THE UNIVERSITY
of EDINBURGH

High Speed Energy Efficient Incoherent Optical Wireless Communications

Dobroslav Tsonev

A thesis submitted for the degree of Doctor of Philosophy.
The University of Edinburgh.
November 2014

Abstract

The growing demand for wireless communication capacity and the overutilisation of the conventional radio frequency (RF) spectrum have inspired research into using alternative spectrum regions for communication. Using optical wireless communications (OWC), for example, offers significant advantages over RF communication in terms of higher bandwidth, lower implementation costs and energy savings. In OWC systems, the information signal has to be real and non-negative. Therefore, modifications to the conventional communication algorithms are required. Multicarrier modulation schemes like orthogonal frequency division multiplexing (OFDM) promise to deliver a more efficient use of the communication capacity through adaptive bit and energy loading techniques. Three OFDM-based schemes – direct-current-biased OFDM (DCO-OFDM), asymmetrically clipped optical OFDM (ACO-OFDM), and pulse-amplitude modulated discrete multitone (PAM-DMT) – have been introduced in the literature.

The current work investigates the recently introduced scheme subcarrier-index modulation OFDM as a potential energy-efficient modulation technique with reduced peak-to-average power ratio (PAPR) suitable for applications in OWC. A theoretical model for the analysis of SIM-OFDM in a linear additive white Gaussian noise (AWGN) channel is provided. A closed-form solution for the PAPR in SIM-OFDM is also proposed. Following the work on SIM-OFDM, a novel inherently unipolar modulation scheme, unipolar orthogonal frequency division multiplexing (U-OFDM), is proposed as an alternative to the existing similar schemes: ACO-OFDM and PAM-DMT. Furthermore, an enhanced U-OFDM signal generation algorithm is introduced which allows the spectral efficiency gap between the inherently unipolar modulation schemes – U-OFDM, ACO-OFDM, PAM-DMT – and the conventionally used DCO-OFDM to be closed. This results in an OFDM-based modulation approach which is electrically and optically more efficient than any other OFDM-based technique proposed so far for intensity modulation and direct detection (IM/DD) communication systems.

Non-linear distortion in the optical front-end elements is one of the major limitations for high-speed communication in OWC. This work presents a generalised approach for analysing non-linear distortion in OFDM-based modulation schemes. The presented technique leads to a closed-form analytical solution for an arbitrary memoryless distortion of the information signal and has been proven to work for the majority of the known unipolar OFDM-based modulation techniques - DCO-OFDM, ACO-OFDM, PAM-DMT and U-OFDM.

The high-speed communication capabilities of novel Gallium Nitride based μm-sized light emitting diodes (μLEDs) are investigated, and a record-setting result of 3.5 Gb/s using a single 50-μm device is demonstrated. The capabilities of using such devices at practical transmission distances are also investigated, and a 1 Gb/s link using a single device is demonstrated at a distance of up to 10 m. Furthermore, a proof-of-concept experiment is realised where a 50-μm LED is successfully modulated using U-OFDM and enhanced U-OFDM to achieve notable energy savings in comparison to DCO-OFDM.

Lay Summary

Demand for wireless communication capacity is growing exponentially and the over-utilisation of the conventional radio frequency (RF) spectrum is expected to significantly limit the advancements in the wireless communications field towards higher data rates. The issues has inspired research into alternative spectrum regions for communication purposes. Using optical wireless communications (OWC), for example, offers a number of significant advantages over RF communication. The field has undergone heavy research over the past decade, leading to a wide range of new communication concepts and a number of impressive high-speed communication demonstrations. Despite the advancements, a lot of research questions remain open.

The current work focuses primarily on novel communication protocols for energy-efficient high-speed OWC. A number of existing concepts are reviewed and their analysis is expanded. A novel inherently unipolar modulation scheme, unipolar orthogonal frequency division multiplexing (U-OFDM), is proposed as an alternative to other existing similar schemes. Furthermore, an enhanced U-OFDM signal generation algorithm is introduced which doubles the communication capacity in comparison to the other similar approaches. This results in an OFDM-based modulation approach which is more energy efficient than any other OFDM-based technique proposed for OWC systems.

Non-linear distortion is one of the major limitations for achieving high-speed data rates in OWC. This work presents a generalised approach for analysing non-linear distortion in OFDM-based modulation schemes. The presented technique leads to a closed-form analytical solution for an arbitrary memoryless distortion of the information signal and has been demonstrated to work for the majority of the known unipolar OFDM-based modulation schemes.

The high-speed communication capabilities of novel micro light emitting diodes (µLEDs) are investigated, and a record-setting result of 3.5 Gb/s is demonstrated. The practical capabilities of these devices are also investigated, and a 1 Gb/s link is demonstrated at a distance of up to 10 m. Furthermore, a proof-of-concept experiment is realised where a µLED is successfully modulated using U-OFDM and enhanced U-OFDM to achieve notable energy savings in comparison to state-of-the-art techniques.

Declaration of originality

I hereby declare that the research recorded in this thesis and the thesis itself was composed and originated entirely by myself in the Institute for Digital Communications (IDCOM) of the School of Engineering at The University of Edinburgh.

The exceptions to the above are, as part of the Ultra-parallel Visible Light Communications (UP-VLC) project:

- The experimental set-up used for the experiments in Section 6.3 which was originally proposed by Mr. Hyunchae Chun, University of Oxford, and Dr. Sujan Rajbhandari, University of Oxford, and was replicated and modified by myself to enable the specific measurements that have been conducted in IDCOM and presented in Section 6.3.

- The measurement results for the experimental work presented in Section 6.4 which have been obtained in collaboration with Dr. Stefan Videv at IDCOM.

I declare that the concepts presented in this thesis have not been used for the purposes of obtaining another degree or professional qualification.

Dobroslav Antonov Tsonev

Acknowledgements

My deepest gratitude goes to my family for their love and support; this thesis would have been impossible without them. I am indebted to my parents, Galya Tsoneva and Anton Tsonev, for shaping me into who I am today. I would like to thank my brother, Hristoslav, for always being beside me and helping me keep it all together in those moments when everybody else seemed like a stranger. Love you, bro!

I offer my sincerest gratitude to my supervisor, Professor Harald Haas, for his support, patience, encouragement and advice throughout my PhD. His huge enthusiasm on research and fathomless knowledge in many areas has deeply inspired me. I fully appreciate his continuous support and encouragement.

My sincere thanks go to Dr. Sinan Sinanović, Dr. Stefan Videv, Dr. Sujan Rajbhandari and Hyunchae Chun for their encouragement, assistance, and insightful comments.

Last but not least, I would like to thank my friends for tirelessly supporting me throughout my studies. I would like to thank Bogo, Harald, Nik and Stefcho personally for being an integral part of my entire academic experience. Thank you, guys! The moments on The Balcony and in The Arena have been some of the best and most inspiring trips I have ever taken throughout my life!

Contents

List of figures

List of tables

Acronyms and abbreviations

2D	two-dimensional
AC	alternating current
ACO-OFDM	asymmetrically clipped optical orthogonal frequency division multiplexing
ADC	analog-to-digital converter
AP	access point
APD	avalanche photodiode
AWG	arbitrary waveform generator
AWGN	additive white Gaussian noise
BER	bit error rate
BPSK	binary phase-shift keying
CLT	central limit theorem
DAC	digital-to-analog converter
DC	direct current
DCO-OFDM	direct-current-biased optical orthogonal frequency division multiplexing
DSP	digital signal processor
EM	electromagnetic
eU-OFDM	enhanced unipolar orthogonal frequency division multiplexing
FEC	forward error correction
FFT	fast Fourier transform
FOV	field of view
GaN	Gallium Nitride
ICI	interchannel interference
IEEE	Institute of Electrical and Electronics Engineers
IFFT	inverse fast Fourier transform
i.i.d.	independent identically distributed
I-L	current-to-light
IM/DD	intensity modulation and direct detection
IR	infrared

IrDA	infrared data association
ISI	intersymbol interference
ITU	International Telecommunication Union
LD	laser diode
LED	light emitting diode
LoS	line-of-sight
LTE	long term evolution
MAC	medium access control
MIMO	multiple–input multiple–output
μ**LED**	μm-sized light emitting diode
M**-PAM**	M-ary pulse-amplitude modulation
M**-QAM**	M-ary quadrature amplitude modulation
NA	numerical aperture
NLoS	non-line-of-sight
OFDM	orthogonal frequency division multiplexing
OOK	on-off keying
OWC	optical wireless communications
PAM-DMT	pulse-amplitude-modulated discrete multitone modulation
PAPR	peak-to-average power ratio
PD	photodiode
PDF	probability density function
PIN	positive-intrinsic-negative
POF	plastic optical fiber
PPM	pulse-position modulation
PRP	power reallocation policy
PSD	power spectral density
PSP	power saving policy
PWM	pulse-width modulation
RCLED	resonant-cavity light emitting diode
RF	radio frequency
RGB	red-green-blue
RRC	root raised cosine
SIM-OFDM	subcarrier-index modulation orthogonal frequency division multiplexing

SM	spatial modulation
SNR	signal-to-noise ratio
SPAD	single-photon avalanche diode
TCA	transconductance amplifier
TIA	transimpedance amplifier
U-OFDM	unipolar orthogonal frequency division multiplexing
UP-VLC	Ultra-parallel Visible Light Communications
UUV	unmanned underwater vehicle
UV	ultraviolet
V-I	voltage-to-current
V-L	voltage-to-light
VL	visible light
VLC	visible light communications

Nomenclature

$\lvert \cdot \rvert$	absolute value operator / cardinality operator
$\binom{\cdot}{\cdot}$	the binomial operator
$[\cdot] * [\cdot]$	the convolution operator
a_k	a random variable indicating whether the kth subcarrier in SIM-OFDM is *active*
A_{di}	the first half – from sample 0 to sample $N_{\text{fft}}/2-1$ – of the ith PAM-DMT or ACO-OFDM frame at "depth d"
$A_{\text{eff}}(\psi)$	effective receiver area
A_{rx}	photodiode area
$A_{u_{\text{s}}}$	area of surface element u_{s}
α	constant factor resulting from a non-linear distortion of a Gaussian random variable, in accordance with the Bussgang theorem
$\bar{\alpha}$	the resulting average constant factor due to the non-linear distortion in the *improved* U-OFDM demodulation algorithm
α_{c}	constant factor due to the non-linear distortion in the *improved* U-OFDM demodulation algorithm for the case when the *active* and *inactive* samples are correctly identified.
$\alpha_{\text{o}-\text{e}}$	the ratio between the average electrical power and the average optical power of the time-domain signal in U-OFDM and eU-OFDM
α_{w}	constant factor due to the non-linear distortion in the *improved* U-OFDM demodulation algorithm for the case when the *active* and *inactive* samples are incorrectly identified.
$\alpha(D)$	the average energy per bit penalty in an eU-OFDM signal with maximum modulation depth of D relative to the energy per bit in an U-OFDM signal
b_{DC}	direct current (DC) bias level in the transmitter front-end
b_k	the kth bit value of block B_{OOK} in SIM-OFDM
B	double-sided bandwidth of the communication system
B_{di}	the second half – from sample $N_{\text{fft}}/2$ to sample $N_{\text{fft}}-1$ – of the ith PAM-DMT or ACO-OFDM frame at "depth d"

B_{OOK}	a block of bits encoded in the subcarrier states of SIM-OFDM
B_{QAM}	a block of bits encoded in M-QAM and modulated onto the *active* subcarriers in SIM-OFMD
BER	the overall average bit-error rate (BER) in SIM-OFDM
BER_k	the overall average bit-error rate (BER) at subcarrier k in SIM-OFDM
$\mathrm{BER}_{\mathrm{MQAM}}(\cdot)$	the bit-error rate (BER) of M-QAM as a function of the signal-to-noise ratio
$\mathrm{BER}_{\mathrm{U}}$	the bit-error rate (BER) of U-OFDM
c	a complex number
c_1	an arbitrary complex number
c_2	an arbitrary complex number
c_3	an arbitrary complex number
C_{PD}	capacitance of the photodiode
d	denotes a given depth in the eU-OFDM information signal
d_{c}	probability for correct detection of an *active* and an *inactive* sample in the *improved* decoder for U-OFDM.
d_k	a variable that indicates whether the detection of the kth subcarrier state in SIM-OFDM is correct
d_{q}	the distance between two neighbouring DAC output levels
d_{tr}	distance between the optical transmitter and the optical receiver
$d_{u,\mathrm{rx}}$	distance between surface element u and the receiver
$d_{u_{\mathrm{s}}}$	distance between the optical source and surface element u_{s}
$d_{u,u_{\mathrm{s}}}$	distance between surface element u and surface element u_{s}
$\mathrm{d}[k]$	the distortion component on the kth subcarrier caused by the non-linearity in the communications system
$\mathrm{d}^i[k]$	the ith realisation of $\mathrm{d}[k]$
$\delta[\cdot]$	the Kronecker delta function
D	Maximum modulation depth in eU-OFDM
$\mathrm{D}(\cdot,\cdot,\cdot,\cdot,\cdot)$	a function used for calculating the moments of a truncated Gaussian distribution, defined in Appendix A
$\mathrm{erf}(\cdot)$	the error function
$\mathrm{E}\{\cdot\}$	statistical expectation
E_{AVG}	the average energy of a given M-QAM constellation used in SIM-OFDM
E_{b}	average energy per bit on a set of equally loaded subcarriers

$E_{\mathrm{b,elec}}$	average electrical energy per bit
$E_{\mathrm{b},k}$	average energy per bit allocated on subcarrier k
$E_{\mathrm{b}k}^{\mathrm{new}}$	average energy per bit on subcarrier k after the non-linear distortion in the communication system
$E_{\mathrm{b,opt}}$	average optical energy per bit
$\mathrm{f_c}(\cdot)$	the mean of the reconstructed bipolar sample in U-OFDM when the *active* and *inacitve* sample are correctly identified in the *improved* U-OFDM demodulation algorithm
$\mathrm{f_{clip}}\{\cdot\}$	operator for clipping an information signal at zero
$\mathrm{f_w}(\cdot)$	the mean of the reconstructed bipolar sample in U-OFDM when the *active* and *inacitve* sample are incorrectly identified in the *improved* U-OFDM demodulation algorithm
F_{s}	sampling frequency in the time domain
ϕ	angle of light emission from the optical transmitter to the receiver
$\phi(\cdot)$	the standard normal distribution probability density function
$\phi_{\frac{1}{2}}$	radiation intensity half angle of an optical source
$\phi_{\frac{1}{2},u_{\mathrm{s}}}$	radiation intensity half angle of reflecting surface element u_{s}
$\phi_{u,\mathrm{rx}}$	angle of light emission from surface element u to the receiver
$\phi_{u_{\mathrm{s}}}$	angle of light emission from the optical source to surface element u_{s}
$\phi_{u,u_{\mathrm{s}}}$	angle of light emission from surface element u to surface element u_{s}
$\mathfrak{F}\{\cdot\}$	the fast Fourier transform (FFT) operator
$\mathrm{G_{oc}}(\psi)$	optical concentrator gain
$\mathrm{G_{of}}(\psi)$	optical filter gain
$\mathrm{h}[n]$	discrete-time sample of the communication channel impulse response
$\mathrm{h}^{-1}[n]$	discrete-time sample of the inverted communication channel impulse response
$\mathrm{h}(t)$	continuous-time communication channel
$\mathrm{H}(0)$	direct current (DC) gain of the optical communication channel due to all possible propagation paths
$\mathrm{H}[k]$	the discrete frequency-domain communications channel response
$\hat{\mathrm{H}}[k]$	the discrete frequency-domain communications channel response estimated at the receiver

$H_{LoS}(0)$	line-of-sight (LoS) direct current (DC) gain of the optical communication channel (no reflections)
$i(t)$	current signal through the transmitter front-end
$\hat{i}(t)$	current signal through the receiver front-end
i_{bias}	bias current level through the LED
i_{min}	the minimum required current through a LED
i_{max}	the maximum allowed current through a LED
I	set of intervals in which a non-linear distortion function is continuous
$I(\cdot)$	the voltage-to-current (V-I) characteristic of a LED
$Im\{\cdot\}$	the imaginary part of a complex number
j	the imaginary number $\sqrt{-1}$
k	frequency-domain subcarrier index
k_{bias}	direct current (DC) bias level in the transmitter front-end as a multiple of the time-domain information signal standard deviation
k_B	the Boltzmann constant equal to 1.381×10^{-23} [J/K]
l	reflection order
m	emission order of a generalised Lambertian emitter
m_b	the majority bit type in SIM-OFDM
m_{u_s}	generalised Lambertian emission order of reflecting surface element u_s
$max\{\cdot\}$	the maximum value operator
M_k	constellation size at subcarrier k
μ_i	the ith constellation point in M-QAM
μ	the mean of a Gaussian random variable
n	time-domain sample index
$n_1[n]$	the samples of an AWGN realisation at the receiver
$n_2[n]$	the samples of an AWGN realisation at the receiver
$n(t)$	a continuous-time realisation of the additive white Gaussian noise (AWGN) at the receiver
$n[n]$	a discrete-time sample realisation of the additive white Gaussian noise (AWGN) at the receiver
n_{ref}	refractive index
N	the number of pilot frame instances used for channel estimation in the practical OFDM implementation

$N[k]$	the frequency-domain component at the kth subcarrier in the realisation of the additive white Gaussian noise (AWGN) process at the receiver
$N^i[k]$	the ith realisation of $N[k]$
$\bar{N}$	the resulting overall noise variance in the *improved* U-OFDM decoder
N_a	number of active (modulated) subcarriers in the frequency domain
N_A	number of active subcarriers per subcarrier block in SIM-OFDM
N_B	the size of a subcarrier block in SIM-OFDM
N_{cp}	length of the cyclic prefix in OFDM
N_{cp}^p	length of the cyclic prefix in OFDM sufficient to remove the effects of the pulse shaping filter between individual OFDM frames
$N_d i$	a U-OFDM frame holding the absolute values of the negative samples and zeros in place of the positive samples of the ith original bipolar OFDM frame at depth d in the eU-OFDM information signal
N_{fft}	number of points used in an FFT and corresponding to the size of an OFDM frame
N_o^{shot}	double-sided power spectral density (PSD) of shot noise in $\left[\frac{A^2}{Hz}\right]$
N_o^{th}	double-sided power spectral density (PSD) of thermal noise in $\left[\frac{A^2}{Hz}\right]$
N_o	double-sided power spectral density (PSD) of additive white Gaussian noise (AWGN) in a receiver system
N_{ref}	number of reflections
N_{total}	number of samples captured by the oscilloscope for the energy consumption estimation of a given modulation scheme
η	spectral efficiency of a specified modulation scheme
η_{ACO}	spectral efficiency of ACO-OFDM
η_{DCO}	spectral efficiency of DCO-OFDM
$\eta_{eU}(D)$	spectral efficiency of eU-OFDM as a function of the maximum modulation depth D
$\eta_{PAM-DMT}$	spectral efficiency of PAM-DMT
$\eta_{SIM-OFDM}$	spectral efficiency of SIM-OFDM
$\eta_{SIM-OFDM}^E$	spectral efficiency of enhanced SIM-OFDM
$\eta_{SIM-OFDM}^{GENERAL}$	spectral efficiency of the generalised enhanced SIM-OFDM
η_U	spectral efficiency of U-OFDM

$\mathrm{p}[t]$ discrete impulse response of the pulse shaping filter

P_0 probability that b_k is equal to 0 in SIM-OFDM

P_1 probability that b_k is equal to 1 in SIM-OFDM

$P_{\mathrm{elec}}^{\mathrm{avg}}$ average electrical power of the time-domain signal

$P_{\mathrm{elec,eU}}^{\mathrm{avg}}$ average electrical power of the time-domain eU-OFDM signal

$P_{\mathrm{opt}}^{\mathrm{avg}}$ average optical power of the time domain signal

$P_{\mathrm{opt,eU}}^{\mathrm{avg}}$ average optical power of the time-domain eU-OFDM signal

$P_d i$ a U-OFDM frame holding the positive samples and zeros in place of the negative samples of the ith original bipolar OFDM frame at depth d in the eU-OFDM information signal

P_{fa} probability that an *inactive* SIM-OFDM subcarrier is incorrectly recognised as *active*

P_{fi} probability that an *active* SIM-OFDM subcarrier is incorrectly recognised as *inactive*

P_{m0} probability that the majority bit type in SIM-OFDM is equal to 0

P_{m1} probability that the majority bit type in SIM-OFDM is equal to 1

P_{mc} probability that the majority bit type in SIM-OFDM is correctly determined at the receiver

P_{mi} probability that the majority bit type in SIM-OFDM is incorrectly determined at the receiver

P_{ne_k} probability that no subcarrier state detection errors have been made up to subcarrier k

P_{qc_k} probability that less than $N_{\mathrm{fft}}/2$ *active* subcarriers have been detected up to subcarrier k

P_{qcne_k} probability that less than $N_{\mathrm{fft}}/2$ *active* subcarriers have been detected up to subcarrier k without any detection errors

P_{rx}^l received optical power at the receiver due to lth light reflection

P_{rx} total optical power at the receiver due to all reflections

$P_{\mathrm{rx},u_{\mathrm{s}}}^l$ received optical power at surface element u_{s} due to the lth reflection

$\bar{P}_{\mathrm{rx}}$ average radiant flux at the receiver

P_{ta} probability that an *active* SIM-OFDM subcarrier is correctly recognised as *active*

P_{ti}	probability that an *inactive* SIM-OFDM subcarrier is correctly recognised as *inactive*
P_{tx}	radiant flux of an optical source in W
PAPR	peak-to-average power ratio (PAPR) of an information signal
$\text{PAPR}_{\text{OFDM}}$	peak-to-average power ratio (PAPR) of a conventional OFDM signal
ψ	light incidence angle at the receiver for light emitted from the optical source
$\psi_{u,u_{\text{s}}}$	light incidence angle at surface element u_{s} for light emitted from surface element u
$\psi_{u_{\text{s}}}$	light incidence angle at surface element u_{s} for light emitted from the optical source
$\psi_{u,\text{rx}}$	light incidence angle at the receiver for light emitted from surface element u
ψ_{FOV}	receiver field-of-view (FOV)
q	elementary charge of an electron equal to 1.602×10^{-19} C
q_{b}	the bit resolution of a DAC
$\text{Q}(\cdot)$	the tail probability of the standard normal distribution
QB1_k	BER contribution of the information encoded in the subcarrier state at subcarrier k in SIM-OFDM
QB2_k	BER contribution of the information encoded in the M-QAM symbol at subcarrier k in SIM-OFDM
R	photodiode responsivity in A/W
R_{b}	the data rate of a communication system in bits/s
$\text{R}(\phi)$	radiation profile of an optical source in 1/sr
R_{TIA}	transimpedance resistor
$\text{Re}\{\cdot\}$	the real part of a complex number
ρ	surface reflectivity coefficient
ρ_u	reflectivity of surface element u
s	an example value of s[n]
s[n]	discrete-time sample of the information signal
s[n, i]	denotes the nth sample of the orthogonal frequency division multiplexing (OFDM) frame at position i; it is assumed that the current frame is at $i = 0$
$\underline{s}[n]$	discrete-time sample of the information signal clipped at zero
$\hat{s}[n]$	discrete-time sample of the matched-filtered and downsampled received information signal

$\mathrm{s}(k, n)$	the contribution of subcarrier k to the value of the time-domain sample at position n
$\mathrm{s}'[t]$	discrete-time upsampled and pulse-shaped information signal
$\mathrm{s}'_\mathrm{p}[t]$	discrete-time upsampled and pulse-shaped information signal corresponding to the *positive* frame in U-OFDM
$\mathrm{s}'_\mathrm{n}[t]$	discrete-time upsampled and pulse-shaped information signal corresponding to the *negative* frame in U-OFDM
$\mathrm{s}'_1[t]$	the portion of the discrete-time upsampled and pulse-shaped information signal which contains the information for the first $N_\mathrm{fft}/2$ samples in a given OFDM frame
$\mathrm{s}'_2[t]$	the portion of the discrete-time upsampled and pulse-shaped information signal which contains the information for the second $N_\mathrm{fft}/2$ samples in a given OFDM frame
$\underline{\mathrm{s}}[t]$	discrete-time predistorted communication signal
$\underline{\mathrm{s}}_d(t)$	the U-OFDM time-domain signal at depth d of the eU-OFDM time-domain signal
$\hat{\underline{\mathrm{s}}}[t]$	discrete-time received information signal
$\mathrm{s}(t)$	continuous-time information signal
$\hat{\mathrm{s}}(t)$	continuous-time received information signal
$\hat{\underline{\mathrm{s}}}_\mathrm{a}[n]$	received *active* samples in U-OFDM
$\hat{\underline{\mathrm{s}}}_\mathrm{i}[n]$	received *inactive* samples in U-OFDM
$\mathrm{s}_\mathrm{eU}(t)$	the time-domain eU-OFDM signal
$\mathrm{sgn}(\cdot)$	the sign function
$\hat{\mathrm{s}}_\mathrm{b}[n]$	the received bipolar signal after the subtraction in the U-OFDM receiver, *i.e.*, $\hat{\mathrm{s}}_\mathrm{b}[n] = \hat{\mathrm{s}}_\mathrm{p}[n] - \hat{\mathrm{s}}_\mathrm{n}[n]$
s'_max	the maximum output level of a DAC
s'_min	the minimum output level of a DAC
$\mathrm{s}_\mathrm{p}[n]$	the samples of a U-OFDM frame holding the positive samples of an originally bipolar OFDM frame
$\hat{\mathrm{s}}_\mathrm{p}[n]$	the received equivalent of $\mathrm{s}_\mathrm{p}[n]$, corrupted by the transmission channel and the AWGN at the receiver
$\mathrm{s}_\mathrm{n}[n]$	the samples of a U-OFDM frame holding the negative samples of an originally bipolar OFDM frame

$\hat{s}_n[n]$	the received equivalent of $s_n[n]$, corrupted by the transmission channel and the AWGN at the receiver
$s'_n[t]$	the oversampled and pulse-shaped discrete-time bipolar part of $s'[t]$ which contains the information of the *negative* block in U-OFDM
$s'_p[t]$	the oversampled and pulse-shaped discrete-time bipolar part of $s'[t]$ which contains the information of the *positive* block in U-OFDM
$\hat{s}_E[n]$	discrete-time sample of the equalised received information signal
$\hat{s}_{E,p}[n]$	the received equalised instance of $s_p[n]$ corrupted by AWGN at the receiver
$\hat{s}_{E,n}[n]$	the received equalised instance of $s_n[n]$ corrupted by AWGN at the receiver
$S[k]$	the value of subcarrier k
$S^i[k]$	the ith realisation of $S[k]$
$\underline{S}[k]$	the value of subcarrier k in the frequency-domain representation of the clipped time-domain information signal
$\hat{S}[k]$	the value of subcarrier k in the frequency-domain representation of the received matched-filtered and downsampled information signal
$\hat{S}^i[k]$	the ith realisation of $\hat{S}[k]$
SNR_{elec}	electrical signal-to-noise ratio
S_{he}	the M-QAM symbol with the highest amplitude for a given constellation size
SNR_{opt}	optical signal-to-noise ratio
σ_s	standard deviation of the time-domain OFDM signal
σ_X	standard deviation of Gaussian random variable X
σ_Y	standard deviation of the noise component Y_n
σ_N^2	variance of the AWGN at the receiver
$\hat{\sigma}_N^2[k]$	the estimated variance of the receiver AWGN at the kth OFDM subcarrier
σ_{NY}	standard deviation of the joint AWGN and Y_n noise components
t	time variable
T	discrete symbol period in the time domain, $T = F_s T_s$
T_k	temperature in K
T_s	time-domain symbol period
u_s	reflecting surface element
U_s	total number of reflecting surface elements
$U(\cdot)$	the unit step function

$v_{\mathrm{c}}(\cdot)$	the variance around the mean of the reconstructed bipolar sample when the *active* and *inactive* samples are correctly identifid in the *improved* U-OFDM algorithm
$\bar{v}_{\mathrm{c}}$	average value of $v_{\mathrm{c}}(\cdot)$ for all possible time-domain samples in U-OFDM.
v_{t}	the value of the detection threshold in SIM-OFDM
$v_{\mathrm{w}}(\cdot)$	the variance around the mean of the reconstructed bipolar sample when the *active* and *inactive* samples are incorrectly identifid in the *improved* U-OFDM algorithm
$\bar{v}_{\mathrm{w}}$	average value of $v_{\mathrm{w}}(\cdot)$ for all possible time-domain samples in U-OFDM.
$\mathrm{V}[n]$	the nth sample of the voltage over the LED captured with the oscilloscope
X	independent identically distributed (i.i.d.) Gaussian random variable
y_{c}	variance of the noise due to the non-linear distortion in the *improved* U-OFDM demodulation algorithm for the case when the *active* and *inactive* samples are correctly identified.
y_{w}	variance of the noise due to the non-linear distortion in the *improved* U-OFDM demodulation algorithm for the case when the *active* and *inactive* samples are incorrectly identified.
Y_{n}	noise component resulting from a non-linear distortion of a Gaussian random variable, in accordance with the Bussgan theorem
$\mathrm{z}(\cdot)$	an arbitrary memoryless distortion function
$\mathrm{z}_{\mathrm{d}}(\cdot)$	the overall memoryless distortion of the information signal up to the demodulator
$\mathrm{z}_{\mathrm{elec}}(\mathrm{s}'[t])$	the current signal flowing through the diode including all distortions up to that point in the system
$\mathrm{z}_{\mathrm{opt}}(s'[t])$	the light intensity output of the diode including all distortions up to that point in the system

Chapter 1
Introduction

The radio frequency (RF) spectrum conventionally used for communication is almost completely depleted, which threatens to leave a significant gap between the capabilities of the state-of-the-art wireless access networks and the exponentially increasing wireless data rate demands. Fortunately, alternative parts of the electromagnetic (EM) spectrum such as millimetre wave radiation and optical radiation can be used for communication. Both regions of the spectrum are currently undergoing heavy research.

The concept of optical wireless communications (OWC) constitutes wireless data communication using the visible light (VL) and the infrared (IR) region of the EM spectrum as a transmission medium. OWC and its subset of visible light communications (VLC) provide a number of advantages over RF and millimetre wave communications, which include, but are not limited to: 1) a large amount of unregulated bandwidth; 2) improved data security at the physical layer; 3) no interference with sensitive electronic equipment. In addition, the existing lighting infrastructure could be re-used for communication, which facilitates easier system deployment and promises to deliver significant energy savings.

The significant research efforts in the field of OWC have led to well-established theoretical models and a number of impressive experimental demonstrations of high-speed OWC links. A lot of the research problems related to the development of energy-efficient optical modulation schemes and to the effects of non-linear distortion on the communication performance still remain open. This work presents a number of new advancements in the field including: further analysis on existing modulation techniques, novel optical modulation methods and new and improved techniques for the analysis of the OWC system performance.

1.1 Motivation

The increasing popularity of smart mobile devices and multimedia streaming applications has led to a tremendous increase in mobile data traffic. By 2017, more than 11 Exabytes of monthly data traffic is expected in wireless networks [1]. At the same time, the available RF spectrum with favourable communication properties, in the range up to $10\,$GHz, has been almost completely utilised [2]. Therefore, it is anticipated that the increasing demands will not be met despite the significant technological advances in the field of mobile communications [3].

In an attempt to tackle the looming spectrum crisis, researchers have focused their efforst to explore unconventional parts of the electromagnetic spectrum in search of additional communication bandwidth. The so-called "millimetre" wave region from $28\,$GHz to $250\,$GHz is gaining a lot of interest [3]. Wave propagation at such short wavelengths, however, is limited mostly to line-of-sight (LoS) scenarios [3]. Millimetre waves provide a promising option for the realisation of multiple–input multiple–output (MIMO) systems as the short wavelength allows multiple antennas to be more easily fit within a relatively small area such as the area available on a hand-held device. Overall, however, as the propagation properties in millimetre wave systems begin to resemble the propagation properties in OWC systems, these short wavelengths begin to lose the ubiquitous coverage advantage that RF wavelengths have over optical wavelengths.

According to the DIN 5031 standard, optical radiation includes electromagnetic radiation in the wavelength range from $100\,$nm up to $1\,$mm. The range between $100\,$nm and $400\,$nm is known as the ultraviolet (UV) spectrum. The range between $400\,$nm and $800\,$nm is the visible radiation spectrum, commonly referred to as the light spectrum. Wavelengths between $800\,$nm and $2.5\,$µm belong to the so-called near IR region, and like the UV waves are not perceivable by the human eye. The concept of OWC typically refers to communication using the visible light spectrum and the infrared spectrum as defined here. The total bandwidth resources in these two regions amount to approximately $630\,$THz, which is thousands of times higher than the bandwidth available in the conventionally-used RF communication spectrum below $10\,$GHz. In addition, both the VL and the IR regions are not subject to regulation. Further benefits of OWC over RF communication include: security at the physical layer is increased due to the inability of light to penetrate solid objects; light does not interfere with sensitive electronic equipment; light can be used in RF-sensitive environments such as airplanes and petrochemical plants; the existing lighting infrastructure could be re-used for simultaneous illumination and communication.

Another approach towards mitigating the effects of the spectrum shortage involves the scaling down of the communication cells' coverage area. Smaller cells serve a lower number of users, which, in turn, translates to higher spectrum resource availability per user [3]. The problem with dense cell deployment, however, is the increased interference between individual access nodes, limiting the degree of frequency reuse which can be achieved. Femtocells and attocells, for example, are envisioned for deployment in indoor environments with a large number of users. The deployment of a large number of such cells is inevitably limited by the generated interference. In order to mitigate the interference problems, researchers have resorted to the introduction of beamforming and beamsteering techniques for RF and millimetre wave communication, which require multiple antenna elements and sophisticated signal processing techniques [3]. As a result, the overall network complexity increases significantly, while the energy efficiency is decreased [3]. Beamforming techniques for OWC involve the introduction of simple passive optical elements, whose properties have been studied and well-understood over the course of many years. Hence, OWC provides a unique advantage over RF communication and millimetre waves with regards to beamforming and beamsteering techniques. Furthermore, the complete inability of optical wavelengths to penetrate opaque objects means that interference between neighbouring cells is always expected to be lower than the interference between neighbouring cells realised with millimetre waves which, despite being severely attenuated, can still penetrate most objects.

Another limiting factor for the use of millimetre waves is the requirement for high-bandwidth high-power amplifiers operating at high frequencies [3]. Such devices are not readily available and are yet to be developed. Information encoding in OWC is limited to intensity modulation and direct detection (IM/DD) where only the envelope of the electromagnetic radiation is modulated [3–5]. The electrical-to-optical transceivers and the optical-to-electrical transceivers are simple light emitting diodes (LEDs), laser diodes (LDs) and photodiodes (PDs). Therefore, communication at such short wavelengths can be easily achieved with standard off-the-shelf components, which have been extensively studied and well-understood. Therefore, OWC systems could be of relatively lower complexity and relatively cheaper to millimetre-wave systems.

Research in OWC has begun with the pioneering work of Gfeller and Bapst in 1979 [6]. The initial studies suggested the feasibility of wireless communication at hundreds of Mb/s and demonstrated links at over a hundred kb/s, which was revolutionary for its time. Since that initial work, research in OWC has produced a deep understanding of the OWC system [4, 7–9]. Some very impressive demonstrations of high-speed OWC links have been made over the past few years. To

name a few: a 1-Gb/s link was demonstrated by Khalid *et. al.* using a commercially available white phosphor-coated LED [10]; a 3.4-Gb/s transmission was shown by Cossu *et al.* using a commercially available red-green-blue (RGB) LED [11]; 1 Gb/s was demonstrated by Azhar *et al.* using white LEDs and a 4×4 MIMO system [12].

Despite the significant research progress in OWC and the impressive experimental results, a lot of questions still remain open at the physical layer. Particularly interesting is the problem of developing a suitable modulation scheme to be used within the context of the IM/DD system. According to the available literature, single-carrier modulation schemes such as pulse-position modulation (PPM), pulse-width modulation (PWM), on-off keying (OOK) and M-ary pulse-amplitude modulation (M-PAM) are the most straightforward candidates in an IM/DD system due to their energy efficiency and robustness to non-linear distortion [4, 7, 13–15]. At high data rates, however, intersymbol interference (ISI) becomes a problem in a bandwidth-limited communication channel. As a result, multi-carrier modulation schemes like orthogonal frequency division multiplexing (OFDM) become advantageous [14–16]. OFDM allows for low-complexity equalisation as well as for adaptive bit and energy loading which enable optimal usage of the communication channel resources. In fact, the highest data rate demonstrations in VLC have all been performed with the help of OFDM [10–12]. Furthermore, OFDM is especially appealing due to the fact that it appears in a number of widely adopted wireless standards such as long term evolution (LTE) and IEEE 802.11. As a result, the OFDM-based OWC system can be more easily integrated into the context of the future heterogeneous networks since the protocol stack from the already available standards can be re-used. Optical OFDM is still a subject of research due to the system's vulnerability to non-linear distortion and due to its rather energy-inefficient nature in IM/DD systems [14–16]. The current work investigates energy-efficient approaches for OFDM implementation in an IM/DD system as well as methods for reducing the high peak-to-average power ratio (PAPR) of the OFDM signal which leads to reduced non-linear distortion of the information signal. Novel work on modelling and evaluating the non-linear distortion effects on OFDM-based modulation signals is also presented. The work culminates with an experimental demonstration of record setting communication rates using VLC and with a proof-of-concept demonstration of a novel newly proposed OFDM-based modulation technique.

1.2   Contributions

In this thesis, a number of OFDM-based modulation schemes for IM/DD systems are investigated. Well-known concepts in the field are studied in more detail compared to what is available in the literature. Performance of the concepts is evaluated such that existing issues with these modulation schemes can be identified and suitable solutions are suggested. As a result, novel and improved modulation techniques are proposed followed by suitable theoretical, simulation and experimental analysis. The analysis of non-linear distortion in the optical system is further extended compared to the existing analytical approaches. The work concludes with practical experimental applications based on the studied OFDM theory leading to new and exciting results in the field.

The newly introduced concept of subcarrier-index modulation orthogonal frequency division multiplexing (SIM-OFDM) is studied in detail. A theoretical performance evaluation of the modulation scheme, which was missing in the literature, is conducted. An inherent flaw is identified in the process, and a solution is proposed, leading to a modified modulation technique termed enhanced SIM-OFDM. The newly proposed scheme is analysed in the context of a linear additive white Gaussian noise (AWGN) channel as a basis for further research on the topic. Despite the reduced PAPR of SIM-OFDM which leads to a reduction of the non-linear distortion in the system, it is concluded that the limited spectral efficiency of the SIM-OFDM concept makes it rather unattractive for high-speed OFDM-based communication. Nevertheless, the scheme is ideal for energy-efficient low-spectral efficiency applications. Furthermore, it can be implemented in an adaptive bit and energy loading scenario, where the SIM-OFDM concept can be combined with the conventional OFDM concept as the SIM-OFDM technique would be suitable for high-frequency subcarriers where the low signal-to-noise ratio (SNR) would not allow high spectral efficiency. The work conducted on SIM-OFDM has led to the publication of [17].

The work on SIM-OFDM has inspired the introduction of a new unipolar OFDM-based modulation scheme termed unipolar orthogonal frequency division multiplexing (U-OFDM). The new scheme is suggested as an alternative to the already existing concepts of asymmetrically clipped optical orthogonal frequency division multiplexing (ACO-OFDM) and pulse-amplitude-modulated discrete multitone modulation (PAM-DMT). Its performance is evaluated in a linear AWGN channel and compared against the performance of the conventional state-of-the-art technique of direct-current-biased optical orthogonal frequency division multiplexing (DCO-OFDM).

An analytical model is created for the performance of U-OFDM, and it is shown that the modulation scheme performs equivalently to ACO-OFDM and PAM-DMT – at exactly $3\,\mathrm{dB}$ of lower energy efficiency compared to a real bipolar OFDM signal, which is assumed to be the performance benchmark. An improved decoding technique is suggested, which allows the aforementioned $3\,\mathrm{dB}$ gap in performance relative to the benchmark to be almost completely closed. A similar improved decoding technique can be devised for ACO-OFDM and PAM-DMT and has even been proposed by other researchers concurrently with the work presented here. A theoretical model for the performance of this improved decoding technique is provided. The loss of spectral efficiency in the modulation process of U-OFDM is identified as a major problem for its application at high spectral efficiencies. This problem also pertains to the generation processes in the other unipolar state-of-the-art techniques ACO-OFDM and PAM-DMT. A solution is devised in the form of a modified technique termed enhanced unipolar orthogonal frequency division multiplexing (eU-OFDM), which exploits the frame structure of the U-OFDM concept and allows multiple U-OFDM information streams to be superimposed on top of each other. The novel concept effectively opens up a new degree of freedom in the signal space of the so-called inherently unipolar modulation schemes, ACO-OFDM, PAM-DMT and U-OFDM, and provides a possible solution to the long-standing problem of spectral efficiency loss in energy efficient unipolar OFDM. The performance of eU-OFDM is analysed theoretically for a linear AWGN channel. Suggestions for an extension of this modified concept to ACO-OFDM and PAM-DMT are also provided. The work conducted on U-OFDM and eU-OFDM has led to the publication of [18, 19].

The current work looks at the problem of analysing non-linear distortion in an OWC system in a novel fashion. The well-known approach of using the Bussgang theorem for the analysis of normally-distributed (OFDM) signals passing through a non-linear system is employed. A novel representation of the non-linear distortion function is proposed. This facilitates the derivation of a closed-form analytical solution for an arbitrary signal distortion. A closed-form solution not only speeds up system analysis, but can also be indispensable in system optimisation procedures when compared to Monte Carlo simulations. Furthermore, pulse shaping techniques, employed for the generation of band-limited analog signals in the digital-to-analog transition step of an OWC system, are investigated in the context of the so-called inherently unipolar OFDM techniques – ACO-OFDM, PAM-DMT, U-OFDM. It is shown that the application of a pulse-shaping filter does not compromise the validity of the analysis technique used to evaluate the effects of non-

linear distortion on the system performance. Furthermore, it is revealed that the three modulation schemes ACO-OFDM, PAM-DMT and U-OFDM perform equivalently in a non-linear AWGN channel. The work conducted on pulse shaping and modelling of non-linear distortion has led to the publication of [20–22].

Following the theoretical research on OFDM-based modulation schemes, a set of experiments is devised for illustrating the merit of the OFDM concept in a number of practical applications. The communication capabilities of a novel Gallium Nitride (GaN) μm-sized light emitting diode (μLED) with a diameter of $50\,\mu m$ are investigated using DCO-OFDM. A record-setting result of over $3\,Gb/s$ is established in collaboration with the partnering institutions of University of Oxford and University of Strathclyde as part of the joint Ultra-parallel Visible Light Communications (UP-VLC) project. An adaptive bit and energy loading algorithm based on the work of Campello [23] is devised. A novel combination of channel estimation techniques is also proposed. It allows for the effects of non-linear distortion to be evaluated in a practical OFDM system. An experimental proof-of-concept OWC link using U-OFDM and eU-OFDM is also demonstrated for the first time, showing significant energy savings when using the proposed inherently unipolar OFDM concepts instead of the conventional technique DCO-OFDM. The conducted experimental work has led to the publication of [24].

1.3   Thesis Layout

The rest of this thesis is organised as follows. Chapter 2 introduces the OWC system and the fundamental concepts necessary for its understanding and modelling. The individual sections focus on the different transmission link scenarios, the front-end elements, the optical free-space channel, the fundamental sources of noise in such a system, and the different signal modulation techniques which have already been introduced in the literature.

Chapter 3 introduces the concept of SIM-OFDM. A theoretical performance analysis is presented and matched to Monte Carlo simulation results. A fundamental flaw is identified in the original concept and an enhanced SIM-OFDM scheme is proposed to solve this issue. Afterwards, a theoretical performance model is presented for the enhanced concept followed by performance evaluation and a conclusion on the merits of the scheme for high-speed OWC.

Chapter 4 presents the U-OFDM concept. A theoretical performance analysis, supported with

Monte Carlo simulations, is provided for both the so-called *conventional* and the so-called *improved* decoders. A disadvantage of the modulation algorithm is identified, after which the eU-OFDM algorithm is presented as a viable solution. The enhanced technique is also analysed in detail, after which a performance comparison to the other state-of-the-art techniques is presented. The chapter concludes with a suggestion for extending the eU-OFDM concept to the other inherently unipolar modulation schemes ACO-OFDM and PAM-DMT.

Chapter 5 presents and overview of the Bussgang theorem and its applications for modelling non-linear distortion in OFDM signals. A novel representation for memoryless non-linear distortions is proposed, which enables the derivation of closed-form solutions when the Bussgang analysis is applied to an arbitrary distortion function. The issue of pulse shaping in relation to the inherently unipolar OFDM-based modulation schemes – ACO-OFDM, PAM-DMT, and U-OFDM – is also discussed. It is shown that the pulse shaping operation does not significantly alter the accuracy of the non-linear analysis. In addition, the chapter also demonstrates the equivalent performance of ACO-OFDM, PAM-DMT, and U-OFDM in a memoryless non-linear AWGN channel.

Chapter 6 presents and experimental investigation of the communication properties of a novel GaN μLED device. It also touches upon various signal processing and adaptive modulation techniques which are employed in the conducted investigation. Furthermore, this chapter presents an experimental proof of concept for an OWC system using U-OFDM and eU-OFDM.

Finally, Chapter 7 summarises the key findings of this work. It draws concluding remarks based on the obtained results. Furthermore, the chapter identifies some of the limitations of the presented work and suggests possible ways in which it can be improved.

1.4   Summary

The optical spectrum has unique physical characteristics, which are expected to significantly aid the efforts against the looming "spectrum crunch". The OWC system has been studied in quite a lot of detail and a deep understanding of the underlying issues has been obtained. Despite the significant research efforts in the field, a lot of the questions remain open. The current work provides further understanding to the common OFDM-based modulation techniques employed in OWC and proposes novel solutions which are expected to significantly improve the system implementation at the physical layer. This chapter lists the major contributions of this thesis and provides an outline of the subsequently presented work.

Chapter 2
Background

The earliest accounts of using light for information transfer can be dated back to more than two thousand years ago. Alexander Graham Bell introduced the first voice transmission system using visible light in the second half of the 19th century. The first concepts of using digital modulation techniques with optical signals for high-speed applications were introduced in 1979 by Gfeller and Bapst. Over the next 35 years, until present day, optical wireless communications (OWC) has undergone significant research and development. Theoretical models have been developed for the accurate analysis of OWC systems. The physical properties of suitable front-end devices have been investigated in detail and appropriate single-carrier and multi-carrier modulation techniques have been developed. These techniques have enabled the demonstration of multi-Gb/s communication systems illustrating the enormous potential of the OWC technology.

2.1 Introduction

Optical communication embodies any form of communication where electromagnetic radiation in the optical spectrum is used to convey information between two distinct points in space. Following this line of thought, acquisition of information regarding the surrounding world using the sense of sight is probably the earliest form of OWC. Some of the first forms of man-engineered OWC schemes can be dated thousands of years ago. For example, the ancient Greeks used signalling fires to indicate an incoming threat. The Greek historian Polybius devised a fire and smoke signalling mechanism where entire messages could be conveyed using the Greek alphabet. Other interesting examples relate to the use of light beacons by the ancient Chinese warriors along the Great Wall of China to indicate an imminent threat. The native Americans are also known to have used smoke signals in order to signal their presence in a possibly hostile territory. Smoke signals are used even nowadays in some traditional practices, for example, to indicate the successful election of a new pope by the cardinals in the Vatican. Lighthouses are still used today to indicate the close proximity of shore lines to incoming ships. The first advanced form of OWC can probably be attributed to Alexander Graham Bell's photophone invention in the second half of the 19th century [25]. The device used Selenium, highly-responsive to light fluctuations, in order to recover a voice signal from a light beam modulated with a reflective membrane that is sensitive to sound vibrations [25].

The modern concept of OWC incorporates the transmission of high-speed digital signals using infrared (IR), visible light (VL), and even ultraviolet (UV) radiation. Work in the field has begun after the invention of the laser diode in the 1960s [26, 27]. The concept of short-range OWC as a means for realizing an access network for independent user terminals, as is the focus of this work, was introduced in the 1979 publication by Gfeller and Bapst [6]. The authors have shown theoretically that using IR communication for realizing a wireless link can deliver transmission speeds at hundreds of Mb/s and have experimentally demonstrated a communication link at a rate of over 100 kb/s. The field of OWC has gone a long way since that pioneering work. In 1993, the infrared data association (IrDA) introduced a protocol standard for infrared communication [28]. In 2006, Afgani *et al.* have presented the first experimental demonstration of orthogonal frequency division multiplexing (OFDM)-based visible light communications (VLC) [29]. In 2009, O'Brien *et al.* have demonstrated a complete transmission system capable of delivering over 300 Mb/s using IR light [30]. The advances in solid state lighting technologies have turned light emitting diodes (LEDs) into the most prominent candidates for off-the-shelf luminaries in

	Directed	Hybrid	Hybrid II	Non-directed
LoS				
non-LoS				
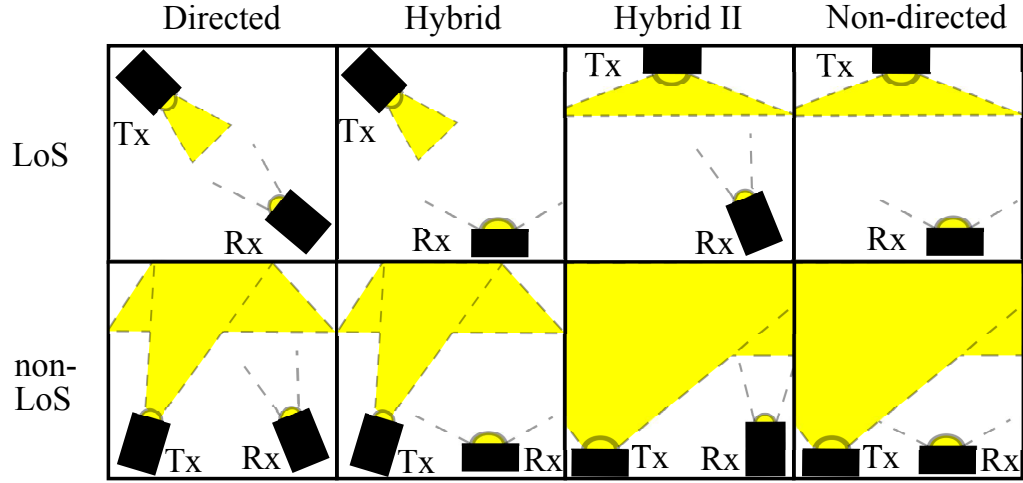
Figure 2.1: *Classification of OWC links according to degree of directionality and according to light propagation through a line-of-sight (LoS) or non-line-of-sight (non-LoS) path.*

the near future [31]. Ciaramella *et al.* have demonstrated a 1-Gb/s wireless link using an off-the-shelf phosphor-coated white LED and an over-3-Gb/s wireless link using an off-the-shelf red-green-blue (RGB) LED. In 2011, the Institute of Electrical and Electronics Engineers (IEEE) introduced a standard for VLC [32].

2.2 Optical Wireless Communication Links

Optical wireless links may be realized in many different configurations. However, it is often useful to classify them according to two main criteria as described in this section. Fig. 2.1 illustrates and summarizes the presented OWC link concepts [4].

The first criterion for link classification is the degree of directionality that is required for the proper operation of the OWC link. Directed links employ transmitters with a narrow light emission pattern and receivers with a narrow field of view (FOV) [4]. Such links are typically useful for energy-efficient high-speed transmission at longer distances [4]. Alignment is critical in such links, and so they are useful mostly in static scenarios. Non-directed links, on the other hand, exhibit a wide emission pattern at the transmitter and a large FOV at the receiver [4]. They are suitable for short-range applications where ubiquitous coverage is desired in order to accommodate for arbitrary motion by mobile users. Hybrid configurations between directed and non-directed links, as described in Fig. 2.1, may exist and are often useful in scenarios where interference
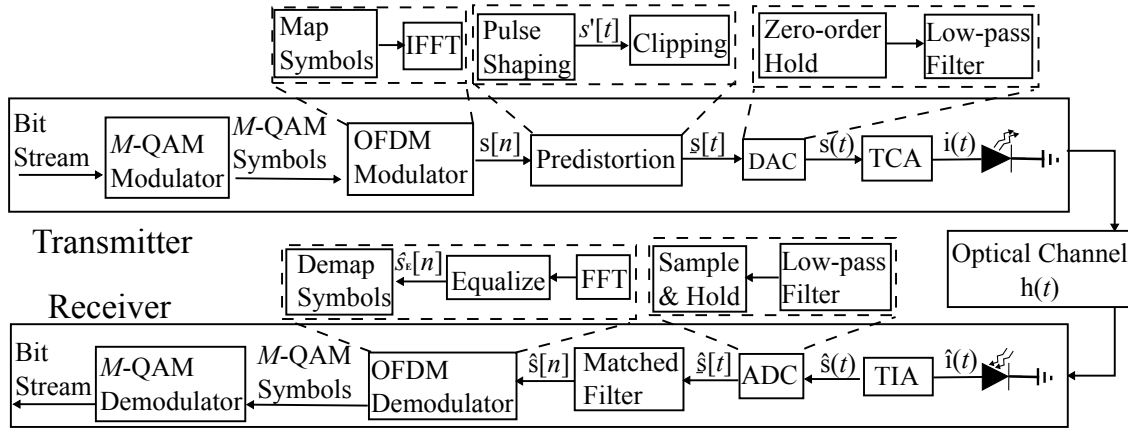
Figure 2.2: *Optical wireless communication system.*

between neighbouring transmitters should be mitigated.

The second criterion for link classification is related to the path along which light propagates from the transmitter to the receiver. The so-called line-of-sight (LoS) links require the existence of a direct and unobstructed propagation path from the transmitter to the receiver through free space. On the contrary, non-line-of-sight (NLoS) links propagate through reflections, without a clear direct path from the transmitter to the receiver [4]. LoS links typically maximize the achievable signal-to-noise ratio (SNR) at the receiver and minimize the impact of signal reflections on the performance [4]. NLoS links, on the other hand, are robust against shadowing effects, which makes them suitable for fulfilling ubiquitous coverage requirements [4].

2.3 Optical Wireless Communication System

A typical OWC system is depicted in Fig. 2.2. An incoming bit stream is divided into data blocks which are mapped to symbols from a known digital modulation scheme such as pulse-width modulation (PWM), pulse-position modulation (PPM), M-ary quadrature amplitude modulation (M-QAM) or M-ary pulse-amplitude modulation (M-PAM). If OFDM is employed, the result-ing data symbols are modulated onto different frequency subcarriers according to one of the fol-lowing schemes: direct-current-biased optical orthogonal frequency division multiplexing (DCO-OFDM), asymmetrically clipped optical orthogonal frequency division multiplexing (ACO-OFDM) or pulse-amplitude-modulated discrete multitone modulation (PAM-DMT). An inverse fast Fourier transform (IFFT) operation produces a time-domain signal when OFDM is used. The discrete

time-domain signal is subjected to a number of pre-distortion techniques that make it suitable for modulating the employed light source. The pre-distortion stage includes oversampling, pulse shaping as well as clipping any values below the allowed minimum or above the allowed maximum. Clipping is performed in order to accommodate the modulated signal within the linear dynamic range of the digital-to-analog converter (DAC), the amplifier, and the LED. The pre-distorted signal is supplied to a DAC which outputs an analog signal. In practice, this stage of the system usually consists of a zero-order-hold electrical circuit or other type of interpolator followed by a low pass filter. The analog output of the DAC is encoded into a current signal, amplified to a suitable level by a transconductance amplifier (TCA) with appropriate bias and passed through the employed electrical-to-optical front-end converter device such as an LED. OWC with incoherent illumination devices is realised as a baseband modulation technique. Therefore, frequency up-conversion is not required. Light intensity at the diode varies with the current. At the receiver side, a photodetector front-end element transforms the variations in the intensity of the received light into variations of a current signal, which is turned into a voltage signal by a transimpedance amplifier (TIA). The resulting voltage signal is discretised at an analog-to-digital converter (ADC) and passed on to the processing circuitry, which performs the demodulation steps including: matched filtering, downsampling, fast Fourier transform (FFT) if OFDM is used, equalisation, and bit demodulation.

2.4   Front-end Elements

2.4.1   Transmitter Front-end

The conversion of electrical signals into optical signals can be realized with the use of LEDs or laser diodes (LDs). LEDs emitting in the visible light spectrum appear to be the most favourable candidates for transmitter front-end elements due to their increasing popularity in illumination applications [5]. A relatively limited emission spectrum at different wavelengths can be achieved through the use of different materials and technologies. Commercially available white LEDs exist as two major variants: 1) RGB LEDs where white light is achieved as a combination of the three main colour components red, green and blue provided by three separate devices [11, 24]; and 2) blue LED chips with a yellow-phosphor coating where the relatively narrow emission of the blue device is absorbed and re-emitted by the phosphor coating resulting in a wide emission profile across the visible light spectrum and effectively rendering white light [10, 24]. The slow

absorption and re-emission time of the phosphor limits the 3-dB modulation bandwidth of the LED to about 2 MHz [24, 33]. In many applications, the addition of a blue filter at the receiver allows the slow signal component from the phosphor to be removed. Modulation speeds of up to 20 MHz have been reported for phosphor-coated commercially available white LEDs with this technique [10, 33]. The modulation speed of the LED is limited by the carrier lifetimes and the innate junction capacitance of the device [24, 34–36]. The carrier lifetime is reduced by increasing the current density in the junction. Therefore, the modulation speed of an LED can be increased by significantly reducing the size of the device. This has led to the introduction of the so-called μm-sized light emitting diodes (μLEDs) [24, 34–36]. A fundamental problem of the small LEDs, however, is the fact that their efficiency drops with an increase in the current density [37].

Unlike LEDs, LDs increase their efficiency as the current-density level increases [37, 38]. That is why, LDs are significantly faster and more efficient than LEDs [4, 37, 38]. Another advantage of LDs over LEDs is their ability to emit light in a very narrow wavelength band, which can significantly increase the possibility for parallel data transmission and, hence, can increase the utilization of the employed electromagnetic spectrum. At the same time, however, the narrow-band emission profile leads to an increased complexity in the design of LD-based illumination devices because precise colour mixing is required for the generation of white light with a suitable colour temperature. The main disadvantage of LDs is their cost [4, 37, 38]. Some other drawbacks include the necessity for additional optics in order to ensure eye-safe radiation levels in an inhabited environment [4]. A diffusive element is required at the output of the transmitter in order to destroy the spatial coherence of the laser light. Such elements with very high efficiency can be designed [4]. Computer-generated holographic diffusers can reach an efficiency of nearly 100% and in addition allow for extreme flexibility in the design of the desired output pattern [4]. Research efforts for increasing the modulation speeds of LEDs without compromising their output efficiency have led to the introduction of techniques from LD design into LED design. Hence, the so-called resonant-cavity light emitting diodes (RCLEDs) have emerged [39, 40].

Depending on the communication scenario, as described in Section 2.2, a specific set of optical elements at the transmitter may be required. The purposes of illumination and ubiquitous communication coverage would generally lead to a requirement for a wide radiation profile. Research has shown that an indoor cellular concept, employing multiple luminaires as access points (APs), achieves the best combination of communication capacity and coverage [41]. Reducing inter-cell interference in such a deployment configuration requires certain limitations on the radiation pro-

file of the transmitter [42,43]. Therefore, depending on the specific indoor environment, a proper combination of optical lenses and diffusive elements would be required at the transmitter. LEDs, in general, tend to be larger in size than LD for the same optical efficiency [37, 38]. Hence, the use of LDs could potentially reduce the design complexity of the transmitter optics. In general, the radiant/luminous intensity of a surface point varies with direction. A generalized Lambertian law has been widely adopted for modelling the intensity of such a source. At an angle of ϕ, the optical radiant intensity of the source can be calculated as [4]:

$$P_{\text{tx}}\text{R}(\phi) = P_{\text{tx}}\frac{m+1}{2\pi}\cos^m(\phi) \ [\text{W/sr}] \tag{2.1}$$

where P_{tx} [W] is the overall transmitted optical power (radiant flux), and $\text{R}(\phi)$ [1/sr] is the radiation profile of the source where the Lambertian emission order m is dependent on the intensity half angle as:

$$m = -\ln(2)/\ln\left(\cos\left(\phi_{\frac{1}{2}}\right)\right). \tag{2.2}$$

A bare LED device, for example, follows the emission profile of a Lambertian source and has a radiation half angle of $\phi_{\frac{1}{2}} = 60°$ ($m = 1$). The design of suitable optical elements allows the emission order to be shaped in accordance with the specifications of the particular application.

2.4.2 Receiver Front-end

A number of photodetector elements can be used for light detection at the receiver side. Some examples include imaging sensors [44, 45], solar panels [46], and even LEDs [47, 48] as suitable photodetectors in a variety of applications. However, these devices generally have a slow frequency response and are rather unsuitable for high-speed communication. The foremost candidates for receiver front-end elements in high-data-rate OWC systems are photodiodes (PDs) [4, 49, 50].

Based on their mode of operation, PDs can be generally divided into three types [4]: ordinary positive-intrinsic-negative (PIN) PDs, avalanche photodiodes (APDs), and single-photon avalanche diodes (SPADs). APDs are essentially PIN diodes operated at high reverse-bias voltages. This mode of operation leads to a high internal gain and, therefore, to high responsivity to light, which makes APDs suitable for applications where the received light signal intensity is

expected to be low. At the same time, the high sensitivity of these devices makes them more susceptible to shot noise, induced by ambient light and even by the information signal itself [4]. The linear operation of APDs can also be compromised when the irradiance over the devices is high. SPADs essentially present a mode of APD operation when the reverse bias is well-beyond the breakdown voltage, the so-called Geiger mode of operation, and, hence, the gain is so high that the reception of a single photon of light can be enough to trigger an avalanche effect inside the device leading to a high output current level [51]. As a consequence, SPADs are only applicable in a scenario where light levels are extremely low. Furthermore, their operation is highly non-linear [51], which makes them suitable for a limited range of data modulation schemes. Since the scope of the current work falls on high-speed communication using OFDM, in the rest of this document, a PD will refer to a PIN PD or an APD, where the appropriate clarifications will be made if the exact mode of operation is important for the presented concepts.

The amount of light that is collected by a PD is proportional to its area, A_{rx}. Therefore, the larger is the area of the device, the more light it can collect, and, hence, the higher is its tolerance to movement and rotation in a mobile communications scenario. The larger PD also relaxes the requirements on the optical output of the transmitter and allows for a wider light transmission profile. At the same time, the larger is the area, the slower is the switching speed of the device and, so, the worse is the frequency response profile. Therefore, there exists an optimal trade-off point between speed and device area depending on the specific application. A straightforward approach towards increasing the collection area of the device is to introduce optics at the receiver in order to increase the receiver's light collection ability. There exist two main groups of optical concentrators [4]: 1) imaging concentrators; and 2) non-imaging concentrators. The imaging concentrators project the original image of the transmitter on the receiver area. They are especially useful in multiple–input multiple–output (MIMO) configurations, where multiple LED transmitters are used to convey independent information streams to the receiver [52–54]. The spatial separation of the different transmitter front-ends allows them to be successfully detected and separated at the receiver with the help of multiple detector elements and signal processing techniques. The imaging concentrators facilitate this source separation at the receiver by preserving the original transmitter image. Non-imaging concentrators, on the other hand, destroy the original image of the transmitter devices and make MIMO techniques with a single optical system infeasible [52]. These concentrators, however, can achieve very high optical gains, close

to the theoretical maximum of [4]:

$$\mathrm{G_{oc}}(\psi) = \begin{cases} \dfrac{n_{\mathrm{ref}}^2}{\sin^2(\psi_{\mathrm{FOV}})}, & |\psi| \leq \psi_{\mathrm{FOV}} \\[2ex] 0, & |\psi| > \psi_{\mathrm{FOV}} \end{cases} \tag{2.3}$$

where ψ is the angle at which light is incident on the receiver; ψ_{FOV} is the receiver FOV, *i.e.*, the incidence angle beyond which the receiver does not accept any light; and n_{ref} is the refractive index of the optics material. In some communication scenarios, the receiver would be expected to detect only a portion of the electromagnetic spectrum, and this portion would be narrower than the spectrum which the PD can detect. Then, an optical filter would be introduced in order to avoid interference from information streams in other parts of the spectrum and in order to avoid the negative effects of strong ambient light sources [4]. Such filters can achieve very narrow bandwidths (less than 1 nm is commercially available) and high optical efficiency. The gain, $\mathrm{G_{of}}(\psi)$, of such a filter would be the integral of the filter response over the emission spectrum of the source [4]. Similarly, the attenuation of interfering light components can be estimated by integrating the filter response over the spectrum of the interfering light. Any losses due to reflections and filter imperfections can be included in $\mathrm{G_{of}}(\psi)$ [4]. The filter gain is expressed as a function of the light incidence angle because the filter response to different wavelengths often would change as the light hits the filter surface at different angles [4]. For most practical applications, such changes would be incremental and, hence, insignificant [4]. The angle of incidence of the incoming light changes the effective collection area of the receiver device due to the geometry of light propagation. The change is proportional to $\cos(\psi)$, and so the overall effective light collection area of the receiver becomes [4]:

$$\mathrm{A_{eff}}(\psi) = \begin{cases} A_{\mathrm{rx}}\mathrm{G_{of}}(\psi)\mathrm{G_{oc}}(\psi)\cos(\psi), & |\psi| \leq \psi_{\mathrm{FOV}} \\[2ex] 0, & |\psi| > \psi_{\mathrm{FOV}}. \end{cases} \tag{2.4}$$

One more important parameter, which needs to be discussed in relation to the receiver front-end, is the responsivity of the PD, $R\,[\mathrm{A/W}]$. It quantifies the amount of current induced at the PD in response to a given amount of incoming optical radiation. The responsivity changes with the light wavelength, therefore, R would typically be calculated by integrating the PD responsivity for individual wavelengths over the electromagnetic spectrum of the transmitted light reaching the PD. The PD responsivity to the interfering signal components can be calculated analogously.

2.5 Optical Wireless Communication Channel

As indicated in Fig. 2.2, the received information signal can be represented as:

$$\hat{s}[n] = h[n] * s[n] + n[n] \tag{2.5}$$

where $h[n]$ indicates the discrete-time communication channel impulse response, $n[n]$ stands for the independent identically distributed instances of additive white Gaussian noise (AWGN) at the receiver and $[\cdot] * [\cdot]$ denotes the convolution operator. The AWGN component $n[n]$ is described in the following section in more detail. The communication channel $h[n]$ encompasses all linear distortion effects from the moment the discrete-time OFDM signal is generated at the signal processor in the transmitter up until the point a discrete-time version of that signal is obtained at the receiver, ready for OFDM demodulation. In a carefully designed system, where all electrical components have been well-chosen to accommodate for the desired communication bandwidth, $h[n]$ is expected to be an effect induced only by the dispersive free-space communication channel. The physical properties of the front-end devices described in Section 2.4 allow an OWC system to be realised as an intensity modulation and direct detection (IM/DD) system only [4]. The phase and the amplitude of the individual electromagnetic waves cannot be modulated, and so information can be reliably encoded only in the signal intensity [4]. A typical receiver element is thousands or even millions of times larger than any wavelength used in OWC [4]. As a result, the received information signal is an average of thousands or millions of different wave modes [4]. Hence, multipath fading effects, typical for radio frequency (RF) communication, are not observed in OWC. The only channel effects in OWC are: geometric path loss due to the free-space propagation of light; and intersymbol interference (ISI) caused by multipath reflections when the maximum delay spread of the channel approaches the duration of the symbols in the information signal. The rest of this section describes how the OWC channel can be derived analytically.

The free-space light intensity loss as a function of the distance d_{tr} between the transmitter and the receiver is proportional to d_{tr}^2 [4]. Therefore, if a transmission source emits light as described in (2.1), and the receiver collects light as described in (2.4), the relationship between transmitted light intensity and received light intensity is [4]:

$$P_{rx}^0 = P_{tx} H_{LoS}(0) = P_{tx} \frac{m+1}{2\pi} \cos^m(\phi) G_{of}(\psi) G_{oc}(\psi) \frac{\cos(\psi) A_{rx}}{d_{tr}^2}, \tag{2.6}$$

20

where $H_{\text{LoS}}(0)$ is the LoS direct current (DC) gain of the optical channel. A non-LoS propagation channel can be modelled by dividing the surface area of reflecting elements into small units that analogously to the receiver absorb light from the source according to (2.6) [4, 55]. The absorbed light is then re-emitted from each unit surface area with a generalized Lambertian pattern according to (2.1). The intensity of the re-emitted light is determined by a surface reflectivity coefficient, ρ, which is specific to each material. The majority of the reflective surfaces are non-smooth and exhibit a Lambertian radiation pattern with a half-angle $\phi_{\frac{1}{2}, u_{\text{s}}} = 60°$ $(m_{u_{\text{s}}} = 1)$. Smooth surfaces have a more directional emission pattern which can be modelled by adjusting the order $m_{u_{\text{s}}}$ of the Lambertian radiation pattern [56]. Following this model, the light incident on a surface unit u_{s} coming from the source can be represented as:

$$P_{\text{rx},u_{\text{s}}}^{0} = P_{\text{tx}} \frac{m+1}{2\pi} \cos^{m}(\phi_{u_{\text{s}}}) \frac{\cos(\psi_{u_{\text{s}}}) A_{u_{\text{s}}}}{d_{u_{\text{s}}}^{2}}, \tag{2.7}$$

where $\phi_{u_{\text{s}}}$, $\psi_{u_{\text{s}}}$, $A_{u_{\text{s}}}$ and $d_{u_{\text{s}}}$ are the corresponding angle of transmission, angle of incidence, surface area and distance for the LoS link from the source to surface element u_{s}. Equation (2.7) effectively represents the light incident on surface element u_{s} due to the LoS path. The light incident on surface element u_{s} after the lth reflection can be calculated as:

$$P_{\text{rx},u_{\text{s}}}^{l} = \sum_{\substack{u=1 \\ u \neq u_{\text{s}}}}^{U_{\text{s}}} \rho_{u} P_{\text{rx},u}^{l-1} \frac{m_{u}+1}{2\pi} \cos^{m_{u}}(\phi_{u,u_{\text{s}}}) \frac{\cos(\psi_{u,u_{\text{s}}}) A_{u_{\text{s}}}}{d_{u,u_{\text{s}}}^{2}}, \tag{2.8}$$

where ρ_{u} is the reflectivity of surface element u, and U_{s} is the total number of surface elements; $\phi_{u,u_{\text{s}}}$, $\psi_{u,u_{\text{s}}}$ and $d_{u,u_{\text{s}}}$ are the corresponding angle of transmission, angle of incidence, and distance for the LoS link from the surface element u to surface element u_{s}. The light collected at the receiver due to the lth reflection can be expressed as:

$$P_{\text{rx}}^{l} = \sum_{u=1}^{U_{\text{s}}} \rho_{u} P_{\text{rx},u}^{l-1} \frac{m_{u}+1}{2\pi} \cos^{m_{u}}(\phi_{u,\text{rx}}) \frac{\cos(\psi_{u,\text{rx}}) A_{\text{rx}}}{d_{u,\text{rx}}^{2}} G_{\text{of}}(\psi) G_{\text{oc}}(\psi), \tag{2.9}$$

where $\phi_{u,\text{rx}}$, $\psi_{u,\text{rx}}$ and $d_{u,\text{rx}}$ are the corresponding angle of transmission, angle of incidence, and distance for the LoS link from the surface element u to the receiver. The total amount of light collected at the receiver from the first N_{ref} reflections is:

$$P_{\text{rx}} = \sum_{l=0}^{N_{\text{ref}}} P_{\text{rx}}^{l} = H(0) P_{\text{tx}}, \tag{2.10}$$

where $H(0)$ is the DC gain of the optical channel due to all possible light propagation paths. In case the symbol period of the designed OWC system approaches the maximum time it takes for significant reflections of the signal to reach the receiver, ISI is likely to occur. The impulse response of the free-space dispersive channel can then be calculated using the hereby described ray-tracing algorithm by additionally estimating the time it takes for light to reach the receiver along each reflection path. The procedure is described in detail in [55].

2.6 Noise in Optical Wireless Communication

Every electrical element introduces a noise component to an information signal. Assuming that all electrical elements in an OWC system are operated in their linear region, *i.e.*, no significant non-linear distortion is introduced to the information signal, the only significant noise contribution that influences the performance is generated in the receiver circuit at the point where the information signal is at its weakest level. Two major noise contributors exist at the optical receiver.

The first noise component is contributed by the so-called "shot noise", resulting from the randomness in the generation of electrons by incoming photons in the PD [4, 7, 57]. It is rather intuitive that higher average light intensities are likely to lead to larger shot noise levels as higher light levels lead to a higher number of random photon-electron interaction events. Typically, ambient light sources contain low-frequency components and their interfering effect can be avoided at the receiver with suitable signal processing techniques. However, the shot noise that they introduce is unavoidable and can have detrimental effects on the communication signal, leading to reduced performance. In case the ambient light intensity is significantly stronger than the intensity of the information signal, shot noise can be described as a random AWGN process whose power spectral density (PSD) is calculated as:

$$N_{\mathrm{o}}^{\mathrm{shot}} = 2qR\bar{P}_{\mathrm{rx}} \ \left[\frac{\mathrm{A}^2}{\mathrm{Hz}}\right], \tag{2.11}$$

where $q = 1.602 \times 10^{-19}\,\mathrm{C}$ is the charge of an electron in coulombs, and $\bar{P}_{\mathrm{rx}}$ is the average received optical power at the receiver. The OWC signal itself can also be responsible for some of the shot noise generated at the receiver. This is especially true in scenarios where the functions of illumination and data communication are performed by the same light emitting device as well as in scenarios where ambient light levels are low [4]. It should also be noted that APD-based receivers are especially vulnerable to shot noise as their high internal gain introduced by
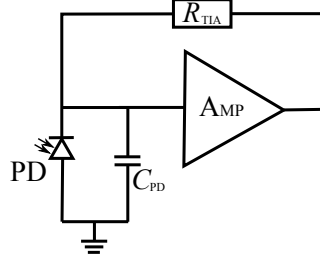
Figure 2.3: *A shunt-feedback transimpedance amplifier. Parameter R_{TIA} represents the feedback resistor in the amplifier configuration, and parameter C_{PD} represents the parasitic capacitance of the photodiode.*

the avalanche effect is usually sufficient to overcome the effect of subsequent thermal noise introduced in the system, but at the same time can amplify and aggravate the shot noise component [4]. The second significant noise component in the receiver system is introduced by thermal noise at the TIA stage. In its largest part, this noise component can be modelled as AWGN [57, 58]. The power of the thermal noise component is dependent on the selected TIA topology and on the parameter values that describe the individual components which are used for the realisation of the amplifier circuit. A typical "shunt-feedback" TIA configuration is shown in Fig. 2.3 [57, 58]. In most TIA topologies, the thermal noise component is dominated by the thermal noise generated at the resistor R_{TIA}. Hence, provided that the modulation bandwidth does not exceed a few hundred MHz, the thermal noise PSD can be calculated as [57, 58]:

$$N_{\mathrm{o}}^{\mathrm{th}} = \frac{4k_{\mathrm{B}}T_{\mathrm{k}}}{R_{\mathrm{TIA}}} \left[\frac{\mathrm{A}^2}{\mathrm{Hz}} \right], \tag{2.12}$$

where $k_{\mathrm{B}} = 1.381 \times 10^{-23}$ [J/K] is the Boltzmann constant in joules per kelvin, and T_{k} [K] is the device temperature in kelvin. The modulation range in which this assumption is valid depends on the particular topology and the particular elements used to realise a given TIA configuration. High modulation speeds, where the bandwidth exceeds a few hundred MHz, require a more thorough calculation of the thermal noise energy where the thermal noise contribution of the other elements in the TIA circuit are taken into account as described in [57, 58].

The AWGN generated by shot noise at the APD and the AWGN generated by thermal noise at the TIA are uncorrelated. Hence, the overall AWGN PSD in the receiver is calculated as [4, 57, 58]:

$$N_{\mathrm{o}} = N_{\mathrm{o}}^{\mathrm{shot}} + N_{\mathrm{o}}^{\mathrm{th}}. \tag{2.13}$$

2.7   Modulation Schemes

The physical properties of the front-end devices described in Section 2.4.1 and Section 2.4.2 do not allow modulation or detection of the amplitude and the phase of the employed electromagnetic wave. As a result, coherent modulation is infeasible in a practical OWC system. Information can be encoded and conveyed only in the intensity of the light emission. As a result, OWC systems can only be realised as IM/DD systems. This means that the modulation signal is real and positive, which puts restrictions on the set of modulation schemes which can be adopted from the field of RF communication in the field of OWC.

2.7.1   Single-carrier Modulation

Real single-carrier modulation techniques from the field of RF communication can be adapted for OWC in a relatively straightforward manner. These include PPM, PWM, on-off keying (OOK), unipolar M-PAM. The single-carrier modulation techniques typically have: 1) lower implementation complexity than multicarrier schemes; 2) better performance in flat fading channels; and 3) less issues with non-linear distortion because their time-domain signal distribution can be more easily shaped and constrained within a desired range in comparison to the signal distribution of multicarrier modulation techniques.

2.7.2   Multi-carrier Modulation

A communication channel with limited coherence bandwidth can lead to ISI at high data rates. In OWC, signal reflections can be a source of ISI when the information symbol period approaches the maximum delay spread of the free space optical channel. With off-the-shelf components, however, the limiting factor for the communication rate is likely to be the limited modulation bandwidth of the front-end devices themselves [10, 11, 24]. The frequency response of most commercially available LEDs can be considered flat for a bandwidth of about 2-20 MHz [10, 11, 24]. This suggests that high-speed OWC is likely to require modulation rates well-beyond the 3-dB modulation bandwidth of the front-end components and an appropriate equalisation technique at the receiver. Hence, OFDM is a very appealing modulation scheme. It enables low-complexity equalisation with single-tap equalisers in the frequency domain as well as adaptive data and energy loading techniques in different regions of the communication bandwidth based

on the communication channel properties. This allows for optimal utilisation of the available communication resources. The highest data rates reported in the field of VLC – over 3 Gb/s for a single LED [24] – have been achieved using OFDM [10, 11, 24]. OFDM also provides a straightforward multiple access scheme at the medium access control (MAC) level, while a multiple access technique has to be implemented additionally for the single-carrier modulation schemes.

The OWC multicarrier modulation techniques presented in this section are modifications of conventional OFDM. The different OFDM frequency subcarriers are modulated with M-QAM symbols in DCO-OFDM and ACO-OFDM and with M-PAM symbols in PAM-DMT. It should be noted that the M-QAM symbols are modulated on the amplitude and phase component of the real time-domain signal and in that sense they do not modulate the electromagnetic wave as in RF communication but the frequency-domain representation of the intensity-modulated signal. A time-domain OFDM frame is obtained by taking the IFFT of a block of N_{fft} M-QAM/M-PAM symbols. A Hermitian symmetry constraint is imposed in the block of symbols before the IFFT. According to the properties of the Fourier transform, this constraint generates a real time-domain signal [5]. The subcarriers at positions $k{=}0$ and $k{=}\frac{N_{\text{fft}}}{2}$, *i.e.* the DC subcarrier and the $180°$ subcarrier, are set to zero as part of the Hermitian symmetry requirement. The resulting real time-domain signal, however, is bipolar in nature. Because an IM/DD system can employ only non-negative signals, the following three different methods have been designed as the state-of-the-art techniques for the generation of unipolar signals, suitable for OWC.

2.7.2.1 DCO-OFDM

The introduction of a positive DC bias around which the bipolar signal can vary, constitutes a straightforward technique for turning a bipolar signal into a unipolar signal. This approach is known in the literature as DCO-OFDM [59]. Fig. 2.4 illustrates the concept.

The spectral efficiency of the scheme is:

$$\eta = \frac{\sum_{k=0}^{\frac{N_{\text{fft}}}{2}-1}(1 - \delta[M_k])\log_2(M_k)}{(N_{\text{fft}} + N_{\text{cp}})} \text{ bits/s/Hz.} \tag{2.14}$$

where the factor $\log_2(M_k)$ indicates the number of bits that are encoded in the M-QAM constellation at subcarrier k; N_{cp} is the length of the cyclic prefix; and $\delta[\cdot]$ denotes the Kronecker delta

(a) Bipolar OFDM before biasing. (b) Biased DCO-OFDM.
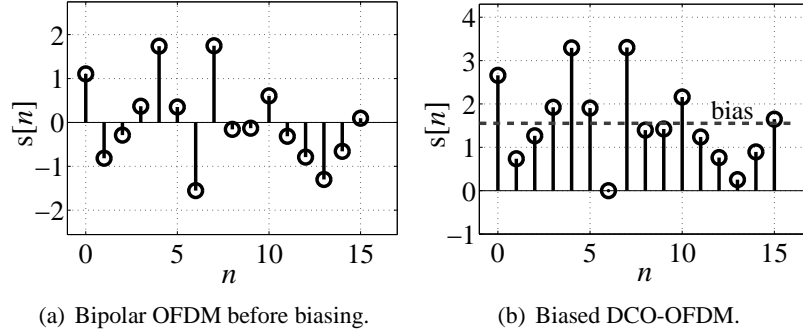
Figure 2.4: *DCO-OFDM Generation. Cyclic prefix is not illustrated.*

function. When all subcarriers are loaded with the same constellation of size M, the spectral efficiency reduces to:

$$\eta_{\text{DCO}} = \frac{\log_2(M)(N_{\text{fft}} - 2)}{2(N_{\text{fft}} + N_{\text{cp}})} \text{ bits/s/Hz}. \tag{2.15}$$

The factors $N_{\text{fft}} - 2$ and $1/2$ occur due to the Hermitian symmetry requirement.
OFDM is characterised by a very high peak-to-average power ratio (PAPR). Based on the calculations provided in [17], a lower bound for the PAPR of real OFDM can be calculated as:

$$\frac{3N_{\text{a}}(\sqrt{M} - 1)}{2\sqrt{M} + 1} \tag{2.16}$$

where N_{a} is the number subcarriers modulated with M-QAM. Following this result, it is clear that it is impractical to introduce a biasing level that ensures all possible time-domain OFDM samples are non-negative. In addition, electronic devices typically have a limited active range with both a lower and an upper bound. Hence, excessive biasing could cause the OFDM signal to be clipped from above. In a practical scenario, the signal would be inevitably clipped on both sides of the distribution. A key design objective is to optimise the signal distribution and biasing in order to ensure high achievable SNR at the receiver while keeping the non-linear distortion due to signal clipping in an acceptable range [14]. Acceptable levels for signal clipping vary with the employed M-QAM constellation size, but typically amount to a few standard deviations on each side of the signal distribution [14]. The time-domain standard deviation of the signal, σ_s, can be computed as:

$$\sigma_{\text{s}}^2 = \frac{1}{N_{\text{fft}}} \sum_{k=0}^{N_{\text{fft}}-1} \log_2(M_k) E_{\text{b}k}, \tag{2.17}$$

where $E_{\mathrm{b}k}$ denotes the energy per bit on the subcarrier with index k.

The average electrical power of the transmitted modulation signal is proportional to [21, 60]:

$$P_{\mathrm{elec}}^{\mathrm{avg}} = \mathrm{E}\{\mathrm{i}^2(t)\}, \tag{2.18}$$

where $\mathrm{i}(t)$ is the current signal through the front-end device. Then, the electrical SNR of the system is defined as [21, 60]:

$$\frac{E_{\mathrm{b,elec}}}{N_{\mathrm{o}}} = \frac{P_{\mathrm{elec}}^{\mathrm{avg}}}{B\eta N_{\mathrm{o}}} = \frac{\mathrm{E}\{\mathrm{i}^2(t)\}}{B\eta N_{\mathrm{o}}}, \tag{2.19}$$

where η is the spectral efficiency of the information signal. The average optical power of the transmitted modulation signal is proportional to [21, 60]:

$$P_{\mathrm{opt}}^{\mathrm{avg}} = \mathrm{E}\left\{\mathrm{i}(t)\right\}. \tag{2.20}$$

Then, the optical SNR of the system is defined as [21, 60]:

$$\frac{E_{\mathrm{b,opt}}}{N_{\mathrm{o}}} = \frac{P_{\mathrm{opt}}^{\mathrm{avg}}}{B\eta N_{\mathrm{o}}} = \frac{\mathrm{E}\left\{\mathrm{i}(t)\right\}}{B\eta N_{\mathrm{o}}}. \tag{2.21}$$

For the remainder of this thesis, it is assumed that the transition from a voltage alternating current (AC) signal, $\mathrm{s}(t)$, to a current AC signal in the TCA is linear with gain 1, unless specifically stated otherwise. It should be pointed out that in a real application, the actual voltage and the equivalent resistance in the front-end components will need to be taken into account when estimating the absolute electrical energy levels consumed in the system. For practical purposes, the energy dissipated in the signal processing components should also be accounted for. In that sense, an estimation of the entire system efficiency in terms of bits transmitted per joule of dissipated electrical energy would be a better performance measure. For the estimation of the optical efficiency, the conversion efficiency between electrical and optical power will also have to be taken into account. For the sake of simplicity, in this work it is assumed that the significant part of the electrical energy in the system is consumed in the transmiter front-end, *i.e.*, in the LED/LD. Normalising the voltage through the front-end device to be equal to the biased information signal amplitude and assuming equivalent resistance of $1\,\Omega$ is a fair assumption which simplifies the conducted analysis and does not introduce any loss of generality in the comparison between the performance of the different modulation schemes presented.

(a) ACO-OFDM before clipping.

(b) ACO-OFDM after clipping and rescaling.
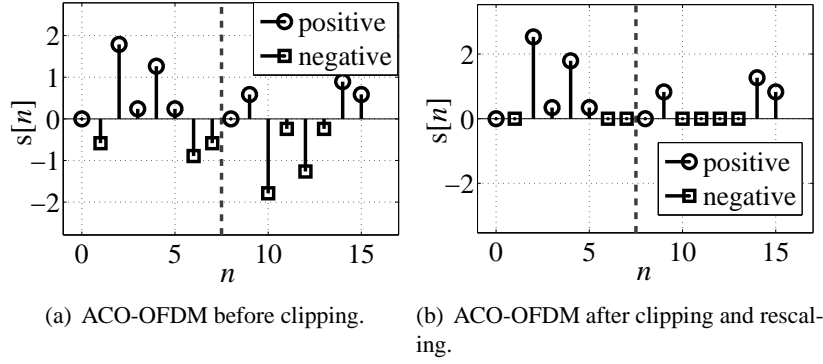
Figure 2.5: *ACO-OFDM Generation. Cyclic prefix is not illustrated.*

The DC-bias in DCO-OFDM causes a substantial increase in both electrical and optical energy consumption. The bias level of the LED can be represented as:

$$b_{\mathrm{DC}} = k_{\mathrm{bias}} \sqrt{\mathrm{E}\left\{\mathrm{s}^2(t)\right\} - \mathrm{E}\left\{\mathrm{s}(t)\right\}^2} = k_{\mathrm{bias}}\sigma_{\mathrm{s}}, \tag{2.22}$$

Then, relative to the original bipolar OFDM signal, the addition of a bias signal causes an energy dissipation increase in DCO-OFDM by approximately [60]:

$$10\log_{10}\left(k_{\mathrm{bias}}^2 + 1\right)\,\mathrm{dB}. \tag{2.23}$$

This approximation is valid if the non-linear effects in the system, such as clipping, do not significantly affect the amount of dissipated energy [60]. For practical approximations, this assumption can be considered valid. For the rest of this work, a biasing level specified in dB would represent the bias level that leads to an electrical energy dissipation increase of that same specified amount in dB, in accordance with the description in (2.23).

2.7.2.2 ACO-OFDM

The bias in DCO-OFDM increases substantially the dissipated electrical energy and the required optical power at the transmitter [14]. The modulation technique known as ACO-OFDM, illustrated in Fig. 2.5, avoids the biasing requirement by exploiting the properties of the Fourier transform in order to generate an inherently unipolar OFDM signal that requires no biasing [61]. In ACO-OFDM, only odd-indexed frequency subcarriers are modulated. This creates a certain symmetry among the bipolar OFDM samples in the time-domain. If $\mathrm{s}(k,n)$ is the contribution of subcarrier value $\mathrm{S}[k]$ to the time sample at position n, then [61]:

28

$$\mathrm{s}(k,n) = \frac{1}{\sqrt{N_{\mathrm{fft}}}} \mathrm{S}[k] \mathrm{e}^{\frac{j2\pi nk}{N_{\mathrm{fft}}}}$$

and

$$\mathrm{s}(k, n + \frac{N_{\mathrm{fft}}}{2}) = \frac{1}{\sqrt{N_{\mathrm{fft}}}} \mathrm{S}[k] \mathrm{e}^{\frac{j2\pi(n+N_{\mathrm{fft}}/2)k}{N_{\mathrm{fft}}}} =$$

$$= \frac{1}{\sqrt{N_{\mathrm{fft}}}} \mathrm{S}[k] \mathrm{e}^{\frac{j2\pi nk}{N_{\mathrm{fft}}}} \mathrm{e}^{j\pi k}. \tag{2.24}$$

When k is odd, $\mathrm{s}(k,n) = -\mathrm{s}(k, n + N_{\mathrm{fft}}/2)$. When k is even, $\mathrm{s}(k,n) = \mathrm{s}(k, n + N_{\mathrm{fft}}/2)$. Hence, if only the odd-indexed subcarriers are modulated and the even-indexed subcarriers are set to zero, the time-domain signal, $\mathrm{s}[n]$, can be described as:

$$\mathrm{s}[n] = -\mathrm{s}[n + N_{\mathrm{fft}}/2]. \tag{2.25}$$

If only the even-indexed subcarriers are modulated and the odd-indexed subcarriers are set to zero, the time-domain signal can be described as:

$$\mathrm{s}[n] = \mathrm{s}[n + N_{\mathrm{fft}}/2]. \tag{2.26}$$

The inverse relations also hold because complex exponential functions are orthogonal to each other. If a time-domain signal has the property in (2.25), in the frequency domain, only the odd-indexed subcarriers are non-zero. Analogously, if a time-domain signal has the property in (2.26), in the frequency domain only the even-indexed subcarriers are non-zero.

Clipping at zero of the negative samples of any time-domain signal, $s[n]$, can be represented as:

$$\underline{\mathrm{s}}[n] = \mathrm{f}_{\mathrm{clip}}\{\mathrm{s}[n]\} = \frac{1}{2}(\mathrm{s}[n] + |\mathrm{s}[n]|) \tag{2.27}$$

In ACO-OFDM, only the odd-indexed subcarriers are modulated with information symbols, while the even-indexed subcarriers are set to zero. Hence, (2.25) applies to the scheme. Therefore, $|\mathrm{s}[n]| = |\mathrm{s}[n + N_{\mathrm{fft}}/2]|$. The created symmetry allows for all negative-valued samples to be set to zero. The resulting distortion $|\mathrm{s}[n]|$ from (2.27), has the property in (2.26). Therefore, it contributes only to the values of the even-indexed subcarriers. The factor $1/2$ appears due to the clipping operation and is consistent with the ACO-OFDM analysis presented in [61]. The

(a) Bipolar PAM-DMT before clipping.   (b) Unipolar PAM-DMT after clipping and rescaling.
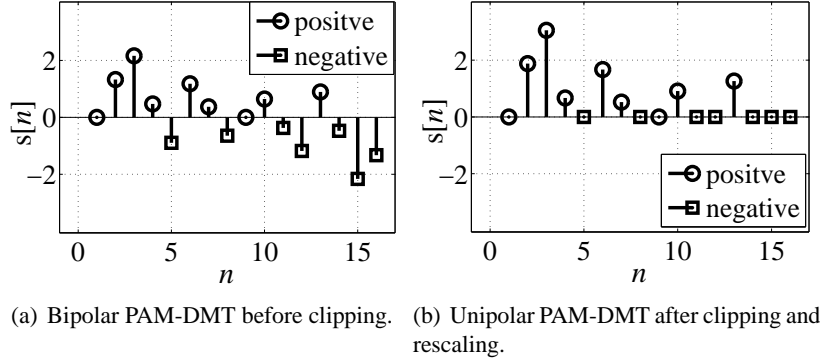
Figure 2.6: *PAM-DMT Generation. Cyclic prefix is not illustrated.*

clipped unipolar signal is rescaled by a factor of $\sqrt{2}$ in order to preserve the amount of dissipated energy. This leads to an overall achieved SNR penalty of $3\,\mathrm{dB}$ [61]. The short proof described here has been developed in the context of the current work. It concisely summarizes the original ACO-OFDM analysis from [61]. Not modulating the even-indexed subcarriers sacrifices approximately half the spectral efficiency, compared to DCO-OFDM. Equation (2.14) can be used to calculate the spectral efficiency of ACO-OFDM. When all subcarriers are loaded with the same constellation of size M, (2.14) reduces to:

$$\eta_{\mathrm{ACO}} = \frac{\log_2(M)N_{\mathrm{fft}}}{4(N_{\mathrm{fft}} + N_{\mathrm{cp}})} \text{ bits/s/Hz.} \tag{2.28}$$

It is clear from (2.15) and (2.28) that the signal generation process in ACO-OFDM sacrifices half of the spectral efficiency in comparison to DCO-OFDM. This means that for the same modulation bandwidth, ACO-OFDM can deliver significant energy savings, but at the cost of half the data rate in comparison to DCO-OFDM.

2.7.2.3 PAM-DMT

PAM-DMT is an inherently unipolar OFDM-based modulation scheme, which is generated similarly to ACO-OFDM. PAM-DMT, however, exploits an alternative property of the FFT. A PAM-DMT time-domain signal is illustrated in Fig. 2.6. In this technique, all frequency subcarriers are modulated with imaginary M-PAM symbols. Due to the imposed Hermitian symmetry in the frequency domain, the PAM-DMT time-domain signal has the property [62]:

$$s[n] = \frac{1}{\sqrt{N_{\mathrm{fft}}}} \sum_{k=0}^{N_{\mathrm{fft}}-1} S[k] e^{\frac{j2\pi kn}{N_{\mathrm{fft}}}} =$$

$$= \frac{1}{\sqrt{N_{\text{fft}}}} \sum_{k=0}^{N_{\text{fft}}-1} \text{S}[k] \left(\cos \frac{2\pi k n}{N_{\text{fft}}} + j \sin \frac{2\pi k n}{N_{\text{fft}}} \right) =$$

$$= \frac{1}{\sqrt{N_{\text{fft}}}} \sum_{k=0}^{N_{\text{fft}}-1} j\text{S}[k] \sin \frac{2\pi k n}{N_{\text{fft}}}. \tag{2.29}$$

In the time-domain, a PAM-DMT frame exhibits an antisymmetry where $\text{s}[0]=0$, $\text{s}[N_{\text{fft}}/2]=0$ if N_{fft} is an even number, and $\text{s}[n]=-\text{s}[N_{\text{fft}}-n]$. Hence, $|\text{s}[0]|=0$, $|\text{s}[N_{\text{fft}}/2]|=0$ if N_{fft} is an even number, and $|\text{s}[n]|=|\text{s}[N_{\text{fft}}-n]|$. Therefore, if all negative time-domain samples are set to zero, as in (2.27), the resulting distortion component $|s[n]|$ exhibits a Hermitian symmetry in the time domain. As a result, the frequency profile of the distortion term is a real-valued signal. Hence, it is completely orthogonal to the information, which is encoded with imaginary values. The proof presented in this work has not been completed in the original PAM-DMT paper [62]. However, with the clipping representation in (2.27), it becomes straightforward to formulate and has been formally completed in the context of the current work. The spectral efficiency of PAM-DMT can be calculated using (2.14), where M denotes the M-PAM modulation order. When all subcarriers are loaded with the same constellation of size M, (2.14) reduces to:

$$\eta_{\text{PAM}-\text{DMT}} = \frac{\log_2(M)(N_{\text{fft}} - 2)}{2(N_{\text{fft}} + N_{\text{cp}})} \text{ bits/s/Hz}. \tag{2.30}$$

In an AWGN channel, $\sqrt{M}$-PAM has approximately the same bit error rate (BER) performance as M-QAM for the same amount of dissipated energy. Therefore, PAM-DMT is comparable to ACO-OFDM in terms of spectral efficiency for the same energy efficiency.

2.8 Non-linear Distortion in OFDM-based OWC Systems

In a practical implementation of an OWC system, non-linear distortion is anticipated. Its effects on the communication performance are an open subject of investigation. A large number of works have been published on the topic of non-linear distortion in an OFDM-based OWC system [14, 15, 63–65]. One popular approach for the analytical evaluation of OFDM's performance in the presence of non-linear distortion has been introduced in [66]. It can be described as follows.

Dardari *et al.* have shown that a non-linear distortion in an OFDM-based system translates into

a signal gain factor and an additional noise component, both of which can be explained and quantified using the Bussgang theorem [66]. In an OFDM frame, for a large number of subcarriers, $N_{\text{fft}} > 64$, the time-domain signal follows a continuous Gaussian distribution [14, 15, 66]. In General, if X is a zero-mean Gaussian random variable and $z(X)$ is an arbitrary memoryless distortion function of X, then using the Bussgang theorem in [67] and Rowe's subsequent work in [68],

$$z(X) = \alpha X + Y_{\text{n}} \tag{2.31}$$

$$E\{XY_{\text{n}}\} = 0, \tag{2.32}$$

where α is a constant, $E\{\cdot\}$ denotes the statistical expectation operator, and Y_{n} is an additive noise component which is not correlated with X. Using equations (2.31) and (2.32), α can be computed as:

$$\alpha = \frac{E\{Xz(X)\}}{\sigma_{\text{x}}^2}, \tag{2.33}$$

where σ_{x} denotes the standard deviation of X. The noise component, Y_{n}, can be quantified with the following equations:

$$E\{Y_{\text{n}}^2\} = E\{z^2(X)\} - \alpha^2 \sigma_{\text{x}}^2 \tag{2.34}$$

$$E\{Y_{\text{n}}\} = E\{z(X)\} \tag{2.35}$$

$$\sigma_{\text{Y}}^2 = E\{Y_{\text{n}}^2\} - E\{Y_{\text{n}}\}^2, \tag{2.36}$$

where σ_{Y}^2 is the variance of Y_{n}. When the FFT operation is applied in the demodulation process at the receiver, in the frequency domain the noise Y_{n} is transformed into additive Gaussian noise in accordance with the central limit theorem (CLT). The noise variance is preserved from the time domain, and the time-domain signal mean contributes only to the DC($k = 0$) subcarrier. Hence, each modulated subcarrier is subjected to additional zero-mean additive Gaussian noise with variance σ_{Y}^2. Overall, the system experiences an increase in the additive Gaussian noise energy by σ_{Y}^2 and a decrease in the information signal energy by a factor of α^2. The achieved

SNR at each frequency subcarrier is calculated as:

$$\frac{E_{\mathrm{b}k}^{\mathrm{new}}}{\sigma_{\mathrm{NY}}^2} = \frac{\alpha^2 E_{\mathrm{b}k}}{\sigma_{\mathrm{n}}^2 + \sigma_{\mathrm{Y}}^2},$$

$$(2.37)$$

where $E_{\mathrm{b}k}^{\mathrm{new}}$ denotes the resulting energy per bit at subcarrier k, $E_{\mathrm{b}k}$ is the initial energy per bit at subcarrier k, σ_{n}^2 is the variance of the channel AWGN, assumed to be the same at all subcarriers, and σ_{NY}^2 is the overall resulting noise variance.

2.9   Summary

Visible light communication has been used for thousands of years. The early concepts have all been dependent on the human ability to recognise different visible light signals until the invention of the photophone by Alexander Graham Bell in the second half of the 19th century. In its contemporary form, suitable for high-speed digital communication, OWC was first presented in 1979 by Gfeller and Bapst. Over the past 35 years, OWC has undergone significant development and has slowly become one of the most prominent candidates for delivering high-speed wireless connectivity.

The physical constraints and the implementation issues of OWC have been studied in a lot of detail. Accurate models of the OWC system as well as accurate models of the individual system components such as the front-end devices and the wireless communication channel have been developed. The generalised Lambertian law is suitable for modelling the light emission profile of an optical transmitter. The same principles can also be used to describe the optical gain of the receiver front-end. Furthermore, reflecting surfaces can be divided into small reflecting elements which can be modelled as simultaneous optical receivers and transmitters whose functionality can be described with the generalised Lambertian law. This enables straightforward ray-tracing algorithms and accurate characterisation of the free-space optical communication channel. The sources of noise in the OWC system have been studied in detail and two dominant sources of AWGN have been identified. The major contributors to AWGN in the communication system are shot noise due to strong ambient light and thermal noise at the TIA stage.

Suitable modifications of the commonly-accepted communication concepts from the field of RF communication have been proposed leading to the demonstration of multi-Gb/s connectivity using VLC. Novel OFDM-based modulation schemes suitable for energy-efficient communication in IM/DD systems have been proposed. These state-of-the-art techniques, including ACO-OFDM and PAM-DMT, can deliver significant energy savings in comparison to the conventional DCO-OFDM scheme. They, however, suffer from an inherent flaw since high energy-efficiency is achieved at the cost of half of the scheme's spectral efficiency. There is a lot of potential for further advancements in the field of OWC as the problem of building an energy-efficient high-speed OWC link is still considered an open subject of investigation. The current work extends the existing research and proposes new solutions to a wide range of problems that have been recognised in the field.

Chapter 3
An Analytical Framework for Subcarrier-Index Modulation OFDM

A novel modulation technique called subcarrier-index modulation orthogonal frequency division multiplexing (SIM-OFDM) has recently been proposed. SIM-OFDM uses different frequency subcarrier states to convey information and supposedly leads to power savings and increased performance in comparison to conventional orthogonal frequency division multiplexing (OFDM). In this chapter, an analytical framework to compute the bit error rate (BER) performance of SIM-OFDM over a linear additive white Gaussian noise (AWGN) communication channel is provided. The new framework offers an accurate estimation of the BER. Furthermore, the performance of SIM-OFDM is compared with the performance of conventional OFDM. It is shown that SIM-OFDM suffers from an error propagation effect, which hinders its ability for power-efficient communication. In the second part of this chapter, a solution to the error-propagation effect is proposed, demonstrating an enhanced SIM-OFDM modulation scheme, which is able to deliver the anticipated performance benefit and offers a further advantage over conventional OFDM in terms of reduced peak-to-average power ratio (PAPR). Overall, however, it is shown that SIM-OFDM is a communication protocol with poor spectral efficiency, which is not likely to deliver high data-rates in wireless communication environments where modulation bandwidth is a scarce resource.

3.1   Introduction

The combination of ever-increasing demand for higher communication speeds and significant reduction in available radio frequency spectrum has forced researchers to investigate the possibilities for new degrees of freedom in the constellation space of the information signal. The concept of multiple–input multiple–output (MIMO) has attracted a lot of interest and a vast number of techniques have been proposed for the successful analysis and implementation of MIMO-based communication systems [12, 69–81]. One such MIMO technique, spatial modulation (SM), was introduced by Mesleh, *et al.* in [76]. SM employs multiple receiver and transmitter elements where only one transmitter element is turned on during the duration of an information symbol. As a result, the unique propagation signature of every symbol transmitted through a different antenna can be used to convey information. The activation of a single transmitter at a given time instance allows interchannel interference (ICI) to be avoided and makes inter-antenna synchronization obsolete. SM has gained a lot of popularity since its introduction in 2006 and has led to many scientific publications in the field [76–81]. The technique described in this chapter, SIM-OFDM, is inspired by the SM concept.

SIM-OFDM is a modification of the conventional OFDM modulation scheme. In conventional OFDM, a number of different frequency subcarriers are modulated with a signal from a modulation scheme such as on-off keying (OOK), M-ary pulse-amplitude modulation (M-PAM) or M-ary quadrature amplitude modulation (M-QAM). The novel approach of SIM-OFDM exploits an additional dimension in the OFDM frame coming from the state of each subcarrier - active or inactive. A detailed description of the modulation scheme can be found in [82]. SIM-OFDM is still a rather unexplored topic. An analytical approach towards deriving its performance in combination with 4-QAM in a fading channel is provided by the authors in [82]. According to the presented results, SIM-OFDM has the potential to outperform the conventional OFDM modulation scheme. However, a complete analytical description of the system BER performance is still missing. This work presents a suitable generalised theoretical model for evaluating SIM-OFDM's performance for an arbitrary M-QAM constellation size in a linear flat AWGN channel. As a result, an underlying issue with the SIM-OFDM frame structure is discovered which deters the modulation scheme's performance. A feasible fix to the problem is presented in combination with a modified BER analysis.

The problem of high PAPR in OFDM has been long-recognised and extensively studied. A large

number of PAPR reduction techniques have already been proposed. Some examples include: clipping and filtering, coding, non-linear companding, tone reservation, tone injection, selective mapping, partial transmit sequence [83]. Some of these techniques promise very significant reduction of the OFDM signal's PAPR distribution. The novel enhanced SIM-OFDM, proposed in this chapter, has an inherent ability to reduce the PAPR in an OFDM based communication system. Consequently, it can be beneficial in communication scenarios which lead to high non-linear distortion of the information signal.

The rest of this chapter is organized as follows. Section 3.2 discusses the existing SIM-OFDM modulation concept and is divided in the following manner: Section 3.2.1 introduces the modulation and demodulation algorithm of SIM-OFDM; Section 3.2.2 presents the analytical framework; and Section 3.2.3 confirms the validity of the theoretical BER estimations through extensive Monte Carlo simulations. Section 3.3 proposes an enhanced SIM-OFDM algorithm with an improved frame structure and is divided as follows: Section 3.3.1 presents the enhanced concept; Section 3.3.2 presents the analytical framework for the enhanced SIM-OFDM algorithm; Section 3.3.3 confirms the validity of the theoretical analysis; and Section 3.3.4 analyses the PAPR of the novel technique. Finally, Section 3.4 provides concluding remarks to the topic.

3.2 Subcarrier-Index Modulation (SIM) OFDM

3.2.1 Concept

In SIM-OFDM, the incoming bit stream is divided into blocks, where each of the blocks has a length of $N_{\text{fft}}(\frac{\log_2(M)}{2} + 1)$, where N_{fft} is the total number of frequency subcarriers in an OFDM frame, and M is the constellation size of the employed M-QAM modulation scheme. Each block of bits is divided into two parts. The first N_{fft} bits of the block form a sub-block, which in the rest of this work will be referred to as B_{OOK}. The remaining $N_{\text{fft}}\frac{\log_2(M)}{2}$ bits form a sub-block, which will be referred to as B_{QAM}. Fig. 3.1 illustrates this. B_{OOK} is inspected and the majority bit type is determined by checking which bit value, 1 or 0, has more occurrences. All subcarriers which have the same relative position inside the OFDM frame as the bits from the majority bit type inside B_{OOK} are classified as *active*, and the rest are classified as *inactive*. *Inactive* subcarriers are assigned the amplitude value $0 + 0\text{j}$. The first $\frac{N_{\text{fft}}}{2}$ *active* subcarriers are assigned amplitude values corresponding to the M-QAM constellation symbols necessary to encode B_{QAM}. The

37
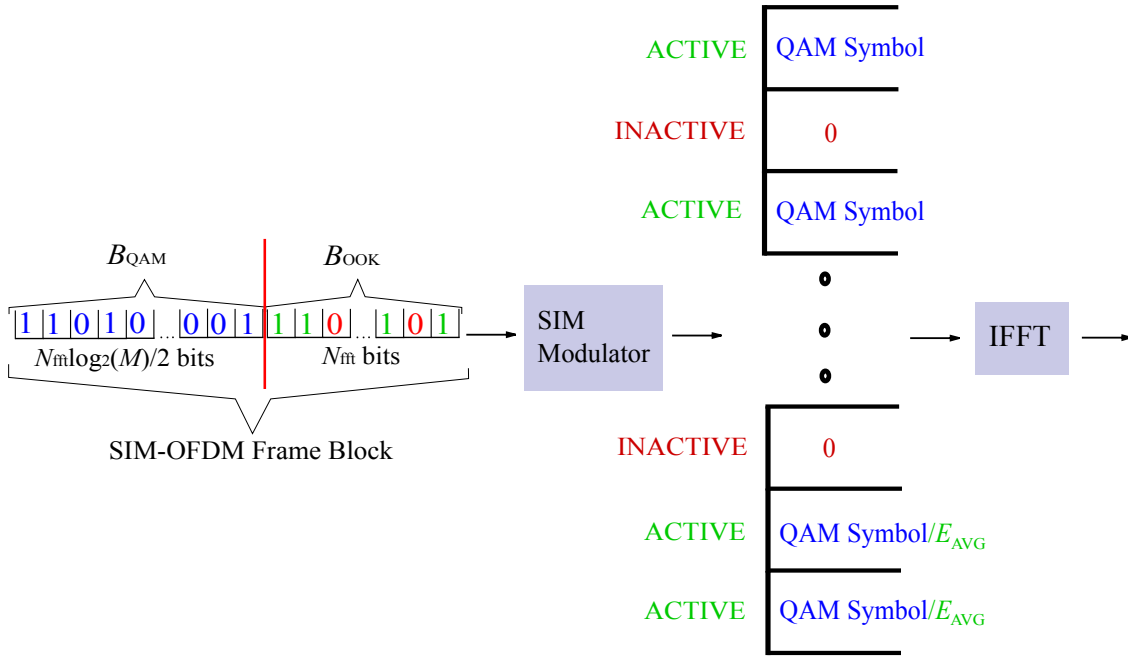
Figure 3.1: *SIM-OFDM subcarrier mapping [82]. In this example, it is assumed that 1 is the majority bit in B_{OOK}. The average energy per M-QAM symbol allocated to excess active subcarriers is denoted by E_{avg}.*

remaining *active* subcarriers are *excess* subcarriers and can be used to signal to the destination the majority bit type of B_{OOK}. They are assigned a value whose energy is equal to the average energy for the given M-QAM scheme. Afterwards, an N_{fft}-point inverse fast Fourier transform (IFFT) operation is performed in order to obtain the time-domain signal, which is transmitted as in conventional OFDM. A slight modification of SIM-OFDM suggests that majority bit type can be signalled either through secure communication channels, or by reserving one particular frequency subcarrier and transmitting the desired value with sufficiently high SNR. In the context of this work, it is assumed that either one of these modifications is employed, and the majority bit type is known at the demodulator. This assumption is considered fair as the majority bit type needs to be signalled once for every SIM-OFDM frame, which for a large N_{fft} requires very little overhead compared to the overall data-rate. Furthermore, such assumption simplifies the analysis tremendously without affecting the achievable BER significantly. It should be noted that in the provided SIM-OFDM description, it is assumed that all subcarriers in the OFDM frame can be used to encode information. In case only a subset of the subcarriers can be utilised, due to frequency-dependent noise or severe channel attenuation in certain frequency bands, the concept

can be easily extended only to those subcarriers that allow reliable communication by omitting the faulty subcarriers. The size of B_{OOK} and B_{QAM} as well as any other relevant parameters would change accordingly. It should also be noted that according to the authors in [82], this modulation scheme can be realised in two configurations: 1) power saving policy (PSP) where the power of the *inactive* subcarriers is saved; and 2) power reallocation policy (PRP) where the unused power from the *inactive* subcarriers is reallocated to the *active* ones, which leads to performance enhancement. A typical OFDM-based communication system implementation would be able to deliver a modulation signal with a range of arbitrary energy levels, which means that a definition of two energy configurations such as PSP and PRP is obsolete from a signal generation perspective. Furthermore, by convention, a fair BER comparison between the energy efficiency of two different modulation schemes requires the use of equal energy per bit as assumed in the rest of this work. In that sense, the two power policies introduced in [82] are not necessarily fair.

Once a signal is received at the destination, it is transformed into the frequency domain with a fast Fourier transform (FFT) operation. Then all subcarriers are inspected. Those, whose energy is above a certain threshold, are marked as *active*, and the rest are marked as *inactive*. It is certain that at least half of the total number of subcarriers need to be detected as *active*. Hence, in case less than $\frac{N_{\text{fft}}}{2}$ *active* subcarriers are detected, the threshold value is decreased by a small step and the inspection is performed again. This procedure is conducted iteratively until at least $\frac{N_{\text{fft}}}{2}$ *active* subcarriers are detected. Then, B_{OOK} is reconstructed from the detected states of the subcarriers and the known majority bit type. Afterwards, the first $\frac{N_{\text{fft}}}{2}$ *active* subcarriers are demodulated according to the respective M-QAM scheme in order to reconstruct B_{QAM}.

3.2.2   Theoretical Bit-error Rate (BER) Analysis

The BER derivation presented in this section is developed under three assumptions. First, the number of OFDM subcarriers, N_{fft}, is large enough, so that the number of *active excess* subcarriers, which do not encode M-QAM symbols, on average, is a very small portion of the overall number of subcarriers. Hence, the performance analysis of the excess subcarriers does not need to be conducted separately from the analysis of the subcarriers which encode M-QAM information. Any inaccuracy is insignificant as confirmed by the Monte Carlo simulations in the presented results. Second, the magnitude of the employed threshold is smaller than the energy

of the M-QAM constellation point with the lowest energy. Otherwise, the constellation points, whose energy is below the threshold by default, would not be recognisable even in high signal-to-noise ratio (SNR) conditions. This would lead to an error floor above zero. The third assumption states that the bit value encoded by the *active* subcarriers, *i.e.* the majority bit value in B_{OOK}, is known at the decoder. It might be passed via the secured communication channels or on a specially-assigned subcarrier in the OFDM frame using OOK with high SNR.

Let k be a variable indicating the position of a subcarrier in the SIM-OFDM frame. The random variable b_k indicates the value of the corresponding bit in B_{OOK}. The probabilities related to b_k are:

$$\mathrm{P}\{b_k = 0\} = P_0 = \frac{1}{2}, \tag{3.1}$$

$$\mathrm{P}\{b_k = 1\} = P_1 = \frac{1}{2}. \tag{3.2}$$

The random variable a_k indicates whether a subcarrier at position k is *active*, indicated by the value 1, or *inactive*, indicated by the value 0. The random variable $m_{\mathrm{b}}=1$ indicates that the majority bits have the value 1 and $m_{\mathrm{b}}=0$ indicates that the majority bits have the value 0. The probabilities related to these two random variables are:

$$P_{\mathrm{m1}} = \mathrm{P}\{m_{\mathrm{b}} = 1|b_k = 1\} = \sum_{i=\frac{N_{\mathrm{fft}}}{2}-1}^{N_{\mathrm{fft}}-1} \binom{N_{\mathrm{fft}}-1}{i} \left(\frac{1}{2}\right)^{N_{\mathrm{fft}}-1}, \tag{3.3}$$

$$P_{\mathrm{m0}} = \mathrm{P}\{m_{\mathrm{b}} = 0|b_k = 0\} = \sum_{i=\frac{N_{\mathrm{fft}}}{2}}^{N_{\mathrm{fft}}-1} \binom{N_{\mathrm{fft}}-1}{i} \left(\frac{1}{2}\right)^{N_{\mathrm{fft}}-1}, \tag{3.4}$$

$$P\{a_k = 1\} = P_1 P_{\mathrm{m1}} + P_0 P_{\mathrm{m0}}, \tag{3.5}$$

$$P\{a_k = 0\} = 1 - P\{a_k = 1\}. \tag{3.6}$$

The variable d_k indicates whether the detection of the kth subcarrier is correct, indicated by 1, or incorrect, indicated by 0. If $a_k = 0$, then the received signal distribution on subcarrier k looks as depicted in Fig. 3.2(a). The mean value $0 + 0j$ corresponds to the transmitted constellation point for an *inactive* subcarrier and the Gaussian variation around it is caused by the AWGN in the receiver system.The red circle marks all points in the complex two-dimensional (2D) space whose energy is equal to the threshold. Equations (3.7) and (3.8) express the detection probabilities for this case in mathematical form; $\sigma_{\mathrm{n}}^2 = BN_{\mathrm{o}}$ is the variance of the AWGN, where B is

the communication bandwidth and N_{o} is the noise power spectral density (PSD), and v_{t} is the threshold value.

(a) *Inactive* subcarrier: $0 + 0j$ transmitted   (b) *Active* subcarrier: $1 + j$ transmitted
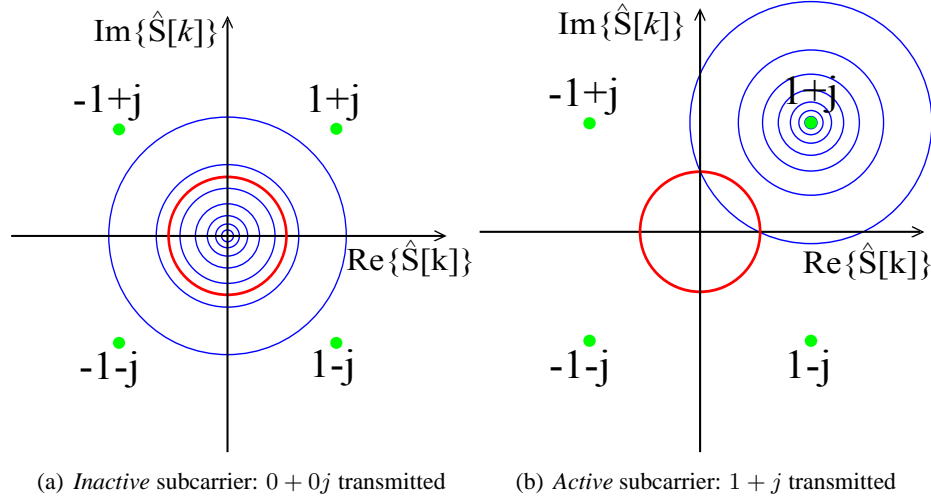
Figure 3.2: *Contour lines of the distribution of the received subcarrier value, $\hat{\mathrm{S}}[k]$, as a function of the transmitted constellation symbol. This specific example depicts a 4-QAM constellation. Lines are not drawn to scale.*

$$\mathrm{P}\{d_k = 1 | a_k = 0\} =$$
$$= \int_{-\sqrt{v_{\mathrm{t}}}}^{\sqrt{v_{\mathrm{t}}}} \int_{-\sqrt{v_{\mathrm{t}} - y^2}}^{\sqrt{v_{\mathrm{t}} - y^2}} \frac{1}{\pi \sigma_{\mathrm{n}}^2} \mathrm{e}^{-\frac{(x)^2 + (y)^2}{\sigma_{\mathrm{n}}^2}} \, \mathrm{d}x \mathrm{d}y =$$
$$= \int_0^{2\pi} \int_0^{\sqrt{v_{\mathrm{t}}}} \frac{1}{\pi \sigma_{\mathrm{n}}^2} \mathrm{e}^{-\frac{r^2}{\sigma_{\mathrm{n}}^2}} r \mathrm{d}r \mathrm{d}\theta =$$
$$= 1 - \mathrm{e}^{-\frac{v_{\mathrm{t}}}{\sigma_{\mathrm{n}}^2}} \tag{3.7}$$

$$\mathrm{P}\{d_k = 0 | a_k = 0\} = 1 - \mathrm{P}\{d_k = 1 | a_k = 0\} \tag{3.8}$$

In case $a_k = 1$, then the received signal distribution is depicted in Fig. 3.2(b). The 2D Gaussian distribution is centred at the transmitted symbol. This occurs with equal probability for each M-QAM constellation point. Hence, in order to calculate the detection error probability, the noise probability density function (PDF) needs to be integrated within the red circle for each point in the M-QAM constellation as its mean value. Then a weighted sum of all results is taken in order to obtain the average detection error probability for an active subcarrier. Equations (3.9) and

41

(3.10) express the related calculations for this case; μ_i indicates constellation point number i.

$$P\{d_k = 0 | a_k = 1\} =$$

$$= \frac{1}{M} \sum_{i=1}^{M} \int_{-\sqrt{v_{\mathrm{t}}}}^{\sqrt{v_{\mathrm{t}}}} \int_{-\sqrt{v_{\mathrm{t}}-y^2}}^{\sqrt{v_{\mathrm{t}}-y^2}} \frac{1}{\pi\sigma_{\mathrm{n}}^2} \mathrm{e}^{-\frac{(x - \mathrm{Re}\{\mu_i\})^2 + (y - \mathrm{Im}\{\mu_i\})^2}{\sigma_{\mathrm{n}}^2}} \mathrm{d}x\mathrm{d}y \qquad (3.9)$$

$$P\{d_k = 1 | a_k = 1\} = 1 - P\{d_k = 0 | a_k = 1\} \qquad (3.10)$$

After a frame passes through the demodulator, each subcarrier can be classified in one of four categories:

- True *active* (ta) - A subcarrier is *active* and recognized as such.

- False *inactive* (fi) - A subcarrier is *active* but recognized as *inactive*.

- True *inactive* (ti) - A subcarrier is *inactive* and recognized as such.

- False *active* (fa) - A subcarrier is *inactive* but recognized as *active*.

With the probabilities of *active*/*inactive* subcarriers and the probabilities of correct/false detection available, the following four probabilities can be derived for each demodulated subcarrier:

$$P_{\mathrm{ta}} = P\{d_k = 1 | a_k = 1\} P\{a_k = 1\} \qquad (3.11)$$

$$P_{\mathrm{fi}} = P\{d_k = 0 | a_k = 1\} P\{a_k = 1\} \qquad (3.12)$$

$$P_{\mathrm{ti}} = P\{d_k = 1 | a_k = 0\} P\{a_k = 0\} \qquad (3.13)$$

$$P_{\mathrm{fa}} = P\{d_k = 0 | a_k = 0\} P\{a_k = 0\} \qquad (3.14)$$

In case $P_{\mathrm{fa}} > P_{\mathrm{fi}}$, then for a large N_{fft} it is almost certain that for the majority of cases more than $\frac{N_{\mathrm{fft}}}{2}$ *active* subcarriers will be detected. Hence, the threshold value will almost never need to be readjusted during the demodulation process. In case $P_{\mathrm{fa}} < P_{\mathrm{fp}}$, then for the majority of cases the threshold value will need to be readjusted by the algorithm. Hence, it is safe to assume that a single threshold value - the first one which causes $P_{\mathrm{fa}} > P_{\mathrm{fi}}$ - can be used for analysing the system performance. A comparison between P_{fa} and P_{fi} can be used to determine whether a given initial threshold value would be effective or it would get readjusted by the demodulation algorithm.

Based on the different cases for correct and wrong detection, the BER in each subcarrier can be determined and hence its contribution towards the overall BER. As described before, the *active/inactive* state of each subcarrier encodes a bit in an OOK fashion. Then, the contribution of each subcarrier towards the overall BER coming from the encoding of B_{OOK} is expressed as:

$$\text{OB}_k = ((P_{\text{ta}} + P_{\text{ti}})P_{\text{mi}} + (P_{\text{fa}} + P_{\text{fi}})P_{\text{mc}})\frac{2}{N_{\text{fft}}\left(\log_2(M) + 2\right)}, \qquad (3.15)$$

where P_{mc} stands for the probability that the majority bit type in B_{OOK} is correctly determined at the decoder, and P_{mi} stands for the probability that the majority bit type is incorrectly determined. The final factor in the equation, $\frac{2}{N_{\text{fft}}(\log_2(M)+2)}$, comes from the fact that there are $N_{\text{fft}}\left(\frac{\log_2(M)}{2} + 1\right)$ bits in the entire frame. Whenever, the subcarrier is correctly identified as *active/inactive*, but the majority bit type is incorrect, the bit at this position in B_{OOK} is wrong, and hence its overall contribution to the BER, OB_k, is 1 out of $N_{\text{fft}}\left(\frac{\log_2(M)}{2} + 1\right)$. The same occurs when the subcarrier is incorrectly identified as *active/inactive*, and the majority bit type is correctly identified. As mentioned before, in this analysis it is assumed that the majority bit type is transmitted independently of the rest of the frame. Hence P_{mc} and P_{mi} are dependant on the method by which they are conveyed to the destination. In this work this is considered insignificant and it is assumed that $P_{\text{mc}} = 1$ and $P_{\text{mi}} = 1 - P_{\text{mc}} = 0$.

The analysis of the BER in B_{OOK} is rather trivial since it resembles regular OOK modulation. However, the analysis of B_{QAM} is more complicated. According to the description in section 3.2.1, it is guaranteed by the modulation scheme that at least $\frac{N_{\text{fft}}}{2}$ active subcarriers will be modulated with an M-QAM symbol. Therefore, for the first $\frac{N_{\text{fft}}}{2}$ subcarriers it is certain that any active subcarrier carries M-QAM information. If a subcarrier is incorrectly determined as *active*, this leads to M-QAM demodulation of a random value, which means that an average of $\frac{1}{2}$ of the demodulated bits will be wrong for the M-QAM symbol attributed to that subcarrier. In case a subcarrier is correctly identified as *active*, two possible cases can occur. In one case, a detection error has been made in any of the previous subcarriers in the frame. This means that the bits decoded for the current subcarrier are misplaced in B_{QAM}. This can be avoided if an equal number of false *active* as well as false *inactive* previous subcarriers have been detected, but the probability for that happening is assumed low and hence not considered for the sake of simplicity. Therefore, the only possibility for the current bits to be in their correct place in B_{QAM} is considered to be when no detection errors have been made for previous subcarriers. Probability for this to happen

is expressed by:

$$P_{\mathrm{ne}_k} = (P_{\mathrm{ta}} + P_{\mathrm{ti}})^{k-1}$$
$$\text{where } k = 1, ..., \frac{N_{\mathrm{fft}}}{2}. \tag{3.16}$$

The value of the correctly detected active subcarrier is demodulated as an M-QAM symbol and the BER is as in the respective M-QAM modulation scheme. The contribution of this case to the BER at subcarrier k is expressed as:

$$\mathrm{QB1}_k = P_{\mathrm{ne}_k} P_{\mathrm{ta}} \mathrm{BER}_{\mathrm{MQAM}} \left(\frac{E_{\mathrm{b}}}{N_{\mathrm{o}}} \right) \frac{2 \log_2(M)}{N_{\mathrm{fft}}(\log_2(M) + 2)}$$
$$\text{where } k = 1, ..., \frac{N_{\mathrm{fft}}}{2}. \tag{3.17}$$

The factor $\frac{2 \log_2(M)}{N_{\mathrm{fft}}(\log_2(M)+2)}$ comes from the fact that $\log_2(M)$ bits are being demodulated and the total number of bits is $\frac{N_{\mathrm{fft}}(\log_2(M)+2)}{2}$; $\mathrm{BER}_{\mathrm{MQAM}}(E_{\mathrm{b}}/N_{\mathrm{o}})$ stands for the BER coming from the respective M-QAM modulation scheme for which a closed-form expression is provided in [84]. The BER in the other two previously described cases – when a detection error has been made for a previous subcarrier and when the current subcarrier is incorrectly identified as *active* – is expressed as:

$$\mathrm{QB2}_k = ((1 - P_{\mathrm{ne}_k})P_{\mathrm{ta}} + P_{\mathrm{fa}}) \frac{\log_2(M)}{N_{\mathrm{fft}}(\log_2(M) + 2)}$$
$$\text{where } k = 1, ..., \frac{N_{\mathrm{fft}}}{2}. \tag{3.18}$$

In this equation, it is assumed that on average half of the decoded bits are wrong.

The analysis for the subcarriers at position $k > \frac{N_{\mathrm{fft}}}{2}$ is similar to the one for the subcarriers at position $k \leq \frac{N_{\mathrm{fft}}}{2}$. In this case, however, it is also necessary to check for the probability that less than $\frac{N_{\mathrm{fft}}}{2}$ *active* subcarriers have been detected at previous positions, since only the first $\frac{N_{\mathrm{fft}}}{2}$ *active* subcarriers are modulated with an M-QAM signal and actually have a contribution to the BER in B_{QAM}. Equation (3.19) expresses the probability, P_{qc_k}, that less than $\frac{N_{\mathrm{fft}}}{2}$ *active* subcarriers have been detected up to the subcarrier at position k for $k > \frac{N_{\mathrm{fft}}}{2}$. Equation (3.20) expresses the probability, P_{qcne_k}, that less than $\frac{N_{\mathrm{fft}}}{2}$ *active* subcarriers have been detected up to subcarrier k without any detection errors. The distinction between the two cases is made because detection errors in previous subcarriers, as stated before, inevitably lead to errors in the bits carried by

the current subcarrier since they are misplaced in B_{QAM}. The separate contributions of a single subcarrier k to the BER in B_{QAM} is expressed in equations (3.21) and (3.22). The total BER contribution of a subcarrier to B_{QAM} is expressed in equation (3.23).

$$P_{\text{qc}_k} = \sum_{i=\frac{N_{\text{fft}}}{2}+k-N_{\text{fft}}-1}^{\frac{N_{\text{fft}}}{2}-1} \binom{k-1}{i}(P_{\text{ta}} + P_{\text{fa}})^i(P_{\text{ti}} + P_{\text{fi}})^{k-1-i}$$
$$\text{where } k = \frac{N_{\text{fft}}}{2} + 1, ..., N_{\text{fft}} \tag{3.19}$$

$$P_{\text{qcne}_k} = \sum_{i=\frac{N_{\text{fft}}}{2}+k-N_{\text{fft}}-1}^{\frac{N_{\text{fft}}}{2}-1} \binom{k-1}{i}(P_{\text{ta}})^i(P_{\text{ti}})^{k-1-i}$$
$$\text{where } k = \frac{N_{\text{fft}}}{2} + 1, ..., N_{\text{fft}} \tag{3.20}$$

$$\text{QB1}_k = P_{\text{qcne}_k} P_{\text{ta}} \text{BER}_{\text{MQAM}}\left(\frac{E_{\text{b}}}{N_{\text{o}}}\right)\frac{2\log_2(M)}{N_{\text{fft}}(\log_2(M)+2)}$$
$$\text{where } k = \frac{N_{\text{fft}}}{2} + 1, ..., N_{\text{fft}} \tag{3.21}$$

$$\text{QB2}_k = ((P_{\text{qc}_k} - P_{\text{qcne}_k})P_{\text{ta}} + P_{\text{qc}}P_{\text{fa}})\frac{\log_2(M)}{N_{\text{fft}}(\log_2(M)+2)}$$
$$\text{where } k = \frac{N_{\text{fft}}}{2} + 1, ..., N_{\text{fft}} \tag{3.22}$$

$$\text{QB}_k = \text{QB1}_k + \text{QB2}_k \tag{3.23}$$

The overall contribution of subcarrier k to the BER is:

$$\text{BER}_k = \text{QB}_k + \text{OB}_k. \tag{3.24}$$

The BER of the system is a sum of the individual BER_k and is expressed as:

$$\text{BER} = \sum_{k=1}^{N_{\text{fft}}} \text{BER}_k. \tag{3.25}$$

For a system under PRP a simple modification of the equations can be adopted in order to closely

45

(a) PSP

(b) PRP
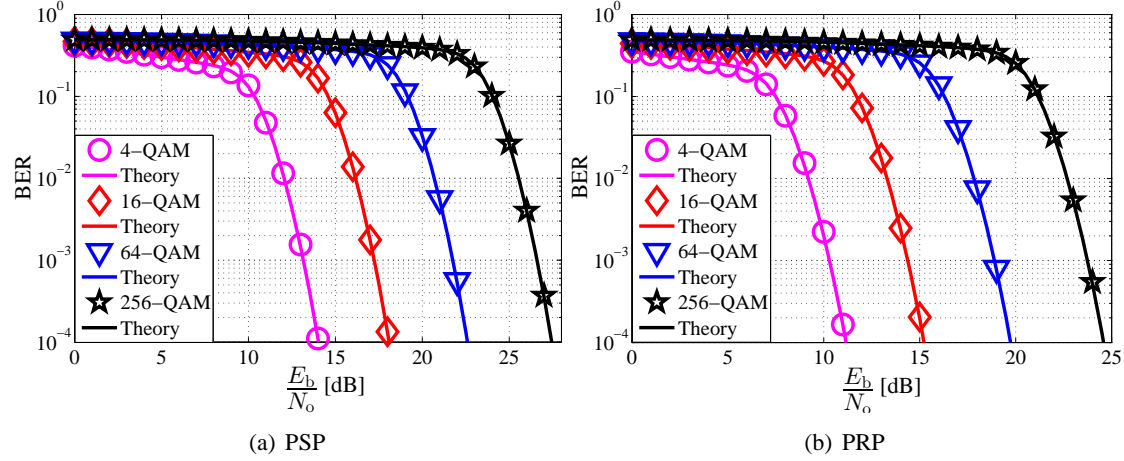
Figure 3.3: *Comparison between theoretical analysis and Monte Carlo simulations for: a) Power saving policy (PSP); and b) Power reallocation policy (PRP).*

approximate the performance. If a large number of subcarriers N_{fft} is used, the assumption can be made that most of the vector realizations of B_{OOK} will be typical sequences. Hence, the number of *active* and *inactive* subcarriers in most signal realisations will be close to the average number of *active* and *inactive* subcarriers. From that, a constant shift of

$$10 \log_{10} \left(1 + \text{P}\{a_k = 0\}/\text{P}\{a_k = 1\}\right) \tag{3.26}$$

can be applied to all BER curves which would produce an accurate approximation of the system performance under PRP.

3.2.3 Results and Discussion

The current section provides a verification of the proposed theoretical analysis through Monte Carlo simulations. In addition, the performance of SIM-OFDM in comparison to conventional OFDM is discussed. The numerical simulations of the SIM-OFDM system are performed with $N_{\text{fft}} = 512$ subcarriers. The Monte Carlo simulation results in comparison to the theoretical model are presented in Fig. 3.3(a) for the PSP and in Fig. 3.3(b) for the PRP. Theoretical results match numerical results quite well, thus, confirming the validity of the analysis from Section 3.2.2. The threshold value, which is used, is half the energy of the M-QAM symbol with the lowest energy. As stated before, it is assumed that the majority bit type in B_{OOK} is known at the demodulator *i.e.* P_{mc}=1 in equation (3.15).
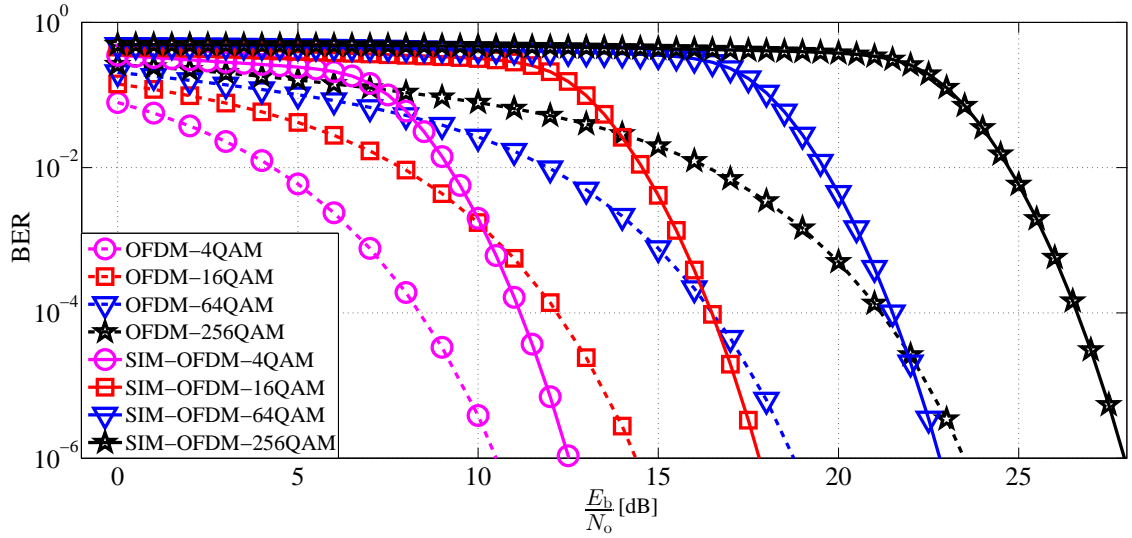
Figure 3.4: *Comparison between the performance of SIM-OFDM and conventional M-QAM OFDM for $M = 4, 16, 64, 256$.*

The performance of SIM-OFDM presented in Fig. 3.3(a) and Fig. 3.3(b) is not fairly estimated. The x-axes of these figures present the SNR in terms of the energy per bit allocated to each M-QAM symbol as in conventional OFDM. However, this does not take into account the fact that a portion of the bits, those contained in B_{OOK}, are encoded by the subcarrier states and not in the complex amplitudes of the subcarriers. For the PSP policy, each frequency subcarrier has the energy corresponding only to the bits encoded in B_{QAM}, in agreement with the original PSP description of the scheme provided in [82]. Thus, the actual $\frac{E_b}{N_o}$ ratio in SIM-OFDM is lower than presented. This is unfair to the SIM-OFDM system. The PRP policy, on the other hand, is only fair for a 4-QAM SIM-OFDM system which has the same spectral efficiency and power as in a conventional OFDM implementation where all subcarriers are fully loaded with 4-QAM. As the order of the M-QAM modulation grows, however, the PRP policy also becomes unfair, but in favour of SIM-OFDM since the spectral efficiency of SIM-OFDM is lower than the spectral efficiency of a fully loaded OFDM frame. Hence, for a fair comparison between SIM-OFDM and OFDM, a fair assessment of the system energy has to be made such that the $\frac{E_b}{N_o}$ ratio is accurate and fair for both systems. Such a comparison is presented in Fig. 3.4. The presented results clearly indicate that SIM-OFDM cannot outperform conventional OFDM in terms of energy efficiency for any given constellation size.

Based on the analysis conducted in Section 3.2.2, two main issues which limit the performance

of SIM-OFDM can be identified. First, an OOK detector at the destination requires the usage of a threshold. The threshold has to be lower than the lowest-energy M-QAM symbol. Otherwise, any symbols with energy below the threshold would not be detected even in high-SNR conditions and this would lead to an error floor above zero. At the same time, a low threshold requirement diminishes the advantage of the OOK encoding when a higher order M-QAM scheme is used. This occurs because even though, on average, a lot of energy is used in a subcarrier for higher order M-QAM, the threshold needs to remain low and below the smallest symbol energy. Hence, the system's ability to correctly distinguish subcarrier states does not improve significantly with an increase of the constellation size since the threshold cannot change significantly. Second, an incorrect detection of a subcarrier state not only leads to incorrect demodulation of the M-QAM symbol it encodes, but also to incorrect demodulation of all subsequent M-QAM symbols. This happens because an incorrect detection of a subcarrier state changes the order in B_{QAM} and misplaces all subsequent bits in that part of the frame. This effect has the most significant impact on the BER performance. Effectively, in order to demodulate an M-QAM symbol correctly, it is necessary not only to detect its subcarrier as *active*, but also to have detected any previous subcarrier states – *active* or *inactive* – correctly. As the total number of subcarriers, N_{fft}, increases, the issue becomes worse. The rest of this chapter proposes a solution to these two problems.

3.3 Enhanced Subcarrier-Index Modulation (SIM) OFDM

3.3.1 Concept

As described in Section 3.2.3, the error propagation effect in SIM-OFDM becomes worse as the number of subcarriers N_{fft} grows. This means that the best performance can be obtained when $N_{\mathrm{fft}} = 2$, which is the minimum number of subcarriers for a non-trivial OFDM frame size. A small SIM-OFDM frame size, however, is impractical due to the overhead from the cyclic prefix and the overhead for signalling the majority bit type to the receiver. Therefore, a solution needs to be developed to limit the error-propagation effect in SIM-OFDM irrespective of the frame size. A slight modification in the way B_{OOK} is encoded can achieve the desired effect. Instead of each bit from B_{OOK} being encoded in a single subcarrier state, it can be encoded in the states of two consecutive subcarriers – a subcarrier pair. Fig. 3.5 illustrates the principle of the new encoding scheme. Whenever a 1 is encountered in B_{OOK}, the first subcarrier of the pair is set as *active* and the second one as *inactive*. Whenever a 0 is encountered in B_{OOK}, the first subcarrier
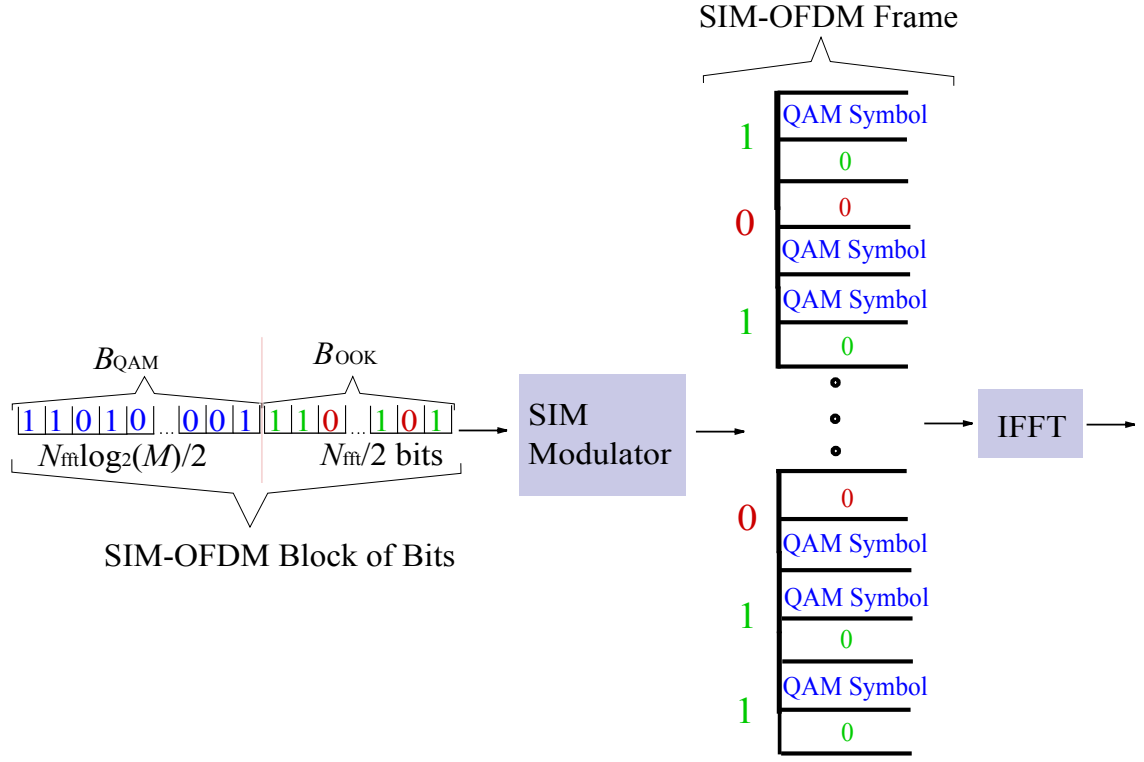
Figure 3.5: *Enhanced SIM-OFDM modulation.*

of the pair is set as *inactive* and the second one as *active*. In this configuration, the size of B_{OOK} which can be represented by the subcarrier states is $\frac{N_{\text{fft}}}{2}$ – half the size than in the original SIM-OFDM scheme. The important difference in this case, however, is that for each pair it is certain that exactly one of the subcarriers is *active*. This means that bits from B_{QAM} cannot be misplaced due to wrong detection of previous subcarrier states. The error is contained within each pair of subcarriers. In addition, bit-majority information for B_{OOK} is not required, and the total number of active subcarriers is constant – $\frac{N_{\text{fft}}}{2}$. A threshold also is not required for the OOK detection. Instead, the subcarrier with higher energy within the pair can be recognised as *active*. The only disadvantage of the enhanced modulation scheme, compared to the original introduced SIM-OFDM, is the slightly reduced spectral efficiency. The spectral efficiency of SIM-OFDM is:

$$\eta_{\text{SIM-OFDM}} = \frac{(\log_2(M)/2 + 1)N_{\text{fft}}}{N_{\text{fft}} + N_{\text{cp}}}, \tag{3.27}$$

while the spectral efficiency of the enhanced SIM-OFDM is:

$$\eta_{\text{SIM}-\text{OFDM}}^{\text{E}} = \frac{(\log_2(M)/2 + 1/2)N_{\text{fft}}}{N_{\text{fft}} + N_{\text{cp}}} \tag{3.28}$$

The spectral efficiency of a complex M-QAM OFDM signal is $\log_2(M)N_{\text{fft}}/(N_{\text{fft}} + N_{\text{cp}})$. It should be noted that the spectral efficiency overhead of the Hermitian symmetry required for the generation of a real signal is not included in the presented spectral efficiency calculations since the SIM-OFDM concept is also applicable to radio frequency (RF) communication. In case a real SIM-OFDM signal is required, the Hermitian symmetry imposed in the frequency domain would further decrease all presented spectral efficiency values in this chapter by a factor of $(N_{\text{fft}} - 2)/(2N_{\text{fft}})$.

The spectral efficiency of the enhanced SIM-OFDM concept can be increased if the subcarrier pairs are expanded to blocks with a total number of subcarriers $N_{\text{B}} > 2$ out of which N_{A} subcarriers are *active* and encode M-QAM information. For example, if $N_{\text{B}} = 8$ is used, there are 70 combinations in which $N_{\text{A}} = 4$ subcarriers are *active*. Therefore, a total of 6 bits ($2^6 = 64 < 70$) from B_{OOK} can be encoded by combinations of *active* subcarriers in a block of $N_{\text{B}} = 8$ subcarriers. This already yields a better spectral efficiency than in (3.28). A generalised expression for the spectral efficiency is:

$$\eta_{\text{SIM}-\text{OFDM}}^{\text{GENERAL}} = \left(\frac{N_{\text{A}}\log_2(M)}{N_{\text{B}}} + \frac{\left\lfloor \log_2\left(\frac{N_{\text{B}}!}{N_{\text{A}}!(N_{\text{B}}-N_{\text{A}})!} \right) \right\rfloor}{N_{\text{B}}} \right) \frac{N_{\text{fft}}}{N_{\text{fft}} + N_{\text{cp}}} \tag{3.29}$$

The closer N_{A} is to N_{B}, the closer is the system spectral efficiency to conventional OFDM. If N_{A} approaches 1, the system starts to resemble pulse-position modulation (PPM). As N_{B} approaches N_{fft}, and N_{A} approaches $\frac{N}{2}$, the system's spectral efficiency gets closer to the spectral efficiency of the original SIM-OFDM.

3.3.2 Theoretical Bit-error-rate Analysis

The BER derivation presented in this section describes the operation of the enhanced SIM-OFDM system for $N_{\text{A}} = 1$ and $N_{\text{B}} = 2$ in a linear AWGN channel. Analysis for a different combination of N_{A} and N_{B} can be conducted in an analogous manner. No fading is assumed since it is not an issue in scenarios related to optical wireless communications (OWC) for which SIM-OFDM is primarily considered. There is no dependence between the different subcarrier pairs in the enhanced SIM-OFDM frame. Therefore, the BER analysis of a single subcarrier pair that follows
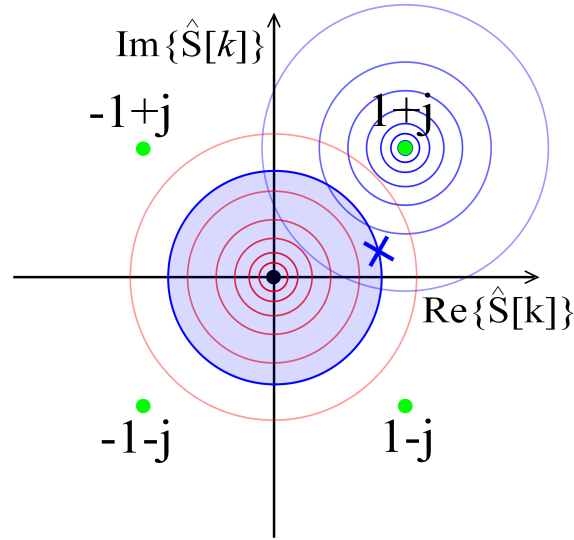
Figure 3.6: *Contour lines of the distribution of the received subcarrier pair as a function of the transmitted constellation symbol. Lines are not drawn to scale.*

applies to the entire system.

At the receiver side, each subcarrier pair is corrupted by AWGN. Hence, the distributions of both received subcarrier values resemble the example illustrated in Fig. 3.6. The '×' sign marks a possible value of the received *active* subcarrier $\hat{S}[k]$. In this case, all values, which the *inactive* subcarrier may take and still be correctly recognized as *inactive*, are contained inside the thick blue circle. Hence, integrating the Gaussian distribution, centred at 0, inside the thick blue circle gives the probability for correctly distinguishing between the *inactive* and *active* subcarrier in the pair. Using some results from [85], this integration can be represented as:

$$P\{d_k = 1 | \hat{S}[k] = x + jy\} =$$
$$= \int_{-\sqrt{|x+jy|^2}}^{\sqrt{|x+jy|^2}} \int_{-\sqrt{|x+jy|^2-b^2}}^{\sqrt{|x+jy|^2-b^2}} \frac{1}{\pi\sigma_n^2} e^{-\frac{(a)^2+(b)^2}{\sigma_n^2}} \mathrm{d}a\mathrm{d}b$$
$$\overset{[85]}{=} \int_0^{2\pi} \int_0^{\sqrt{|x+jy|^2}} \frac{1}{\pi\sigma_n^2} e^{-\frac{r^2}{\sigma_n^2}} r\mathrm{d}r\mathrm{d}\theta$$
$$= 1 - e^{-\frac{|x+jy|^2}{\sigma_n^2}}, \tag{3.30}$$

where $d_k = 1$ when the subcarriers are correctly distinguished, and $d_k = 0$ when they are not. The variable $\hat{S}[k]$ stands for the complex value of the received *active* subcarrier, and $\sigma_n^2 = BN_o$ stands for the variance of the AWGN. Equation (3.31) expresses the probability density that the

value of the *active* subcarrier takes the value $x + \mathrm{j}y$. There is an equal probability, $\frac{1}{M}$, that the original value of the subcarrier, before the addition of the AWGN, is equal to any one of the M constellation points. Hence, the probability density that the subcarrier value at the receiver is equal to $x + \mathrm{j}y$ is expressed as a weighted sum of M different probability densities coming from the Gaussian functions centred at the M constellation points:

$$P\{\hat{S}[k] = x + \mathrm{j}y\} =$$

$$= \frac{1}{M} \sum_{i=1}^{M} \frac{1}{\pi \sigma_{\mathrm{n}}^2} e^{-\frac{(x - \mathrm{Re}\{\mu_i\})^2 + (y - \mathrm{Im}\{\mu_i\})^2}{\sigma_{\mathrm{n}}^2}} \tag{3.31}$$

Symbol μ_i marks constellation point number i while $\mathrm{Re}\{\mu_i\}$ and $\mathrm{Im}\{\mu_i\}$ denote the real and imaginary part of μ_i, respectively. Equation (3.32) expresses the probability for correctly determining the *active* and the *inactive* subcarrier in a pair. Equation (3.33) expresses the complementary probability – that the *active* and the *inactive* subcarrier are incorrectly determined.

$$P\{d_k = 1\} = \int_{-\infty}^{\infty} \int_{-\infty}^{\infty} P\{d_k = 1 | \hat{S}[k] = x + \mathrm{j}y\} P\{\hat{S}[k] = x + \mathrm{j}y\} \mathrm{d}x\mathrm{d}y$$

$$= 1 - \frac{1}{2M} \sum_{i=1}^{M} e^{-\frac{|\mu_i|^2}{2\sigma_{\mathrm{n}}^2}} \tag{3.32}$$

$$P\{d_k = 0\} = 1 - P\{d_k = 1\} \tag{3.33}$$

Based on the calculated detection probabilities, the BER performance for the system can be calculated. When the subcarrier states are incorrectly detected, the bit from B_{OOK}, which they encode, is erroneous. That bit amounts to $\frac{1}{\log_2(M)+1}$ of all the bits encoded in a subcarrier pair. Hence, the contribution of B_{OOK} to the BER is expressed as:

$$\mathrm{BER}_{B_{\mathrm{OOK}}} = P\{d_k = 0\} \frac{1}{\log_2(M) + 1}. \tag{3.34}$$

A wrong detection of a subcarrier state leads to M-QAM demodulation of an unmodulated subcarrier, which adds additional errors to the frame. Such an event occurs with very high probability in the four M-QAM symbols closest to 0. Probability for wrong detection of any other symbol in the constellation is low in comparison. The four symbols closest to 0 encode bits which differ by only one bit on average when the M-QAM constellation is Gray-mapped. Hence, in the majority of cases only 1 bit is wrong in B_{QAM} for wrong subcarrier detection. This assumption might not hold in low-SNR regions, however, for SNR values of practical interest, it appears to be

correct, as confirmed by the results presented in the next section. Hence, the first part of the BER contribution of B_{QAM} is the same as the BER contribution of (3.34). If a subcarrier state is correctly identified, there still exists the possibility that the M-QAM demodulation leads to errors. This effect is characterised by the well-known BER analysis for M-QAM, $\mathrm{BER}_{\mathrm{MQAM}}(\mathrm{E_b}/\mathrm{N_o})$, presented in [84]. It can be used in order to complete $\mathrm{BER}_{B_{\mathrm{QAM}}}$ which is the contribution of B_{QAM} to the overall BER. The final factor indicates that the bits encoded by M-QAM symbols are $\frac{\log_2(M)}{\log_2(M)+1}$ of all the bits encoded in a subcarrier pair:

$$\mathrm{BER}_{B_{\mathrm{QAM}}} = \mathrm{P}\{d_k = 0\}\frac{1}{\log_2(M)+1} + \mathrm{P}\{d_k = 1\}\mathrm{BER}_{\mathrm{MQAM}}\left(\frac{E_{\mathrm{b}}}{N_{\mathrm{o}}}\right)\frac{\log_2(M)}{\log_2(M)+1}. \quad (3.35)$$

The final expression for the BER of the enhanced SIM-OFDM system is as follows:

$$\mathrm{BER}_{\mathrm{SIM-OFDM}} = \mathrm{BER}_{B_{\mathrm{OOK}}} + \mathrm{BER}_{B_{\mathrm{QAM}}}. \quad (3.36)$$

3.3.3 Results and Discussion

The current section confirms the validity of the analytical approach from Section 3.3.2 through Monte Carlo simulations. The numerical simulations of the enhanced SIM-OFDM are performed for N_{A}=1 and N_{B}=2 in accordance with the analysis from Section 3.3.2. The results are shown in Fig. 3.7. The presented results indicate a very good agreement between the theoretical model suggested in Section 3.3.2 and the conducted Monte Carlo simulations, which confirms the validity of the analytical approach.

A comparison between the enhanced SIM-OFDM concept and conventional OFDM is shown in Fig. 3.8. For the same M-QAM modulation order, SIM-OFDM requires less energy per bit than OFDM to achieve a given target BER. At the same time, M-QAM SIM-OFDM is less spectrally-efficient than M-QAM OFDM as illustrated in (3.28). This means that for the same amount of system bandwidth and the same constellation size, SIM-OFDM requires less energy per bit, but is capable of delivering lower data-rate. In the absence of any additional constraints, such as non-linear distortion or processing power, it is fair to make an energy-efficiency comparison only between systems with the same spectral efficiency. Due to the fractional part in (3.28), for the presented results, it is not possible to find a comparison between realisations of SIM-OFDM and OFDM with equivalent spectral efficiency. Nevertheless, the presented curves clearly illustrate that SIM-OFDM does not show superior performance to conventional OFDM for high-
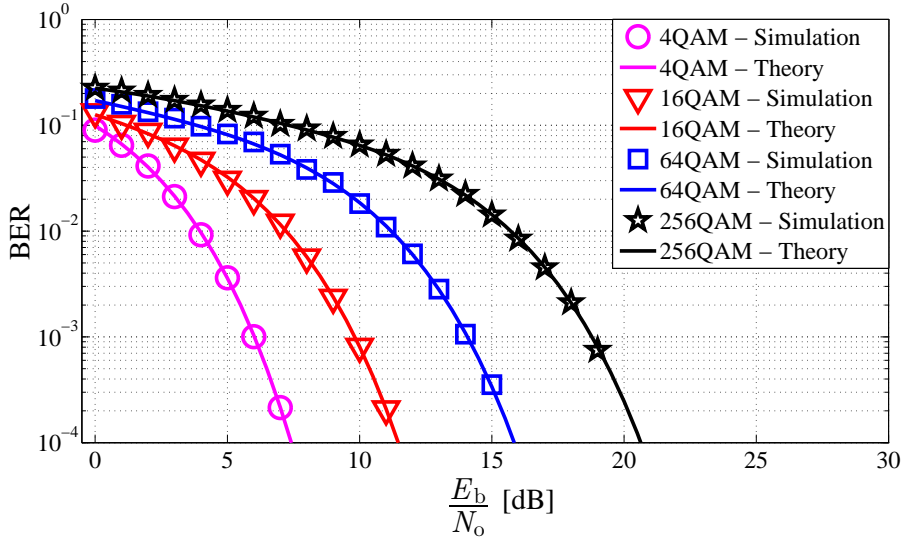
Figure 3.7: *Comparison between theoretical analysis and Monte Carlo simulations for the performance of enhanced SIM-OFDM (N_A=1 and N_B=2). A linear AWGN channel is assumed.*

throughput scenarios where high spectral efficiency is required. For example, 16-QAM OFDM is both energy and spectrally more efficient than 64-QAM SIM-OFDM. The extra $\frac{1}{2}$ bit/s/Hz gained from the subcarrier-state encoding (1 bit/s/Hz in the original SIM-OFDM) leads to a sacrifice of $\log_2(M)$ bits/s/Hz per *inactive* subcarrier, which means that for $M > 2$, SIM-OFDM has a loss in spectral efficiency compared to OFDM for the same constellation size. At the same time, the energy gain introduced by SIM-OFDM is not really substantial enough to justify the loss in the spectral efficiency. For example, for M=4, the energy gain of SIM-OFDM compared to OFDM is about 1 dB. As M increases, this gain is reduced as it originates from: 1) the extra bit on top of the M-QAM symbol which increases the energy per symbol; and 2) the OOK/PPM-like encoding of the bits in B_{OOK} that utilises the high energy of each M-QAM symbol in an OOK/PPM fashion. As M increases, the extra energy per symbol from the additional bit and the extra B_{OOK} bit with low BER become a smaller and smaller portion of the overall information frame. As a result, the benefit of their utilisation is reduced. The spectral efficiency of the scheme can be increased as described in Section 3.3.1 and denoted by (3.29). However, that would lead to an increase in BER as the additional *active* subcarriers lead to more possibilities for errors in the subcarrier-state detection and to less additional energy per M-QAM symbol. Overall, the BER performance would not be better than presented in Fig. 3.8, which means that any potential energy savings compared to OFDM would not be significant enough to justify the realisation of
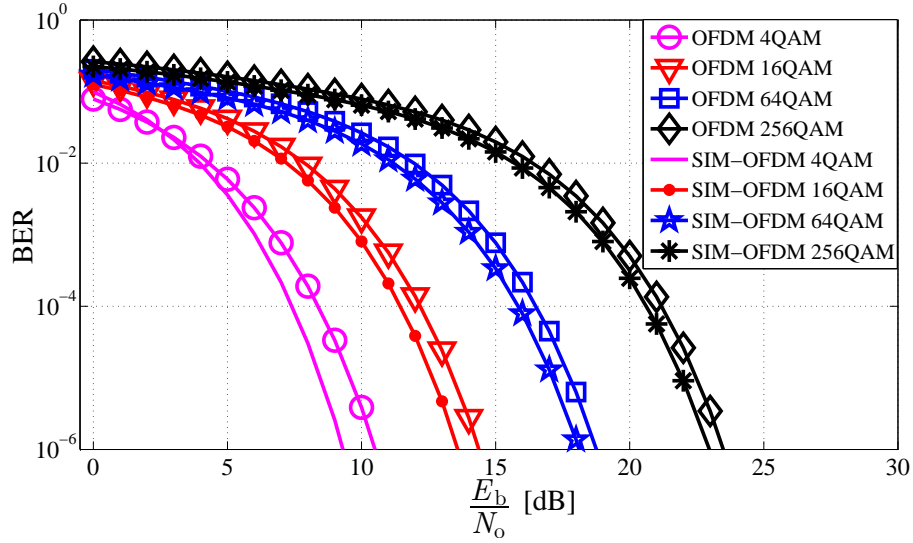
Figure 3.8: *Comparison between enhanced SIM-OFDM (N_A=1 and N_B=2) and conventional OFDM performance. A linear AWGN channel is assumed.*

this more complicated SIM-OFDM modulation scheme.

3.3.4 Peak-to-average Power Ratio (PAPR)

Conventional OFDM suffers from a high PAPR, which can present a considerable problem in electrical components with a limited dynamic range, such as amplifiers, digital-to-analog converters (DACs), analog-to-digital converters (ADCs) and light emitting diodes (LEDs) [84]. The structure of the enhanced SIM-OFDM frame leads to a reduction of the PAPR when compared to conventional OFDM. This is highly beneficial, especially in the context of OWC where both the average and the peak light intensity are further limited by eye safety regulations [86].

The PAPR is defined as the ratio of the maximum achievable power at any point in time, $\max\{s^2[n]\}$, and the average power of the signal, $E\{s^2[n]\}$, [84]:

$$\text{PAPR} = \frac{\max\{s^2[n]\}}{E\{s^2[n]\}}. \tag{3.37}$$

The time domain signal, $s[n]$, to be transmitted in an OFDM system is calculated as:

$$s[n] = \frac{1}{\sqrt{N_{\text{fft}}}} \sum_{k=0}^{N_{\text{fft}}-1} S[k] e^{\frac{j2\pi kn}{N_{\text{fft}}}}, \tag{3.38}$$

55
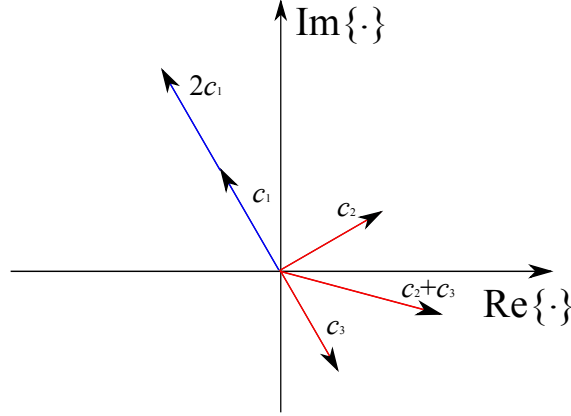
Figure 3.9: *Graphical representation of sum of complex numbers with the same power -*
$c_1, c_2, c_3 \in \mathbb{C}$; $|c_1|^2 = |c_2|^2 = |c_3|^2$; $|2c_1|^2 > |c_2 + c_3|^2$

where $S[k]$ is the value assigned to the kth subcarrier. In conventional OFDM, the peak power occurs at $s[n]$ when

$$S[k] = ce^{\frac{-j2\pi kn}{N_{\text{fft}}}}, \ c \in \mathbb{C}. \tag{3.39}$$

The complex exponential in (3.38) is cancelled by the complex exponential in (3.39) and the result is a summation of N_{fft} equal complex numbers c. When two complex numbers are summed, they yield a result with the highest possible amplitude when their phases are equal and their amplitudes are as high as possible. Fig. 3.9 illustrates the concept graphically. Hence, (3.39) guarantees a peak value at $s[n]$ when c has the highest possible amplitude. The maximum power is achieved at $s[0]$ when each subcarrier is modulated with the same constellation symbol with the highest possible energy. That symbol is marked as S_{he}. Then $s[0] = \sqrt{N_{\text{fft}}}S_{\text{he}}$ and $|s[0]|^2 = s[0]s[0]^* = N_{\text{fft}}S_{\text{he}}S_{\text{he}}^*$. For a square M-QAM constellation, $S_{\text{he}} = (\sqrt{M} - 1) + j(\sqrt{M} - 1)$ and $S_{\text{he}}S_{\text{he}}^* = 2(\sqrt{M} - 1)^2$ [84]. Hence, the maximum power is:

$$\max\{s^2[n]\} = 2N_{\text{fft}}(\sqrt{M} - 1)^2. \tag{3.40}$$

Note that this result is correct only when the M-QAM constellation points take odd integer values in both the real and imaginary dimension as is the common representation of M-QAM constellations. In some scenarios, the constellation could be rescaled in order to meet a certain constraint such as a pre-determined average power of the communication signal. In any such scenario, the results for $\max\{s^2[n]\}$ and $E\{s^2[n]\}$ presented here would still be valid but would include the

scaling factor used for the normalisation of the signal.

The average power of the signal is equal to the average frame energy divided by the number of points in time domain. The average frame energy is equal to the average energy per subcarrier multiplied by the number of subcarriers. The average energy per subcarrier is equal to the average energy in an M-QAM symbol, when all subcarriers are equally loaded. Hence, using [84],

$$\mathrm{E}\{\mathrm{s}^2[n]\} = \frac{E_{\mathrm{AVG}}N_{\mathrm{fft}}}{N_{\mathrm{fft}}} \overset{[84]}{=} \frac{2(M-1)}{3}. \tag{3.41}$$

From (3.40) and (3.41), the PAPR for conventional OFDM can be calculated as:

$$\mathrm{PAPR}_{\mathrm{OFDM}} = \frac{\max\{\mathrm{s}^2[n]\}}{\mathrm{E}\{\mathrm{s}^2[n]\}} = \frac{3N_{\mathrm{fft}}(\sqrt{M}-1)^2}{M-1} = \frac{3N_{\mathrm{fft}}(\sqrt{M}-1)}{\sqrt{M}+1}. \tag{3.42}$$

An alternative derivation of (3.42) is proposed in [84].

Since in the enhanced SIM-OFDM a number of subcarriers are always "switched off", *i.e.* set to 0, the condition in (3.39) cannot be fulfilled. A complex exponential never takes the value 0; its amplitude is always 1. Hence, in the enhanced SIM-OFDM, (3.39) is always violated, and it is not possible to allocate all the signal energy at a single point in the time domain. This already suggests a reduction of the peak power value. Adding zeros to the expression in (3.38) means that a smaller number of complex values have to be summed in order to obtain s[n]. For a peak-power value, they still should have the highest possible power and be the same due to the property of complex numbers, described in Fig. 3.9. Hence, the peak value is achieved at s[0] when all *active* subcarriers are modulated with S_{he}. If N_{a} is the total number of *active* subcarriers, then:

$$\max\{\mathrm{s}^2[n]\} = \left(\frac{1}{\sqrt{N_{\mathrm{fft}}}}N_{\mathrm{a}}S_{\mathrm{he}}\right)\left(\frac{1}{\sqrt{N_{\mathrm{fft}}}}N_{\mathrm{a}}S_{\mathrm{he}}\right)^* = \frac{2}{N_{\mathrm{fft}}}N_{\mathrm{a}}^2(\sqrt{M}-1)^2, \tag{3.43}$$

$$\mathrm{E}\{\mathrm{s}^2[n]\} = \frac{E_{\mathrm{AVG}}N_{\mathrm{a}}}{N_{\mathrm{fft}}} = \frac{2N_{\mathrm{a}}(M-1)}{3N}, \tag{3.44}$$

$$\mathrm{PAPR} = \frac{\max\{\mathrm{s}^2[n]\}}{\mathrm{E}\{\mathrm{s}^2[n]\}} = \frac{3N_{\mathrm{a}}(\sqrt{M}-1)^2}{M-1} = \frac{3N_{\mathrm{a}}(\sqrt{M}-1)}{\sqrt{M}+1}. \tag{3.45}$$

Equations (3.43)–(3.45) are a generalisation of equations (3.40)–(3.42) for an arbitrary number of *active* subcarriers. The PAPR depends on both the number of *active* subcarriers, expressed by N_{a}, and the modulation order, expressed by the ratio $\frac{3(\sqrt{M}-1)}{\sqrt{M}+1}$. The lowest PAPR is achieved in frequency shift keying (FSK) because $N_{\mathrm{a}} = 1$ and there is no additional subcarrier modulation.

The highest PAPR is achieved in the case of conventional M-QAM OFDM when $N_a = N_{fft}$, and both N_{fft} and M are as high as possible. The advantage of SIM-OFDM over conventional OFDM comes from the fact that in general it has less *active* subcarriers. For example, M-QAM SIM-OFDM with $N_A = 1$ and $N_B = 2$ has half the PAPR when compared to M-QAM OFDM for any total number of subcarriers, N_{fft}.

3.4 Summary

In this chapter, a novel, simple and accurate analytical framework to compute the BER of SIM-OFDM in a linear AWGN channel has been proposed. As a result of the analysis, a propagation error effect within the SIM-OFDM frame has been discovered. In order to correct this issue, an enhanced SIM-OFDM modulation scheme has been proposed. Analytical results and Monte Carlo simulations have shown that the SIM-OFDM concept is inherently unable to provide high data-rate communication in a system with limited bandwidth due to its lower spectral efficiency when compared to conventional OFDM. Nevertheless, SIM-OFDM could be successfully applied in low-data-rate systems as it provides a reduction of the energy requirements and the PAPR in comparison to conventional OFDM. The original concept of encoding an additional bit into the subcarrier states leads to interesting possibilities for further research and has become an inspiration for the unipolar orthogonal frequency division multiplexing (U-OFDM) concept presented in the next chapter.

Chapter 4
Unipolar Orthogonal Frequency Division Multiplexing

A novel modulation technique named unipolar orthogonal frequency division multiplexing (U-OFDM) is proposed. U-OFDM is a method for the generation of an inherently non-negative orthogonal frequency division multiplexing (OFDM) signal which could lead to significant energy savings in comparison to the conventional approach for OFDM implementation in optical wireless communications (OWC) named direct-current-biased optical orthogonal frequency division multiplexing (DCO-OFDM). Furthermore, a closed-form framework to compute the bit error rate (BER) of U-OFDM over a linear additive white Gaussian noise (AWGN) communication channel is provided in this chapter. A performance comparison of U-OFDM and other state-of-the-art techniques for unipolar OFDM signal generation is also provided. An inherent disadvantage of the known inherently unipolar modulation schemes, such as asymmetrically clipped optical orthogonal frequency division multiplexing (ACO-OFDM), pulse-amplitude-modulated discrete multitone modulation (PAM-DMT) and U-OFDM, is the necessity to sacrifice half of the spectral efficiency in the modulation process when compared to DCO-OFDM. In order to compensate for this disadvantage, an improved U-OFDM modulation scheme named enhanced unipolar orthogonal frequency division multiplexing (eU-OFDM) is also proposed, and it is shown that the enhanced concept can make up for the spectral efficiency loss in U-OFDM while still providing significant energy benefits over DCO-OFDM. All results and conclusions have been supported by a detailed theoretical analysis and Monte Carlo simulations.

4.1   Introduction

The physical properties of commercially available light emitting diodes (LEDs) and photodiodes (PDs), which are the foremost candidates for low-cost front-end devices in OWC, allow OWC to be realised as an intensity modulation and direct detection (IM/DD) system only. Light emitted by of-the-shelf LEDs is incoherent and so information can be reliably encoded only in the signal intensity. The phase and the amplitude of the light wave cannot be modulated or detected with LEDs and PDs. Therefore, an OWC system can be realised only as an IM/DD system. This limits the set of conventional modulation schemes that can be adopted from the field of radio frequency (RF) communications and directly translated into OWC. Signal modulation techniques such as on-off keying (OOK), pulse-position modulation (PPM), and M-ary pulse-amplitude modulation (M-PAM) are relatively straightforward to implement as they provide real signals that can be directly mapped to light intensity. As transmission rates increase, however, the limited modulation bandwidth of the front-end devices and the limited bandwidth of the OWC channel lead to intersymbol interference (ISI) in the time-domain modulation signal. Hence, a technique such as OFDM becomes more appropriate as a modulation scheme. OFDM enables simple cost-effective equalisation with single-tap equalisers in the frequency domain. In addition, data and energy can be loaded adaptively in different frequency bands according to the channel properties. This results in an optimal exploitation of the communication resources. Furthermore, at a system level, OFDM provides a straightforward and low-complexity multiple access scheme, which has to be implemented additionally for other modulation schemes such as OOK, PPM and M-PAM.

In practice, OFDM is realised in a digital signal processor (DSP) by taking an inverse fast Fourier transform (IFFT) of a block of symbols from a conventional modulation scheme such as M-ary quadrature amplitude modulation (M-QAM). This operation effectively maps the M-QAM symbols to different frequency bands of the resulting time-domain signal. The procedure, however, produces complex-valued bipolar time-domain samples, while intensity modulation requires real non-negative signals. Hence, the OFDM signal has to be modified before it becomes suitable for an IM/DD system. A real signal can be obtained by imposing a Hermitian symmetry in the information block on which an IFFT operation is applied during the signal generation procedure. The resulting time-domain samples, however, would still be bipolar. A number of different approaches for obtaining a unipolar signal exist in the literature. One straightforward method is to add a bias value to all samples, which would make the resulting signal non-negative. This approach is known as DCO-OFDM. The direct current (DC) biasing leads to a significant increase

62

in the energy consumption compared to conventional OFDM in a bipolar system. For example, a minimum bias, resulting in an energy penalty of about 6 dB compared to bipolar OFDM, is required for 4-QAM DCO-OFDM. Hence, researchers have explored alternative methods for generation of unipolar signals. This has led to the introduction of new inherently non-negative modulation schemes such as ACO-OFDM [61] and PAM-DMT [62]. These modulation techniques exploit the properties of the fast Fourier transform (FFT) and the OFDM frame structure in order to create a symmetric time-domain signal in which any negative values can simply be reduced to zero without compromising the information in the OFDM frame, and, thus, a unipolar signal without the use of biasing can be realised. The clipping of the negative values in ACO-OFDM and M-PAM leads to a an electrical energy penalty of 3 dB when compared to conventional bipolar OFDM. The scheme presented in this chapter, U-OFDM, is inspired by the concept of subcarrier-index modulation orthogonal frequency division multiplexing (SIM-OFDM) in an attempt to close the 3 dB gap between OFDM and ACO-OFDM for bipolar signals, whilst generating a unipolar signal, which does not require biasing. It should be noted that the concepts presented for U-OFDM in the first part of this chapter have also been introduced by another research group as Flip-OFDM in [87] and in [88]. The concept of U-OFDM and Flip-OFDM have been developed in parallel completely independently from each other and within roughly the same time frame. It is interesting to note that all four approaches – ACO-OFDM, PAM-DMT, Flip-OFDM and U-OFDM – achieve the same performance in both a linear and a non-linear AWGN channel as will be illustrated later in the context of this work [18, 21, 61, 62, 87, 88]. For an equivalent M-QAM/M-PAM modulation order, the spectral efficiency of each of these four methods is halved in comparison to DCO-OFDM. However, the energy penalty in comparison to a bipolar OFDM signal is only 3 dB for any M-QAM/M-PAM constellation size. Thus, the premise is that a larger constellation can be used in ACO-OFDM, PAM-DMT and U-OFDM in order to compensate for the loss in spectral efficiency from the modulation technique, but the energy efficiency can still be better than in DCO-OFDM. Improved decoders which are equivalent in performance have been developed for ACO-OFDM [89], U-OFDM [18] and Flip-OFDM [88]. Even though, to the best of the author's knowledge, such an improved decoder is not presented in the literature for PAM-DMT, it would be straightforward to design. The improved decoders make the power efficiency of all four schemes almost equivalent to the case for a bipolar OFDM signal but can only work for a flat-fading communication channel. A serious problem for the inherently non-negative modulation schemes arises from the decreased spectral efficiency, which requires M-QAM DCO-OFDM to be compared to M^2-QAM ACO-OFDM/U-OFDM/Flip-OFDM and to

M-PAM PAM-DMT in order to keep the achievable data rate equivalent for systems with equivalent bandwidth. This causes a substantial loss of energy efficiency compared to DCO-OFDM in all four schemes for a spectral efficiency above 1 bit/s/Hz [90]. Dissanayake et. al. have proposed a technique to simultaneously transmit ACO-OFDM and DCO-OFDM in an attempt to close the spectral efficiency gap [91]. However, this method still requires a DC-bias for the generation of DCO-OFDM. The second part of this chapter proposes a solution to the problem of spectral efficiency loss in U-OFDM, which could be extended to ACO-OFDM and PAM-DMT relatively straightforwardly.

The rest of this chapter is organized as follows. Section 4.2 presents the U-OFDM modulation concept and is divided in the following manner: Section 4.2.1 introduces the modulation and demodulation algorithm of U-OFDM; Section 4.2.2 presents the analytical framework; and Section 3.2.3 confirms the validity of the theoretical BER estimations through extensive Monte Carlo simulations. Section 4.3 proposes an enhanced U-OFDM algorithm with an improved frame structure and is divided as follows: Section 4.3.1 presents the enhanced concept; Section 4.3.3 presents the analytical framework for the enhanced U-OFDM algorithm, and Section 4.3.4 confirms the validity of the theoretical analysis. Section 4.4 discusses the possibility for extension of the enhanced U-OFDM concept to the other inherently unipolar modulation schemes: ACO-OFDM and PAM-DMT. Finally, Section 3.4 provides concluding remarks to the topic.

4.2 Unipolar OFDM (U-OFDM)

4.2.1 Concept

The concept of U-OFDM is an algorithm for the generation of an inherently unipolar modulation signal which presents an alternative to the already familiar techniques of ACO-OFDM and PAM-DMT. The modulation process begins with conventional generation of a real bipolar OFDM signal such as the one in Fig. 4.1. The sign of a real time-domain sample amounts to exactly one bit of information. All additional information in the sample is represented by its absolute value. Absolute values are always positive. Therefore, the absolute value of a bipolar time-domain signal is a unipolar signal which can be used for transmission in IM/DD systems. Such a signal, however, has two problems. First, the one-bit information for all signs has to somehow be correctly conveyed to the destination. Second, the use of a non-linear transformation such
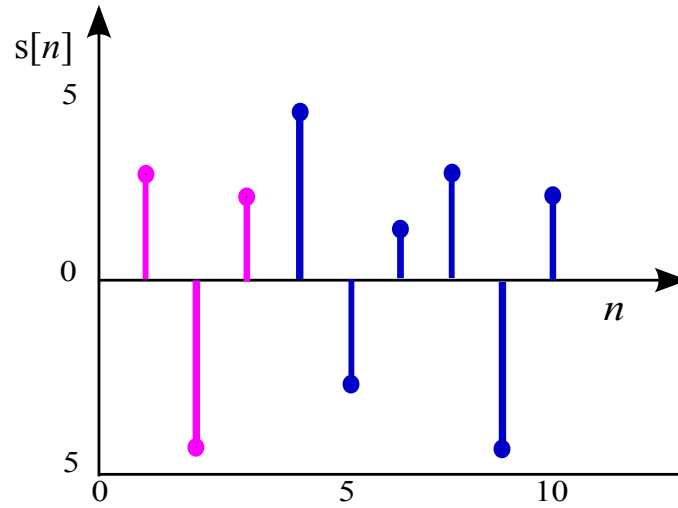
Figure 4.1: *A typical real OFDM time-domain signal. The first three samples constitute the cyclic prefix.*
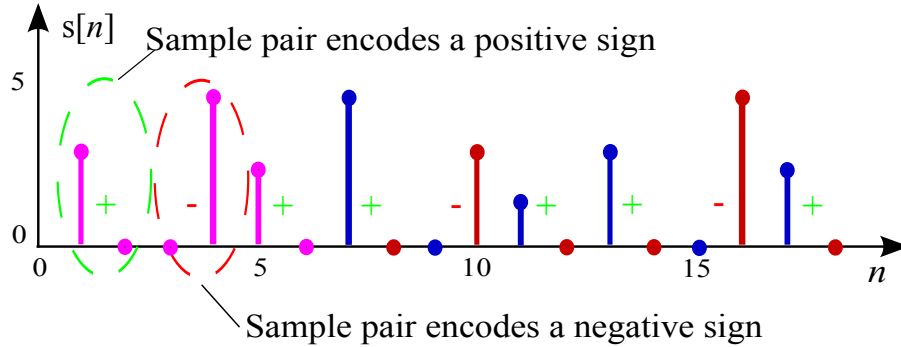
Figure 4.2: *A unipolar time domain signal. The first six samples constitute the cyclic prefix.*

as obtaining the absolute value of a signal creates a waveform whose frequency profile is significantly different than initially intended. This effect is very detrimental to the OFDM concept where adaptive bit and energy loading in the frequency domain is used in order to optimise performance in a non-flat channel. A solution to the first issue can be devised from Section 3.3.1 which introduced a very simple concept for encoding exactly one bit of information into the position of an arbitrary information symbol. Following that same line of thought, each time-domain sample can be encoded into a pair of new time-domain samples. If the original OFDM sample is positive, the first sample of the new pair is set as *active*, and the second sample is set as *inactive*. If, on the other hand, the original OFDM sample is negative, the first sample of the new pair is set as *inactive*, and the second sample is set as *active*. *Active* samples are set equal to the absolute value of the bipolar OFDM sample they correspond to, and *inactive* samples are set

65
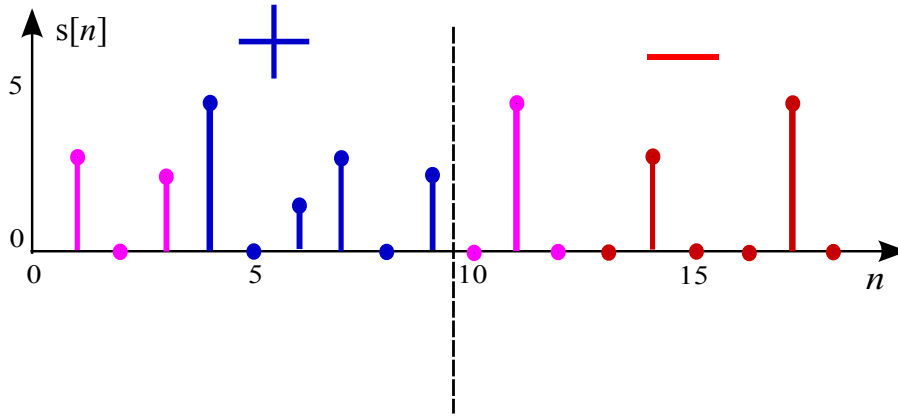
Figure 4.3: *A U-OFDM time domain signal. The first frame contains only positive samples of the original bipolar OFDM signal. The second frame contains only negative samples of the original bipolar OFDM signal. First three samples of each frame constitute the cyclic prefix.*

to zero. That is how the signal illustrated in Fig. 4.2 can be obtained from the signal in Fig. 4.1. Fig. 4.2 only illustrates how the signs of the bipolar samples can be encoded in the position of the *active* sample in a pair. The described operation for sign encoding is still non-linear and changes the frequency profile of the original OFDM signal. This issue has been circumvented by an additional change in the signal structure. The actual U-OFDM signal is obtained when the first samples of each pair are grouped in their original order to form the so called *positive* block while the second samples are grouped in their original order to form the so called *negative* block. The *positive* block is transmitted first and the *negative* block is transmitted second. That is how the signal illustrated in Fig. 4.3 is obtained. This operation can also be described as the act of taking all negative samples from the original bipolar frame, replacing them with zeros and then flipping their values and transmitting them in a second frame where the positions of the original positive samples are occupied by zeros. This description of the signal generation process has inspired the name Flip-OFDM used by the authors in [87]. Alternatively, the same modulation procedure can be expressed as the act of transmitting two copies of the original bipolar frame one after the other. The first copy corresponds to the *positive* block. The second copy corresponds to the *negative* block and has been multiplied by -1 in order to switch the signs of the samples. The signal is made unipolar by removing any negative values from both copies by clipping at zero. After both U-OFDM frames are received at the destination, the original bipolar frame can be recovered by subtracting the second U-OFDM frame from the first one. Afterwards, the demodulation process continues with conventional OFDM demodulation of the reconstructed bipolar signal. In the

context of this work, this demodulation algorithm will be referred to as *conventional* U-OFDM demodulation. The following paragraph explains why the U-OFDM signal structure avoids the non-linearity effects from the clipping-at-zero operation.

As presented in (2.27), the clipping of a signal $\mathrm{s}[n]$ at zero can be represented as:

$$\underline{\mathrm{s}}[n] = \mathrm{f_{clip}}\{\mathrm{s}[n]\} = \frac{1}{2}(\mathrm{s}[n] + |\mathrm{s}[n]|). \tag{4.1}$$

If $\mathrm{s}[n]$ represents the samples of the original bipolar frame, then the transmitted samples from the first corresponding U-OFDM frame would be equal to:

$$\mathrm{s_p}[n] = \frac{1}{2}(\mathrm{s}[n] + |\mathrm{s}[n]|). \tag{4.2}$$

The values of the second corresponding U-OFDM frame would be equal to:

$$\mathrm{s_n}[n] = \frac{1}{2}(-\mathrm{s}[n] + |-\mathrm{s}[n]|) = \frac{1}{2}(-\mathrm{s}[n] + |\mathrm{s}[n]|). \tag{4.3}$$

After the signal is transmitted through the dispersive channel $\mathrm{h}[n]$, corrupted by AWGN, and equalized at the receiver, the respective U-OFDM frames become:

$$\hat{\mathrm{s}}_{\mathrm{E,p}}[n] = \frac{1}{2}(\mathrm{s}[n] + |\mathrm{s}[n]|) + \mathrm{n_1}[n] * \mathrm{h}^{-1}[n] \tag{4.4}$$

and

$$\hat{\mathrm{s}}_{\mathrm{E,n}}[n] = \frac{1}{2}(-\mathrm{s}[n] + |\mathrm{s}[n]|) + \mathrm{n_2}[n] * \mathrm{h}^{-1}[n], \tag{4.5}$$

where $*$ denotes the convolution operator, $\mathrm{h}^{-1}[n]$ is the inverse of the dispersive channel $\mathrm{h}[n]$, $\mathrm{n_1}[n]$ and $\mathrm{n_2}[n]$ are AWGN realisations at the receiver. The reconstructed original bipolar frame then becomes:

$$\hat{\mathrm{s}}_{\mathrm{E}}[n] = \hat{\mathrm{s}}_{\mathrm{E,p}}[n] - \hat{\mathrm{s}}_{\mathrm{E,n}}[n] = \frac{1}{2}(\mathrm{s}[n] + |\mathrm{s}[n]|) + \mathrm{n_1}[n] * \mathrm{h}^{-1}[n] -$$
$$- \frac{1}{2}(-\mathrm{s}[n] + |\mathrm{s}[n]|) - \mathrm{n_2}[n] * \mathrm{h}^{-1}[n] = \mathrm{s}[n] + (\mathrm{n_1}[n] - \mathrm{n_2}[n]) * \mathrm{h}^{-1}[n]. \tag{4.6}$$

The reconstructed signal, $\hat{\mathrm{s}}_{\mathrm{E}}[n]$, consists of the original signal, $\mathrm{s}[n]$, and a Gaussian noise component which is coloured according to the inverted frequency profile of the channel $\mathrm{h}[n]$. Despite the

time-domain representation of (4.4) – (4.6), it should be noted that the equalisation step does not need to be performed in the time domain. The subtraction step can also be performed either in the time domain or the frequency domain, but a time-domain operation would be the preferred choice as it would halve the number of required FFT operations. Therefore, the most cost-effective sequence of demodulation steps would be subtraction → FFT → equalisation. Two observations should be made regarding the U-OFDM signal. First, the clipping term $|s[n]|$ is common for both U-OFDM frames and is completely removed by the subtraction operation. Any frequency components outside the desired spectrum resulting from the clipping operation are contained in that term. Hence, the spectrum of the estimated bipolar signal $\hat{s}[n]$ is not adversely affected by the clipping operation. Second, the noise in both U-OFDM frames is combined leading to a signal-to-noise ratio (SNR) penalty of 3 dB compared to conventional bipolar OFDM transmission.

Since U-OFDM employs two frames to transmit the same information as conventional OFDM, the spectral efficiency of U-OFDM:

$$\eta_{\mathrm{U}} = \frac{\eta_{\mathrm{DCO}}}{2} = \frac{\log_2(M)(N_{\mathrm{fft}} - 2)}{4(N_{\mathrm{fft}} + N_{\mathrm{cp}})} \text{ bits/s/Hz}, \tag{4.7}$$

is half the spectral efficiency of DCO-OFDM, presented in (2.15), and roughly the same as the spectral efficiency of ACO-OFDM, presented in (2.28). It should be noted that this is true when the FFT size for all three modulation schemes is the same. Then, U-OFDM experiences double the initial latency to decode a single information frame because two consecutive frames need to be received in order for the demodulation process to begin. The authors in [87] have made the case that Flip-OFDM/U-OFDM is computationally more efficient than ACO-OFDM as it requires a smaller FFT size for decoding the same information per frame. This is true for the case when the two U-OFDM/Flip-OFDM frames have a combined length equal to one ACO-OFDM frame. Then, the information latency in both schemes would be the same. However, in that case, since the FFT size of U-OFDM/Flip-OFDM is half the FFT size of ACO-OFDM, the overhead of the cyclic prefix is doubled. This means that the spectral efficiency of U-OFDM/Flip-OFDM would be less than the spectral efficiency of ACO-OFDM. For a large number of practical scenarios, when the cyclic prefix length is small, this does not introduce a significant difference. However, it would lead to a significant sacrifice of U-OFDM/Flip-OFDM throughput in high-speed communication scenarios, when the cyclic prefix length is expected to constitute a large portion of the frame size. Therefore, if equal spectral efficiency between ACO-OFDM and U-OFDM/Flip-OFDM is assumed for an arbitrary communication scenario, computational efficiency of U-OFDM/Flip-

OFDM over ACO-OFDM cannot be claimed.

As already described, the subtraction operation in the demodulation process of U-OFDM causes the noise in each pair of U-OFDM frames to combine leading to a 3-dB SNR penalty. Following the logic used for the demodulation algorithm in Section 3.3.1, an alternative demodulation method can be proposed in an attempt to reduce the SNR penalty. Each pair of samples, as illustrated in Fig. 4.2, encodes the amplitude and the sign of the original bipolar sample. In the same way, the value of each *active* sample in Fig. 4.3 encodes the absolute value of the original bipolar OFDM sample while its position encodes the sign. If the receiver is able to detect which is the *active* sample at each position of the U-OFDM frames, it can successfully guess the original sign and simply discard the *inactive* sample since it carries no further information, just noise. This procedure is ideally expected to remove half of the AWGN variance from the reconstructed bipolar signal in comparison to the decoder employing a subtraction operation, and, thus, it is expected to improve the performance. A simple and efficient way to guess the *active* sample is by comparing the amplitudes of the two samples at each position in a pair of U-OFDM frames - the sample with the higher amplitude is marked as *active*. After reconstruction of the bipolar signal, the demodulation process continues with conventional OFDM demodulation. In the context of this work, this decoding scheme will be referred to as the *improved* U-OFDM decoder. A similar approach for ACO-OFDM demodulation has been reported very recently by Asadzadeh et. al. in [89], leading to the equivalent improvement in performance as illustrated in this work. It would be fairly straightforward to design the same decoding scheme for PAM-DMT as well, following the logic used in [89]. Something to note regarding the *improved* decoder is that this technique is only applicable in relatively flat communication channels where the ISI is negligible. If the ISI is considerable, then this demodulator requires equalisation to be performed in the time domain. In addition, since this method discards half of the U-OFDM samples, the channel attenuation at different frequency subcarriers is not consistent. This renders use of adaptive bit loading techniques difficult. Furthermore, when present, low-frequency noise from ambient light flickering and the baseline wander effect in electrical circuits would further hinder the operation of the *improved* demodulation algorithm. This should be taken into account in a practical implementation. In OWC, the communication channel would often be flat, especially when a strong line-of-sight (LoS) propagation path is present. As a result, the *improved* decoder could be applied selectively, when the channel conditions are favourable, as it requires only a small modification in the processing algorithm compared to the *conventional* decoder.

4.2.2 Theoretical Bit-error-rate Analysis

This section presents a theoretical BER analysis of U-OFDM in a linear AWGN channel. The analysis of the *conventional* U-OFDM decoder is trivial as the only difference to conventional bipolar OFDM performance that needs to be taken into account is the combining of AWGN in the subtraction operation. Therefore, the theoretical BER for this demodulation scheme can be obtained by adding 3 dB to the SNR requirements of conventional bipolar OFDM for an arbitrary desired BER. The rest of this section presents the theoretical approach for analysing the performance of the *improved* demodulator for U-OFDM in an AWGN channel. In the context of the following mathematical formulas, σ_n is the standard deviation of the AWGN, *i.e.* , $\sigma_\mathrm{n} = \sqrt{BN_\mathrm{o}}$, where B denotes the double-sided signal bandwidth and N_o denotes the AWGN power spectral density (PSD); σ_s is the standard deviation of the real bipolar OFDM signal, $\mathrm{s}[n]$, before it is encoded in U-OFDM, as described in (2.17); $\mathrm{sgn}(s)$ is the sign function, *i.e.* ,

$$\mathrm{sgn}(s) = \begin{cases} -1 & , \ s < 0 \\ 0 & , \ s = 0 \\ 1 & , \ s > 0; \end{cases} \tag{4.8}$$

$\phi(x)$ is the standard normal distribution probability density function, *i.e.* ,

$$\phi(x) = \frac{1}{\sqrt{2\pi}} \mathrm{e}^{-\frac{x^2}{2}}, \tag{4.9}$$

$\mathrm{Q}(x)$ is the tail probability of the standard normal distribution, *i.e.* ,

$$\mathrm{Q}(x) = \frac{1}{\sqrt{2\pi}} \int_x^\infty \mathrm{e}^{-\frac{u^2}{2}} \mathrm{d}u, \tag{4.10}$$

and $\mathrm{erf}(x)$ is the error function, *i.e.* ,

$$\mathrm{erf}(x) = \frac{2}{\sqrt{\pi}} \int_0^x \mathrm{e}^{-u^2} \mathrm{d}u. \tag{4.11}$$

Modelling the performance of the *improved* U-OFDM decoder analytically is not a trivial task due to the fact that during the demodulation procedure each individual sample in the time domain is subjected to a varying non-linear transformation, which depends on two independent random variables from the AWGN. This is caused by the *active*-sample selection procedure. The distri-
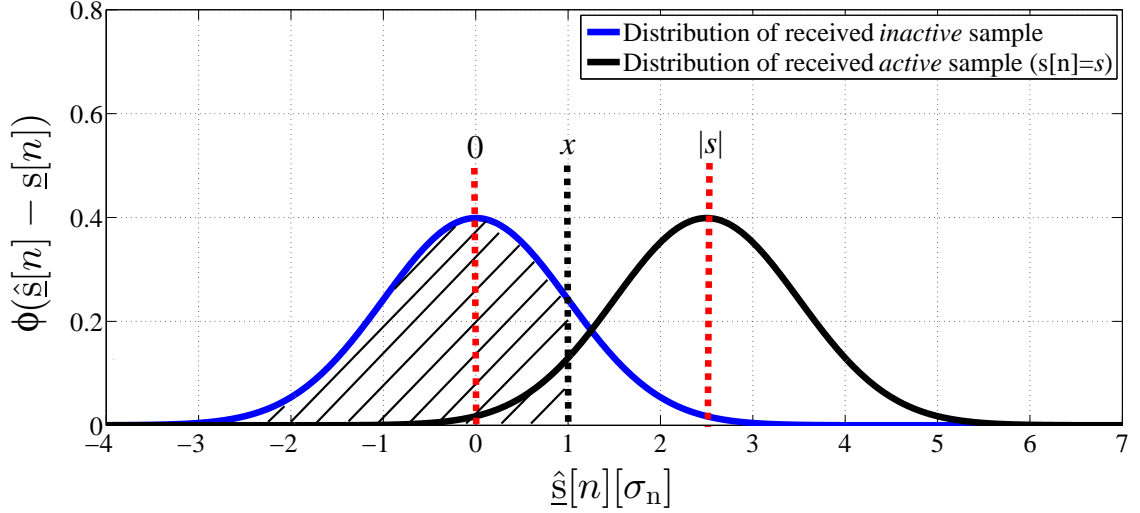
Figure 4.4: *Distribution of the received U-OFDM samples $\hat{\underline{s}}[n]$. The received U-OFDM samples are expressed in multiples of the AWGN standard deviation. The transmitted* active *sample has a value of $|s_a[n]| = |s|$ and the transmitted* inactive *sample has a value of 0. In this example, $|s| = 2.5\sigma_n$. The probability that the received active sample, $\hat{\underline{s}}_a[n]$, has a value of x is expressed by $1/\sigma_n\phi((x-|s|)/\sigma_n)dx$, and the probability that the received* inactive *sample, $\hat{\underline{s}}_i[n]$, has a value lower than x is denoted in the figure by the shaded area under the blue/left curve and expressed as $1 - Q(x/\sigma_n)$. Similarly, the probability that $\hat{\underline{s}}_i[n]$ takes the value x is expressed by $1/\sigma_n\phi(x/\sigma_n)dx$, and the probability that $\hat{\underline{s}}_a[n]$ takes a value lower than x is denoted by the shaded area under the black/right curve and expressed as $1 - Q((x-|s|)/\sigma_n)$.*

bution of a pair of received *active-inactive* samples is depicted in Fig. 4.4. The original *inactive* sample at the transmitter has a value of 0, so the received *inactive* sample, corrupted with AWGN from the receiver circuit, has a Gaussian distribution centred around the original value of 0. Similarly, the original *active* sample at the transmitter has a value of s, so the received *active* sample, corrupted with AWGN, has a Gaussian distribution centred around the original value of s. Let's assume that the received *active* sample takes the value of x due to the AWGN. In order to *correctly* detect it as *active* at the demodulator, the value of the *inactive* sample has to take a value smaller than x. From Fig. 4.4, the probability that the *active* sample takes the value x and at the same time the *inactive* sample takes a value smaller than x is:

$$P\{\hat{\underline{s}}_a[n] = x \cap \hat{\underline{s}}_i[n] \leq x\} = P\{\hat{\underline{s}}_a[n] = x\}P\{\hat{\underline{s}}_i[n] \leq x\} =$$

$$= \frac{1}{\sigma_{\mathrm{n}}} \phi\left(\frac{x - |s|}{\sigma_{\mathrm{n}}}\right)\left(1 - Q\left(\frac{x}{\sigma_{\mathrm{n}}}\right)\right) \mathrm{d}x. \tag{4.12}$$

This event is equivalent to the joint event of *correct* detection and the received *active* sample having a value of x. The probability of *correct* detection alone is the sum of the probabilities of all possible events $\{\hat{\underline{s}}_{\mathrm{a}}[n] = x \cap \hat{\underline{s}}_{\mathrm{i}}[n] \leq x\}$. Hence,

$$P\{\hat{\underline{s}}_{\mathrm{a}}[n] \geq \hat{\underline{s}}_{\mathrm{i}}[n]\} = \int_{-\infty}^{\infty} \frac{1}{\sigma_{\mathrm{n}}} \phi\left(\frac{x - |s|}{\sigma_{\mathrm{n}}}\right)\left(1 - Q\left(\frac{x}{\sigma_{\mathrm{n}}}\right)\right) \mathrm{d}x = \frac{1}{2} + \frac{1}{2}\mathrm{erf}\left(\frac{|s|}{2\sigma_{\mathrm{n}}}\right). \tag{4.13}$$

The probability that the *active* sample has the value x, given that it has been *correctly* detected, is:

$$P\left\{\hat{\underline{s}}_{\mathrm{a}}[n] = x | \hat{\underline{s}}_{\mathrm{a}}[n] \geq \hat{\underline{s}}_{\mathrm{i}}[n]\right\} = \frac{P\{\hat{\underline{s}}_{\mathrm{a}}[n] = x \cap \hat{\underline{s}}_{\mathrm{i}}[n] \leq x\}}{P\{\hat{\underline{s}}_{\mathrm{a}}[n] \geq \hat{\underline{s}}_{\mathrm{i}}[n]\}} =$$

$$= \frac{\frac{1}{\sigma_{\mathrm{n}}} \phi\left(\frac{x - |s|}{\sigma_{\mathrm{n}}}\right)\left(1 - Q\left(\frac{x}{\sigma_{\mathrm{n}}}\right)\right)}{\int_{-\infty}^{\infty} \frac{1}{\sigma_{\mathrm{n}}} \phi\left(\frac{u - |s|}{\sigma_{\mathrm{n}}}\right)\left(1 - Q\left(\frac{u}{\sigma_{\mathrm{n}}}\right)\right) \mathrm{d}u} \mathrm{d}x = \frac{\frac{1}{\sigma_{\mathrm{n}}} \phi\left(\frac{x - |s|}{\sigma_{\mathrm{n}}}\right)\left(1 - Q\left(\frac{x}{\sigma_{\mathrm{n}}}\right)\right)}{\frac{1}{2} + \frac{1}{2}\mathrm{erf}\left(\frac{|s|}{2\sigma_{\mathrm{n}}}\right)} \mathrm{d}x. \tag{4.14}$$

Therefore, (4.14) provides the probability that the original bipolar OFDM sample, $s[n] = s$, is mapped to $\mathrm{sgn}(s)x$ at the receiver when *correct* detection of the *active* sample occurs. This mapping is not deterministic and varies due to the AWGN at the receiver even when the same pair of *active* and *inactive* samples is transmitted. In order to create a more deterministic view of the transformation which each original bipolar sample undergoes in the event of *correct* detection, it can be assumed that each bipolar sample is mapped to the mean of $\mathrm{sgn}(s)x$ plus an additional noise component which represents the variation around that mean. The mean of $\mathrm{sgn}(s)x$ can be calculated as:

$$f_{\mathrm{c}}(s) = \int_{-\infty}^{\infty} \mathrm{sgn}(s)x \frac{\frac{1}{\sigma_{\mathrm{n}}} \phi\left(\frac{x - |s|}{\sigma_{\mathrm{n}}}\right)\left(1 - Q\left(\frac{x}{\sigma_{\mathrm{n}}}\right)\right)}{\int_{-\infty}^{\infty} \frac{1}{\sigma_{\mathrm{n}}} \phi\left(\frac{u - |s|}{\sigma_{\mathrm{n}}}\right)\left(1 - Q\left(\frac{u}{\sigma_{\mathrm{n}}}\right)\right) \mathrm{d}u} \mathrm{d}x =$$

$$= \frac{s - \mathrm{sgn}(s) \int_{-\infty}^{\infty} \frac{x}{\sigma_{\mathrm{n}}} \phi\left(\frac{x - |s|}{\sigma_{\mathrm{n}}}\right) Q\left(\frac{x}{\sigma_{\mathrm{n}}}\right) \mathrm{d}x}{\frac{1}{2} + \frac{1}{2}\mathrm{erf}\left(\frac{|s|}{2\sigma_{\mathrm{n}}}\right)} =$$

$$= \frac{s - \mathrm{sgn}(s)\left(|s|\left(\frac{1}{2} - \frac{1}{2}\mathrm{erf}\left(\frac{|s|}{2\sigma_n}\right)\right) - \frac{\sigma_{\mathrm{n}}}{2\sqrt{\pi}}e^{-\frac{s^2}{4\sigma_{\mathrm{n}}^2}} + \right)}{\frac{1}{2} + \frac{1}{2}\mathrm{erf}\left(\frac{|s|}{2\sigma_n}\right)}. \tag{4.15}$$

The variance of the noise component can be calculated as:

$$v_c(s) = \int_{-\infty}^{\infty} x^2 \frac{\frac{1}{\sigma_n}\phi\left(\frac{x-|s|}{\sigma_n}\right)\left(1 - Q\left(\frac{x}{\sigma_n}\right)\right)}{\int_{-\infty}^{\infty} \frac{1}{\sigma_n}\phi\left(\frac{u-|s|}{\sigma_n}\right)\left(1 - Q\left(\frac{u}{\sigma_n}\right)\right)du} dx - f_c^2(s) =$$

$$= \frac{\int_{-\infty}^{\infty} \frac{x^2}{\sigma_n}\phi\left(\frac{x-|s|}{\sigma_n}\right)\left(1 - Q\left(\frac{x}{\sigma_n}\right)\right)dx}{\frac{1}{2} + \frac{1}{2}\text{erf}\left(\frac{|s|}{2\sigma_n}\right)} - f_c^2(s) =$$

$$= \frac{\frac{\sigma_n^2 + s^2}{2}\left(1 + \text{erf}\left(\frac{|s|}{2\sigma_n}\right)\right) + \frac{3}{4}\frac{|s|}{\sqrt{\pi}}\sigma_n e^{-\frac{s^2}{4\sigma_n^2}}}{\frac{1}{2} + \frac{1}{2}\text{erf}\left(\frac{|s|}{2\sigma_n}\right)} - f_c^2(s). \tag{4.16}$$

The communication channel is assumed to be flat when the *improved* decoder is employed. As a result, the original bipolar OFDM frame can be loaded evenly in the frequency domain, which means that its time-domain samples can be approximated by independent identically distributed (i.i.d.) Gaussian random variables when the FFT size is greater or equal to 64, $N_{\text{fft}} \geq 64$ due to the central limit theorem (CLT) [14, 92]. Due to the flat channel, the received U-OFDM samples would not experience any dependence in time either. At the same time, the AWGN components at each time instance are also independent. Hence, the realisations of the noise component described in (4.16) are independent from each other. As a result, due to the CLT, the noise component is transformed into an AWGN component by the FFT operation in the demodulator. The noise variance is preserved from the time domain while the noise mean value reflects only on the DC subcarrier which is not used for communication.

Following the logic described so far and the description in Fig. 4.4, the probability that the *inactive* sample takes the value x and at the same time the *active* sample takes a value smaller than x, *i.e.* , the *inactive* sample is misinterpreted as *active*, is:

$$P\{\hat{\underline{s}}_i[n] = x \cap \hat{\underline{s}}_a[n] < x\} = P\{\hat{\underline{s}}_i[n] = x\}P\{\hat{\underline{s}}_a[n] < x\} =$$

$$= \frac{1}{\sigma_n}\phi\left(\frac{x}{\sigma_n}\right)\left(1 - Q\left(\frac{x - |s|}{\sigma_n}\right)\right)dx \tag{4.17}$$

The probability of *incorrect* detection alone is the sum of the probabilities of all possible events $\{\hat{\underline{s}}_i[n] = x \cap \hat{\underline{s}}_a[n] < x\}$. Hence,

$$P\{\hat{\underline{s}}_a[n] < \hat{\underline{s}}_i[n]\} = \int_{-\infty}^{\infty} \frac{1}{\sigma_n}\phi\left(\frac{x}{\sigma_n}\right)\left(1 - Q\left(\frac{x - |s|}{\sigma_n}\right)\right)dx = \frac{1}{2} - \frac{1}{2}\text{erf}\left(\frac{|s|}{2\sigma_n}\right). \tag{4.18}$$

Alternatively, this probability can be expressed as $1 - \mathrm{P}\{\hat{\underline{s}}_a[n] \geq \hat{\underline{s}}_i[n]\}$. The probability that the *inactive* sample has the value x, given that it has been *incorrectly* detected as *active*, is:

$$
\mathrm{P}\left\{\hat{\underline{s}}_i[n] = x | \hat{\underline{s}}_a[n] < \hat{\underline{s}}_i[n]\right\} = \frac{\mathrm{P}\{\hat{\underline{s}}_i[n] = x \cap \hat{\underline{s}}_a[n] < x\}}{\mathrm{P}\{\hat{\underline{s}}_a[n] < \hat{\underline{s}}_i[n]\}} =
$$

$$
= \frac{\frac{1}{\sigma_n}\phi\left(\frac{x}{\sigma_n}\right)\left(1 - Q\left(\frac{x - |s|}{\sigma_n}\right)\right)}{\int_{-\infty}^{\infty}\frac{1}{\sigma_n}\phi\left(\frac{u}{\sigma_n}\right)\left(1 - Q\left(\frac{u - |s|}{\sigma_n}\right)\right)\mathrm{d}u}\mathrm{d}x = \frac{\frac{1}{\sigma_n}\phi\left(\frac{x}{\sigma_n}\right)\left(1 - Q\left(\frac{x - |s|}{\sigma_n}\right)\right)}{\frac{1}{2} - \frac{1}{2}\mathrm{erf}\left(\frac{|s|}{2\sigma_n}\right)}\mathrm{d}x. \tag{4.19}
$$

Therefore, (4.19) provides the probability that the original bipolar OFDM sample, $s[n] = s$, is mapped to $-\mathrm{sgn}(s)x$ at the receiver when the *inactive* sample is *incorrectly* detected as *active*. This mapping is not deterministic and varies due to the AWGN at the receiver even when the same pair of *active* and *inactive* samples is transmitted. In order to create a more deterministic view of the transformation which each original bipolar sample undergoes in the event of incorrect detection, it can be assumed that the bipolar sample is mapped to the mean of $-\mathrm{sgn}(s)x$ plus an additional noise component which represents the variation around that mean. The mean of $-\mathrm{sgn}(s)x$ can be calculated as:

$$
\mathrm{f}_w(s) = \int_{-\infty}^{\infty} -\mathrm{sgn}(s)x\frac{\frac{1}{\sigma_n}\phi\left(\frac{x}{\sigma_n}\right)\left(1 - Q\left(\frac{x - |s|}{\sigma_n}\right)\right)}{\int_{-\infty}^{\infty}\frac{1}{\sigma_n}\phi\left(\frac{u}{\sigma_n}\right)\left(1 - Q\left(\frac{u - |s|}{\sigma_n}\right)\right)\mathrm{d}u}\mathrm{d}x =
$$

$$
= \frac{\mathrm{sgn}(s)\int_{-\infty}^{\infty}\frac{x}{\sigma_n}\phi\left(\frac{x}{\sigma_n}\right)Q\left(\frac{x - |s|}{\sigma_n}\right)\mathrm{d}x}{\frac{1}{2} - \frac{1}{2}\mathrm{erf}\left(\frac{|s|}{2\sigma_n}\right)} =
$$

$$
= -\frac{\mathrm{sgn}(s)\frac{\sigma_n}{2\sqrt{\pi}}e^{-\frac{s^2}{4\sigma^2}}}{\frac{1}{2} - \frac{1}{2}\mathrm{erf}\left(\frac{|s|}{2\sigma_n}\right)}. \tag{4.20}
$$

The variance of the noise component can be calculated as:

$$
\mathrm{v}_w(s) = \int_{-\infty}^{\infty} x^2\frac{\frac{1}{\sigma_n}\phi\left(\frac{x}{\sigma_n}\right)\left(1 - Q\left(\frac{x - |s|}{\sigma_n}\right)\right)}{\int_{-\infty}^{\infty}\frac{1}{\sigma_n}\phi\left(\frac{u}{\sigma_n}\right)\left(1 - Q\left(\frac{u - |s|}{\sigma_n}\right)\right)\mathrm{d}u}\mathrm{d}x - \mathrm{f}_w^2(s) =
$$

$$
= \frac{\int_{-\infty}^{\infty}\frac{x^2}{\sigma_n}\phi\left(\frac{x}{\sigma_n}\right)\left(1 - Q\left(\frac{x - |s|}{\sigma_n}\right)\right)\mathrm{d}x}{\frac{1}{2} - \frac{1}{2}\mathrm{erf}\left(\frac{|s|}{2\sigma_n}\right)} - \mathrm{f}_w^2(s) =
$$

$$
= \frac{\frac{\sigma_n^2}{2} + \frac{|s|}{4\sqrt{\pi}}\sigma_n e^{-\frac{s^2}{4\sigma_n^2}} - \frac{\sigma_n^2}{2}\mathrm{erf}\left(\frac{|s|}{2\sigma_n}\right)}{\frac{1}{2} + \frac{1}{2}\mathrm{erf}\left(\frac{|s|}{2\sigma_n}\right)} - \mathrm{f}_w^2(s). \tag{4.21}
$$

As in the case for *correct* distinction between the *active* and *inactive* sample, the noise component in the case for *incorrect* detection is transformed into an AWGN component in the frequency domain by the FFT operation at the demodulator.

According to the Bussgang theorem, introduced in Section 2.8, a zero-mean Gaussian random variable, X, subjected to a non-linear transformation, $z(X)$, has the following properties:

$$z(X) = \alpha X + Y_n \tag{4.22}$$

$$E\{XY_n\} = 0 \tag{4.23}$$

$$\alpha = \text{const.} \tag{4.24}$$

Based on these properties, the constant α and the variance of the noise Y_n can be calculated for the two separate cases of *correct* and *incorrect* detection of the *active* and *inactive* samples. In the case for *correct* detection, the original bipolar sample, $s[n]$, is mapped to $f_c(s)$. In that case, the variance of Y_n and α can be calculated as:

$$\alpha_c = \frac{E\{sf_c(s)\}}{\sigma_s^2} = \frac{\int_{-\infty}^{\infty} sf_c(s)\frac{1}{\sigma_s}\phi\left(\frac{s}{\sigma_s}\right) ds}{\sigma_s^2} \tag{4.25}$$

$$y_c = E\{Y_{n,c}^2\} - E\{Y_{n,c}\}^2 = E\{f_c^2(s)\} - \alpha_c^2\sigma_s^2 - E\{f_c(s)\}^2 =$$
$$= E\{f_c^2(s)\} - \alpha_c^2\sigma_s^2 = \int_{-\infty}^{\infty} f_c^2(s)\frac{1}{\sigma_s}\phi\left(\frac{s}{\sigma_s}\right) ds - \alpha_c^2\sigma_s^2. \tag{4.26}$$

It is apparent from (4.15) that $f_c(s)$ is an odd function, so its mean in (4.26) is zero. In the case for *incorrect* detection of the *active* and *inactive* samples, the variance of Y_n and α can be calculated as:

$$\alpha_w = \frac{E\{sf_w(s)\}}{\sigma_s^2} = \frac{\int_{-\infty}^{\infty} sf_w(s)\frac{1}{\sigma_s}\phi\left(\frac{s}{\sigma_s}\right) ds}{\sigma_s^2} \tag{4.27}$$

$$y_w = E\{Y_{n,w}^2\} - E\{Y_{n,w}\}^2 = E\{f_w^2(s)\} - \alpha_w^2\sigma_s^2 - E\{f_w(s)\}^2 =$$
$$= E\{f_w^2(s)\} - \alpha_w^2\sigma_s^2 = \int_{-\infty}^{\infty} f_w^2(s)\frac{1}{\sigma_s}\phi\left(\frac{s}{\sigma_s}\right) ds - \alpha_w^2\sigma_s^2. \tag{4.28}$$

It is apparent from (4.20) that $f_w(s)$ is an odd function, so its mean in (4.28) is zero. The noise

component Y_n is not correlated with the signal, according to the Bussgang theorem. At the same time, the detection events at each *active-inactive* sample pair are independent as well. Consequently, Y_n is transformed by the FFT operation at the demodulator into AWGN and its variance adds to the variance of the AWGN in the frequency domain.

The variances in (4.16) and (4.21) are given as functions of s, the realization of the signal $s[n]$. On average, over the entire duration of the OFDM frame they are equal to:

$$\bar{v}_c = \int_{-\infty}^{\infty} v_c(s) \frac{1}{\sigma_s} \phi\left(\frac{s}{\sigma_s}\right) ds \tag{4.29}$$

and

$$\bar{v}_w = \int_{-\infty}^{\infty} v_w(s) \frac{1}{\sigma_s} \phi\left(\frac{s}{\sigma_s}\right) ds. \tag{4.30}$$

Using (4.13), the average probability for *correct* detection of an *active* time sample, d_c, is:

$$d_c = \int_{-\infty}^{\infty} \frac{1}{\sigma_s} \phi\left(\frac{s}{\sigma_s}\right) \left(\frac{1}{2} + \frac{1}{2}\text{erf}\left(\frac{|s|}{2\sigma_n}\right)\right) ds. \tag{4.31}$$

For a large number of samples in a U-OFDM frame, the number of *correctly* and *incorrectly* detected *active* samples will have a ratio which corresponds to the probabilities for *correct* and *incorrect* detection – d_c and $1 - d_c$, respectively. Hence, the average gain factor, $\bar{\alpha}$, and the average noise variance in frequency domain, $\bar{N}$, become:

$$\bar{\alpha} = d_c \alpha_c + (1 - d_c)\alpha_w \tag{4.32}$$

$$\bar{N} = d_c(\bar{v}_c + y_c) + (1 - d_c)(\bar{v}_w + y_w) \tag{4.33}$$

The achieved average electrical signal-to-noise ratio (SNR_{elec}) can be plugged in the well-known formula for the BER of M-QAM [93]. Hence, the performance of U-OFDM is calculated as:

$$\text{BER}_U = \text{BER}_{\text{MQAM}}\left(\frac{\alpha^2 E_{\text{b,elec}}}{\bar{N}}\right) \tag{4.34}$$

The comparison between theoretical model and Monte Carlo simulations of the system perfor-

76
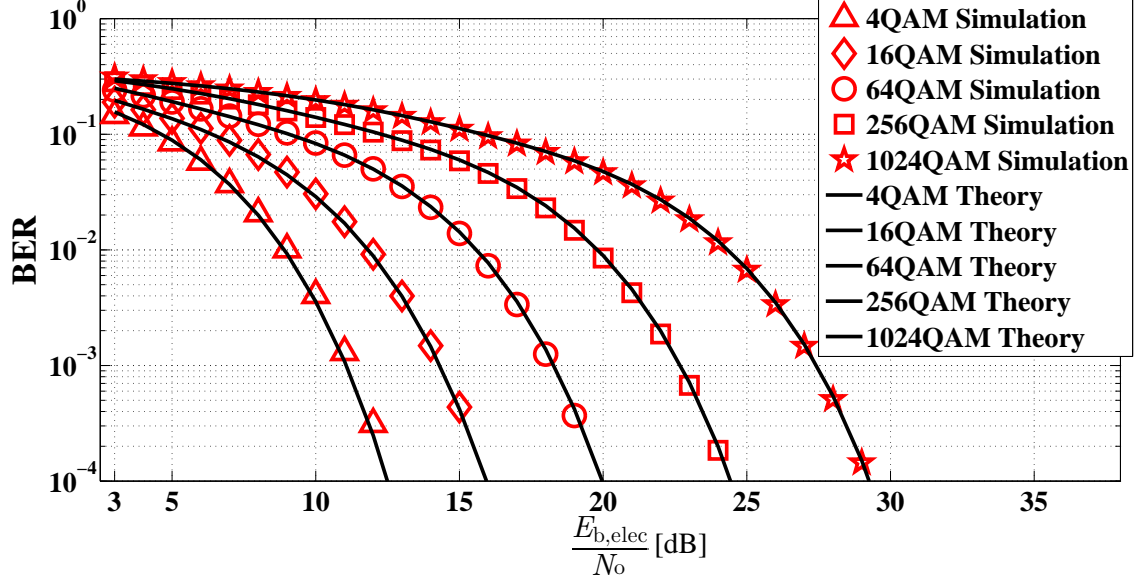
Figure 4.5: *Theoretical U-OFDM performance vs. Monte Carlo simulations*

mance is presented in Fig. 4.5. There is good agreement between the presented model and the conducted simulations.

From (2.19) and (2.21), the ratio between the achieved optical signal-to-noise ratio ($\mathrm{SNR_{opt}}$), and the achieved electrical SNR ($\mathrm{SNR_{elec}}$) can be expressed as the ratio between the average optical power, $P_{\mathrm{opt}}^{\mathrm{avg}}$ presented in (2.20), and the average electrical power, $P_{\mathrm{elec}}^{\mathrm{avg}}$ presented in (2.18). Half of the U-OFDM time-domain samples are equal to zero and the other half follow a clipped Gaussian distribution. Hence, using the statistics of the clipped Gaussian distribution [14], the ratio between the optical power and the electrical power of the signal can be expressed as:

$$\alpha_{\mathrm{o-e}} = \frac{P_{\mathrm{opt}}^{\mathrm{avg}}}{P_{\mathrm{elec}}^{\mathrm{avg}}} = \frac{\phi(0)\sigma_{\mathrm{s}}}{\sigma_{\mathrm{s}}^2/2} = \frac{2\phi(0)}{\sigma_{\mathrm{s}}}. \tag{4.35}$$

The ratio $\alpha_{\mathrm{o-e}}$ can be used to obtain the equivalent $\mathrm{SNR_{elec}}$ for a given value of $\mathrm{SNR_{opt}}$. Thus, since an analytical formula for the BER performance of the system as a function of the electrical SNR has been provided, the BER performance of the system can be evaluated analytically as a function of the optical SNR as well. This concept applies for both the *conventional* demodulation algorithm and the *improved* demodulation algorithm. For the *improved* algorithm, the BER as a
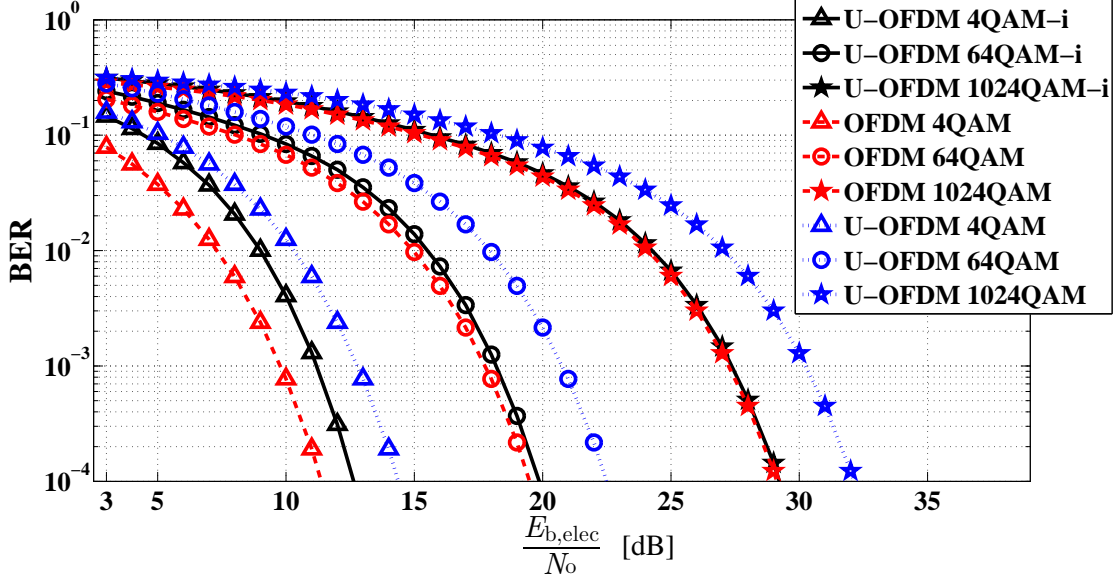
Figure 4.6: *Performance improvement introduced by the* improved *decoder for U-OFDM. The letter "i" denotes the curves for the* improved *decoder. The performance of OFDM for bipolar real signals is illustrated in this figure.*

function of SNR_{opt} is calculated as:

$$BER_U = BER_{MQAM} \left(\frac{\alpha^2 \alpha_{o-e} E_{b,opt}}{\bar{N}} \right). \tag{4.36}$$

4.2.3 Results and Discussion

This section evaluates the performance of U-OFDM in a linear AWGN channel. The AWGN channel is a good approximation of the OWC channel for the system scenarios described in Chapter 2. Any frequency-dependent channel effects as well as non-linear distortion effects are specific for a particular system realisation and a particular deployment scenario. Therefore, they are not included in the analysis, and the linear AWGN channel is adopted as an appropriate fundamental scenario for the evaluation of U-OFDM's performance. Furthermore, in this section, a comparison is made between the performance of the conventional DCO-OFDM scheme presented in Section 2.7.2.1 and the performance of U-OFDM. Since it is practically impossible to avoid clipping effects from below in DCO-OFDM due to the high peak-to-average power ratio (PAPR) of the OFDM signal, as described in Section 2.7.2.1, clipping of any negative values

in DCO-OFDM is the only non-linear distortion adopted in this study.

As already described previously, the *improved* U-OFDM decoder is aimed at closing the 3-dB gap between the performance of a bipolar OFDM signal and the performance of the *conventional* U-OFDM decoder. Fig. 4.6 illustrates the degree to which the *improved* decoder is able to complete the task. For an M-QAM constellation size of 4, the *improved* decoder closes most of the performance gap, but is still about 1.3 dB away from the target. As the constellation size increases, the gap is reduced. For $M = 64$, for example, the performance difference between bipolar OFDM and the *improved* U-OFDM is approximately 0.4 dB. For $M = 1024$, the difference is 0.1 dB. Higher constellation sizes lead to more energy per symbol on average, thus, leading to more signal power per time-domain sample. This, in turn, reduces the probability for making errors in the sample selection process conducted in the *improved* U-OFDM decoding algorithm, and therefore increases the performance improvement relative to the *conventional* U-OFDM decoding algorithm.

The performance of the *conventional* U-OFDM decoder is compared against the performance of DCO-OFDM in Fig. 4.7 and Fig. 4.8 in terms of electrical and optical energy requirements, respectively. It should be noted that binary phase-shift keying (BPSK) OFDM and 4-QAM OFDM perform equivalently in an AWGN channel, and as a result, BPSK DCO-OFDM and 4-QAM DCO-OFDM perform equivalently. Therefore, they are represented by a single BER curve. It should also be pointed out that the biasing levels for DCO-OFDM have been optimised for BER$=[10^{-4}; 10^{-3}]$ through Monte Carlo simulations, *i.e.*, lower bias levels in any of the presented cases would lead to higher BER values while higher bias levels would lead to an increase in the signal power without reducing the BER. In terms of electrical energy dissipation, the *conventional* U-OFDM decoder exhibits performance improvement over DCO-OFDM only in the case of 4-QAM U-OFDM vs. BPSK DCO-OFDM. The improvement is approximately 4 dB. For higher constellations, U-OFDM exhibits either similar or worse performance than DCO-OFDM. It is evident that, as the constellation size increases, U-OFDM requires significantly larger M-QAM constellations in order to achieve the same spectral efficiency, and, as a result, suffers in performance. In terms of optical energy dissipation, U-OFDM again has an advantage over DCO-OFDM only for the case of 4-QAM U-OFDM vs. BPSK DCO-OFDM, where the performance improvement is approximately 1.4 dB at a BER of 10^{-4}. For higher constellations, the optical efficiency of U-OFDM becomes worse than the efficiency of DCO-OFDM. The *improved* decoder could improve the performance of U-OFDM with up to 3 dB as shown in Fig. 4.6.
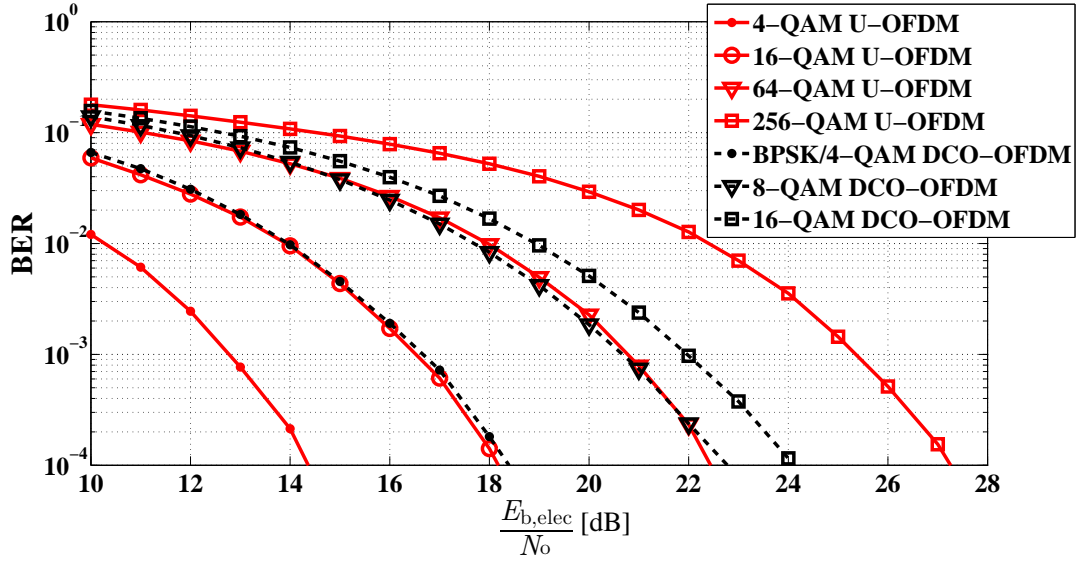
Figure 4.7: *Performance of the* conventional *decoder for U-OFDM in comparison to the performance of DCO-OFDM. The presented BER curves are generated as a function of the electrical SNR as defined in (2.19). The biasing levels for BPSK/4-QAM, 8-QAM, and 16-QAM DCO-OFDM have been set to 6 dB, 7 dB and 7.5 dB according to the biasing representation in (2.23).*
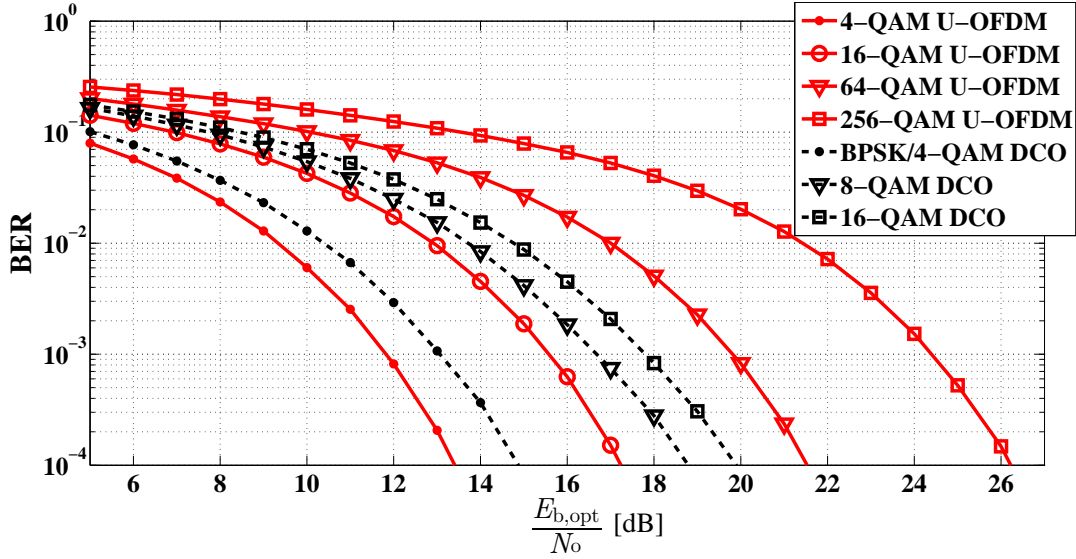
Figure 4.8: *Performance of the* conventional *decoder for U-OFDM in comparison to the performance of DCO-OFDM. The presented BER curves are generated as a function of the optical SNR as defined in (2.21). The biasing levels for BPSK/4-QAM, 8-QAM, and 16-QAM DCO-OFDM have been set to 6 dB, 7 dB and 7.5 dB according to the biasing representation in (2.23).*

However, it is applicable only in favourable communication channel conditions as described at the end of Section 4.2. Furthermore, the *improved* decoder would be insufficient to compensate the electrical energy loss for U-OFDM constellation sizes larger than $M{=}256$ and the optical power loss for U-OFDM constellation sizes larger than $M{=}16$ as can be inferred from the results presented in Fig. 4.7 and Fig. 4.8, respectively. Clearly, a solution to the spectral efficiency loss in U-OFDM is required.

4.3 Enhanced Unipolar Orthogonal Frequency Division Multiplexing (U-OFDM)

The results in Section 4.2.3 show the great potential for energy savings introduced by a unipolar OFDM-based modulation scheme that requires no biasing. At the same time, the loss in spectral efficiency, introduced by the proposed OFDM modulation scheme, clearly diminishes the energy-saving effect of U-OFDM at low spectral efficiency and even completely eliminates any energy-saving benefit at higher spectral efficiency. Furthermore, if moderately high spectral efficiency, in the order of 4b/s/Hz or 5 b/s/Hz, is required, an impractical constellation size, in the order of 65536 or 1048576, would be necessary. Hence, in order for U-OFDM to become suitable for high-speed communication, an appropriate solution to the problem of spectral efficiency loss in the generation process has to be devised. The current section proposes an approach for solving this issue. It is referred to as eU-OFDM.

4.3.1 Concept

The eU-OFDM concept is described in Fig. 4.9. The scheme combines multiple U-OFDM information streams in a single unipolar time-domain signal. All signal generation steps are performed in the digital domain and after a conventional digital-to-analog conversion, the resulting analog signal can modulate the LED without any biasing apart from the minimum requirement to turn on the LED. A single discrete U-OFDM signal in the time domain would look exactly as the information stream at *Depth 1* in Fig. 4.9. A frame P contains the positive samples of an originally bipolar OFDM frame and zeros in the places of the negative samples. A frame N holds the absolute values of the negative samples of that same bipolar OFDM frame and zeros in the places of the positive samples. The signal at *Depth 1* is generated following the procedure described in
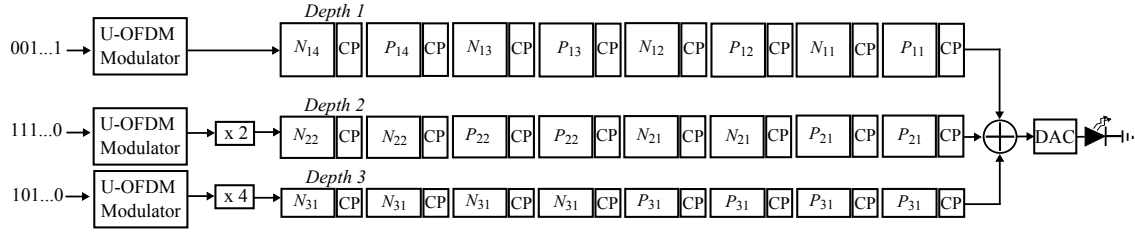
Figure 4.9: *Illustration of the enhanced U-OFDM concept up to* Depth 3. *CP denotes the individual cyclic prefix of a frame.* P_{di} *denotes the unipolar frame which contains the positive samples of the ith originally bipolar OFDM frame at* Depth d. N_{di} *denotes the unipolar frame which contains the absolute values of the negative samples of the ith originally bipolar OFDM frame at* Depth d. *The digital-to-analog converter (DAC) block represents the required operations, including signal amplification, for transition from a digital signal to an analog signal, capable of driving the LED frontend.*

Section 4.2.1. A second U-OFDM information signal, depicted at *Depth 2*, is superimposed over the signal at *Depth 1*, and it does not affect the ability of the receiver processor to separate the two signals if the following structure is followed. At *Depth 2*, each U-OFDM frame is replicated and transmitted twice, where the second frame instance is an exact copy of the first one. Hence, in Fig. 4.9, the second frame at *Depth 2* is an exact replica of the first frame, the fourth frame is an exact replica of the third frame, *etc*. This is denoted by the frame labels. Since at *Depth 2* each U-OFDM frame is transmitted twice, the amplitude of each frame instance is scaled by $\sqrt{1/2}$ in order to keep the utilised energy per bit constant. A third signal, at *Depth 3*, can be introduced similarly to the second signal, however, the individual U-OFDM frames are replicated four times where the amplitude of each frame instance is scaled by $\sqrt{1/4}$, again in order to preserve the dissipated energy per bit. Additional information signals can be added, where at depth d, each U-OFDM frame is replicated 2^{d-1} times and its amplitude is scaled by $1/\sqrt{2^{d-1}}$.

After the information signal is received, the data signal at *Depth 1* can be demodulated straight away with the *conventional* U-OFDM decoding algorithm. Every second frame, holding the negative values of the original bipolar OFDM frame, is subtracted from its preceding frame, holding the positive values of the original bipolar OFDM frame. Then, the conventional OFDM demodulator is applied on the obtained bipolar frames. For example, at *Depth 1*, the first bipolar frame is recovered with the operation $P_{11} - N_{11}$, the second bipolar frame is recovered with the operation $P_{12} - N_{12}$ and so forth. No additional signals interfere with the successful demodulation because

82

the interference that falls on P_{11} is equivalent to the interference that falls on N_{11}, caused by $P_{21} + P_{31}$ in the presented example. Hence, the subtraction operation cancels out both interference terms. Analogously, the interference is removed from all subsequent frames at *Depth 1*. Hence, the bits encoded at *Depth 1* can be successfully recovered with the conventional U-OFDM demodulator. Once the demodulation at *Depth 1* is complete, the demodulated bits can be remodulated again in order to recover the transmitted U-OFDM signal at *Depth 1*. This signal is then subtracted from the overall received signal, and the result contains only the information streams at *Depth 2* and above. Every two equivalent frames at *Depth 2* are summed. For example, the first and the second frame at *Depth 2* are summed, the third and the fourth frames are summed, *etc.*. Afterwards, the demodulation process continues with *conventional* U-OFDM demodulation – exactly the same way as for the recovery of the information at *Depth 1*. Again, subsequent streams do not hinder the process because the interference from all subsequent streams is structured in such a way that it is completely removed by the subtraction operation. After the bits at *Depth 2* are recovered, they are remodulated and the result is subtracted from the remaining received signal. This iterative procedure continues until the information at all depths is decoded.

4.3.2 Spectral Efficiency

The newly-introduced scheme has increased spectral efficiency when compared to U-OFDM. The spectral efficiency of the modified scheme can be calculated as the sum of the spectral efficiencies of the different streams at all depths:

$$\eta_{\mathrm{eU}}(D) = \sum_{d=1}^{D} \frac{\eta_{\mathrm{U}}}{2^{d-1}} = \eta_{\mathrm{U}} \sum_{d=1}^{D} \frac{1}{2^{d-1}}, \tag{4.37}$$

where D is the maximum employed modulation depth in the new scheme. It equals the total number of U-OFDM streams that are superimposed in the generated modulation signal. As the maximum modulation depth is increased, the spectral efficiency of eU-OFDM increases as shown in Table 4.1.

D	1	2	3	4	5	6	7
$\frac{\eta_{\mathrm{eU}}(D)}{\eta_{\mathrm{DCO}}}$ [%]	50	75	87.5	93.75	96.88	98.44	99.22

Table 4.1: *Spectral efficiency of eU-OFDM as a function of the maximum modulation depth D.*

For a large modulation depth, $\eta_{\mathrm{eU}}(D)$ converges to η_{DCO}, the spectral efficiency of DCO-OFDM, defined in (2.15):

$$\lim_{D\to\infty} \eta_{\mathrm{eU}}(D) = \eta_{\mathrm{U}} \lim_{D\to\infty} \sum_{d=1}^{D} \frac{1}{2^{d-1}} = 2\eta_{\mathrm{U}} = \eta_{\mathrm{DCO}}. \tag{4.38}$$

Two practical issues should be considered at this point. First, OFDM transmission cannot start before at least a full block of bits, required for the generation of one full OFDM frame, is available at the transmitter. In real-time streaming applications, this introduces a latency of at least one frame length. When eU-OFDM is used, the latency increases with the modulation depth because the binary data for at least 2^D-1 OFDM frames has to be available to the processor at the transmitter before one full eU-OFDM data block, as the one depicted in Fig. 4.9, can be modulated for transmission. At the receiver site, some latency is also expected because at least 2^d frames have to be received before the demodulation at depth d can be completed. Second, it can be assumed that the FFT/IFFT operation dominates the computational complexity at the receiver [87]. The eU-OFDM demodulation process requires additional FFT/IFFT operations to be performed at the receiver compared to the demodulation processes in U-OFDM and OFDM. If all subtraction procedures in the eU-OFDM demodulator are performed in the time domain, the total number of FFT/IFFT operations is approximately double the number of FFT/IFFT operations required in OFDM because every demodulated frame has to be remodulated and, therefore, an additional IFFT operation is required. When the communication channel is not flat, this approach would introduce additional complexity in the equalisation process because the remodulated signal components would have to be distorted by the channel transfer characteristic before they are subtracted from the overall received signal. Therefore, it might be more practical if all subtraction operations in the demodulation process are performed in the frequency domain after the FFT operation. Then, in every eU-OFDM frame, equalization has to be performed only once for the entire information signal, and no channel effects would have to be introduced to the remodulated signal. In such an implementation, however, the number of required FFT/IFFT operations is roughly four times higher than in conventional OFDM demodulation. This occurs because every remodulated frame has to be split into two frames, one holding the positive values of the bipolar frame and the other holding the negative values of the bipolar frame, according to the U-OFDM algorithm, and then both of these frames have to be translated into the frequency domain with an FFT in order to be subtracted from the overall received signal. In summary, this leads to four

FFT/IFFT operations per OFDM frame in comparison to DCO-OFDM. The implementation of eU-OFDM also introduces additional memory costs compared to OFDM because the data equivalent of 2^D OFDM frames has to be buffered for the complete demodulation of one full eU-OFDM block as the one shown in Fig. 4.9. The presented implementation issues put a practical limit on the highest eU-OFDM modulation depth that can be implemented with a given hardware budget. In practical applications, the hardware complexity is not expected to be problematic because for a relatively small maximum modulation depth, the gap in spectral efficiency between eU-OFDM and DCO-OFDM is almost completely closed. For example, for D=3 and D= 5, η_{eU} is already 87.5% and 96.88% of η_{DCO}, respectively, which means the difference is practically negligible. A more detailed analysis of the eU-OFDM implementation cost can be addressed in future work.

4.3.3 Theoretical Bit-error-rate Analysis

4.3.3.1 Electrical Power

A real bipolar time-domain OFDM signal follows a Gaussian distribution with average electrical power of $\mathrm{E}\{\mathrm{s}^2(t)\}=\sigma_{\mathrm{s}}^2$, where σ_{s} is the standard deviation of the time-domain waveform $\mathrm{s}(t)$ [15, 21]. Therefore, half of the time-domain samples in a U-OFDM signal follow a Gaussian distribution truncated at zero and the other half of the samples are equal to zero [18, 21]. As a result, it is straightforward to show that the average power of the time-domain U-OFDM signal is $\sigma_{\mathrm{s}}^2/2$ [18, 21]. The eU-OFDM signal is a combination of superimposed independent U-OFDM signals, and, therefore, its average time-domain electrical power grows with the number of signals that are superimposed. It can be derived as [21, 60]:

$$
\begin{aligned}
P_{\mathrm{elec,eU}}^{\mathrm{avg}} &= \mathrm{E}\{\mathrm{s}_{\mathrm{eU}}^2(t)\} = \mathrm{E}\left\{\left(\sum_{d=1}^{D}\underline{\mathrm{s}}_d(t)\right)^2\right\} \\
&= \sum_{d=1}^{D}\mathrm{E}\left\{\underline{\mathrm{s}}_d^2(t)\right\} + \sum_{d_1=1}^{D}\sum_{\substack{d_2=1 \\ d_1\neq d_2}}^{D}\mathrm{E}\left\{\underline{\mathrm{s}}_{d_1}(t)\right\}\mathrm{E}\left\{\underline{\mathrm{s}}_{d_2}(t)\right\} \\
&= \frac{\sigma_{\mathrm{s}}^2}{2}\sum_{d=1}^{D}\frac{1}{2^{d-1}} + \sum_{d_1=1}^{D}\sum_{\substack{d_2=1 \\ d_1\neq d_2}}^{D}\frac{\phi(0)\sigma_{\mathrm{s}}}{\sqrt{2^{d_1-1}}}\frac{\phi(0)\sigma_{\mathrm{s}}}{\sqrt{2^{d_2-1}}} \\
&= \frac{\sigma_{\mathrm{s}}^2}{2}\left(2-\frac{1}{2^{D-1}}\right) + \frac{\sigma_{\mathrm{s}}^2}{2}4\phi^2(0)\sum_{d_1=1}^{D}\sum_{\substack{d_2=1 \\ d_1\neq d_2}}^{D}\frac{1}{\sqrt{2^{d_1+d_2}}},
\end{aligned}
\tag{4.39}
$$

where $s_{eU}(t)$ is the eU-OFDM waveform in the time domain, $\underline{s}_d(t)$ is the U-OFDM signal at depth d, and $\phi(0)$ is the probability density function (PDF) of the standard normal distribution. The time-domain expectation of the U-OFDM signal at depth d is $E\{\underline{s}_d(t)\} = \phi(0)\sigma_s/\sqrt{2^{d-1}}$. It is used in the calculation of (4.39) and can be derived from the statistics of the truncated Gaussian distribution described in [14]. The average number of bits that are encoded in a eU-OFDM signal is $2 - 1/2^{D-1}$ times more than the number of bits that are encoded in a U-OFDM signal during the same time interval. Therefore, the increase in the required SNR per bit in eU-OFDM compared to U-OFDM for the same M-QAM constellation size is the ratio of the average electrical power calculated in (4.39) and the average electrical power of the U-OFDM signal, $\sigma_s/2$, divided by the ratio of the bits encoded in the two modulation schemes, $2 - 1/2^{D-1}$. Hence, the increase in the required SNR for eU-OFDM is:

$$\alpha(D) = 1 + \frac{4\phi^2(0)}{2 - 1/2^{D-1}} \sum_{d_1=1}^{D} \sum_{\substack{d_2=1 \\ d_1 \neq d_2}}^{D} \frac{1}{\sqrt{2^{d_1+d_2}}}. \tag{4.40}$$

The electrical SNR of the system is defined as in (2.19):

$$\frac{E_{b,\text{elec}}}{N_o} = \frac{P_{\text{elec,eU}}^{\text{avg}}}{B\eta_{eU}N_o} = \frac{E\{s_{eU}^2(t)\}}{B\eta_{eU}N_o}, \tag{4.41}$$

where B is the used double-sided communication bandwidth and N_o is the double-sided PSD of the AWGN at the receiver. Fig. 4.10(a) shows $\alpha(D)$ for different values of the maximum modulation depth. The average SNR penalty of eU-OFDM in comparison to U-OFDM converges to about $4\,\text{dB}$ as the spectral efficiency converges to the spectral efficiency of DCO-OFDM. As described in Section 4.2.2, U-OFDM suffers a constant SNR penalty of $3\,\text{dB}$ in comparison to a bipolar OFDM signal. Therefore, when this penalty is combined with the maximum penalty of about $4\,\text{dB}$ in Fig. 4.10(a), it can be concluded that irrespective of the employed M-QAM constellation size, eU-OFDM suffers a maximum electrical SNR penalty of about $7\,\text{dB}$ in comparison to a bipolar OFDM signal. The results in Section 4.2.3 indicate that DCO-OFDM suffers a penalty of about 7 dB in terms of electrical SNR requirements relative to a bipolar OFDM signal for BPSK and 4-QAM. Furthermore, the penalty increases when larger M-QAM constellations are used because larger constellations are more sensitive to non-linear distortion, and therefore, higher biasing levels are required in order to reduce the clipping effect on any negative signal samples. Therefore, depending on the used M-QAM constellation size, eU-OFDM is expected

(a) Average penalty per bit as a function of the maximum modulation depth.

(b) Penalty per additional bit at a specific depth.
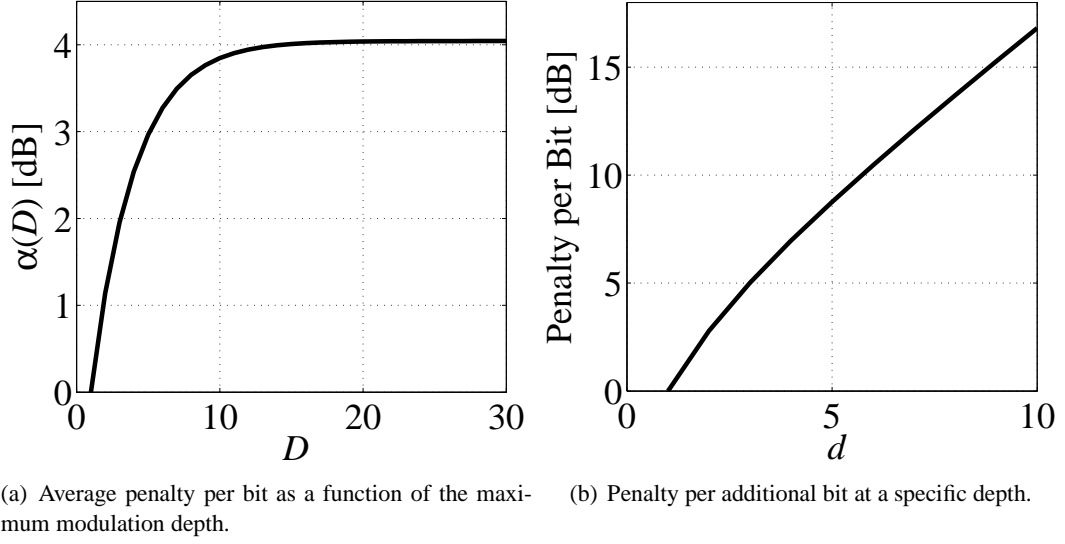
Figure 4.10: *Energy penalty with increasing modulation depth.*

to have comparable or significantly better performance than DCO-OFDM.

At this point, note the additional electrical energy per bit that is introduced at each modulation depth, d, shown in Fig. 4.10(b). The presented curve shows the additional electrical energy per additional bit that is introduced when an additional U-OFDM signal is introduced to the overall information signal. The results are normalised to the energy per bit at *Depth 1*. Since the additional signals are added on top of an already existing time-domain signal, the additional electrical energy per additional bit that they introduce increases significantly with the modulation depth. This means that introducing additional U-OFDM streams to close the spectral efficiency gap between eU-OFDM and DCO-OFDM becomes energy inefficient very quickly. When the additional latency, the increased hardware complexity and the size of the spectral efficiency gap, illustrated in Table 4.1, are also taken into consideration, it becomes evident that a practical implementation of eU-OFDM is likely to be realised for a maximum modulation depth of not more than a few streams. In case it is important that the spectral efficiency gap is closed completely, an alternative eU-OFDM implementation can be considered with different M-QAM constellation sizes at each depth. For example, two 16-QAM streams match the spectral efficiency of 8-QAM DCO-OFDM; a 64-QAM stream at *Depth 1* in combination with a 16-QAM stream at *Depth 2* or a combination of a 32-QAM stream at *Depth 1* and two subsequent 16-QAM streams at *Depth 2* and *Depth 3* is enough to achieve the same spectral efficiency as 16-QAM DCO-OFDM. A detailed study of the optimal constellation size combinations can be addressed in future work.
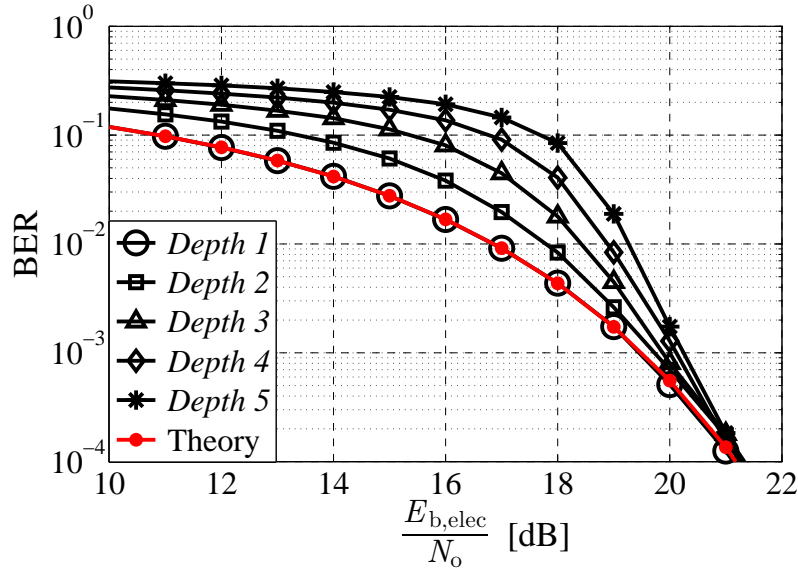
Figure 4.11: *The performance of* 16-*QAM eU-OFDM at different depths as a function of the electrical SNR. Note that the electrical energy per bit represents the average electrical energy per bit for all streams combined in accordance with the definition in (4.39) and (4.41). The curve named "Theory" represents the theoretically performance bound.*

A theoretical bound for the BER of eU-OFDM as a function of the electrical SNR can be estimated using the well-established formula for calculating the BER of conventional real bipolar M-QAM OFDM [93]. The only necessary modification in that formula is a scaling of the required SNR by a factor of 2α to account for the 3-dB performance degradation in U-OFDM and to account for the SNR penalty incurred in eU-OFDM. The proposed theoretical bound is equivalent to the BER curve for the information stream at *Depth 1* in eU-OFDM because in that stream any distortion is caused only by the AWGN process at the receiver since any inter-stream interference is completely removed by the subtraction operation in the demodulation procedure. The BER of the U-OFDM signals at higher depths increases with the depth because the performance is affected by the BER at lower depths. Any errors in the bit demodulation at a given depth propagate into the performance of the data streams at subsequent depths because they translate into imperfections in the iterative signal cancellation algorithm. This results in reduced signal quality at all subsequent U-OFDM streams. With an increase in the SNR, the bit errors are reduced. As a result, the performance at all depths converges to the performance of the stream at *Depth 1*. This performance trend is illustrated in Fig. 4.11. The presented results show good agreement between the theoretical performance bound and the results of the Monte Carlo simulations conducted.

4.3.3.2 Optical Power

The average optical power of the time-domain eU-OFDM signal is [21, 60]:

$$P_{\text{opt,eU}}^{\text{avg}} = \text{E}\left\{s_{\text{eU}}(t)\right\} = \text{E}\left\{\sum_{d=1}^{D} \underline{s}_d(t)\right\} = \sum_{d=1}^{D} \text{E}\left\{\underline{s}_d(t)\right\} \tag{4.42}$$

$$= \phi(0)\sigma_{\text{s}} \sum_{d=1}^{D} \frac{1}{\sqrt{2^{d-1}}}.$$

The optical SNR of the system is defined as in (2.21) [21, 60]:

$$\frac{E_{\text{b,opt}}}{N_{\text{o}}} = \frac{P_{\text{opt,eU}}^{\text{avg}}}{B\eta_{\text{eU}}N_{\text{o}}} = \frac{\text{E}\left\{s_{\text{eU}}(t)\right\}}{B\eta_{\text{eU}}N_{\text{o}}}. \tag{4.43}$$

The ratio of (4.39) and (4.42) can be used to establish a relationship between the electrical SNR and the optical SNR. Hence, for a given value of the optical SNR, the equivalent achieved electrical SNR can be calculated using this relationship. Then, the closed-form BER bound as a function of the electrical SNR can be used to establish a performance bound as a function of the optical SNR. Fig. 4.12 illustrates the close agreement between the proposed theoretical bound and the Monte Carlo simulations conducted. All calculations presented in this section are valid for an ideal front-end transmitter device under the assumption that modulation using eU-OFDM does not require biasing of the LED. However, a typical LED requires a minimum bias voltage at which the device "turns on" and begins to emit light. In the estimation of the optical efficiency of the system, a zero bias can be assumed, because before the LED "turns on" any light intensity output is negligible. However, when the electrical efficiency of the system is estimated, the bias should be taken into account. If the bias level is small relative to the dynamic range of the information signal, it would not introduce considerable variations in the estimated energy efficiency relative to an ideal system. Furthermore, the "turn on" bias level is device-specific. Consequently, it is disregarded in the presented theoretical study for matters of simplicity.

4.3.4 Results and Discussion

This section presents the performance of eU-OFDM in a linear AWGN channel. Appendix C presents a study which illustrates why an investigation in a flat AWGN channel is sufficient for comparing the performance of different OFDM based modulation schemes. As in Section 4.2.3, the only non-linear effect considered in this section is the effect of clipping any negative val-
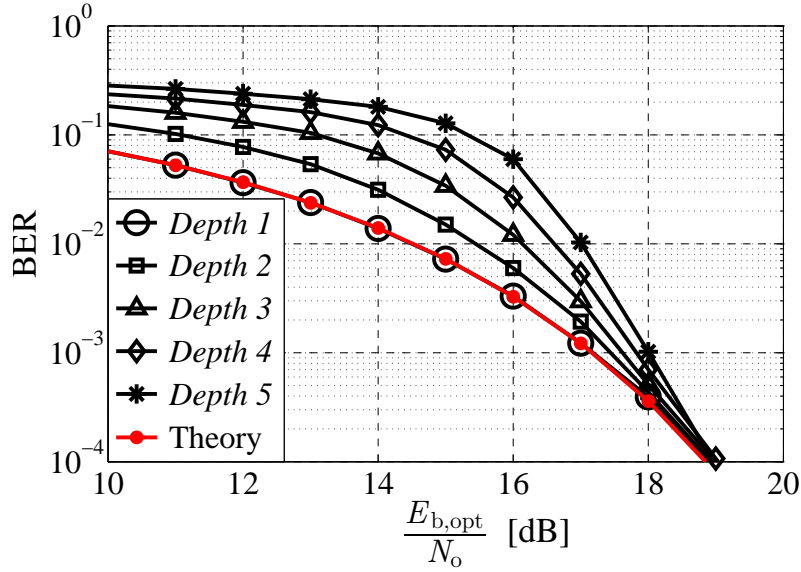
Figure 4.12: *The performance of 16-QAM eU-OFDM at different depths as a function of the optical SNR. Note that the optical energy per bit represents the average optical energy per bit for all streams combined in accordance with the definition in (4.42) and (4.43). The curve named "Theory" represents the theoretical performance bound.*

ues in the information signal due to the electrical characteristics of an ideal LED. The novel scheme, eU-OFDM, generates a strictly positive signal and, therefore, it completely avoids clipping of the signal from below, while DCO-OFDM is subjected to this non-linear effect. In the presented study, the maximum depth of eU-OFDM is chosen to be $D{=}3$ because at this depth, the larger part of the spectral efficiency gap between DCO-OFDM and U-OFDM is closed. In addition, for this value of D, the implementation complexity is still quite manageable and the theoretical/simulation results provided in this section can be compared against experimental results described in Chapter 6. Therefore, in all results presented in this section, the spectral efficiency of eU-OFDM is 87.5% of the spectral efficiency of DCO-OFDM, in agreement with Table 4.1.

The average BER achieved for the decoded information at all depths in eU-OFDM is compared against the BER of DCO-OFDM and U-OFDM for different M-QAM constellation sizes. Fig. 4.13 presents the BER results for constellation sizes $M = [2, 4, 8, 16]$ as a function of the electrical SNR. For U-OFDM, an actual constellation size of M^2 is used for each respective value of M, so that equal spectral efficiency can be achieved by the three schemes. The results have been presented for BER values down to 10^{-4} because most forward error correction (FEC) codes in practice are able to deliver reliable communication at such BERs [94]. The electrical efficiency
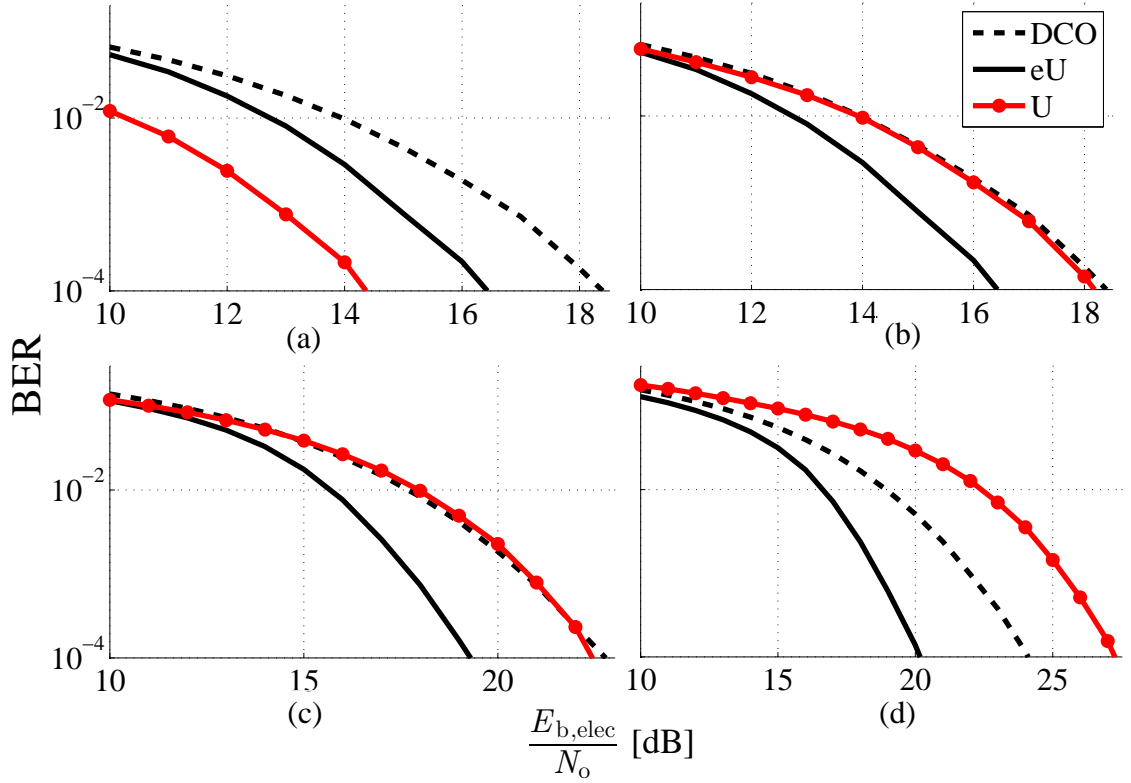
Figure 4.13: *Comparison between the performance of eU-OFDM, U-OFDM, and DCO-OFDM for different M-QAM modulation orders as a function of the electrical SNR: (a) BPSK; (b) 4-QAM; (c) 8-QAM; (d) 16-QAM. The optimum bias levels for BPSK, 4-QAM, 8-QAM, and 16-QAM DCO-OFDM are estimated using Monte Carlo simulations and set at 6 dB, 6 dB, 7 dB, and 7.5 dB, respectively, following the description in (2.23).*

improvement of eU-OFDM over DCO-OFDM begins at around 2 dB for BPSK and increases to about 4 dB for 16-QAM. In DCO-OFDM, the bias levels for the different M-QAM constellations are optimised through Monte Carlo simulations and appear to be in agreement with previous work as in [14, 95]. The introduced bias levels are deemed optimal because in each of the presented cases adding less bias leads to more clipping distortion and, therefore, to higher BER for a given SNR. At the same time, adding more bias leads to higher energy dissipation without any reduction of the BER. The bias levels are expressed as the estimated SNR increase in dB relative to a bipolar OFDM signal as described in (2.23). In eU-OFDM, for a maximum depth of $D=3$, the SNR penalty is $\alpha \approx 1.95$ dB according to Fig. 4.10(a). This SNR penalty is constant irrespective of the constellation size. Therefore, the apparent increase in energy efficiency of eU-OFDM over DCO-OFDM with an increase in the M-QAM modulation order can be explained and even quan-
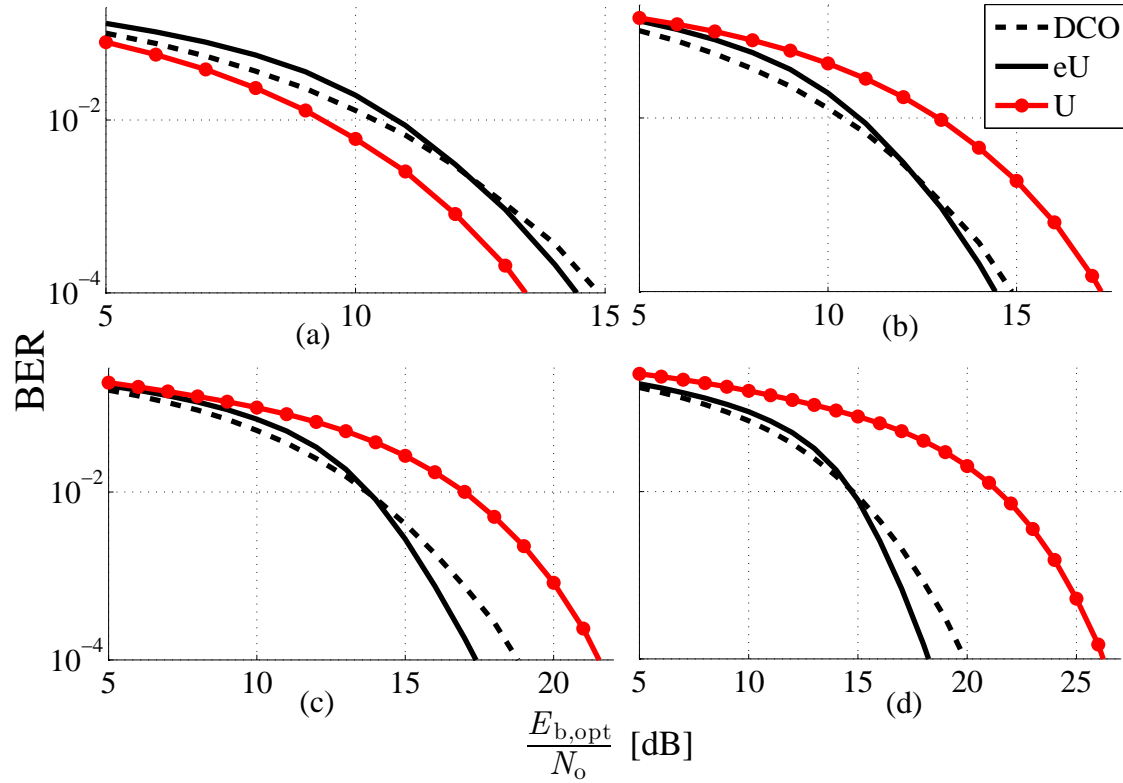
Figure 4.14: *Comparison between the performance of eU-OFDM, U-OFDM, and DCO-OFDM for different M-QAM modulation orders as a function of the optical SNR: (a) BPSK; (b) 4-QAM; (c) 8-QAM; (d) 16-QAM. The optimum bias levels for BPSK, 4-QAM, 8-QAM, and 16-QAM DCO-OFDM are estimated using Monte Carlo simulations and set at 6 dB, 6 dB, 7 dB, and 7.5 dB, respectively, following the description in (2.23).*

tified. Fig. 4.13 also clearly illustrates the loss in energy efficiency for U-OFDM as the spectral efficiency increases. In Fig. 4.13(a), 4-QAM U-OFDM is more energy-efficient than both BPSK eU-OFDM and BPSK DCO-OFDM. In Fig. 4.13(b)-4.13(c), 16-QAM U-OFDM and 64-QAM U-OFDM are less energy efficient than 4-QAM eU-OFDM and 8-QAM eU-OFDM, respectively, while at the same time exhibiting approximately the same efficiency as 4-QAM DCO-OFDM and 8-QAM DCO-OFDM. In Fig. 4.13(d), 256-QAM U-OFDM is evidently less energy efficient than both 16-QAM eU-OFDM and 16-QAM DCO-OFDM. Fig. 4.14 presents the same performance trends in all three investigated modulation schemes as a function of the optical SNR. For BPSK and 4-QAM, eU-OFDM exhibits an efficiency advantage of about 0.5 dB over DCO-OFDM. This optical power advantage reaches almost 2 dB for 16-QAM. At the same time, U-OFDM exhibits an advantage only for a constellation size of $M = 4$ compared with BPSK eU-OFDM and BPSK
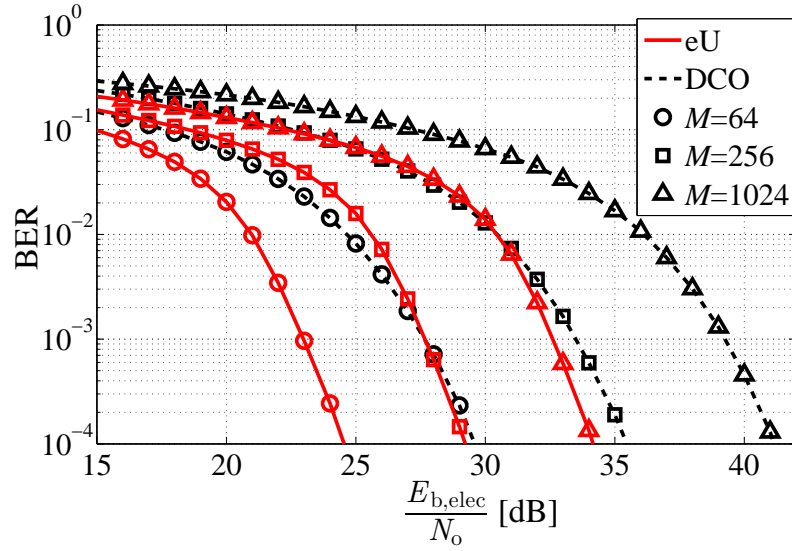
Figure 4.15: *Performance of eU-OFDM compared against the performance of DCO-OFDM for different M-QAM modulation orders as a function of the electrical SNR. The optimum bias levels for 64-QAM, 256-QAM, and 1024-QAM DCO-OFDM are estimated using Monte Carlo simulations and set at 9.5 dB, 11 dB, and 13 dB, respectively, following the description in (2.23).*

DCO-OFDM in Fig. 4.14(a).

A performance comparison between eU-OFDM and DCO-OFDM is presented for higher spectral efficiency values as well. Fig. 4.15 and Fig. 4.16 show results for $M = [64, 256, 1024]$. In this study, U-OFDM is not considered because it was already demonstrated that the scheme clearly loses its energy advantage over both eU-OFDM and DCO-OFDM for 256-QAM U-OFDM compared to 16-QAM eU-OFDM/DCO-OFDM. The results presented in Fig. 4.15 and Fig. 4.16 show that for 1024-QAM, eU-OFDM can reach savings of approximately $7\,\mathrm{dB}$ in electrical energy dissipation over DCO-OFDM and savings of approximately $3\,\mathrm{dB}$ in required optical power. Such results can make a significant difference in future high-speed OWC systems.

4.4 Extension to Other Unipolar OFDM-based Modulation Schemes

The concept described in this paper is based on the unique time-domain structure in every pair of U-OFDM frames. Analogous unique structures are also present in the other two well-known unipolar OFDM modulation schemes – ACO-OFDM and PAM-DMT. Hence, the eU-OFDM concept could be extended to ACO-OFDM and PAM-DMT.
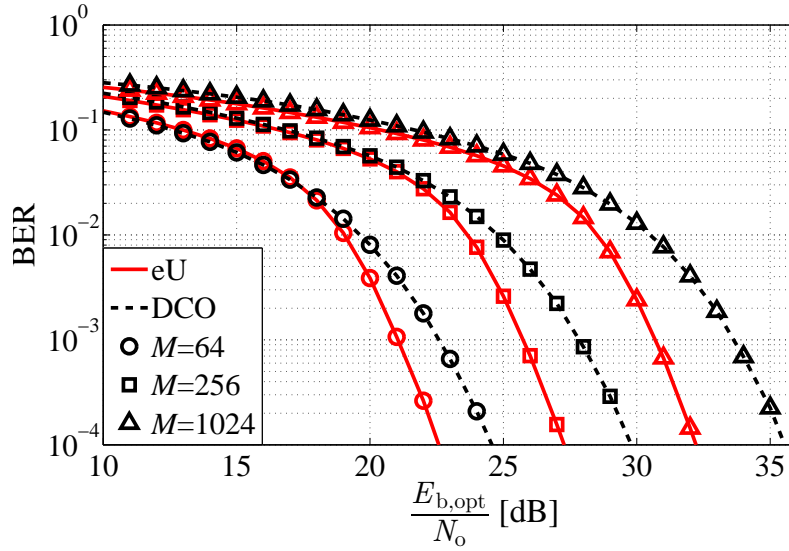
Figure 4.16: *Performance of eU-OFDM compared against the performance of DCO-OFDM for different M-QAM modulation orders as a function of the optical SNR. The optimum bias levels for 64-QAM, 256-QAM, and 1024-QAM DCO-OFDM are estimated using Monte Carlo simulations and set at 9.5 dB, 11 dB, and 13 dB, respectively, following the description in (2.23).*

4.4.1 Asymmetrically-clipped Optical OFDM (ACO-OFDM)

In ACO-OFDM, only the odd subcarriers are modulated. As a consequence, the samples within one time-domain frame of the bipolar signal, $s[n]$, before the asymmetrical clipping have the property: $s[n] = -s[n + N_{\text{fft}}/2]$ as shown in Section 2.7.2.2 [21, 61]. If only the even subcarriers are modulated, the time-domain frame has the property: $s[n] = s[n + N_{\text{fft}}/2]$ [21]. The opposite relations also hold as described in Section 2.7.2.2. Therefore, as long as the interference in the first half of the frame, from sample 0 to sample $N_{\text{fft}}/2-1$, is equivalent to the interference in the second half of the frame, from sample $N_{\text{fft}}/2$ to sample $N_{\text{fft}}-1$, any distortion due to interference falls only on the even subcarriers in the frequency domain. Hence, it is orthogonal to the information, which is modulated only on the odd subcarriers [21, 61]. A way to enhance the data rate of ACO-OFDM is presented in Fig. 4.17.

The demodulation process at the receiver would be applied in the same manner as for eU-OFDM. The information at *Depth 1* can be recovered directly as in conventional ACO-OFDM because all subsequent data streams are arranged such that they reflect only on the even subcarriers in the frequency domain. After the first stream is decoded, the information can be remodulated again and subtracted from the overall signal. Then, frames which are equivalent at *Depth 2* can
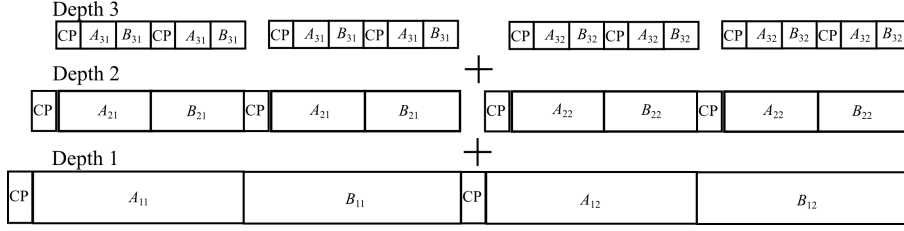
Figure 4.17: *Illustration of the enhanced ACO-OFDM concept up to depth 3. CP indicates the unique cyclic prefix of each frame. A_{di} indicates the first half – from sample 0 to sample $N_{\text{fft}}/2-1$ – of the ith ACO-OFDM frame at Depth d. B_{di} indicates the second half – from sample $N_{\text{fft}}/2$ to sample $N_{\text{fft}}-1$ – of the ith ACO-OFDM frame at Depth d.*
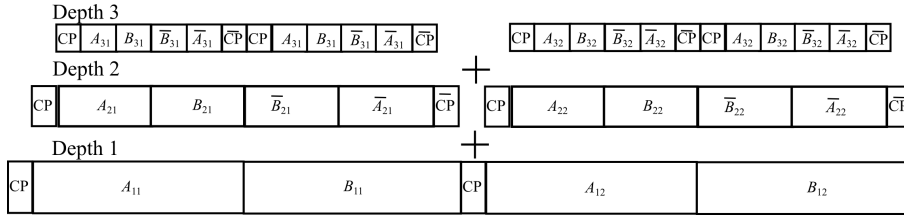
Figure 4.18: *Illustration of the enhanced PAM-DMT concept up to depth 3. CP indicates the unique cyclic prefix of each frame. A_{di} indicates the first half – from sample 0 to sample $N_{\text{fft}}/2-1$ – of the ith PAM-DMT frame at Depth d. B_{di} indicates the second half – from sample $N_{\text{fft}}/2$ to sample $N_{\text{fft}}-1$ – of the ith PAM-DMT frame at Depth d. Furthermore, $A_{di}[n] = \bar{A}_{di}[N_{\text{fft}}/2 - 1 - n]$ and $B_{di}[n] = \bar{B}_{di}[N_{\text{fft}}/2 - 1 - n]$ so that the Hermitian symmetry of the interference at each depth is satisfied.*

be recombined and the demodulation procedure can continue as for the stream at *Depth 1*. The algorithm can be applied until the information from all streams is recovered.

4.4.2 Pulse-amplitude-modulated Discrete Multitone Modulation (PAM-DMT)

In PAM-DMT, all subcarriers are modulated with imaginary symbols from an M-PAM scheme as described in Section 2.7.2.3 [21, 62]. In case the interference over a single PAM-DMT frame duration possesses a Hermitian symmetry in the time-domain, its frequency profile is a real signal. Hence, the interference is completely orthogonal to the useful information which is encoded in imaginary symbols [21]. A way to introduce additional PAM-DMT data within the modulation signal is presented in Fig. 4.18.

The demodulation process at the receiver is analogous to the demodulation process of eU-OFDM and the demodulation process of the proposed enhanced version of ACO-OFDM from Section 4.4.1. The information at *Depth 1* can be recovered directly. Afterwards, the data is remodulated and then subtracted from the overall signal. Then, the identical frames at *Depth 2* can be recombined, after which they can be demodulated as the data at *Depth 1*. The information at all additional depths is recovered in a similar fashion.

4.5   Summary

A novel modulation approach for the generation of energy-efficient unipolar OFDM signals, coined U-OFDM, has been introduced in this chapter. The scheme offers significant energy savings in terms of electrical energy consumption and optical power requirements when compared to the conventional DCO-OFDM. All benefits, however, come at a 50% reduction in the scheme's spectral efficiency. When equal spectral efficiency is assumed, U-OFDM manages to outperform DCO-OFDM only for relatively small M-QAM constellation sizes. A modified approach, termed eU-OFDM, has been proposed as a solution to the spectral efficiency reduction problem in U-OFDM. Using this approach, the spectral efficiency gap between U-OFDM and DCO-OFDM is practically closed, while significant power savings are attained.

The problem of spectral efficiency loss has been a long-lasting issue in the inherently unipolar state-of-the-art techniques including: ACO-OFDM, PAM-DMT and the novel U-OFDM. The solution proposed in this chapter in the form of eU-OFDM exploits the OFDM frame structure in a novel way and allows multiple information streams to be transmitted simultaneously. The novel concept effectively introduces a new degree of freedom in the signal space of U-OFDM, ACO-OFDM and PAM-DMT. For the first time, the spectral efficiency of DCO-OFDM has been matched by an inherently unipolar OFDM-based modulation scheme which does not require an increase in the M-QAM modulation order and still attains manageable implementation complexity as well as significant energy benefits.

Chapter 5
Non-linear Distortion in OFDM-based Modulation Schemes for OWC

Non-linear distortion is anticipated in an optical wireless communications (OWC) system. During the design process, it is important that one fully understands and is able to quantify the effects of non-linear distortion on the system performance. The orthogonal frequency division multiplexing (OFDM) modulation signals are particularly vulnerable to non-linear distortion due to the generally high peak-to-average power ratio (PAPR) they possess. There exist multiple approaches for analysing the effects of non-linear distortion on an OFDM-based information signal. One particularly popular approach proves that in the frequency domain, non-linear distortion effectively translates into additional Gaussian noise, whose statistics can be estimated with the help of the Bussgang theorem.

The current work provides an extension to the Bussgang theorem approach where a novel method for approximating non-linear distortion allows a closed-form theoretical solution to be obtained for an arbitrary distortion function. The technique can be applied to most existing OFDM-based modulation schemes in OWC, in particular: direct-current-biased optical orthogonal frequency division multiplexing (DCO-OFDM), asymmetrically clipped optical orthogonal frequency division multiplexing (ACO-OFDM), pulse-amplitude-modulated discrete multitone modulation (PAM-DMT), unipolar orthogonal frequency division multiplexing (U-OFDM). The latter three are shown to have equivalent performance in a non-linear additive white Gaussian noise (AWGN) channel, thus, providing further evidence that these concepts are, in essence, three different approaches towards the same energy-efficiency goal.

5.1 Introduction

In an OWC system, an information signal is subject to a number of linear and non-linear distortions. The linear distortions like signal attenuation and intersymbol interference (ISI) can be compensated at the receiver with amplifiers and equalisers. The non-linear distortions, however, are often irreversible. Some examples include: quantisation effects in the digital-to-analog converters (DACs) at the transmitter and quantisation effects in the analog-to-digital converters (ADCs) at the receiver, as well as the effects of the non-linear output characteristic of a light emitting diode (LED). That is why, during the system design process, it is necessary to be able to characterise and evaluate distortion effects as completely as possible.

A number of possible sources of non-linear distortion exist in an OWC system. An electronic device usually has a limited dynamic range and often a non-linear characteristic within that dynamic range. Furthermore, transitions between the digital signal domain and the analog signal domain always lead to signal quantisation effects even if the electrical components behave almost ideally. As indicated in the system description in Fig. 2.2, a processed digital time-domain signal has to be passed through a DAC in order to obtain a signal, which can be used to modulate the LED. As a rule of thumb, an increase in the resolution of a DAC increases the design complexity and cost. At the same time, decreasing the resolution leads to more pronounced signal quantisation effects. In addition, non-linear distortion is always anticipated in OFDM-based systems due to the high PAPR of the information signal and the limited range of the electronic components which leads to clipping effects. An adequate analysis of the distortion effects on an information signal allows for making informed choices between cost and accuracy in the design of the DAC and ADC components.

The most prominent source of non-linear distortion in an OWC system is the LED at the analog front-end of the transmitter. The voltage-to-current (V-I) relationship in an LED is not linear. However, when a suitable V-I transducer is designed, this transition step in the system can be almost completely linearised. However, the current-to-light (I-L) relationship between the current through the LED and the emitted light intensity is also non-linear. Furthermore, there is inevitably a minimum and a maximum allowed current level at which the diode can properly operate. Therefore, the OFDM signal is inevitably clipped during the processing stage in order to ensure that the analog signal fits within the active range of the LED. Analogously, non-linear effects due to the non-linear relationship between light intensity, current and voltage are also

present in the photodiode (PD) at the receiver. However, this front-end device is anticipated to operate in a much smaller range, which means that the distortion is expected to be insignificant compared to the distortion incurred at the transmitter.

A number of publications on non-linear distortion in OFDM-based modulation schemes already exist in the literature [14, 15, 63–66, 96–99]. A large number of these works are focused specifically on the non-linear distortions that occur in an OWC system [14, 15, 63–65]. The analysis of the non-linear distortion effects is often quite complicated. Some general procedures for obtaining an analytical solution [66] have been introduced in the literature. However, a closed-form solution is not always feasible. The current work presents a novel complete generalised procedure which *always* leads to a closed-form analytical solution. It can be applied to all the cases presented in [14, 15, 63–65] as well as to any other arbitrary memoryless non-linear distortion, which can be anticipated in an OWC system using OFDM modulation. The specific case studies presented in the current work provide a complete picture of the important non-linear effects at the OWC transmitter, where the most significant non-linear distortion is anticipated. The application of pulse shaping techniques is also considered in the context of non-linear distortion unlike in previous works on the same subject [14, 15, 63–65].

The rest of this chapter is organised as follows. Section 5.2 introduces the concept of pulse shaping and describes the effect of common pulse shapes on the investigated OFDM-based modulation schemes, specifically focusing on the inherently unipolar OFDM algorithms: 1) ACO-OFDM in Section 5.2.1; 2) PAM-DMT in Section 5.2.2; and 3) U-OFDM in Section 5.2.3. Section 5.3 introduces the generalised algorithm for the analysis of non-linear distortion in an OFDM-based communication system. Section 5.4 explains how the analytical framework can be applied to the different OFDM-based modulation schemes analysed in this work, including: 1) DCO-OFDM in Section 5.4.1; 2) ACO-OFDM in Section 5.4.2; 3) PAM-DMT in Section 5.4.3; and 4) U-OFDM in Section 5.4.4. Section 5.5 confirms the validity of the analysis by means of Monte Carlo simulations, and presents the effects of non-linear distortion on the system performance for different transmission scenarios. Finally, Section 5.6 provides concluding remarks.

5.2 Pulse Shaping

A pulse shaping operation enables a set of digital samples to be mapped to a continuous analog signal with desirable properties. It is often employed in communication channels with limited bandwidth. The typical flat bandwidth response of off-the-shelf LEDs, for example, is around 2 MHz for white phosphor-coated LEDs and up to 20 MHz when blue filtering at the receiver is employed or when a colour LED is used [33]. It is usually desirable that the frequency profile of the transmitted information signal fits within the flat bandwidth of the front-end elements in order to avoid significant distortion.

Different pulse shaping filters have different time-domain properties as well as a different bandwidth span. A commonly-employed pulse shape is the square pulse which corresponds to the zero-order hold function of a DAC [100]. This shape is of low implementation complexity and has a duration in the time domain which is limited to the period of a single information symbol. However, it spans an infinite spectrum profile. Therefore, it cannot be realised without distortion to the information signal. In practice, when square pulses are used, the signal would also be low-pass filtered following the zero-order hold element in order to limit the frequency profile of the resulting signal. A common reference point for the bandwidth is the first zero crossing in the frequency domain, which occurs at $1/T_\mathrm{s}$ if T_s is the symbol duration in the time domain. Another very similar shape is the triangle pulse, which corresponds to a first order interpolation technique [100]. This shape is effectively the convolution of two square pulses, so the magnitude of its out-of-band components is reduced and the overall signal profile is improved to some extent (theoretically it is still infinite). The pulse duration, however, spans over two symbol periods in the time domain which causes the time-domain information samples to be convoluted. Exact recovery of the original discrete information signal (with no ISI) requires very accurate sampling at the receiver. Furthermore, matched filtering cannot be done without introducing ISI. In theory, the sinc function is the most bandwidth efficient interpolation filter [100]. It requires a bandwidth of $1/2T_\mathrm{s}$, so it is approximately two times more efficient than a square pulse low-passed at the first zero crossing in the frequency domain. However, the sinc spans a time-domain impulse response with an infinite duration. This means that for practical purposes the shape has to be truncated. Also, due to the longer impulse response, this pulse shape requires more processing during the pulse shaping and the matched filtering operations. In addition, time jitter can introduce significant ISI. For these reasons, the raised-cosine filter and its modified version, the root-raised cosine filter, are typically used in practical implementations. They enable the generation of an interpo-
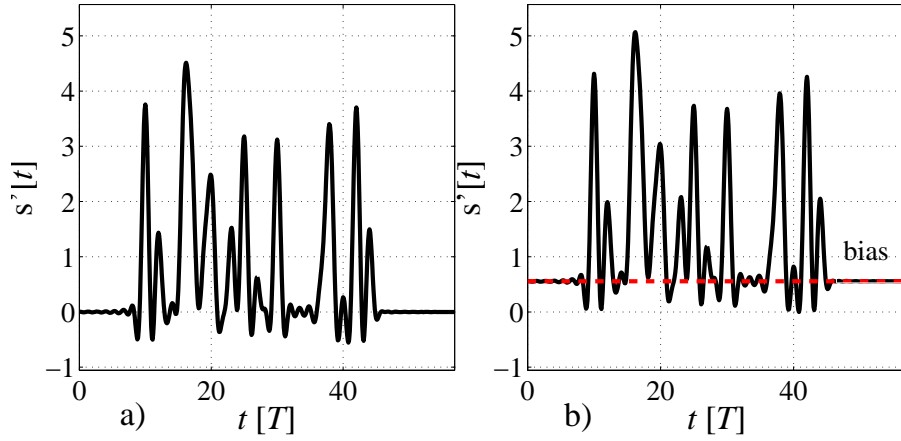
Figure 5.1: *(a) The ACO-OFDM signal pulse-shaped after the negative samples are initially removed. (b) The pulse-shaped ACO-OFDM signal after the addition of a bias level necessary to make it unipolar.*

lation pulse with an arbitrary frequency span between $1/2T_s$ and $1/T_s$ depending on a specified roll-off factor. The raised cosine allows the designer to trade between the length of the pulse in the time domain and the bandwidth requirement of the information signal. In practice, these filters are implemented by oversampling the discrete information signal, interpolating it with the desired pulse shape and then supplying it to a DAC, which consists of a zero-order hold and a low-pass filter as illustrated in Fig. 2.2.

As described in Section 2.7 and Section 4.2.1, the information signals in ACO-OFDM, PAM-DMT, and U-OFDM are turned into unipolar signals after the negative samples are removed. A bipolar pulse shape like the sinc and the raised-cosine filter transform a *unipolar* signal into a *bipolar* signal. An example is shown in Fig. 5.1. This issue can be resolved by introducing a bias level which makes all samples non-negative. However, the effect of this process is an increase in the electrical energy of the signal by approximately 2-3 dB, according to Monte Carlo simulations. Alternatively, all negative samples after the pulse shaping operation can be clipped at zero again, but this leads to the distortion illustrated in Fig. 5.2. If the pulse shaping operation is performed before the negative samples in ACO-OFDM, PAM-DMT, and U-OFDM are clipped, then, the clipping operation would produce a unipolar pulse-shaped information signal. Furthermore, as shown in (2.27), the clipping operation leads to a unipolar signal that can be represented as the sum of the original bipolar signal and a distortion term which contains frequency components both inside and outside the desired bandwidth. The useful signal is preserved inside the limited bandwidth and is not affected by the distortion term as described in Section 2.7. The
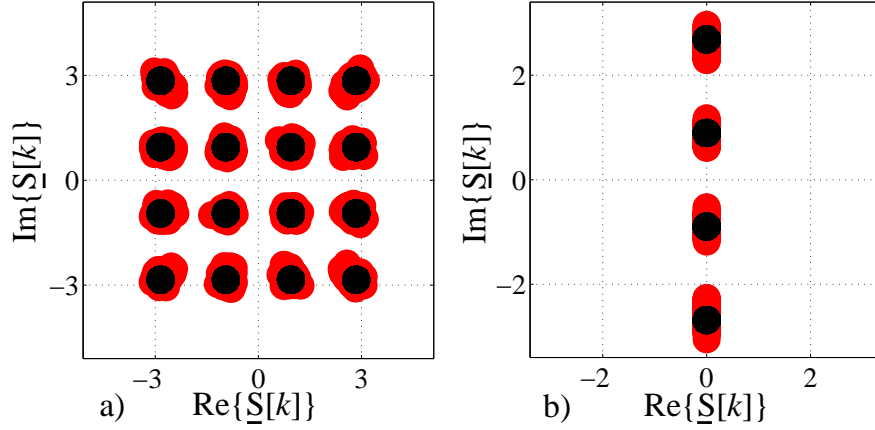
Figure 5.2: *(a) Distortion in ACO-OFDM/U-OFDM after clipping the negative samples of the pulse-shaped signal. (b) Distortion in PAM-DMT after the negative samples of the pulse-shaped signal are clipped.*

rest of this section provides a detailed proof to this claim.

Given that F_{s} denotes the sampling frequency, T_{s} denotes the time-domain symbol period, $T = F_{\mathrm{s}}T_{\mathrm{s}}$, and $\mathrm{p}[t]$ denotes the discrete pulse shape, then the portion of the oversampled pulse-shaped discrete bipolar signal (before any negative values are clipped), which contains the information in a given OFDM frame can be expressed as:

$$
\mathrm{s}'[t] = \sum_{n=N_{\mathrm{fft}}-N_{\mathrm{cp}}}^{N_{\mathrm{fft}}-1} \mathrm{s}[n,0]\mathrm{p}[t-(n-N_{\mathrm{fft}})T] + \sum_{n=0}^{N_{\mathrm{fft}}-1} \mathrm{s}[n,0]\mathrm{p}[t-nT] +
$$
$$
+ \sum_{n=N_{\mathrm{fft}}-N_{\mathrm{cp}}}^{N_{\mathrm{fft}}-N_{\mathrm{cp}}+N_{\mathrm{cp}}^{\mathrm{P}}-1} \mathrm{s}[n,1]\mathrm{p}[t-(N_{\mathrm{fft}}+N_{\mathrm{cp}})T-(n-N_{\mathrm{fft}})T]. \qquad (5.1)
$$

In 5.1, $N_{\mathrm{cp}}^{\mathrm{P}}$ stands for the length of the cyclic prefix that is sufficient to remove any effects of $\mathrm{p}[t]$ between individual OFDM frames, and $\mathrm{s}[n,0]$ denotes the nth sample of the OFDM frame at position 0, assumed to be the current frame. The portion of the discrete-time pulse-shaped bipolar signal which is relevant for sampling the first $\frac{N_{\mathrm{fft}}}{2}$ points of the frame at position 0 can be expressed as:

$$
\mathrm{s}'_1[t] = \sum_{n=N_{\mathrm{fft}}-N_{\mathrm{cp}}}^{N_{\mathrm{fft}}-1} \mathrm{s}[n,0]\mathrm{p}[t-(n-N_{\mathrm{fft}})T] + \sum_{n=0}^{N_{\mathrm{fft}}/2-1} \mathrm{s}[n,0]\mathrm{p}[t-nT] +
$$

$$+ \sum_{n=N_{\text{fft}}/2}^{N_{\text{fft}}/2-1+N_{\text{cp}}^{\text{P}}} \text{s}[n,0]\text{p}[t-nT] \tag{5.2}$$

The discrete-time pulse-shaped bipolar signal relevant for sampling the next $\frac{N_{\text{fft}}}{2}$ points of the OFDM frame at position 0 can be expressed as:

$$\text{s}'_2[t] = \sum_{n=N_{\text{fft}}/2-N_{\text{cp}}}^{N_{\text{fft}}/2-1} \text{s}[n,0]\text{p}[t-nT] + \sum_{n=N_{\text{fft}}/2}^{N_{\text{fft}}-1} \text{s}[n,0]\text{p}[t-nT]+$$
$$+ \sum_{n=N_{\text{fft}}-N_{\text{cp}}}^{N_{\text{fft}}-N_{\text{cp}}+N_{\text{cp}}^{\text{P}}-1} \text{s}[n,1]\text{p}[t-(N_{\text{fft}}+N_{\text{cp}})T-(n-N_{\text{fft}})T]. \tag{5.3}$$

The discrete-time pulse-shaped unipolar signal, ready for digital-to-analog conversion and transmission, can be expressed as

$$\underline{\text{s}}[t] = \sqrt{2}\text{f}_{\text{clip}}\left\{\text{s}'[t]\right\} = \frac{1}{\sqrt{2}}\left(\text{s}'[t] + |\text{s}'[t]|\right), \tag{5.4}$$

where the factor $\sqrt{2}$ is applied in ACO-OFDM and PAM-DMT in order to equalise the transmission energy. At the receiver, the discrete-time samples of a given frame after matched filtering can be expressed as:

$$\hat{\text{s}}[n] = \left(\underline{\text{s}}[t] * \text{h}[t] + \text{n}[t]\right) * \text{p}[t]\big|_{t=nT} =$$
$$= \left(\frac{1}{\sqrt{2}}\left(\text{s}'[t] + |\text{s}'[t]|\right) * \text{h}[t] + \text{n}[t]\right) * \text{p}[t]\Big|_{t=nT} =$$
$$= \begin{cases} \left(\frac{1}{\sqrt{2}}\left(\text{s}_1'[t]+|\text{s}_1'[t]|\right) *\text{h}[t]+\text{n}[t]\right) *\text{p}[t]\big|_{t=nT}, n<\frac{N_{\text{fft}}}{2} \\ \left(\frac{1}{\sqrt{2}}\left(\text{s}_2'[t]+|\text{s}_2'[t]|\right) *\text{h}[t]+\text{n}[t]\right) *\text{p}[t]\big|_{t=nT}, \frac{N_{\text{fft}}}{2} \le n \end{cases}, \tag{5.5}$$

where $[] * []$ denotes the convolution operator, $\text{n}[t]$ denotes the AWGN process at the receiver, and $\text{h}[t]$ denotes the discrete time-domain impulse response of the communications channel. The cyclic prefix is assumed to be of sufficient length in order to remove any ISI between individual OFDM frames due to the channel and to turn the *continuous*-time convolution of the unipolar information signal, $\underline{\text{s}}[t]$, and the channel, $\text{h}[t]$, into circular convolution in the *discrete* time domain. Hence, the ISI effect can be completely reversed by equalisation. Assuming perfect channel

state information, the time-domain representation of the equalised samples at the receiver can be expressed as:

$$
\begin{aligned}
\hat{s}_E[n] &= \left(\underline{s}[t] + n[t] * h^{-1}[t]\right) * p[t]\Big|_{t=nT} = \\
&= \left(\frac{1}{\sqrt{2}}\left(s'[t] + |s'[t]|\right) + n[t] * h^{-1}[t]\right) * p[t]\Big|_{t=nT} = \\
&= \begin{cases} \left(\frac{1}{\sqrt{2}}\left(s_1'[t] + |s_1'[t]|\right) + n[t]*h^{-1}[t]\right)*p[t]\Big|_{t=nT}, & n < \frac{N_{fft}}{2} \\ \left(\frac{1}{\sqrt{2}}\left(s_2'[t] + |s_2'[t]|\right) + n[t]*h^{-1}[t]\right)*p[t]\Big|_{t=nT}, & \frac{N_{fft}}{2} \le n \end{cases}
\end{aligned} \tag{5.6}
$$

5.2.1 ACO-OFDM

From Section 2.7.2.2, in ACO-OFDM, $s[n] = -s[n + N_{fft}/2]$. Therefore, $s'_1[t] \approx -s'_2[t + \frac{N_{fft}}{2}T]$ except for the third terms of the expressions in (5.2) and (5.3). The differences occur because in the time domain, $p[t]$ spans a non-causal impulse response beyond a single information symbol duration and beyond the boundaries of the OFDM frame. When $N_{cp}^p << N_{fft}$, however, these differences are practically insignificant. This result implies that $|s'_1[t]| \approx \left|s'_2[t + \frac{N_{fft}}{2}T]\right|$. At the receiver, the distortion term in the first $\frac{N_{fft}}{2}$ points, $\frac{1}{\sqrt{2}}|s'_1[t]| * h[t] * p[t]\Big|_{nT}$, is equivalent to the distortion term in the second $\frac{N_{fft}}{2}$ points, *i.e.*, $\frac{1}{\sqrt{2}}|s'_2[t]| * h[t] * p[t]\Big|_{nT}$, because $|s'_1[t]| \approx \left|s'_2\left[t + \frac{N_{fft}}{2}T\right]\right|$. Therefore, the distortion due to clipping reflects only on the even subcarriers as in (2.26).

5.2.2 PAM-DMT

From Section 2.7.2.3, in PAM-DMT, $s[n] = -s[N_{fft} - n]$. Therefore, based on the representations in (5.2) and (5.3), $s'_1[t] \approx -s'_2[N_{fft}T - t]$. There are differences in the first term in (5.2) and the third term in (5.3). The differences are caused by the non-causal time-domain impulse response of $p[t]$. However, they are not significant if $N_{cp}^p << N_{fft}$. Therefore, it can be concluded that $|s'_1[t]| \approx |s'_2[N_{fft}T - t]|$. The impulse response of the pulse-shaping filter is an even function. Hence, $p[t] = p[-t]$. In equation (5.6), the distortion term after the equalisation procedure at the receiver consists of $\frac{1}{\sqrt{2}}|s'_1[t]| * p[t]\Big|_{t=nT}$ and $\frac{1}{\sqrt{2}}|s'_2[t]| * p[t]\Big|_{t=nT}$. It is Hermitian symmetric in the time domain. Therefore, the distortion translates into a real signal component in the frequency domain and is orthogonal to the useful information as explained in Section 2.7.2.3.

5.2.3 U-OFDM

As described in Section 4.2.1, the U-OFDM bipolar (before clipping of the negative values) *discrete*-time signal is encoded in two consecutive frames. The oversampled and pulse-shaped discrete-time bipolar part of $s'[t]$ which contains the information of the *positive* block can be expressed as $s'_p[t]$ in the form of equation (5.1). The oversampled and pulse-shaped discrete-time bipolar part of $s'[t]$ which contains the information of the *negative* block can be expressed in the same form as $s'_n[t]$. If $s_p[n]$ are the bipolar time-domain information symbols of the *positive* block, and $s_n[n]$ are the bipolar time-domain information symbols of the *negative* block, then by design $s_p[n] = -s_n[n]$. Hence, a closer inspection of equation (5.1) reveals that $s'_p[t] = -s'_n[t]$ except for the third terms in the presented summation. The differences appear because $p[t]$ spans a non-causal impulse response. When $N_{cp}^p << N_{fft}$, these differences are not significant. The samples of the positive frame and the samples of the negative frame after matched filtering at the receiver become respectively:

$$\hat{s}_p[n] = \left(\frac{1}{2} \left(s'_p[t] + |s'_p[t]| \right) * h[t] + n_1[t] \right) * p[t] \Big|_{t=nT} \tag{5.7}$$

$$\hat{s}_n[n] = \left(\frac{1}{2} \left(s'_n[t] + |s'_n[t]| \right) * h[t] + n_2[t] \right) * p(t) \Big|_{t=nT} \tag{5.8}$$

where $n_1[t]$ and $n_2[t]$ are two independent identically-distributed realisations of the AWGN at the receiver. At the receiver, the original bipolar OFDM samples are reconstructed by subtracting the samples of the *negative* block from the samples of the *positive* block:

$$\hat{s}_b[n] = \hat{s}_p[n] - \hat{s}_n[n] =$$
$$= \left(\frac{1}{2} \left(s'_p[t] - s'_n(t) \right) * h[t] + n_1[t] - n_2[t] \right) * p(t) \Big|_{t=nT}. \tag{5.9}$$

The non-linear distortion terms, $\frac{1}{2}|s'_p[t]| * h[t] * p[t]\big|_{t=nT}$ and $\frac{1}{2}|s'_n[t]| * h[t] * p[t]\big|_{t=nT}$, are equivalent and as such are completely removed by the subtraction operation in the demodulation process. The noise variance doubles due to the subtraction as shown in Section 4.2.1.

One important implication of these proofs is that the pulse shaping process can be incorporated in the non-linear distortion framework for ACO-OFDM, PAM-DMT, and U-OFDM described in the rest of this section. When pulse shaping is applied after the negative values in these schemes

are clipped at zero, then the distribution of the samples in the time domain pulse-shaped signal changes. This compromises the accuracy of the analysis. To elaborate, the time-domain OFDM samples follow a Gaussian distribution. Hence, in ACO-OFDM, PAM-DMT, and U-OFDM, the positive samples alone as well as the negative samples alone follow a Gaussian distribution clipped at zero. The pulse shaping process is a linear operation, which linearly combines the discrete-time samples of an OFDM frame, scaled by the sample values of a pulse-shaping filter's impulse response. Linearly combining samples which follow a clipped Gaussian distribution does not render samples that follow the same distribution. On the other hand, linearly combining samples which follow a Gaussian distribution generates samples which also follow a Gaussian distribution. Therefore, if the pulse shaping operation is performed before the signal is clipped at zero, the pulse-shaped samples after the clipping operation follow a clipped Gaussian distribution. This distribution enables the analysis presented in the rest of this section.

5.3 Complete Framework for a Closed-form Theoretical Analysis of Non-linear Distortion in OFDM-based OWC

The non-linear distortion analysis approach described in Section 2.8 has been used in a number of works in an analytical or semi-analytical fashion [14, 15, 66]. The resulting analytical solution, however, is never guaranteed to be in closed-form. Every time a closed-form solution is required with this approach, an additional creative step is required because the derivation has to be tailored according to the non-linear distortion function under investigation. In this section, a general derivation procedure is presented. It *always* leads to a closed-form analytical solution for an arbitrary memoryless distortion function. The concept can be easily applied to most of the OFDM-based modulation schemes presented in this work. The remainder of this section introduces the modified technique and describes how it can be applied to DCO-OFDM, ACO-OFDM, PAM-DMT, and U-OFDM.

An arbitrary memoryless distortion function, $z(X)$, can be represented with a set of intervals, I, having cardinality, $|I|$, and with a set of continuous polynomials which can be considered as accurate approximations of the function in each of the respective intervals. Such polynomials can be generated by interpolation of empirical data, or by polynomial expansion techniques such as Taylor polynomial expansion. The selected polynomial degree can set the accuracy of the

approximation. Then, the function $z(x)$ becomes:

$$z(x) = \sum_{i=1}^{|I|} \sum_{j=0}^{n_i} c_{i,j} x^j \left(U(x - x_{\min,i}) - U(x - x_{\max,i}) \right) \tag{5.10}$$

where i denotes the ith function interval, n_i is the polynomial order in interval i, $c_{i,j}$ denotes the jth coefficient of the polynomial in interval i, $U(x)$ is the unit step function, so $x_{\min,i}$ and $x_{\max,i}$ are the lower and the upper boundary of interval i, respectively. Using this representation, the attenuation factor α in (2.33) becomes:

$$
\begin{aligned}
\alpha &= \frac{E\{Xz(X)\}}{\sigma_{\mathrm{x}}^2} = \frac{1}{\sigma_{\mathrm{x}}^2} \int_{-\infty}^{\infty} x z(x) \frac{1}{\sigma_{\mathrm{x}}} \phi\left(\frac{x}{\sigma_{\mathrm{x}}}\right) \mathrm{d}x \\
&= \frac{1}{\sigma_{\mathrm{x}}^2} \int_{-\infty}^{\infty} \left\{ \sum_{i=1}^{|I|} \sum_{j=0}^{n_i} c_{i,j} x^{j+1} \left(U(x - x_{\min,i}) - U(x - x_{\max,i}) \right) \right\} \frac{1}{\sigma_{\mathrm{x}}} \phi\left(\frac{x}{\sigma_{\mathrm{x}}}\right) \mathrm{d}x \\
&= \frac{1}{\sigma_{\mathrm{x}}^2} \sum_{l=1}^{|I|} \sum_{j=0}^{n_i} c_{i,j} \int_{x_{\min,i}}^{x_{\max,i}} x^{j+1} \frac{1}{\sigma_{\mathrm{x}}} \phi\left(\frac{x}{\sigma_{\mathrm{x}}}\right) \mathrm{d}x \\
&\overset{(A.4)}{=} \frac{1}{\sigma_{\mathrm{x}}^2} \sum_{i=1}^{|I|} \sum_{j=0}^{n_i} c_{i,j} \left. \frac{\mathrm{d}^{j+1} D(t, x_{\min,i}, x_{\max,i}, 0, \sigma_{\mathrm{x}})}{\mathrm{d}t^{j+1}} \right|_{t=0}
\end{aligned} \tag{5.11}
$$

where the function $D(t, a, b, \mu, \sigma_{\mathrm{x}})$ is defined in (A.1). The time-domain signal variance, $\sigma_{\mathrm{x}}^2 = \sigma_{\mathrm{s}}^2$, is derived in (2.17). It should be noted that after the pulse shaping operation, the variance of the oversampled time-domain signal distribution is not constant over time and that the individual time-domain samples are not really independently distributed. However, in [66], Dardari *et al.* have shown that for the commonly-used pulse shapes in practice this does not compromise the validity of the analysis technique. The simulations conducted in this work and the results presented in the next section also support this claim. The calculations that characterise the statistics of Y_{n} in (2.34)-(2.36) can be expressed as:

$$
\begin{aligned}
E\{Y_{\mathrm{n}}\} &= E\{z(X)\} = \int_{-\infty}^{\infty} z(x) \frac{1}{\sigma_{\mathrm{x}}} \phi\left(\frac{x}{\sigma_{\mathrm{x}}}\right) \mathrm{d}x \\
&= \int_{-\infty}^{\infty} \left\{ \sum_{i=1}^{|I|} \sum_{j=0}^{n_i} c_{i,j} x^j \left(U(x - x_{\min,i}) - U(x - x_{\max,i}) \right) \right\} \frac{1}{\sigma_{\mathrm{x}}} \phi\left(\frac{x}{\sigma_{\mathrm{x}}}\right) \mathrm{d}x \\
&= \sum_{i=1}^{|I|} \sum_{j=0}^{n_l} c_{i,j} \int_{x_{\min,i}}^{x_{\max,i}} x^j \frac{1}{\sigma_{\mathrm{x}}} \phi\left(\frac{x}{\sigma_{\mathrm{x}}}\right) \mathrm{d}x
\end{aligned}
$$

$$\overset{(A.4)}{=} \sum_{i=1}^{|I|} \sum_{j=0}^{n_i} c_{i,j} \left. \frac{\mathrm{d}^j \mathrm{D}(t, x_{\min,i}, x_{\max,i}, 0, \sigma_{\mathrm{x}})}{\mathrm{d}t^j} \right|_{t=0}, \tag{5.12}$$

$$
\begin{aligned}
\mathrm{E}\{\mathrm{z}^2(X)\} &= \int_{-\infty}^{\infty} \mathrm{z}^2(x) \frac{1}{\sigma_{\mathrm{x}}} \phi\left(\frac{x}{\sigma_{\mathrm{x}}}\right) \mathrm{d}x \\
&= \int_{-\infty}^{\infty} \left\{ \sum_{i=1}^{|I|} \sum_{j=0}^{n_i} c_{i,j} x^j \left(\mathrm{U}(x - x_{\min,i}) - \mathrm{U}(x - x_{\max,i}) \right) \right\}^2 \frac{1}{\sigma_{\mathrm{x}}} \phi\left(\frac{x}{\sigma_{\mathrm{x}}}\right) \mathrm{d}x \\
&= \sum_{i=1}^{|I|} \sum_{j=0}^{n_i} \sum_{j'=0}^{n_i} c_{i,j} c_{i,j'} \int_{x_{\min,i}}^{x_{\max,i}} x^{j+j'} \frac{1}{\sigma_{\mathrm{x}}} \phi\left(\frac{x}{\sigma_{\mathrm{x}}}\right) \mathrm{d}x \\
&\overset{(A.4)}{=} \sum_{i=1}^{|I|} \sum_{j=0}^{n_i} \sum_{j'=0}^{n_i} c_{i,j} c_{i,j'} \left. \frac{\mathrm{d}^{j+j'} \mathrm{D}(t, x_{\min,i}, x_{\max,i}, 0, \sigma_{\mathrm{x}})}{\mathrm{d}t^{j+j'}} \right|_{t=0}. \tag{5.13}
\end{aligned}
$$

With the help of equations (A.1), (A.5), (A.6) and the standard rules for differentiation, it is rather straightforward to obtain closed-form expressions for (5.11), (5.12) and (5.13). The procedure is also easily programmable on a computer. A simple example of how to compute (5.11), (5.12) and (5.13) in closed-form is presented in Appendix B.

The presented analysis based on the Bussgang theorem is valid for zero-mean Gaussian signals. The four modulation schemes - DCO-OFDM, ACO-OFDM, PAM-DMT, U-OFDM - are all non-zero-mean modified versions of the original bipolar zero-mean OFDM signal. As a result, the modifications have to be taken into account in the analysis in order to correctly interpret the effects of the non-linear distortion. All manipulations of the original bipolar OFDM signal up to the point where an inverse fast Fourier transform (IFFT) operation is performed during the demodulation procedure at the receiver have to be considered. For example, if $z_1(x)$ is a memoryless distortion at one stage in the system, for instance, caused by clipping of the signal, $z_2(x)$ is a subsequent memoryless distortion, for example caused by quantisation at the DAC, $z_3(x)$ is a third memoryless distortion, for example, caused by adding a positive signal bias, then the overall distortion effect after the three separate consecutive distortions is $z(s'[t]) = z_3(z_2(z_1(s'[t])))$. Regardless if a distortion is linear or non-linear, it can and should be incorporated in the analysis provided that it is memoryless. In this work, it is assumed that no distortion with memory is present in the system or any such distortion can be completely equalised, for example ISI.

5.4 Application to OFDM-based Modulation Schemes

5.4.1 DC-biased Optical OFDM (DCO-OFDM)

The presented analytical framework can be applied to DCO-OFDM straightforwardly as it would be applied to conventional bipolar OFDM. The positive bias of the signal can be analysed as part of the overall non-linear transformation and its effects do not need to be considered separately like in other similar works [14, 15].

5.4.2 Asymmetrically-clipped Optical OFDM (ACO-OFDM)

The clipping at zero operation in the modulation process of ACO-OFDM is a non-linear transformation, but has no adverse effect on the odd subcarriers of the system. A slight modification in the analytical procedure has to be made in order to account for this effect. In ACO-OFDM, the bipolar time-domain OFDM signal before clipping of the negative samples consists of a set of positive samples and a set of negative samples. The two sets of samples have identical distribution and identical contribution to the value of each modulated subcarrier in the frequency domain [61]. As a result, when one of the sets is set to zero, this has no adverse effect on the useful signal apart from an amplitude attenuation factor of 0.5. Since only the positive samples are used in the transmission, the non-linear distortion in the system pertains only to the set of positive samples. As a result, the effect of the non-linear distortion on the modulated subcarriers is the same as if the same distortion function mirrored around zero is applied on the unclipped bipolar OFDM signal. Hence, in the calculation process, the intervals of the non-linear transform can be specified from 0 to ∞. Then (5.11),(5.12) and (5.13) can be calculated for the interval $[0; \infty]$ and scaled by 2 to account for the complementary identical half of the signal distribution. With this modification, the analysis equations become:

$$\alpha = \frac{2}{\sigma_{\mathrm{x}}^2} \sum_{i=1}^{|\mathrm{I}|} \sum_{j=0}^{n_l} c_{l,j} \left. \frac{\mathrm{d}^{j+1}\mathrm{D}(t, x_{\min,i}, x_{\max,i}, 0, \sigma_{\mathrm{x}})}{\mathrm{d}t^{j+1}} \right|_{t=0} \tag{5.14}$$

$$\mathrm{E}\{Y\} = 2 \sum_{i=1}^{|\mathrm{I}|} \sum_{j=0}^{n_i} c_{i,j} \left. \frac{\mathrm{d}^{j}\mathrm{D}(t, x_{\min,i}, x_{\max,i}, 0, \sigma_{\mathrm{x}})}{\mathrm{d}t^{j}} \right|_{t=0} \tag{5.15}$$

$$\mathrm{E}\{[\mathrm{z}^2(X)\} =$$

111

$$= 2 \sum_{i=1}^{|\mathrm{I}|} \sum_{j=0}^{n_i} \sum_{j'=0}^{n_i} c_{i,j} c_{i,j'} \left. \frac{\mathrm{d}^{j+j'} \mathrm{D}(t, x_{\min,i}, x_{\max,i}, 0, \sigma_{\mathrm{x}})}{\mathrm{d}t^{j+j'}} \right|_{t=0} \tag{5.16}$$

The estimated noise variance due to the distortion, σ_{Y}^2, has to be halved before it is added to the variance of the AWGN, because the noise has no correlation with the signal and, therefore, distributes evenly on both odd and even subcarriers. The signal-to-noise ratio (SNR) should be further scaled by a factor of 0.5 due to the removal of the negative samples. Then in the analysis of ACO-OFDM, the achieved SNR in (2.37) becomes:

$$\frac{E_{\mathrm{b}j}^{\mathrm{new}}}{\sigma_{\mathrm{NY}}^2} = \frac{\alpha^2 E_{\mathrm{b}j}}{2(\sigma_{\mathrm{N}}^2 + \frac{\sigma_{\mathrm{Y}}^2}{2})} \tag{5.17}$$

It should be noted that the originally negative samples that are clipped to zero do not influence the modulated subcarrier values because having a value of zero, they are excluded from any contribution in the IFFT transform at the receiver. If these samples, are distorted, however, and have a value which is different from zero, they begin to influence the result in the frequency domain. Therefore, it is not enough to only analyse the distortion of the positive samples, as described in this section, but the distortion of the clipped samples should also be taken into account. Let's define the overall distortion of the information signal up to the demodulator as $z_{\mathrm{d}}(s'[t])$; this is just the distortion to the signal without including the distortion due to the AWGN. If $z_{\mathrm{d}}(0) \neq 0$, then the zeros generated due to clipping of the negative samples are distorted. Their distortion distorts the information in the the odd subcarriers which is avoided when these samples are 0. In order to account for this effect, $z_{\mathrm{d}}(0)$ can be interpreted as a direct current (DC) shift and subtracted from $z_{\mathrm{d}}(s'[t])$. Then, the analysis described in this section can be applied without having to additionally model the distortion coming from the distorted clipped samples. Hence, the effective overall distortion function on the positive OFDM samples is:

$$z(s'[t])_{s'[t] \geq 0} = z_{\mathrm{d}}(s'[t])_{s'[t] \geq 0} - z_{\mathrm{d}}(0) \tag{5.18}$$

5.4.3 Pulse-amplitude-modulated Discrete Multitone Modulation (PAM-DMT)

The time-domain information signal in PAM-DMT possesses the same statistical properties as the information signal in ACO-OFDM. The power of the additive Gaussian noise introduced by

the non-linearity distortion is equally split between the real and the imaginary components of the subcarriers in the frequency domain. As a result, the non-linearity distortion analysis for PAM-DMT is exactly the same as for ACO-OFDM. It should be noted that PAM-DMT uses M-ary pulse-amplitude modulation (M-PAM) while ACO-OFDM uses M^2-QAM for modulation of the frequency subcarriers at the same spectral efficiency of the system. In a real additive Gaussian noise channel, M-PAM and M^2-QAM have identical bit error rate (BER) performance.

5.4.4 Unipolar Orthogonal Frequency Division Multiplexing (U-OFDM)

In the modulation process for U-OFDM, the signs of the negative samples are switched, the samples are transmitted as positive samples and then turned back into negative samples by the subtraction operation at the demodulator as described in Section 4.2.1. As a result, any non-linear transformation of the bipolar OFDM signal is symmetric around zero, *i.e.*, $z(s'[t]) = -z(-s'[t])$. Because all time-domain samples are transmitted as positive samples, $z(s'[t])_{s'[t]\leq 0}$ is a mirrored version of $z(s'[t])_{s'[t]\geq 0}$. Therefore, $z(s'[t]) = -z(-s'[t])$ in the calculations of (5.11),(5.12) and (5.13). Alternatively, because the Gaussian probability density function (PDF) of OFDM is symmetric around zero, it is possible to specify $z(s'[t])$ only in the interval $[0;\infty]$ and perform the calculations of (5.11),(5.12) and (5.13) only in this interval. If this approach is adopted, in all calculations, the final result has to be doubled to account for the negative half of the signal distribution just as in the analysis case for ACO-OFDM and PAM-DMT. The subtraction operation at the demodulator effectively doubles the system AWGN. Hence (2.37) is calculated as:

$$\frac{E_{\mathrm{b}j}^{\mathrm{new}}}{\sigma_{\mathrm{NY}}^2} = \frac{\alpha^2 E_{\mathrm{b}j}}{2\sigma_{\mathrm{N}}^2 + \sigma_{\mathrm{Y}}^2} \tag{5.19}$$

Note that the bipolar signal is obtained by subtracting the *negative* block from the *positive* block at the demodulator. However, when all zero samples corresponding to clipped negative samples from the original bipolar signal are distorted to $z_{\mathrm{d}}(0)\neq 0$, then all originally positive samples are shifted by $-z_{\mathrm{d}}(0)$ after the subtraction operation and all originally negative samples are shifted by $z_{\mathrm{d}}(0)$, where $z_{\mathrm{d}}(s'[t])$ is the non-linear distortion function up to the subtraction operation at the demodulator. This means that the subtraction operation at the demodulator introduces additional distortion, which has to be accounted for by subtracting $z_{\mathrm{d}}(0)$ from $z_{\mathrm{d}}(s'[t])$, i.e., the resulting overall non-linear distortion function is:

$$z(s'[t])_{s'[t]\geq 0} = z_{\mathrm{d}}(s'[t])_{s'[t]\geq 0} - z_{\mathrm{d}}(0). \tag{5.20}$$

The analysis of ACO-OFDM, PAM-DMT, and U-OFDM indicates that all three schemes experience exactly the same SNR deterioration for the same non-linear distortion effects because the time-domain information signals in the three schemes are characterised by equivalent statistical properties for the same spectral efficiency. This conclusion is also supported by the numerical results presented in the following section. Therefore, in addition to the equivalent performance in a linear AWGN channel, the three schemes are expected to exhibit equivalent performance in a non-linear AWGN channel as well. Hence, this work provides further evidence that the three schemes are simply three different but equally-valid approaches towards the same energy-efficiency goal.

5.5 Numerical Results

This section investigates the joint effect of three non-linear distortions at the OWC transmitter. The effects under investigation include clipping which accounts for the limited dynamic range of the electronic devices, quantisation effects in the DAC, and the I-L output characteristic of the LED. Non-linearities at the receiver site are not included in the investigation because they are considered negligible in comparison to the non-linear effects at the transmitter. The non-linear distortion at the receiver can be analysed analogously using the concepts presented in Section 5.3 and Section 5.4. In the analysis and in the numerical simulations presented in this section, the oversampled pulse-shaped signal $s'[t]$ has an oversampling ratio of 10.

For comparison purposes, the average electrical energy per bit, $E_{b,elec}$, and average optical energy per bit, $E_{b,opt}$, consumed at the transmitter have been defined as in (2.19) and (2.21), but the non-linear transfer characteristics have also been included in the SNR definition:

$$E_{b,elec} = \frac{P_{elec}^{avg}}{B\eta} = \frac{E[z_{elec}^2(s'[t])]}{B\eta}, \tag{5.21}$$

$$E_{b,opt} = \frac{P_{opt}^{avg}}{B\eta} = \frac{E[z_{opt}(s'[t])]}{B\eta}, \tag{5.22}$$

where P_{elec}^{avg} denotes the average electrical power of the time-domain information signal, proportional to the mean square of the electrical signal; P_{opt}^{avg} is the average optical power of the time-domain information signal, proportional to the average intensity of the time-domain optical signal; η is the spectral efficiency of the respective modulation scheme defined in (2.15), (2.28),

(2.30) or (4.7); $z_{elec}(s'[t])$ is the current signal flowing through the diode including all distortions up to that point in the system; $z_{opt}(s'[t])$ is the light intensity output of the diode including all distortions up to that point in the system; B is the double-sided signal bandwidth in Hz. For the examples presented in this section, $z_{elec}(s'[t])$ includes clipping of the signal, quantisation effects at the DAC as well as the addition of a positive bias level, while $z_{opt}(s'[t])$ includes also the I-L output characteristic of the diode.

The zero-order-hold DAC investigated in this work has a limited range of output amplitudes between s'_{min} and s'_{max}, and also has a finite bit resolution, q_b. The discrete output levels of the device are assumed to be equally spaced in the interval $[s'_{min}; s'_{max}]$, and the distance between any two levels is assumed to be:

$$d_q = \frac{s'_{max} - s'_{min}}{2^{q_b} - 1}. \tag{5.23}$$

Each quantisation threshold is set in the middle between two neighbouring quantisation levels. For instance, the threshold between s'_{min} and $s'_{min} + d_q$ is set at $s'_{min} + d_q/2$. The values of s'_{min} and s'_{max} are a function of the desired DAC accuracy and of the LED active range, $[i_{min}; i_{max}]$. Therefore, these signal limits account for the combined clipping effect at the DAC and at the LED. In the presented investigations, the resolution of the DAC is set to q_b=8 bits.

After the information signal is quantised by the DAC output characteristic, it is biased by a constant positive signal and is passed through the LED output characteristic. The LED output characteristic is a continuous function, specified in the interval $[i_{min}; i_{max}]$. It represents the transition from a current signal to an optical signal in the device. The output characteristic of the LED used in this study is obtained through interpolation of the data presented in the device datasheet [101]. A third-degree polynomial is used in the interpolation procedure. The calculated coefficients are provided in Table 5.1. The relationship between the device current and the radiated luminous flux

Interval	$c_{i,3}$	$c_{i,2}$	$c_{i,1}$	$c_{i,0}$
$i = 1 \Leftrightarrow i(t) < i_{min}$	0	0	0	0.1947
$i = 2 \Leftrightarrow i_{min} < i(t) < i_{max}$	0.2855	-1.0886	2.0565	-0.0003
$i = 3 \Leftrightarrow i_{max} < i(t)$	0	0	0	1.2531

Table 5.1: *Polynomial coefficients of the LED output characteristic: $c_{i,j}$ is the coefficient of degree j in interval i.*

has been adopted from the datasheet as a suitable representation of the relationship between the

current and the optical radiation power.

The information signal is contained in the current signal through the LED. The initial (before distortion and biasing) average energy per bit of the original bipolar OFDM signal is defined as E_b. The actual dissipated electrical energy per bit at the LED is defined as $E_{b,elec}$ assuming that the device resistance is normalised to 1Ω and taking into account the quantisation effects and the addition of a bias level, *i.e.*, $E_{b,elec} = E\{i^2(t)\}/(B\eta) = E\{(z_3(z_2(z_1(s'[t]))) + i_{bias})^2\}/(B\eta)$ where $z_1(s'[t])$ denotes the clipping effect on the oversampled pulse-shaped signal, $s'[t]$, $z_2(\cdot)$ denotes the quantisation effect of the DAC, and $z_3(\cdot)$ denotes the conversion step from a voltage signal to a current signal, which is assumed linear with gain 1. For the evaluation of the optical efficiency of the system, the quantity $E_{b,opt}$ is defined as $E_{b,opt} = E\{z_4(z_3(z_2(z_1(s'[t])))) + i_{bias})\}/(B\eta)$ where $z_4(\cdot)$ denotes the transition step from a current signal to an optical signal in the LED, characterised by the polynomial described in Table 5.1.

The typical 3-dB modulation bandwidth of white commercially-available LEDs is in the order of 2MHz [33]. This bandwidth is assumed in the presented investigations. The coherence bandwidth of a typical indoor optical channel is in the order of 90 MHz, which is significantly higher than the assumed modulation bandwidth of the LED [33]. Therefore, the channel can be assumed flat within the communication bandwidth and ISI does not have to be considered. In an alternative scenario, where ISI becomes an issue, the non-linearity analysis presented in this work still applies provided that channel knowledge is available at the receiver, and the information signal can be equalised. In the following investigation, the current signal at the receiver is assumed to be:

$$\hat{i}(t) = z_4(i(t))H(0)R \qquad (5.24)$$

where $H(0)$ is the optical channel gain define in Section 2.5, and R is the PD responsivity. Taking into account the LED emission spectrum and the PD responsivity to the different optical wavelengths, the average responsivity to white light is calculated as $R = 0.52$ [102]. This value is used in the numerical simulations. The optical channel gain depends on a number of different factors as described in Section 2.5. In the current investigation, the channel gain is arbitrarily selected depending on the M-ary quadrature amplitude modulation (M-QAM) modulation order in use. The aim is to use a channel gain which requires the LED to be operated in its full active region because then the energy advantage of ACO-OFDM, PAM-DMT, and U-OFDM over DCO-

OFDM should be most pronounced. If the information signal requires a small modulation depth of the LED and varies only slightly around the bias level, the energy consumption depends almost entirely on the bias level, which means that there will be relatively small performance differences between the four schemes.

In an OWC system, the main contributor to the AWGN is expected to be shot noise at the photo detector due to background light. The power spectral density of the noise in this study is specified in the order of $N_\mathrm{o}{=}10^{-21}$ W/Hz in agreement with other similar work [33]. This value is used in all numerical simulations. Then, the variance of the AWGN is $\sigma_\mathrm{N}^2{=}BN_\mathrm{o}$.

Fig. 5.3-5.5 present the investigation results which compare 4-QAM DCO-OFDM, 16-QAM ACO-OFDM, 4-PAM PAM-DMT, and 16-QAM U-OFDM - all with equivalent spectral efficiency of $1 \, \mathrm{bit/s/Hz}$. The assumed optical channel gain is $H(0){=}4{\times}10^{-6}$ because this value allows all the investigated schemes to achieve BER values in the order of 10^{-3} and 10^{-4} - within the requirements of most forward error correction (FEC) codes required for successful communication [15, 33, 94] - and at the same time to use the active region of the LED as fully as possible.

In the conducted investigation, the bias levels for ACO-OFDM, PAM-DMT, and U-OFDM are set to $i_\mathrm{bias} = 0.1 \, \mathrm{A}$, while the bias level for DCO-OFDM is set to $i_\mathrm{bias} = 0.19 \, \mathrm{A}$. The distribution region $[-3\sigma; 3\sigma]$ is quantised for DCO-OFDM, and the distribution region $[0; 3\sigma]$ is quantised for the other schemes. Any signal values which fall outside the presented regions are clipped. These clipping levels are set as the default clipping levels. The AWGN power is constant. In order to increase the SNR in the system, the information signal through the LED has to be amplified. However, if the modulation signal falls outside the allowed operational range of the LED when amplified, it is clipped further due to the non-linear output characteristic of the LED, presented in Table 5.1. As a result, the BER curves presented in Fig. 5.3-5.5 are V-shaped. There is a clear dip in the curves because at first, an amplification of the information signal increases the SNR, however, after a certain point, the clipping distortion becomes more dominant than the improvement due to the increase in the transmitted power. For the performance comparison between the different schemes, the power of the transmitted signal is used rather than the power of the received signal because it gives a better illustration of the energy efficiency in the system where most of the energy is consumed at the transmitter. The achieved SNR at the receiver can be calculated by using the power levels presented in Fig. 5.3-5.5 and by taking into account the optical channel gain, the responsivity gain and the noise power at the receiver.
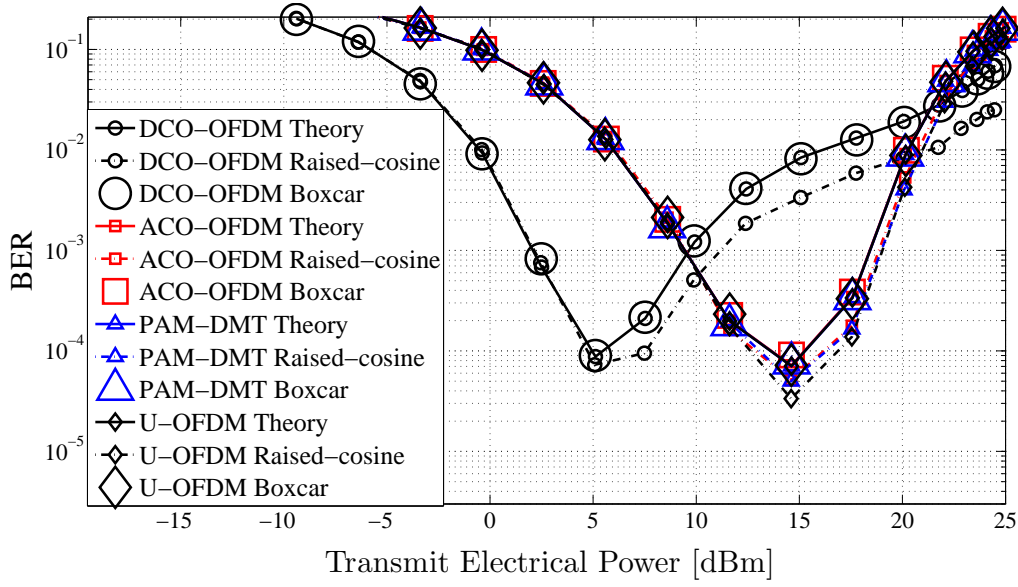
Figure 5.3: *A performance comparison between* 4*-QAM DCO-OFDM,* 16*-QAM ACO-OFDM,* 4*-PAM PAM-DMT, and* 16*-QAM U-OFDM in terms of the electrical power at the transmitter* P_{elec}^{avg}*. The power dissipation due to the bias level is not taken into account.*
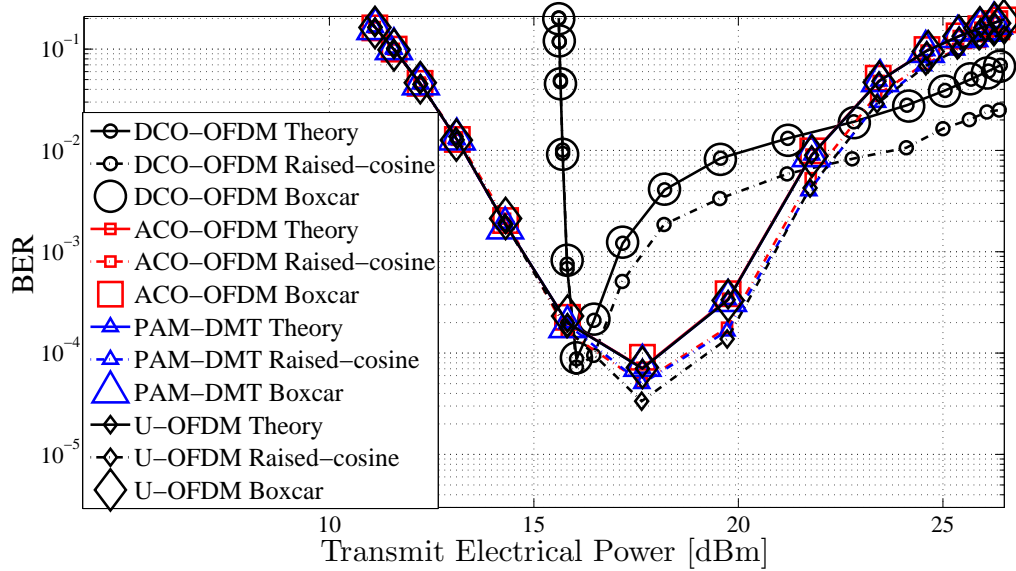
Figure 5.4: *A performance comparison between* 4*-QAM DCO-OFDM,* 16*-QAM ACO-OFDM,* 4*-PAM PAM-DMT, and* 16*-QAM U-OFDM in terms of the electrical power at the transmitter* P_{elec}^{avg}*. The power requirement estimation includes the contribution of the bias level to the electrical power dissipation.*
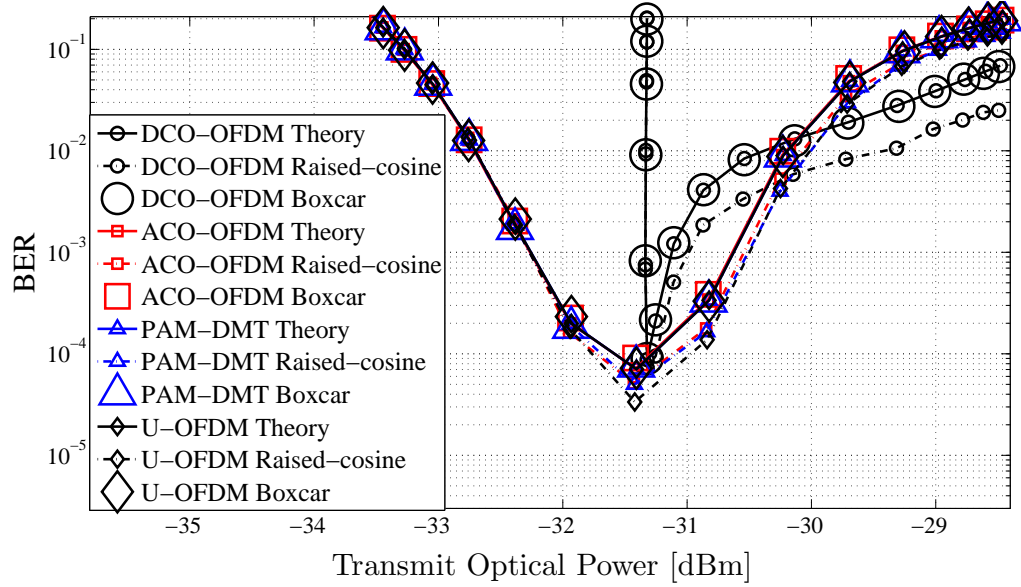
Figure 5.5: *A performance comparison between* 4-*QAM DCO-OFDM,* 16-*QAM ACO-OFDM,* 4-*PAM PAM-DMT, and* 16-*QAM U-OFDM in terms of the optical power at the transmitter* $P_{\mathrm{opt}}^{\mathrm{avg}}$. *The bias level contribution to the power dissipation is taken into account.*

Fig. 5.3 presents the electrical energy efficiency of the four schemes if the bias level is not taken into account. As expected, for bipolar signals, DCO-OFDM clearly outperforms the other three schemes. The benefits of the latter, however, are caused by the biasing requirement. This is shown in Fig. 5.4, where ACO-OFDM, PAM-DMT, and U-OFDM require approximately 1dB less energy per bit for a BER of 10^{-3} and approximately the same energy for a BER of 10^{-4} compared to DCO-OFDM. The results in Fig. 5.5 indicate that DCO-OFDM is approximately 1dB less optically efficient than the other three schemes for a BER of 10^{-3}, and approximately 0.3dB worse for a BER of 10^{-4}. The presented curves clearly demonstrate that the BER values decrease as expected with the increase in the SNR up to a certain point. Afterwards, the active region of the LED is completely depleted, and any increase in the signal power leads to increase in the clipping distortion and, hence, to higher BER. Overall, the conducted theoretical analysis matches quite well the results of the Monte Carlo simulations for square pulse shapes. When a root-raised cosine filter is used to pulse shape the information signal, the Monte Carlo results are slightly better than the theory because the matched filter at the receiver filters out the frequency components of the distortion noise which fall outside the signal bandwidth. Nevertheless, the results for the root-raised cosine filter follow closely the theoretical approximation and confirm
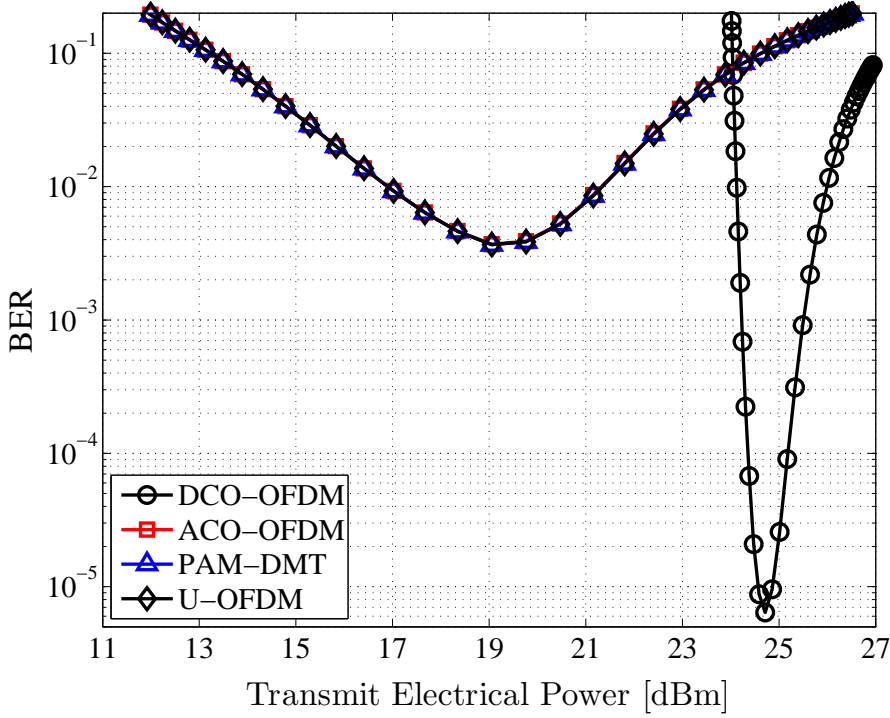
Figure 5.6: *Low channel gain, $H(0)$=2x10^{-6}, scenario which illustrates the advantage of a smaller constellation. The performance of 4-QAM DCO-OFDM, 16-QAM ACO-OFDM, 4-QAM PAM-DMT, and 16-QAM U-OFDM is compared.*

the validity of the presented analytical framework. For practical calculations, the presented analysis can serve as a good approximation of a lower bound on the performance of a system which employs a pulse shaping filter with limited bandwidth. To the best of the author's knowledge, other techniques for the analysis of non-linear distortion which are present in the literature do not even consider bandlimited pulse shaping filters and work with simple square pulse shapes (Boxcar filter) for which the analysis presented in this work is exact [14, 15, 63–65]. The BER curves for ACO-OFDM, PAM-DMT, and U-OFDM fall on top of each other as predicted by the theoretical analysis. This clearly demonstrates the equivalent performance of the three schemes in a non-linear AWGN channel. The requirement for bigger M-QAM constellations in ACO-OFDM, PAM-DMT, and U-OFDM makes these schemes more vulnerable to non-linear distortion when compared to DCO-OFDM. Larger constellations are more vulnerable to distortion. An example is presented in Fig. 5.6 where the channel gain is decreased to $H(0) = 2\times10^{-6}$, the bias level in DCO-OFDM is set to $i_{\text{bias}} = 0.5\,\text{A}$, and it is kept at $i_{\text{bias}} = 0.1\,\text{A}$ in the other three schemes. Despite the higher energy requirement, in this scenario DCO-OFDM is still able to achieve a BER of 10^{-4}. On the other hand, the other three schemes do not even reach a BER of 10^{-3}. This

120
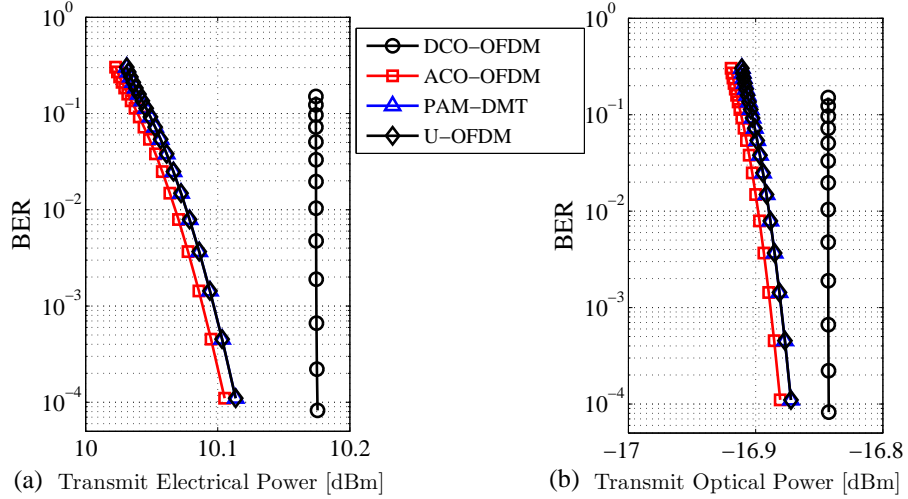
Figure 5.7: *Performance comparison of 4-QAM DCO-OFDM, 16-QAM ACO-OFDM, 4-QAM PAM-DMT, and 16-QAM U-OFDM in a high channel gain, $H(0)=4\text{x}10^{-4}$, scenario: (a) Electrical power efficiency (in terms of $P_{\text{elec}}^{\text{avg}}$) including energy dissipation due to the bias current; (b) Optical power efficiency (in terms of $P_{\text{opt}}^{\text{avg}}$) including the bias level.*

example illustrates how a slight change in the channel conditions can make a big difference in the selection of a modulation scheme for a given system configuration.

The final investigation is performed for a scenario where the channel gain is significantly higher, $H(0) = 4{\times}10^{-4}$. In this case, the required modulation depth of the information signal is much lower than in the other cases and the main contribution to energy consumption is the positive bias level of the signal. Fig. 5.7 presents the results for this example. The bias level of DCO-OFDM is $i_{\text{bias}} = 0.1018\,\text{A}$, which is the minimum bias level required to fully accommodate the information signal. The bias level in the other three schemes is kept at the minimum level of $i_{\text{bias}} = 0.1\,\text{A}$. The difference in the electrical energy efficiency between DCO-OFDM and the other three schemes is approximately $0.06\,\text{dB}$. The difference in the optical power requirement is approximately $0.04\,\text{dB}$. All four schemes are almost equivalent in their energy requirements because the main contributor to the energy dissipation is the bias of the LED. Note that the power efficiency of ACO-OFDM, PAM-DMT, and U-OFDM is always expected to be lower than the theoretical values presented in the respective introductory papers - [61], [62], [18] - because any clipped values that are ideally set to zero at the modulator, are actually set to the bias level at the transmitter and, therefore, also contribute to the power dissipation.

5.6 Summary

In this section, a complete analytical approach for the analysis of memoryless non-linear distortion in an OWC system has been presented. The novel approach enables the analysis of an arbitrary distortion function and the derivation of analytical solutions in closed form. The concept is valid for four OFDM-based modulation schemes proposed for intensity modulation and direct detection (IM/DD) systems: DCO-OFDM, ACO-OFDM, PAM-DMT and U-OFDM. An investigation has been conducted on the joint distortion effects caused by quantisation in a DAC and by the non-linear relationship between the electrical current and the emitted light in an LED. These distortion effects are anticipated to be the major sources of non-linearity in an OWC system. Monte Carlo simulations conducted exhibit good agreement with the proposed theory, thus confirming the validity of the analysis technique.

The analytical work as well as the numerical results presented in this section indicate that ACO-OFDM, PAM-DMT, and U-OFDM exhibit equivalent performance in a non-linear AWGN channel, which suggests that the schemes are three different but equally valid approaches towards energy efficiency. The presented performance analysis shows that the optimal choice of a modulation scheme is strongly dependent on the communications scenario and can vary. The theoretical analysis approach presented here provides a quick and accurate way to estimate system performance and to optimise the system parameters without computationally expensive Monte Carlo simulations and numerical integration. Further work on the subject can include an analytical approach for modelling the effects of non-linear distortion on the performance of the enhanced U-OFDM concept, presented in Section 4.3.1.

Chapter 6
Experimental Demonstration of High-speed Optical Wireless Communication Using OFDM

This chapter presents a performance investigation of a visible light communications (VLC) system based on a single novel Gallium Nitride (GaN) µm-sized light emitting diode (µLED). A device of such size exhibits a frequency profile with a 3-dB modulation bandwidth of at least 60 MHz - significantly higher than the typical commercially-available white lighting light emitting diodes (LEDs). The modulation scheme used in this investigation is orthogonal frequency division multiplexing (OFDM). It enables the non-flat frequency response of the device to be used in an optimal fashion. Adaptive data and energy loading techniques are successfully applied in order to achieve a demonstration of optical wireless communication at speeds exceeding 3 Gb/s. To date, this is the fastest demonstration of a wireless VLC system using a single LED.

The chapter presents a systematic study of the achievable data rates, the practical transmission distances and the coverage area that are achievable with a wireless VLC link using a single GaN µLED with a diameter of 50 µm. The work on GaN µLEDs is extended by discussing the possible deployment scenarios at a practical transmission distance of at least 1 m and the feasibility of a Gb/s wireless link at a distance of up to 10 m without the need for complex optics is demonstrated. All results have been obtained indoors at ambient lighting levels of 1000 lx. The results presented in this chapter illustrate the enormous potential of the technology and demonstrate that high-speed VLC is not limited to short-range applications.

The inherently unipolar OFDM modulation schemes, asymmetrically clipped optical orthogonal frequency division multiplexing (ACO-OFDM) and pulse-amplitude-modulated discrete multi-tone modulation (PAM-DMT), presented in Chapter 2.7 have been studied theoretically quite

extensively. The novel unipolar modulation schemes, unipolar orthogonal frequency division multiplexing (U-OFDM) and enhanced unipolar orthogonal frequency division multiplexing (eU-OFDM), presented in this work have also been studied quite extensively in Chapter 4 and Chapter 5. However, very little work seems to have been done on practical implementation of such modulation schemes. To the best of the author's knowledge, the current work presents the first experimental proof-of-concept demonstration of both U-OFDM and eU-OFDM and clearly demonstrates the significant energy advantages that these two schemes can introduce in an optical wireless communications (OWC) system, consistent with the theoretical results from Chapter 4.

6.1 Introduction

Incoherent solid-state lighting elements such as LEDs are very prominent VLC transmitters due to their low cost and high availability. They are envisioned as the most likely candidates for VLC front-end devices. Several physical challenges are limiting the communication speeds in VLC and are hindering the future development of high-speed commercial VLC systems [10]. One major challenge is the slow modulation response of commercial white luminaires based on a blue LED chip with a yellow phosphor coating, popular for lighting applications. The relatively long carrier life-time of the yellow phosphor leads to a slow response time and restricts the flat modulation bandwidth of the device to several MHz [10]. A common workaround for this issues is the application of a blue short-pass filter at the receiver, which removes the slow component from the modulated signal and enables flat modulation frequencies of up to 20 MHz [10]. Despite the bandwidth limitation of the LEDs, signal processing techniques such as equalization, high-order modulation/multiplexing, and parallel data transmission have enabled communication of up to 1 Gb/s using a single commercially-available phosphor-coated LED and up to 3 Gb/s using commercially-available red-green-blue LEDs [10, 12, 103].

Significant research effort is being directed towards the development of faster LEDs. An example of such novel devices are resonant-cavity light emitting diodes (RCLEDs) [39]. The application of an RCLED has enabled demonstrations of communication links of up to 3 Gb/s over a plastic optical fiber (POF) [40]. Other devices with comparable modulation bandwidth can be manufactured by reducing the innate junction capacitance of the diodes and by controlling the differential carrier lifetimes through injected current density. For example, in [34], μLEDs with small diameters, of the order of tens of μm, are introduced. The reduced size of the LEDs leads to notable improvements in their modulation frequency response. VLC links with a transmission speed of up to 512 Mb/s [34] and up to 1 Gb/s [35] have been successfully demonstrated for such μLEDs using on-off keying (OOK) modulation. Another similar device has been used in [36] for a demonstration of a 1.07 Gb/s communication link over a POF.

In this chapter, the communication capabilities of GaN μLEDs [34] in combination with OFDM are investigated in Experiment I. An experimental measurement of the μLED bandwidth and a physical demonstration of an OFDM-based system are presented. OFDM is chosen because it allows cost-effective equalisation with single-tap equalisers in the frequency domain. Moreover, this modulation scheme allows adaptive data and energy allocation to different frequency regions

based on the properties of the communication system. In addition, the scheme can easily avoid low-frequency distortion effects caused by ambient light interference and by the baseline wander effect in the electrical components. The purpose of the experiment is to establish the maximum modulation bandwidth and the highest data rates that can be achieved with a μLED. As a result, to the best of the author's knowledge, the fastest single-link wireless VLC system is presented in this chapter.

The high-speed demonstration in Experiment I is realised at a short transmission distance of 5 cm. The main reason for the limited distance is the use of a wide-bandwidth positive-intrinsic-negative (PIN) photodiode (PD) receiver without dedicated optics, suitable for precise measurements. The current chapter also presents Experiment II in which an alternative avalanche photodiode (APD) receiver with dedicated optics is used. This allows the wireless link to be established over practical distances for indoor OWC. The feasibility of a Gb/s communication link is demonstrated in a wide indoor distance range between 1 m and 10 m. A discussion on coverage and practical applications is also conducted. In particular, Experiment II includes: 1) Study I in which the goal is to investigate the possibility of establishing a Gb/s transmission over a range of distances from 1 m to 2.5 m where the LED emission profile is optimised at each transmission distance; 2) Study II in which the goal is to demonstrate that high-speed transmission can be achieved within the range from 1 m to 2.5 m even if the LED transmission profile is not optimised for transmission at each distance; In essence, this study resembles the application of a μLED in a mobile application, where the receiver can move in three dimensions relative to the transmitter; 3) Study III in which the goal is to demonstrate that a Gb/s transmission can be established even at longer transmission distances of up to 10 m, which could be ideal for the realisation of high-speed indoor wireless links intended to replace longer wires.

Following the high-speed wireless link demonstration, an energy-efficient OFDM realisation is also presented in Experiment III. In this experiment, the feasibility of U-OFDM and the feasibility of eU-OFDM is demonstrated for the first time in a proof-of-concept realisation of a VLC link. The measured results clearly indicate that a LED can be operated at a minimum biasing level, and despite the issues of reduced communication bandwidth and significant non-linear distortion, an inherently-unipolar OFDM-based modulation scheme such as U-OFDM and eU-OFDM can be realised and significant energy savings can be achieved, consistent with the simulation results presented in Chapter 4.

The rest of this chapter is organized as follows. Section 6.2 discusses the possible applications and deployment scenarios for µLEDs. Section 6.3 presents the first high-speed transmission investigation where: a description of the experimental set-up is provided in Section 6.3.1; the modulation parameters are described in Section 6.3.2; the experimental results are presented in Section 6.3.3 including the communication channel characteristics in Section 6.3.3.1 and the achievable data rates in Section 6.3.3.2. Section 6.4 presents the second high-speed transmission investigation at practical indoor distances where: the experimental set-up is described in Section 6.4.1; the modulation parameters are shown in Section 6.4.2; the results of the study are presented in Section 6.4.3 where the results of Study I are presented in Section 6.4.3.1, the results of Study II are presented in Section 6.4.3.2 and the results of Study III are presented in Section 6.4.3.3. Section 6.5 presents the energy-efficiency demonstration using U-OFDM and eU-OFDM where: the experimental set-up and the modulation parameters are introduced in Section 6.5.1; a number of signal processing techniques necessary for the investigation are described in Section 6.5.2 where a novel empirical technique for evaluating the performance effects of non-linear distortion is described in Section 6.5.2.1, a signal pre-distortion technique required for the successful implementation of the modulation schemes is described in Section 6.5.2.2, and the technique for estimating the energy dissipated by the modulation signal is described in Section 6.5.2.3; the performance results and a comparison to direct-current-biased optical orthogonal frequency division multiplexing (DCO-OFDM) is provided in Section 6.5.3. Finally, Section 6.6 provides concluding remarks.

6.2   Envisioned Usage Scenarios

The typical ceiling heights in indoor environments range from $2.5\,\mathrm{m}$ to $3.5\,\mathrm{m}$. Conventionally, luminaires are mounted at the height of the ceiling or up to approximately $0.5\,\mathrm{m}$ below. The typical mobile receivers for high-speed communication access are anticipated to be located in the range between an average desk height of about $0.85\,\mathrm{m}$ up to the average human height of about $1.75\,\mathrm{m}$. Therefore, wireless VLC transmission in indoor environments is likely to encompass links at distances of up to approximately 2–3 m. An example office deployment is presented in Fig. 6.1(a).

In a practical µLED deployment scenario, where simultaneous illumination and high-speed data communication have to be provided by the light sources, a large array of µLED devices would

be required since a single µLED with a diameter of $50\mu m$ has a maximum output power of about $4.5\,\mathrm{mW}$. Alternatively, a hybrid system consisting of high power white LEDs and high bandwidth µLEDs could be used to meet the requirements for simultaneous illumination and communication. The results presented in this chapter have two important implications. Firstly, the high-speed communication experiments illustrate the potential of the µLED technology and demonstrate that the novel devices can be modulated at very high frequencies of up to 800 MHz. Secondly, the presented results on achievable coverage enable a quick practical estimation of the number of devices that are required in a given application with specific coverage requirements. The results demonstrate the possibility for achieving unprecedented extremely dense deployments of high-speed parallel data links ($>\,1\,\mathrm{Tb/s/m^2}$) using µLEDs. Note that indoor lighting with simultaneous high-speed wireless access is not the only application for a µLED. A device of such size can be easily integrated into a typical electronic display. Moreover, any indicator light can be easily turned into a high-speed data access port. Such µLEDs can replace wire interfaces in high-speed data links at short distances and have the potential to play a significant role in the future concept of "the internet of things". For illumination purposes, white light emission can be achieved through combination of a µLED with a number of novel colour-converter materials [104] or through the introduction of additional red and green devices as in commercially-available red-green-blue (RGB) LEDs.

An alternative application of a GaN µLED is high-speed underwater communication. A potential deployment scenario in such a context is depicted in Fig. 6.1(b). An unmanned underwater vehicle (UUV) can be used for taking measurements or retrieving data from fixed underwater sensors such as the ones mounted on other UUVs, bridge foundations, oil platforms, *etc.* Blue light, centred at a wavelength of $450\,\mathrm{nm}$, is a good choice for underwater wireless communication as it suffers relatively low attenuation in that propagation medium.

6.3 Experiment I

6.3.1 Experimental Set-up

The OFDM-based experimental system set-up is presented in Fig. 6.2. First, a pseudo-random bit stream is generated and encoded into M-ary quadrature amplitude modulation (M-QAM) symbols. The resulting M-QAM symbols are modulated onto different frequency subcarriers

(a) Office

(b) Underwater
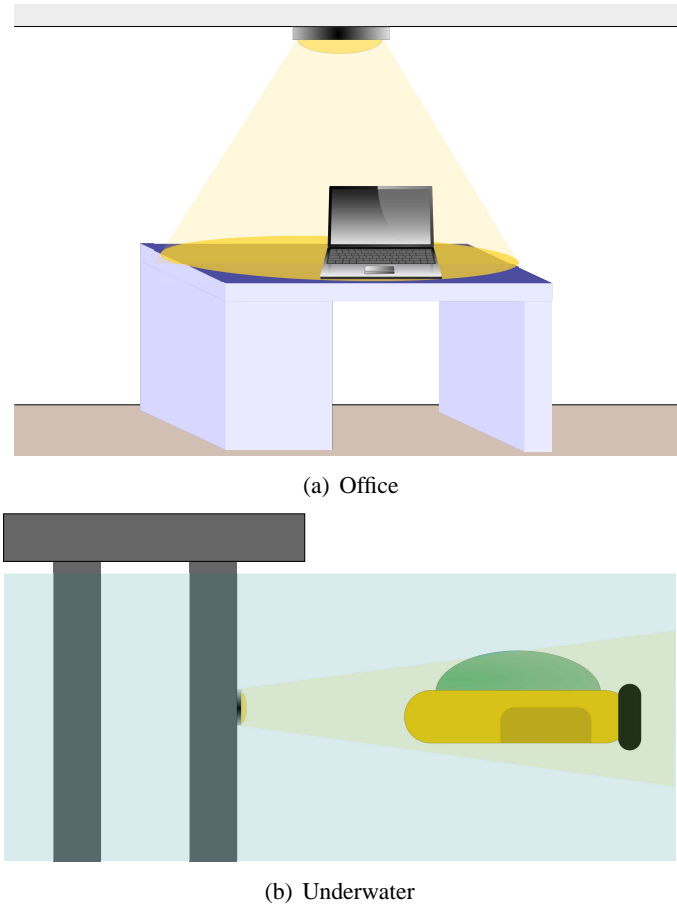
Figure 6.1: *Envisioned system deployments*

and rescaled accordingly if adaptive energy loading is employed. Afterwards, an inverse fast Fourier transform (IFFT) operation is applied on a block of symbols. This generates a discrete time-domain signal, which is up-sampled by a factor of 2 and pulse-shaped with a discrete root raised cosine (RRC) filter with a roll-off factor of 0.1. The pulse-shaping filter confines the frequency profile of the information signal within a desired bandwidth, thus reducing intersymbol interference (ISI) effects when compared with the square pulse which is used when no pulse shaping is applied. The small roll-off factor of the filter causes the frequency requirements of the system to approach the theoretical Nyquist rate set by an ideal sinc pulse [93]. The use of the RRC filter also allows for straightforward and accurate matched-filtering at the receiver, thus eliminating any excess additive white Gaussian noise (AWGN) in the receiver system. Following the pulse-shaping operation, any signal values outside the allowed operational range set by the electrical properties of the µLED, are clipped. All digital processing is performed in MATLAB®.
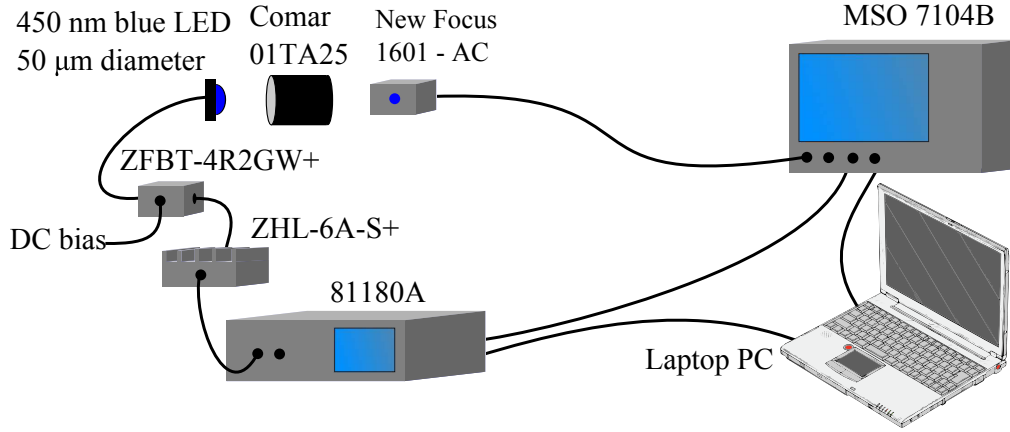
Figure 6.2: *Experimental set-up for Experimet I.*

The resulting conditioned discrete signal is sent to an arbitrary waveform generator (AWG), Agilent 81180A, which maps it to an analog signal. The analog output of the generator is amplified with a high-power amplifier, Mini-Circuits ZHL-6A-S+, which drives the μLED by modulating the voltage over the device. The selected μLED emits blue light with a relatively narrow wavelength distribution centred around 450 nm and has a maximum optical radiation of approximately 4.5 mW [34]. A constant direct current (DC) bias level is added to the information signal using a bias-T, Mini-Circuits ZFBT-4R2GW+. The light emission from the μLED is collected via an optical condenser 01TA25 from Comar Optics and imaged onto a high-speed photodetector, New Focus 1601-AC. The analog output of the photodetector is captured by a digital oscilloscope, Agilent MSO7104B. Afterwards, the digitized information signal is processed in MATLAB® with a sequence of processing steps that include: synchronisation, matched-filtering, down-sampling, fast Fourier transform (FFT), equalisation, and M-QAM demodulation.

6.3.2 Modulation Parameters

The modulation scheme employed in the current investigation is DCO-OFDM, described in Section 2.7.2.1. As a prerequisite of the Hermitian symmetry imposed in the OFDM frame, the DC subcarrier and the π-shifted subcarrier are set to zero. In addition, half of the subcarriers are fixed as complex conjugates of the other half of the subcarriers. In an OFDM frame, a total of N_{fft} subcarriers are equally distributed in the bandwidth range $[-1/2T_{\text{s}}; 1/2T_{\text{s}}]$ where T_{s} is the time-domain sampling period which corresponds to the Nyquist rate. Some subcarriers might

130

be left unmodulated in order to avoid distortion effects from ambient light sources and from the DC-wander effect. Certain subcarriers can also be omitted if signal-to-noise ratio (SNR) levels are not sufficient in a given frequency band. The spectral efficiency of the scheme, η, is defined in (2.14) and the double-sided bandwidth of the system is calculated as:

$$B = \frac{1}{T_\mathrm{s}} \text{ Hz.} \tag{6.1}$$

Then, the data rate of the system is:

$$R_\mathrm{b} = B\eta \text{ bits/s.} \tag{6.2}$$

In this experiment, the FFT size is set to $N_\mathrm{fft}{=}1024$. After exhaustive experiments, the optimal cyclic prefix length is determined to be $N_\mathrm{cp}{=}5$.

The active range of the μLED is limited in terms of a minimum and a maximum signal level. Hence, clipping of the OFDM signal, which has a high peak-to-average power ratio (PAPR) as described in (2.16), is practically unavoidable. Exhaustive experiments have shown that clipping levels at -3.2σ_s and 3.2σ_s, where σ_s is the standard deviation of the time-domain signal, described in (2.17), lead to an optimal utilisation of the limited μLED active range. The optimal bias level is determined to be at a voltage of $V_\mathrm{bias}{=}5.2$ V corresponding to a bias current of $I_\mathrm{bias}{=}40$ mA. The peak-to-peak voltage swing of the modulating signal is set at $V_\mathrm{pp} = 3.5$ V in order to utilise the full dynamic range of the μLED. The sampling frequency of the AWG is fixed at $F_\mathrm{s}{=}3.2\,\mathrm{Gs/s}$, which results in a maximum achievable single-sided bandwidth of $B/2{=}800$MHz since a RRC pulse shaping filter with an oversampling ratio of 2 is also applied to the digital signal.

6.3.3 Results and Discussion

6.3.3.1 Communication Channel

The communication channel is estimated with a set of pilot OFDM frames that consist of pseudo-random 4-QAM symbols with equal energy. The absolute channel gain and the absolute achieved SNR, obtained using error vector magnitude estimation, are shown in Fig. 6.3 as a function of the subcarrier index. The channel gain follows the frequency profile of the μLED. The 3-dB attenuation point occurs at around 30 MHz. However, overall the channel gain decreases quite gradually and the channel is suitable for M-QAM modulation in almost the full bandwidth up to
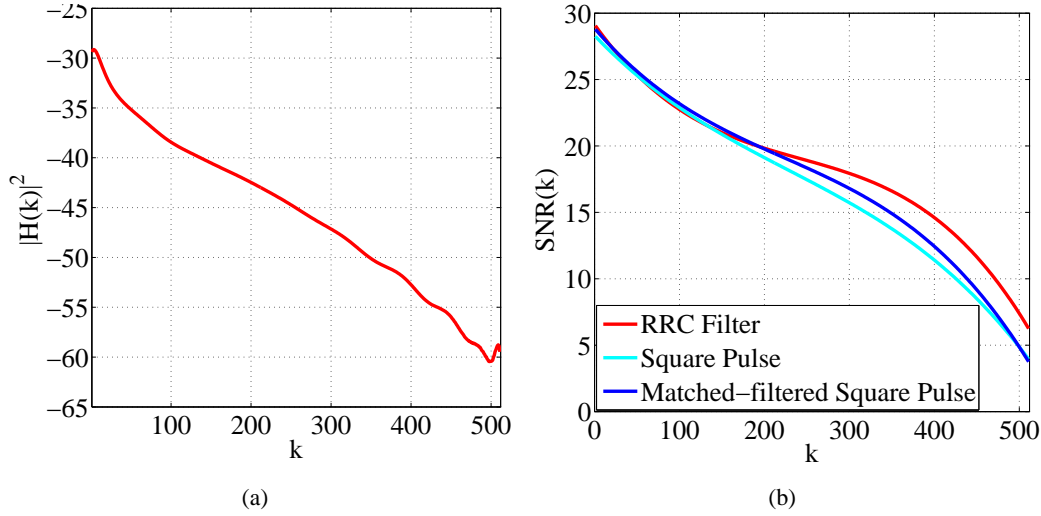
Figure 6.3: *Estimated: (a) channel gain; and (b) SNR.*

a frequency of about 800 MHz. The estimated achievable SNR in the communication channel follows closely the estimated channel gain. This suggests that the AWGN power spectral density in the system is uniform within the communication bandwidth. The estimated SNR values at the low-frequency subcarriers are slightly lower than expected when compared with the channel gain. This effect is attributed to the non-linear distortion in the system which limits the achievable SNR. The effect is discussed in more detail in Section 6.5.2.1. Note that in the presented results in Fig. 6.3(b) the achievable SNR is estimated both for the case when an RRC filter pulse shaping at the transmitter with matched-filtering at the receiver is applied to the communication signal and for the case when a simple square pulse without matched filtering is applied to the information signal. The conclusion is that the RRC filter notably improves the SNR with improvement in the order of 2–3 dB in the higher frequency range. In order to show that the improved frequency profile of the RRC filter is the main reason for the improvement and not the matched filter, an SNR estimation is also performed for an oversampled and matched-filtered version of the square-pulse information signal. The matched-filter shows consistent improvement over the case where no matched filter is applied. However, the achieved SNR is still clearly lower than the SNR achieved after the application of the RRC filter. The conclusion is that the introduction of an RRC filter pulse-shaping technique leads to a notable difference in the practical implementation of an OFDM-based VLC system.
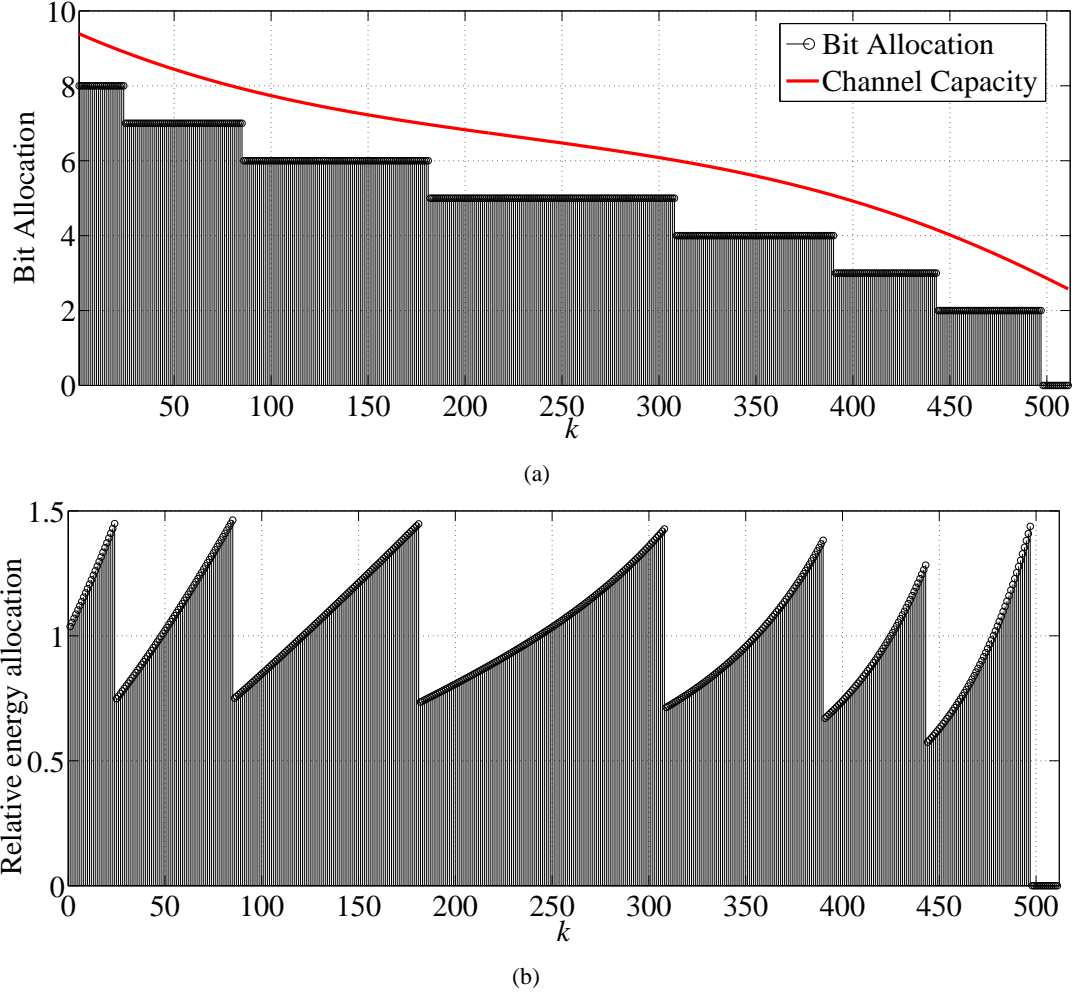
Figure 6.4: *Allocated: (a) bits; and (b) energy.*

6.3.3.2 Adaptive Bit and Energy Loading

The adaptive bit and energy loading algorithm adopted in the current experiment is based on the work of Campello, who has defined the optimal bit and energy loading conditions for the problems of rate maximisation and performance margin maximisation in [23]. A number of other works exist on the subject. For example, Fasano *et al.* have proposed algorithms for margin and rate maximisation of a constrained multicarrier system in [105]. The algorithm used in the current study, presented in Algorithm 1, resembles the rate maximization algorithm in [105]. Other notable publications on the subject include: 1) Sonalkar and Shively's algorithm for a constrained system, which adopts a bit removal approach and successfully reduces the compu-

tational complexity [106]; 2) Levin's algorithm which operates in the logarithmic domain for reduced complexity and successfully incorporates the necessary overhead for Reed Solomon and Trellis forward error correction (FEC) codes [107]; 3) Fasano and Di Blasio's dynamic loading algorithm which reduces the complexity by modifying the previous bit and energy allocation in the OFDM frame rather than conducting the entire allocation process [108]; and 4) Lee at al.'s algorithm which extends the adaptive bit and energy loading concepts to a multiuser system [109].

For the current experimental set-up, the optimal bit allocation according to the algorithm is shown in Fig. 6.4(a). The achievable communication capacity for the estimated SNR values on the different subcarriers is also presented in the same figure [95]. The gap between the M-QAM bit loading and the capacity can only be closed using channel coding techniques. In general, however, the M-QAM bit loading follows the communication capacity trend, and the achieved throughput is close to the theoretical maximum. Fig. 6.4(b) shows the energy that is assigned to each subcarrier. The adaptive algorithm attempts to ensure a constant achieved SNR on all received subcarriers that have been loaded with the same M-QAM constellation. The optimally-loaded modulation signal achieves a data-rate of R_{b}=3.75 Gb/s with a BER=2×10^{-3}. Based on the International Telecommunication Union (ITU) recommendations, the addition of a FEC code with an overhead of about 7%, such as the RS(1023,1007)/BCH(2047/1952), is expected to guarantee reliable communication for the achieved bit error rate (BER) [110]. Because of the FEC overhead, the actual achievable throughput becomes R_{b}=3.5 Gb/s.

Algorithm 1 Adaptive Bit and Energy Loading

$total\_allocated\_energy \leftarrow 0$

set all subcarrier constellations to zero

set the allocated energy on all subcarriers to zero

set the candidate constellations for all subcarriers to BPSK

while $total\_allocated\_energy \leq total\_available\_energy$ **do**

    $(energy\_requirement, selected\_subcarrier) \leftarrow$ find the subcarrier that requires the smallest additional energy to upgrade to its candidate constellation

    if $total\_allocated\_energy + energy\_requirement \leq total\_available\_energy$ **then**

        upgrade selected_subcarrier to its candidate constellation

        upgrade energy on selected_subcarrier to the required energy for the upgraded constellation

        upgrade the candidate constellation for selected_subcarrier to the next available constellation size

        $total\_allocated\_energy \leftarrow total\_allocated\_energy + energy\_requirement$

    end if

end while
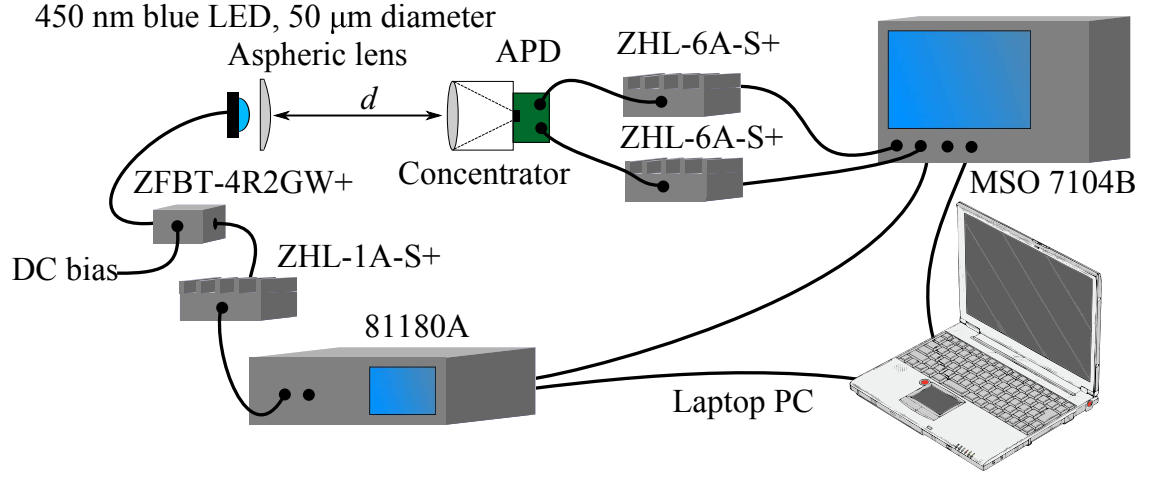
Figure 6.5: *Experimental set-up for Experiment II.*

6.4 Experiment II

6.4.1 Experimental Set-up

Fig. 6.5 presents a diagram of the experimental OFDM-based VLC system set-up for Experiment II. The system control interface is implemented in MATLAB®, and the procedure is operated by a laptop computer. The system functionality is very similar to the functionality in Experiment I and is described as follows. First, a pseudo-random bit stream is encoded into a sequence of M-QAM symbols. Afterwards, the generated M-QAM symbols are assigned to different frequency subcarriers and rescaled to appropriate amplitude levels if adaptive energy loading is employed. An IFFT operation is applied on a block of M-QAM symbols, and a discrete time-domain modulation signal is produced. The samples are conditioned for digital-to-analog conversion by oversampling and a pulse shaping operation with a RRC filter. Following the pulse-shaping procedure, any values outside the allowed dynamic range of the µLED, are clipped. All digital processing steps are implemented in MATLAB®. The conditioned pulse-shaped digital signal is sent to an AWG, Agilent 81180A, which performs digital-to-analog conversion via a zero-order-hold digital-to-analog converter (DAC). The analog output of the generator is amplified with a high-power amplifier, Mini-Circuits ZHL-1A-S+. A DC bias level is introduced to the modulation signal using a bias-T, Mini-Circuits ZFBT-4R2GW+. The biased signal is used to drive the µLED by modulating the voltage over the device. The same µLED as in Experiment I, emitting blue light with a relatively narrow distribution and a peak wavelength of
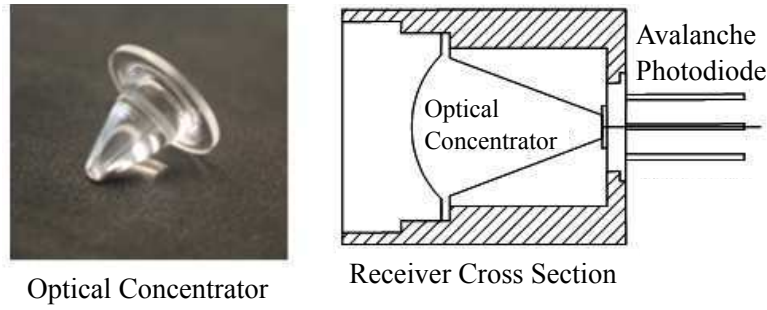
Figure 6.6: *Receiver configuration for Experiment II, originally proposed in [105].*

$450\,\text{nm}$, is used in this experiment [34]. The maximum optical radiation of the µLED is around $4.5\,\text{mW}$. In order to facilitate transmission at longer distances, the light output of the µLED is collimated using an aspheric lens, Thor Labs ACL108 with a diameter of $1\,\text{cm}$ and a focal distance of $8\,\text{mm}$. At the receiver, the incoming light is first passed through a Brightline Fluorescence $447/60\,\text{nm}$ filter. The blue filter is used to reduce the collected ambient light which is responsible for additional shot noise energy and reduces the linear range of the employed APD receiver. The receiver constitutes a custom-designed polymethyl methacrylate optical concentrator (with a field of view (FOV) of $30°$) and a 1.95-mm-in-diameter photodetector, Pacific Silicon Sensor AD1900-9-TO5i. The analog output of the APD is turned into a voltage signal with a differential transimpedance amplifier (TIA), Maxim MAX3665. Figure 6.6 provides a description of the non-imaging concentrator and a cross section illustration of the receiver. More details on the receiver system are provided in [111], where this receiver configuration is first introduced. The differential output of the TIA is further amplified by a pair of Mini-Circuits ZHL-6A-S+ amplifiers, and, afterwards, it is sampled and digitized by a digital oscilloscope, Agilent MSO7104B. The second amplifier stage is introduced in order to increase the voltage swing of the oscilloscope input, which improves the overall quality of the received signal before the processing stage. The frequency response of the complete receiver system (APD + amplifiers + oscilloscope) is provided in Fig. 6.7(a). The digitised received signal, retrieved from the oscilloscope, is processed in MATLAB$^{®}$ with a sequence of steps that include: synchronisation, matched-filtering, downsampling, FFT, equalisation, and M-QAM demodulation.

6.4.2 Modulation Parameters

The modulation parameters in Experiment II are very similar to the parameters in Experiment I with a few small differences. First, an RRC filter with an oversampling ratio of 4 and a roll-

(a) Frequency response of the receiver.

(b) Estimated channel SNR.
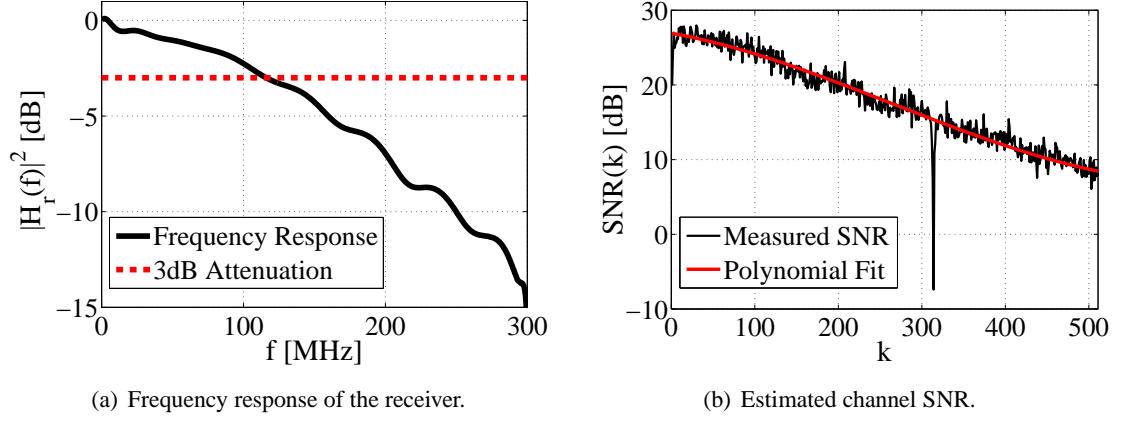
Figure 6.7: *Receiver characteristics.*

off factor of 0.1 is employed in Experiment II since the lower modulation bandwidth utilised in this experiment allows for higher degree of oversampling by the AWG. In relation to this, the single-sided communication bandwidth is set to 250 MHz due to the lower bandwidth of the APD receiver compared with the bandwidth of the PIN receiver used in Experiment I. Exhaustive experiments have shown that the achievable SNR at this rate, depicted in Fig. 6.7(b), is sufficient to accommodate at least 4-QAM on the high-frequency subcarriers (where the SNR is the lowest), and no significant increase in terms of data rate is achieved if more bandwidth is used. The Nyquist rate criterion and the oversampling ratio of 4 in the RRC filter translate into a sampling rate of 2 Gs/s at the AWG. Most of the other parameters in this experiment have been kept the same as in Experiment I, described in Section 6.3.2. The only other difference is the selection of a lower peak-to-peak voltage swing of the information signal for which a level of $2.5\,V$ is selected since higher voltage levels do not seem to introduce a notable performance difference. The system performs adaptive bit and energy loading on the different subcarriers according to Algorithm 1.

6.4.3 Results and Discussion

Three performance investigations are conducted in this experiment. The first study investigates the feasibility to design a single-µLED VLC system which supports a target data-rate of 1 Gb/s at fixed practical distances for an indoor communication scenario. The second study investigates the system performance in terms of achievable data-rate at various short-range distances after the transmission profile of the µLED has been optimized for a target data-rate of 1 Gb/s at a distance of $2\,m$ – approximately the average transmission distance for a mobile receiver in an

indoor deployment scenario as described in Section 6.2. In essence, the first study represents a fixed point-to-point transmission link, while the second study represents a mobile point-to-point transmission with a fixed transmitter configuration. The third study investigates the feasibility of longer transmission, which spans beyond the expected typical requirements for most indoor scenarios. Such a link can be used to replace cable connections in a large indoor space, in airplanes, ships, *etc*. The presented performance results can easily be scaled to a large number of μLEDs, which can be combined in a single transmitter array in order to provide increased communication coverage or to provide extremely high data rates by exploiting the possibility for high-density deployment of individual parallel transmission links. All results, presented for the three studies, have been obtained at office ambient lighting levels of $1000\,\text{lx}$. This demonstrates that strong background lighting does not hinder the performance of the presented high-speed communication system which uses an APD receiver. All results have been achieved at a BER $<3\times10^{-3}$ for which a number of FEC codes with an overhead of 7% can provide reliable communication [110].

6.4.3.1 Study I

At different indoor distances, the light emission profile of the transmitter is adjusted such that a spot of light is generated, where the data-rate achievable at the centre of the spot is $1\,\text{Gb/s}$ after taking into account the 7% overhead for the FEC code. Once the link is realised, the receiver is moved towards the edge of the spot in order to estimate the coverage provided by the transmitter light emission profile. The achievable data-rate is estimated at the point where the received signal variance drops by $3\,\text{dB}$. The distance from the centre is recorded for this point. A second measurement is performed at the visible edge of the spot. The data rate is again estimated and the distance is recorded in order to determine the visible coverage of the transmitter. The estimated data-rate is presented in Fig. 6.8(a) and the spot coverage is shown in Fig. 6.9. At a transmission distance between $1\,\text{m}$ and $2.5\,\text{m}$, a $1\,\text{Gb/s}$ transmission can be achieved by adjusting the μLED emission profile which is accomplished by varying the distance between the device and the aspheric lens used for light collimation.

An interesting observation can be made based on the presented results. If the noise at the receiver is independent of the information signal, when the variance of the received signal is decreased by $3\,\text{dB}$, this should translate into a $3\,\text{dB}$ decrease in the achieved SNR. In turn, this would result into a spectral efficiency decrease of approximately $1\,\text{bit/s/Hz}$, according to the Shannon

(a) Data-rate – Study I

(b) Data-rate – Study II
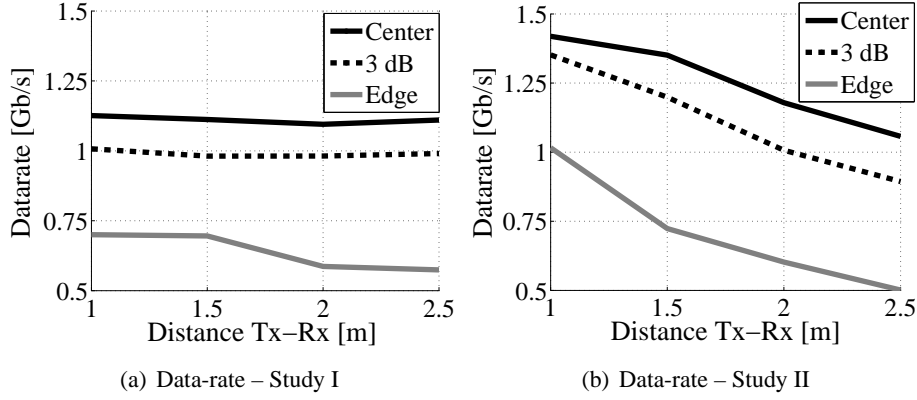
Figure 6.8: *Achievable data-rate for different distances between the transmitter and the receiver. The FEC overhead (assumed to be 7%) is not included in the presented results.*

capacity formula and approximately $1 - 2$ bit/s/Hz according to the typical SNR requirements for M-QAM [93]. Since the communication bandwidth is 250 MHz, the achievable data-rate should decrease by approximately $250 - 500$ Mb/s. From the results in Fig. 6.8(a), it is clear that the data-rate decreases less than expected. Therefore, it can be concluded that the dominant source of noise at the receiver is dependent on the information signal and decreases as the received signal level decreases.

As shown in Fig. 6.9, at most transmission distances, the 3-dB signal energy attenuation occurs at approximately the same distance of about 6 mm from the centre of the light spot and the visible edge of the light spot occurs at around 17 mm. This indicates that the light emission profile is quite collimated. Nevertheless, as the transmission distance increases, the losses due to imperfections in the light collimation increase and the achievable data rate gradually decreases towards the spot edge. At the same time, the light distribution within the spot is not uniform for the different distances due to imperfections in the lens. This effect is responsible for variations in the 3-dB attenuation distance from the spot centre. It is especially pronounced at a transmission distance of 1 m, where the 3-dB attenuation occurs at around 12 mm from the spot centre. The effect of non-uniform light distribution within a light spot can be corrected with the addition of a holographic diffuser at the transmitter.

The results of this study demonstrate the feasibility of a practical VLC system using μLEDs. However, in a deployment scenario where substantial coverage is desired, such a system would require an array of μLEDs. On the other hand, the confined coverage which a single μLED
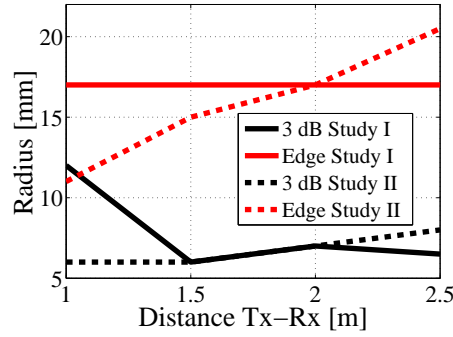
Figure 6.9: *Light spot radius at different distances between the transmitter and the receiver.*

can achieve enables high-density deployment of communication links which could significantly boost the data-rate per unit of coverage area. In relation to this, it should be noted that dense deployment of wireless links in radio frequency (RF) can only be achieved through beamforming and beamforming in RF is achieved with multiple antennas and multiple transmitter chains that require high energy dissipation as well as high computational and hardware complexity. As demonstrated in this experiment, beamforming in VLC is possible with a single LED device and simple passive optical components.

6.4.3.2 Study II

In this study, the light emission profile of the transmitter is optimised such that the data-rate achieved at the centre of the light spot is approximately 1 Gb/s at a distance of 2 meters . Then, the receiver is placed at different distances from the transmitter and the data-rate and coverage are characterized in the manner described in Section 6.4.3.1. The results are presented in Fig. 6.8(b) and Fig. 6.9. The light emission is optimised for transmission at 2 m. As the receiver is moved further from the source, the light beam diverges. This increases the overall link coverage. However, the achievable data-rate decreases due to the reduced SNR at the receiver. When the receiver is moved towards the source, the light beam becomes narrower. As a result, the spot coverage decreases, and the data-rate increases due to the improved SNR. For transmission distances shorter than 2 m, data-rates beyond 1 Gb/s are achievable at the expense of reduced coverage. Because of the high received light intensity at shorter distances, non-linear effects at the receiver appear as the APD approaches saturation. Nevertheless, all communication results are well-within the limits for FEC.

6.4.3.3   Study III - 10 **Meter Transmission**

In the third study, the distance between the transmitter and the receiver is set to 10 meters. Data-rate and coverage measurements are performed twice. During the first measurement, the receiver configuration is used as it is, while during the second measurement an additional aspheric lens, Edmund Optics Plano-Convex lens with a 75-mm diameter and focal length, is introduced at the receiver. In the first measurement, a data rate of 451.4 Mbps is achieved. In the second measurement, the additional lens improves the light collection significantly, and, as a result, the data-rate can reach 1.1 Gb/s (without FEC). At this transmission distance, the 3 dB signal attenuation point is at a distance of 2.5 cm from the spot centre. The visible spot radius is about 4 cm. The achieved results are consistent with the fact that light diverges more at longer transmission distances due to the imperfect light collimation. Therefore, the data-rate can be improved by using better transmitter optics, which improves light collimation, or, alternatively, the receiver optics can be modified to allow for improved light collection.

6.5   Energy-efficient OFDM Communication

The high-speed communication capabilities of µLEDs using OFDM have been demonstrated in Experiment I and Experiment II. Experiment III aims at demonstrating the possibility of using U-OFDM and eU-OFDM for modulating the µLEDs, which is expected to lead to a significant reduction in the energy consumption at the transmitter and to a significant reduction in the required optical power. The latter is desired in low-illumination scenarios such as dimming applications. Adaptive bit loading has not been utilised in this experiment because fixed constellation loading allows the results from this study to be more easily related to the theoretical results presented in Section 4.3.4.

6.5.1   Experimental Set-up

The set-up for this investigation is presented in Fig. 6.10. The modulation procedure begins with the generation of a discrete OFDM/U-OFDM/eU-OFDM signal using MATLAB®. The signal generation process includes a series of steps: pseudo-random bit generation, M-QAM modulation, IFFT, oversampling, and pulse shaping. For U-OFDM and eU-OFDM, the pulse shaping procedure is performed after the *positive* and the *negative* frames are generated but before any
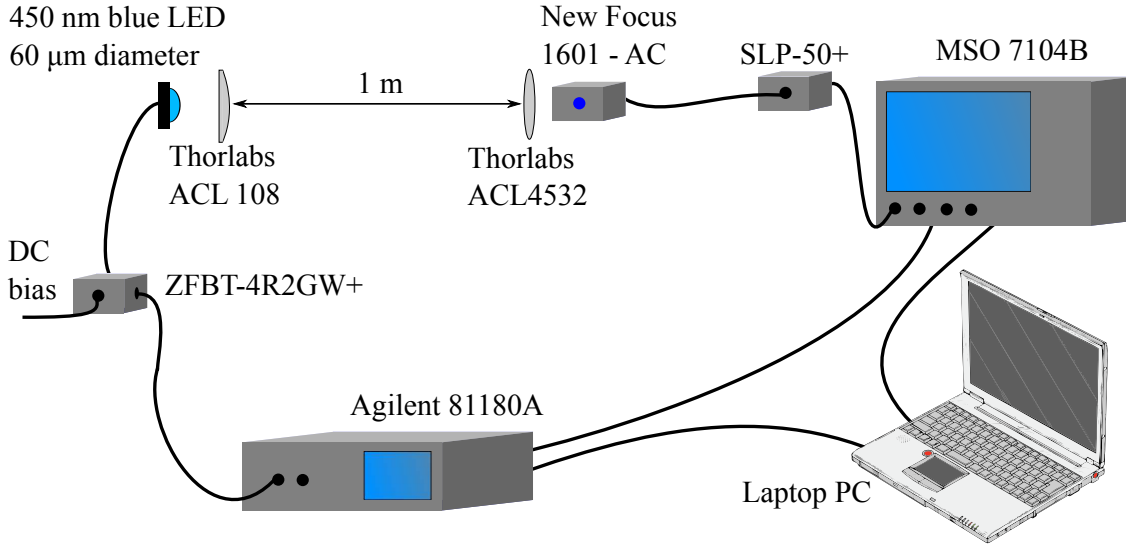
Figure 6.10: *Experimental set-up for Experiment III.*

negative values are removed, as described in Section 5.2. The discrete time samples of the resulting signal are sent to an AWG, Agilent 81180A, which outputs an analog waveform by performing digital-to-analog conversion with a 12-bit zero-order-hold DAC. The output signal from the AWG is used to directly modulate the voltage over the LED. The AWG employs a DC-coupled output amplifier with a maximum voltage swing of $2\,\mathrm{V}$ and a maximum DC offset of $1.5\,\mathrm{V}$. At the same time, the LED has a turn-on voltage of $\approx 3\,\mathrm{V}$. Therefore, in order to utilise the active region of the device for transmission of the information signal, bias is added to the information signal using a bias-T, Mini Circuits ZFBT-4R2GW+. The LED emission is collimated with an aspheric lens, Thorlabs ACL108, and directed towards the receiver. An aspheric lens, Thorlabs ACL4532, collects the light at the receiver site and focuses it on a PIN photodetector, New Focus 1601-AC. The output of the photodetector is a continuous analog signal which is filtered with a commercial low-pass filter, Mini Circuits SLP-50+, in order to remove any excess noise from the signal due to the large bandwidth ($> 1\,\mathrm{GHz}$) of the photodetector. The output of the filter is captured with a digital oscilloscope, Agilent MSO7104B, which performs digital to analog conversion with a 12-bit analog-to-digital converter (ADC). The digitised signal is processed in MATLAB® with a series of steps that include: synchronisation, matched filtering, down-sampling, FFT, channel estimation, equalisation, and M-QAM demodulation. Any additional demodulation steps which are required in U-OFDM and eU-OFDM are performed in accordance with the demodulation process described in Section 4.2 and 4.3.1.

The parameters which describe the OFDM techniques used in this section are: 1) an FFT size of N_{fft}=1024, where only 501 subcarriers are modulated with unique M-QAM symbols due to the Hermitian symmetry requirement described in Section 2.7.2 and because the first 10 subcarriers are omitted due to the baseline wandering effect; 2) cyclic prefix length of N_{cp}=5; 3) a single-sided communication bandwidth of $B/2$=20 MHz for DCO-OFDM and U-OFDM where the achievable SNR is expected to be relatively flat based on the results in Experiment I; the bandwidth for eU-OFDM is set to $B/2$=23 MHz in order to compensate for the spectral efficiency difference since a maximum modulation depth of D=3 is used in eU-OFDM; 4) digital clipping of the OFDM time-domain signal at $-3\sigma_{\text{s}}$ and $3\sigma_{\text{s}}$, in order to reduce the high PAPR of the OFDM signal; the range of $[-3\sigma; 3\sigma]$ contains more than 99.7% of the signal distribution, and according to the results presented in Section 4.3.4, it is more than enough to ensure that the digital clipping does not limit the performance of the communication system for the presented modulation orders; in U-OFDM and eU-OFDM, every single information stream is clipped at $[0; 3\sigma]$; 5) RRC pulse shaping with an oversampling factor of 4 and a roll-off factor of 0.1.

6.5.2 Signal Processing Techniques

6.5.2.1 Channel Estimation

For bit and energy loading at the transmitter as well as for equalisation at the receiver, the communication channel has to be accurately estimated. Therefore, a suitable channel estimation technique should be employed. The received signal can be expressed as:

$$\hat{S}[k] = H[k]S[k] + N[k], \tag{6.3}$$

where $H[k]$ is the complex channel gain in the frequency domain, $S[k]$ is the transmitted signal in the frequency domain, and $N[k]$ is the frequency-domain realisation of the AWGN process at the receiver. It is assumed that $H[k]$ contains all frequency-dependent attenuation and phase rotation of the information signal from the moment the signal is generated in the OFDM/U-OFDM/eU-OFDM modulation process at the transmitter until the moment it is demodulated at the receiver.

In order to allow for better characterisation of the communication channel, two separate estimation techniques have been used. In the first technique, multiple identical copies of a single OFDM pilot frame are transmitted in series. The AWGN is assumed to be zero-mean. Therefore, when N

identical copies of the pilot frame are transmitted, the communication channel can be estimated using a conventional mean estimator as follows:

$$\hat{H}[k] = \frac{\sum\limits_{i=1}^{N} \hat{S}^i[k]}{N S[k]} = \frac{\sum\limits_{i=1}^{N} \left\{ H[k]S[k] + N^i[k] \right\}}{N S[k]}. \tag{6.4}$$

The noise variance, *i.e.*, the noise energy, can be estimated using a conventional variance estimator as follows:

$$\hat{\sigma}_{\mathrm{N}}^2[k] = \frac{\sum\limits_{i=1}^{N} \left| \hat{S}^i[k] - \hat{H}[k]S[k] \right|^2}{N-1}. \tag{6.5}$$

In the rest of this chapter, the described channel and noise variance estimation technique is referred to as Estimator I. The estimated channel gain can be used in the equalisation procedure. The estimated channel gain and the estimated noise variance can be used to estimate the achievable SNR levels at each subcarrier in the OFDM frame. The SNR estimation can be used to determine how much data can be transmitted on a given subcarrier. As a result, modulation of some subcarriers might be avoided or the modulating symbols could be pre-equalised to ensure equivalent performance for all subcarriers that are loaded with the same constellation size. It should be noted that the SNR quantity described in this section does not take into account the energy dissipated in the DC component of the information signal. As a result, It is different from the SNR defined in (2.19). Another aspect of the communication system that should be discussed is the inherent non-linearity of a real OWC channel. Non-linear distortion occurs in the digital-to-analog/analog-to-digital conversion, in the electrical-to-optical transition in the LED front-end, and in the transition step from an optical signal to an electrical signal in the photodetector. The DAC of the employed AWG and the ADC of the oscilloscope have 12-bit precision, which is enough to consider any non-linear distortion from these elements insignificant for the achievable SNR levels reported in this chapter. The PIN photodetector is operated in a range which appears to also introduce negligible distortion to the information signal. Therefore, it is safe to assume that any significant non-linear distortion in the system is expected to be caused by the LED output characteristic. The received time-domain information signal without the AWGN takes the following form:

$$\hat{s}[n] = h[n] * z(s[n]) \tag{6.6}$$

where $z(\cdot)$ denotes the non-linear electrical-to-optical conversion step at the LED, $[\cdot] * [\cdot]$ denotes the convolution operator, and $\mathrm{h}[n]$ is the time-domain impulse response of the communication channel. According to the analysis in Chapter 5, a time-domain non-linear distortion of an OFDM signal translates into an SNR penalty in the frequency domain. Estimator I is designed for a linear AWGN channel. When the communication system contains significant non-linear distortion, Estimator I is unable to capture its effect because (6.4) actually estimates:

$$\hat{\mathrm{H}}[k] = \frac{\mathfrak{F}\{\hat{\mathrm{s}}[n]\}}{\mathrm{S}[k]} = \frac{\mathrm{H}[k]\mathrm{S}[k] + \mathrm{d}[k]}{\mathrm{S}[k]} \tag{6.7}$$

rather than the true communication channel frequency response $\mathrm{H}[k]$. In (6.7), $\mathfrak{F}\{\cdot\}$ denotes the FFT operation and $\mathrm{d}[k]$ is the non-linear distortion in the frequency domain. When the non-linear distortion is significant, $\mathrm{d}[k]$ could lead to inaccurate estimation of the communication channel. It also compromises the estimation of the noise variance in (6.5), because the way Estimator I is defined, $\mathrm{d}[k]$ does not contribute to the estimated noise variance. Therefore, in the high SNR communication scenarios, where the non-linear distortion is the limiting factor for the performance, the SNR levels estimated with Estimator I could be inaccurate. As a result, a second estimation approach, named Estimator II, is introduced in conjunction with Estimator I. In Estimator II, multiple different realisations of an OFDM pilot frame are transmitted sequentially instead of one frame copy being sent multiple times as in Estimator I. In Estimator II, the communication channel is estimated as:

$$\hat{\mathrm{H}}[k] = \frac{1}{N}\sum_{i=1}^{N}\frac{\hat{\mathrm{S}}^i[k]}{\mathrm{S}^i[k]} = \frac{1}{N}\sum_{i=1}^{N}\frac{\mathrm{H}[k](\mathrm{S}^i[k] + \mathrm{d}^i[k]) + \mathrm{N}^i[k]}{\mathrm{S}^i[k]}. \tag{6.8}$$

In (6.8), both the AWGN realisations and the non-linear distortion terms are averaged out during the channel estimation procedure. Therefore, the channel estimation procedure is expected to be more accurate when the non-linear distortion is the limiting factor for the system performance. Furthermore, the technique in Estimator II improves the accuracy of the noise variance estimation procedure because the non-linear distortion term contributes to the sum in (6.5). In certain practical scenarios, where the non-linearity distortion is significant, it can be beneficial to apply both Estimator I and Estimator II in order to evaluate how much the non-linear distortion affects the performance of the communication system. This, in turn, can be used when optimising the active range of the LED.

(a) V-I characteristic of the LED.

(b) V-L characteristic of the LED.
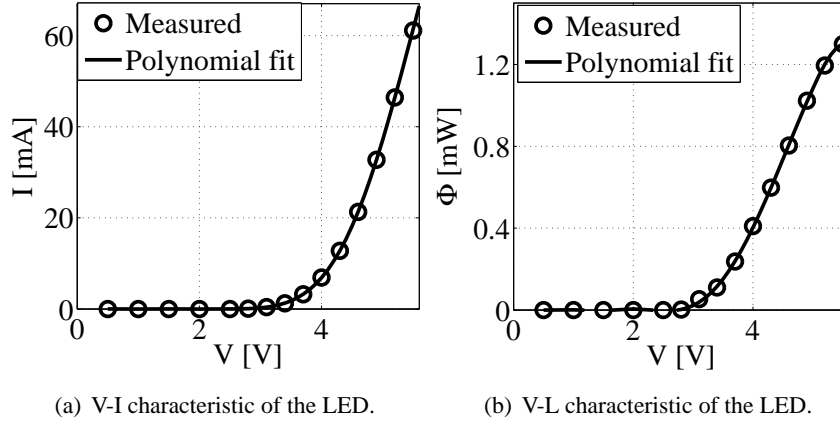
Figure 6.11: *LED characteristics.*

6.5.2.2 Non-linear Distortion

The main source of non-linear distortion in the presented communication set-up is the output characteristic of the LED. The voltage-to-current (V-I) characteristic of the LED is non-linear as illustrated by the measured data presented in Fig. 6.11(a). The current-to-light (I-L) characteristic of the LED can be assumed linear for the most part of the device active region. For high current values, however, the light output of the device tends to saturate as the output efficiency of the LED decreases with increasing current density and increasing temperature. As the information signal modulates the voltage over the LED, Fig. 6.11(b) presents the input-output (voltage-to-light (V-L)) relationship of the LED. The active region of the device starts at around 3V, where the light output begins.

For energy efficiency purposes, the LED should be operated as low as possible in its active region. This part of the region, however, causes significant non-linear distortion to the information signal as can be inferred from the data in Fig. 6.11(b). The same conclusion can be made from Fig. 6.12(a) and Fig. 6.12(b). In Fig. 6.12(a), the channel gain for DCO-OFDM estimated with Estimator I exhibits noticeable variation, while the curve computed with Estimator II appears smooth. This is a good indication that the non-linear distortion is significant. The data in Fig. 6.12(b) leads to the same conclusion because the SNR values at the different subcarriers of DCO-OFDM computed with Estimator II are about 3 dB lower than the SNR values computed with Estimator I. A non-linear pre-distortion technique described in [112] was attempted in order to mitigate the effects of the non-linearity. The technique consists of simply computing the inverse of the V-L function presented in Fig. 6.11(b) and then passing the discrete modulation signal

(a) Channel gain.

(b) SNR before pre-distortion.

(c) SNR after pre-distortion.

(d) SNR after pre-equalisation.
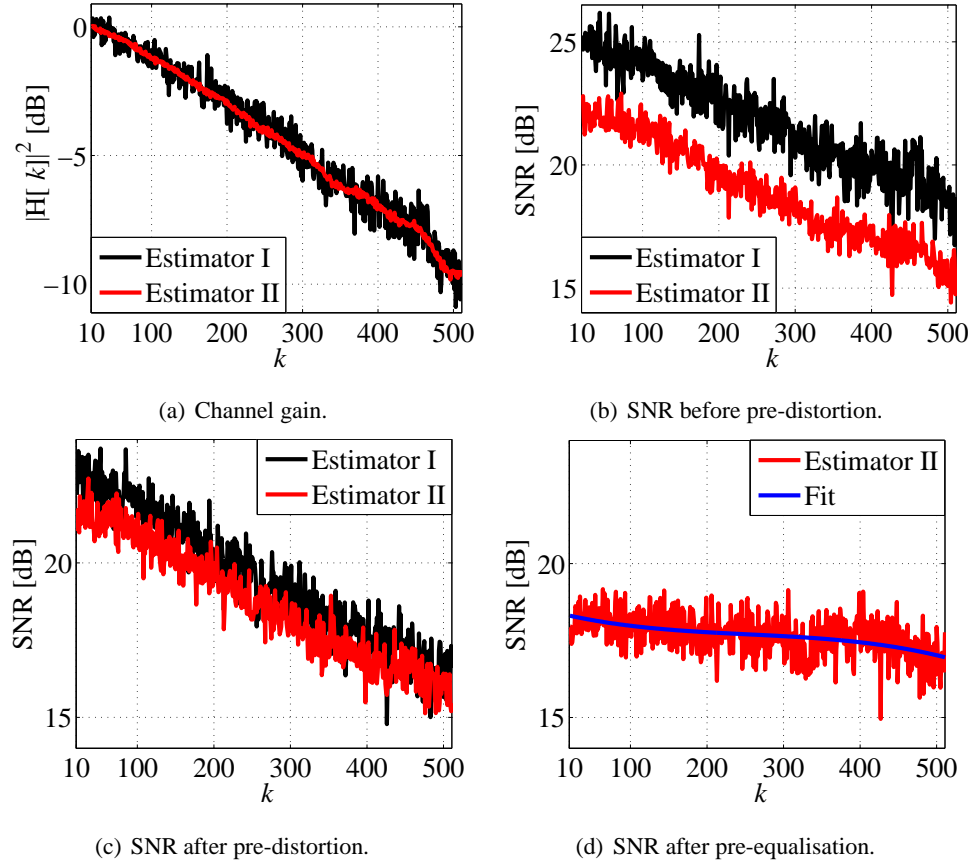
Figure 6.12: *Communication channel characteristics estimated for an OFDM signal centred at around 3.5 V with a peak-to-peak voltage swing of about 1 V. Subcarriers with indices [0; 10] have not been used for communication due to significant DC-wandering effects at the transmitter, caused by AC-coupling in the bias-T.*

through that inverse function before converting it to an analog signal. The effect of this pre-distortion technique is illustrated in Fig. 6.12(c) where the SNR curves estimated with Estimator I and Estimator II are closely adjacent to each other. This suggests that the non-linearity has been significantly reduced. It is interesting to note, however, that the SNR after the pre-distortion does not appear to be better than the SNR estimated with Estimator II before the pre-distortion technique. The BER results obtained during the experiments have also confirmed that the pre-distortion technique does not seem to improve the performance of DCO-OFDM. However, the pre-distortion is very beneficial for U-OFDM and eU-OFDM. When no pre-distortion is applied, both schemes exhibit performance outside the FEC limits. Both U-OFDM and eU-OFDM appear to be more sensitive to non-linear distortion than DCO-OFDM. The effect is likely to arise from the fact that the time-domain information signal in both schemes is concentrated in a more

non-linear part of the LED active range compared with the information signal in DCO-OFDM. The higher modulation depths of eU-OFDM are especially vulnerable to this effect because the imperfections in the time-domain signal due to non-linear distortion add up in the demodulation process. When no pre-distortion is used, U-OFDM and eU-OFDM require significant bias in order to be realised in the relatively linear region of the LED V-L characteristic. This tends to significantly reduce any energy advantage they have over DCO-OFDM. When the pre-distortion is applied, both U-OFDM and eU-OFDM can be realised with minimum biasing requirements and demonstrate a significant energy advantage over DCO-OFDM.

When operated at low current density, *i.e.*, at low bias currents, the LED appears to have a slower frequency response. It is clear from Fig. 6.12(a) that the frequency response of the LED is not flat. In order to ensure equivalent received SNR levels at all OFDM subcarriers, a pre-equalisation technique has been employed. It consists of rescaling the energy allocated to each subcarrier inversely proportional to the SNR values computed with Estimator II and presented in Fig. 6.12(c). As a result, the achieved SNR profile looks flat as shown in Fig. 6.12(d).

6.5.2.3 Estimation of Energy Dissipation

In order to estimate the average electrical power dissipated at the transmitter front-end, the voltage over the LED is probed and captured with the oscilloscope. Afterwards, the V-I characteristic of the LED is used in order to estimate the current which flows through the device. The average electrical power for each modulation scheme is estimated as:

$$P_{\text{elec}}^{\text{avg}} = \frac{\sum_{n=1}^{N_{\text{total}}} V[n] I(V[n])}{N_{\text{total}}}, \tag{6.9}$$

where $V[n]$ is the nth discrete voltage sample captured by the oscilloscope, $I(\cdot)$ is the V-I characteristic presented in Fig. 6.11(a), and N_{total} is the total number of discrete voltage samples captured with the oscilloscope.

In order to compare the optical efficiency of the different modulation schemes, the average irradiance level at the receiver is measured with a commercially available spectral irradiance receiver, Labsphere E1000. The irradiance receiver is positioned in place of the receiver lens. The average irradiance level is measured for each scheme while the LED is being modulated with the respective information signal.

148

6.5.3   Performance Results

The current section presents a performance comparison between DCO-OFDM, U-OFDM and eU-OFDM for the communication set-up presented in Section 6.5.1 using the electrical and optical power metrics presented in Section 6.5.2.3. A number of system-related factors cause the results presented here to differ from the results presented in Section 4.3.4 and would have to be modelled in future work for a good match between theory and experimental measurements. First, the frequency response of the transmission system is not flat and needs to be equalised through pre-distortion. This leads to an SNR penalty. Second, the free-space optical channel loss has to be accounted for in order to establish an accurate relationship between the transmitted optical power and the received optical power. Third, the frequency response of the receiver system including any absolute gain factors needs to be characterised experimentally in addition to the AWGN levels at the receiver. Fourth, the non-linear relationship between voltage, current and light in the LED, as well as the significant turn-on voltage requirement (almost 3 V), introduce additional differences that have to be accurately modelled and estimated for a good match between the theoretical/numerical results and the experimental results. Finally, the non-linear relationship between voltage and current leads to differences between the method for estimating electrical power in the simulation results presented in Section 4.3.4 and the experimental results presented in the current section. Nevertheless, the performance trends, derived from the theoretical analysis and the Monte Carlo simulations, can be identified in the results presented in Fig. 6.13 and Fig. 6.14.

When compared with binary phase-shift keying (BPSK) eU-OFDM and BPSK DCO-OFDM, 4-QAM U-OFDM is more efficient both in terms of electrical and optical power. The difference to eU-OFDM in terms of both electrical and optical power is approximately 1.5 dB at a BER of 10^{-3} and almost 2 dB at a BER of 10^{-4}. Compared with BPSK DCO-OFDM, 4-QAM U-OFDM requires 3.5 dB less electrical power and 3 dB less optical power for a BER of 10^{-3}, and it also requires 4 dB less electrical power and 3.5 dB less optical power for a BER of 10^{-4}. The 16-QAM U-OFDM scheme performs worse than 4-QAM eU-OFDM using approximately equivalent optical power and 1 dB more electrical power at a BER of 10^{-3}. For a BER of 10^{-4}, the difference between U-OFDM and eU-OFDM is approximately 3 dB in terms of electrical power and approximately 1 dB in terms of optical power in favour of eU-OFDM. At the same time, 4-QAM DCO-OFDM is approximately 1 dB worse than 4-QAM eU-OFDM in terms of electrical power at a BER of 10^{-3} and 2 dB worse at a BER of 10^{-4}. In terms of optical power,
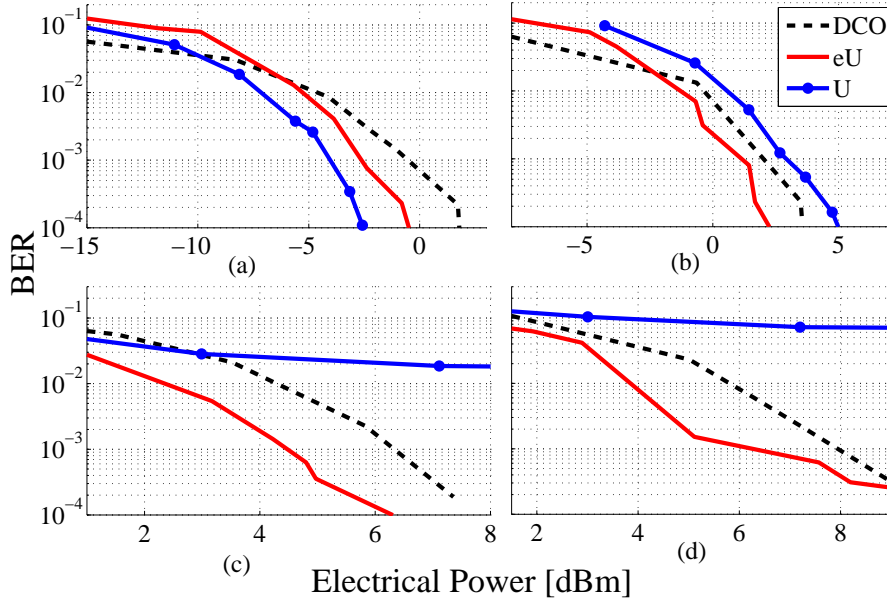
Figure 6.13: *Performance comparison as a function of the electrical power dissipated in the LED: (a) BPSK DCO-OFDM/eU-OFDM vs. 4-QAM U-OFDM (20 Mb/s); (b) 4-QAM DCO-OFDM/eU-OFDM vs. 16-QAM U-OFDM (40 Mb/s); (c) 8-QAM DCO-OFDM/eU-OFDM vs. 64-QAM U-OFDM (60 Mb/s); (d) 16-QAM DCO-OFDM/eU-OFDM vs. 256-QAM U-OFDM (80 Mb/s).*

DCO-OFDM is $0.7\,\mathrm{dB}$ worse at a BER of 10^{-3} and $1\,\mathrm{dB}$ worse at a BER of 10^{-4} when compared with eU-OFDM. The non-linear distortion introduces a noticeable effect on the 16-QAM U-OFDM signal and the corresponding curves in Fig. 6.13(b) and Fig. 6.14(b) exhibit a noticeable change in slope for a BER lower than 10^{-3}. In Fig. 6.13(c), 8-QAM eU-OFDM exhibits a $2\,\mathrm{dB}$ improvement over DCO-OFDM in electrical power dissipation for a BER of 10^{-3} and a BER of 10^{-4}. At the same time, the optical power requirement of 8-QAM eU-OFDM is approximately $1\,\mathrm{dB}$ less than the optical power requirement of 8-QAM DCO-OFDM for both a BER of 10^{-3} and a BER of 10^{-4}. The U-OFDM scheme for $M \geq 64$ could not be realised within the FEC limits due to the non-linear distortion. The non-linear pre-distortion procedure does not appear to improve the performance when the signal exceeds $4.5\,\mathrm{V}$. This could be due to non-linearity in the upper part of the LED active region which is not memoryless, so a more complicated pre-distortion procedure, like the one in [113], should be applied. For 16-QAM, eU-OFDM is again more efficient than DCO-OFDM with $2\,\mathrm{dB}$ of electrical power improvement and $1.5\,\mathrm{dB}$ of optical power improvement at a BER of 10^{-3}. At a BER close to 10^{-4}, the eU-OFDM scheme requires approximately the same electrical and optical power as 16-QAM DCO-OFDM as the non-linear distortion limits the system performance. For higher M-QAM constellation sizes, eU-OFDM
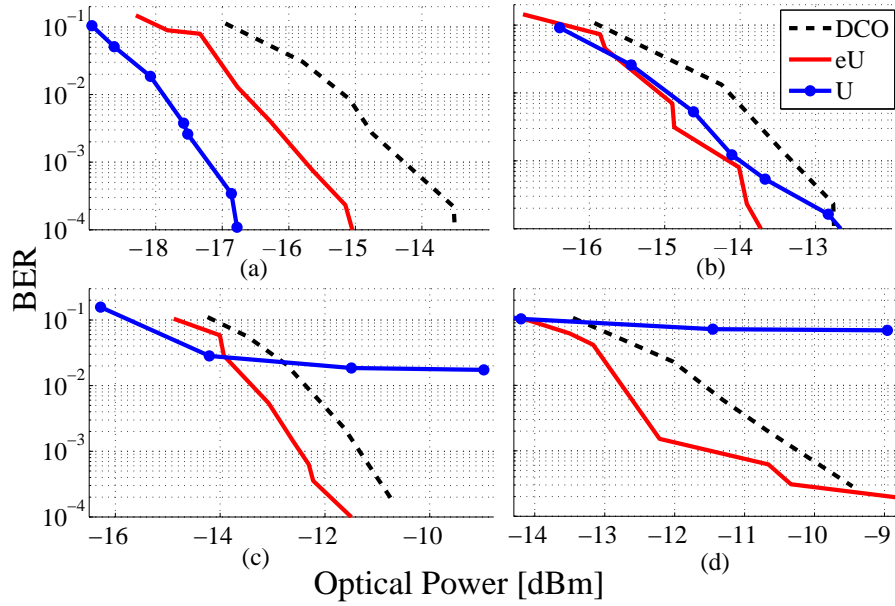
Figure 6.14: *Performance comparison as a function of the optical power measured at the receiver: (a) BPSK DCO-OFDM/eU-OFDM vs. 4-QAM U-OFDM (20 Mb/s); (b) 4-QAM DCO-OFDM/eU-OFDM vs. 16-QAM U-OFDM (40 Mb/s); (c) 8-QAM DCO-OFDM/eU-OFDM vs. 64-QAM U-OFDM (60 Mb/s); (d) 16-QAM DCO-OFDM/eU-OFDM vs. 256-QAM U-OFDM (80 Mb/s).*

could not be realised within the FEC limits.

Non-linear distortion due to the LED output characteristic appears to limit the performance of the eU-OFDM OWC system. The memoryless pre-distortion technique described in Section 6.5.2.2 improves the performance significantly. In a future implementation, the issue of non-linearity could be avoided by introducing a transconductance amplifier (TCA) which modulates the current through the LED rather than the voltage over the device. The LED efficiency drop could be reduced with appropriate heat-sinking techniques. Furthermore, the issue of LED efficiency drooping at high current densities suggests that energy-efficient implementations, both for communication and illumination applications, would benefit from a system configuration with multiple LEDs operated in parallel at the lower end of their active region. This could reduce the non-linear distortion in eU-OFDM as it would enable the output power to be scaled linearly with the number of output devices.

6.6   Summary

The results presented in this chapter have demonstrated the feasibility of a 3.5-Gb/s optical wireless link using a single Gallium Nitride µLED and OFDM modulation which allows for adaptive bit and energy loading leading to an optimal utilisation of the communication resources. To the best of the author's knowledge, this is the highest achieved data rate in a single-LED wireless VLC demonstration up-to-date. The demonstration has been performed for a narrow-field-of-view link over a 5-cm distance. The coverage can be improved with the introduction of dedicated optics, with ganging of multiple µLEDs in order to increase the transmitted optical power or with the introduction of a more sensitive photodetector such as an APD.

The feasibility of a Gb/s link has been demonstrated for a GaN µLED using simple lenses and an APD photodetector over a practical distance ranging from a few meters, for a potential indoor short-distance scenario, to at least $10\,\mathrm{m}$ for a longer-distance transmission. In the context of energy and spectrally efficient wireless communications, this is an important result taking into account the total output optical power of 4.5 mW of the µLED and comparing it to RF systems. These results suggest great implications for a large number of potential VLC applications. The area coverage of a single µLED is in the order of a few cm^2, and so is insufficient for ubiquitous coverage. Yet, it is more than enough to avoid stringent alignment requirements. The introduction of integrated arrays of multiple transmitter devices could be sufficient to provide simultaneous illumination and Gb/s communication in an indoor environment.

A proof-of-concept experimental investigation of VLC using eU-OFDM modulation and U-OFDM modulation has been presented in this chapter. The results of the study indicate that both techniques can be realised in practice and can deliver significant energy savings over the conventional DCO-OFDM. The most significant limitation for the use of U-OFDM and eU-OFDM in practical OWC systems is expected to be the non-linear distortion. Techniques for non-linear distortion mitigation, such as signal pre-distortion, can enable both schemes to be realised. Future work on non-linear distortion reduction by the use of improved predistortion techniques and by the use of transmitter front-end devices with more linear output characteristics is expected to enable even higher performance results to be achieved with eU-OFDM.

Chapter 7
Conclusions, Limitations and Future work

In this thesis, a number of unipolar orthogonal frequency division multiplexing (OFDM)-based modulation schemes suitable for intensity modulation and direct detection (IM/DD) systems have been investigated. The well-known concepts of direct-current-biased optical orthogonal frequency division multiplexing (DCO-OFDM), asymmetrically clipped optical orthogonal frequency division multiplexing (ACO-OFDM) and pulse-amplitude-modulated discrete multitone modulation (PAM-DMT) have been studied in more detail compared to what is already available in the literature. Some of the existing issues with these modulation schemes have been identified and suitable solutions have been suggested. The work has led to novel and improved modulation techniques for which suitable theoretical, simulation and experimental analysis has been presented. The non-linear distortion in the optical system has been analysed from a new point of view and the existing analytical concepts have been further extended with a technique that always leads to a closed-form analytical solution. The work concludes with experimental demonstrations of high-speed optical wireless communications (OWC) using OFDM and a proof-of-concept demonstration of unipolar orthogonal frequency division multiplexing (U-OFDM) and enhanced unipolar orthogonal frequency division multiplexing (eU-OFDM) leading to the energy savings predicted by the presented theoretical work.

7.1   Summary and Conclusions

The recently introduced concept of subcarrier-index modulation orthogonal frequency division multiplexing (SIM-OFDM) has been studied in detail. A novel accurate analytical framework to compute the bit error rate (BER) of SIM-OFDM in a linear additive white Gaussian noise (AWGN) channel has been proposed. As a result of the analysis, a propagation error effect within the SIM-OFDM frame has been discovered. The error propagation limits the performance of SIM-OFDM and does not allow the scheme to deliver the anticipated energy savings in comparison to conventional OFDM. An enhanced SIM-OFDM modulation scheme has been proposed as a means to correct this issue. The performance of the new scheme has been analysed in a linear AWGN channel, which can serve as a basis for further research on the topic. The modified structure of the enhanced SIM-OFDM successfully avoids the error propagation effect and allows the scheme to deliver energy efficiency improvements in the order of $1\,\mathrm{dB}$ in comparison to OFDM. Furthermore, the frame structure used in the enhanced SIM-OFDM leads to a reduction of the time-domain signal peak-to-average power ratio (PAPR), which has been found to be proportional to the number of *active* subcarriers employed in the scheme.

Even though the enhanced SIM-OFDM offers an inherently reduced PAPR and lower energy requirements in comparison to conventional OFDM, the limited spectral efficiency of the novel concept makes it unattractive for high-speed OFDM-based communication. Nevertheless, SIM-OFDM can be used in energy-efficient low-spectral-efficiency applications. Furthermore, SIM-OFDM can also be used in adaptive bit and energy loading scenarios, where the SIM-OFDM concept can be combined with the conventional OFDM concept because SIM-OFDM is suitable for modulation of those subcarriers where the signal-to-noise ratio (SNR) is low and does not allow for high spectral efficiency modulation. This enables better utilisation of the communication channel resources.

A novel unipolar OFDM-based modulation scheme termed U-OFDM has been proposed. The novel scheme is an alternative to the concepts of ACO-OFDM and PAM-DMT. A theoretical framework has been presented for evaluating the performance of U-OFDM in a linear AWGN channel which has been compared against the performance of the commonly adopted state-of-the-art technique of DCO-OFDM. It has been shown that U-OFDM performs equivalently to ACO-OFDM and PAM-DMT with a $3\,\mathrm{dB}$ lower energy efficiency compared to a real bipolar OFDM information signal, which can be considered as a performance benchmark. An improved

decoding technique has been suggested, and this improved decoder can improve the performance of U-OFDM with up to $3\,$dB in a linear AWGN channel, ideally closing the gap to the benchmark performance. An accurate theoretical framework for evaluating the performance of this improved decoding technique has been proposed. All benefits of U-OFDM, however, come at a 50% reduction in the scheme's spectral efficiency. The same problem is observed in the generation processes of the other unipolar state-of-the-art techniques ACO-OFDM and PAM-DMT. As a result, when the spectral efficiency of DCO-OFDM is matched by introducing a larger modulation order, U-OFDM, and similarly ACO-OFDM and PAM-DMT, cannot deliver any benefits over DCO-OFDM for spectral efficiency values higher than $0.5\,$bits/s/Hz.

A solution to the issue of the spectral efficiency loss has been proposed in the form of a modified technique named eU-OFDM, where the structure of the U-OFDM frame can be exploited in order to combine multiple individual information streams and, thus, increase the overall spectral efficiency of the scheme while still retaining a lot of its energy efficiency. The performance of eU-OFDM has been analysed theoretically for a linear AWGN channel. It has been shown that in a linear AWGN channel, eU-OFDM always performs with an energy requirement which is a fixed multiple of the energy required in a bipolar real OFDM signal for a given BER. Consequently, as the modulation order of the scheme increases, the energy advantage of eU-OFDM over DCO-OFDM increases as the latter requires higher bias levels, and thus more energy, for higher modulation orders because larger constellations can tolerate less non-linear distortion due to signal clipping. The electrical energy advantage of eU-OFDM over DCO-OFDM starts at approximately $2\,$dB for binary phase-shift keying (BPSK) and increases to approximately $7\,$dB for 1024-QAM at a maximum modulation depth of $D{=}3$. At the same time, the optical power requirement of eU-OFDM is approximately the same as the optical power requirement of DCO-OFDM for BPSK and approximately $3\,$dB lower for 1024-QAM. The presented simulation results suggest that eU-OFDM can achieve very significant energy efficiency benefits over DCO-OFDM or can potentially deliver higher data rates in dimming applications since the optical power required in eU-OFDM is less than in DCO-OFDM for a given data rate and BER. Suggestions for an extension of the eU-OFDM concept to ACO-OFDM and PAM-DMT have also been provided.

The problem of analysing non-linear distortion in an OWC system has been investigated from a novel point of view. The already known approach of using the Bussgang theorem for analysing the performance of OFDM signals in a non-linear system has been extended by introducing a novel representation of the non-linear distortion function as a set of polynomials. This represen-

tation enables the derivation of a very accurate closed-form analytical performance evaluation. The derivation procedure can be applied for an arbitrary memoryless distortion function, and the algorithm can be easily automated following the proposed framework. This analytical approach can be very beneficial for the automation of the performance analysis of OFDM-based systems in which the information signal is subjected to non-linear distortion. Furthermore, this approach could significantly reduce the computational efforts and simulation times in optimisation procedures for OFDM-based systems with non-linear distortion when compared to a Monte Carlo simulation approach. Pulse shaping techniques have been introduced in the non-linearity analysis for the investigated OFDM-based techniques – DCO-OFDM, ACO-OFDM, PAM-DMT and U-OFDM. It has been shown that the use of a pulse-shaping filter does not compromise the validity of the analysis technique for evaluating the effects of non-linear distortion on the system performance. Furthermore, it has been demonstrated, both theoretically and through numerical simulations, that ACO-OFDM, PAM-DMT and U-OFDM perform equivalently in a non-linear AWGN channel.

The communication capabilities of a novel Gallium Nitride (GaN) μm-sized light emitting diode (μLED) with a diameter of $50\,\mu$m have been investigated using DCO-OFDM. It has been shown that such devices can be modulated with bandwidths of up to $800\,$MHz, and a record-setting data rate of $3.5\,$Gb/s has been achieved using an adaptive bit and energy loading algorithm. To the best of the author's knowledge, this is the fastest single-link wireless visible light communications (VLC) system demonstration up-to-date. In addition, the feasibility of a Gb/s OWC link over a transmission distance of up-to $10\,$m has been demonstrated for a GaN μLED using simple lenses. The coverage provided by a single μLED is in the order of a few cm^2, and is not sufficient for ubiquitous coverage in a typical indoor scenario. However, this is more than enough to avoid stringent alignment requirements for realising fixed links at shorter distances. An integrated array of a large number of such transmitter devices could provide simultaneous illumination and high-speed communication in an indoor environment. The limited coverage of a single device, however, allows for the deployment of very high data densities, in the order of $> 1\,\text{Tb/s/m}^2$, which is unprecedented in wireless communications.

Finally, a proof-of-concept experiment has been conducted in order to demonstrate the plausibility and the high potential of U-OFDM and eU-OFDM. The demonstrated results indicate that both techniques are practically feasible and tend to deliver the anticipated energy efficiency. At low spectral efficiency of $0.5\,$bit/s/Hz, 4-QAM U-OFDM achieves the best results in comparison

to eU-OFDM and DCO-OFDM with an electrical energy efficiency improvement of 3.5 dB and a lower optical power requirement of 3 dB in comparison to DCO-OFDM. For higher spectral efficiencies, eU-OFDM achieves the best results by delivering improvements in electrical energy dissipation of approximately 2 dB and improvements in the optical power requirement of approximately 1 dB in comparison to DCO-OFDM for all of the presented cases. Non-linear distortion has proven to be a limitation for the realisation of U-OFDM and eU-OFDM in an OWC system. Signal processing techniques, such as signal pre-distortion, can mitigate the non-linearity issues and improve the system performance.

7.2   Limitations and Future Work

The analytical work presented for SIM-OFDM in Chapter 3 follows closely the results of the conducted numerical simulations. However, the performance analysis has been performed for an ideal flat linear AWGN channel. The presented energy efficiency results in combination with the reduced spectral efficiency of the modulation approach have been considered as sufficient evidence to dismiss SIM-OFDM as a suitable scheme for high-speed optical wireless communication. Nevertheless, it could be suitable for energy-efficient applications where high spectral efficiency is not required. In that sense, a more realistic communication channel including non-linear effects of the transmitter and receiver system in both optical an radio frequency (RF) communication should be considered in the analysis. Furthermore, in RF communication, the effect of channel fading on the system performance should be analysed. The suitability of different forward error correction (FEC) coding techniques used in conventional OFDM also should be investigated in potential applications of SIM-OFDM.

The novel modulation schemes proposed in Chapter 4 have been analysed in the context of a linear AWGN channel, which is a fair starting point for analysing the performance of a modulation scheme in an IM/DD communication system. The effects of non-linear distortion on U-OFDM have been analysed in Chapter 5. However, an adequate theoretical approach for modelling the effects of non-linear distortion on the performance of eU-OFDM has not been provided. This is because the proposed non-linearity analysis is based on the Bussgang theorem and is valid only for signals with Gaussian distribution. The distribution of eU-OFDM is the convolution of the distributions of the individual U-OFDM signals used in the scheme, and, as a result, it is not

Gaussian. Further work on the subject may include the design of an adequate analytical technique for modelling the effects of non-linear distortion on the performance eU-OFDM. Furthermore, in a practical communication system, appropriate channel estimation and FEC techniques have to be used, and the applicability of the conventional techniques used in OFDM is yet to be investigated for the newly proposed modulation schemes. The use of different modulation orders at the different depths in eU-OFDM should also be analysed in future work. In practical applications, the effects of different synchronisation techniques on the system performance would have to be evaluated for U-OFDM and eU-OFDM as well.

The non-linearity analysis presented in Chapter 5 gives very accurate analytical predictions in closed form for the performance of the investigated modulation schemes which can be subjected to arbitrary distortion effects. Nevertheless, the proposed approach is only valid for memoryless non-linear distortion effects. For modulation frequencies in the flat region of the light emitting diode (LED) response, the assumption of memoryless non-linear distortion can be considered fair. In general, however, the non-linear distortion effects in LEDs are not memoryless, as confirmed by others [113]. Therefore, for modulation frequencies beyond the 3-dB bandwidth of the LED, the provided analytical approach could begin to disagree with experimental measurements. Another assumption in the analysis is the independent and identical Gaussian distribution of the time-domain OFDM samples. The assumption for an independent identically distributed (i.i.d.) time-domain signal is only valid when all frequency subcarriers are loaded with equal energy. Therefore, when adaptive bit and energy loading is employed in the OFDM modulation process, the accuracy of the theoretical model could decrease. Furthermore, the Gaussianity assumption of the time-domain signal is only true for an OFDM frame size of $N_{\text{fft}} > 64$, which means that for smaller frame sizes, the model could be inaccurate.

The experimental results presented in Chapter 6 do not take into account the overhead required for estimating the communication channel, which, depending on the scenario, will inevitably lead to a reduction in the achievable data rates. All processing has been performed offline. The implementation cost and complexity of a real-time OFDM system at such high data rates has to be addressed when a practical realisation of the system is considered. In that sense, the implementation of a suitable FEC code is likely to be limited by the implementation complexity and by the hardware cost. As a result, more strict requirements on the achievable BER might be required depending on the selected FEC algorithm. Adaptive bit and energy loading has not be demonstrated in the proof-of-concept experiment for U-OFDM and eU-OFDM. Instead, a fixed constellation

size with pre-equalisation according to the channel properties has been chosen in order to illustrate that the expected performance trend of the two schemes obtained in the analysis in Chapter 4 is achievable in practice. Further work on the subject may include the introduction of adaptive bit and energy loading as well as modulation of the µLED at the maximum possible rate in order to demonstrate the ability of the schemes to reach high-speed communication rates comparable to the high-speed data rates demonstrated for DCO-OFDM.

Appendix A

Derivation of the D-Function for Equations (5.11), (5.12) and (5.13)

$$
\begin{aligned}
\mathrm{D}(t, a, b, \mu, \sigma_{\mathrm{x}}) &= \int_a^b \mathrm{e}^{xt} \frac{1}{\sqrt{2\pi\sigma_{\mathrm{x}}^2}} \mathrm{e}^{-\frac{(x-\mu)^2}{2\sigma_{\mathrm{x}}^2}} \, \mathrm{d}x \\
&= \int_a^b \frac{1}{\sqrt{2\pi\sigma_{\mathrm{x}}^2}} \mathrm{e}^{-\frac{-2xt\sigma_{\mathrm{x}}^2 + x^2 - 2\mu x + \mu^2}{2\sigma_{\mathrm{x}}^2}} \, \mathrm{d}x \\
&= \int_a^b \frac{1}{\sqrt{2\pi\sigma_{\mathrm{x}}^2}} \mathrm{e}^{-\frac{x^2 - 2(t\sigma_{\mathrm{x}}^2 + \mu)x + \mu^2}{2\sigma_{\mathrm{x}}^2}} \, \mathrm{d}x \\
&= \int_a^b \frac{1}{\sqrt{2\pi\sigma_{\mathrm{x}}^2}} \mathrm{e}^{-\frac{x^2 - 2(t\sigma_{\mathrm{x}}^2 + \mu)x + t^2\sigma_{\mathrm{x}}^4 + 2t\sigma_{\mathrm{x}}^2\mu + \mu^2 - t^2\sigma_{\mathrm{x}}^4 - 2t\sigma_{\mathrm{x}}^2\mu}{2\sigma_{\mathrm{x}}^2}} \, \mathrm{d}x \\
&= \mathrm{e}^{\frac{t^2\sigma_{\mathrm{x}}^2}{2} + t\mu} \int_a^b \frac{1}{\sqrt{2\pi\sigma_{\mathrm{x}}^2}} \mathrm{e}^{-\frac{x^2 - 2(t\sigma_{\mathrm{x}}^2 + \mu)x + (t\sigma_{\mathrm{x}}^2 + \mu)^2}{2\sigma_{\mathrm{x}}^2}} \, \mathrm{d}x \\
&= \mathrm{e}^{\frac{t^2\sigma_{\mathrm{x}}^2}{2} + t\mu} \int_a^b \frac{1}{\sqrt{2\pi\sigma_{\mathrm{x}}^2}} \mathrm{e}^{-\frac{(x - \mu - t\sigma_{\mathrm{x}}^2)^2}{2\sigma_{\mathrm{x}}^2}} \, \mathrm{d}x \\
&= \mathrm{e}^{\frac{t^2\sigma_{\mathrm{x}}^2}{2} + t\mu} \left(\mathrm{Q}\left(\frac{a - \mu - t\sigma_{\mathrm{x}}^2}{\sigma_{\mathrm{x}}} \right) - \mathrm{Q}\left(\frac{b - \mu - t\sigma_{\mathrm{x}}^2}{\sigma_{\mathrm{x}}} \right) \right),
\end{aligned}
\tag{A.1}
$$

where $\mathrm{Q}(x)$ is defined as the tail probability of the standard normal distribution, and $\phi(x)$ is defined as the probability density function (PDF) of the standard normal distribution:

$$
\mathrm{Q}(x) = \frac{1}{\sqrt{2\pi}} \int_x^\infty \mathrm{e}^{-\frac{u^2}{2}} \, \mathrm{d}u,
\tag{A.2}
$$

$$
\phi(x) = \frac{1}{\sqrt{2\pi}} \mathrm{e}^{-\frac{x^2}{2}}.
\tag{A.3}
$$

161

$$\frac{\mathrm{d}^n \mathrm{D}(t, a, b, \mu, \sigma_{\mathrm{x}})}{\mathrm{d}t^n}\Bigg|_{t=0} \overset{(A.1)}{=}$$

$$= \frac{\mathrm{d}^n}{\mathrm{d}t^n} \int_a^b \mathrm{e}^{xt} \frac{1}{\sqrt{2\pi\sigma_{\mathrm{x}}^2}} \mathrm{e}^{-\frac{(x-\mu)^2}{2\sigma_{\mathrm{x}}^2}} \,\mathrm{d}x \Bigg|_{t=0}$$

$$= \int_a^b \frac{\mathrm{d}^n}{\mathrm{d}t^n} \mathrm{e}^{xt} \frac{1}{\sqrt{2\pi\sigma_{\mathrm{x}}^2}} \mathrm{e}^{-\frac{(x-\mu)^2}{2\sigma_{\mathrm{x}}^2}} \,\mathrm{d}x \Bigg|_{t=0}$$

$$= \int_a^b x^n \mathrm{e}^{xt} \frac{1}{\sqrt{2\pi\sigma_{\mathrm{x}}^2}} \mathrm{e}^{-\frac{(x-\mu)^2}{2\sigma_{\mathrm{x}}^2}} \,\mathrm{d}x \Bigg|_{t=0}$$

$$= \int_a^b x^n \frac{1}{\sqrt{2\pi\sigma_{\mathrm{x}}^2}} \mathrm{e}^{-\frac{(x-\mu)^2}{2\sigma_{\mathrm{x}}^2}} \,\mathrm{d}x \tag{A.4}$$

$$\frac{\mathrm{d}Q\left(\frac{x-\mu-t\sigma_{\mathrm{x}}^2}{\sigma_{\mathrm{x}}}\right)}{\mathrm{d}t} = \phi\left(\frac{x-\mu-t\sigma_{\mathrm{x}}^2}{\sigma_{\mathrm{x}}}\right)\sigma_{\mathrm{x}} \tag{A.5}$$

$$\frac{\mathrm{d}\phi\left(\frac{x-\mu-t\sigma_{\mathrm{x}}^2}{\sigma_{\mathrm{x}}}\right)}{\mathrm{d}t} = \phi\left(\frac{x-\mu-t\sigma_{\mathrm{x}}^2}{\sigma_{\mathrm{x}}}\right)\left(\frac{x-\mu-t\sigma_{\mathrm{x}}^2}{\sigma_{\mathrm{x}}}\right)\sigma_{\mathrm{x}} \tag{A.6}$$

162

Appendix B
Example of Non-linear Distortion Analysis in Closed Form

This example demonstrates the application of (5.11), (5.12) and (5.13) for a clipping distortion of the orthogonal frequency division multiplexing (OFDM) information signal at values $x_{\min}$ and $x_{\max}$. The non-linear distortion function is presented in Fig. B.1. The intervals and polynomial coefficients corresponding to the non-linear distortion function are presented in Table B.1.

For the presented non-linear distortion function, (5.11) takes the form:

$$
\begin{aligned}
\alpha &= \frac{1}{\sigma_{\mathrm{x}}^2} \sum_{i=1}^{|I|} \sum_{j=0}^{n_i} c_{i,j} \left. \frac{\mathrm{d}^{j+1} \mathrm{D}(t, x_{\min,i}, x_{\max,i}, 0, \sigma_{\mathrm{x}})}{\mathrm{d}t^{j+1}} \right|_{t=0} \\
&= \frac{1}{\sigma_{\mathrm{x}}^2} \left(x_{\min} \frac{\mathrm{d}\mathrm{D}(t, -\infty, x_{\min}, 0, \sigma_{\mathrm{x}})}{\mathrm{d}t} + x_{\max} \frac{\mathrm{d}\mathrm{D}(t, x_{\max}, \infty, 0, \sigma_{\mathrm{x}})}{\mathrm{d}t} \right. \\
&\quad \left. + \frac{\mathrm{d}^2 \mathrm{D}(t, x_{\min}, x_{\max}, 0, \sigma_{\mathrm{x}})}{\mathrm{d}t^2} \right)\Bigg|_{t=0}
\end{aligned}
\tag{B.1}
$$

Equation (5.12) takes the form:

$$
\begin{aligned}
\mathrm{E}\{Y_{\mathrm{n}}\} &= \sum_{i=1}^{|I|} \sum_{j=0}^{n_i} c_{i,j} \left. \frac{\mathrm{d}^{j} \mathrm{D}(t, x_{\min,i}, x_{\max,i}, 0, \sigma_{\mathrm{x}})}{\mathrm{d}t^{j}} \right|_{t=0}, \\
&= \left(x_{\min} \mathrm{D}(t, -\infty, x_{\min}, 0, \sigma_{\mathrm{x}}) + x_{\max} \mathrm{D}(t, x_{\max}, \infty, 0, \sigma_{\mathrm{x}}) \right. \\
&\quad \left. + \frac{\mathrm{d}\mathrm{D}(t, x_{\min}, x_{\max}, 0, \sigma_{\mathrm{x}})}{\mathrm{d}t} \right)\Bigg|_{t=0}
\end{aligned}
\tag{B.2}
$$

Equation (5.13) takes the form:

$$
\begin{aligned}
\mathrm{E}\{z^2(X)\} &= \sum_{i=1}^{|I|} \sum_{j=0}^{n_i} \sum_{j'=0}^{n_i} c_{i,j} c_{i,j'} \left. \frac{\mathrm{d}^{j+j'} \mathrm{D}(t, x_{\min,i}, x_{\max,i}, 0, \sigma_{\mathrm{x}})}{\mathrm{d}t^{j+j'}} \right|_{t=0} \\
&= \left(x_{\min}^2 \mathrm{D}(t, -\infty, x_{\min}, 0, \sigma_{\mathrm{x}}) + x_{\max}^2 \mathrm{D}(t, x_{\max}, \infty, 0, \sigma_{\mathrm{x}}) \right. \\
&\quad \left. + \frac{\mathrm{d}^2 \mathrm{D}(t, x_{\min}, x_{\max}, 0, \sigma_{\mathrm{x}})}{\mathrm{d}t^2} \right)\Bigg|_{t=0}
\end{aligned}
\tag{B.3}
$$
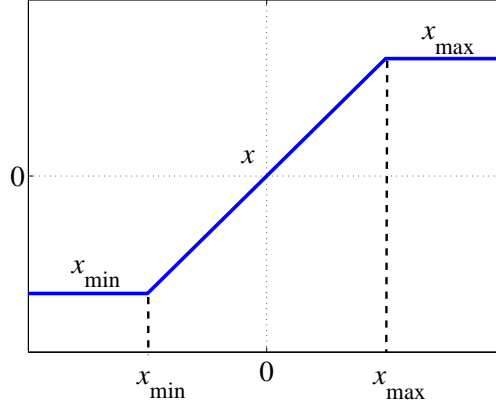
Figure B.1: *Non-linear distortion function corresponding to clipping of the signal at $x_{\min}$ and $x_{\max}$.*

Interval	$c_{i,1}$	$c_{i,0}$
$i = 1 \Leftrightarrow -\infty < x < x_{\min}$	0	$x_{\min}$
$i = 2 \Leftrightarrow x_{\min} < x < x_{\max}$	1	0
$i = 3 \Leftrightarrow x_{\max} < x < \infty$	0	$x_{\max}$

Table B.1: *Polynomial coefficients of the non-linear distortion function.*

Using Appendix A, the derivatives of the D-Function necessary to complete the calculations can be computed as:

$$D(t, a, b, 0, \sigma_x)|_{t=0} = Q\left(\frac{a}{\sigma_x}\right) - Q\left(\frac{b}{\sigma_x}\right) \tag{B.4}$$

$$\frac{dD(t, a, b, 0, \sigma_x)}{dt} = t\sigma_x^2 e^{\frac{t^2\sigma_x^2}{2}}\left(Q\left(\frac{a - t\sigma_x^2}{\sigma_x}\right) - Q\left(\frac{b - t\sigma_x^2}{\sigma_x}\right)\right) +$$
$$e^{\frac{t^2\sigma_x^2}{2}}\left(\phi\left(\frac{a - t\sigma_x^2}{\sigma_x}\right)\sigma_x - \phi\left(\frac{b - t\sigma_x^2}{\sigma_x}\right)\sigma_x\right) \tag{B.5}$$

$$\left.\frac{dD(t, a, b, 0, \sigma_x)}{dt}\right|_{t=0} = \phi\left(\frac{a}{\sigma_x}\right)\sigma_x - \phi\left(\frac{b}{\sigma_x}\right)\sigma_x \tag{B.6}$$

$$\frac{d^2D(t, a, b, 0, \sigma_x)}{dt^2} = t^2\sigma_x^4 e^{\frac{t^2\sigma_x^2}{2}}\left(Q\left(\frac{a - t\sigma_x^2}{\sigma_x}\right) - Q\left(\frac{b - t\sigma_x^2}{\sigma_x}\right)\right) +$$

$$\sigma_x^2 e^{\frac{t^2 \sigma_x^2}{2}} \left(Q\left(\frac{a - t\sigma_x^2}{\sigma_x} \right) - Q\left(\frac{b - t\sigma_x^2}{\sigma_x} \right) \right) +$$

$$2t\sigma_x^2 e^{\frac{t^2 \sigma_x^2}{2}} \left(\phi\left(\frac{a - t\sigma_x^2}{\sigma_x} \right) \sigma_x - \phi\left(\frac{b - t\sigma_x^2}{\sigma_x} \right) \sigma_x \right) +$$

$$e^{\frac{t^2 \sigma_x^2}{2}} \left(\phi\left(\frac{a - t\sigma_x^2}{\sigma_x} \right) \left(\frac{a - t\sigma_x^2}{\sigma_x} \right) \sigma_x^2 - \phi\left(\frac{b - t\sigma_x^2}{\sigma_x} \right) \left(\frac{b - t\sigma_x^2}{\sigma_x} \right) \sigma_x^2 \right) \qquad \text{(B.7)}$$

$$\left. \frac{d^2 D(t,a,b,0,\sigma_x)}{dt^2} \right|_{t=0} = \sigma_x^2 \left(Q\left(\frac{a}{\sigma_x} \right) - Q\left(\frac{b}{\sigma_x} \right) + \phi\left(\frac{a}{\sigma_x} \right) \left(\frac{a}{\sigma_x} \right) - \phi\left(\frac{b}{\sigma_x} \right) \left(\frac{b}{\sigma_x} \right) \right)$$

$$\text{(B.8)}$$

Then (B.1), (B.2), and (B.3) become:

$$\alpha = \frac{1}{\sigma_x^2} \left(-x_{min} \phi\left(\frac{x_{min}}{\sigma_x} \right) \sigma_x + x_{max} \phi\left(\frac{x_{max}}{\sigma_x} \right) \sigma_x + \sigma_x^2 \left(Q\left(\frac{x_{min}}{\sigma_x} \right) - Q\left(\frac{x_{max}}{\sigma_x} \right) \right) +$$

$$x_{min} \phi\left(\frac{x_{min}}{\sigma_x} \right) \sigma_x - x_{max} \phi\left(\frac{x_{max}}{\sigma_x} \right) \sigma_x \right) = Q\left(\frac{x_{min}}{\sigma_x} \right) - Q\left(\frac{x_{max}}{\sigma_x} \right), \qquad \text{(B.9)}$$

$$E\{Y_n\} = x_{min} \left(Q\left(\frac{-\infty}{\sigma_x} \right) - Q\left(\frac{x_{min}}{\sigma_x} \right) \right) + x_{max} \left(Q\left(\frac{x_{max}}{\sigma_x} \right) - Q\left(\frac{\infty}{\sigma_x} \right) \right) +$$

$$\phi\left(\frac{x_{min}}{\sigma_x} \right) \sigma_x - \phi\left(\frac{x_{min}}{\sigma_x} \right) \sigma_x =$$

$$x_{min} \left(1 - Q\left(\frac{x_{min}}{\sigma_x} \right) \right) + x_{max} Q\left(\frac{x_{max}}{\sigma_x} \right) + \phi\left(\frac{x_{min}}{\sigma_x} \right) \sigma_x - \phi\left(\frac{x_{max}}{\sigma_x} \right) \sigma_x,$$

$$\text{(B.10)}$$

$$E\{z^2(X)\} = x_{min}^2 \left(Q\left(\frac{-\infty}{\sigma_x} \right) - Q\left(\frac{x_{min}}{\sigma_x} \right) \right) + x_{max}^2 \left(Q\left(\frac{x_{max}}{\sigma_x} \right) - Q\left(\frac{\infty}{\sigma_x} \right) \right) +$$

$$\sigma_x^2 \left(Q\left(\frac{x_{min}}{\sigma_x} \right) - Q\left(\frac{x_{max}}{\sigma_x} \right) + \phi\left(\frac{x_{min}}{\sigma_x} \right) \left(\frac{x_{min}}{\sigma_x} \right) - \phi\left(\frac{x_{max}}{\sigma_x} \right) \left(\frac{x_{max}}{\sigma_x} \right) \right) =$$

$$x_{min}^2 \left(1 - Q\left(\frac{x_{min}}{\sigma_x} \right) \right) + x_{max}^2 Q\left(\frac{x_{max}}{\sigma_x} \right) +$$

$$\sigma_x^2 \left(Q\left(\frac{x_{min}}{\sigma_x} \right) - Q\left(\frac{x_{max}}{\sigma_x} \right) + \phi\left(\frac{x_{min}}{\sigma_x} \right) \left(\frac{x_{min}}{\sigma_x} \right) - \phi\left(\frac{x_{max}}{\sigma_x} \right) \left(\frac{x_{max}}{\sigma_x} \right) \right)$$

$$\text{(B.11)}$$

Appendix C

On the Performance of eU-OFDM in a Non-flat Communication Channel

When subjected to the same communication channel, the individual subcarriers between the different orthogonal frequency division multiplexing (OFDM)-based modulation techniques are subjected to the same channel attenuation (the channel frequency response can be considered flat per individual subcarrier). As a result, the signal-to-noise ratio (SNR) penalty due to the channel attenuation in each technique is the same. In order to illustrate this effect, a simple investigation has been conducted using the free-space dispersive visible light communications (VLC) channel presented in [114]. An estimation for the VLC channel is presented in Fig. 3 of the cited source. In this study, the initial delay of $10\,\text{ns}$ in the impulse response has been ignored and the channel response has been sampled at a rate of $2\,\text{Gsamples/s}$ (communication bandwidth of $1\,\text{GHz}$) up to $25\,\text{ns}$, where the last notable contributions of the reflections appear to arrive at the destination. As a result, the digital representation of the VLC channel response used in the simulation appears as in Fig. C.1(a). The channel gain for the different modulated subcarriers (fast Fourier transform (FFT) size of 2048) is presented in Fig. C.1(b).
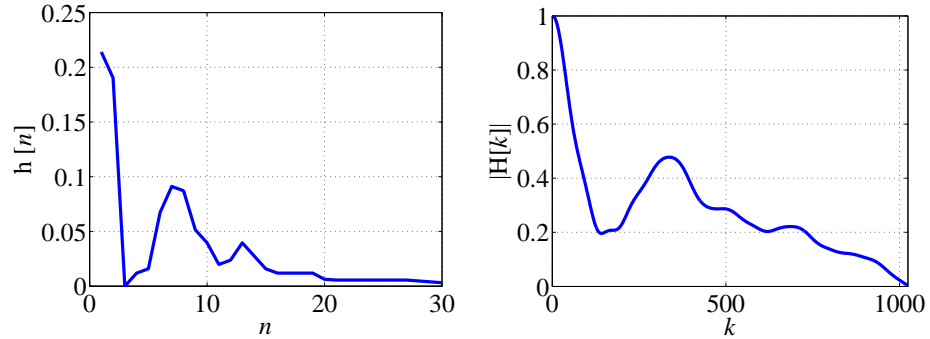
(a) Channel impulse response in the time domain (30 taps).

(b) Channel gain in the frequency domain (FFT size of 2048 with 1024 subcarriers which can be modulated due to the required Hermitian symmetry).

Figure C.1: *Dispersive channel used to illustrate the effects on eU-OFDM and DCO-OFDM.*

A comparison between the performance of enhanced unipolar orthogonal frequency division multiplexing (eU-OFDM) and direct-current-biased optical orthogonal frequency division multiplexing (DCO-OFDM) has been presented for different M-ary quadrature amplitude modulation (M-QAM) constellation sizes in Fig. C.2-C.5. In all of the presented cases, it is clear that the performance difference between eU-OFDM and DCO-OFDM is almost equivalent for both the flat channel and the highly dispersive channel (only the slopes of the curves change due to uneven SNR between the subcarriers within one frame; pre-equalization is not used in this simulation). The results confirm the claim that a comparison in a flat channel is sufficient for comparing the performance of two OFDM-based modulation schemes.

(a) Flat channel 4-QAM.

(b) Dispersive channel 4-QAM.
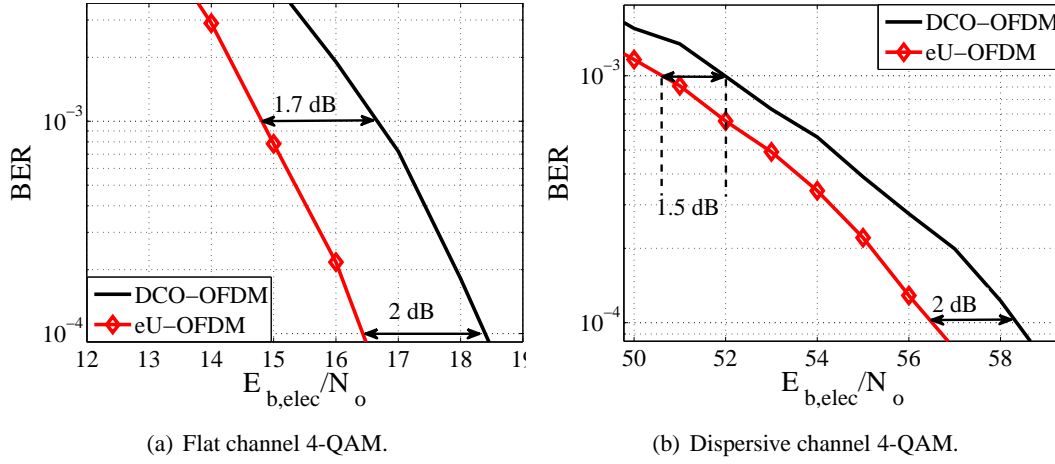
Figure C.2: *Performance difference between 4-QAM eU-OFDM and 4-QAM DCO-OFDM for a flat channel and a highly dispersive channel.*

(a) Flat channel 16-QAM.

(b) Dispersive channel 16-QAM.
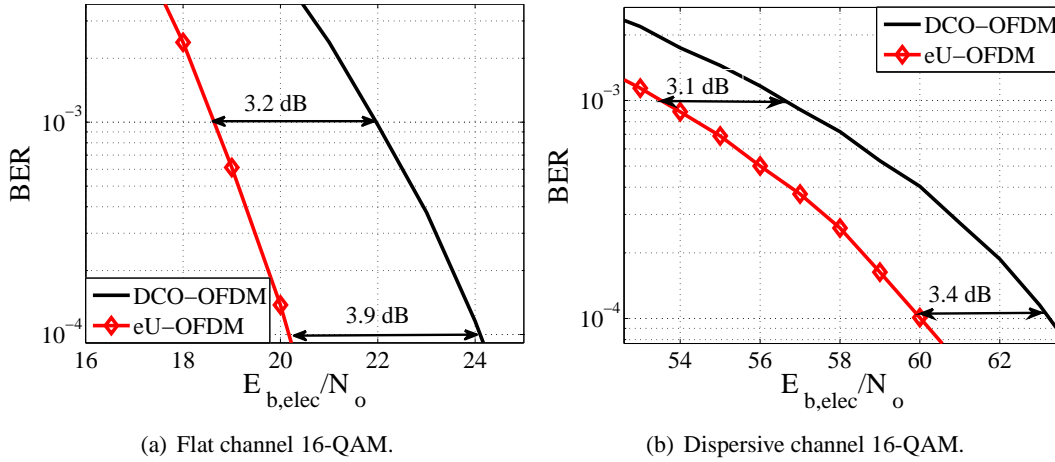
Figure C.3: *Performance difference between 16-QAM eU-OFDM and 16-QAM DCO-OFDM for a flat channel and a highly dispersive channel.*

(a) Flat channel 64-QAM.

(b) Dispersive channel 64-QAM.
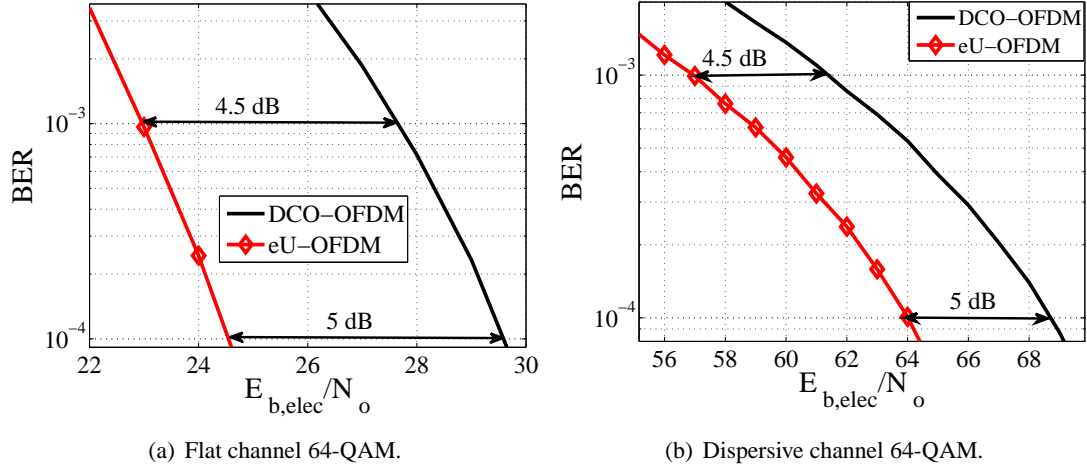
Figure C.4: *Performance difference between 64-QAM eU-OFDM and 64-QAM DCO-OFDM for a flat channel and a highly dispersive channel.*

(a) Flat channel 256-QAM.

(b) Dispersive channel 256-QAM.
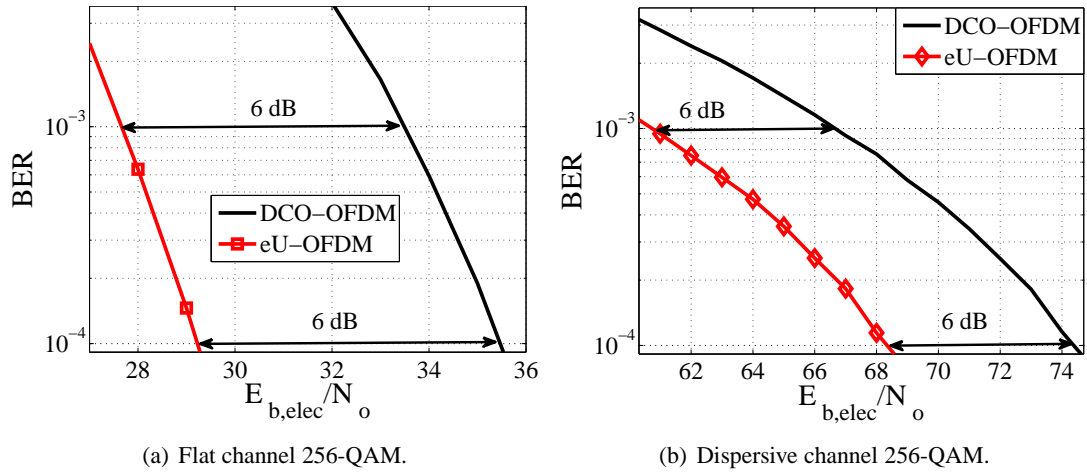
Figure C.5: *Performance difference between 256-QAM eU-OFDM and 256-QAM DCO-OFDM for a flat channel and a highly dispersive channel.*

Appendix D
Selected Publications

The following articles have resulted from the work presented in this thesis.

D.1 Journal Articles

D. Tsonev, S. Sinanovic, and H. Haas, "Complete Modeling of Nonlinear Distortion in OFDM-based Optical Wireless Communication," J. Lightw. Technol., vol. 31, no. 18, pp.3064–3076, Sep. 15, 2013.

D. Tsonev, H. Chun, S. Rajbhandari, J. J. D. McKendry, S. Videv, E. Gu, M. Haji, S. Watson, A. E. Kelly, G. Faulkner, M. D. Dawson, H. Haas and D. OBrien, "A 3-Gb/s Single-LED OFDM-based Wireless VLC Link Using a Gallium Nitride μLED," IEEE Photon. Technol. Lett., vol. 26, no. 7, pp. 637–640, Apr. 2014.

D. Tsonev, S. Videv, and H. Haas, "Unlocking Spectral Efficiency in Intensity Modulation and Direct Detection Systems," J. Sel. Areas Commun., (to appear).

D.2 Magazine Articles

H. Burchard, N. Serafimovski, D. Tsonev, S. Videv, and H. Haas, "VLC: Beyond Point-to-point Communication," Comm. Mag., vol. 52, no. 7, pp.98–105, Jul. 2014.

D.3 Conference Papers

D. Tsonev, S. Sinanovic, and H. Haas, "Enhanced Subcarrier Index Modulation (SIM) OFDM," in GLOBECOM Workshops (GC Wkshps), IEEE. Houston, Texas, USA: IEEE, Dec. 5–9, 2011, pp. 728–732.

D. Tsonev, S. Sinanovic, and H. Haas, "Novel Unipolar Orthogonal Frequency Division Multiplexing (U-OFDM) for Optical Wireless," in Proc. of the Vehicular Technology Conference (VTC Spring), IEEE. Yokohama, Japan: IEEE, May 6–9 2012, pp. 1–5.

D. Tsonev, S. Sinanovic, and H. Haas, "Pulse Shaping in Unipolar OFDM-based Modulation Schemes," in GLOBECOM Workshops (GC Wkshps), IEEE, Anaheim, California, USA: IEEE, Dec. 3–7 2012, pp. 1208–1212.

D. Tsonev, S. Sinanovic, and H. Haas, "Practical MIMO Capacity for Indoor Optical Wireless Communication with White LEDs," in Proc. of the Vehicular Technology Conference (VTC Spring), IEEE, Dresden, Germany: IEEE, Jun. 2–5 2013, pp. 1–5.

D. Tsonev, S. Sinanovic, and H. Haas, "A Novel Analytical Framework for Modeling Nonlinear Distortions in OFDM-based Optical Wireless Communication," in Proc. of the International Conference on Communications in China (ICCC), IEEE, Xián, China: IEEE, Aug. 12–14, pp.147–152. [invited]

D. Tsonev, S. Videv, and H. Haas, "Light Fidelity (Li-Fi): Towards All Optical Networking," in Proc. of SPIE Photonics West, SPIE, San Francisco, CA, USA: SPIE, Feb. 1–6, pp. 1–10. [invited]

D. Tsonev and H. Haas, "Avoiding Spectral Efficiency Loss in Unipolar OFDM for Optical Wireless Communication," in Proc. of the International Conference on Communications (ICC). Sydney, Australia: IEEE, Jun., 10–14 2014, pp. 3336–3341.

Complete Modeling of Nonlinear Distortion in OFDM-Based Optical Wireless Communication

Dobroslav Tsonev, Sinan Sinanovic, and Harald Haas

Abstract—**This paper presents a complete analytical framework for modeling memoryless nonlinear effects in an intensity modulation and direct detection optical wireless communication system based on orthogonal frequency division multiplexing. The theory employs the Bussgang theorem, which is widely accepted as a means to characterize the impact of nonlinear distortions on normally distributed signals. This paper proposes a new method to generalize this approach, and it describes how a closed-form analytical expression for the system bit error rate can be obtained for an arbitrary memoryless distortion. Major distortion effects at the transmitter stage such as quantization and nonlinearity from the light emitting diode are analyzed. Four known orthogonal-frequency-division-multiplexing-based modulation schemes for optical communication are considered in this paper: direct-current-biased optical OFDM, asymmetrically clipped optical OFDM, pulse-amplitude-modulated discrete multitone modulation, and unipolar orthogonal frequency division multiplexing.**

Index Terms—**Nonlinear distortion, orthogonal frequency division multiplexing (OFDM), optical modulation, wireless communication.**

I. INTRODUCTION

WIRELESS data rates have been growing exponentially in the past decade. According to some recent forecasts, in 2015 more than 6 Exabytes of wireless data would be required per month [1]. The continuously enhanced wireless communication standards will not be able to fully satisfy the future demand for mobile data throughput because the available radio frequency (RF) spectrum is very limited. Hence, an expansion of the wireless spectrum into a new and largely unexplored domain—the visible light spectrum—has the potential to change the face of future wireless communications. The advantages of an optical wireless system include among others: 1) vast amount of unused bandwidth; 2) no licensing fees; 3) low-cost front end devices; and 4) no interference with sensitive electronic systems. In addition, the existing lighting infrastructure can be used for the realization of visible light communication.

Optical wireless communication (OWC) using incoherent off-the-shelf illumination devices, which are the foremost

candidates for mass-produced front-end elements, is realizable as an intensity modulation and direct detection (IM/DD) system. This means that only signal intensity can be detected reliably. Hence, without modification it is not possible to use all digital modulation techniques known in RF communication. Unipolar techniques like on-off keying, pulse-position modulation, and pulse-amplitude modulation (M-PAM) can be adopted in a relatively straightforward way. As transmission rates increase, however, unwanted intersymbol interference (ISI) appears. Hence, more resilient techniques such as orthogonal frequency division multiplexing (OFDM) are preferred. OFDM allows equalization to be performed with single-tap equalizers in the frequency domain, which reduces design complexity and equalization cost. It also allows different frequency subcarriers to be adaptively loaded with information according to the channel characteristics. This enables more optimal usage of the channel, especially when attenuation or interference is significant in certain frequency bands [2]. Conventional OFDM signals are bipolar and complex-valued. However, they have to be both real and unipolar in IM/DD systems. It is possible to transform an OFDM signal into a real signal by imposing Hermitian symmetry on the subcarriers in the frequency domain. Furthermore, a number of possible approaches to deal with the issue of bipolarity in OFDM signals have been proposed. The current paper focuses on four of them, in particular: direct-current-biased optical OFDM (DCO-OFDM), asymmetrically clipped optical OFDM (ACO-OFDM) [3], pulse-amplitude-modulated discrete multitone modulation (PAM-DMT) [4], and unipolar orthogonal frequency division multiplexing (U-OFDM) [5]. It analytically characterizes their performance in a nonlinear additive white Gaussian noise (AWGN) channel which is typical for an OWC system. Some of the schemes—DCO-OFDM and ACO-OFDM—have already been analyzed in the context of certain nonlinearities that are present in OWC [6]–[10]. This paper gives a more complete analysis encompassing the joint effect of a number of different distortions which to the best of the authors' knowledge have not been analyzed jointly in OWC and have never been analyzed for PAM-DMT and U-OFDM. An interesting observation is that the concepts presented for U-OFDM have been previously introduced in Flip-OFDM [11]. In addition, the four schemes, ACO-OFDM, PAM-DMT, U-OFDM, and Flip-OFDM, perform equivalently in a simple AWGN channel [3]–[5], [11].

An information signal in an OWC system undergoes a number of distortions, including nonlinear ones. Linear distortions such as attenuation and ISI can be compensated with amplifiers, equalizers, and signal processing. Nonlinear distortions, however, often make irreversible changes to the signal.
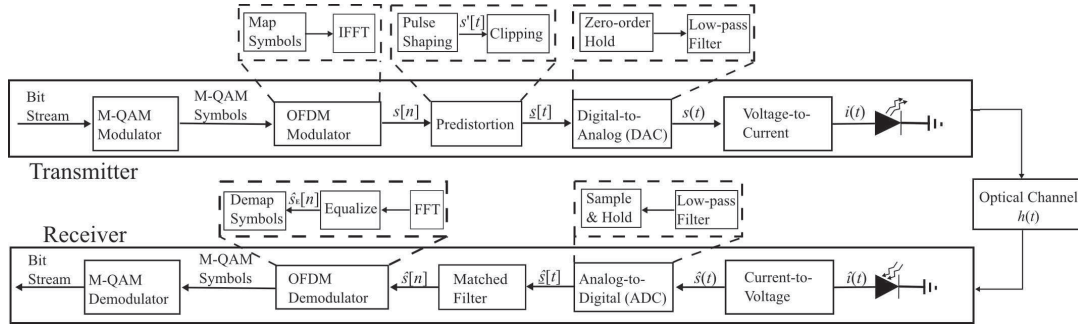
Fig. 1.   Optical wireless communication system.

Therefore, it is necessary to be able to characterize and evaluate distortion effects as fully as possible. Such examples include quantization effects in the digital-to-analog converters (DACs) and analog-to-digital converters (ADCs), as well as the effects caused by the nonlinear output characteristic of a light emitting diode (LED). A number of works have been published on distortion in OFDM-based modulation schemes [6]–[10], [12]–[16]. A significant number of them focus specifically on the nonlinear distortions present in an OWC system [6]–[10]. The analysis of nonlinear distortion is not straightforward. Even though general procedures have been introduced for obtaining an analytical solution [12], a closed-form solution is not always available. This paper describes a complete general procedure which *always* leads to a closed-form solution. It can be used to solve the problems presented in [6]–[10] as well as to analyze any other arbitrary memoryless nonlinear distortion, which can be part of an OWC system based on OFDM. The specific case study in this paper involves a complete set of the significant nonlinear effects at the transmitter combining distortion due to quantization at the DAC as well as distortion due to the nonlinear characteristic of the LED. Pulse shaping has also been considered unlike in previous works on the subject [6]–[10].

The rest of this paper is organized as follows. Section II provides a description of the OWC system. Section III describes the modulation schemes under investigation. Section IV discusses the issues incurred by pulse shaping techniques in IM/DD transmission systems. Section V introduces the expected nonlinearities in an OWC system. Section VI presents the theoretical approach for obtaining a closed-form assessment of the performance. Section VII confirms analytical solutions with numerical simulations. Finally, section VIII provides concluding remarks.

II. OWC System

The diagram of an OWC system is presented in Fig. 1. The incoming bits are divided into data chunks and mapped to symbols from a known modulation scheme such as quadrature amplitude modulation (M-QAM) or M-PAM. The M-QAM/M-PAM symbols are modulated onto different frequency subcarriers according to one of the following schemes: DCO-OFDM, ACO-OFDM, PAM-DMT, U-OFDM. Then, the resulting time domain signal is subjected to a number of predistortion techniques, which condition it for transmission. This block includes oversampling, pulse shaping as well as clipping any values below the allowed minimum or above the allowed maximum. Clipping is performed because a DAC, an amplifier, and an LED can only operate in a limited range, specified by their electrical properties. The conditioned signal is fed to a DAC which outputs an analog signal. This stage of the system consists of a zero-order-hold element or other type of interpolator followed by a low-pass filter. The output signal from the zero-order hold is continuous in time. However, because the signal has discrete amplitude levels, corresponding to the samples of the oversampled pulse-shaped and clipped signal $s'[t]$, it is analyzed in terms of the discrete time-domain signal $s'[t]$. It is assumed that the oversampling is sufficient, and the pulse shaping operation is such that the low-pass filter after the zero-order hold outputs a continuous-time signal which is equivalent to the signal at its input for all practical considerations. Hence, in the analysis, nonlinear transformations of the signal $s'[t]$ are investigated. The analog output of the DAC is encoded into a current signal by a voltage-to-current transducer with appropriate bias and supplied to the LED. OFDM-based OWC with incoherent off-the-shelf illumination devices can only be realized as a baseband communication technique. Therefore, frequency up-conversion is not required and, thus, has not been considered in the presented analysis. Light intensity at the diode varies with the current. At the receiver side, a photo diode transforms the variations in the intensity of the received light into variations of a current signal, which is turned into a voltage signal by a transimpedance amplifier. The resulting signal is discretized at an ADC and passed on to the processing circuitry, which includes a matched filter, an OFDM demodulator with an equalizer, as well as a bit demodulator.

III. OFDM Modulation Schemes

The modulation schemes presented in this paper are modifications of conventional OFDM. The subcarriers in the frequency domain are modulated with M-QAM symbols in the case of DCO-OFDM, ACO-OFDM, and U-OFDM and with M-PAM symbols in the case of PAM-DMT. A time-domain block of samples is obtained by taking the inverse fast Fourier transform of a block of N_{FFT} complex M-QAM/M-PAM symbols.

174
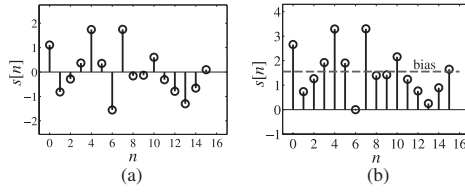
Fig. 2. DCO-OFDM Generation. Cyclic prefix is not illustrated. (a) Bipolar OFDM before biasing. (b) Biased DCO-OFDM.

Fig. 3. ACO-OFDM Generation. Cyclic prefix is not illustrated. (a) ACO-OFDM before clipping. (b) ACO-OFDM after clipping.

Hermitian symmetry is imposed, which, according to the properties of the Fourier transform, generates a real time-domain signal [17]. The subcarriers at positions $k = 0$ and $k = \frac{N_{\text{FFT}}}{2}$ are set to zero in order to satisfy the requirements of the Hermitian symmetry. The real time-domain signal is bipolar in nature. An LED can convey only positive signals when it is active. Hence, the following four different methods have been designed for the generation of unipolar signals, suitable for OWC.

A. DCO-OFDM

DCO-OFDM generates a unipolar signal by introducing a DC bias. Fig. 2 illustrates the concept. The spectral efficiency of the scheme is

$$\eta_{\text{DCO}} = \frac{\log_2(M)(N_{\text{FFT}} - 2)}{2(N_{\text{FFT}} + N_{\text{cp}})} \text{bits/s/Hz} \quad (1)$$

provided that all available carriers are loaded with M-QAM. The factors $N_{\text{FFT}} - 2$ and 0.5 occur due to the Hermitian symmetry requirement. N_{cp} is the length of the cyclic prefix.

OFDM has a very high peak-to-average power ratio (PAPR). Following the calculations presented in [18], a lower bound for the PAPR of real signals can be calculated as follows:

$$\frac{3N_{\text{a}}\left(\sqrt{M} - 1\right)}{2\sqrt{M} + 1} \quad (2)$$

where N_{a} is the number of modulated carriers in the frequency domain. Therefore, it is impractical to introduce a biasing level which ensures that all possible time samples are positive. In addition, electronic elements have an operational range, which is limited both in terms of a minimum and a maximum value. Hence, an OFDM signal would be clipped both from above and from below in order to fit within the required range. A typical value of a few signal standard deviations is used in practice for clipping on each side of the signal distribution. This distortion is easily modeled by the upper and lower limit of the DAC. This modeling approach is adopted in this paper.

B. ACO-OFDM

Biasing in DCO-OFDM increases the dissipated electrical and optical energy at the transmitter by a substantial amount. The dissipated electrical energy is proportional to $\text{E}[i^2(t)] = \text{E}[(i_{\text{signal}}(t) + i_{\text{bias}}(t))^2]$, and the dissipated optical energy is proportional to $\text{E}[i(t)] = \text{E}[i_{\text{signal}}(t) + i_{\text{bias}}(t)]$, where $E[\cdot]$ denotes statistical expectation. ACO-OFDM, illustrated in Fig. 3,
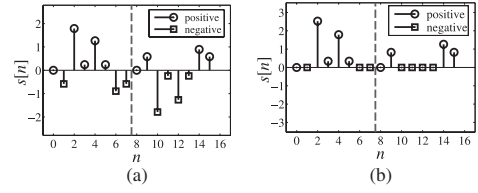
avoids the biasing requirement of DCO-OFDM by exploiting the properties of the Fourier transform so that a unipolar signal can be generated without biasing. As presented in [3], only odd frequency subcarriers are modulated. This creates a symmetry between samples in the time-domain OFDM frame. In general, if $s(k, n)$ is the contribution of subcarrier $S[k]$ to the sample at time n, then [3]

$$s(k, n) = \frac{1}{\sqrt{N_{\text{FFT}}}} S[k] e^{\frac{j 2\pi n k}{N_{\text{FFT}}}}$$

$$s\left(k, n + \frac{N_{\text{FFT}}}{2}\right) = \frac{1}{\sqrt{N_{\text{FFT}}}} S[k] e^{\frac{j 2\pi (n + N_{\text{FFT}}/2) k}{N_{\text{FFT}}}}$$

$$= \frac{1}{\sqrt{N_{\text{FFT}}}} S[k] e^{\frac{j 2\pi n k}{N_{\text{FFT}}}} e^{j\pi k}. \quad (3)$$

For odd values of k, $s(k, n) = -s(k, n + N_{\text{FFT}}/2)$. For even values of k, $s(k, n) = s(k, n + N_{\text{FFT}}/2)$. Hence, if only the odd subcarriers in an OFDM frame are modulated, the time-domain signal, $s[n]$, has the property

$$s[n] = -s[n + N_{\text{FFT}}/2]. \quad (4)$$

If only the even subcarriers in an OFDM frame are modulated, the time-domain signal has the property:

$$s[n] = s[n + N_{\text{FFT}}/2]. \quad (5)$$

Because complex exponential functions are orthogonal to each other, if a signal has the property in (4), this means that in the frequency domain only odd samples contain information. Similarly, if a signal has the property in (5), then in the frequency domain only its even samples contain information. Clipping the negative samples of an arbitrary time-domain signal, $s[n]$, can be represented as

$$\text{CLIP}(s[n]) = \frac{1}{2}(s[n] + |s[n]|). \quad (6)$$

In ACO-OFDM, only the odd subcarriers are modulated. Hence, (4) applies. Therefore, $s[n] = -s[n + N_{\text{FFT}}/2]$. Then, $|s[n]| = |s[n + N_{\text{FFT}}/2]|$. This symmetry allows all negative values to be removed. The clipping distortion $|s[n]|$, described in (6), has the property stipulated in (5), and so it distorts only the even subcarriers. The factor 0.5 occurs from the clipping and is consistent with the analysis presented in [3]. An additional factor of $\sqrt{2}$ is introduced to rescale the unipolar signal and normalize the amount of dissipated energy, which would lead to an overall signal-to-noise ratio (SNR) performance penalty of 3 dB. This short proof describes the analysis in [3] in a more
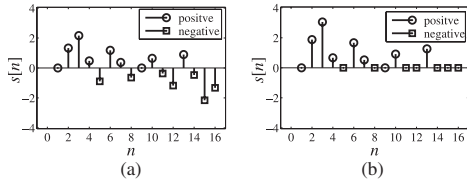
Fig. 4. PAM-DMT Generation. Cyclic prefix is not illustrated. (a) Bipolar PAM-DMT before clipping. (b) Unipolar PAM-DMT after clipping and rescale.

Fig. 5. U-OFDM Generation. Cyclic prefixes are not illustrated. (a) Bipolar OFDM. (b) Unipolar U-OFDM.

concise manner. Not using the even subcarriers sacrifices about half the spectral efficiency, compared to DCO-OFDM, and it becomes

$$\eta_{\text{ACO}} = \frac{\log_2(M)N_{\text{FFT}}}{4(N_{\text{FFT}} + N_{\text{cp}})} \text{bits/s/Hz}. \tag{7}$$

C. PAM-DMT

In PAM-DMT, illustrated in Fig. 4, the frequency subcarriers in an OFDM frame are modulated with imaginary symbols from the M-PAM modulation scheme. Due to Hermitian symmetry in the frequency domain, the PAM-DMT time-domain signal becomes [4]

$$s[n] = \frac{1}{\sqrt{N_{\text{FFT}}}} \sum_{k=0}^{N_{\text{fft}}-1} S[k] e^{\frac{j2\pi kn}{N_{\text{FFT}}}} = \tag{8}$$

$$= \frac{1}{\sqrt{N_{\text{FFT}}}} \sum_{k=0}^{N_{\text{FFT}}-1} S[k] \left(\cos \frac{2\pi kn}{N_{\text{FFT}}} + j \sin \frac{2\pi kn}{N_{\text{FFT}}} \right)$$

$$= \frac{1}{\sqrt{N_{\text{FFT}}}} \sum_{k=0}^{N_{\text{FFT}}-1} jS[k] \sin \frac{2\pi kn}{N_{\text{FFT}}}. \tag{9}$$

The time-domain structure of a PAM-DMT frame exhibits an antisymmetry, where $s[0] = 0$, $s[N_{\text{FFT}}/2] = 0$ if N_{FFT} is even, and $s[n] = -s[N_{\text{FFT}} - n]$. This means that $|s[0]| = 0$, $|s[N_{\text{FFT}}/2]| = 0$, if N_{FFT} is even, and $|s[n]| = |s[N_{\text{FFT}} - n]|$. Therefore, if the negative values are removed, as described in (6), the distortion term $|s[n]|$ has Hermitian symmetry in the time domain. This means that in the frequency domain, the distortion is transformed into a real-valued signal. Hence, it is completely orthogonal to the useful information. This proof has not been formally completed in [4], but it is straightforward with the representation of clipping in (6). The spectral efficiency of PAM-DMT is

$$\eta_{\text{PAM-DMT}} = \frac{\log_2(M)(N_{\text{FFT}} - 2)}{2(N_{\text{FFT}} + N_{\text{cp}})} \text{bits/s/Hz} \tag{10}$$

where M denotes the order of M-PAM modulation. It should be noted that $\sqrt{M}$-PAM has roughly the same performance as M-QAM in an AWGN channel. This makes PAM-DMT comparable to ACO-OFDM in spectral efficiency for the same bit error rate (BER) performance.

D. U-OFDM

In U-OFDM, all possible subcarriers in the frequency domain are modulated as in DCO-OFDM. After the time-domain signal is obtained, it is divided into two blocks: a positive and a negative one. The positive block is a copy of the original signal frame, where all negative samples are set to zero. The negative block is a copy of the original signal frame, where all samples are multiplied by -1 to switch signs. After this operation, the negative samples are set to zero. The principle of how both blocks form the original OFDM frame can be observed in Fig. 5(a). The two blocks are transmitted separately. This can be seen in Fig. 5(b). The cyclic prefixes are omitted in the given examples for simplicity of illustration. The increased number of samples in the time domain decreases the spectral efficiency by a factor of 0.5 compared to DCO-OFDM, and it becomes

$$\eta_{\text{U}} = \frac{\log_2(M)(N_{\text{FFT}} - 2)}{4(N_{\text{FFT}} + N_{\text{cp}})} \text{bits/s/Hz}. \tag{11}$$

At the demodulator, the original OFDM frame is obtained by subtracting the negative block from the positive one. This effectively doubles the noise at each resulting sample, and so the performance of U-OFDM becomes the same as the performance of ACO-OFDM and PAM-DMT, where the clipping introduces an SNR penalty of 3 dB.

IV. PULSE SHAPING

An LED is modulated with a continuous electrical signal, and it emits a continuously varying light signal. A digital implementation of OFDM generates discrete values which need to be encoded into an analog signal, suitable to modulate the LED. The pulse shaping operation allows digital samples to be mapped to continuous pulse shapes. The selection of the pulse-shaping filters is important because the communication channel restricts the bandwidth of the signals which can be successfully propagated to the receiver. The maximum modulation frequency of off-the-shelf white LEDs is in the order of 2 MHz and in the order of 20 MHz when blue filtering is applied at the receiver [19]. The transmitted information signals must be tailored to fit in that frequency range in order to avoid distortion. Different pulse shapes have different time-domain properties as well as different bandwidth requirements. An example of a pulse shape is a square pulse which corresponds to the zero-order hold function of a DAC [20]. This shape is easy to implement and has a time duration which is perfectly limited within a symbol period. However, it requires an infinite
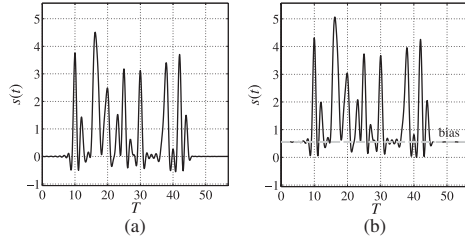
Fig. 6.   (a) ACO-OFDM pulse-shaped after removing the negative values. (b) Addition of necessary bias to make the pulse-shaped signal unipolar.

Fig. 7.   (a) Distortion in ACO-OFDM/U-OFDM after clipping the negative values of the pulse-shaped unipolar signal. (b) Distortion in PAM-DMT after clipping the negative values of the pulse-shaped unipolar signal.

bandwidth. Therefore, it is not possible to realize it without distorting the received signal. In practice, if square pulses are used as an interpolation technique, the signal is low-pass-filtered afterward to incorporate only a desired portion of the frequencies, for example, until the first zero crossing in the frequency domain. This occurs at $1/T_{\mathrm{s}}$ if T_{s} is the symbol period. A similar shape is the triangle pulse, which corresponds to a first-order interpolation of discrete samples [20]. This shape is characterized with an improved bandwidth profile and a longer time-domain duration compared to the square pulse. Exact recovery of the transmitted signal, without ISI, requires accurate sampling at the receiver. Theoretically, the most bandwidth efficient interpolation filter is the sinc function [20]. Its bandwidth requirement is $1/2T_{\mathrm{s}}$, so it is two times more efficient than a square pulse low-pass-filtered at the first zero crossing. However, it spans an impulse response with an infinite duration in the time domain. This means that in practice the shape is truncated, and due to the longer impulse response, it requires more processing. In addition, time jitter can introduce significant ISI. For this reason, the raised-cosine filter and its modified version, the root-raised cosine filter, are used in many practical implementations. They allow the generation of an interpolation pulse with an arbitrary bandwidth requirement between $1/2T_{\mathrm{s}}$ and $1/T_{\mathrm{s}}$ dependent on an adjustable roll-off factor. The raised cosine filter gives the designer the freedom to choose between the length of the pulse in the time domain and the frequency requirement of the shape. In practice, these filters are implemented by oversampling the discrete signal, interpolating it with a discrete pulse shape and then supplying it to the DAC, which typically consists of a zero-order hold and a low-pass filter as described in Fig. 1. Signals in ACO-OFDM, PAM-DMT, and U-OFDM are made unipolar after clipping of the negative values. Bipolar pulse shapes like the sinc and the raised-cosine filter turn a *unipolar* signal before pulse shaping into a *bipolar* signal after pulse shaping. An example is presented in Fig. 6. The issue can be solved by introducing a bias to account for the negative values. This leads to an increase in the energy consumption of approximately 3 dB. Alternatively, the negative values after pulse shaping can be clipped at zero again, but this leads to the distortion presented in Fig. 7. Therefore, it is important to implement pulse shaping before the negative values in ACO-OFDM, PAM-DMT, and U-OFDM are removed. Then, as described in (6), the clipping operation leads to a unipolar signal that consists of the
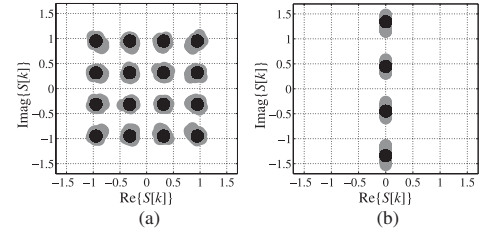
original bipolar signal and a distortion term which is present both inside and outside the desired bandwidth. The useful signal, however, remains within the bandwidth limit and is not affected by the distortion term as described in Section III. The rest of this section provides a proof.

The sampling frequency is denoted by F_{s}, T_{s} denotes the symbol period, $T = F_{\mathrm{s}}T_{\mathrm{s}}$ denotes the discrete-time symbol period, and $p[t]$ denotes the digital pulse shape. Then, the part of the oversampled pulse-shaped discrete bipolar signal, which contains the information of a given frame, is expressed as

$$
\begin{aligned}
s'[t] = &\sum_{n=N_{\mathrm{FFT}}-N_{\mathrm{cp}}}^{N_{\mathrm{FFT}}-1} s[n,0]p[t-(n-N_{\mathrm{FFT}})T] \\
&+ \sum_{n=0}^{N_{\mathrm{FFT}}-1} s[n,0]p[t-nT] + \sum_{n=N_{\mathrm{FFT}}-N_{\mathrm{cp}}}^{N_{\mathrm{FFT}}-N_{\mathrm{cp}}+N_{\mathrm{cp}}^{\mathrm{p}}-1} \\
&\times s[n,1]p[t-(N_{\mathrm{FFT}}+N_{\mathrm{cp}})T-(n-N_{\mathrm{FFT}})T] \quad (12)
\end{aligned}
$$

where $N_{\mathrm{cp}}^{\mathrm{p}}$ is the length of the cyclic prefix sufficient to remove the effects of $p[t]$, and $s[n,0]$ indicates the nth sample of the OFDM frame at position 0, i.e., the current frame. The discrete-time pulse-shaped bipolar signal relevant for sampling the first $\frac{N_{\mathrm{FFT}}}{2}$ points of the current frame can be expressed as

$$
\begin{aligned}
s'_1[t] = &\sum_{n=N_{\mathrm{FFT}}-N_{\mathrm{cp}}}^{N_{\mathrm{FFT}}-1} s[n,0]p[t-(n-N_{\mathrm{FFT}})T] \\
&+ \sum_{n=0}^{N_{\mathrm{FFT}}/2-1} s[n,0]p[t-nT] \\
&+ \sum_{n=N_{\mathrm{FFT}}/2}^{N_{\mathrm{FFT}}/2-1+N_{\mathrm{cp}}^{\mathrm{p}}} s[n,0]p[t-nT]. \quad (13)
\end{aligned}
$$

The discrete-time pulse-shaped bipolar signal relevant for sampling the next $\frac{N_{\mathrm{FFT}}}{2}$ points of the current frame can be expressed as

$$s_2'[t] = \sum_{n=N_{\mathrm{FFT}}/2-N_{\mathrm{cp}}}^{N_{\mathrm{FFT}}/2-1} s[n,0]p[t-nT]$$

$$+ \sum_{n=N_{\mathrm{FFT}}/2}^{N_{\mathrm{FFT}}-1} s[n,0]p[t-nT] + \sum_{n=N_{\mathrm{FFT}}-N_{\mathrm{cp}}}^{N_{\mathrm{FFT}}-N_{\mathrm{cp}}+N_{\mathrm{cp}}^{\mathrm{p}}-1}$$

$$\times s[n,1]p[t-(N_{\mathrm{FFT}}+N_{\mathrm{cp}})T-(n-N_{\mathrm{FFT}})T]. \quad (14)$$

The discrete-time unipolar signal, ready for digital-to-analog conversion and transmission, can be expressed as

$$\underline{s}[t] = \sqrt{2}\mathrm{CLIP}\left(s'[t]\right) = \frac{1}{\sqrt{2}}\left(s'[t] + |s'[t]|\right). \quad (15)$$

At the receiver, the samples of a given frame after match filtering can be expressed as

$$\hat{s}[n] = \left(\underline{s}[t] * h[t] + n[t]\right) * p[t]\big|_{t=nT}$$

$$= \left(\frac{1}{\sqrt{2}}\left(s'[t] + |s'[t]|\right) * h[t] + n[t]\right) * p[t]\bigg|_{t=nT}$$

$$= \begin{cases} \left(\frac{1}{\sqrt{2}}\left(s_1'[t]+|s_1'[t]|\right)*h[t]+n[t]\right)*p[t]\big|_{t=nT}, & n < \frac{N_{\mathrm{FFT}}}{2} \\ \left(\frac{1}{\sqrt{2}}\left(s_2'[t]+|s_2'[t]|\right)*h[t]+n[t]\right)*p[t]\big|_{t=nT}, & \frac{N_{\mathrm{FFT}}}{2} \le n \end{cases}$$

$$\quad (16)$$

where $*$ denotes convolution, $n[t]$ denotes AWGN, and $h[t]$ denotes the impulse response of the channel in discrete time. The cyclic prefix is sufficient to remove ISI and to turn the *continuous*-time convolution with the channel, $h(t)$, into a circular convolution in *discrete* time with the channel, $h[t]$. Assuming perfect channel knowledge, the equalized samples at the receiver are expressed as

$$\hat{s}_{\mathrm{E}}[n] = \left(\underline{s}[t] + n[t] * h^{-1}[t]\right) * p[t]\big|_{t=nT}$$

$$= \left(\frac{1}{\sqrt{2}}\left(s'[t] + |s'[t]|\right) + n[t] * h^{-1}[t]\right) * p[t]\bigg|_{t=nT}$$

$$= \begin{cases} \left(\frac{1}{\sqrt{2}}\left(s_1'[t]+|s_1'[t]|\right)+n[t]*h^{-1}[t]\right)*p[t]\big|_{t=nT}, & n<\frac{N_{\mathrm{FFT}}}{2} \\ \left(\frac{1}{\sqrt{2}}\left(s_2'[t]+|s_2'[t]|\right)+n[t]*h^{-1}[t]\right)*p[t]\big|_{t=nT}, & \frac{N_{\mathrm{FFT}}}{2} \le n. \end{cases}$$

$$\quad (17)$$

A. ACO-OFDM

In ACO-OFDM, $s[n] = -s[n + N_{\mathrm{FFT}}/2]$. Therefore, $s_1'[t] \approx -s_2'[t + \frac{N_{\mathrm{FFT}}}{2}T]$ except for the third terms in (13) and (14). Differences appear because in the time domain $p[t]$ spans beyond a single symbol duration and beyond the boundaries of the OFDM frame. However, this effect is not significant when $N_{\mathrm{cp}}^{\mathrm{p}} << N_{\mathrm{FFT}}$. As a consequence, $|s_1'[t]| \approx |s_2'[t + \frac{N_{\mathrm{FFT}}}{2}T]|$. At the receiver, the distortion term in the first $\frac{N_{\mathrm{FFT}}}{2}$ points, $\frac{1}{\sqrt{2}}|s_1'[t]| * h[t] * p[t]|_{nT}$, is the same as the distortion term in the second $\frac{N_{\mathrm{FFT}}}{2}$ points, $\frac{1}{\sqrt{2}}|s_2'[t]| * h[t] * p[t]|_{nT}$, because $|s_1'[t]| \approx |s_2'[t + \frac{N_{\mathrm{FFT}}}{2}T]|$. Therefore, distortion falls on the even subcarriers only as described in Section III-B.

B. PAM-DMT

In PAM-DMT, $s[n] = -s[N_{\mathrm{FFT}} - n]$. Therefore, with the representations in (13) and (14), $s_1'[t] \approx -s_2'[N_{\mathrm{FFT}}T - t]$. Again, differences appear between the first term in (13) and the third term in (14). The differences are caused by the time-domain span of $p[t]$ but are not significant for $N_{\mathrm{cp}}^{\mathrm{p}} \ll N_{\mathrm{FFT}}$. Hence, it can be concluded that $|s_1'[t]| \approx |s_2'[N_{\mathrm{FFT}}T - t]|$. The pulse-shaping filter's impulse response is an even function, so $p[t] = p[-t]$. From (17), the distortion term after equalization consists of $\frac{1}{\sqrt{2}}|s_1'[t]| * p[t]\big|_{t=nT}$ and $\frac{1}{\sqrt{2}}|s_2'[t]| * p[t]\big|_{t=nT}$. It maintains Hermitian symmetry, and hence, noise due to distortion is orthogonal to useful information as described before in Section III-C.

C. U-OFDM

The U-OFDM bipolar *discrete* signal is encoded in two consecutive frame blocks. The oversampled discrete-time bipolar part of $s'[t]$ which contains the information of the positive frame block can be expressed with the representation in (12) and denoted as $s'^p[t]$. The oversampled discrete-time bipolar part of $s'[t]$ which contains the information of the negative frame block can be expressed with the representation in (12) and denoted as $s'^n[t]$. If $s^{\mathrm{p}}[n]$ denotes the original bipolar samples of the positive frame block, and $s^{\mathrm{n}}[n]$ denotes the original bipolar samples of the negative frame block, then by design $s^{\mathrm{p}}[n] = -s^{\mathrm{n}}[n]$. Hence, a closer look at (12) shows that $s'^p[t] = -s'^n[t]$ except for the third terms in the summation. The differences appear due to the time-domain span of $p[t]$ but are not significant when $N_{\mathrm{cp}}^{\mathrm{p}} \ll N_{\mathrm{FFT}}$. Then, the samples of the positive frame block and the negative frame block after match filtering at the receiver become, respectively:

$$\hat{s}^{\mathrm{p}}[n] = \left(\frac{1}{2}\left(s'^p[t] + |s'^p[t]|\right) * h[t] + n_1[t]\right) * p[t]\bigg|_{t=nT} \quad (18)$$

$$\hat{s}^{\mathrm{n}}[n] = \left(\frac{1}{2}\left(s'^n[t] + |s'^n[t]|\right) * h[t] + n_2[t]\right) * p[t]\bigg|_{t=nT} \quad (19)$$

where $n_1[t]$ and $n_2[t]$ are two independent identically distributed instances of the AWGN process. The bipolar samples at the receiver can be reconstructed by subtracting the received samples of the negative frame block from the received samples of the positive frame block

$$\hat{s}^{\mathrm{b}}[n] = \hat{s}^{\mathrm{p}}[n] - \hat{s}^{\mathrm{n}}[n]$$

$$= \left(\frac{1}{2}\left(s'^p[t] - s'^n[t]\right) * h[t] + n_1[t] - n_2[t]\right) * p[t]\bigg|_{t=nT}. \quad (20)$$

The nonlinear distortion terms $\frac{1}{2}|s'^p[t]| * h[t] * p[t]|_{t=nT}$ and $\frac{1}{2}|s'^n[t]| * h[t] * p[t]|_{t=nT}$ are equal and so are completely removed by the subtraction operation. The noise doubles as described in Section III-D.

An important implication of these proofs is that pulse shaping can also be incorporated in the analysis of the nonlinear distortions for ACO-OFDM, PAM-DMT, and U-OFDM. If pulse shaping is applied after clipping at zero, then the distribution of samples in the time domain changes, and that compromises the

accuracy of the analysis. OFDM samples in the time domain follow a Gaussian distribution when the number of carriers is greater than 64 [8], [10], [12]. Hence, the positive samples of ACO-OFDM, PAM-DMT, and U-OFDM follow the distribution of a Gaussian function, clipped at zero. Pulse shaping is a linear operation, which linearly combines the discrete samples of an OFDM frame, scaled by the samples of a pulse-shaping filter. Linearly combining samples that follow a clipped Gaussian distribution results in samples that follow a different distribution. Hence, pulse shaping after clipping at zero produces a signal which cannot be analyzed with the Bussgang theorem. On the other hand, combining samples that follow a Gaussian distribution results in samples that again follow a Gaussian distribution. Hence, if the pulse shaping is done before the clipping at zero, the pulse-shaped samples follow a Gaussian distribution and after the clipping operation they follow a clipped Gaussian distribution. This enables the use of the Bussgang theorem and the analysis presented in this paper.

V. NONLINEARITIES IN OWC

There are a number of possible sources of nonlinear distortion in an OWC system. Electronic devices have limited dynamic ranges and often nonlinear characteristics within the dynamic range. Furthermore, transitions between the digital and the analog domain lead to signal quantization effects.

The processed digital time-domain signal needs to be passed through a DAC in order to obtain a signal, which can be used to drive the LED. An increase in the resolution of a DAC increases the design complexity and cost. Decreasing the resolution leads to signal quantization. In addition, nonlinear distortion occurs from the limited range of the device which leads to clipping. An accurate analysis of the distortion effects caused to a signal allows for making informed choices between cost, range, and accuracy of the DAC.

LEDs and photodiodes (PDs) are another source of nonlinearity. The voltage–current relationship at an LED is not linear. With the design of suitable V-to-I transducers, this transition step in the system can be almost completely linearized. However, the relationship between the current through the LED and the produced light intensity is also not linear. In addition, there is a minimum and a maximum allowed current level so that the diode can operate properly. This means that the OFDM signal should be clipped at the processing step in order to become suitable for transmission through the LED. The same effects due to the nonlinear relationships between light intensity, current, and voltage are present in the PD. However, this device operates in a much smaller range, which means that distortion is not as significant as in the LED.

VI. NONLINEARITY ANALYSIS

For a large number of subcarriers, $N_{\text{FFT}} > 64$, an OFDM time-domain signal can be approximated by a set of independent identically distributed random variables with a continuous Gaussian distribution [8], [10], [12]. According to [12], a nonlinear distortion in an OFDM-based system can be described with a gain factor and an additional noise component, both of

which can be explained and quantified with the help of the Bussgang theorem. If X is a zero-mean Gaussian random variable and $z(X)$ is an arbitrary memoryless distortion on X, then, following the Bussgang theorem in [21] and Rowe's subsequent work in [22]

$$z(X) = \alpha X + Y \tag{21}$$

$$E[XY] = 0. \tag{22}$$

In these equations, α is a constant, $E[\cdot]$ stands for statistical expectation, and Y is a noise component not correlated with X. Using (21) and (22), α can be derived as

$$\alpha = \frac{E[Xz(X)]}{\sigma_{\text{x}}^2} \tag{23}$$

where σ_{x} is the standard deviation of X. The noise component Y can be quantified as follows:

$$E[Y^2] = E[z^2(X)] - \alpha^2 \sigma_{\text{x}}^2 \tag{24}$$

$$E[Y] = E[z(X)] \tag{25}$$

$$\sigma_{\text{Y}}^2 = E[Y^2] - E[Y]^2 \tag{26}$$

where σ_{Y}^2 denotes the variance of Y. When the fast Fourier transform (FFT) is applied at the system receiver, in the frequency domain the noise Y is transformed into additive Gaussian noise due to the central limit theorem. The variance of Y in the frequency domain is again σ_{Y}^2, and its time-domain average contributes only to the 0th subcarrier. Therefore, at each modulated subcarrier an additional zero-mean additive Gaussian noise component with variance σ_{Y}^2 is present. Overall the system experiences an increase in the additive Gaussian noise power by σ_{Y}^2 and a decrease in the useful signal power by a factor of α^2. This approach has been used in a number of works to analyze nonlinearities in an analytical or semianalytical fashion [8], [10], [12]. The analytical solution, however, is not guaranteed to be in a closed form. Whenever a closed-form solution is desired, an additional step is required as the derivation needs to be tailored to the respective nonlinear distortion function. In this paper, a general derivation approach which leads to a closed-form analytical solution with arbitrary accuracy for an arbitrary memoryless distortion function is proposed. It is applicable to the four OFDM-based modulation schemes investigated in this paper. The rest of this section introduces the modified technique and describes how it can be applied to DCO-OFDM, ACO-OFDM, PAM-DMT, and U-OFDM.

An arbitrary distortion function $z(X)$ can be expressed as a set of intervals I with cardinality $|I|$ and a set of continuous polynomials which accurately approximate $z(X)$ in those intervals. The polynomials can be generated through interpolation of empirical data, or with a polynomial expansion of a function. The polynomial degree sets the accuracy of the approximation. Then, $z(x)$ can be represented as

$$z(x) = \sum_{l=1}^{|I|} \sum_{j=0}^{n_l} c_{l,j} x^j \left(U(x - x_{\min,l}) - U(x - x_{\max,l}) \right) \quad (27)$$

where l denotes the lth interval, n_l denotes the order of the polynomial in interval l, $c_{l,j}$ denotes the jth polynomial coefficient in interval l, and $U(x)$ is the unit step function. Moreover, $x_{\min,l}$ and $x_{\max,l}$ denote the lower and upper boundaries of interval l. Then, α can be calculated as

$$\alpha = \frac{E[Xz(X)]}{\sigma_x^2} = \frac{1}{\sigma_x^2} \int_{-\infty}^{\infty} xz(x) \frac{1}{\sigma_x} \phi\left(\frac{x}{\sigma_x}\right) dx$$

$$= \frac{1}{\sigma_x^2} \int_{-\infty}^{\infty} \left\{ \sum_{l=1}^{|I|} \sum_{j=0}^{n_l} c_{l,j} x^{j+1} \left(U(x - x_{\min,l}) \right. \right.$$

$$\left. \left. - U(x - x_{\max,l}) \right) \right\} \frac{1}{\sigma_x} \phi\left(\frac{x}{\sigma_x}\right) dx$$

$$= \frac{1}{\sigma_x^2} \sum_{l=1}^{|I|} \sum_{j=0}^{n_l} c_{l,j} \int_{x_{\min,l}}^{x_{\max,l}} x^{j+1} \frac{1}{\sigma_x} \phi\left(\frac{x}{\sigma_x}\right) dx$$

$$\stackrel{(46)}{=} \frac{1}{\sigma_x^2} \sum_{l=1}^{|I|} \sum_{j=0}^{n_l} c_{l,j} \left. \frac{d^{j+1} D(t, x_{\min,l}, x_{\max,l}, 0, \sigma_x)}{dt^{j+1}} \right|_{t=0} \quad (28)$$

where function $D(t, a, b, \mu, \sigma_x)$ is defined in the Appendix. The variance of the time domain signal, σ_x^2, can be calculated with the following formula for DCO-OFDM and U-OFDM

$$\sigma_x^2 = \frac{1}{N_{FFT}} \sum_{j=0}^{N_{FFT}-1} \log_2(M_j) E_{bj}. \quad (29)$$

For ACO-OFDM and PAM-DMT, the time-domain variance can be calculated as

$$\sigma_x^2 = \frac{2}{N_{FFT}} \sum_{j=0}^{N_{FFT}-1} \log_2(M_j) E_{bj} \quad (30)$$

where M_j is the size of the signal constellation and E_{bj} is the energy per bit at the jth subcarrier. The factor of two for ACO-OFDM and PAM-DMT results from the power rescaling after clipping of the negative samples. It should be noted that after pulse shaping, the variance of the oversampled signal is not constant over time. However, the authors of [12] have shown that for commonly used pulse shapes this does not influence the validity of the analysis. Results in this paper confirm this finding. The calculations necessary to complete the statistical description of Y can be expressed as

$$E[Y] = E[z(X)] = \int_{-\infty}^{\infty} z(x) \frac{1}{\sigma_x} \phi\left(\frac{x}{\sigma_x}\right) dx$$

$$= \int_{-\infty}^{\infty} \left\{ \sum_{l=1}^{|I|} \sum_{j=0}^{n_l} c_{l,j} x^j \left(U(x - x_{\min,l}) \right. \right.$$

$$\left. \left. - U(x - x_{\max,l}) \right) \right\} \frac{1}{\sigma_x} \phi\left(\frac{x}{\sigma_x}\right) dx$$

$$= \sum_{l=1}^{|I|} \sum_{j=0}^{n_l} c_{l,j} \int_{x_{\min,l}}^{x_{\max,l}} x^j \frac{1}{\sigma_x} \phi\left(\frac{x}{\sigma_x}\right) dx$$

$$\stackrel{(46)}{=} \sum_{l=1}^{|I|} \sum_{j=0}^{n_l} c_{l,j} \left. \frac{d^j D(t, x_{\min,l}, x_{\max,l}, 0, \sigma_x)}{dt^j} \right|_{t=0} \quad (31)$$

$$E[z^2(X)] = \int_{-\infty}^{\infty} z^2(x) \frac{1}{\sigma_x} \phi\left(\frac{x}{\sigma_x}\right) dx$$

$$= \int_{-\infty}^{\infty} \left\{ \sum_{l=1}^{|I|} \sum_{j=0}^{n_l} c_{l,j} x^j \left(U(x - x_{\min,l}) \right. \right.$$

$$\left. \left. - U(x - x_{\max,l}) \right) \right\}^2 \frac{1}{\sigma_x} \phi\left(\frac{x}{\sigma_x}\right) dx$$

$$= \sum_{l=1}^{|I|} \sum_{j=0}^{n_l} \sum_{k=0}^{n_l} c_{l,j} c_{l,k} \int_{x_{\min,l}}^{x_{\max,l}} x^{j+k} \frac{1}{\sigma_x} \phi\left(\frac{x}{\sigma_x}\right) dx$$

$$\stackrel{(46)}{=} \sum_{l=1}^{|I|} \sum_{j=0}^{n_l} \sum_{k=0}^{n_l} c_{l,j} c_{l,k}$$

$$\times \left. \frac{d^{j+k} D(t, x_{\min,l}, x_{\max,l}, 0, \sigma_x)}{dt^{j+k}} \right|_{t=0}. \quad (32)$$

With the help of the Appendix and the standard differentiation rules, it is straightforward to obtain closed-form expressions for (28), (31), and (32). The procedure can easily be programmed on a computer. The resulting SNR at each frequency subcarrier can be calculated according to the following relationship:

$$\frac{E_{bj}^{new}}{\sigma_{NY}^2} = \frac{\alpha^2 E_{bj}}{\sigma_N^2 + \sigma_Y^2} \quad (33)$$

where E_{bj}^{new} is the resulting energy per bit of the jth subcarrier, E_{bj} is the initial energy per bit of the jth subcarrier, σ_N^2 is the variance of the channel AWGN, and σ_{NY}^2 is the overall noise variance. Closed-form analytical expressions for the BER in M-PAM and M-QAM as a function of the SNR exist in the literature [20].

The Bussgang analysis presented so far is valid for zero-mean signals with Gaussian distribution. All four optical modulation schemes—DCO-OFDM, ACO-OFDM, PAM-DMT, U-OFDM—are modifications of the original zero-mean OFDM signal and need to be treated with care for a correct assessment of the nonlinearity effects. The analysis should take into account all effects on the signal up to the point where an FFT operation is performed by the OFDM demodulator at the receiver. Let's assume that $z_1(x)$ is a memoryless distortion at one stage of the system, for example caused by clipping the signal within the allowed range; $z_2(x)$ is a memoryless distortion at another stage, for example due to quantization at the DAC; $z_3(x)$ is a third memoryless distortion, for example the addition of a bias level. Then, the overall distortion after the three separate consecutive distortions is $z(s'[t]) = z_3(z_2(z_1(s'[t])))$. It does not matter whether a distortion is linear or nonlinear. It can always

be incorporated in the analysis if it is memoryless. This paper assumes that there is no distortion with memory or any such distortion can be completely equalized, for example ISI.

For comparison purposes, the average electrical energy per bit $E_{b,elec}$ and the average optical energy per bit $E_{b,opt}$ dissipated at the transmitter are defined as

$$E_{b,elec} = \frac{P_{elec}^{avg}}{B\eta} = \frac{E[z_{elec}^2(s'[t])]}{B\eta} \tag{34}$$

$$E_{b,opt} = \frac{P_{opt}^{avg}}{B\eta} = \frac{E[z_{opt}(s'[t])]}{B\eta} \tag{35}$$

where P_{elec}^{avg} is the average electrical power of the signal, proportional to the mean square of the electrical signal; P_{opt}^{avg} is the average optical power of the signal, proportional to the average intensity of the optical signal; η is the respective spectral efficiency defined for the various schemes in (1), (7), (10), and (11); $z_{elec}(s'[t])$ is the current signal at the diode; $z_{opt}(s'[t])$ is the light intensity signal at the diode; B is the signal bandwidth in hertz. For the examples which are presented in this paper, $z_{elec}(s'[t])$ includes clipping, quantization effects at the DAC, and biasing, while $z_{opt}(s'[t])$ includes the current-to-light output characteristic of the diode in addition.

A. DCO-OFDM

The proposed analysis can be applied to DCO-OFDM in a straightforward manner. The biasing of the signal can be considered as part of the nonlinear transform. It does not need to be added separately like it has been done in other works [8], [10].

B. ACO-OFDM

The modulation process of ACO-OFDM includes clipping at zero. This operation is a nonlinear transform, but does not affect the odd carriers of the system. As a consequence, a slight modification needs to be made to the analysis in order to account for this effect. The modified approach is described in the rest of this section. In ACO-OFDM, the bipolar OFDM signal before clipping consists of a set of positive samples and a set of negative samples. The two sets have identical contribution to each modulated value in the frequency domain [3]. Therefore, setting one set to zero does not distort the useful signal except for a factor of 0.5. This means that the nonlinearity analysis can be conducted only on the positive samples. The result is the same as if the effect of a symmetrical distortion function on the bipolar OFDM signal is analyzed. Hence, for the calculations, the intervals of the nonlinear transform can be specified from 0 to ∞. Then, (28), (31), and (32) can be calculated in the interval $[0; \infty]$ and scaled by 2 to account for the negative half of the signal distribution. The equations become

$$\alpha = \frac{2}{\sigma_x^2} \sum_{l=1}^{|I|} \sum_{j=0}^{n_l} c_{l,j} \left. \frac{d^{j+1} D(t, x_{min,l}, x_{max,l}, 0, \sigma_x)}{dt^{j+1}} \right|_{t=0} \tag{36}$$

$$E[Y] = 2 \sum_{l=1}^{|I|} \sum_{j=0}^{n_l} c_{l,j} \left. \frac{d^j D(t, x_{min,l}, x_{max,l}, 0, \sigma_x)}{dt^j} \right|_{t=0} \tag{37}$$

$$E[z^2(X)] = 2 \sum_{l=1}^{|I|} \sum_{j=0}^{n_l} \sum_{k=0}^{n_l} c_{l,j} c_{l,k}$$
$$\times \left. \frac{d^{j+k} D(t, x_{min,l}, x_{max,l}, 0, \sigma_x)}{dt^{j+k}} \right|_{t=0}. \tag{38}$$

The removal of the negative samples does not influence the odd subcarriers, as previously explained in Section III. The calculated noise variance, σ_Y^2, needs to be halved before addition to the AWGN variance because the noise is evenly distributed on both odd and even subcarriers. There is a 0.5 factor to the SNR, stemming from the removal of the negative samples. Then for ACO-OFDM, (33) becomes

$$\frac{E_{bj}^{new}}{\sigma_{NY}^2} = \frac{\alpha^2 E_{bj}}{2(\sigma_N^2 + \frac{\sigma_Y^2}{2})}. \tag{39}$$

It should be noted that the zeroes from clipped negative samples need to preserve their value in order not to influence the modulated subcarriers. The overall distortion of the signal up to the demodulator is $z_d(s'[t])$; this distortion does not include the addition of AWGN. If $z_d(0) \neq 0$, then the zeros obtained from clipping the negative samples are distorted. The distortion on the clipped zero values in the time domain adds distortion on the odd subcarriers in the frequency domain. This effect is avoided when the clipped values are zero. If $z_d(0)$ is interpreted as a dc shift and subtracted from $z_d(s'[t])$, then the modified Bussgang analysis described in this section can be applied without having to additionally model the distortion resulting from the distorted clipped samples. Hence, the overall distortion, experienced by the nonzero ACO-OFDM samples is

$$z(s'[t])_{s'[t] \geq 0} = z_d(s'[t])_{s'[t] \geq 0} - z_d(0). \tag{40}$$

C. PAM-DMT

The time-domain signal of PAM-DMT has the same statistical properties as the ACO-OFDM signal. In addition, the power of the additive Gaussian noise from the nonlinearity is equally split between real and imaginary components in the frequency domain. Therefore, the nonlinearity analysis of PAM-DMT is exactly the same as for ACO-OFDM. It should be kept in mind that PAM-DMT employs M-PAM while ACO-OFDM employs M^2-QAM for the same spectral efficiency. In an additive Gaussian noise environment, M-PAM and M^2-QAM perform identically in terms of BER.

D. U-OFDM

In U-OFDM, the signs of negative samples are switched, they are transmitted as positive samples and switched back at the demodulator. As a result, the nonlinear distortion on the bipolar OFDM signal is symmetric around zero, i.e., $z(s'[t]) = -z(-s'[t])$. Any two bipolar samples with the same absolute value experience exactly the same nonlinear distortion. Hence, $z(s'[t])_{s'[t] \leq 0}$ is formed as a mirrored version of $z(s'[t])_{s'[t] \geq 0}$ according to $z(s'[t]) = -z(-s'[t])$. Alternatively, it can be stated that due to the symmetry of the Gaussian probability density function (PDF), $z(s'[t])$ can be specified only in the interval

$[0; \infty]$ for the calculations of (28), (31), and (32). Each of the equations, however, needs to be doubled to account for the negative half of the distribution as is the case for ACO-OFDM and PAM-DMT. The subtraction of the negative block from the positive block effectively doubles the system AWGN. Hence, (33) is modified as

$$\frac{E_{\mathrm{b}j}^{\mathrm{new}}}{\sigma_{\mathrm{NY}}^2} = \frac{\alpha^2 E_{\mathrm{b}j}}{2\sigma_{\mathrm{N}}^2 + \sigma_{\mathrm{Y}}^2}. \qquad (41)$$

It should be noted that in the demodulator the bipolar signal is obtained by subtracting the negative block from the positive one. If all zeroes corresponding to clipped negative samples from the original signal are transformed to $z_{\mathrm{d}}(0) \neq 0$, then the subtraction operation shifts all positive samples by $-z_{\mathrm{d}}(0)$ and all negative samples by $z_{\mathrm{d}}(0)$. The function $z_{\mathrm{d}}(s'[t])$ is the overall nonlinearity distortion which the signal experiences on its path to the demodulator. The subtraction operation in the demodulation process effectively adds additional distortion, which needs to be accounted for by subtracting $z_{\mathrm{d}}(0)$ from $z_{\mathrm{d}}(s'[t])$, i.e., the resulting overall nonlinearity becomes

$$z(s'[t])_{s'[t] \geq 0} = z_{\mathrm{d}}(s'[t])_{s'[t] \geq 0} - z_{\mathrm{d}}(0) \qquad (42)$$

as in ACO-OFDM and PAM-DMT.

The analyses of ACO-OFDM, PAM-DMT, and U-OFDM show that all three schemes experience exactly the same SNR deterioration for the same nonlinearity effects. This occurs because the three schemes exhibit the same statistical properties in the time domain when their spectral efficiencies are equivalent. This finding is also supported by the results in the next section. Therefore, in addition to the equivalent performance in a simple AWGN channel, the three schemes exhibit the same performance in a nonlinear AWGN channel.

VII. NUMERICAL RESULTS

In this section, the joint effect of three nonlinear distortions at the OWC transmitter is illustrated. These include clipping to account for the limited dynamic range of the electronic devices, quantization from a low-resolution DAC, and the current-to-light output characteristic of the LED. Nonlinearities at the receiver are not examined since they are negligible in comparison to the ones present at the transmitter. They could be analyzed in an analogous manner using the concepts presented in Section VI. In the following case study, the oversampled pulse-shaped signal $s'[t]$ has an oversampling ratio of 10.

The zero-order hold has a limited range of output amplitudes between s'_{min} and s'_{max}, and a finite number of bits q. The different levels of the device are equally spaced in the interval $[s'_{\mathrm{min}}; s'_{\mathrm{max}}]$ at a distance of

$$d_{\mathrm{q}} = \frac{s'_{\mathrm{max}} - s'_{\mathrm{min}}}{2^q - 1}. \qquad (43)$$

Each quantization threshold is set in the middle between two consecutive quantization levels. For example, the threshold between s'_{min} and $s'_{\mathrm{min}} + d_{\mathrm{q}}$ is set at $s'_{\mathrm{min}} + d_{\mathrm{q}}/2$. The values of s'_{min} and s'_{max} are determined by the desired accuracy of the DAC and by the allowed operational range of the LED, $[i_{\mathrm{min}}; i_{\mathrm{max}}]$. Therefore, they account for the clipping effects in-

TABLE I
POLYNOMIAL COEFFICIENTS $c_{l,k}$ IN INTERVAL l AND OF DEGREE k

Interval	$c_{l,3}$	$c_{l,2}$	$c_{l,1}$	$c_{l,0}$
$l = 1 \Leftrightarrow i(t) < i_{\mathrm{min}}$	0	0	0	0.1947
$l = 2 \Leftrightarrow i_{\mathrm{min}} < i(t) < i_{\mathrm{max}}$	0.2855	-1.0886	2.0565	-0.0003
$l = 3 \Leftrightarrow i_{\mathrm{max}} < i(t)$	0	0	0	1.2531

troduced by the DAC and the LED. In the conducted simulations, the resolution of the DAC is set to $q = 8$ bits.

After the signal values are quantized by the DAC output function, they are biased by a constant and are passed through the LED. The LED output function is a continuous function, specified in the interval $[i_{\mathrm{min}}; i_{\mathrm{max}}]$. According to the device datasheet [23], $i_{\mathrm{min}} = 0.1$ A and $i_{\mathrm{max}} = 1$ A. The LED output function corresponds to a transition from a current signal to an optical signal. The output characteristic of the LED has been obtained through interpolation of data from the device datasheet. A third degree polynomial has been used in the interpolation, and its coefficients are presented in Table I. The relationship between radiant flux (power) and luminous flux (power) is linear. Therefore, since only the relationship between current through the device and luminous flux is available in the datasheet, it has been adopted as an accurate representation of the relationship between the current and the radiation power.

It is assumed that the modulating signal is contained in the current signal through the LED. The initial average energy per bit of the original bipolar OFDM signal $s[n]$ is E_{b}. The actual dissipated electrical energy per bit at the LED assuming that the resistance is normalized to $1\,\Omega$ and including the quantization effects and biasing is $E_{\mathrm{b,elec}} = \mathrm{E}[i^2(t)]/(B\eta) = \mathrm{E}[(z_3(z_2(z_1(s'[t]))) + i_{\mathrm{bias}})^2]/(B\eta)$. In this formula, $z_1(s'[t])$ is the clipping effect in the preprocessing step applied on the oversampled pulse-shaped signal $s'[t]$; $z_2(x)$ is the quantization effect of the DAC; $z_3(x)$ is the conversion from voltage to current, which is assumed to be linear with gain 1. In order to evaluate the optical efficiency of the system, a third quantity is defined as $E_{\mathrm{b,opt}} = \mathrm{E}[z_4(z_3(z_2(z_1(s'[t]))) + i_{\mathrm{bias}})]/(B\eta)$, where $z_4(x)$ expresses the transition from current to optical signal in the LED, specified by the polynomial in Table I.

The modulation bandwidth of white-light LEDs is 2 MHz [19]. The coherence bandwidth of the optical channel is around 90 MHz [19], which is much higher than the modulation frequency of the LED. Hence, ISI does not need to be considered. In an alternative scenario, where ISI is an issue, the presented nonlinearity framework is still applicable as long as channel knowledge is available at the receiver, and the signal can be equalized. In the assumed system configuration, the received current signal can be expressed as

$$\hat{i}(t) = z_4(i(t))h_{\mathrm{G}}\gamma \qquad (44)$$

where h_{G} is the channel gain due to dispersion of light, and γ is the responsivity of the PD. Using the profile of the LED light spectrum and the PD responsivity to different optical wavelengths [24], the receiver responsivity to white light is calculated as $\gamma = 0.52$. The channel gain depends on a number of factors–distance, receiver area, angle with respect to the transmitter. In this paper, h_{G} is selected depending on the M-QAM
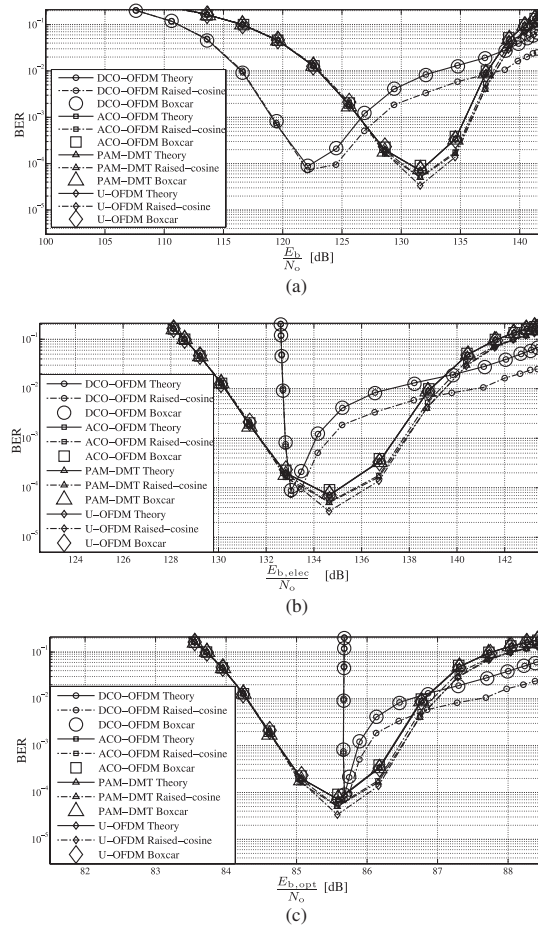
Fig. 8. Comparison between 4-QAM DCO-OFDM, 16-QAM ACO-OFDM, 4-PAM PAM-DMT, and 16-QAM U-OFDM in terms of electrical and optical SNR. (a) Comparison of bipolar signals. Bias not taken into account. (b) Comparison of unipolar signals including contribution of bias to electrical power dissipation. (c) Comparison of unipolar signals in terms of optical power requirements. Bias contribution to power dissipation included.

modulation order that is used. The aim is to operate the LED in the full range of its active region because then the improvements of ACO-OFDM, PAM-DMT, and U-OFDM over DCO-OFDM are demonstrated. In the cases when the optical signal varies only slightly around the biasing point, the energy consumption depends almost entirely on the biasing level, which makes the energy dissipation almost constant for the four schemes.

The main source of AWGN in an OWC system is shot noise at the photo detector caused by background light. The power spectral density of shot noise is $N_o = 10^{-21}$ W/Hz according to [19]. The variance of the AWGN is calculated as $\sigma_N^2 = BN_o$.

Fig. 8 presents a working example which compares 4-QAM DCO-OFDM, 16-QAM ACO-OFDM, 4-PAM PAM-DMT, and 16-QAM U-OFDM—all with the same spectral efficiency of

1 bit/s/Hz. The simulated channel gain is $h_G = 4 \times 10^{-6}$, since this value allows all the presented schemes to reach BER values in the order of 10^{-3} and 10^{-4}—required for successful communication [10], [19]. At the same time, this value of the channel gain requires almost full utilization of the LED active range. The bias levels for ACO-OFDM, PAM-DMT, and U-OFDM are set to $i_{bias} = 0.1$ A, since this is the minimum biasing requirement of the LED. The selected simulation parameters set the minimum bias level for DCO-OFDM at $i_{bias} = 0.19$ A. The distribution region $[-3\sigma; 3\sigma]$ is quantized for DCO-OFDM, and the region $[0; 3\sigma]$ is quantized for the other three schemes. Anything outside those regions is clipped. These clipping levels are chosen to be the default clipping levels as they introduce negligible nonlinear distortion according to simulations. Since the AWGN power is constant, higher SNR values can be achieved by amplifying the information signal through the LED. However, if that signal falls outside the allowed operational range of the device when amplified, it is further clipped at the predistortion step in order to satisfy the electrical properties of the LED. Hence, the BER curves presented in this section are V-shaped. The dip in the plots emerges because after a certain point the distortion due to clipping outweighs the improvement due to the SNR increase. Fig. 8(a) shows the electrical energy efficiency of the four schemes when the energy dissipation due to biasing is neglected. As expected for bipolar signals, DCO-OFDM performs better than the other three schemes. The benefits of the latter, however, are due to the biasing requirement, and this can be observed in Fig. 8(b). In that figure, ACO-OFDM, PAM-DMT, and U-OFDM require about 1 dB less energy per bit than DCO-OFDM for BER $= 10^{-3}$ and about the same energy for BER $= 10^{-4}$. According to Fig. 8(c), DCO-OFDM is about 1 dB less optically efficient than the other three schemes for BER $= 10^{-3}$ and about 0.3 dB less efficient for BER $= 10^{-4}$. It is interesting to note that, as expected, the BER values decrease with the increase in SNR up to a certain point. Afterward, the active region of the LED is exhausted, and the increase in power leads to increase in clipping, and hence, to more nonlinear distortion. It should also be noted that the theoretical analysis coincides well with the Monte Carlo simulation results for square pulse shapes (Boxcar filter). The Monte Carlo results for a root-raised-cosine filter are slightly better than the other results because the matched filter at the receiver eliminates some of the distortion noise which falls outside the desired signal bandwidth. Nonetheless, the root-raised-cosine filter results follow closely the theoretical results and confirm validity of the new analytical framework. For practical purposes, the presented analysis can serve as a good lower bound approximation for the performance of systems which employ pulse shapes with limited bandwidth. To the best of the authors' knowledge, other available techniques for analysis of nonlinear distortion in OWC do not consider bandlimited pulse shapes. They assume simple square pulses (Boxcar filter) [6]–[10] for which an exact analysis is provided in this paper. The curves for ACO-OFDM, PAM-DMT, and U-OFDM fall almost on top of each other as predicted by the theoretical analysis. This highlights the very similar performance of the three schemes.

ACO-OFDM, PAM-DMT, and U-OFDM exhibit better energy efficiency than DCO-OFDM. However, they require a
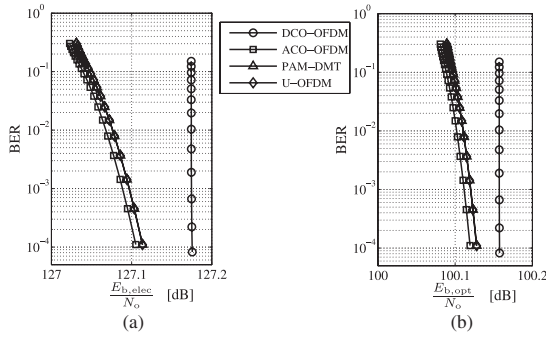
Fig. 9. Comparison of 4-QAM DCO-OFDM, 16-QAM ACO-OFDM, 4-QAM PAM-DMT, and 16-QAM U-OFDM for a high channel gain, $h_{\rm G} = 4 \times 10^{-4}$, scenario: (a) Electrical power efficiency including bias current; (b) Optical power efficiency including bias level.

bigger M-QAM constellation size for the same spectral efficiency. Larger constellations are more vulnerable to distortion. This vulnerability can put the three schemes at a disadvantage in certain scenarios. Such an example occurs if the channel gain is decreased to $h_{\rm G} = 2 \times 10^{-6}$. In this case, the minimum biasing requirement of DCO-OFDM becomes $i_{\rm bias} = 0.5$ A, and it is kept at $i_{\rm bias} = 0.1$ A for the other three schemes. In spite of the worse performance in the previous simulation, in this scenario DCO-OFDM becomes the better choice. It is still able to achieve a BER of 10^{-4}, while all three other schemes cannot even reach a BER of 10^{-3}. This example shows that a minor change of the system parameters such as a factor of two in the channel gain can be decisive in the selection of a modulation scheme.

Fig. 9 presents a case for a significantly higher channel gain, $h_{\rm G} = 4 \times 10^{-4}$. In this scenario, the information signal energy requirement is small. Hence, the main contributor to energy consumption is the biasing level. The bias of DCO-OFDM is set to $i_{\rm bias} = 0.1018$ A, which is the minimum required bias that is able to accommodate the information signal without severe clipping distortion. The bias of the other three schemes is kept at the minimum, $i_{\rm bias} = 0.1$ A. The electrical energy advantage of ACO-OFDM, PAM-DMT, and U-OFDM over DCO-OFDM is in the order of 0.06 dB, while the difference in the optical energy requirement is in the order of 0.04 dB. The four schemes are almost equivalent in performance because the main contributor to energy dissipation is the bias of the LED. It should be noted that the electrical energy efficiency of ACO-OFDM, PAM-DMT, and U-OFDM is lower than presented in the papers which originally introduced these concepts— [3]–[5]. The reason for this is that all clipped values which are set to zero at the modulator actually cannot be lower than the minimum required current at the LED and so also contribute to the power dissipation.

The analyzed schemes achieve higher spectral efficiency when the M-QAM/M-PAM modulation order is increased. This leads to more variance in the time-domain signal as described in (29) and (30), which for the same system parameters leads to more distortion. At the same time, bigger constellations are

more sensitive to noise. Therefore, for higher spectral efficiencies and assuming the same OWC system parameters, the BER performance suffers from additional deterioration.

VIII. CONCLUSION

A complete analytical framework has been presented for the analysis of memoryless nonlinear distortion in an OWC system. It allows for the analysis of an arbitrary distortion function and guarantees closed-form solutions. The concept has been successfully applied to four separate OFDM-based modulation schemes proposed for IM/DD systems: DCO-OFDM, ACO-OFDM, PAM-DMT, and U-OFDM. Examples have been given for the joint distortion effects from quantization at a DAC element, as well as for distortion from the nonlinear relationship between electrical current and emitted light in an LED, which are the major sources of nonlinearity in an OWC system. Monte Carlo simulations show very good agreement with the proposed theory, thus confirming validity of the approach.

Analytical derivations as well as numerical results exhibit equivalent performance of ACO-OFDM, PAM-DMT, and U-OFDM in a nonlinear AWGN channel. The findings suggest that these schemes are three separate and equally valid approaches with respect to spectrum efficiency and energy efficiency. A brief analysis demonstrates that the optimal choice of a modulation scheme depends on the operating conditions and can change with variations in the system parameters. The presented framework provides a quick and accurate way to estimate system performance without computationally expensive Monte Carlo simulations and numerical integration. Thus, it enables system optimization as the influence of a large range of system parameters can be evaluated exhaustively with reasonable computational complexity.

APPENDIX

This section presents the necessary formulas for derivation of a closed-form solution in the proposed novel analytical framework. The formulas are defined as follows:

$$\mathrm{D}(t,a,b,\mu,\sigma_{\rm x}) = \int_a^b e^{xt}\frac{1}{\sqrt{2\pi\sigma_{\rm x}^2}}e^{-\frac{(x-\mu)^2}{2\sigma_{\rm x}^2}}\,\mathrm{d}x$$

$$= \int_a^b \frac{1}{\sqrt{2\pi\sigma_{\rm x}^2}}e^{-\frac{-2xt\sigma_{\rm x}^2+x^2-2\mu x+\mu^2}{2\sigma_{\rm x}^2}}\,\mathrm{d}x$$

$$= \int_a^b \frac{1}{\sqrt{2\pi\sigma_{\rm x}^2}}e^{-\frac{x^2-2(t\sigma_{\rm x}^2+\mu)x+\mu^2}{2\sigma_{\rm x}^2}}\,\mathrm{d}x$$

$$= \int_a^b \frac{1}{\sqrt{2\pi\sigma_{\rm x}^2}}e^{-\frac{x^2-2(t\sigma_{\rm x}^2+\mu)x+t^2\sigma_{\rm x}^4+2t\sigma_{\rm x}^2\mu+\mu^2-t^2\sigma_{\rm x}^4-2t\sigma_{\rm x}^2\mu}{2\sigma_{\rm x}^2}}\,\mathrm{d}x$$

$$= e^{\frac{t^2\sigma_{\rm x}^2}{2}+t\mu}\int_a^b \frac{1}{\sqrt{2\pi\sigma_{\rm x}^2}}e^{-\frac{x^2-2(t\sigma_{\rm x}^2+\mu)x+(t\sigma_{\rm x}^2+\mu)^2}{2\sigma_{\rm x}^2}}\,\mathrm{d}x$$

$$= e^{\frac{t^2\sigma_{\rm x}^2}{2}+t\mu}\int_a^b \frac{1}{\sqrt{2\pi\sigma_{\rm x}^2}}e^{-\frac{(x-\mu-t\sigma_{\rm x}^2)^2}{2\sigma_{\rm x}^2}}\,\mathrm{d}x$$

$$= e^{\frac{t^2\sigma_{\rm x}^2}{2}+t\mu}\left(\mathrm{Q}\left(\frac{a-\mu-t\sigma_{\rm x}^2}{\sigma_{\rm x}}\right) - \mathrm{Q}\left(\frac{b-\mu-t\sigma_{\rm x}^2}{\sigma_{\rm x}}\right)\right) \quad (45)$$

where $Q(x)$ is the tail probability of the standard normal distribution, and $\phi(x)$ is its PDF.

$$\frac{\mathrm{d}^n D(t, a, b, \mu, \sigma_\mathrm{x})}{\mathrm{d}t^n}\bigg|_{t=0} \overset{(45)}{=}$$

$$= \frac{\mathrm{d}^n}{\mathrm{d}t^n} \int_a^b e^{xt} \frac{1}{\sqrt{2\pi\sigma_\mathrm{x}^2}} e^{-\frac{(x-\mu)^2}{2\sigma_\mathrm{x}^2}} \, \mathrm{d}x \bigg|_{t=0}$$

$$= \int_a^b \frac{\mathrm{d}^n}{\mathrm{d}t^n} e^{xt} \frac{1}{\sqrt{2\pi\sigma_\mathrm{x}^2}} e^{-\frac{(x-\mu)^2}{2\sigma_\mathrm{x}^2}} \, \mathrm{d}x \bigg|_{t=0}$$

$$= \int_a^b x^n e^{xt} \frac{1}{\sqrt{2\pi\sigma_\mathrm{x}^2}} e^{-\frac{(x-\mu)^2}{2\sigma_\mathrm{x}^2}} \, \mathrm{d}x \bigg|_{t=0}$$

$$= \int_a^b x^n \frac{1}{\sqrt{2\pi\sigma_\mathrm{x}^2}} e^{-\frac{(x-\mu)^2}{2\sigma_\mathrm{x}^2}} \, \mathrm{d}x \tag{46}$$

$$\frac{\mathrm{d}Q\left(\frac{x-\mu-t\sigma_\mathrm{x}^2}{\sigma_\mathrm{x}}\right)}{\mathrm{d}t} = \phi\left(\frac{x-\mu-t\sigma_\mathrm{x}^2}{\sigma_\mathrm{x}}\right)\sigma_\mathrm{x} \tag{47}$$

$$\frac{\mathrm{d}\phi\left(\frac{x-\mu-t\sigma_\mathrm{x}^2}{\sigma_\mathrm{x}}\right)}{\mathrm{d}t} = \phi\left(\frac{x-\mu-t\sigma_\mathrm{x}^2}{\sigma_\mathrm{x}}\right)\left(\frac{x-\mu-t\sigma_\mathrm{x}^2}{\sigma_\mathrm{x}}\right)\sigma_\mathrm{x} \tag{48}$$

REFERENCES

[1] (2011). "Visible Light Communication (VLC)—A potential solution to the global wireless spectrum shortage," GBI Res., Tech. Rep., [Online]. Available: http://www.gbiresearch.com/

[2] J. A. C. Bingham, "Multicarrier modulation for data transmission: An idea whose time has come," *IEEE Commun. Mag.*, vol. 28, no. 5, pp. 5–14, May 1990.

[3] J. Armstrong and A. Lowery, "Power efficient optical OFDM," *Electron. Lett.*, vol. 42, no. 6, pp. 370–372, Mar. 16, 2006.

[4] S. C. J. Lee, S. Randel, F. Breyer, and A. M. J. Koonen, "PAM-DMT for intensity-modulated and direct-detection optical communication systems," *IEEE Photon. Technol. Lett.*, vol. 21, no. 23, pp. 1749–1751, Dec. 2009.

[5] D. Tsonev, S. Sinanović, and H. Haas, "Novel unipolar orthogonal frequency division multiplexing (U-OFDM) for optical wireless," presented at IEEE Vehicular Technol. Conf., Yokohama, Japan, May 2012.

[6] I. Neokosmidis, T. Kamalakis, J. W. Walewski, B. Inan, and T. Sphicopoulos, "Impact of nonlinear LED transfer function on discrete multitone modulation: Analytical approach," *J. Lightw. Technol.*, vol. 27, no. 22, pp. 4970–4978, 2009.

[7] H. Elgala, R. Mesleh, and H. Haas, "A study of LED nonlinearity effects on optical wireless transmission using OFDM," in *Proc. 6th IEEE Int. Conf. Wireless Opt. Commun. Netw.*, Cairo, Egypt, Apr. 28–30, 2009, pp. 1–5.

[8] S. Dimitrov, S. Sinanovic, and H. Haas, "Clipping noise in OFDM-based optical wireless communication systems," *IEEE Trans. Commun.*, vol. 60, no. 4, pp. 1072–1081, Apr. 2012.

[9] H. Elgala, R. Mesleh, and H. Haas, "Impact of LED nonlinearities on optical wireless OFDM systems," in *Proc. 2010 IEEE 21st Int. Symp. Pers. Indoor Mobile Radio Commun.*, Sep. 2010, pp. 634–638.

[10] S. Dimitrov, S. Sinanovic, and H. Haas, "Signal shaping and modulation for optical wireless communication," *J. Lightw. Technol.*, vol. 30, no. 9, pp. 1319–1328, May 2012.

[11] N. Fernando, Y. Hong, and E. Viterbo, "Flip-OFDM for optical wireless communications," in *Proc. Inf. Theory Workshop*, IEEE. Paraty, Brazil: IEEE, Oct., 16–20 2011, pp. 5–9.

[12] D. Dardari, V. Tralli, and A. Vaccari, "A theoretical characterization of nonlinear distortion effects in OFDM systems," *IEEE Trans. Commun.*, vol. 48, no. 10, pp. 1755–1764, Oct. 2000.

[13] A. Bahai, M. Singh, A. Goldsmith, and B. Saltzberg, "A new approach for evaluating clipping distortion in multicarrier systems," *IEEE J. Sel. Areas Commun.*, vol. 20, no. 5, pp. 1037–1046, Jun. 2002.

[14] X. Li and L. J. CiminiJr., "Effects of clipping and filtering on the performance of OFDM," *IEEE Commun. Lett.*, vol. 2, no. 5, pp. 131–133, May 1998.

[15] D. J. G. Mestdagh, P. Spruyt, and B. Biran, "Analysis of clipping effect in DMT-based ADSL systems," in *Proc. IEEE Int. Conf. Commun.*, vol. 1, New Orleans, LA, USA, May 1–5, 1994, pp. 293–300.

[16] B. Inan, S. C. J. Lee, S. Randel, I. Neokosmidis, A. M. J. Koonen, and J. W. Walewski, "Impact of LED nonlinearity on discrete multitone modulation," *IEEE/OSA J. Opt. Commun. Netw.*, vol. 1, no. 5, pp. 439–451, Oct. 2009.

[17] H. Elgala, R. Mesleh, and H. Haas, "Indoor optical wireless communication: Potential and state-of-the-art," *IEEE Commun. Mag.*, vol. 49, no. 9, pp. 56–62, Sep. 2011.

[18] D. Tsonev, S. Sinanović, and H. Haas, "Enhanced subcarrier index modulation (SIM) OFDM," in *Proc. IEEE Global Commun. Conf.*, Houston, TX, USA, Dec. 5–9, 2011, pp. 728–732.

[19] J. Grubor, S. Randel, K. Langer, and J. Walewski, "Bandwidth efficient indoor optical wireless communications with white light emitting diodes," in *Proc. 6th Int. Symp. Commun. Syst., Netw. Digital Signal Process.*, vol. 1, Graz, Austria, Jun. 23–25, 2008, pp. 165–169.

[20] J. G. Proakis and D. K. Manolakis, in *Digital Signal Processing: Principles, Algorithms and Application*, T. Robbins, Ed., 4th ed. Englewood Cliffs, NJ, USA: Prentice-Hall, Apr. 2006.

[21] J. Bussgang, "Cross correlation function of amplitude-distorted Gaussian signals," Res. Lab. Electron., Massachusetts Inst. Technol., Cambridge, MA, USA, Tech. Rep. 216, Mar. 1952.

[22] H. E. Rowe, "Memoryless nonlinearities with Gaussian inputs: Elementary results," *Bell Syst. Tech. J.*, vol. 61, no. 7, pp. 1519–1525, Sep. 1982.

[23] OSRAM GmbH. (2008, Feb.). "Datasheet: OS-PCN-2008-002-A OSTAR LED." [Online]. Available: http://www.osram.de

[24] Vishay Semiconductors. (2012, Aug.). "Datasheet: BPV10 silicon PIN photodiode, RoHS compliant." [Online]. Available: www.vishay.com/docs/81502/bpv10.pdf

Dobroslav Tsonev (S'11) received the BSc degree in electrical engineering and computer science in 2008 from Jacobs University Bremen, Bremen, Germany and the MSc degree in communication engineering with a specialization in electronics in 2010 from the Munich Institute of Technology, Munich, Germany. Currently, he is pursuing a PhD degree in electrical engineering at the University of Edinburgh. His main research interests lie in the area of optical wireless communication with an emphasis on visible light communication.

Sinan Sinanovic (S'98-M'07) is a lecturer at Glasgow Caledonian University. He has obtained his Ph.D. in electrical and computer engineering from Rice University, Houston, Texas, in 2006. In the same year, he joined Jacobs University Bremen in Germany as a post doctoral fellow. In 2007, he joined the University of Edinburgh in the UK where he has worked as a research fellow in the Institute for Digital Communications. While working with Halliburton Energy Services, he has developed acoustic telemetry receiver which was patented. He has also worked for Texas Instruments on development of ASIC testing. He is a member of the Tau Beta Pi engineering honor society and a member of Eta Kappa Nu electrical engineering honor society. He won an honorable mention at the International Math Olympiad in 1994.

Harald Haas (S'98–A'00–M'03) holds the Chair of Mobile Communications in the Institute for Digital Communications (IDCOM) at the University of Edinburgh, Edinburgh, U.K., and he currently is the CSO of a university spin-out company pureVLC Ltd. His main research interests are in interference coordination in wireless networks, spatial modulation, and optical wireless communication. He holds more than 23 patents. He has published more than 50 journal papers including a Science article and more than 170 peer-reviewed conference papers. Nine of his papers are invited papers. He has co-authored a book entitled Next Generation Mobile Access Technologies: Implementing TDD (Cambridge, U.K.: Cambridge Univ. Press, 2008). Since 2007, he has been a Regular High Level Visiting Scientist supported by the Chinese 111 program at Beijing University of Posts and Telecommunications (BUPT). Prof. Haas was an invited speaker at the TED Global conference 2011, and his work on optical wireless communication was listed among the 50 best inventions in 2011 in Time Magazine. In 2011 he has received a prestigious Fellowship of the Engineering and Physical Sciences Research Council (EPSRC) in the UK.

185

A 3-Gb/s Single-LED OFDM-Based Wireless VLC Link Using a Gallium Nitride μLED

Dobroslav Tsonev, Hyunchae Chun, Sujan Rajbhandari, Jonathan J. D. McKendry, *Member, IEEE*, Stefan Videv, Erdan Gu, Mohsin Haji, Scott Watson, Anthony E. Kelly, Grahame Faulkner, Martin D. Dawson, *Fellow, IEEE*, Harald Haas, *Member, IEEE*, and Dominic O'Brien, *Member, IEEE*

Abstract—This letter presents a visible light communication (VLC) system based on a single 50-μm gallium nitride light emitting diode (LED). A device of this size exhibits a 3-dB modulation bandwidth of at least 60 MHz—significantly higher than commercially available white lighting LEDs. Orthogonal frequency division multiplexing is employed as a modulation scheme. This enables the limited modulation bandwidth of the device to be fully used. Pre- and postequalization techniques, as well as adaptive data loading, are successfully applied to achieve a demonstration of wireless communication at speeds exceeding 3 Gb/s. To date, this is the fastest wireless VLC system using a single LED.

Index Terms—Visible light communication, OFDM, optical modulation, optical wireless communication.

I. Introduction

WIRELESS data traffic is growing exponentially. Recent forecasts indicate that it will be challenging to satisfy the data-rate demands of mobile users because the available radio frequency (RF) communication spectrum is very limited [1]. A potential solution to the looming spectrum crisis lies in the migration of wireless communication into the visible light spectrum. Using visible light offers a number of advantages over RF: 1) 100s of THz license-free bandwidth; 2) simple front-end devices; 3) no interference with sensitive electronic equipment; 4) possibility for integration into the existing lighting infrastructure.

Incoherent solid-state lighting elements such as LEDs are the most likely candidates for VLC transmitters. Several

challenges are hindering the development of commercial VLC systems [2]. Among them is the slow modulation response of commercial white LEDs based on blue LEDs with a yellow phosphor coating. The slow response time of the phosphor restricts the modulation bandwidth of the device to several MHz [2]. The application of a blue filter at the receiver removes the slow component from the modulated signal and enables modulation frequencies of up to 20 MHz [2]. Despite the bandwidth limitation of the LEDs, techniques such as equalization, high-order modulation/multiplexing, and parallel data transmission have enabled communication of up to 1 Gb/s using a single phosphor-coated LED and up to 3 Gb/s using red-green-blue LEDs [2]–[4].

Significant research effort is being directed towards the development of faster LEDs. Among them are resonant-cavity light emitting diodes (RCLEDs) [5]. Using an RCLED has enabled communication links of up to 3 Gb/s over a plastic optical fiber (POF) [6]. Devices with comparable modulation bandwidth can be manufactured by reducing the innate junction capacitance of diodes and by controlling the differential carrier lifetimes through injected current density. In [7], a light emitting diode with a diameter of 50 μm (μLED) is introduced. The significantly-reduced size of the device leads to notable improvements in its frequency response. VLC links with a speed of up to 512 Mb/s [7] and up to 1 Gb/s [8] have been successfully established for such μLEDs using on-off keying (OOK) modulation. For a similar device, a 1.07 Gb/s communication link over a POF has been reported in [9].

In this letter, the communication capabilities of Gallium Nitride μLEDs [7] in conjunction with Orthogonal frequency division multiplexing (OFDM) are investigated. A characterization of the μLED bandwidth and an actual experimental realization of an OFDM-based system are presented. OFDM is selected because it allows cost-effective equalization with single-tap equalizers in the frequency domain. Moreover, OFDM allows adaptive data and energy allocation to different frequency bands based on the communication system properties. In addition, the scheme provides an easy way to avoid low-frequency interference caused by ambient light and by the baseline wander in electrical components. In the current work, a comparison is made between the performance of two techniques for overcoming the effects of frequency-dependent signal attenuation: 1) fixed-rate subcarrier loading with pre-equalization; and 2) adaptive bit and energy loading. As a result, to the best of the authors' knowledge, the fastest single-link wireless VLC system is presented in this letter.

Fig. 1.   Experimental set-up.

The rest of this letter is organized as follows. Section II provides a description of the experimental setup. Section III presents the experimental results and offers a discussion. Finally, Section IV provides concluding remarks.

II. SYSTEM DESCRIPTION

A. Experimental Set-Up Parameters

Fig. 1 presents a diagram of the experimental OFDM-based VLC system set-up. First, an incoming bit stream is encoded into M-ary quadrature amplitude modulation (M-QAM) symbols. Then, the resulting M-QAM symbols are assigned to different frequency subcarriers and rescaled accordingly if pre-equalization is employed. Afterwards, an inverse fast Fourier transform (IFFT) operation is applied on a block of symbols, which produces a discrete time-domain signal. This signal is conditioned for transmission by clipping any values outside the allowed operational range set by the electrical properties of the μLED. All digital processing steps are performed in MATLAB®. Afterwards, the conditioned digital signal is supplied to an arbitrary waveform generator (AWG), Agilent N8241A, which maps it to an analog signal. The analog signal is amplified with a high-power amplifier, Mini-Circuits ZHL-6A, which drives the μLED. The μLED emits blue light with a wavelength distribution centered around 450 nm and has a maximum optical power of around 4.5 mW [7]. A direct current (DC) bias from a laser driver is added to the drive signal using a bias-T, Mini-Circuits ZFBT-6GW. Light from the μLED is imaged onto a high-speed photodetector, New Focus 1601FS-AC, using a high numerical aperture (NA) microscope objective, model 40OA65 from Comar Optics. The output signal of the photodetector is captured by a digital oscilloscope, Agilent MSO7104B. Afterwards, it is processed in MATLAB with a sequence of steps that include: synchronization, fast Fourier transform (FFT), equalization, and M-QAM demodulation.

The distance between the transmitter and the receiver is set at 5 cm. This is limited by the optical power of the μLED

and the small area of the photodiode (PD). It can be increased further with the addition of improved μLEDs, improved optics, an avalanche PD detector, or additional transmitter elements whose combined radiation power provides a sufficient signal-to-noise ratio (SNR) at the receiver.

B. OFDM Parameters and Operating Condition

VLC with incoherent illumination devices can only be realized as an intensity modulation and direct detection (IM/DD) system. Hence, modulation signals have to be both real and unipolar. However, conventional OFDM signals are both complex and bipolar in nature.

It is possible to obtain a real OFDM signal by imposing Hermitian symmetry in the IFFT operation during the signal generation step [2], [3]. As a prerequisite, the DC subcarrier and the π-shifted subcarrier are set to zero. In addition, half of the subcarriers are set as complex conjugates of the other half. In OFDM, a total of N_{fft} subcarriers are equally distributed in the frequency range $[-1/2T_s; 1/2T_s]$ where T_s is the sampling period in the time domain. Data loading can be omitted on some subcarriers in order to avoid interference stemming from ambient light sources and from the DC-wander effect. Subcarriers can also be left unused if SNR levels are not sufficient in a certain frequency band. The spectral efficiency of the scheme is:

$$\eta = \frac{\sum_{k=0}^{\frac{N_{\text{fft}}}{2}-1} \text{sgn}(M_k) \log_2 M_k}{N_{\text{fft}} + N_{\text{cp}}} \text{ bits/s/Hz} \tag{1}$$

where N_{fft} is the FFT size, M_k is the constellation size on the kth subcarrier, N_{cp} is the size of the cyclic prefix in the time domain, and $\text{sgn}(x)$ is the sign function. The single-sided bandwidth of the system is calculated as:

$$B = \frac{1}{2T_s} \text{ Hz} \tag{2}$$

Then, the data rate of the system is:

$$D = 2B\eta \text{ bits/s} \tag{3}$$

187

Fig. 2. Estimated: (a) channel gain; and (b) SNR.

Fig. 3. Power spectrum density of 64-QAM DCO-OFDM with the last (a) 100 and (b) 60 subcarriers unused.
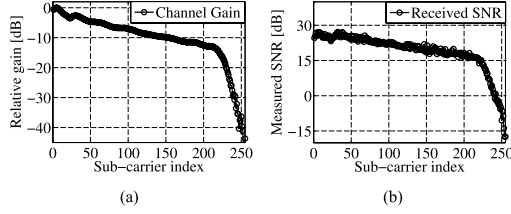
In this letter, the FFT size is N_{fft}=512. The optimal cyclic prefix length is set to N_{cp}=5 after exhaustive experiments.

A bipolar OFDM signal can be employed in an IM/DD system if a suitable DC-bias is applied [2], [3]. This allows the bipolar OFDM signal to vary around a fixed positive operating point. The resulting scheme is known as DC-biased optical OFDM (DCO-OFDM). The time-domain OFDM signal is characterized by a very high peak-to-average power ratio (PAPR), which grows with the number of IFFT points. The dynamic range of the μLED is limited in terms of a minimum and a maximum signal level. Hence, clipping of the signal on both sides of the time-domain distribution is practically unavoidable. In the current work, exhaustive experiments have determined that clipping levels at -3.2σ and 3.2σ, where σ is the standard deviation of the time-domain signal:

$$\sigma^2 = \frac{2 \sum_{k=0}^{\frac{N_{\text{fft}}}{2}-1} E_{\text{b}k} \log_2 M_k}{N_{\text{fft}}}, \qquad (4)$$

lead to an optimal utilization of the limited μLED dynamic range. In (4), $E_{\text{b}k}$ is defined as the energy per bit on the kth subcarrier. The optimal biasing point is determined to be at a voltage of V_{bias}=5.2 V which corresponds to a bias current of I_{bias}=40 mA. The peak-to-peak voltage swing of the modulating signal is set at $V_{\text{pp}} = 2.5$ V in order to utilize the full dynamic range of the μLED. The sampling frequency of the AWG is fixed at F_{s}=1.25 Gs/s, which results in a maximum achievable single-sided bandwidth of B=625MHz.

C. Channel Gain and SNR Per Sub-Carrier

Channel estimation is performed with a pilot sequence that consists of random binary phase-shift keying (BPSK) symbols with constant energy. The relative channel gain and the absolute SNR values, obtained through error vector magnitude estimation, are shown in Fig. 2 for the different frequency subcarriers. The channel attenuation follows closely the frequency profile of the μLED whose 3-dB attenuation occurs at a frequency of 60 MHz. The remaining elements in the system are guaranteed to have a flat bandwidth up to a frequency of at least 500 MHz. This assumption is supported by Fig. 2(a) where the gain factor experiences a sudden drop after subcarrier 220 which corresponds to a frequency of about 540 MHz. The estimated SNR profile of the communication channel follows closely the estimated frequency profile, see Fig. 2(b). This suggests that the additive white Gaussian noise (AWGN) distribution in the system is uniform within
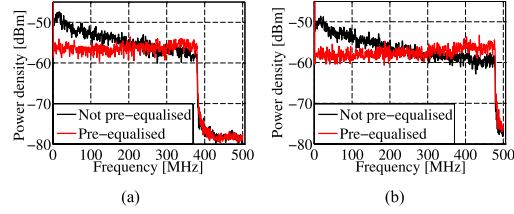
the communication bandwidth. The SNR values at the low-frequency subcarriers are slightly lower than expected. This is attributed to low-frequency noise from ambient light and from the baseline wander effect. Nevertheless, the SNR on these subcarriers is sufficient for successful communication.

III. RESULTS AND DISCUSSION

In the current study, two approaches are employed for maximizing the utilization of the μLED communication capabilities. In the first approach, a fixed M-QAM constellation size is employed on all modulated subcarriers. Energy pre-equalization is used in an attempt to equalize the achievable SNR values on each subcarrier at the receiver. In the second approach, both the constellation size and the energy on each subcarrier are determined based on the achievable SNR at that particular frequency. Based on widely-accepted results from information theory, it is expected that the adaptive bit and energy loading will exhibit better results as it provides more freedom in the signal optimization procedure [10].

A. Fixed-Rate With Pre-Equalization

Pre-equalization consists of applying the inverse function of the system frequency response on all subcarriers before transmission. This effectively scales the energy in each frequency band with the inverse of the system gain. Hence, after propagating to the receiver, all subcarriers should exhibit the same average energy level. The power spectral density (PSD) of the received signal for the case without pre-equalization and for the case with pre-equalization is illustrated in Fig. 3. This shows pre-equalization leads to uniform SNR distribution on all subcarriers. In the current experimental setup, the highest data rate with this approach can be achieved for a constellation size of M=64. Fig. 3(a) illustrates the signal PSD when the last 100 subcarriers are not used, *i.e.*, the signal bandwidth is about 380 MHz. Fig. 3(b) illustrates the case when the last 60 subcarriers are omitted, *i.e.*, the signal bandwidth reaches 480 MHz. The case in Fig. 3(a) achieves higher SNR values and so a lower bit error rate (BER) because the signal energy is distributed over a smaller frequency range. The system throughput, however, is also lower than in the case presented in Fig. 3(b) where the data rate reaches a value of D=2.8 Gb/s for a BER<0.002. Based on the recommendations of the International Telecommunication Union (ITU), it is expected that the addition of a forward error correction (FEC) code with an overhead of about 7%, such
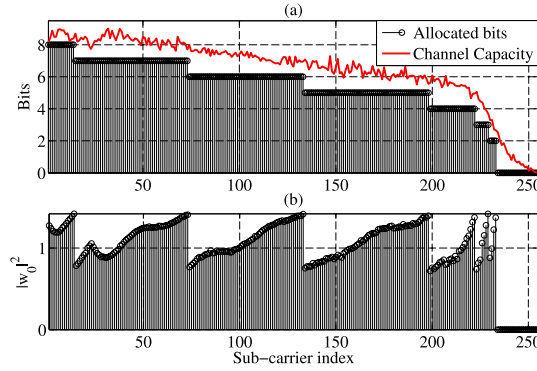
Fig. 4.   Allocated: (a) bits; and (b) energy.
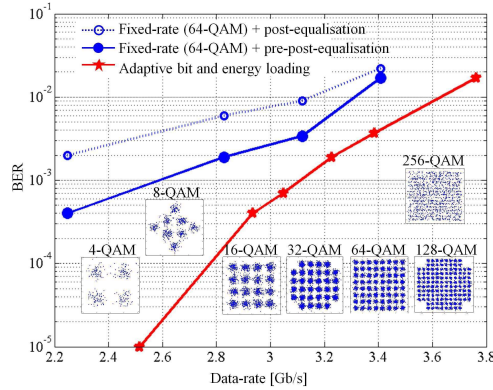
Fig. 5.   BER results and received constellations for $D=3.22$ Gb/s with adaptive bit and energy loading.

as the RS(1023,1007)/BCH(2047/1952), can guarantee reliable communication for BER<0.002 [11]. Due to the overhead, the throughput decreases to $D=2.63$ Gb/s.

B. Adaptive Bit and Energy Loading

The algorithm in the current approach is based on the work of Levin [12]. The optimal bit allocation for the current set-up can be observed in Fig. 4(a). The theoretical system capacity for the achieved SNR values on the different subcarriers is also shown [13]. The small gap between the system throughput and the capacity can only be closed through channel coding techniques. Fig. 4(b) shows the assigned energy on each subcarrier. The algorithm aims to ensure a constant SNR on all received subcarriers with the same constellation size. This optimized modulation signal achieves $D=3.22$ Gb/s with a BER<0.002. With the 7% overhead for FEC, the data rate becomes $D=3$ Gb/s. In general, reducing the data rate allows the BER to be improved even without FEC. The results are summarized in Fig. 5. The received M-QAM constellations are also shown.

IV. CONCLUSION

The feasibility of a 3-Gb/s wireless link with a single Gallium Nitride μLED is demonstrated in the current work. OFDM is employed as a modulation scheme because it allows optimal usage of a frequency-dependent communication system. Two separate approaches are tested for optimization of the communication system utilization: 1) pre-equalization; and 2) adaptive bit and energy loading. The latter is shown to be better with a maximum achieved data rate of $D=3$ Gb/s. To the best of the authors' knowledge, this is the fastest single-link wireless VLC system demonstration up-to-date.

The system throughput in the presented scenario is limited not only by the μLED properties, but also by the characteristics of the additional electrical components. The sampling rate of the AWG and the frequency response of the amplifier limit the modulation bandwidth. Work to further improve the data rate is under way. The current demonstration is performed for a narrow-field-of-view link over a 5-cm distance. The coverage can be improved with the introduction of dedicated optics as well as with ganging of multiple μLEDs in order to increase the transmitted optical power.

ACKNOWLEDGEMENT

REFERENCES

[1] D. O'Brien, G. Parry, and P. Stavrinou, "Optical hotspots speed up wireless communication," *Nature Photon.*, vol. 1, pp. 245–247, May 2007.

[2] A. M. Khalid, G. Cossu, R. Corsini, P. Choudhury, and E. Ciaramella, "1-Gb/s transmission over a phosphorescent white LED by using rate-adaptive discrete multitone modulation," *IEEE Photon. J.*, vol. 4, no. 5, pp. 1465–1473, Oct. 2012.

[3] A. Azhar, T. Tran, and D. O'Brien, "A Gigabit/s indoor wireless transmission using MIMO-OFDM visible-light communications," *IEEE Photon. Technol. Lett.*, vol. 25, no. 2, pp. 171–174, Jan. 15, 2013.

[4] F. Wu, *et al.*, "Performance comparison of OFDM signal and CAP signal over high capacity RGB-LED-based WDM visible light communication," *IEEE Photon. J.*, vol. 5, no. 4, pp. 7901507-1–7901507-7, Aug. 2013.

[5] R. Baets, D. Delbeke, R. Bockstaele, and P. Bienstman, "Resonant-cavity light-emitting diodes: A review," *Proc. SPIE*, vol. 4996, pp. 74–86, Jul. 2003.

[6] L. Geng, J. Wei, R. Penty, I. White, and D. Cunningham, "3 Gbit/s LED-based step index plastic optical fiber link using multilevel pulse amplitude modulation," in *Proc. IEEE OFC/NFOEC*, Anaheim, CA, USA, Mar. 2013, pp. 1–3.

[7] J. McKendry, *et al.*, "Visible-light communications using a CMOS-controlled micro-light-emitting-diode array," *J. Lightw. Technol.*, vol. 30, no. 1, pp. 61–67, Jan. 1, 2012.

[8] J. McKendry, *et al.*, "High-speed visible light communications using individual pixels in a micro light-emitting diode array," *IEEE Photon. Technol. Lett.*, vol. 22, no. 18, pp. 1346–1348, Sep. 15, 2010.

[9] J. Wun, *et al.*, "GaN-based miniaturized cyan light-emitting diodes on a patterned sapphire substrate with improved fiber coupling for very high-speed plastic optical fiber communication," *IEEE Photon. J.*, vol. 4, no. 5, pp. 1520–1529, Oct. 2012.

[10] J. G. Proakis, *Digital Communications*, 4th ed. New York, NY, USA: McGraw-Hill, 2000.

[11] "Forward error correction for high bit-rate DWDM submarine systems," ITU, Geneva, Switzerland, Tech. Rep. ITU-T G.975.1, Nov. 2013.

[12] H. E. Levin, "A complete and optimal data allocation method for practical discrete multitone systems," in *Proc. IEEE Global Telecommun. Conf.*, vol. 1. San Antonio, TX, USA, Nov. 2001, pp. 369–374.

[13] S. Dimitrov and H. Haas, "Information rate of OFDM-based optical wireless communication systems with nonlinear distortion," *J. Lightw. Technol.*, vol. 31, no. 6, pp. 918–929, Mar. 15, 2013.

VLC: Beyond Point-to-Point Communication

Harald Burchardt, Nikola Serafimovski, Dobroslav Tsonev, Stefan Videv, and Harald Haas

ABSTRACT

Due to the large growth of mobile communications over the past two decades, cellular systems have resorted to fuller and denser reuse of bandwidth to cope with the growing demand. On one hand, this approach raises the achievable system capacity. On the other hand, however, the increased interference caused by the dense spatial reuse inherently limits the achievable network throughput. Therefore, the spectral efficiency gap between users' demand and network capabilities is ever growing. Most recently, visible light communication has been identified as well equipped to provide additional bandwidth and system capacity without aggregating the interference in the mobile network. Furthermore, energy-efficient indoor lighting and the large amount of indoor traffic can be combined inherently. In this article, VLC is examined as a viable and ready complement to RF indoor communications, and advancement toward future communications. Various application scenarios are discussed, presented with supporting simulation results, and the current technologies and challenges pertaining to VLC implementation are investigated. Finally, an overview of recent VLC commercialization is presented.

INTRODUCTION

Since the introduction of mobile technologies over 30 years ago, wireless communications have evolved into a utility similar to water and electricity, fundamental to the socio-economic growth of modern society. To support the ever growing demand for mobile communications, cellular networks have had to evolve from simple local service providers to massively complex cooperative systems. Indeed, meeting this exponentially growing demand (Fig. 1) is the main challenge for wireless communications over the next decade(s).

LOOMING SPECTRUM CRISIS

Figure 1 illustrates the discrepancy between traffic demand and network capacity as a result of the continued proliferation of mobile communications. From Shannon's initial work in information theory, it is clear that the capacity of a wireless link (and, by extension, of a network) is directly proportional to the available bandwidth. On one hand, the system capacity in previous generations of cellular networks was diminished by limiting the spatial reuse of frequencies in an attempt to minimize interference. On the other hand, the most recent generation of wireless technologies, Long-Term Evolution (LTE) and beyond, rely on full frequency reuse along with advanced interference management algorithms to maximize the system capacity (i.e., each cell may use the entire available bandwidth). Nonetheless, in spite of employing interference management, there is a trade-off between bandwidth use and link connectivity.

Future networks are moving toward more heterogeneous architectures where multiple access points (APs) (e.g., macro-, pico-, femto-cells, relays, and/or remote radio heads) are available in each cell [1]. This will lead to even denser spatial reuse of resources. These heterogeneous networks (HetNets) provide enhanced coverage in standard cellular networks and improve the capacity of the system. As an example, Ericsson's recent acquisition of BelAir is specifically aimed at advancing Ericsson networks to heterogeneous deployments, offering "small cell" WiFi integration into traditional macro-base station (BS) coverage. Unfortunately, the increased frequency reuse introduces both inter- and intracell interference, which limits the achievable capacity of the network. To this extent, the conventional methods for capacity improvement, enhanced spatial reuse and intercell interference coordination (ICIC), will be unable to support the growing demand for mobile communications. Therefore, a new radio frequency (RF)-orthogonal communication medium is required to fill the ever increasing capacity gap.

CLOSING THE SPECTRAL EFFICIENCY GAP WITH VLC

Visible light communication (VLC) relies on the visible light (VL) spectrum for communication rather than the cluttered, scarce, and expensive RF spectra used today for wireless communications. In fact, VL is not regulated, and can therefore be used freely for communication purposes, significantly reducing the costs for operators. Thus, VLC presents a viable alternative to traditional communication methods and may be used as a complement to current RF communications [3, 4].

Harald Burchardt and Nikola Serafimovski are with pureLiFi Ltd.

Dobroslav Tsonev, Stefan Videv, and Harald Haas are with the University of Edinburgh.

Furthermore, recent studies indicate that a substantial portion (> 70 percent) of wireless traffic originates indoors [5]. Signal propagation through walls, however, severely inhibits the operation of indoor data services, which is attracting considerable interest in providing wireless communications directly indoors. Indeed, VLC is well suited to fill this function as:
• Most indoor environments are illuminated.
• VL cannot penetrate solid objects.
• VL can easily be directed through optics.
• As previously mentioned, it is interference-orthogonal to the cellular network.

These characteristics permit very close spacing between VLC nodes, thereby increasing the spatial reuse of resources, providing higher data density, and resulting in increased network capacity. In addition, in an attempt to reduce the carbon footprint of the information and communication technology (ICT) industry, there has been a research drive for more energy-efficient networks [6]. In this context, another advantage of VLC systems is that the energy used for communication in VLC is essentially free due to the lighting requirement(s) of indoor spaces; that is, no extra energy is required for information transmission, with minimal additional power to drive the necessary circuitry for communication.

DIFFERENCES BETWEEN RF AND VLC

Although both VL and RF communication employ electromagnetic radiation as the information medium, the two concepts differ significantly in their inherent properties. Waves in the visible region of the spectrum cannot penetrate through most surfaces that are present in everyday surroundings. Radio waves, on the other hand, are particularly apt at providing sufficient connectivity through the majority of commonly used materials. As previously mentioned, this offers very interesting benefits. Information may be contained within the confined space of the specific premises where a VLC system is deployed. This practically eliminates the possibility of casual eavesdropping. More important, it eliminates interference between spatially isolated communication systems, removing one of the biggest challenges in RF communications.

With the current state of off-the-shelf illumination components and photodetectors, VLC is realizable as an intensity modulation and direct detection (IM/DD) scheme. This means that only the signal intensity is used to convey information, which although more limiting than RF, is also advantageous. The wavelength of VL (380 nm to 750 nm) is much smaller than the typical area of a photodetector, which effectively removes multipath fading (as opposed to RF communication) from the system. In addition, signals in the optical domain do not interfere with the operation of sensitive electronic systems and can be used in a variety of applications where RF is not allowed, e.g., hospitals, aircraft, chemical plants). Indeed, the goal of VLC is not to replace RF, but rather to complement it in the context of HetNets where the best of both physical domains and resulting propagation characteristics are employed.
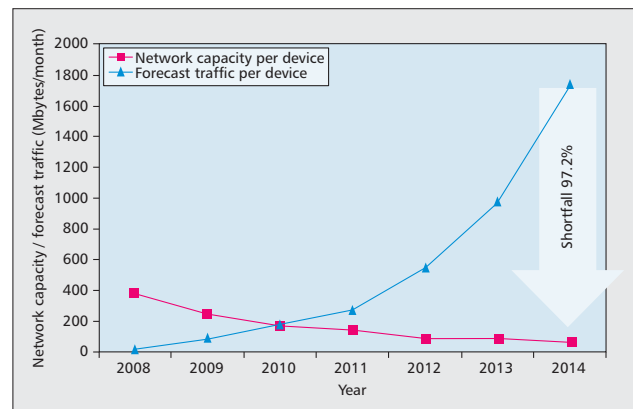
Figure 1. The predicted, almost exponential, increase in demand of mobile communications services over the last few years [2] and the corresponding network capacity evolution. (Source: GBI Research.)

POTENTIAL APPLICATIONS FOR VLC

INFRASTRUCTURE

Wireless HetNets are widely seen as the future of mobile communications, as smaller and smaller cells are used to offload and localize traffic. Indeed, the simple concept of cell-size reduction has increased the system spectral efficiency by a factor of 2700 over the last 50 years [7]. To this extent, even smaller VLC atto-cells are just a logical progression to provide the next 1000 times system capacity increase. There are two important aspects to consider with small cells, the first being coordination with the macro network, and the second the integration of WiFi capabilities with Third Generation Partnership Project (3GPP) technologies. This enables, for example, mobile users to connect to WiFi APs automatically based on authentication information held in a mobile operator's customer database.

In this context, the term "light fidelity (Li-Fi)" is defined as the subset of VLC that exhibits *high-speed*, *bidirectional*, and *fully networked* communications; the Li-Fi Consortium has already begun promoting this technology. Li-Fi is envisioned to fill a complementary role along with WiFi to offload traffic from the macro BSs. The key to a high-performing system is not merely to increase the link-level spectral efficiency. In fact, the most relevant aspect to a mobile vendor is the area spectral efficiency (ASE), that is, what mobile data rates can be offered for each user. In this context, Li-Fi is shown to provide at least an order of magnitude improvement in the ASE [8]. In addition, one of the key obstacles to the widespread application and integration of WiFi in modern communication systems is the interoperability of the 3GPP technology with the WiFi standards. Principally, Li-Fi requires adapting only the front-ends and physical layers of typical femto- or picocells, while the above-lying protocols, authentication, channels, and so on can remain (fundamentally) unchanged.

However, a VLC standardization drive would

VLC could also enable indoor as well as improve city canyon navigation where GPS signaling is weak or nonexistent. Due to the simplicity of its front-end hardware, it can play a significant role in enabling the Internet of Things and machine-to-machine communications in general.

need to account for some of the VL-specific problems such as intra- and inter-frame flicker, dimming, visibility patterns, and others. The new standard, which would be based around orthogonal frequency-division multiplexing (OFDM), could stipulate that only subcarriers above a certain frequency may be used for modulation. In this manner, the system would always avoid flicker issues. Similarly, dimming could be achieved by reducing the average signal power. For example, if direct-current-biased optical OFDM (DCO-OFDM) is used, it would mean a lower biasing point, as well as potentially shallower modulation depth for the signal (of course, this may result in a diminished signal-to-noise ratio, SNR). This facilitates rapid development and deployment of Li-Fi technology complementary to the current RF BSs with unique advantages (i.e., high ASE, security, and lack of electromagnetic interference, as mentioned earlier). To this extent, the future implementation of VLC technology should focus on retaining the system architectures outlined in 3GPP and be designed to comply with such standards.

A well designed HetNet should make use of its elements in an efficient manner. Each link in the network is employed when it is most relevant for the respective task. Just as optical fibers and cables are most appropriate for high-speed backbone functionality, and RF communication is suitable for APs with good coverage, VLC communication is best suited for high data rates, and a secure interface between a BS and a mobile station (MS). Such a connection is not needed constantly. A lot of the time, a mobile device is simply dormant, waiting for an incoming data transmission or for the user to request one. For these tasks to be negotiated successfully, a constant connection is required. Such a connection can be provided by the existing well established RF connectivity. The heavy load of the high-speed data transfer can then be allocated to the VLC network. If a VLC connection is not possible, the MS may be served with RF until an appropriate optical AP is nearby.

Finally, the discussion regarding the practicality, performance, and future of VLC is not constrained by the underlying technology of the physical illumination devices. Currently, the most widespread devices are traditional light emitting diodes (LEDs); however, other technologies are emerging as well — organic-based LEDs, micro-LEDs, as well as resonant cavity LEDs — which are fundamentally all electronics devices capable of data transmission. Thus, the research community is investing significant effort into manufacturing devices that are capable of simultaneous illumination and communication.

OTHER APPLICATIONS FOR VLC

VLC could also enable indoor as well as improve city canyon navigation where GPS signaling is weak or nonexistent. Due to the simplicity of its front-end hardware, it can play a significant role in enabling the Internet of Things and machine-to-machine communications in general. Car-to-car communications [9] may be one of the first implementation scenarios as manufacturers are beginning to make a move toward solid-state lighting solutions.

Other possible areas that stand to benefit from the practical implementation of VLC include museums, hospitals, and underwater communications [2, 10]. Museums could exploit the already present light fixtures to not only illuminate their exposition pieces, but also continuously transmit information about them. This could redefine the way automated tours are executed. Hospitals could achieve ubiquitous networking without any detriment to equipment that is sensitive to RF radiation. This should improve hospital care and reduce staff workload.

Underwater communications stand likely to benefit most. RF and sound communication are unable to provide fast wireless connectivity under water. Although VLC will also face challenges in that particular propagation environment, it should deliver significant data rate improvements when conditions allow, and otherwise fall back to existing technology (e.g., sound waves) to provide basic connectivity.

CHALLENGES OF VLC PRACTICAL IMPLEMENTATION AND INTEGRATION

MODULATION

Realization of VLC as an IM/DD system means that only positive and real signals can be successfully transmitted. This limits the modulation schemes that can be employed. Early work in the field suggested on-off keying (OOK) and pulse-position modulation (PPM) as viable techniques. However, the bandwidth of the front-end elements and the optical channel is limited. This leads to the requirement for multi-level schemes like unipolar pulse-amplitude modulation (PAM) in order to achieve higher throughput. As the communication speeds increase, the limited communication bandwidth leads to intersymbol interference (ISI). Hence, a more sophisticated scheme like OFDM becomes the prime candidate for VLC.

Conventional OFDM generates complex bipolar signals. Therefore, modifications have to be made before it becomes suitable for VLC. A commonly accepted method to generate a real time domain OFDM signal is to impose Hermitian symmetry on the carriers in the frequency domain. The resulting waveform, however, is still bipolar and needs to be modified further. A number of different techniques for the creation of unipolar signals exist. A straightforward approach is called DCO-OFDM. It involves the addition of a bias current to the bipolar signal, making it unipolar [11]. However, the addition of the direct current (DC)-bias increases the power dissipation of the time domain signal significantly when compared to the bipolar case.

In order to avoid this DC bias, alternative techniques such as asymmetrically clipped optical OFDM (ACO-OFDM) exploit the properties of the OFDM frame to generate a signal that does not need biasing. In ACO-OFDM, only the odd subcarriers in the frequency domain are modulated, which leads to a symmetric time domain signal [11]. The symmetry allows negative values to simply be set to zero without affecting the encoded information as all distortion falls on the even subcarriers in the frequen-

cy domain. Other similar approaches that exploit different properties of the OFDM frame but effectively achieve the same result are: PAM discrete multitone modulation (PAM-DMT), unipolar OFDM (U-OFDM), and flip-OFDM.

A modulation signal can be linearly encoded in the current that flows through an LED. The relationship between the current and the emitted light is not linear, as illustrated in Fig. 2. OFDM-based systems are particularly sensitive to the described nonlinear effects due to their high peak-to-average power ratio (PAPR). One approach to counter nonlinearity is to operate the LED in a small range where its output characteristic is linear enough. However, the dispersive nature of non-coherent light and the resulting high path loss require the use of as much of the device active region as possible. Another approach is to pre-distort the signal such that the output of the LED has the desired shape. This, however, is limited by the accuracy of the digital-to-analog conversion and inconsistencies in the nonlinearity of the LED output characteristic. Currently, the question of combating nonlinearity is one of the biggest challenges for VLC systems.

MULTIPLE ACCESS

As with any communication system, however, the ability to serve multiple users is crucial. Both time-division multiple access (TDMA) and code-division multiple access (CDMA) are viable alternatives for addressing the multiple access limitation of Li-Fi. Indeed, TDMA was utilized within the OMEGA project for the optical wireless medium access control (MAC) [12], whereas optical CDMA uses codes to separate users over the channel. To this extent, the underlying modulation scheme is irrelevant for enabling multiple access in an optical wireless system.

However, since OFDM is widely considered as the most viable modulation technique for VLC, orthogonal frequency-division multiple access (OFDMA) is the natural extension to provide multiple access. OFDMA can be employed in VLC in a similar manner to RF communications, where each user is allocated a portion of the total available subcarriers in each time slot. Furthermore, subcarrier allocations may be varied over time, such that users' potentially varying traffic requirements and channel conditions can be accommodated.

It should be noted that due to the constraints of VLC (Table 1), not all OFDM subcarriers are available for communication, as discussed earlier. However, this will not retard the multiple access capabilities of the system, but simply limit the number of subcarriers allocatable to each user.

UPLINK

In general, most demonstrations of VLC technology up until now have focused on maximizing the communication speed over a point-to-point *unidirectional* channel [2, 10]. However, in order to realize the envisioned Li-Fi communication systems, it is clear that the first logical step is the establishment of bidirectional communication (i.e., uplink transmission). This is not straightforward, as employing the same VL band in both
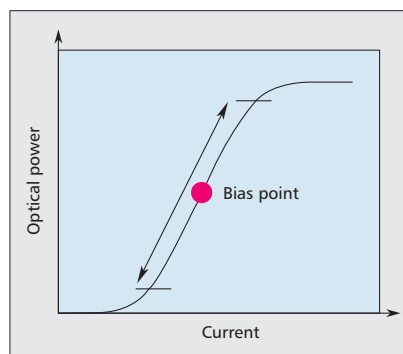
Figure 2. Typical LED output characteristic is nonlinear in three aspects: i) a minimum current is required for photon emission to occur; ii) light emission saturates after a certain current level; and iii) the relationship between current and light output intensity is nonlinear even within the range between minimum and maximum allowed current.

System	Information	Signal	
RF	Carried on electric field	Complex valued	Bipolar
VLC	Carried on optical intensity	Real valued	Unipolar

Table 1. RF vs. VLC.

directions would result in large self-interference at a transceiver due to cross-talk, unless physical separation of the photo diode (PD) and LED can be administered. However, just as in RF communications, there are two methods to support this bidirectionality: time-division duplexing (TDD) and wavelength-division duplexing (WDD) (termed frequency-division duplexing, FDD, in RF).

WDD employs separate (non-overlapping) frequency bands for downlink and uplink, such that cross-talk between a transceiver's LED and PD is eliminated. For example, the near-infrared band may be utilized for uplink transmission, avoiding interference to/from the VL band. However, because this band is outside the visible region, eye safety must be ensured by transmit power limitation. TDD, on the other hand, allows the use of the same VL band, but downlink and uplink are not performed simultaneously. But a VL transmitter at the device may be uncomfortable from a user perspective, and the power requirements for such a source may make it impractical for device integration.

Finally, another perspective to solve this problem is to make use of the already existing infrastructure (i.e., RF communication). Through the proliferation of WiFi and mobile connectivity, the VLC downlink is maintained while essentially piggybacking the RF networks in order to provide uplink transmission. However, seamless connectivity between networks and fixed mobile convergence are long-standing problems in RF, and therefore, this must be
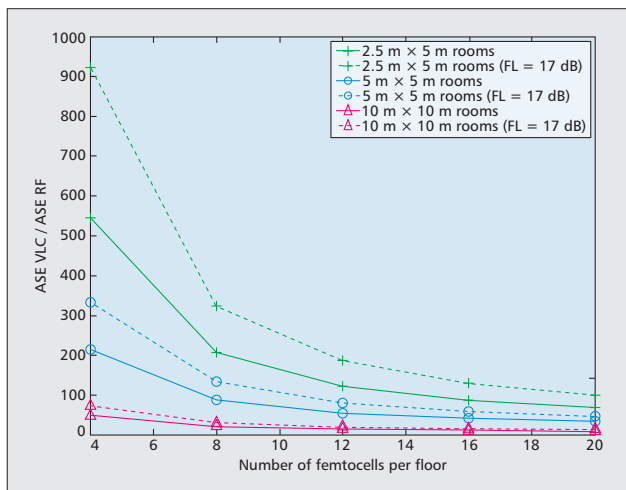
Figure 3. The ratio of VLC ASE and RF ASE for different floor layouts.

solved before Li-Fi can be properly integrated in future RF HetNets.

RESULTS

This section present results from previous studies, indicating the enormous potential VLC has for future networks in a multitude of application scenarios.

HETNET ASE

Earlier, the evolution of wireless networks toward heterogeneous architectures is described, where multiple tiers of communication can be located within the area normally served solely by a macrocell. The reduced spatial separation when reusing the RF spectra results in more interference; using Li-Fi indoors can mitigate this interference.

In [8], a comparison of the achievable ASE of RF femtocells and a VLC network in a two-tier HetNet is examined, yielding the results displayed in Fig. 3.

Depending on the size of the apartments emulating the indoor environment (proportional to the number of walls) and the number of femto-APs allocated in the building, a Li-Fi system can achieve over 900 times the ASE of a corresponding femtocell network. Of course, this gain diminishes for larger rooms and additional femtocells; nonetheless, Fig. 3 shows that this gain is always positive, indicating a unanimous benefit when utilizing non-interfering VL spectrum rather than RF.

MULTI-BAND COVERAGE

In the early days of mobile communications, a cellular network was generally separated into clusters, within which the system bandwidth was split and divided among neighbouring cells to mitigate co-channel interference (CCI). The latest generation of wireless technologies, however, employ full frequency reuse, using intelligent ICIC to control interference.

One of the core advantages of VLC is the vast available spectrum in comparison to RF. Instead of having to divide a set system bandwidth into multiple orthogonal bands, it is now possible to simply add a non-overlapping section of VL spectrum, and thus not only enhance the system bandwidth, but also curtail CCI caused by dense spatial reuse.

Such a process is described in [13], with the results shown in Fig. 4. By adding additional wavelengths, it is evident from Fig. 4 that:
• The dead zones in the coverage area are substantially reduced.
• The achievable signal quality (and consequently rate) have been significantly augmented.

Moreover, the utilization of multiple VL spectra allows for enhanced data density, as physically overlapping cells can transmit on different frequencies and increase the available bandwidth per unit area, and thus the ASE.

INITIAL MULTIPLE-INPUT MULTIPLE-OUTPUT INVESTIGATION

The finite bandwidth of front-end devices limits the speed of a communication system. Different laboratory experiments have shown communication capability of a single link up to 3 Gb/s [10]. However, in order to go well beyond the Gb/s rate, it is likely that multiple-input multiple-output (MIMO) would need to be employed in VLC.

Currently, there are two possible implementations of MIMO receiver systems, one based on PDs and the other on imaging type sensors. Utilizing PDs has the advantage that the hardware implementation is relatively simple. On the other hand, imaging sensors facilitate easy separation of MIMO channels. However, the speed and accuracy of their present hardware implementations considerably limit their application in VLC-MIMO.

Recent studies of MIMO have shown that for a well distributed configuration of transmitters, receiver elements with angle diversity have the potential to reach very high communication capacity that scales almost linearly with the MIMO order employed [14]. Figure 5 illustrates two possible MIMO configurations and the corresponding capacity distributions across an empty 5 m × 5 m × 3 m room for three different heights of the receiver. As apparent from the results, the capacity is distributed quite uniformly and grows about linearly with the number of MIMO elements. This stems from the possibility to isolate information streams in space.

The concept of spatial modulation (SM) and spatial shift keying (SSK) are shown to be particularly applicable in an optical wireless system [15], where a low-complexity multiple-transmitter generalized SSK (GSSK) signaling technique for short-range indoor VLC is presented. In a transmitter with N_t number of transmit elements, this signaling technique is capable of achieving a spectral efficiency of N_t b/s/Hz. GSSK supplies higher spectral efficiency than the conventional OOK and PPM techniques. Moreover, the GSSK transmitter is much simpler than that of an equivalent regular PAM system with similar

spectral efficiency, avoiding challenges such as LED nonlinearity.

CHALLENGES OF VLC COMMERCIALIZATION

If VLC is to become widespread, a number of challenges pertaining to its commercialization must be addressed. In particular, the drive toward an industry standard, possible market penetration, and applications must be considered. A number of suitable application scenarios are identified later. However, these applications must offer a sufficient incentive for potential companies, and the standard must look ahead of the current technology.

STANDARDIZATION

Some consideration has already been given to VLC standardization. Most notably, the IEEE 802.15.7 standard was established in 2009 for short-range optical wireless communications using VL where the physical (PHY), MAC, and logical link control (LLC) layers are specified with very high associated LED bandwidths. Furthermore, the VLC Consortium (VLCC) has developed several standards for VLC, published by the Japanese electronics standards body. In addition, the Infrared Data Association (IrDA) has created standards for point-to-point short-range optical communications, with data rates from 1 Gb/s.

However, recent research showing successful use of OFDM for VLC may drive the need for new standardization. By considering O-OFDM, chiefly enabled through the use of variable current drivers and first demonstrated as a viable transmission technique at TED Global in 2011, a VLC system can achieve significant improvements in spectral efficiency, and simplify both multiple access and mobility considerations. Because the PHY layer of an O-OFDM system is so different from the existing VLC standards, the MAC and associated higher layers are also different. Therefore, if O-OFDM is to be at the heart of the latest evolution of VLC, a new standardization drive is required. The nature of O-OFDM means that only the optical front-end and lower-level PHY would require changes to seamlessly integrate a VLC system with the existing higher-layer definitions of either LTE or 802.11. However, the potential of VLC is in the PHY layer with the same features as cellular communication, where it can replace the standard RF front-end with an optical alternative. This consideration means that VLC can rely on readily available IEEE 802.11 or LTE protocol stacks. By removing the need to standardize the entire communication system, VLC may be employed in a large-scale network with minimal infrastructure and coordination efforts. Such a combination narrows the focus of any standardization effort. In addition, since the publication of the IEEE 802.15.7 standard, research in the area of VLC has increased. Among the key findings are the increased system performance resulting from the application of both OFDM and the MIMO concept, which emphasizes the need for a new industry-driven standard.
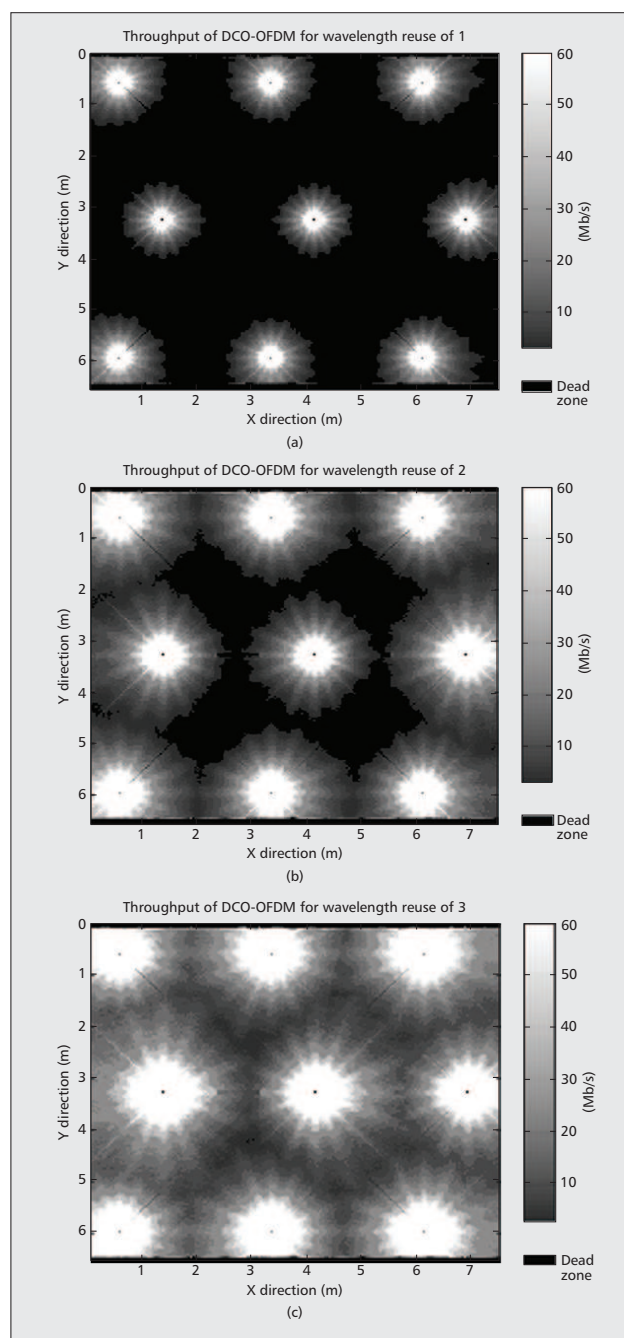
Figure 4. Throughput of DCO-OFDM estimated via a Monte Carlo ray-tracing global irradiation simulation in a computer-aided design airplane cabin model. Signal contributions from both line-of-sight and non-line-of-sight propagation paths are considered. Wavelength sets of [940 nm], [940 nm, 870 nm], and [940 nm, 870 nm, 840 nm] are employed in the different scenarios with wavelength reuse factor of 1, 2, and 3, respectively: a) wavelength reuse of 1; b) wavelength reuse of 2; c) wavelength reuse of 3.
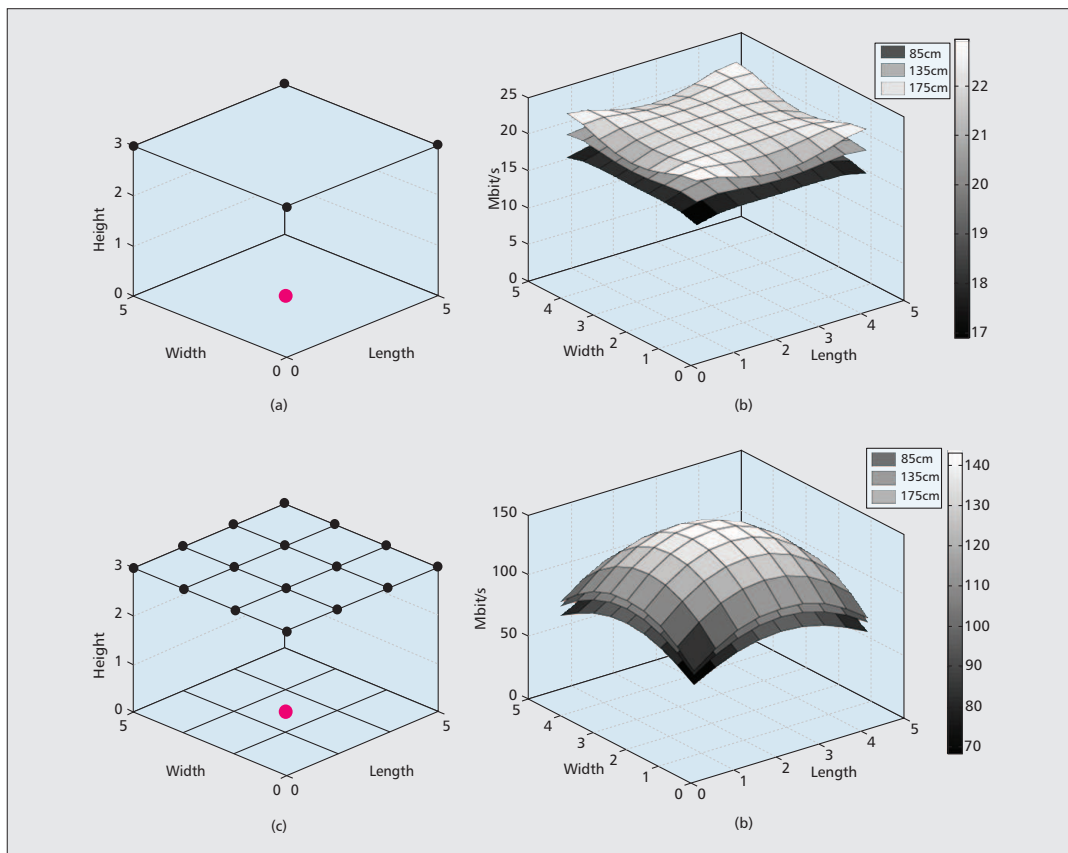
Figure 5. Transmitter layout and room capacity for different MIMO configurations. Black dots indicate transmitter positions, the red dot on the floor their directions. Emission pattern is Lambertian. High-power off-the-shelf illumination devices are assumed, limiting the capacity to well below the values reported in laboratory experiments: a) 4 × 4 MIMO configuration; b) capacity distribution for 4 × 4 MIMO; c) 16 × 16 MIMO configuration; d) capacity distribution for 16 × 16 MIMO.

MARKET CONDITIONS

Despite the need for standardization, companies are actively working on commercializing VLC technology. The VLC market is projected to grow as LED lighting becomes more prolific. The VLC market applications have been outlined. In addition, VLC is particularly well suited to provide last mile connectivity; indeed, projects such as the Reasonable Optical Near Joint Access (RONJA) initiative are deployed to service this demand. Furthermore, the U.S. Department of Energy estimates that faster adoption rate of LED lighting in the United States over the next 20 years can deliver energy savings of about US$265 billion and reduce the demand for lighting electricity by 33 percent in 2027. This highlights the inevitable growth and proliferation of LED devices along with the associated VLC market potential [2].

The VLC link is untethered in the sense that a user is independent of any one AP and can acquire the same information from other optical APs, providing mobility and seamless handover. Moreover, each communication link can serve multiple distinct user devices. This is the future of indoor Li-Fi applications, which at present are providing data connectivity in point-to-point scenarios. Nonetheless, indoor networking applications account for the largest overall market share. This market for VLC is expected to grow further from around US$83 million in 2012 to around US$4.5 billion in 2018, increasing at a rate of around 84 percent annually from 2013 to 2018. To this extent, indoor network applications compose around 70 percent of the global VLC market, and the growth of indoor commercial connectivity will be the major driver of this market [10].

CONCLUSION

In this article, VLC has been introduced as a unique and viable alternative to RF indoor communication strategies, and furthermore a plethora of application scenarios for future systems have been presented. VLC furthers the concept of ever smaller cells to deliver wireless data at exponentially increasing rates, now and in the future. It is clear that wherever there is man-made light, there

is an opportunity for high-speed wireless connectivity complementary to RF networks and thus interference-free. Furthermore, the vast unused VL spectrum can provide the necessary bandwidth to meet the ever growing demands for mobile traffic. The fact that more secure indoor networks can be established through VLC is a further advantage. VLC, it seems, is destined to provide ubiquitous wireless access in the next generation(s) of mobile communication.

Being a relatively modern technology, there are, of course, many challenges that VLC systems are currently facing. Apart from the inherent nonlinearity of LEDs and limits of LED bandwidth, aspects such as signal modulation, power delivery to the transceiver, and multiple access pose difficulties for the immediate proliferation of VLC. However, since such technical challenges have already been conquered in RF through decades of research, VLC is well equipped to go along a similar but much accelerated path. Furthermore, while the current abundance and maturity of RF communications may impede the commercialization and standardization of VLC technologies, there is no doubt that VLC will be needed in future communications generations. Thus, its proliferation has already begun.

REFERENCES

[1] D. Lopez-Perez *et al.*, "Enhanced Intercell Interference Coordination Challenges in Heterogeneous Networks," *IEEE Wireless Commun.*, vol. 18, no. 3, June 2011, pp. 22–30.

[2] "Visible Light Communication (VLC) — A Potential Solution to the Global Wireless Spectrum Shortage," GBI Research tech. rep., 2011; http://www.gbiresearch.com/.

[3] M. B. Rahaim, A. M. Vegni, and T. D. C. Little, "A Hybrid Radio Frequency and Broadcast Visible Light Communication System," *Proc. IEEE GLOBECOM 2011 Wksps.*, Dec. 5–9 2011, pp. 792–96.

[4] J.-P. Javaudin *et al.*, "OMEGA ICT Project: Towards Convergent Gigabit Home Networks," *Proc. IEEE PIMRC 2008*, Cannes, France, Sept. 15–18 2008, pp. 1–5.

[5] V. Chandrasekhar, J. Andrews, and A. Gatherer, "Femtocell Networks: A Survey," *IEEE Commun. Mag.*, vol. 46, no. 9, 2008, pp. 59–67.

[6] G. Auer *et al.*, "How Much Energy Is Needed to Run a Wireless Network?," *IEEE Wireless Commun.*, vol. 18, no. 5, 2011, pp. 40–49.

[7] W. Webb, *Wireless Communications: The Future*, Wiley, 2007.

[8] I. Stefan, H. Burchardt, and H. Haas, "Area Spectral Efficiency Performance Comparison between VLC and RF Femtocell Networks," *Proc. IEEE ICC*, Budapest, Hungary, June 2013, pp. 1–5.

[9] N. Kumar *et al.*, "Visible Light Communication for Intelligent Transportation in Road Safety Applications," *Proc. Int'l. Wireless Commun. and Mobile Computing Conf.*, 2011, pp. 1513–18.

[10] Markets and Markets, "Visible Light Communication (VLC)/Li-Fi Technology & Free Space Optics (FSO) Market (2013–2018)," tech. rep., Jan. 2013.

[11] J. Armstrong and A. Lowery, "Power Efficient Optical OFDM," *IEEE Electronics Letters*, vol. 42, no. 6, Mar. 16, 2006, pp. 370–72.

[12] "ICT-213311 OMEGA: Deliverable D4.3 Optical Wireless MAC Specification," http://www.ict-omega.eu/publications/deliverables.html, Nov. 2009; accessed Oct. 2013.

[13] S. Dimitrov *et al.*, "On the Throughput of an OFDM-Based Cellular Optical Wireless System for an Aircraft Cabin," *Proc. Euro. Conf. Antennas and Propagation*, Rome, Italy, Apr. 11–15 2011, invited paper.

[14] D. Tsonev, S. Sinanović, and H. Haas, "Practical MIMO Capacity for Indoor Optical Wireless Communications," *VTC Spring*, Dresden, Germany, June 2–5 2013, pp. 1–5.

[15] W. Popoola, E. Poves, and H. Haas, "Error Performance of Generalised Space Shift Keying for Indoor Visible Light Communications," *IEEE Trans. Commun.*, 2013, pp. 1–9.

BIOGRAPHIES

HARALD BURCHARDT (harald.burchardt@purelifi.com) received his B.Sc. in electrical engineering and computer science in 2007 from Jacobs University Bremen, Germany, and his M.Sc. in communications engineering in 2009 from the Technical University of Munich. He recently completed his Ph.D. degree at the Institute for Digital Communications, the University of Edinburgh, United Kingdom, where the focus of his research was on interference management in heterogeneous networks. He is currently working for pureLi-Fi as the director of product management, working with major companies to assist them in integrating Li-Fi technology. His experience includes DoCoMo Euro-Labs and Rohde & Schwarz GmbH in Munich, Germany; he holds a patent and has filed three more in the field of communications engineering.

NIKOLA SERAFIMOVSKI (nikola.serafimovski@purelifi.com) is currently working for pureLiFi as the director of product marketing. His experience with T-Mobile and T-Home in Macedonia focused on mobile network deployment and analysis as well as database application development. He worked for the UK-China Science Bridges project to successfully demonstrate the world's first practical implementation of the spatial modulation MIMO concept. He received a B.Sc. in electrical engineering and computer science and an M.Sc. in communications, systems, and electronics, both from Jacobs University Bremen. He earned his Ph.D. in digital communications and signal processing from the University of Edinburgh.

DOBROSLAV TSONEV [S'11] (d.tsonev@ed.ac.uk) received his B.Sc. degree in electrical engineering and computer science in 2008 from Jacobs University Bremen and his M.Sc. degree in communication engineering with a specialization in electronics in 2010 from the Munich Institute of Technology. Currently, he is pursuing a Ph.D. degree in electrical engineering at the University of Edinburgh. His main research interests lie in the area of optical wireless communication with an emphasis on visible light communication.

STEFAN VIDEV (s.videv@ed.ac.uk) received his B.Sc. in electrical engineering and computer science in 2007 from Jacobs University, and his M.Sc. in communications, systems, and electronics in 2009 from the same university. He was awarded his Ph.D. in 2013 for his thesis, *Techniques for Green Radio Cellular Communications*, from the University of Edinburgh. He is currently employed as a research fellow at the University of Edinburgh and working in the field of visible light communications. His research focus at the moment is on indoor VLC, and his interests include prototyping high-speed communication systems, smart resource allocation, and energy-efficient communications.

HARALD HAAS [SM'98, AM'00, M'03] (h.haas@ed.ac.uk) holds the Chair for Mobile Communications at the University of Edinburgh. He has pioneered and coined Li-Fi listed among the 50 best inventions in *Time Magazine* 2011. He was an invited speaker at TED Global 2011, and his talk has been watched online more than 1.4 million times. His research interests are in optical wireless communications, interference management in cellular systems, and large-scale MIMO systems. He holds 23 patents, and has published 270 conference and journal papers. Recently, he has been awarded the prestigious Established Career Fellowship from the Engineering and Physical Sciences Research Council (EPSRC) of the United Kingdom. He is cofounder and CSO of pureLiFi Ltd. He was the recipient of the Tam Dalyell Prize 2013 awarded by the University of Edinburgh for excellence in engaging the public with science.

Enhanced Subcarrier Index Modulation (SIM) OFDM

Dobroslav Tsonev, Sinan Sinanovic and Harald Haas

Institute for Digital Communications, Joint Research Institute for Signal and Image Processing,
The University of Edinburgh, EH9 3JL, Edinburgh, UK
Email: {*dtsonev,s.sinanovic, h.haas*} @ed.ac.uk

Abstract—**A novel modulation technique coined SIM-OFDM was recently proposed. SIM-OFDM uses different frequency carrier states to convey information and leads to increased performance in comparison to conventional OFDM. Additionally, its innovative structure can lead to a decrease of the peak system power, which is highly beneficial in the context of optical wireless communication. One of the issues of the original SIM-OFDM scheme is a potential bit error propagation which could lead to significant burst errors. The current paper proposes a modified technique which avoids bit error propagation whilst retaining the benefits of the concept.**

I. INTRODUCTION

SIM-OFDM is a modification of the classical OFDM modulation scheme. In OFDM a number of different frequency carriers are modulated with a signal from a scheme such as Quadrature Amplitude Modulation (QAM). The novel approach of SIM-OFDM tries to exploit an additional "new" dimension in the OFDM frame coming from the state of each subcarrier – active or inactive. This additional dimension is employed to transmit information in an On-Off Keying (OOK) fashion. A detailed description of SIM-OFDM can be found in [1].

The motivation behind this new concept lies in an attempt to optimize power usage, which is crucial in the current climate of "green communication systems" [2]. Each active carrier receives the energy of an M-QAM symbol and the energy of the additional bit encoded in OOK fashion. The individual performances of QAM and OOK are thus improved. Overall, this leads to performance improvement of SIM-OFDM on an energy-per-bit basis.

SIM-OFDM is still a rather unexplored topic. An analytical approach towards deriving its performance in a fading channel is given in [1]. The same paper reports that SIM-OFDM has the potential to outperform the traditional OFDM modulation scheme in terms of bit error rate (BER). However, to the best of our knowledge, a complete analytical description of its BER performance does not exist in literature. SIM-OFDM suffers from bit error propagation in the presence of Additive White Gaussian Noise (AWGN). This work provides a proposition for a modified scheme which solves the issue of bit error propagation. A further benefit of our modified approach is reduction of the Peak-to-average power ratio (PAPR) which comes from the new enhanced structure of SIM-OFDM.

The rest of this paper is organized as follows. Section II gives a brief description of the SIM-OFDM modulation scheme and its demodulator. Section III describes the new enhanced modulation scheme. Section IV shows an analytical BER derivation of the enhanced SIM-OFDM. Section V presents the numerical simulation results, which demonstrate the close match between analysis and Monte Carlo simulations of the system performance. Section VI discusses the PAPR of the modified approach. Finally, section VII gives concluding remarks to the topic.

II. SIM-OFDM
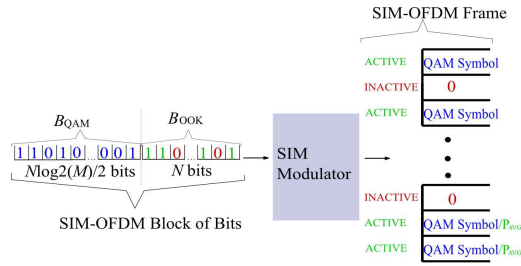
Fig. 1. SIM-OFDM carrier modulation scheme. Assumption for this example is that 1 is the majority bit in B_{OOK}

In SIM-OFDM the incoming bit stream is divided into blocks of bits, each having a length of $N(\frac{\log_2(M)}{2}+1)$, where N is the number of subcarriers, and M is the constellation size of the respective M-QAM modulation scheme. Each of these blocks is divided into two parts. The first N bits of the block form a subblock, which in the rest of this paper will be refered to as B_{OOK}. The remaining $N\frac{\log_2(M)}{2}$ bits form a second subblock, which will be refered to as B_{QAM}. This is further illustrated in Fig. 1. Before transmission B_{OOK} is inspected and the majority bit type is determined by checking which bit value, 1 or 0, has more occurences. This is done because all carriers which have the same position inside the OFDM frame as the bits from the majority bit type in B_{OOK} will be classified as "active", and the rest will be classified as "inactive". Inactive carriers are given the amplitude value $0 + j0$ where $j = \sqrt{-1}$. The first $\frac{N}{2}$ active carriers will be given amplitude values corresponding to M-QAM constellation symbols necessary to encode B_{QAM}. The remaining active carriers can be used to signal to the receiver what the majority bit type of B_{OOK} is, and they will be assigned a signal whose power is equal to the average power for the given M-QAM scheme. This is followed by an N-point Inverse Fast Fourier Transform (IFFT) in order to obtain the time-domain signal. A slight modification of SIM-OFDM suggests that majority bit type can be signaled either through secure communication

channels, or by reserving one particular frequency carrier and transmitting the desired value with sufficiently high signal-to-noise ratio (SNR). This leads to a slight improvement in the SIM-OFDM performance.

Upon reception, the signal is transformed using a Fast Fourier Transform as in traditional OFDM. Then all subcarriers are inspected. Those subcarriers whose power is above a certain threshold are marked as active, and the rest are marked as inactive. Then B_{OOK} is reconstructed from the detected states of the carriers and the known majority bit type. Afterwards, the first $\frac{N}{2}$ active carriers are demodulated according to the respective M-QAM scheme in order to reconstruct B_{QAM}.

There are two main issues which limit the performance of SIM-OFDM. First, an OOK detector at the destination requires the usage of a threshold. The threshold, however, needs to be below the power of the M-QAM symbol with the lowest power. Otherwise, any symbol below the threshold would be unrecognizable even in high SNR conditions, and that would lead to an error floor above zero. On the other hand, a low threshold requirement diminishes the advantage of OOK when a higher order M-QAM scheme is used. This happens because even though on average a lot of power is used in a subcarrier for higher order M-QAM, the threshold needs to be below the smallest symbol power. Hence, the system's ability to correctly distinguish subcarrier states does not improve significantly since the threshold cannot change much. Second, an incorrect detection of a carrier state not only leads to incorrect demodulation of the M-QAM symbol it encodes, but also to incorrect demodulation of all subsequent QAM symbols. This happens because an incorrect detection of a carrier state changes the order in B_{QAM} and misplaces all subsequent bits in that part of the frame. This effect has the biggest impact on the BER performance. Effectively, in order to demodulate an M-QAM symbol correctly, it is necessary not only to detect its carrier as active, but also to have detected any previous carriers – active or inactive – correctly. As the total number of carriers, N, increases, the issue becomes worse. The main contribution of this paper is a solution to these two problems.

III. ENHANCED SIM-OFDM

As mentioned in section II, the error propagation becomes worse as the number of subcarriers, N, grows. However, a slight modification in the way B_{OOK} is encoded can limit this effect. Instead of each bit from B_{OOK} being encoded in a single subcarrier state, it can be encoded in the states of two consecutive carriers – a carrier pair. Fig. 2 illustrates the principle of the new encoding scheme. Whenever a 1 is encountered in B_{OOK}, the first carrier of the pair is set as active and the second one as passive. Whenever a 0 is encountered in B_{OOK}, the first carrier of the pair is set as passive and the second one as active. Effectively, now the size of B_{OOK}, which can be represented by carrier states, is $\frac{N}{2}$ – half the size than in the original SIM-OFDM scheme. The benefit, however, is that for each pair it is certain that exactly one of the carriers is active. This means that bits from B_{QAM} can no longer be misplaced due to wrong detection of previous subcarrier states. The error that can be made is limited within

each pair of carriers. In addition, there is no longer a need to define a bit-majority in B_{OOK}, and the total number of active carriers is always the same – $\frac{N}{2}$. The number of active carriers within each pair is known and is always one, so there is no need to use a threshold for OOK detection. Instead, the carrier with higher power can be recognized as active, which would lead to better performance in the carrier state detection.

The only disadvantage of the modified scheme, compared to the former SIM-OFDM, is the slightly reduced spectral efficiency. Spectral efficiency of SIM-OFDM, measured in bits/carrier, is

$$\eta_{\text{SIM}-\text{OFDM}}^{\text{OLD}} = \frac{\log_2(M)}{2} + 1, \tag{1}$$

while the spectral efficiency of the modified SIM-OFDM is

$$\eta_{\text{SIM}-\text{OFDM}}^{\text{NEW}} = \frac{\log_2(M)}{2} + \frac{1}{2} \tag{2}$$

For comparison purposes, the spectral efficiency of QAM-encoded OFDM is $\log_2(M)$. This negative characteristic can be mitigated for SIM-OFDM when carrier pairs are expanded to blocks with a total number of subcarriers $L > 2$. For example, if $L = 8$ is used, there are 70 combinations in which 4 out of 8 subcarriers are set as active. This means a total of 6 bits ($2^6 = 64 < 70$) from B_{OOK} can be represented by combinations of active subcarriers in a block of 8 subcarriers, which already yields a better spectral efficiency than in (2). If the number of subcarriers in the block is L, and the number of active carriers within the block is L_{a}, a general expression for the spectral efficiency becomes

$$\eta_{\text{SIM}-\text{OFDM}}^{\text{GENERAL}} = \frac{L_{\text{a}}\log_2(M)}{L} + \frac{\lfloor\log_2(\frac{L!}{L_{\text{a}}!(L-L_{\text{a}})!})\rfloor}{L} \tag{3}$$

If L_{a} is chosen to be close to L, the system gets closer to conventional OFDM. If L is chosen to be close to N, and L_{a} approaches 1, the system starts to resemble PPM. As L approaches N, and L_{a} approaches $\frac{N}{2}$, the system gets closer to the original SIM-OFDM.

Fig. 2. Modified SIM-OFDM modulation approach.

IV. ENHANCED SIM-OFDM BER DERIVATION

The BER derivation that follows describes the operation of the system for $L_{\text{a}} = 1$ and $L = 2$ in the presence of AWGN.

199

Analysis for a different combination of L_a and L can be made in an analogous manner. No fading is assumed since it is not an issue in scenarios related to optical wireless communication for which SIM-OFDM is primarily considered. There is no dependence between the separate subcarrier pairs in the enhanced SIM-OFDM frame. Therefore, the BER analysis of one pair applies to the entire system.

Each carrier pair is received with an addition of AWGN. Hence, the distributions of both carrier amplitudes resemble the example illustrated in Fig. 3. The 'X' marks a possible value of the amplitude of the active carrier. In this case, all values, which the inactive carrier may take and still be correctly recognized as inactive, are contained inside the thick circle. Hence, integrating the Gaussian distribution, centered at 0, inside the thick circle would give the probability for correctly distinguishing between the passive and active carrier in the pair. Using some results from [3], this integration is represented by (4), where d is 1 when carriers are correctly distinguished or 0 when they are not. The symbol c stands for the amplitude of the active carrier, and N_o stands for the power of the noise.

$$
\begin{aligned}
P(d=1|c&=x+jy) = \\
&= \int_{-\sqrt{|x+jy|^2}}^{\sqrt{|x+jy|^2}} \int_{-\sqrt{|x+jy|^2-b^2}}^{\sqrt{|x+jy|^2-b^2}} \frac{1}{\pi N_o} e^{-\frac{(a)^2+(b)^2}{N_o}} \mathrm{d}a\mathrm{d}b \overset{[3]}{=} \\
&\overset{[3]}{=} \int_{0}^{2\pi} \int_{0}^{\sqrt{|x+jy|^2}} \frac{1}{\pi N_o} e^{-\frac{r^2}{N_o}} r \mathrm{d}r \mathrm{d}\theta = \\
&= 1 - e^{-\frac{|x+jy|^2}{N_o}}
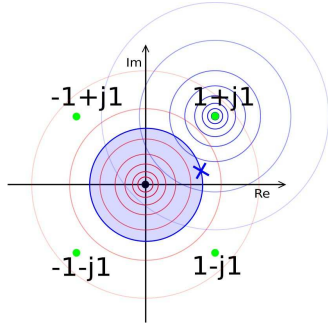\end{aligned} \tag{4}
$$

Fig. 3.   Contour lines of the distribution of the received carrier pair as a function of the transmitted constellation symbol. Lines are not drawn to scale.

Equation (5) expresses the probability density that the amplitude of the active carrier takes the value $x+jy$. There is an equal probability, $\frac{1}{M}$, that the value of the carrier before the addition of AWGN was equal to any one of the M constellation points. Hence, the probability density that the carrier value at the receiver is equal to $x+jy$ is expressed as a weighted sum of M different probability densities coming from the Gaussian functions centered at the M constellation points. Symbol μ_k marks constellation point number k. Symbols $\Re\{\mu_k\}$ and $\Im\{\mu_k\}$ denote the real and imaginary part of μ_k.

$$
\begin{aligned}
P(c=x&+jy) = \\
&= \frac{1}{M}\sum_{k=1}^{M} \frac{1}{\pi N_o} e^{-\frac{(x-\Re\{\mu_k\})^2+(y-\Im\{\mu_k\})^2}{N_o}}
\end{aligned} \tag{5}
$$

Equation (6) expresses the probability for correctly determining the active and inactive subcarrier in a pair. Equation (7) expresses the complementary probability - that the active and inactive subcarrier are incorrectly determined.

$$
\begin{aligned}
P_1 = P(d&=1) \\
&= \int_{-\infty}^{\infty} \int_{-\infty}^{\infty} P(d=1|c=x+jy)P(c=x+jy)\mathrm{d}x\mathrm{d}y \\
&= 1 - \frac{1}{2M}\sum_{k=1}^{M} e^{-\frac{|\mu_k|^2}{2N_o}}
\end{aligned} \tag{6}
$$

$$
P_0 = P(d=0) = 1 - P(d=1) \tag{7}
$$

Based on the calculated detection probabilities, the BER performance for the system can be calculated. When the carrier states are incorrectly determined, the bit from B_{OOK}, which they encode, is in error. That bit amounts to $\frac{1}{\log_2(M)+1}$ part of all the bits encoded in a carrier pair. Hence, the BER contribution of B_{OOK} is expressed as

$$
\mathrm{BER}_{B_{OOK}} = P_0 \frac{1}{\log_2(M)+1} \tag{8}
$$

An erroneous detection of a subcarrier state leads to the attempt of M-QAM demodulation of an unmodulated subcarrier, which adds additional errors to the frame. Such erroneous detection occurs with very high probability in the four M-QAM symbols close to 0. Probability that wrong detection occurs for any of the other symbols in the constellation is low in comparison to the probability for those four. Those four symbols encode bits which differ by only one bit on average when the M-QAM constellation is Gray encoded. Hence, in most of the cases only 1 bit will be wrong in B_{QAM} for wrong subcarrier detection. This is especially true for high SNR and high modulation order, M. Hence, the first part of the BER contribution of B_{QAM} is the same as in (8). Whenever a subcarrier state is correctly determined, there still exists the possibility that the QAM demodulation will lead to errors. Subcarrier state detection is not independent from the QAM demodulation process since both depend on the same subcarrier value. However, the Gray mapping of the constellation leads to very similar BER for all symbols, especially for high SNR. This happens because symbols are mostly mistaken for their neighbouring symbols. Hence, the BER of M-QAM, MQAM_{BER} defined in [4], can be used almost independently from the carrier state detection in (9) in order to complete $\mathrm{BER}_{B_{QAM}}$ which is the contribution of B_{QAM} to the overall bit error rate. This assumption is confirmed by numerical results in V and should become more accurate as SNR increases since distributions converge towards the original QAM constellation points. The final factor indicates that the bits encoded by M-QAM are $\frac{\log_2(M)}{\log_2(M)+1}$ of

200

all the bits encoded in a carrier pair.

$$\text{BER}_{B_{\text{QAM}}} = \text{P}_0 \frac{1}{\log_2(M)+1} + \text{P}_1 \text{MQAM}_{\text{BER}} \frac{\log_2(M)}{\log_2(M)+1} \tag{9}$$

The final expression for the bit error rate of the modified SIM-OFDM system is as follows:

$$\text{BER}_{\text{SIM-OFDM}} = \text{BER}_{B_{\text{OOK}}} + \text{BER}_{B_{\text{QAM}}} \tag{10}$$
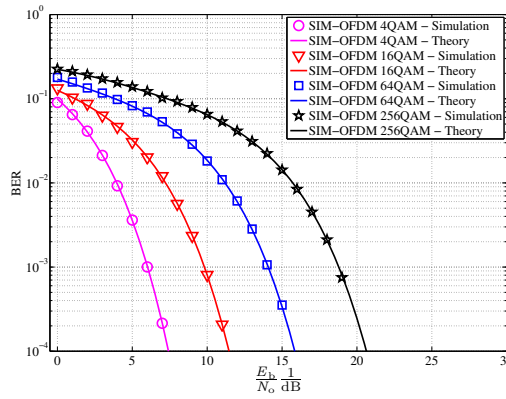
V. NUMERICAL RESULTS

Fig. 4. Comparison between theoretical model and Monte Carlo simulations for modified SIM-OFDM (L=2, L_{a}=1) performance in the presence of AWGN

The numerical simulations of the modified SIM-OFDM were performed for $L = 2$ and $L_{\text{a}} = 1$ in accordance with the analysis in section IV. The results that compare the analytical model with Monte Carlo simulations are presented in Fig. 4. The Monte Carlo simulations are obtained for 1000 SIM-OFDM frames with errors.

In order to fairly compare SIM-OFDM with conventional OFDM on a power-per-bit basis, each active carrier should receive the energy of its M-QAM symbol and additional energy to account for the bit encoded in the carrier states. The comparison can be observed in Fig. 5. For the same QAM modulation order, SIM-OFDM requires less energy per bit than OFDM to achieve a target BER, which leads to an energy gain. At the same time, M-QAM SIM-OFDM is less spectrally efficient than M-QAM OFDM as illustrated in (2). This decreases its performance for high orders of M. However, SIM-OFDM effectively improves the BER performance when high spectral efficiency is not required. For example, 4-QAM SIM-OFDM produces a BER curve which is not achievable by 4-QAM OFDM without the use of coding. SIM-OFDM with less active carriers than the presented version – $L = 2$, $L_a = 1$ – has the potential to produce even more energy efficient schemes.
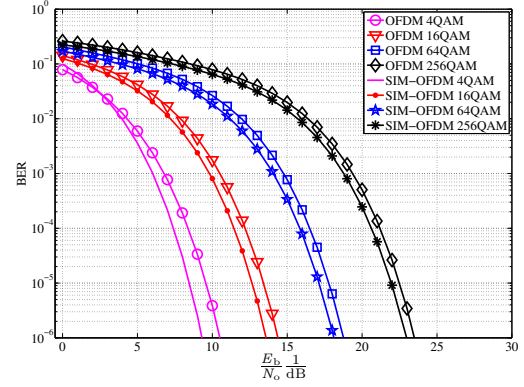

Fig. 5. Comparison between modified SIM-OFDM (L=2, L_{a}=1) and conventional OFDM performance in the presence of AWGN

VI. PEAK-TO-AVERAGE POWER RATIO

Conventional OFDM modulation suffers from a high PAPR, which can present a considerable problem to amplifier and quantizer design in the system [4]. This aspect of SIM-OFDM is worth discussing because the structure of the modified SIM-OFDM frame leads to reduction of the PAPR, which is highly beneficial especially in the context of optical wireless systems where power is limited by eye safety regulations [5].

PAPR is defined as the ratio of the maximum achievable power at any point in time, P_{MAX}, and the average power of the signal, P_{AVG} [4]:

$$\text{PAPR} = \frac{P_{\text{MAX}}}{P_{\text{AVG}}} \tag{11}$$

The time domain signal, $x[n]$, to be transmitted in an OFDM system is calculated as

$$x[n] = \frac{1}{\sqrt{N}} \sum_{k=0}^{N-1} X[k] e^{\frac{j2\pi k n}{N}} \tag{12}$$

where $X[k]$ is the value assigned to the kth subcarrier. In conventional OFDM, the peak power in time occurs at $x[a]$ when

$$X[k] = b e^{\frac{-j2\pi k a}{N}}, \ b \in \mathbb{C} \tag{13}$$

The complex exponential in (12) is cancelled by the complex exponential in (13) and the result is a summation of N equal complex numbers b. When two complex numbers with the same power are summed, they yield a result with the highest possible power when both numbers are the same. Fig. 6 illustrates the concept graphically. Hence, (13) guarantees a peak value at $x[a]$ when b has the highest possible power. The maximum power is achieved at $x[0]$ when each subcarrier is modulated with the same constellation symbol with the highest possible power. That symbol is marked as S$_{\text{HP}}$. Then $x[0] = \sqrt{N}$S$_{\text{HP}}$ and $x[0]x[0]^* = N$S$_{\text{HP}}$S$_{\text{HP}}^*$. For a square M-QAM modulation S$_{\text{HP}} = (\sqrt{M}-1) + \text{j}(\sqrt{M}-1)$ and
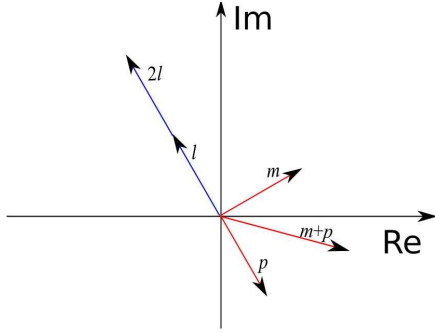
201

Fig. 6. Graphical representation of sum of complex numbers with the same power - $l, m, p \in \mathbb{C}$; $|l|^2 = |m|^2 = |p|^2$; $|2l|^2 > |m + p|^2$

$S_{HP}S_{HP}{}^* = 2(\sqrt{M} - 1)^2$ [4]. Hence, the maximum power is

$$P_{\text{MAX}} = 2N(\sqrt{M} - 1)^2 \qquad (14)$$

The average power is equal to the average frame energy divided by the number of points in time domain. The average frame energy is equal to the average energy per carrier multiplied by the number of carriers. The average energy per carrier is equal to the average energy in an M-QAM symbol. Hence, using [4],

$$P_{\text{AVG}} = \frac{E_{\text{AVG}}}{N} = \frac{E_{\text{AVG}}^{\text{QAM}} N}{N} = E_{\text{AVG}}^{\text{QAM}} \overset{[4]}{=} \frac{2(M-1)}{3} \qquad (15)$$

From (14) and (15), the PAPR for conventional OFDM can be calculated as

$$\text{PAPR}_{\text{OFDM}} = \frac{P_{\text{MAX}}}{P_{\text{AVG}}} = \frac{3N(\sqrt{M}-1)^2}{M-1} = \frac{3N(\sqrt{M}-1)}{\sqrt{M}+1} \qquad (16)$$

An alternative derivation of (16) can be found in [4].

In SIM-OFDM, a number of subcarriers are "switched off", *i.e.*, set to 0. A complex exponential, however, never takes the value 0; its power is always 1. Hence, it is not possible to allocate all the signal energy at a single point in time anymore. This already suggests a reduction of the peak power value. Adding zeros to the expression in (12) only means that a smaller number of complex numbers need to be summed in order to obtain $x[n]$. They still need to have the highest possible power and be the same due to the property of complex numbers, described in Fig. 6. Hence, the peak value is achieved at $x[0]$ when all active carriers are modulated with S_{HP}. If N_a is the total number of active carriers, then

$$P_{\text{MAX}} = \left(\frac{1}{\sqrt{N}} N_a S_{HP}\right)\left(\frac{1}{\sqrt{N}} N_a S_{HP}\right)^* = \frac{2}{N} N_a^2 (\sqrt{M}-1)^2 \qquad (17)$$

$$P_{\text{AVG}} = \frac{E_{\text{AVG}}}{N} = \frac{E_{\text{AVG}}^{\text{QAM}} N_a}{N} = \frac{2N_a(M-1)}{3N} \qquad (18)$$

$$\text{PAPR} = \frac{P_{\text{MAX}}}{P_{\text{AVG}}} = \frac{3N_a(\sqrt{M}-1)^2}{M-1} = \frac{3N_a(\sqrt{M}-1)}{\sqrt{M}+1} \qquad (19)$$

Equations (17)-(19) are a generalization of equations (14)-(16) for an arbitrary number of active carriers. The PAPR depends on both the number of active carriers, expressed by N_a, and the way they are modulated, expressed by the ratio $\frac{3(\sqrt{M}-1)}{\sqrt{M}+1}$. The best PAPR is achieved in Frequency Shift Keying (FSK) because $N_a = 1$ and there is no carrier modulation. The worst PAPR is achieved in the case of conventional M-QAM OFDM when $N_a = N$, and both N and M are as high as possible. An advantage of SIM-OFDM over conventional OFDM comes from the fact that in general it has less active carriers. For example, M-QAM SIM-OFDM has half the PAPR when compared to M-QAM OFDM for any number of carriers.

VII. CONCLUSION

A modification of the recently proposed SIM-OFDM was presented in this paper. The new scheme demonstrates improvement over conventional OFDM in terms of energy requirement at low spectral efficiency. It is a potential technique in the design of communication systems with a strong nonlinear characteristic where a low PAPR is required such as in optical wireless communications where incoherent light from off-the-shelf light emitting diodes is used to modulate data [6]. An alternative application are uplink channels, where high data rates are not of crucial importance, but energy efficiency. SIM-OFDM can be beneficial in scenarios with a high density of access points, for example in visual light communication uplinks where sophisticated coding schemes require additional design and processing complexity. Further research to investigate SIM-OFDM's performance in comparison to different coding methods and PAPR reduction techniques can fully characterize it as a novel modulation scheme.

REFERENCES

[1] R. Abualhiga and H. Haas, "Subcarrier-Index Modulation OFDM," in *Proc. of the International Symposium on Personal, Indoor and Mobile Radio Communications (PIMRC)*, Tokyo, Japan, Sep. 13–16, 2009.

[2] D. Grace, J. Chen, T. Jiang, and P. Mitchell, "Using Cognitive Radio to Deliver 'Green' Communications," in *Proc. of the 4th International Conference on Cognitive Radio Oriented Wireless Networks and Communications (CROWNCOM)*. Hannover, Germany: IEEE, Jun. 22-24, 2009, pp. 1–6.

[3] M.-S. Alouini and A. Goldsmith, "A Unified Approach for Calculating Error Rates Of Linearly Modulated Signals over Generalized Fading Channels," *IEEE Transactions on Communications*, vol. 47, no. 9, pp. 1324–1334, 1999.

[4] F. Xiong, *Digital Modulation Techniques*, 2nd ed. Artech House Publishers, 2006.

[5] R. J. Green, H. Joshi, M. D. Higgins, and M. S. Leeson, "Recent Developments in Indoor Optical Wireless," *IET Communications*, vol. 2, no. 1, pp. 3–10, Jan. 2008.

[6] S. Dimitrov and H. Haas, "On the Clipping Noise in an ACO-OFDM Optical Wireless Communication System," in *IEEE Global Communications Conference (IEEE GLOBECOM 2010)*, Miami, Florida, USA, 6–10 Dec. 2010.

202

Novel Unipolar Orthogonal Frequency Division Multiplexing (U-OFDM) for Optical Wireless

Dobroslav Tsonev, Sinan Sinanovic and Harald Haas
Institute for Digital Communications, Joint Research Institute for Signal and Image Processing,
The University of Edinburgh, EH9 3JL, Edinburgh, UK
Email: {dtsonev,s.sinanovic, h.haas}@ed.ac.uk

Abstract—A novel modulation technique coined U-OFDM is proposed. U-OFDM uses different time sample states and an innovative rearrangement of the Orthogonal Frequency Division Multiplexing (OFDM) frame which allow for the creation of unipolar OFDM signals required for Optical Wireless Communication (OWC) with Light Emitting Diodes (LEDs). In comparison to similar techniques like DC-biased Optical OFDM (DCO-OFDM) and Asymmetrically Clipped Optical OFDM (ACO-OFDM), U-OFDM is both optically and electrically more power efficient in an Additive White Gaussian Noise (AWGN) channel, which is prevalent in an optical wireless system.

I. Introduction

The demand for wireless data rates is growing exponentially. It is forecast that globally in 2015 more than 6 Exabyte of data will be sent through wireless networks per month [1]. Continuously increasing amounts of data traffic have led to new and refined wireless communication standards that significantly improve the usage, and hence the spectral efficiency of the scarce and limited radio frequency (RF) spectrum. Despite the improvements in current cellular standards, the demand for mobile data throughput outstrips the supply because the available RF spectrum is very limited. Hence, an expansion of wireless communications into a new and largely unexplored physical domain – the visible light spectrum – is very appealing. The main advantages of an optical wireless system are: (a) enormous amount of unregulated bandwidth, (b) no licensing requirements, (c) low-cost front end devices, and (d) no interference with the operation of sensitive electronic systems. Additionally, most of the existing lighting infrastructure can be reused for communication, and there are no known health concerns related to visible light as long as eye-safety regulations are met.

The physical properties of LEDs and Photodiodes (PDs) characterize a Visible Light Communication (VLC) system as an Intensity Modulation/Direct Detection (IM/DD) system. It means that only signal intensity and no phase and amplitude can be conveyed. This limits the set of modulation schemes which can be employed. Techniques like On-Off Keying (OOK), Pulse Position Modulation (PPM), and Pulse Amplitude Modulation (PAM) can be applied in a straight-forward fashion for the purpose of OWC. With the increase of transmission rates, however, Intersymbol Interference (ISI) becomes an issue. Hence, the usage of a more resilient technique like OFDM becomes desirable. On one hand, it allows equalization to be performed with single tap equalizers in the frequency domain, which simplifies design. On the other hand, OFDM allows different frequency carriers to be

adaptively loaded with bits according to the channel properties. This improves performance, especially in channels where signal attenuation is significant [2]. It is possible to generate real OFDM signals by imposing Hermitian symmetry on the carriers in frequency domain at the expense of half the spectral efficiency. The bipolar nature of OFDM signals, however, introduces an additional problem in VLC since LEDs can only convey unipolar signals in light intensity. The issue can be solved by introducing a DC-bias, which increases the power requirement of the system and cannot be easily optimized for any constellation size if Quadrature Amplitude Modulation (M-QAM) is used to modulate the different OFDM carriers. This technique is known as DCO-OFDM. A power efficient alternative to DCO-OFDM is ACO-OFDM, which uses the properties of the Fourier Transform and asymmetrical clipping to create unipolar signals in time domain [3]. ACO-OFDM, however, has half of the spectral efficiency of DCO-OFDM and a 3 dB performance disadvantage for bipolar signals when compared to OFDM [4]. A third novel modulation approach, in which carrier states are used to convey information is described in [5]. The idea is a modification for improved performance of Subcarrier-Index Modulation OFDM (SIM-OFDM) described in [6]. It has been developed in an attempt to create a modulation scheme with inherently reduced Peak-to-average Power Ratio (PAPR) for the purposes of VLC. The newly proposed modulation scheme, U-OFDM, is inspired by the concept from [5] in an attempt to close the 3 dB gap between OFDM and ACO-OFDM for bipolar signals, whilst generating a unipolar signal, which does not require the biasing of DCO-OFDM for OWC.

The rest of this paper is organized as follows. Section II provides a description of the U-OFDM modulation scheme and its demodulator. Section III describes the new modulation scheme's performance in an AWGN channel. Section IV presents a theoretical approach for assessing the performance of the system. Finally, section V gives concluding remarks.

II. U-OFDM

A typical discrete real bipolar OFDM signal in time domain is illustrated in Fig. 1. A DC shift can be added to the signal, so that DCO-OFDM is obtained for optical wireless communication. This is illustrated in Fig. 2. The DC bias in this example is equal to the absolute value of the lowest sample in the figure. In practice, OFDM has a very high PAPR. The DC shift would have a typical value of a few standard deviations of the original OFDM signal distribution, and any remaining negative values would be clipped. The required bias
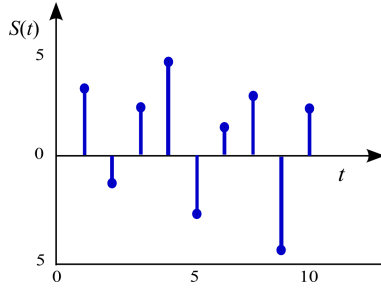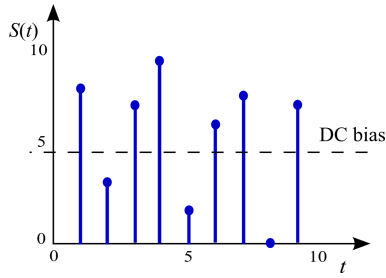
Fig. 1. Typical real OFDM time domain signal

Fig. 2. Typical DCO-OFDM time domain signal

Fig. 3. A unipolar time domain signal

Fig. 4. U-OFDM time domain signal

depends on the desired BER and constellation size as described in [4]. In Fig. 2 it is easy to visualize that the power of the signal is being increased by the DC shift when compared to the original signal in Fig. 1.

Unipolar signals do not require a DC shift and lead to higher power efficiency. ACO-OFDM is a state of the art technique for achieving unipolar OFDM signals. As described in [3], the method modulates only odd carriers in the OFDM frame, which leads to a certain symmetry between positive and negative values in time domain. In effect, all negative values can simply be ignored and replaced with zeros. Any distortion, caused by the clipping of the negative values, is projected on the even carriers in frequency domain. The resulting unipolar signal can be used for the purposes of OWC. By ignoring half of the carriers in frequency domain, however, ACO-OFDM has half the spectral efficiency of DCO-OFDM for the same order of M-QAM modulation. In addition, ACO-OFDM has a 3 dB disadvantage in power efficiency for bipolar signals when compared to conventional OFDM for the same M-QAM modulation order.

U-OFDM is a simple alternative technique which provides the benefit of unipolar signals. The modulation process begins with conventional modulation of an OFDM signal. After a real bipolar OFDM signal such as the one in Fig. 1 is obtained, it is transformed into a unipolar signal by encoding each time sample into a pair of new time samples. If the original OFDM sample is positive, the first sample of the new pair is set as "active", and the second sample is set as "inactive". If, on the other hand, the original OFDM sample is negative, the first sam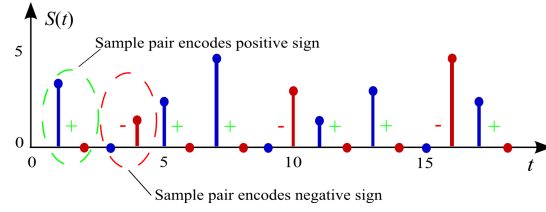ple of the new pair is set as "inactive", and the second sample is set as "active". Active sam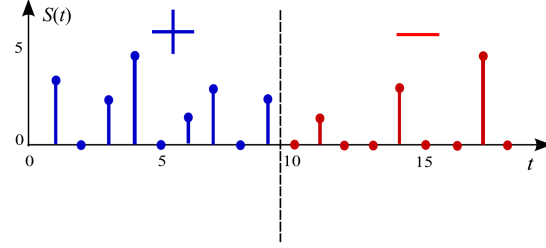ples are set equal to the absolute value of the original OFDM sample they correspond to, and inactive samples are set to zero. That is how the signal illustrated in Fig. 3 is obtained from the signal in Fig. 1. Fig. 3 only illustrates how the signs of the bipolar samples are encoded in the position of the active sample in a pair. The actual U-OFDM signal is obtained when the first samples of each pair are grouped in their original order to form the so called "positive" block while the second samples are grouped in their original order to form the so called "negative" block. The positive block is transmitted first and the negative block is transmitted second. That is how the signal illustrated in Fig. 4 is obtained. It can be used for transmission through the LED. The idea behind the rearrangement procedure is to obtain two blocks which can be linearly combined in order to obtain the original bipolar OFDM signal. This is done so that when both blocks are transmitted through an ISI channel, their frequency components will be attenuated in the same way. The linear recombination will ensure that the symbols encoded in the frequency components of the original bipolar OFDM signal will be subjected to the same attenuation effects by the channel. Cyclic prefixes are not illustrated in the given example. Since the length of the OFDM frame is doubled, the spectral efficiency of U-OFDM is about half the spectral efficiency of DCO-OFDM and the same as the spectral efficiency of ACO-OFDM. There is a necessity for a second cyclic prefix to separate the positive and negative blocks. However, for a large number of carriers its influence on the spectral efficiency will be negligible.

Once the U-OFDM signal is received, there are two ways in which it can be demodulated. The first way consists of subtracting the negative signal block from the positive one, and afterwards continuing the demodulation process with conventional demodulation of an OFDM signal since the result of the subtraction would be identical to the original bipolar

OFDM signal. When demodulated this way, the proposed scheme performs 3 dB worse than bipolar OFDM for the same M-QAM modulation order. This is due to the fact that the subtraction of the negative block from the positive one effectively doubles the AWGN variance at each resulting point. The U-OFDM performance is exactly the same as the reported performance of ACO-OFDM in [4]. An alternative demodulation method allows for a significant improvement of the scheme performance. Each pair of samples as illustrated in Fig. 3 encodes the amplitude and the sign of the original bipolar sample. If the receiver is able to detect which is the active sample in a pair, it can successfully guess the original sign and simply discard the passive sample since it carries no further information. This procedure is ideally expected to remove about half of the noise variance, and hence improve the performance. A simple and efficient way to achieve this is by comparing the amplitudes of the samples in each pair - the one with higher amplitude will be marked as active. A similar approach for ACO-OFDM demodulation has been reported very recently by Asadzadeh et. al. in [7].

III. U-OFDM Performance

Performance of U-OFDM has been simulated in an AWGN channel. No fading is observed in IM/DD systems, and so the AWGN channel is a sufficient model for the evaluation of optical wireless systems. The rest of this work presents only the performance of the improved demodulation scheme for U-OFDM since the other case completely resembles the behavior of ACO-OFDM and is trivial. For comparison purposes the quantities electrical energy per bit ($E_{b,elec}$) and optical energy per bit ($E_{b,opt}$) are introduced in [4] as the average electrical and optical energy per bit consumed in the system. Then Electrical Signal-to-noise Ratio (SNR_{elec}) and Optical Signal-to-noise Ratio (SNR_{opt}) would be defined as

$$SNR_{elec} = \frac{E_{b,elec}}{N_o} \qquad (1)$$

$$SNR_{opt} = \frac{E_{b,opt}}{N_o} \qquad (2)$$

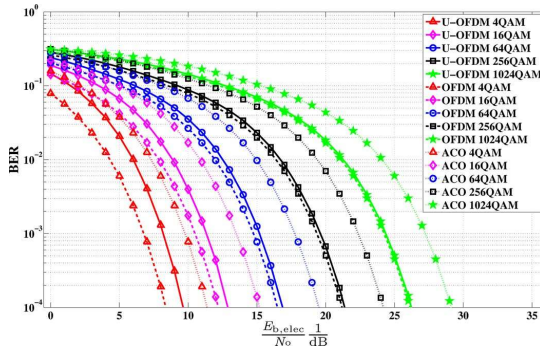where $N_o/2$ is the variance of the AWGN. The bit error rate

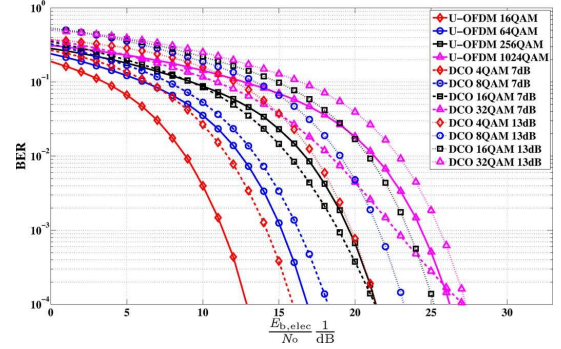Fig. 5. U-OFDM vs OFDM and ACO-OFDM for bipolar signals

Fig. 6. U-OFDM vs DCO-OFDM performance for different values of SNR_{elec}

(BER) performance of U-OFDM as a function of SNR_{elec} is compared to the performances of OFDM and ACO-OFDM for bipolar signals in Fig. 5. The theoretical BER curves of M-QAM are used for the performance of OFDM, and the same curves with a 3 dB shift are used for the performance of ACO-OFDM in agreement with the analysis from [4]. The new improved ACO-OFDM demodulation technique from [7] is not taken into account. The curves for the improved U-OFDM are obtained with Monte Carlo simulations. The simulations are conducted for 1024 carriers per U-OFDM frame. As expected, U-OFDM cannot surpass conventional bipolar OFDM for the same M-QAM modulation due to the additional detection of active samples in time domain which is not always perfect. However, it has noticeably better performance than ACO-OFDM of the same modulation order. The performance improvement reaches almost 3 dB for higher order M-QAM modulation where U-OFDM approaches conventional OFDM. The difference between U-OFDM and ACO-OFDM curves also illustrates the reduction of the required power caused by the improved demodulator. The performances of U-OFDM and DCO-OFDM are compared in Fig. 6. ACO-OFDM creates unipolar signals. Therefore, its performance does not need to be considered again. The BER curves are plotted against SNR_{elec}. The energy consumed by DCO-OFDM depends on the choice of a biasing point. Consistence with the work presented in [4] will be kept for comparison purposes. Hence, the DC shift of DCO-OFDM is defined in [4] as

$$B_{DC} = k\sqrt{E[S^2(t)]} \qquad (3)$$

where $S(t)$ is the bipolar OFDM signal in time domain before the shift and k denotes the ratio of the DC shift and the standard deviation. This is defined in the same work as a bias of $10\log_{10}(k^2+1)$ dB. In consistence with the work in [4], bias levels of 7 dB and 13 dB are chosen for DCO-OFDM. They are not necessarily the optimum biasing points for the different modulation orders. Estimation of the optimum biasing points and a better comparison is a subject of further research. The spectral efficiency of U-OFDM is half the spectral efficiency of DCO-OFDM. That is why the orders of M-QAM modulation are chosen such that the spectral efficiencies of U-OFDM and DCO-OFDM are the same. For example, 16-QAM U-OFDM
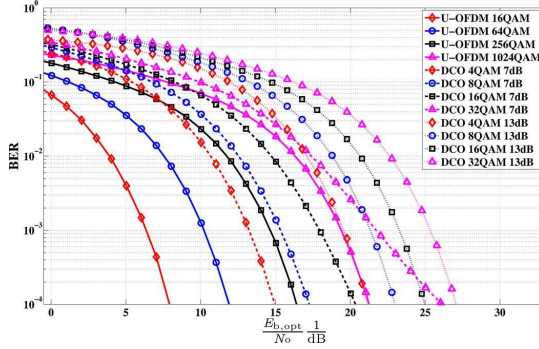
Fig. 7. U-OFDM vs DCO-OFDM performance for different values of SNR_{opt}

should be compared to 4-QAM DCO-OFDM, 64-QAM U-OFDM should be compared to 8-QAM DCO-OFDM, etc. For a $\text{BER} = 10^{-4}$, U-OFDM performs better or the same as DCO-OFDM in all the presented cases.

In order to compare the optical efficiencies of the systems, we adopt the conditions,

$$P_{\text{opt}}^{\text{DCO}} = \text{E}[S_{\text{DCO}}(t)] = 1 \tag{4}$$

$$P_{\text{opt}}^{\text{U}} = \text{E}[S_{\text{U}}(t)] = 1 \tag{5}$$

for consistency with the work done in [4] where subbscripts DCO and U denote time domain signals of DCO-OFDM and U-OFDM respectively. $P_{\text{opt}}^{\text{DCO}}$ and $P_{\text{opt}}^{\text{U}}$ stand for the average optical power of the DCO-OFDM and U-OFDM time domain signals. If these conditions are fullfilled, by using [4], we can write

$$\frac{E_{\text{b,opt}}^{\text{DCO}}}{N_{\text{o}}} = \frac{k^2}{1+k^2} \frac{E_{\text{b,elec}}^{\text{DCO}}}{N_{\text{o}}} \tag{6}$$

$$\frac{E_{\text{b,opt}}^{\text{U}}}{N_{\text{o}}} = \frac{1}{\pi} \frac{E_{\text{b,elec}}^{\text{U}}}{N_{\text{o}}} \tag{7}$$

Using the relations defined in (6) and (7), the performances of U-OFDM and DCO-OFDM for different values of SNR_{opt} are compared in Fig. 7. U-OFDM surpasses DCO-OFDM in performance for all presented cases, regardless of BER.

It should be noted that the relations in (6) and (7) are only true for the conditions in (4) and (5). The relationship between optical and electrical power efficiency of the system changes as the average power of the signal is varied. The previous remark about the optimum biasing levels of DCO-OFDM applies in this case as well.

IV. THEORETICAL PERFORMANCE OF U-OFDM

A theoretical approach for analyzing the performance of the improved demodulator for U-OFDM in an AWGN channel is presented in this section. In the context of the following mathematical formulas, σ_{n} is the standard deviation of the AWGN, i.e., $\sigma_{\text{n}} = \sqrt{N_{\text{o}}/2}$, σ_{s} is the standard deviation of the

real OFDM signal, $S(t)$, before it is encoded in U-OFDM, i.e., $\sigma_{\text{s}} = \sqrt{E_{\text{b,elec}} \log_2(M)/2}$, $\text{sgn}(s)$ is the sign function, i.e.,

$$\text{sgn}(s) = \begin{cases} -1 & \text{if } s < 0 \\ 0 & \text{if } s = 0 \\ 1 & \text{if } s > 0 \end{cases} \tag{8}$$

$\phi(x)$ is the standard normal distribution probability density function, i.e.,

$$\phi(x) = \frac{1}{\sqrt{2\pi}} e^{-\frac{x^2}{2}} \tag{9}$$

and $Q(x)$ is the tail probability of the standard normal distribution, i.e.,

$$Q(x) = \frac{1}{\sqrt{2\pi}} \int_x^\infty e^{-\frac{u^2}{2}} \, \mathrm{d}u \tag{10}$$

Modeling a U-OFDM system analytically is a cumbersome task due to the fact that during demodulation each individual sample in time domain is subjected to a different nonlinear transformation, which depends on two independent random variables from the AWGN. As a starting point, we look at the statistics of the value of a *correctly* detected active sample, which is a random variable. The mean of that variable can be viewed as a nonlinear transform to which the original $S(t)$ sample, s, is subjected. That function has the following form:

$$f_{\text{c}}(s) = \frac{s - \text{sgn}(s) \int_{-\infty}^\infty \frac{x}{\sigma_{\text{n}}} \phi\left(\frac{x-|s|}{\sigma_{\text{n}}}\right) Q\left(\frac{x}{\sigma_{\text{n}}}\right) \, \mathrm{d}x}{\int_{-\infty}^\infty \frac{1}{\sigma_{\text{n}}} \phi\left(\frac{x-|s|}{\sigma_{\text{n}}}\right) \left(1 - Q\left(\frac{x}{\sigma_{\text{n}}}\right)\right) \, \mathrm{d}x} \tag{11}$$

In addition, the variance of the *correctly* detected sample has the following value

$$v_{\text{c}}(s) = \frac{\int_{-\infty}^\infty \frac{x^2}{\sigma_{\text{n}}} \phi\left(\frac{x-|s|}{\sigma_{\text{n}}}\right) \left(1 - Q\left(\frac{x}{\sigma_{\text{n}}}\right)\right) \, \mathrm{d}x}{\int_{-\infty}^\infty \frac{1}{\sigma_{\text{n}}} \phi\left(\frac{x-|s|}{\sigma_{\text{n}}}\right) \left(1 - Q\left(\frac{x}{\sigma_{\text{n}}}\right)\right) \, \mathrm{d}x} - f_{\text{c}}^2(s) \tag{12}$$

Due to the Central Limit Theorem (CLT), that variance will be part of the variance of the AWGN in frequency domain after the Fast Fourier Transform (FFT) is performed in the demodulation process. For the *incorrectly* detected active sample, the mean and variance have the following form

$$f_{\text{w}}(s) = \frac{\text{sgn}(s) \int_{-\infty}^\infty \frac{x}{\sigma_{\text{n}}} \phi\left(\frac{x}{\sigma_{\text{n}}}\right) Q\left(\frac{x-|s|}{\sigma_{\text{n}}}\right) \, \mathrm{d}x}{\int_{-\infty}^\infty \frac{1}{\sigma_{\text{n}}} \phi\left(\frac{x}{\sigma_{\text{n}}}\right) \left(1 - Q\left(\frac{x-|s|}{\sigma_{\text{n}}}\right)\right) \, \mathrm{d}x} \tag{13}$$

$$v_{\text{w}}(s) = \frac{\int_{-\infty}^\infty \frac{x^2}{\sigma_{\text{n}}} \phi\left(\frac{x}{\sigma_{\text{n}}}\right) \left(1 - Q\left(\frac{x-|s|}{\sigma_{\text{n}}}\right)\right) \, \mathrm{d}x}{\int_{-\infty}^\infty \frac{1}{\sigma_{\text{n}}} \phi\left(\frac{x}{\sigma_{\text{n}}}\right) \left(1 - Q\left(\frac{x-|s|}{\sigma_{\text{n}}}\right)\right) \, \mathrm{d}x} - f_{\text{w}}^2(s) \tag{14}$$

Using the Bussgang theorem, introduced in [8], a Gaussian random variable, X, subjected to a nonlinear transformation, $f(X)$, has the following properties

$$f(X) = \alpha X + Y \tag{15}$$
$$\text{E}[XY] = 0 \tag{16}$$
$$\alpha = \text{const.} \tag{17}$$

206

Based on these properties, the constant α and the variance of the noise Y are calculated for the two separate cases we have defined:

$$\alpha_c = \frac{\int_{-\infty}^{\infty} s f_c(s) \frac{1}{\sigma_s} \phi\left(\frac{s}{\sigma_s}\right) ds}{\sigma_s^2} \qquad (18)$$

$$y_c = \mathrm{E}[Y_c^2] = \int_{-\infty}^{\infty} f_c^2(s) \frac{1}{\sigma_s} \phi\left(\frac{s}{\sigma_s}\right) ds - \alpha_c^2 \sigma_s^2 \qquad (19)$$

$$\alpha_w = \frac{\int_{-\infty}^{\infty} s f_w(s) \frac{1}{\sigma_s} \phi\left(\frac{s}{\sigma_s}\right) ds}{\sigma_s^2} \qquad (20)$$

$$y_w = \mathrm{E}[Y_w^2] = \int_{-\infty}^{\infty} f_w^2(s) \frac{1}{\sigma_s} \phi\left(\frac{s}{\sigma_s}\right) ds - \alpha_w^2 \sigma_s^2 \qquad (21)$$

The variance of Y will also be added to the variance of the AWGN in frequency domain. The variances in (12) and (14) are given as functions of the realization of the signal $S(t)$. On average they will be equal to

$$\bar{v}_c = \int_{-\infty}^{\infty} v_c(s) \frac{1}{\sigma_s} \phi\left(\frac{s}{\sigma_s}\right) ds \qquad (22)$$

and

$$\bar{v}_w = \int_{-\infty}^{\infty} v_w(s) \frac{1}{\sigma_s} \phi\left(\frac{s}{\sigma_s}\right) ds \qquad (23)$$

The probability for correct detection of an active time sample, d_c, is

$$d_c = \int_0^{\infty} \frac{2}{\sigma_s} \phi\left(\frac{s}{\sigma_s}\right) Q\left(\frac{s}{\sqrt{2}\sigma_n}\right) ds \qquad (24)$$

For a large number of samples in a U-OFDM frame, the number of *correctly* and *incorrectly* detected active samples will have a ratio which corresponds to the probabilities for *correct* and *incorrect* detection. Hence, the average gain factor, $\bar{\alpha}$, and the average noise variance in frequency domain, $\bar{N}$, become

$$\bar{\alpha} = d_c \alpha_c + (1 - d_c)\alpha_w \qquad (25)$$

$$\bar{N} = d_c(\bar{v}_c + y_c) + (1 - d_c)(\bar{v}_w + y_w) \qquad (26)$$

$$\mathrm{SNR}_{\mathrm{elec}} = \frac{\alpha^2 E_{\mathrm{b,elec}}}{\bar{N}} \qquad (27)$$

The achieved average $\mathrm{SNR}_{\mathrm{elec}}$ from (27) can be plugged in the well-known formula for M-QAM BER performance [9]. Hence, the performance of U-OFDM can be calculated as

$$\mathrm{BER}_U = \mathrm{BER}_{\mathrm{QAM}}\left(\frac{\alpha^2 E_{\mathrm{b,elec}}}{\bar{N}}\right) \qquad (28)$$

The comparison between theoretical model and Monte Carlo simulations of the system performance is presented in Fig. 8. There is good agreement between the presented model and the conducted simulations.
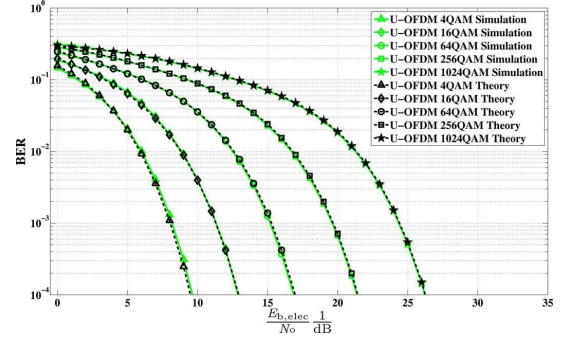

Fig. 8. Theoretical U-OFDM performance vs. Monte Carlo simulations

V. Conclusion

A novel multicarrier modulation scheme for optical wireless communication has been presented in this paper. The new scheme demonstrates improvement over some known multicarrier schemes for OWC. It provides the same benefits as the already known ACO-OFDM modulation scheme as well as an improved demodulation scheme for better power efficiency in an AWGN channel. When compared to DCO-OFDM, it shows better performance in terms of BER for the presented scenarios. The current work additionally provides a good theoretical analysis for the performance of the presented scheme in an AWGN channel.

References

[1] "Visible light communication (vlc) - a potential solution to the global wireless spectrum shortage," GBI Research, Tech. Rep., 2011. [Online]. Available: http://www.gbiresearch.com/
[2] J. Bingham, "Multicarrier modulation for data transmission: an idea whose time has come," *Communications Magazine, IEEE*, vol. 28, no. 5, pp. 5 –14, may 1990.
[3] J. Armstrong and A. Lowery, "Power Efficient Optical OFDM," *Electronics Letters*, vol. 42, no. 6, pp. 370–372, Mar. 16, 2006.
[4] J. Armstrong and B. J. C. Schmidt, "Comparison of Asymmetrically Clipped Optical OFDM and DC-Biased Optical OFDM in AWGN," *Communications Letters, IEEE*, vol. 12, no. 5, pp. 343–345, May 2008.
[5] D. Tsonev, S. Sinanović, and H. Haas, "Enhanced Subcarrier Index Modulation (SIM) OFDM," in *GLOBECOM Workshops (MMCOM'11), 2011 IEEE*, Houston, Texas, USA, 5–9 Dec. 2011.
[6] R. Abualhiga and H. Haas, "Subcarrier-Index Modulation OFDM," in *Proc. of the International Symposium on Personal, Indoor and Mobile Radio Communications (PIMRC)*, Tokyo, Japan, Sep. 13–16, 2009.
[7] K. Asadzadeh, A. Dabbo, and S. Hranilovic, "Receiver Design for Asymmetrically Clipped Optical OFDM," in *GLOBECOM Workshops (Optical Wireless Communications), 2011 IEEE*, Houston, Texas, USA, 5–9 Dec. 2011.
[8] J. Bussgang, "Cross Correlation Function of Amplitude-Distorted Gaussian Signals," Research Laboratory for Electronics, Massachusetts Institute of Technology, Cambridge, MA, Technical Report 216, Mar. 1952.
[9] J. G. Proakis, *Digital Communications*, 4th ed., ser. McGraw-Hill Series in Electrical and Computer Engineering, S. W. Director, Ed. McGraw-Hill Higher Education, December 2000.

Pulse Shaping in Unipolar OFDM-based Modulation Schemes

Dobroslav Tsonev, Sinan Sinanović and Harald Haas

Institute for Digital Communications, Joint Research Institute for Signal and Image Processing,
The University of Edinburgh, EH9 3JL, Edinburgh, UK
Email: {d.tsonev,s.sinanovic, h.haas}@ed.ac.uk

Abstract—**This paper discusses the issue of pulse shaping in unipolar orthogonal-frequency-division-multiplexing-based modulation schemes for intensity modulation/direct detection systems. Three previously presented schemes, asymmetrically clipped optical OFDM, pulse-amplitude-modulated discrete multitone modulation, and unipolar orthogonal frequency division multiplexing, are investigated. The current work demonstrates how both unipolar and bipolar pulse shapes can be used for the generation of unipolar *continuous*-time signals.**

I. Introduction

Wireless data traffic is increasing exponentially [1]. Despite the continuous improvements in wireless communication technology, it is expected that the future demand cannot be met because the radio frequency spectrum has been almost completely utilised. A potential solution to the emerging problem is the development of optical wireless communication. Main advantages of an optical wireless system are: (a) a lot of unregulated bandwidth, (b) license-free operation, (c) low-cost front end devices, (d) no interference with the operation of sensitive electronic systems, (e) reuse of the existing lighting infrastructure, and (f) no health concerns related to visible light as long as eye-safety regulations are met [2].

The physical properties of light emitting diodes (LEDs) and photodiodes (PDs) characterise a visible light communication (VLC) system as an intensity modulation/direct detection (IM/DD) system. In other words, only signal intensity and no phase or amplitude can be conveyed. This fact limits the set of modulation schemes which can be employed. Techniques like on-off keying (OOK), pulse-position modulation (PPM), and pulse-amplitude modulation (PAM) can be applied in a straightforward fashion. With the increase of transmission rates, however, intersymbol interference (ISI) becomes an issue. Hence, a more resilient technique like orthogonal frequency division multiplexing (OFDM) becomes desirable. Conventional OFDM signals are complex and bipolar in nature. It is possible to generate real OFDM signals by imposing Hermitian symmetry on the carriers in frequency domain at the expense of half the spectral efficiency [2]. The bipolarity of signals, however, introduces an additional problem in VLC since LEDs can only be modulated with strictly positive signals. The issue can be solved by introducing a DC-bias, which increases the power dissipation of the system and cannot be easily optimised for all constellation sizes of quadrature amplitude modulation (M-QAM) used to modulate the different OFDM carriers. This technique is known as DC-biased optical OFDM (DCO-OFDM). Three power-efficient alternatives to DCO-OFDM have been proposed in

previous works: asymmetrically clipped optical OFDM (ACO-OFDM) [3], pulse-amplitude-modulated discrete multitone modulation (PAM-DMT) [4], unipolar orthogonal frequency division multiplexing (U-OFDM) [5]. They use different properties of the OFDM frame for generation of unipolar signals, which do not require DC-biasing and achieve better power efficiency. To the best of our knowledge, all three techniques have been discussed in the context of *digital* signal processing without special consideration of the pulse shaping necessary for the generation of *continuous*-time bandlimited signals. The current work will focus on this issue and demonstrate that while special considerations need to be taken in the signal generation process, all the modulation concepts can be realised with commonly used pulse shapes. DCO-OFDM is not considered in this paper since it does not have the same issues because unipolarity is achieved through biasing in the analog domain.

The rest of this paper is organised as follows. Section II provides a description of the unipolar modulation schemes. Section III describes the problem which arises when bipolar pulses are used for the generation of a *continuous*-time signal and how it can be avoided. Section IV gives a theoretical justification to the solution proposed in Section III. Section V presents numerical results to confirm the theory. Finally, section VI gives concluding remarks.

II. Unipolar Modulation Schemes

A. ACO-OFDM

ACO-OFDM was introduced in [3]. In this scheme only odd subcarriers are modulated in frequency domain, which creates a certain symmetry in time domain. In general, if $s(k, n)$ is the contribution of subcarrier $S[k]$ to the sample at time n, then [3]

$$s(k, n) = \frac{1}{\sqrt{N_{\text{fft}}}} S[k] e^{\frac{j 2\pi n k}{N_{\text{fft}}}}$$

$$s(k, n + \frac{N_{\text{fft}}}{2}) = \frac{1}{\sqrt{N_{\text{fft}}}} S[k] e^{\frac{j 2\pi (n + N_{\text{fft}}/2)k}{N_{\text{fft}}}} =$$

$$= \frac{1}{\sqrt{N_{\text{fft}}}} S[k] e^{\frac{j 2\pi n k}{N_{\text{fft}}}} e^{j \pi k} \qquad (1)$$

If k is odd, $s(k, n) = -s(k, n + N_{\text{fft}}/2)$, and if k is even, $s(k, n) = s(k, n + N_{\text{fft}}/2)$. Then, if only the odd subcarriers in an OFDM frame are modulated, the time domain signal, $s[n]$, has the property

$$s[n] = -s[n + N_{\text{fft}}/2] \qquad (2)$$

208

If only the even subcarriers in an OFDM frame are modulated, the time-domain signal has the property

$$s[n] = s[n + N_{\text{fft}}/2] \qquad (3)$$

Due to the orthogonality of the complex exponential functions, the property in (2) implies that only the odd subcarriers contain information, and the property in (3) implies that only the even subcarriers contain information. Clipping at zero of an arbitrary time-domain signal, $s[n]$, can be represented as

$$\text{CLIP}(s[n]) = \frac{1}{2}(s[n] + |s[n]|) \qquad (4)$$

Because only the odd subcarriers are modulated in ACO-OFDM, equation (2) applies to the scheme. Therefore, $s[n] = -s[n + N_{\text{fft}}/2]$. Then $|s[n]| = |s[n + N_{\text{fft}}/2]|$. Hence, the clipping distortion $|s[n]|$, described in (4), possesses the property in (3) and falls on the even subcarriers only. The factor $\frac{1}{2}$ is consistent with the halving of the amplitudes, described in [3]. An additional factor of $\sqrt{2}$ should be used to preserve the amount of dissipated power, which would lead to an overall signal-to-noise ratio (SNR) penalty of 3dB. This simple proof is an alternative to the one presented in [3].

B. PAM-DMT

PAM-DMT was introduced in [4]. It modulates the carriers of an OFDM frame with symbols from the PAM modulation scheme, which are multiplied by $j = \sqrt{-1}$, and thus made imaginary. Due to the Hermitian symmetry in frequency domain of the OFDM frame, the PAM-DMT time-domain signal becomes [4]

$$
\begin{aligned}
s[n] &= \frac{1}{\sqrt{N_{\text{fft}}}} \sum_{k=0}^{N_{\text{fft}}-1} S[k] e^{\frac{j2\pi kn}{N_{\text{fft}}}} = \\
&= \frac{1}{\sqrt{N_{\text{fft}}}} \sum_{k=0}^{N_{\text{fft}}-1} S[k] \left(\cos \frac{2\pi kn}{N_{\text{fft}}} + j \sin \frac{2\pi kn}{N_{\text{fft}}} \right) = \\
&= \frac{1}{\sqrt{N_{\text{fft}}}} \sum_{k=0}^{N_{\text{fft}}-1} jS[k] \sin \frac{2\pi kn}{N_{\text{fft}}}
\end{aligned} \qquad (5)
$$

The structure of PAM-DMT exhibits an antisymmetry where $s[0]=0$, $s[N_{\text{fft}}/2]=0$ if N_{fft} is even, and $s[n]=-s[N_{\text{fft}}-n]$. This means that $|s[0]|=0$, $|s[N_{\text{fft}}/2]|=0$ if N_{fft} is even, and $|s[n]|=|s[N_{\text{fft}}-n]|$. Therefore, after the clipping operation, described in (4), the distortion term $|s[n]|$ will possess Hermitian symmetry in time domain. This means that in frequency domain, the distortion will be translated into a real signal. Hence, it will be completely orthogonal to the original signal. The authors of [4] have not formally completed this proof. However, with the representation of clipping in (4), it is rather straightforward as presented here.

C. U-OFDM

U-OFDM was introduced in [5]. However, the authors in [6] present a very similar concept as Flip-OFDM. In the context of this work, the scheme will be referred to as U-OFDM. The idea is to separate a bipolar OFDM frame in two separate frames - positive and negative. The positive frame is a copy of the bipolar frame, where all negative values have been replaced with zeros. The negative frame is a copy of the bipolar frame where all samples are multiplied by -1, and again the negative ones are replaced with zeros. Therefore, the positive frame conveys the positive values in a unipolar positive signal, and the negative frame conveys the negative values in a unipolar positive signal. At the demodulator, they can be recombined by subtracting the negative frame from the positive one.

III. PULSE SHAPING

Pulse shaping is used in communication systems for the generation of *continuous*-time signals that possess specific characteristics. A simple pulse shape is the Boxcar filter (a square pulse that corresponds to the zero-order hold function of a digital-to-analog converter (DAC)) [7]. It is easy to implement and simple to work with. However, it requires infinite bandwidth, which is very wasteful in wireless communications. The most spectrum efficient pulse shape is the sinc function $\text{sinc}(t) = \frac{\sin(\pi t)}{\pi t}$ [7]. However, it has a long impulse response, which is prone to ISI due to time jitter and is hard to realise. That is why the raised-cosine filter and its modified version the root-raised-cosine filter present a more practical alternative. In addition, other pulse shapes like the hat function (a triangular pulse that corresponds to linear interpolation of samples) and the Gaussian filter exist. To the best of our knowledge, pulse shaping has not been considered for the schemes presented in Section II. It, however, is an integral part of any communication system and raises additional questions regarding the signal properties in the context of ACO-OFDM, PAM-DMT, and U-OFDM.

The three modulation approaches as presented in [3], [5], and [4] describe the process of generating a *discrete* unipolar signal. Discrete signals cannot be directly translated into *continuous* signals with the same properties if the bandwidth is limited. A *continuous*-time signal, $s(t)$, can be represented as a superposition of different copies of the pulse-shaping filter's impulse response, $p(t)$, scaled by the samples of the *discrete*-time signal, $s[n]$. It is presented in (6) where F indicates the frame order, $s[n, F]$ indicates the *discrete* signal $s[n]$ in frame F, N_{fft} indicates the number of fast Fourier transform (FFT) points in a single frame, N_{cp} indicates the length of the cyclic prefix, which is formed by the last N_{cp} points of $s[n, F]$. It is assumed that the phase is known, so $F=0$ corresponds to the current frame, and $t=0$ corresponds to the first sample position. If $p(t)$ is bipolar, and $s[n]$ is unipolar, $s(t)$ will tend to be bipolar as well. That is why, bipolar pulse shapes like the sinc function and the root-raised-cosine filter cannot be applied in a straightforward way to unipolar *discrete*-time signals. Unipolar shapes like the Boxcar filter, the hat function, and the Gaussian filter, can easily generate unipolar signals, but raise questions about how bandwidth efficient they are as well as how match filtering would be applied without generating intersymbol interference. The root-raised-cosine filter is a very practical pulse-shaping technique, which completely avoids ISI if there is no time jitter and provides an easy way to do match filtering. That is why, it will be used as the shaping pulse in the context of this paper. Fig. 1(a) illustrates the *continuous*-time signal generated by shaping a unipolar *discrete* ACO-OFDM signal with a root-raised-cosine filter. The result has negative values. This can be

$$s(t) = \sum_{F=-\infty}^{\infty} \left(\sum_{n=N_{\mathrm{fft}}-N_{\mathrm{cp}}}^{N_{\mathrm{fft}}-1} s[n,F]p(t-F(N_{\mathrm{fft}}+N_{\mathrm{cp}})T_{\mathrm{s}}-(n-N_{\mathrm{fft}})T_{\mathrm{s}}) + \sum_{n=0}^{N_{\mathrm{fft}}-1} s[n,F]p(t-F(N_{\mathrm{fft}}+N_{\mathrm{cp}})T_{\mathrm{s}}-nT_{\mathrm{s}}) \right) \quad (6)$$

amended by introducing a DC-bias as in Fig. 1(b). However, it would increase the average power consumption approximately by 3dB, which would greatly reduce the power efficiency of the scheme. Alternatively, the negative values could be clipped, but this would lead to the distortion illustrated in Fig. 2(a). The other two schemes PAM-DMT and U-OFDM have exactly the same problem with a very similar performance degradation.
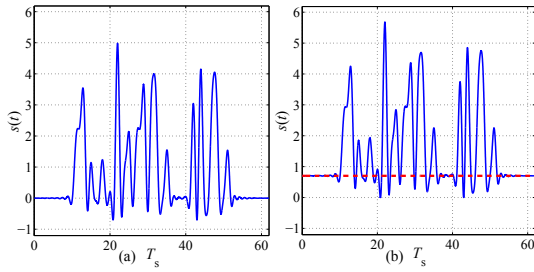

Fig. 1. (a) *Discrete* unipolar ACO-OFDM signal, shaped with a root-raised-cosine filter. (b) Signal from (a), biased to avoid clipping distortion.
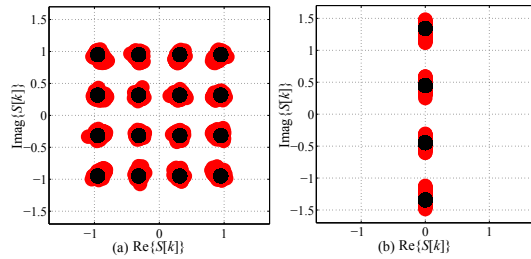

Fig. 2. (a) Distortion in the 16-QAM constellation after clipping negative values of the *continuous*-time signal. (b) Distortion in the 4-PAM constellation after clipping negative values of the *continuous*-time signal.

The rest of this paper will show that a bipolar pulse shape like the root-raised-cosine filter can be used without performance degradation in the previously described unipolar schemes if the *discrete*-time signal is kept bipolar and clipping is done after the pulse shaping operation. Fig. 3(a) illustrates a bipolar *discrete* ACO-OFDM signal shaped with a root-raised-cosine filter. Fig. 3(b) presents the signal, clipped after the pulse shaping operation. The next section shows analytically why the wave form from Fig. 3(b) retains the modulation concepts described in Section II, and distortion is avoided.

IV. CONTINUOUS-TIME ANALYSIS

The complete *continuous*-time signal is presented in (6). Assume that the channel impulse response is causal, $h(t<0)=0$, and that the cyclic prefixes completely remove the ISI
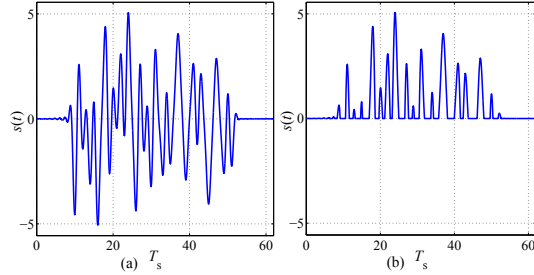

Fig. 3. (a) *Discrete* bipolar ACO-OFDM signal, shaped with a root-raised-cosine filter. (b) Signal from (a), made unipolar through clipping.

between the different OFDM frames. Hence, the portion of the *continuous*-time signal at the transmitter, which is relevant for sampling of the current frame, $F=0$, at the receiver, can be expressed as:

$$s(t) = \sum_{n=N_{\mathrm{fft}}-N_{\mathrm{cp}}}^{N_{\mathrm{fft}}-1} s[n]p(t-(n-N_{\mathrm{fft}})T_{\mathrm{s}}) + \sum_{n=0}^{N_{\mathrm{fft}}-1} s[n]p(t-nT_{\mathrm{s}}) +$$
$$+ \sum_{n=N_{\mathrm{fft}}-N_{\mathrm{cp}}}^{N_{\mathrm{fft}}-N_{\mathrm{cp}}+N_{\mathrm{cp}}^{\mathrm{P}}-1} s[n,1]p(t-(N_{\mathrm{fft}}+N_{\mathrm{cp}})T_{\mathrm{s}}-(n-N_{\mathrm{fft}})T_{\mathrm{s}}) \quad (7)$$

where $N_{\mathrm{cp}}^{\mathrm{P}}$ is the length of the cyclic prefix sufficient to remove the effects of $p(t)$, and $s[n] = s[n,0]$. The *continuous*-time signal relevant for sampling the first $\frac{N_{\mathrm{fft}}}{2}$ points of the current frame can be expressed as

$$s_1(t) = \sum_{n=N_{\mathrm{fft}}-N_{\mathrm{cp}}}^{N_{\mathrm{fft}}-1} s[n]p(t-(n-N_{\mathrm{fft}})T_{\mathrm{s}}) + \sum_{n=0}^{N_{\mathrm{fft}}/2-1} s[n]p(t-nT_{\mathrm{s}}) +$$
$$+ \sum_{n=N_{\mathrm{fft}}/2}^{N_{\mathrm{fft}}/2-1+N_{\mathrm{cp}}^{\mathrm{P}}} s[n]p(t-nT_{\mathrm{s}}) \quad (8)$$

The *continuous*-time signal relevant for sampling the second $\frac{N_{\mathrm{fft}}}{2}$ points of the current frame can be expressed as

$$s_2(t) = \sum_{n=N_{\mathrm{fft}}/2-N_{\mathrm{cp}}}^{N_{\mathrm{fft}}/2-1} s[n]p(t-nT_{\mathrm{s}}) + \sum_{n=N_{\mathrm{fft}}/2}^{N_{\mathrm{fft}}-1} s[n]p(t-nT_{\mathrm{s}}) +$$
$$+ \sum_{n=N_{\mathrm{fft}}-N_{\mathrm{cp}}}^{N_{\mathrm{fft}}-N_{\mathrm{cp}}+N_{\mathrm{cp}}^{\mathrm{P}}-1} s[n,1]p(t-(N_{\mathrm{fft}}+N_{\mathrm{cp}})T_{\mathrm{s}}-(n-N_{\mathrm{fft}})T_{\mathrm{s}}) \quad (9)$$

The *continuous*-time unipolar signal, ready for transmission, can be expressed as

$$s_{\mathrm{c}}(t) = \sqrt{2}\,\mathrm{CLIP}\left(s(t)\right) = \frac{1}{\sqrt{2}}\left(s(t)+|s(t)|\right) \quad (10)$$

210

Therefore, at the receiver, the samples of a given frame after match filtering can be expressed as

$$\hat{s}_{\mathrm{h}}[n] = (s_{\mathrm{c}}(t) * h(t) + n(t)) * p(t)|_{t=nT_{\mathrm{s}}} =$$

$$= \left(\frac{1}{\sqrt{2}} (s(t) + |s(t)|) * h(t) + n(t) \right) * p(t) \Bigg|_{t=nT_{\mathrm{s}}} =$$

$$= \begin{cases} \left(\frac{1}{\sqrt{2}} (s_1(t) + |s_1(t)|) * h(t) + n(t) \right) * p(t) \Big|_{t=nT_{\mathrm{s}}}, n \le \frac{N_{\mathrm{fft}}}{2} - 1 \\ \left(\frac{1}{\sqrt{2}} (s_2(t) + |s_2(t)|) * h(t) + n(t) \right) * p(t) \Big|_{t=nT_{\mathrm{s}}}, \frac{N_{\mathrm{fft}}}{2} \le n \end{cases}$$

$$(11)$$

where $*$ denotes convolution and $n(t)$ denotes additive white Gaussian noise (AWGN). The cyclic prefix is sufficient to remove interference and to turn the *continuous*-time convolution with the channel, $h(t)$, into a circular convolution in *discrete* time, which can be completely reversed by equalisation. Hence, assuming the channel can be perfectly estimated, the equalised samples at the receiver can be expressed as

$$\hat{s}[n] = (s_{\mathrm{c}}(t) + n(t)) * p(t)|_{t=nT_{\mathrm{s}}} =$$

$$= \left(\frac{1}{\sqrt{2}} (s(t) + |s(t)|) + n(t) \right) * p(t) \Bigg|_{t=nT_{\mathrm{s}}} =$$

$$= \begin{cases} \left(\frac{1}{\sqrt{2}} (s_1(t) + |s_1(t)|) + n(t) \right) * p(t) \Big|_{t=nT_{\mathrm{s}}}, n \le \frac{N_{\mathrm{fft}}}{2} - 1 \\ \left(\frac{1}{\sqrt{2}} (s_2(t) + |s_2(t)|) + n(t) \right) * p(t) \Big|_{t=nT_{\mathrm{s}}}, \frac{N_{\mathrm{fft}}}{2} \le n \end{cases}$$

$$(12)$$

A. ACO-OFDM

From the properties of ACO-OFDM, $s[n] = -s[n + N_{\mathrm{fft}}/2]$. Hence, in this scheme $s_1(t) \approx -s_2(t + \frac{N_{\mathrm{fft}}}{2}T_{\mathrm{s}})$ except for the third terms in (8) and (9). The differences appear due to the noncausal nature of $p(t)$ but are not significant when $N_{\mathrm{cp}}^{\mathrm{p}} << N_{\mathrm{fft}}$. This also implies $|s_1(t)| \approx |s_2(t + \frac{N_{\mathrm{fft}}}{2}T_{\mathrm{s}})|$. At the receiver, the distortion term in the first $\frac{N_{\mathrm{fft}}}{2}$ points, $\frac{1}{\sqrt{2}}|s_1(t)| * h(t) * p(t)\big|_{nT_{\mathrm{s}}}$, is the same as the distortion term in the second $\frac{N_{\mathrm{fft}}}{2}$ points, $\frac{1}{\sqrt{2}}|s_2(t)| * h(t) * p(t)\big|_{nT_{\mathrm{s}}}$, because $|s_1(t)| \approx |s_2\left(t + \frac{N_{\mathrm{fft}}}{2}T_{\mathrm{s}}\right)|$. Hence, distortion will fall on the even subcarriers as in (3).

B. PAM-DMT

From the properties of PAM-DMT, $s[n] = -s[N_{\mathrm{fft}} - n]$. Hence, using the representations in (8) and (9), $s_1(t) \approx -s_2(N_{\mathrm{fft}}T_{\mathrm{s}} - t)$. Differences are observed between the first term in (8) and the third term in (9) as well as between a single point in the third term of (8) and a single point in the first term of (9). The differences appear due to the noncausal nature of $p(t)$ but are not significant for $N_{\mathrm{cp}}^{\mathrm{p}} << N_{\mathrm{fft}}$. This also implies $|s_1(t)| \approx |s_2(N_{\mathrm{fft}}T_{\mathrm{s}} - t)|$. The impulse response of the pulse-shaping filter is even. Therefore, $p(t) = p(-t)$. Hence, a closer look at equation (12) shows that the distortion term after equalisation, formed by $\frac{1}{\sqrt{2}}|s_1(t)| * p(t)\Big|_{t=nT_{\mathrm{s}}}$ and $\frac{1}{\sqrt{2}}|s_2(t)| * p(t)\Big|_{t=nT_{\mathrm{s}}}$, keeps its Hermitian symmetry, and so it is orthogonal to the useful information as described in Section II-B.

C. U-OFDM

The U-OFDM bipolar *discrete* signal is encoded in two consecutive frames. The *continuous*-time bipolar part of $s(t)$ which needs to be sampled for the positive frame can be expressed before transmission as $s_{\mathrm{up}}(t)$ in the form of equation (7). The *continuous*-time bipolar part of $s(t)$ which holds the information of the negative frame can be expressed in the same form as $s_{\mathrm{un}}(t)$. If $s_{\mathrm{up}}[n]$ are the original bipolar samples of the positive frame, and $s_{\mathrm{un}}[n]$ are the original bipolar samples of the negative frame, then by design $s_{\mathrm{up}}[n] = -s_{\mathrm{un}}[n]$. Hence, a closer look at equation (7) shows that $s_{\mathrm{up}}(t) = -s_{\mathrm{un}}(t)$ except for the third terms in the summation. The differences appear due to the noncausal nature of $p(t)$ but are not significant when $N_{\mathrm{cp}}^{\mathrm{p}} << N_{\mathrm{fft}}$. Then, after match filtering at the receiver, the samples of the positive frame and the samples of the negative frame become respectively

$$\hat{s}_{\mathrm{hup}}[n] = \left(\frac{1}{2} (s_{\mathrm{up}}(t) + |s_{\mathrm{up}}(t)|) * h(t) + n_1(t) \right) * p(t) \Bigg|_{t=nT_{\mathrm{s}}}$$

$$(13)$$

$$\hat{s}_{\mathrm{hun}}[n] = \left(\frac{1}{2} (s_{\mathrm{un}}(t) + |s_{\mathrm{un}}(t)|) * h(t) + n_2(t) \right) * p(t) \Bigg|_{t=nT_{\mathrm{s}}}$$

$$(14)$$

where $n_1(t)$ and $n_2(t)$ are two independent identically-distributed instances of the AWGN process. The bipolar samples at the receiver can be reconstructed by subtracting the samples of the negative frame from the samples of the positive frame

$$\hat{s}_{\mathrm{hb}}[n] = \hat{s}_{\mathrm{hup}}[n] - \hat{s}_{\mathrm{hun}}[n] =$$

$$= \left(\frac{1}{2} (s_{\mathrm{up}}(t) - s_{\mathrm{un}}(t)) * h(t) + n_1(t) - n_2(t) \right) * p(t) \Bigg|_{t=nT_{\mathrm{s}}}$$

$$(15)$$

The nonlinear distortion terms $\frac{1}{2}|s_{\mathrm{up}}(t)| * h(t) * p(t)\big|_{t=nT_{\mathrm{s}}}$ and $\frac{1}{2}|s_{\mathrm{un}}(t)| * h(t) * p(t)\big|_{t=nT_{\mathrm{s}}}$ are equal and so are completely removed by the subtraction operation. The noise doubles as shown in [5] and [6].

For all three schemes, a cyclic suffix with length $N_{\mathrm{cp}}^{\mathrm{p}}$ could be added at the end of each frame to counter the effect of subsequent frames and remove the ISI and resulting distortion due to the noncausal impulse response of the pulse-shaping filter. The value of $N_{\mathrm{cp}}^{\mathrm{p}}$ depends on $p(t)$.

V. NUMERICAL RESULTS

Monte Carlo simulations with 16-QAM ACO-OFDM, 16-QAM U-OFDM, and 4-PAM PAM-DMT have been conducted in order to confirm the theory from Section IV. Figs. 4(a)-4(c) present the results for $N_{\mathrm{fft}}=64$ and a cyclic prefix with length $N_{\mathrm{cp}}=5$. The channel has been assumed flat with gain 1. As can be observed from the examples, the original signal is almost completely recovered if clipping is done after the pulse shaping. Nevertheless, some distortion is still present due to the noncausal impulse response of the shaping filter. Figs. 4(d)-4(f) present the results for $N_{\mathrm{fft}}=64$ and the addition of a cyclic suffix with length $N_{\mathrm{cp}}^{\mathrm{p}}=5$. The cyclic suffix improves
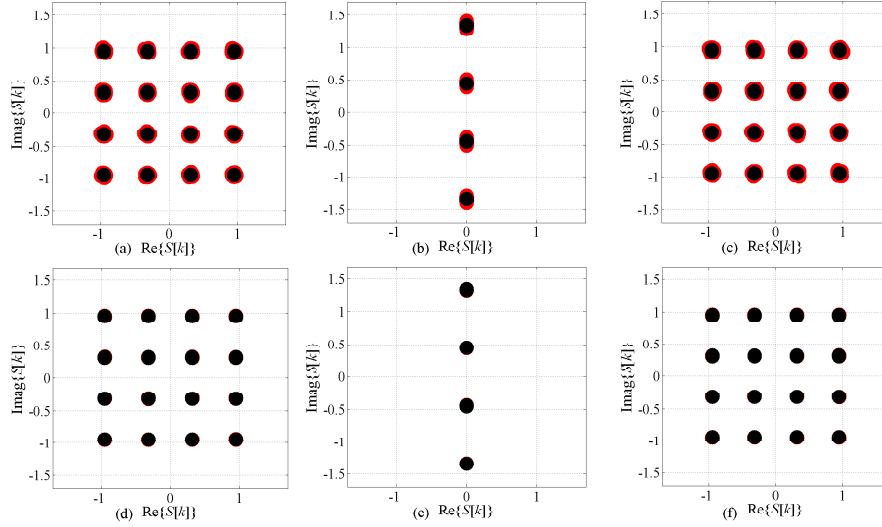
211

Fig. 4. (a) 16-QAM ACO-OFDM with a prefix only. (b) 4-PAM PAM-DMT with a prefix only. (c) 16-QAM U-OFDM with a prefix only. (d) 16-QAM ACO-OFDM with a prefix and a suffix. (e) 4-PAM PAM-DMT with a prefix and a suffix. (f) 16-QAM U-OFDM with a prefix and a suffix.

TABLE I
SDR VALUES FOR 16-QAM ACO-OFDM, 16-QAM U-OFDM, AND 4-PAM PAM-DMT FOR DIFFERENT NUMBER OF FRAME CARRIERS

N_{fft}	ACO-OFDM SDR [dB]		PAM-DMT SDR [dB]		U-OFDM SDR [dB]	
	Prefix Only	Prefix & Suffix	Prefix Only	Prefix & Suffix	Prefix Only	Prefix & Suffix
16	35.43	58.06	37.17	60.35	36.69	57.77
64	41.18	63.48	42.88	65.33	42.92	62.88
256	47.16	67.65	48.21	69.19	47.96	67.66

the recovered signal as expected. We define signal-to-distortion ratio (SDR) as

$$\text{SDR} = \frac{\text{E}\left[S^2[k]\right]}{\text{E}\left[\left(S[k] - \bar{S}[k]\right)^2\right]} \qquad (16)$$

where $\bar{S}[k]$ denotes the distorted carrier values after pulse shaping and clipping, $\text{E}[\cdot]$ denotes expectation. Table I shows the SDR for a varying number of carriers, N_{fft}. It also shows the SDR for cases with and without a suffix. Increasing the number of carriers improves the SDR as the influence of subsequent frames becomes a smaller part of the overall signal. Adding a cyclic suffix improves the SDR significantly as it removes a big portion of the ISI caused by the pulse-shaping filter.

VI. CONCLUSION

Pulse shaping is an integral part of a communication system. Pulse shaping filters differ in terms of bandwidth requirements, ISI, and polarity. *Discrete* unipolar signals require unipolar pulse shapes to avoid bipolarity without additional power dissipation. If pulse shaping is applied before clipping, bipolar pulse-shaping filters can be used for the three modulation schemes ACO-OFDM, U-OFDM, and PAM-DMT, and in-band interference can be avoided. The structure of the interference terms suggests that even out-of-band interference could

be avoided between systems that employ the same modulation concept. This could be a subject of further investigation.

REFERENCES

[1] "Visible Light Communication (VLC) - A Potential Solution to the Global Wireless Spectrum Shortage," GBI Research, Tech. Rep., 2011. [Online]. Available: http://www.gbiresearch.com/
[2] H. Elgala, R. Mesleh, and H. Haas, "Indoor Optical Wireless Communication: Potential and State-of-the-Art," *IEEE Commun. Mag.*, vol. 49, no. 9, pp. 56–62, Sep. 2011, ISSN: 0163-6804.
[3] J. Armstrong and A. Lowery, "Power Efficient Optical OFDM," *Electronics Letters*, vol. 42, no. 6, pp. 370–372, Mar. 16, 2006.
[4] S. C. J. Lee, S. Randel, F. Breyer, and A. M. J. Koonen, "PAM-DMT for Intensity-Modulated and Direct-Detection Optical Communication Systems," *IEEE Photonics Technology Letters*, vol. 21, no. 23, pp. 1749–1751, Dec. 2009.
[5] D. Tsonev, S. Sinanović, and H. Haas, "Novel Unipolar Orthogonal Frequency Division Multiplexing (U-OFDM) for Optical Wireless," in *Proc. of the Vehicular Technology Conference (VTC Spring)*, IEEE. Yokohama, Japan: IEEE, May 6–9 2012, to appear.
[6] N. Fernando, Y. Hong, and E. Viterbo, "Flip-OFDM for Optical Wireless Communications," in *Information Theory Workshop (ITW)*, IEEE. Paraty, Brazil: IEEE, Oct., 16–20 2011, pp. 5–9.
[7] J. G. Proakis and D. K. Manolakis, *Digital Signal Processing: Principles, Algorithms and Application*, 4th ed., T. Robbins, Ed. Prentice Hall, Apr. 2006.

212

Practical MIMO Capacity for Indoor Optical Wireless Communication with White LEDs

Dobroslav Tsonev*, Sinan Sinanovic [†] and Harald Haas*

* *Institute for Digital Communications, The University of Edinburgh, EH9 3JL, Edinburgh, UK*

[†] *School of Engineering and Built Environment, Glasgow Caledonian University, G4 0BA, Glasgow, UK*

Email: d.tsonev@ed.ac.uk, sinan.sinanovic@gcu.ac.uk, h.haas@ed.ac.uk

Abstract—**Multiple-input-multiple-output systems provide a potential approach for achieving high communication capacities in optical wireless. A small amount of publications based on different scenarios are available. The current work will illustrate that a very good distribution of communication capacity can be achieved for certain configurations. In particular, we look at angle diversity receivers which are able to successfully identify transmitter directions. The investigated scenarios include 4x4 and 16x16 multiple-input-multiple-output configurations.**

I. INTRODUCTION

Solid state lighting has seen remarkable improvements over the past two decades. Energy-efficient illumination devices such as light emitting diodes (LEDs) have gained large popularity due to the cheaper and superior lighting capabilities they provide. More than that, they offer good modulation capabilities, around 2 MHz for white light and up to 20 MHz for blue light [1], which enable high speed data transmission. This development has come at a point in time when demand for data traffic is growing exponentially. It is estimated that by 2015 more than 6 exabytes of data would be transferred through wireless networks [2]. Despite the great improvements in communication standards and electronics, the satisfaction of this demand is deterred by the limited available bandwidth. The radio frequency (RF) spectrum has been almost completely utilised. At a certain point, it would be physically impossible to increase signal speeds unless a new physical domain - such as the optical spectrum - is utilised. This part of the spectrum has further benefits. It offers thousands of times more bandwidth; it is unregulated; it does not interfere with sensitive electronic equipment; it has no anticipated negative effects on human health, and systems can be built with low-cost front-end devices which are increasingly employed in the lighting infrastructure anyway.

The concept of multiple-input-multiple-output (MIMO) systems comes from RF communication where the communication environment subjects the transmitted signals to a number of physical phenomena like fading, refraction, reflection etc. These effects decorrelate the gain and phase between different antenna elements at the receiver and the transmitter which allows information to be successfully divided into different streams. The modulation speeds of off-the-shelf LEDs, 2-20 MHz [1], and the significantly higher coherence bandwidth of indoor optical wireless channels make MIMO a very good candidate for achieving high speed data transmission.

The current state of commercial optical components allows optical wireless to be realised as an intensity modulation/direct detection (IM/DD) system. In such a realisation, the phase of optical waves cannot be reconstructed leading to the usage of signal intensity as the only means to convey information. In addition, the rather small propagation environments of indoor optical wireless lead to very similar channel gains between front-end devices which are close in space and thus lead to very low channel diversity. Overall, MIMO in optical wireless communication (OWC) is challenging to translate from the RF domain.

A limited number of publications are available on the subject of optical MIMO systems [3]–[5]. Two types of optical MIMO realisations can be identified based on their receiver configuration: non-imaging and imaging [3]. In an imaging system, a single lens projects an image of each transmitter on a matrix of photodetectors. The high diversity, resulting from the large number of receiving elements, creates a full-rank channel matrix, and so the information can be successfully recovered [6]. This approach has certain limitations when unconstrained movement needs to be allowed within the communication space [3]. Individual detector elements would have small gains especially when combined with large field of view (FOV) optics. Furthermore, we believe that the single imaging lens leads to limitations in the receiver shape, which we believe is going to be crucial for systems with good coverage and independent communication streams. Systems with a nonimaging receiver have a number of optical detectors which operate independently and have individual concentrator optics. The benefit of this approach is that large gains can be achieved for individual receiving elements with narrow FOV [7]. The disadvantage of such a configuration is that it is very sensitive to misalignment of the frontend elements.

O'Brien concludes in [8] that the "ideal" MIMO system will probably be a compromise between imaging and nonimaging configurations. We agree with this conclusion and suggest that a compromise could be found in angle diversity receivers, which employ a number of nonimaging detector elements at various angles thus achieving both good coverage and high gains [7]. We believe that such systems with a large number of detectors provide enough design flexibility to construct a receiver with good coverage, gain and ability to align itself with optical transmitters. A simple example of such a device is illustrated in Fig. 1. For a spherically-shaped receiver with a
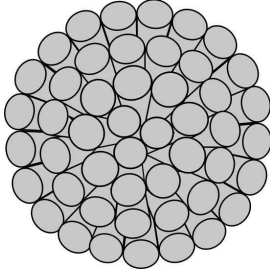
Fig. 1.   Example of an angle diversity receiver.

Fig. 2.   Quantities related to transfer of light between a source and a destination.

large number of detectors that have a narrow FOV, each of the transmitters will always be in good alignment with at least one detector provided that there is no shadowing. The greater the number of detectors is and the narrower their FOV is, the better will be the ability of the receiver to distinguish the different streams. The independence of the nonimaging detectors allows more flexibility in the construction of different receiver shapes. The principles from the imaging receiver could be used to perform good alignment algorithmically with the processing circuitry. In a way, the receiver we are proposing emulates the imaging receiver but with simpler optics and more design flexibility. As a first step of the design process, the current work will describe the communication capacity in a typical indoor optical MIMO system in which the receiver elements have managed to capture the locations of the transmitters perfectly. Future work will include constructing an optimal receiver shape and performing a good alignment algorithm.

The rest of this paper is organised as follows. Section II provides a description of the communication channel model and how it is estimated. Section III describes the simulation setup. Section IV gives numerical values for the capacity distribution across a standard indoor environment. Finally, section V provides concluding remarks.

II. Optical MIMO Channel Model

A typical l by k MIMO system is described by the following equation:

$$\mathbf{y} = \mathbf{Hx} + \mathbf{n} \tag{1}$$

where $\mathbf{x} = [x_1, x_2, ..., x_l]$ are the symbols emitted from each of the l transmitters, $\mathbf{y} = [y_1, y_2, ..., y_k]$ are the values received at each of the k receivers, $\mathbf{H}$ describes the gain factors between the different front end elements, and $\mathbf{n} = [n_1, n_2, ..., n_k]$ are simply independent identically distributed (i.i.d.) realisations of the additive white Gaussian noise (AWGN) processes which corrupt samples at the receivers.

At a receiver with area A_r, the received optical power, P_r, radiated from a point source with optical power of P_t is [7], [9], [10]:

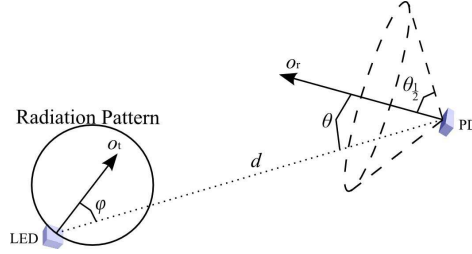$$P_r = P_t \frac{m+1}{2\pi} \cos^m(\phi) G_{of}(\lambda) G_{oc}(\theta) \frac{\cos(\theta) A_r}{d^2} \tag{2}$$

where m is the mode number of the source; ϕ is the angle at which light is emitted relative to the normal vector of the transmitter plane; θ is the angle at which the light is received relative to the normal vector of the receiver plane; d is the distance between the devices; G_{of} is the gain of the optical filter; G_{oc} is the gain of the optical concentrator; $\theta_{\frac{1}{2}}$ is the semiangle of the optical concentrator. An illustration of the quantities is presented in Fig. 2. The mode number of the source, m, specfies the order of directionality and can be calculated as [9]:

$$m = \frac{-\ln(2)}{\ln\left(\cos\left(\phi_{\frac{1}{2}}\right)\right)} \tag{3}$$

where $\phi_{\frac{1}{2}}$ is the transmitter semiangle. The optical concentrator gain, G_{oc}, is ideally equal to [7]:

$$G_{oc}(\theta) = \begin{cases} \frac{r^2}{\sin^2\left(\theta_{\frac{1}{2}}\right)}, & |\theta| \le \theta_{\frac{1}{2}} \\ 0, & |\theta| > \theta_{\frac{1}{2}} \end{cases} \tag{4}$$

where r is the refractive index of the optical concentrator material. According to [7] and [11], this theoretical limit for a concentrator gain can be closely approached with existing design techniques. Hence, it will be used as the concentrator model in this work. The optical filter gain, G_{of}, will be specified as:

$$G_{of}(\lambda) = \begin{cases} g_o, & \lambda_1 \le \lambda \le \lambda_2 \\ 0, & \text{otherwise} \end{cases} \tag{5}$$

where the optical filter gain is considered independent of the light incidence angle, θ, as the detector FOV assumed in this work is sufficiently narrow. In addition, the authors in [7] state that it is possible to circumvent the filter dependency on the light incidence angle if the filter is applied as a coating of the optical concentrator.

If $\mathbf{p}_t$ is the position vector of the transmitter, $\mathbf{p}_r$ is the position vector of the receiver, $\mathbf{o}_t$ is the orientation vector of the transmitter (orthogonal to the transmitter plane) and $\mathbf{o}_r$ is the orientation vector of the receiver (orthogonal to the receiver plane), then the angles ϕ and θ are described by [10]:

$$\cos(\phi) = \frac{\mathbf{o}_t \cdot (\mathbf{p}_r - \mathbf{p}_t)}{d} \tag{6}$$

$$\cos(\theta) = \frac{\mathbf{o}_{\mathrm{r}} \cdot (\mathbf{p}_{\mathrm{t}} - \mathbf{p}_{\mathrm{r}})}{d} \tag{7}$$

where, $\cdot$, denotes a vector dot product, and the distance between the transmitter and receiver, d, can be calculated as [10]:

$$d = \sqrt{(\mathbf{p}_{\mathrm{t}} - \mathbf{p}_{\mathrm{r}})^{\mathrm{T}} \cdot (\mathbf{p}_{\mathrm{t}} - \mathbf{p}_{\mathrm{r}})} \tag{8}$$

where $[]^{\mathrm{T}}$ denotes the transpose operator.

In order to create a ray tracing algorithm which follows the multiple reflections of light that travel across a room and reach the receiver, the surfaces in the room can be divided into small rectangles. Those can be modelled as receivers with area A which absorb light according to (2) and reemit a portion of it just like the original source. This approach is well-described in [10]. Depending on the material from which each surface is constructed, the radiation pattern it has is different, but the majority of surfaces can be modelled as ideal Lambertian sources with a semiangle of ϕ=60º. The light portion which is reemitted after absorption varies typically between ρ=0.4 and ρ=0.9 of the absorbed light [9]. In this work, light path has been traced up to the fifth reflection. The reflectivity of wall surfaces has been assumed as ρ=0.65.

An OWC channel has two main contributors to signal disturbances: shot noise from ambient light reaching the photodiode (PD) and thermal noise from the transimpedance amplifier at the receiver. In a well-lit environment, the thermal noise is significantly weaker than the shot noise for modulation frequency, B, up to 20 MHz [7], [12]. That is why, the current work will consider only shot noise as a significant contributor to signal disturbances. The power spectral density of shot noise can be calculated as [7]:

$$N_{\mathrm{o}} = 2qRP_{\mathrm{n}} \quad \left[\frac{\mathrm{A}^2}{\mathrm{Hz}}\right] \tag{9}$$

where $q = 1.60217646\mathrm{x}10^{-19}$ C is the charge of an electron in coulombs, R is the responsivity of the PD in A/W, and P_{n} is the power of the optical noise reaching the detector.

Theoretical capacity of MIMO optical wireless Gaussian channels is not readily available to the best of our knowledge. However, if we are not concerned with the exact power dissipation of a system, the capacity equation for RF MIMO channels can be used. MIMO capacity in a RF system is described in [13] and its formula is repeated here for convenience:

$$C = B \log_2 \left(\det \left(\mathbf{I} + \frac{P_{\mathrm{s}}}{N} \mathbf{H}\mathbf{H}^{\mathrm{H}} \right) \right) \mathrm{bit/s} \tag{10}$$

where $\det()$ denotes a determinant, $\mathbf{I}$ is the identity matrix, $[]^{\mathrm{H}}$ denotes the Hermitian conjugate of a matrix, P_{s} denotes the variance of the signal at a single transmitter, and N stands for the variance of the AWGN which can be calculated as N=BN_{o}. This formula describes the capacity if no channel state information is available at the transmitter. We adopt it because it suggests a simpler system design without feedback from the receiver. The absolute channel capacity is achieved when the channel matrix, $\mathbf{H}$, is available at the transmitter and bits are encoded adaptively according to the respective channel quality.

III. INDOOR COMMUNICATION SETUP

For consistency, the current work considers a 5.0 m x 5.0 m x 3.0 m empty room. The same setup is used in a number of other publications [3], [10], [12]. A 4×4 and a 16×16 MIMO schemes have been simulated in three different cases. In the first case, the receiver is at a distance of 85 cm from the floor (the approximate height of a desk) in consistence with the work in [3], [10], [12]. In the second case, the receiver is at a distance of 135 cm from the floor (the approximate height of a handheld device when used in a mobile scenario). In the third case, the receiver is at a distance of 175 cm from the floor (the approximate height of an average human's ear). An actual realisation of an angle diversity receiver, as illustrated in Fig. 1, would have more detectors than what is simulated here. We assume that the alignment algorithm has managed to successfully determine the 4 or 16 detectors, depending on the MIMO scheme, that have the best view of the different transmitters, and we simulate the capacity that can be achieved with those detectors only. At each position in the room, we assume that the detectors are directed at the exact positions of the transmitters. The transmitters are fixed at positions displayed in Fig. 3.
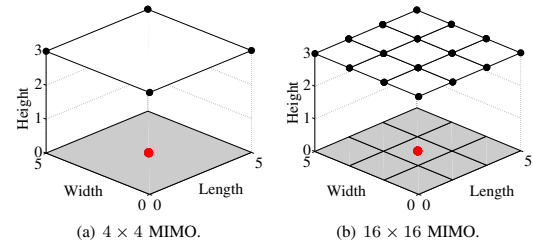

(a) 4×4 MIMO. (b) 16×16 MIMO.

Fig. 3.   Communication setup for different scenarios. Black spots indicate transmitters. Red spot on the floor has position $\mathbf{p}_{\mathrm{d}} = [2.5, 2.5, 0]$ and indicates the direction of all transmitters.

Each transmitter uses an OSTAR LE CW E3A high-power illumination LED for white light communication or an OSTAR LE W E2B high-power illumination LED for blue light communication. Each photodetector uses an OSRAM SFH 213 PIN PD. The modulation bandwidth is considered as $B = 2$ MHz for white light, and $B = 10$ MHz for blue light. The white light bandwidth is consistent with devices from other sources like [1]. The blue light modulation bandwidth of 20 MHz specified in [1] is the highest we have seen reported so far and exceeds the one we have measured. The devices which are used in [1] are not specified. The LED devices have a Lambertian emitter pattern with a semiangle of $\phi_{\frac{1}{2}} = 60º$. This means that the mode number of the source is $m = 1$ when calculated according to (3). The PD has a semiangle of $\theta_{\frac{1}{2}} = 10°$ and a plastic concentrator with refractive index of $r = 1.54$. Then, the optical concentrator gain can be calculated according to (4). The blue filter has a very sharp transfer characteristic that allows blue light in the range between λ_1=430 nm and λ_2=490 nm with a gain of g_{o}=0.9. The PD

sensitivity to white light has been calculated as $R = 0.33$ A/W and to blue light as $R = 0.15$ A/W for the OSTAR LE CW E3A LED. The same values have been calculated as $R = 0.27$ A/W for white light and as $R = 0.15$ A/W for blue light for the OSTAR LE W E2B. These values are lower than the ones specified in [1] and [12]. Without loss of generality, devices with better parameters could be used in order to improve signal-to-noise ratio (SNR) values at the receiver. The portion of blue light in the emitted spectrum by OSTAR LE CW E3A is 0.11 while it is 0.27 for OSTAR LE W 2EB which makes the latter more beneficial for blue light communication. The allowed current for both devices is in the range 0.1 A $- 1$ A with optical efficiency of about 25 lm/W. The radiated optical power was measured at 3.6×10^{-3} W/lm. The assumption is that the distribution of a Gaussian signal between -3σ and 3σ (99.73% of distribution) needs to be fit in the LED active range of 0.9 A in order to avoid significant clipping effects. That makes a maximum signal variance of $\sigma^2 = (0.9/6)^2 = 0.0225$ A^2. The power spectral density of the ambient noise, which we have measured in a well-lit room with a combination of sunlight and fluorescent light, is around 10^{-21} A^2/Hz for white light, which is in the order of magnitude presented by [1]. The blue light filter reduces the amount of ambient noise which falls on the receiver. Considering that sunlight has an almost uniform wavelength distribution and the fact that we have a sharp filter that passes only light between $\lambda = 430$ nm and $\lambda = 460$ nm, we assume that roughly about 15% of the shot noise will be present for the blue light receiver.

IV. NUMERICAL RESULTS

Capacity estimations are performed for white light communication and for blue light communication with the setup from Section III. Fig. 4 presents the capacity distribution across the room for white light. Fig. 5 presents the capacity distribution with blue light filtering. It seems that white light communication has the potential for higher capacities than blue light despite the higher frequencies achievable with the latter. This is due to the fact that the SNR values of the received signal are insufficient for the blue-light system to take advantage of the higher bandwidth. It also seems that the communication system is at a point where it is very sensitive to SNR changes. This can be verified by changing the parameter for blue light sensitivity of the PD to $R = 0.28$ A/W, the amount of transmitted blue light to 0.5 of the overall LED emission, and the modulation frequency to 20 MHz as in [1]. The achieved capacity with blue light communication increases dramatically as illustrated in Fig. 6.

It is hard to put an absolute theoretical limit to achievable communication throughput because a great number of parameters are a subject of design variation. We have shown that very good transmission speeds are possible with existing off-the-shelf components. We also believe that improved speeds can be realised not only through selection of devices with improved parameters, but also through better transmitter configurations. Furthermore, an angle diversity receiver of the type illustrated in Fig. 1 can allow not only for automatic
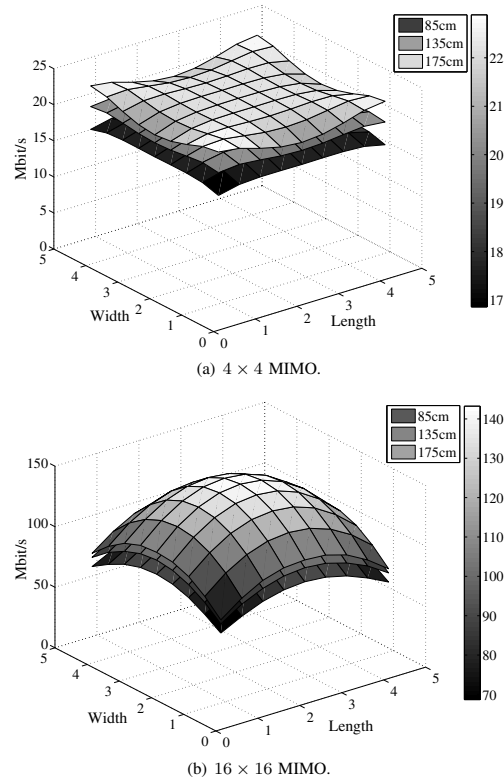

(a) 4×4 MIMO.

(b) 16×16 MIMO.

Fig. 4. Capacity distribution of white light communication for different MIMO schemes.

alignment, but also for improved SNR values since more than one detector is likely to pick up the individual transmitter signals which could lead to high diversity gains. The most important result from the conducted experiments is that communication capacity changes gradually for a moving receiver across a typical office space. Furthermore, even with multiple light reflections, narrow FOV receivers are able to decrease interchannel interference (ICI) allowing for the realisation of MIMO communication schemes.

V. CONCLUSION

The current work has investigated the achievable communication capacity in a typical 5.0 m x 5.0 m x 3.0 m office space by means of an optical wireless MIMO system. Fixed transmitters with wide illumination angles have been selected in combination with narrow FOV photodetectors. The communication scenario assumes an angle diversity receiver with multiple detector elements. At any given time, each transmitter is within the FOV of at least one detector. Assuming that such detectors are successfully identified from the large array of detector elements, we have shown that very good communication capacity distribution is available for such a system.
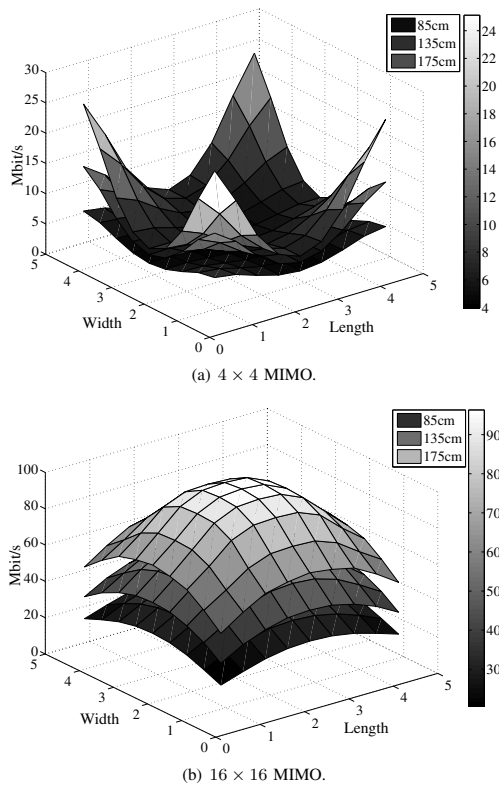
(a) 4×4 MIMO.

(b) 16×16 MIMO.

Fig. 5. Capacity distribution of blue light communication for different MIMO schemes.

(a) 4×4 MIMO.

(b) 16×16 MIMO.

Fig. 6. Capacity distribution of blue light communication for different MIMO schemes with parameters from [1].

Plans for further work include the design of the proposed angle diversity receiver and exact simulation of achievable data rates for specific receiver alignment algorithms.

REFERENCES

[1] J. Grubor, S. Randel, K. Langer, and J. Walewski, "Bandwidth Efficient Indoor Optical Wireless Communications with White Light Emitting Diodes," in *In the Proceeding of the 6th International Symposium on Communication Systems, Networks and Digital Signal Processing*, vol. 1, Graz, Austria, Jun. 23–25, 2008, pp. 165–169.
[2] "Visible Light Communication (VLC) - A Potential Solution to the Global Wireless Spectrum Shortage," GBI Research, Tech. Rep., 2011. [Online]. Available: http://www.gbiresearch.com/
[3] L. Zeng, D. O'Brien, H. Minh, G. Faulkner, K. Lee, D. Jung, Y. Oh, and E. T. Won, "High Data Rate Multiple Input Multiple Output (MIMO) Optical Wireless Communications using White LED Lighting," *IEEE J. Select. Areas Commun.*, vol. 27, no. 9, pp. 1654–1662, Dec. 2009.
[4] R. Mesleh, R. Mehmood, H. Elgala, and H. Haas, "Indoor MIMO Optical Wireless Communication Using Spatial Modulation," in *IEEE International Conference on Communications (ICC)*, Cape Town, South Africa, May 22–27 2010, pp. 1–5.
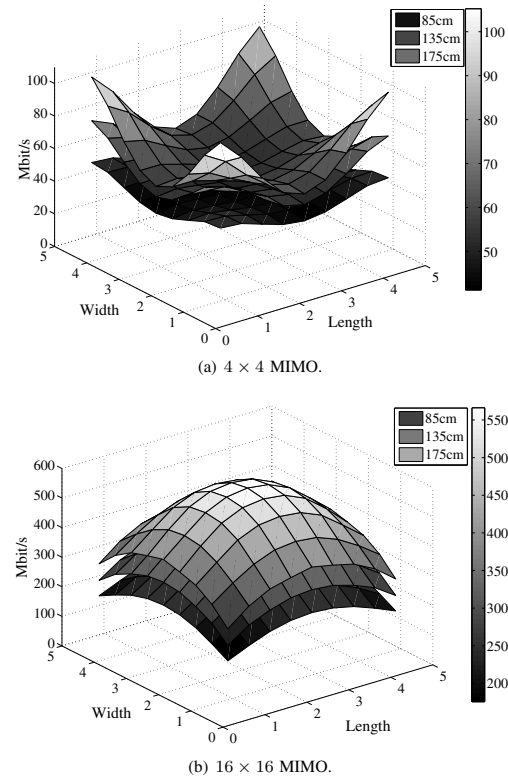[5] T. Fath and H. Haas, "Performance Comparison of MIMO Techniques for Optical Wireless Communications in Indoor Environments," *IEEE Transactions on Communications (IEEE TCOM)*, vol. PP, no. 99, pp. 1–10, Dec. 2012.
[6] S. Hranilovic, *Wireless Optical Communication Systems*, 1st ed. Springer, Sep. 1996.
[7] J. M. Kahn and J. R. Barry, "Wireless Infrared Communications," *Proceedings of the IEEE*, vol. 85, no. 2, pp. 265–298, Feb. 1997.
[8] D. O'Brien, "Multi-Input Multi-Output (MIMO) indoor optical wireless communications," in *Conference Record of the Forty-Third Asilomar Conference on Signals, Systems and Computers*, Nov. 2009, pp. 1636–1639.
[9] F. R. Gfeller and U. Bapst, "Wireless In-House Data Communication Via Diffuse Infrared Radiation," *Proceedings of the IEEE*, vol. 67, no. 11, pp. 1474–1486, Nov. 1979.
[10] J. Barry, J. Kahn, W. Krause, E. Lee, and D. Messerschmitt, "Simulation of multipath impulse response for indoor wireless optical channels," *IEEE J. Select. Areas Commun.*, vol. 11, no. 3, pp. 367–379, Apr. 1993.
[11] X. Ning, R. Winston, and O. J., "Dielectric totally internally reflecting concentrators," *OSA Applied Optics*, vol. 26, pp. 300–305, Jan. 1987.
[12] T. Komine and M. Nakagawa, "Fundamental Analysis for Visible–Light Communication System using LED Lights," *IEEE Transactions on Consumer Electronics*, vol. 50, no. 1, pp. 100–107, Feb. 2004.
[13] E. Telatar, "Capacity of Multi-Antenna Gaussian Channels," *European Transaction on Telecommunication*, vol. 10, no. 6, pp. 585–595, Nov. / Dec. 1999.

A Novel Analytical Framework for Modeling Nonlinear Distortions in OFDM-based Optical Wireless Communication

Invited Paper

Dobroslav Tsonev [*], Sinan Sinanovic [†] and Harald Haas [*]

[*] *Institute for Digital Communications, Joint Research Institute for Signal and Image Processing,*
The University of Edinburgh, EH9 3JL, Edinburgh, UK
Email: {dtsonev, h.haas} @ed.ac.uk

[†] *School of Engineering and Built Environment,*
Glasgow Caledonian University, Glasgow, G4 0BA, UK
Email: sinan.sinanovic@gcu.ac.uk

Abstract—This paper presents an analytical framework to determine the impact of nonlinear distortions in an optical wireless communication system that employs orthogonal frequency division multiplexing (OFDM). The presented theory applies the Bussgang theorem, which has been widely used for the analysis of nonlinear effects on normally-distributed signals. This work proposes a new method to complete the well-known OFDM analysis approach based on the Bussgang theorem and describes how a closed-form analytical solution can be obtained for an arbitrary memoryless distortion. The framework is tested in a DC-biased optical OFDM system assuming two specific examples of nonlinear distortion caused by: (a) signal quantisation, and (b) a nonlinear light emitting diode (LED) characteristic.

Index Terms—optical wireless communication (OWC), DC-biased optical OFDM (DCO-OFDM), nonlinear distortion.

I. Introduction

Demand for wireless data communication is growing exponentially. It is expected that by 2016, more than 10 Exabytes of monthly traffic would be required in mobile networks [1]. Despite the significant improvements in communication standards, it is very likely that the demand will not be met. The main reason for this is the significantly reduced radio frequency (RF) spectrum availability within the licensed bands. In the past decade, a lot of research efforts have been directed towards finding alternative communication bandwidth. A major candidate for providing a complementary alternative to RF communication is optical wireless communication (OWC). The optical spectrum features thousands of times more unregulated bandwidth than its RF counterpart. Furthermore, optical radiation does not interfere with the operation of sensitive electronic systems. This means that OWC can be employed in environments that are sensitive to RF radiation such as hospitals, airplanes, petrochemical plants, etc. In addition, OWC can be realised in conjunction with RF where they both complement each other in a high-throughput heterogeneous network. Existing lighting infrastructure could be reused for the deployment of OWC. The energy used for illumination could serve for communication purposes as well. This has

the potential to reduce operational costs significantly and to decrease the environmental impact of wireless services.

The physical properties of available low-cost front-end devices, such as light emitting diodes (LEDs) and photodiodes (PDs), allow OWC to be realised as an intensity modulation and direct detection (IM/DD) system. This is because the light emitted by LEDs is incoherent and so information can be encoded only in the signal intensity. Phase and amplitude of the light wave cannot be modulated or detected. This limits the set of conventional modulation schemes that can be applied. Therefore, traditional pulsed modulation techniques such as on-off keying (OOK), pulse-position modulation (PPM), and pulse-amplitude modulation (PAM) have been used in OWC. However, with the increase of transmission rates, the limited bandwidth of the optical wireless communication channel leads to intersymbol interference (ISI). Hence, orthogonal frequency division multiplexing (OFDM) becomes a more appropriate modulation scheme. It enables simple equalisation with single-tap equalisers in the frequency domain as well as adaptive bit-loading of different frequency subcarriers according to the channel properties, which results in a more optimal use of the communication resources. At a system level, OFDM provides a simple and straightforward multiple access scheme. In OOK, PPM and PAM, the multiple access technique would need to be added separately, and the options are limited since, for example, frequency division multiple access (FDMA) cannot be used.

Whenever a signal is passed through an OWC system, it undergoes a number of distortions. Linear distortions, such as attenuation and ISI, can be compensated by amplifiers and equalisers. Nonlinear distortions, however, are often irreversible. Examples include quantisation effects in the digital-to-analog converters (DACs) and the effects caused by the nonlinear output characteristic of an LED. Performance analysis of OWC systems requires the designer to characterise and evaluate nonlinear distortion effects. A number of works have dealt with characterising distortion in OFDM-based modula-
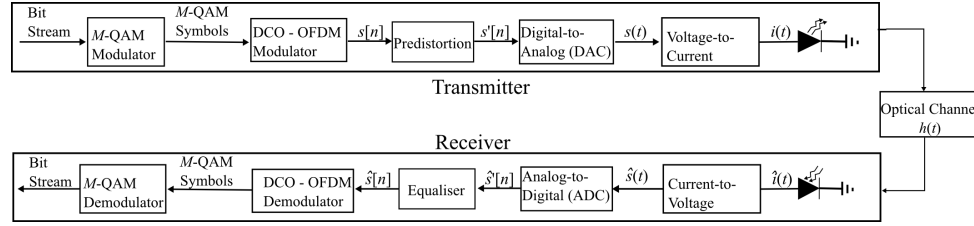
Fig. 1. Optical Wireless Communication System

tion schemes [2–9]. Papers [2–5] look at applications in RF communication, and so only some general analysis principles they present are applicable to OWC. The other works, [6–9], focus specifically on the nonlinear distortions in an OWC system. For example, the authors in [6] look at distortion caused by the nonlinear relationship between current input and light output in an LED within the active range of the device. The actual distortion function is continuous, and the presented case neglects some nonlinear effects such as clipping. Papers [8, 9] analyse the clipping effects only, and the work in [7] looks at the overall LED nonlinearity but in a semi-analytic fashion. Analysis of nonlinear distortions can be a cumbersome task. Although general procedures for obtaining an analytical solution exist [2], a closed-form solution is not always easily obtainable. The current work attempts to completely solve the problem by establishing a general framework which *always* leads to a closed-form solution regardless of the type of memoryless nonlinearity. This framework, for example, can be applied to all the problems presented in [6–9] as well as any other arbitrary memoryless nonlinear distortion in an OWC OFDM-based system. Closed-form solutions do not require high computational complexity as those that require numerical evaluation of integrals. Compared to Monte Carlo simulations, closed-form solutions reduce simulation times tremendously, which can prove to be invaluable in optimization procedures.

The remainder of this paper is organised as follows. Section II introduces the OWC system. Section III presents the framework. Section IV discusses the results. Finally, Section V concludes the paper.

II. OWC SYSTEM

The block-diagram of an OWC system is presented in Fig. 1. The incoming bit stream is fed to the modulator where it is mapped to symbols from a known modulation scheme such as M-level quadrature amplitude modulation (M-QAM). These symbols are put on different frequency subcarriers and modulated according to DC-biased optical OFDM (DCO-OFDM). The time domain signal, obtained after multicarrier modulation, is conditioned for transmission. This block includes clipping any values outside the allowed range, as well as pulse shaping and any other required predistortion. Clipping is performed because an LED can only operate above its turn-on voltage and below its maximum allowed current. The conditioned signal is fed to a DAC which outputs an

analog signal. The analog signal is then passed through a voltage-to-current transducer with appropriate bias according to the LED requirements and fed to the diode. At the receiver side, the photodiode transforms optical intensity levels into proportional current variations, which are turned into voltage by the transimpedance amplifier. The resulting signal is passed through an analog-to-digital converter (ADC) and fed to the processing circuitry, which includes an equaliser, DCO-OFDM demodulator, and an M-QAM demodulator.

The modulation scheme presented in this paper is a modification of conventional OFDM. Each subcarrier in frequency domain is modulated with a symbol from the M-QAM modulation scheme. The time domain signal is obtained by taking the inverse fast Fourier transform (IFFT) of N_{FFT} M-QAM symbols. Hermitian symmetry is imposed, such that a real time domain signal can be obtained according to the properties of the Fourier transform [8, 9]. As a result, subcarriers at positions $k = 0$ and $k = \frac{N_{\text{FFT}}}{2}$ are set to zero. The Hermitian symmetry constraint ensures the generation of a real signal in time domain. This signal, however, is bipolar in nature. An LED can convey only positive signals when it is active. Hence, a DC-bias is introduced in order to generate a unipolar signal, suitable for OWC. This DC-bias is realised by means of an analog circuit as part of the LED driver.

In the context of the current work, the optical wireless communication channel, $h(t)$, is considered to be flat fading, i.e., $h(t)=\delta(t)$. This assumption is made in order to simplify the analysis. In practice, the channel will not be flat fading, which leads to ISI. This occurs if high-speed communication is realised, where the symbol rate exceeds the coherence bandwidth of the communication channel. The effects of $h(t)$ will be reversed by the equaliser at the receiver stage. Memoryless distortions do not include effects such as ISI. However, in OWC the significant nonlinearity effects, which limit performance, happen before the information signal experiences the memory effects of the channel. Therefore, after equalisation, the nonlinearly-distorted signal will have exactly the same form as before it was passed through the channel, $h(t)$. The only notable difference observed at the different frequency subcarriers will be the amount of additive white Gaussian noise (AWGN) as it will be amplified by the equaliser function. Hence, in a practical high-data-rate scenario, the analysis presented here keeps its merits. This is because the method allows the analysis of the most significant nonlinear distortion

148

effects even if the channel is not flat fading. In particular, those nonlinear effects include the signal quantisation distortion introduced by the DAC and the transition between current and light at the LED. The latter nonlinearity occurs due to the physical properties of the device, in which the amount of emitted light is not linearly proportional to the amount of injected current.

III. NONLINEARITY ANALYSIS

A number of different approaches are proposed for the analysis of OFDM-based systems that undergo nonlinear distortions [2–9]. We adopt the one described by Dardari *et al.* in [2]. It states that a nonlinear distortion in an OFDM-based system results in an attenuation factor and additional noise component, both of which modify the resulting signal-to-noise ratio (SNR) of the system and can be computed using the Bussgang theorem. For a large number of subcarriers, $N_{\mathrm{FFT}} > 64$, the samples of the time-domain OFDM signal can be approximated by the realisations of independent identically-distributed Gaussian random variables. This approximation holds, even when not all the subcarriers in the frequency domain are loaded with information such as is the case with alternative modulation schemes like asymmetrically clipped optical OFDM (ACO-OFDM) where only the odd subcarriers in a frame are modulated [8, 10]. The approximation is also valid in cases where guard intervals are inserted in one or both ends of the OFDM spectrum provided that the number of subcarriers in the guard intervals is much smaller than the total number of subcarriers. According to the Bussgang theorem [11], if X is a zero-mean Gaussian random variable, and $g(X)$ is an arbitrary distortion on X, then

$$g(X) = \alpha X + Y_{\mathrm{n}} \tag{1}$$

$$\mathrm{E}[XY_{\mathrm{n}}] = 0 \tag{2}$$

where α is a constant, $\mathrm{E}[\cdot]$ denotes statistical expectation, and Y_{n} is a noise component not correlated with X. From (1) and (2), α can be calculated as:

$$\alpha = \frac{\mathrm{E}[Xg(X)]}{\sigma^2} \tag{3}$$

where σ^2 is the variance of X. The expectation of Y_{n}^2 can be calculated as:

$$\mathrm{E}[Y_{\mathrm{n}}^2] = \mathrm{E}[g^2(X)] - \alpha^2\sigma^2. \tag{4}$$

The expectation of Y_{n} can be calculated as:

$$\mathrm{E}[Y_{\mathrm{n}}] = \mathrm{E}[g(X)]. \tag{5}$$

The variance of Y_{n} can then be calculated as:

$$\mathrm{Var}[Y_{\mathrm{n}}] = \mathrm{E}[Y_{\mathrm{n}}^2] - \mathrm{E}[Y_{\mathrm{n}}]^2. \tag{6}$$

Due to the central limit theorem (CLT), when the fast Fourier transform (FFT) is applied in the demodulator for $N_{\mathrm{FFT}} > 64$, the noise Y_{n} is transformed into additive Gaussian noise [2, 8, 9]. The variance of the noise is preserved. Hence, each

modulated subcarrier experiences additional zero-mean additive Gaussian noise with variance $\mathrm{Var}[Y_{\mathrm{n}}^2]$. An exception occurs in special cases like clipping at zero in modulation schemes such as ACO-OFDM and pulse-amplitude-modulated discrete multitone modulation (PAM-DMT) [12]. However, for common nonlinear distortions encountered in electrical components such as in the cases presented in the current work, the assumption of equal noise distribution in the frequency domain holds. In future work, it will be shown that with a slight modification the concepts presented here can be extended to modulation schemes such as ACO-OFDM and PAM-DMT. In frequency domain, the resulting SNR at each subcarrier can be calculated according to:

$$\frac{E_{\mathrm{b}j}^{\mathrm{new}}}{N_{\mathrm{o}}^{\mathrm{new}}} = \frac{\alpha^2 E_{\mathrm{b}j}^{\mathrm{old}}}{N_{\mathrm{o}} + \mathrm{Var}[Y_{\mathrm{n}}^2]} \tag{7}$$

where $E_{\mathrm{b}j}^{\mathrm{new}}$ is the resulting energy per bit of the jth subcarrier, $E_{\mathrm{b}j}^{\mathrm{old}}$ is the initial energy per bit of the jth subcarrier, $N_{\mathrm{o}}^{\mathrm{new}}$ is the resulting noise variance, and N_{o} is the variance of the channel AWGN. The presented Bussgang analysis is valid for zero-mean Gaussian signals. The analysed scheme, DCO-OFDM, is not zero-mean. The biasing level should be taken into account. It can be modeled as part of the nonlinear transformation, applied on the original zero-mean OFDM signal. The Bussgang approach has been used in a number of works [2, 8, 9]. However, a closed-form solution has either been impossible or it has been specifically tailored to the respective nonlinear distortion. The rest of this paper will show that there is a general approach which can always lead to a closed-form analytical solution with arbitrary accuracy.

A distortion function $g(X)$ can be represented by a set of intervals I with cardinality $|I|$ and a set of continuous polynomials which accurately approximate the function in those intervals. The polynomials can be generated with various interpolation techniques for a set of empirical data, or with polynomial expansion techniques for analytical functions. The degrees of the polynomials can give arbitrary accuracy to the approximation. Then $g(x)$ can be represented as:

$$g(x) = \sum_{l=1}^{|I|} \sum_{j=0}^{n_l} c_{l,j} x^j \left(U(x - x_{\min,l}) - U(x - x_{\max,l})\right) \tag{8}$$

where l is the lth interval, n_l is the degree of the polynomial in interval l, $c_{l,j}$ indicates the jth polynomial coefficient in interval l, $U(x)$ is the unit step function, $x_{\min,l}$ and $x_{\max,l}$ denote the boundaries of interval l. With this representation, α can be calculated as:

$$\alpha = \frac{\mathrm{E}[Xg(X)]}{\sigma^2} = \frac{1}{\sigma^2} \int_{-\infty}^{\infty} xg(x)\frac{1}{\sigma}\phi\left(\frac{x}{\sigma}\right)\mathrm{d}x$$

$$= \frac{1}{\sigma^2} \sum_{l=1}^{|I|} \sum_{j=0}^{n_l} c_{l,j} \int_{x_{\min,l}}^{x_{\max,l}} x^{j+1}\frac{1}{\sigma}\phi\left(\frac{x}{\sigma}\right)\mathrm{d}x$$

$$\overset{(20)}{=} \frac{1}{\sigma^2} \sum_{l=1}^{|I|} \sum_{j=0}^{n_l} c_{l,j} \left.\frac{\mathrm{d}^{j+1}D(t, x_{\min,l}, x_{\max,l}, 0, \sigma)}{\mathrm{d}t^{j+1}}\right|_{t=0} \tag{9}$$

149

where $D(t, a, b, \mu, \sigma)$ and $\phi(x)$ are defined in Appendix A. The variance of the time domain signal, σ^2, can be calculated as follows:

$$\sigma^2 = \frac{1}{N_{\text{FFT}}} \sum_{j=1}^{N_{\text{FFT}}} \log_2(M_j) E_{\text{b}j}$$

(10)

where M_j is the constellation size and $E_{\text{b}j}$ is the energy per bit at the jth subcarrier. $\text{E}[Y_{\text{n}}]$ can be calculated as:

$$\text{E}[Y_{\text{n}}] = \text{E}[g(X)] = \int_{-\infty}^{\infty} g(x) \frac{1}{\sigma} \phi\left(\frac{x}{\sigma}\right) \mathrm{d}x$$
$$= \sum_{l=1}^{|I|} \sum_{j=0}^{n_l} c_{l,j} \int_{x_{\text{min},l}}^{x_{\text{max},l}} x^j \frac{1}{\sigma} \phi\left(\frac{x}{\sigma}\right) \mathrm{d}x$$
$$\overset{(20)}{=} \sum_{l=1}^{|I|} \sum_{j=0}^{n_l} c_{l,j} \left.\frac{\mathrm{d}^j D(t, x_{\text{min},l}, x_{\text{max},l}, 0, \sigma)}{\mathrm{d}t^j}\right|_{t=0}.$$

(11)

$\text{E}[g^2(x)]$ can be calculated as:

$$\text{E}[g^2(X)] = \int_{-\infty}^{\infty} g^2(x) \frac{1}{\sigma} \phi\left(\frac{x}{\sigma}\right) \mathrm{d}x$$
$$= \sum_{l=1}^{|I|} \sum_{j=0}^{n_l} \sum_{k=0}^{n_l} c_{l,j} c_{l,k} \int_{x_{\text{min},l}}^{x_{\text{max},l}} x^{j+k} \frac{1}{\sigma} \phi\left(\frac{x}{\sigma}\right) \mathrm{d}x$$
$$\overset{(20)}{=} \sum_{l=1}^{|I|} \sum_{j=0}^{n_l} \sum_{k=0}^{n_l} c_{l,j} c_{l,k} \left.\frac{\mathrm{d}^{j+k} D(t, x_{\text{min},l}, x_{\text{max},l}, 0, \sigma)}{\mathrm{d}t^{j+k}}\right|_{t=0}.$$

(12)

Taking the derivative of the D-Function with respect to the variable t and setting $t = 0$ in the result, allows to compute expressions of the form $\int_a^b x^j f_X(x) \mathrm{d}x$, where X is a Gaussian random variable. These expressions are essential for the evaluation of (9), (11) and (12). Using Appendix A and the standard differentiation rules, it is straightforward to obtain closed-form expressions for (9), (11) and (12). The procedure is easily programmable as well.

The computational complexity of the final closed-form solution is limited by the tail probability function of the standard normal distribution, denoted by $Q(x)$ and defined in Appendix A. This function represents a numerical integral which has been well-characterised, tabulated, and widely-used in practice for decades. A good number of closed-form approximations to $Q(x)$ exist both in theory as well as in practical software for numerical analysis such as MATLAB. The authors in [8, 9], for example, use the Q-function in their closed-form solutions. The number of calls to this function in the framework presented in the current paper depends on the number of intervals in which the distortion function is continuous and on the number of polynomial terms which are necessary to approximate the distortion function within those intervals. For the nonlinearities analysed in [6–9], for example, only up to 3 intervals with a maximum polynomial order of 2 is required. In fact, the same closed-form solutions as in [8, 9] could be obtained with the approach presented in this work.

IV. Numerical Examples

Two separate distortion functions have been analysed in the context of the current work. One represents the effects of digital-to-analog conversion while the other one represents the distortion caused by the diode's electrical-to-optical conversion. Pulse shaping is not considered in the presented scenarios. It is shown in [2] that the impact of pulse shaping is negligible for commonly-used pulse shapes.

For comparison purposes we define a number of quantities. The spectral efficiency of DCO-OFDM is:

$$\eta = \frac{(N_{\text{FFT}} - 2) \log_2(M)}{N_{\text{FFT}} + N_{\text{cp}}} \text{ bits/s/Hz,}$$

(13)

where N_{cp} is the length of the cyclic prefix and $s(t)$ is the time-domain signal illustrated in Fig. 1. The electrical energy per bit is defined as:

$$E_{\text{b,elec}} = \frac{\text{E}[s^2(t)]}{B\eta},$$

(14)

where B is the communication bandwidth. The optical energy per bit is defined as:

$$E_{\text{b,opt}} = \frac{\text{E}[s(t)]}{B\eta}.$$

(15)

1) Quantisation: An example of the nonlinearity effects of quantisation in the DAC is proposed in the current work. A quantiser can always be approximated by zero-degree polynomials within the intervals formed by its thresholds. The quantiser example in this work is specified between two values y_{min} and y_{max}, which are the lowest and highest possible output after the quantisation. The device is specified as a q-bit quantiser, which means that there are 2^q possible output levels. The distance between output values is set evenly as:

$$d_{\text{q}} = \frac{y_{\text{max}} - y_{\text{min}}}{2^q - 1}.$$

(16)

The interval boundaries are set at $-\infty$, $y_{\text{min}} + d_{\text{q}}/2 - x_{\text{bias}}$, $y_{\text{max}} - d_{\text{q}}/2 - x_{\text{bias}}$, ∞ and at equal multiples of d_{q} between $y_{\text{min}} + d_{\text{q}}/2 - x_{\text{bias}}$ and $y_{\text{max}} - d_{\text{q}}/2 - x_{\text{bias}}$, where x_{bias} is the DC bias of DCO-OFDM. For simplicity, all other stages of the system are considered to be linear with gain 1. A comparison between the presented theory and Monte Carlo simulations is depicted in Fig. 2 for electrical power efficiency and in Fig. 3 for optical power efficiency. A modulation order of $M{=}16$ for M-QAM is presented in three different cases. In the first two cases, the time-domain signal is clipped at -3σ and 3σ, while in the last case it is clipped at -1σ and 3σ. The first two cases use a resolution of 8 bits and 4 bits, respectively. The last case uses a resolution of 8 bits. There is a very close match between the results obtained from the novel analytical framework and Monte Carlo simulations. The slight mismatch for the high bit error rate (BER) values is due to inaccuracy in the formula for theoretical performance of M-QAM [13]. Naturally, the BER cannot exceed 0.5.
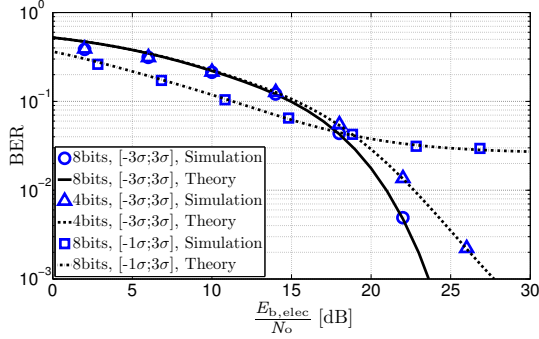
Fig. 2. DCO-OFDM performance as a function of ratio between electrical signal power at transmitter and AWGN power. The DC-bias of the system is included in the calculations of the SNR requirement.

Fig. 4. DCO-OFDM performance as a function of ratio between electrical signal power at transmitter and AWGN power. The DC-bias of the system is included in the calculations of the SNR requirement.

Fig. 3. DCO-OFDM performance as a function of ratio between optical signal power at transmitter and AWGN power. The DC-bias of the system is included in the calculations of the SNR requirement.

Fig. 5. DCO-OFDM performance as a function of ratio between optical signal power at transmitter and AWGN power. The DC-bias of the system is included in the calculations of the SNR requirement.

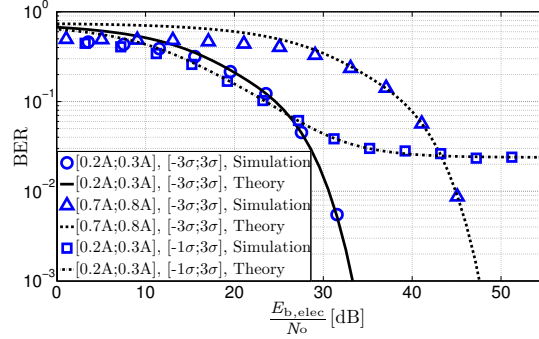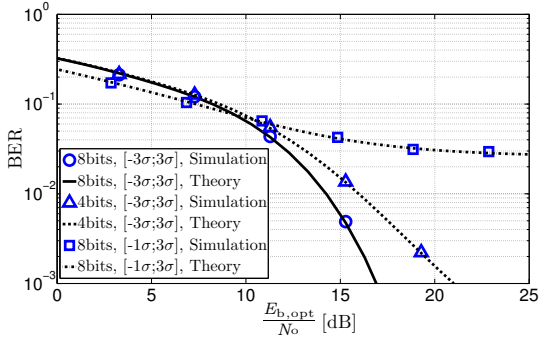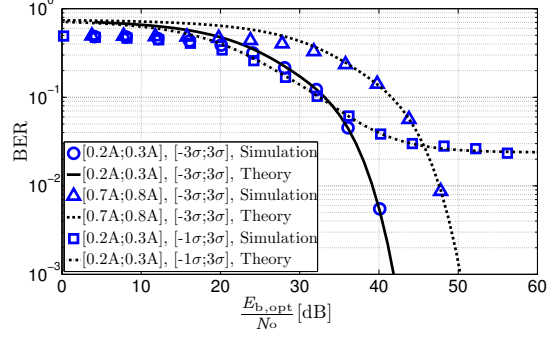*2) LED Nonlinearity:* The nonlinear relationship between current and light intensity is analysed for DCO-OFDM. For simplicity, all other stages of the system are assumed linear with gain 1. The LED characteristic is obtained from [14]. The minimum allowed current is set to $I_{\min}$=0.1 A. The maximum allowed current is set to $I_{\max}$=1 A. The electrical signal, $i(t)$, at the diode is only subjected to clipping distortion, while the light signal, $g(x)$, also experiences the transfer characteristic of the diode and represents the overall system distortion in (1). The diode characteristic is normalised in the LED datasheet to light flux Φ=430 lm at current $i(t)$=700 mA. In this work, it is approximated with zero-degree polynomials in the intervals $[-\infty; 0.1\,\text{A}]$ and $[1\,\text{A}; \infty]$ and with a third-degree polynomial in the interval $[0.1\,\text{A}; 1\,\text{A}]$. A modulation order of M=16 for M-QAM is presented in three different cases. In the first two cases, the time-domain signal is clipped at -3σ and 3σ, while in the last case it is clipped at -1σ and 3σ. In the first two cases the diode is operated in the region $[0.2\,\text{A}; 0.3\,\text{A}]$ and $[0.7\,\text{A}; 0.8\,\text{A}]$ respectively. In the last case the diode is operated in the region $[0.2\,\text{A}; 0.3\,\text{A}]$. A comparison between

the presented theory and Monte Carlo simulations is depicted in Fig. 4 for electrical power efficiency and in Fig. 5 for optical power efficiency. The figures illustrate very close match between the results obtained by the novel analytical framework and Monte Carlo simulations. Again, the slight mismatch for the high BER values is due to inaccuracy in the formula for theoretical performance of M-QAM [13]. An interesting observation with respect to dimming is that if the LED is operated close to the maximum optical power or close to the minimum optical power, performance does not seem to change significantly. The only notable difference is that in the case with higher DC-bias the energy requirement increases by around 14 dB for a BER of less than 10^{-3}.

V. CONCLUSION

A complete analytical approach has been presented for the analysis of memoryless nonlinear distortion in an OWC system. It allows for the analysis of an arbitrary distortion function and allows for the generation of closed-form solutions. The concept has been applied to a DCO-OFDM modulated IM/DD system. However, it can be applied equally-

well to alternative OFDM-based modulation schemes such as ACO-OFDM, PAM-DMT, unipolar OFDM (U-OFDM) [15] and Flip-OFDM [16] as will be demonstrated in future work. Examples have been given for distortion effects from quantisation in DAC elements, as well as for distortion stemming from the nonlinear relationship between electrical current and emitted light in an LED. It is interesting to note that these two nonlinear effects can be combined and analysed jointly as will be demonstrated in future work. Monte Carlo simulations show very good agreement with the results obtained from the proposed theory. This confirms the validity of the approach.

APPENDIX A

We define the D-Function as follows:

$$
\begin{aligned}
D(t, a, b, \mu, \sigma) &= \int_a^b e^{xt} \frac{1}{\sqrt{2\pi\sigma^2}} e^{-\frac{(x-\mu)^2}{2\sigma^2}} \mathrm{d}x \\
&= \int_a^b \frac{1}{\sqrt{2\pi\sigma^2}} e^{-\frac{-2xt\sigma^2 + x^2 - 2\mu x + \mu^2}{2\sigma^2}} \mathrm{d}x \\
&= \int_a^b \frac{1}{\sqrt{2\pi\sigma^2}} e^{-\frac{x^2 - 2(t\sigma^2 + \mu)x + \mu^2}{2\sigma^2}} \mathrm{d}x \\
&= \int_a^b \frac{1}{\sqrt{2\pi\sigma^2}} e^{-\frac{x^2 - 2(t\sigma^2 + \mu)x + t^2\sigma^4 + 2t\sigma^2\mu + \mu^2 - t^2\sigma^4 - 2t\sigma^2\mu}{2\sigma^2}} \mathrm{d}x \\
&= e^{\frac{t^2\sigma^2}{2} + t\mu} \int_a^b \frac{1}{\sqrt{2\pi\sigma^2}} e^{-\frac{x^2 - 2(t\sigma^2 + \mu)x + (t\sigma^2 + \mu)^2}{2\sigma^2}} \mathrm{d}x \\
&= e^{\frac{t^2\sigma^2}{2} + t\mu} \int_a^b \frac{1}{\sqrt{2\pi\sigma^2}} e^{-\frac{(x - \mu - t\sigma^2)^2}{2\sigma^2}} \mathrm{d}x \\
&= e^{\frac{t^2\sigma^2}{2} + t\mu} \left(Q\left(\frac{a - \mu - t\sigma^2}{\sigma}\right) - Q\left(\frac{b - \mu - t\sigma^2}{\sigma}\right) \right)
\end{aligned}
\tag{17}
$$

where $Q(x)$ is defined as the tail probability of the standard normal distribution, and $\phi(x)$ is defined as the probability density function (pdf) of the standard normal distribution:

$$
Q(x) = \frac{1}{\sqrt{2\pi}} \int_x^\infty e^{-\frac{u^2}{2}} \mathrm{d}u
\tag{18}
$$

$$
\phi(x) = \frac{1}{\sqrt{2\pi}} e^{-\frac{x^2}{2}}
\tag{19}
$$

$$
\begin{aligned}
\left. \frac{\mathrm{d}^n D(t, a, b, \mu, \sigma)}{\mathrm{d}t^n} \right|_{t=0} &= \left. \frac{\mathrm{d}^n}{\mathrm{d}t^n} \int_a^b e^{xt} \frac{1}{\sqrt{2\pi\sigma^2}} e^{-\frac{(x-\mu)^2}{2\sigma^2}} \mathrm{d}x \right|_{t=0} \\
&= \left. \int_a^b \frac{\mathrm{d}^n}{\mathrm{d}t^n} e^{xt} \frac{1}{\sqrt{2\pi\sigma^2}} e^{-\frac{(x-\mu)^2}{2\sigma^2}} \mathrm{d}x \right|_{t=0} \\
&= \left. \int_a^b x^n e^{xt} \frac{1}{\sqrt{2\pi\sigma^2}} e^{-\frac{(x-\mu)^2}{2\sigma^2}} \mathrm{d}x \right|_{t=0} \\
&= \int_a^b x^n \frac{1}{\sqrt{2\pi\sigma^2}} e^{-\frac{(x-\mu)^2}{2\sigma^2}} \mathrm{d}x
\end{aligned}
\tag{20}
$$

$$
\frac{\mathrm{d}Q\left(\frac{x - \mu - t\sigma^2}{\sigma}\right)}{\mathrm{d}t} = \phi\left(\frac{x - \mu - t\sigma^2}{\sigma}\right) \sigma
\tag{21}
$$

$$
\frac{\mathrm{d}\phi\left(\frac{x - \mu - t\sigma^2}{\sigma}\right)}{\mathrm{d}t} = \phi\left(\frac{x - \mu - t\sigma^2}{\sigma}\right)\left(\frac{x - \mu - t\sigma^2}{\sigma}\right) \sigma
\tag{22}
$$

ACKNOWLEDGEMENT

REFERENCES

[1] "Visible Light Communication (VLC) - A Potential Solution to the Global Wireless Spectrum Shortage," GBI Research, Tech. Rep., 2011. [Online]. Available: http://www.gbiresearch.com/

[2] D. Dardari, V. Tralli, and A. Vaccari, "A Theoretical Characterization of Nonlinear Distortion Effects in OFDM Systems," *IEEE Transactions on Communications*, vol. 48, no. 10, pp. 1755–1764, Oct. 2000.

[3] A. Bahai, M. Singh, A. Goldsmith, and B. Saltzberg, "A New Approach for Evaluating Clipping Distortion in Multicarrier Systems," *IEEE Journal on Selected Areas in Communications*, vol. 20, no. 5, pp. 1037–1046, Jun. 2002.

[4] X. Li and J. Cimini, L.J., "Effects of Clipping and Filtering on the Performance of OFDM," *IEEE Communications Letters*, vol. 2, no. 5, pp. 131–133, May 1998.

[5] D. J. G. Mestdagh, P. Spruyt, and B. Biran, "Analysis of Clipping Effect in DMT-based ADSL Systems," in *Proc. IEEE International Conference on Communications ICC 1994*, vol. 1, New Orleans, LA, USA, 1–5 May 1994, pp. 293–300.

[6] I. Neokosmidis, T. Kamalakis, J. W. Walewski, B. Inan, and T. Sphicopoulos, "Impact of Nonlinear LED Transfer Function on Discrete Multitone Modulation: Analytical Approach," *Lightwave Technology*, vol. 27, no. 22, pp. 4970–4978, 2009.

[7] H. Elgala, R. Mesleh, and H. Haas, "Impact of LED nonlinearities on optical wireless OFDM systems," in *2010 IEEE 21st International Symposium on Personal Indoor and Mobile Radio Communications (PIMRC)*, sept 2010, pp. 634 – 638.

[8] S. Dimitrov, S. Sinanovic, and H. Haas, "Clipping Noise in OFDM-based Optical Wireless Communication Systems," *IEEE Transactions on Communications (IEEE TCOM)*, vol. 60, no. 4, pp. 1072–1081, Apr. 2012.

[9] ——, "A Comparison of OFDM-based Modulation Schemes for OWC with Clipping Distortion," in *Proc. of the 2nd Optical Wireless Communications (OWC) Workshop in conjunction with IEEE Global Telecommunications Conference (IEEE GLOBECOM 2011)*, Houston, Texas, USA, 5–9 Dec. 2011.

[10] J. Armstrong and A. Lowery, "Power Efficient Optical OFDM," *Electronics Letters*, vol. 42, no. 6, pp. 370–372, Mar. 16, 2006.

[11] J. Bussgang, "Cross Correlation Function of Amplitude-Distorted Gaussian Signals," Research Laboratory for Electronics, Massachusetts Institute of Technology, Cambridge, MA, Technical Report 216, Mar. 1952.

[12] S. C. J. Lee, S. Randel, F. Breyer, and A. M. J. Koonen, "PAM-DMT for Intensity-Modulated and Direct-Detection Optical Communication Systems," *IEEE Photonics Technology Letters*, vol. 21, no. 23, pp. 1749–1751, Dec. 2009.

[13] F. Xiong, *Digital Modulation Techniques*, 2nd ed. Artech House Publishers, 2006.

[14] OSRAM GmbH, "Datasheet: OS-PCN-2008-002-A OSTAR LED," Retrieved from http://www.osram.de, Feb. 2008.

[15] D. Tsonev, S. Sinanović, and H. Haas, "Novel Unipolar Orthogonal Frequency Division Multiplexing (U-OFDM) for Optical Wireless," in *Proc. of the Vehicular Technology Conference (VTC Spring)*, IEEE. Yokohama, Japan: IEEE, May 6–9 2012.

[16] N. Fernando, Y. Hong, and E. Viterbo, "Flip-OFDM for Unipolar Communication Systems," *IEEE Transactions on Communications*, vol. 60, no. 12, pp. 3726–3733, Dec. 2012.

152

Light Fidelity (Li-Fi): Towards All-Optical Networking

Dobroslav Tsonev, Stefan Videv and Harald Haas

Institute for Digital Communications,
Li-Fi R&D Centre,
The University of Edinburgh, EH9 3JL, Edinburgh, UK

ABSTRACT

Motivated by the looming radio frequency (RF) spectrum crisis, this paper aims at demonstrating that optical wireless communication (OWC) has now reached a state where it can demonstrate that it is a viable and matured solution to this fundamental problem. In particular, for indoor communications where most mobile data traffic is consumed, light fidelity (Li-Fi) which is related to visible light communication (VLC) offers many key advantages, and effective solutions to the issues that have been posed in the last decade. This paper discusses all key component technologies required to realize optical cellular communication systems referred to here as optical attocell networks. Optical attocells are the next step in the progression towards ever smaller cells, a progression which is known to be the most significant contributor to the improvements in network spectral efficiencies in RF wireless networks.

Keywords: Li-Fi, VLC, optical wireless, visible light communications, optical attocell

1. INTRODUCTION

Thirty years after the introduction of the first commercially-available mobile communication systems, wireless connectivity has evolved into a fundamental commodity like gas and electricity. The exponential increase in mobile data traffic during the past two decades has led to the massive deployment of wireless systems. As a consequence, the limited available RF spectrum is subject to an aggressive spatial reuse and co-channel interference has become a major capacity limiting factor. Therefore, there have been many independent warnings of a looming "RF spectrum crisis"[1] as the mobile data demands continue to increase while the network spectral efficiency saturates despite newly-introduced standards and great technological advancements in the field. It is estimated that by 2017, more than 11 exabytes of data traffic will have to be transferred through mobile networks every month.[2] Most recently, VLC has been identified as a potential solution for mitigating the looming RF spectrum crisis.

Over the past decade, significant research efforts have been directed towards exploring alternative parts of the electromagnetic spectrum* that could potentially offload a large portion of the network traffic from the overcrowded RF domain. Very interesting results have recently been reported from the use of millimeter wave (mmWave) communication in the 28 GHz region as well as from the use of infrared and visible light. The latter is particularly enticing as lighting is a commodity that has been integrated in virtually every inhabited environment and sophisticated infrastructures already exist. The use of the visible light spectrum for high speed data communication is enabled by the emergence of the light emitting diode (LED) which at the same time is at the heart of the next wave of energy-efficient illumination. In that sense, the concept of combining the functions of illumination and communication offers the potential for tremendous cost savings and carbon footprint reductions. First, the deployment of VLC access points (APs) becomes straightforward as the existing lighting infrastructure

---

Further author information: (Send correspondence to H.H.)

D.T.: E-mail: d.tsonev@ed.ac.uk, Telephone: +44 (0)131 651 3492

S.V.: E-mail: s.videv@ed.ac.uk, Telephone: +44 (0)131 651 3492

H.H.: E-mail: h.haas@ed.ac.uk, Telephone: +44 (0)131 650 5591

*The preferred region of the RF spectrum for use in terrestrial mobile communication is between 0 - 10 GHz due to certain radio propagation characteristics. As wireless communications has changed over the last decade, the authors believe that it is worthwhile to reconsider the importance of these "preferential" propagation characteristics for future wireless systems.

can be reused, and there exist off-the-shelf technologies such as power-line communication (PLC) and power-over-Ethernet (PoE) as viable backhaul solutions for retrofit installations, and new installations respectively. Second, because lighting is on most of the time in indoor environments even during day time, the energy used for communication would practically be zero as a result of the piggy-backing of data on illumination. However, even if illumination is not required energy efficient intensity modulation (IM) techniques exist that would allow data communication even if the lights are visually off.[3] These are already compelling benefits, but the case does not end there. The visible light spectrum includes 100s of THz of license free bandwidth, 10,000 times more than the entire RF spectrum up to 30 GHz, including the mmWave spectrum. Optical radiation, in general, does not interfere with other radio waves or with the operation of sensitive electronic equipment. Therefore, it is ideal for providing wireless coverage in areas which are sensitive to electromagnetic radiation – some examples include: hospitals, airplanes, petrochemical and nuclear power plants, etc. Furthermore, the inability of light to propagate through walls offers an inherent level of network security. The same feature can be exploited to eliminate interference between neighboring cells.

During the last ten years, there have been continuous reports of improved point-to-point link data rates using off-the-shelf white LEDs under experimental lab conditions. Recently, data rates in excess of 1 Gbps has been reported using off-the-shelf phosphor-coated white LEDs,[4] and 3.4 Gbps has been demonstrated with an off-the-shelf red-green-blue (RGB) LED.[5] Another similar Gigabit/s wireless system with phosphor-coated white LEDs has been demonstrated[6] using a 4×4 multiple-input-multiple-output (MIMO) configuration. To the best of the authors' knowledge, the highest speed that has ever been reported from a *single* color incoherent LED is 3.5 Gbps.[7] The experiment was led by researchers of the University of Edinburgh. A theoretical framework for the achievable capacity of a intensity modulation and direct detection (IM/DD) systems using orthogonal frequency division multiplexing (OFDM) has been established in,[8] and a closed-form solution on the impact of non-linearties on the achievable signal-to-noise ratio in practical OFDM based VLC systems is reported in.[9] To date, research in the field of OWC has been focused on successful implementations of physical-link connections and proofs of the concept.[10] For the realization of a mobile communication system, however, a full networking solution is required. This is what we refer to as Li-Fi: the *networked*, *mobile*, *high-speed* VLC solution for wireless communication.[11] The vision is that a Li-Fi wireless network would complement existing heterogenous RF wireless networks, and would provide significant spectrum relief by allowing cellular and wireless-fidelity (Wi-Fi) systems to off-load a significant portion of wireless data traffic. The current paper summarizes some of the research conducted so far and looks at the different aspects of the communication system with a particular focus on wireless networking. The rest of this paper is structured as follows: Section 2 looks at the modulation scheme requirements of Li-Fi which is based on IM/DD; Section 3 discusses the different possibilities for achieving multiple access; Section 4 summarizes the uplink concepts; Section 5 introduces the optical "attocell" concept; Section 6 summarizes interference mitigation techniques for optical attocell networks; and finally, Section 7 provides concluding remarks.

2. SIGNAL MODULATION IN OWC

A seamless all-optical wireless network would require ubiquitous coverage provided by the optical front-end elements. This necessitates the usage of a large amount of Li-Fi enabled lighting units. The most likely candidates for front-end devices in VLC are incoherent solid-state lighting LEDs due to their low cost. Due to the physical properties of these components, information can only be encoded in the intensity of the emitted light, while the actual phase and amplitude of the light wave cannot be modulated. This significantly differentiates VLC from RF communications.

VLC can only be realized as an IM/DD system, which means that the modulation signal has to be both *real valued* and *unipolar*. This limits the application of the well-researched and developed modulation schemes from the field of RF communications. Techniques such as on-off keying (OOK), pulse-position modulation (PPM), pulse-width modulation (PWM) and unipolar M-ary pulse-amplitude modulation (M-PAM) can be applied in a relatively straightforward fashion. As the modulation speeds are increased, however, these particular modulation schemes begin to suffer from the undesired effects of intersymbol interference (ISI) due to the non-flat frequency response of the OWC channel. Hence, a more resilient technique such as OFDM is required. OFDM allows adaptive bit and energy loading of different frequency sub-bands according to the communication channel

properties.[12] This leads to optimal utilization of the available resources. OFDM achieves the throughput capacity in a non-flat communication channel even in the presence of nonlinear distortion.[8] Such channel conditions are introduced by the transfer characteristic of an off-the-shelf LED that has a maximum 3 dB modulation bandwidth in the order of 20 MHz.[4,5] In fact, the record-breaking results presented in[4–6] have all been achieved using OFDM with, to the best of the authors' knowledge, the first experimental OFDM results for VLC reported in.[13] Further benefits of this modulation scheme include simple equalization with single-tap equalizers in the frequency domain as well as the ability to avoid low-frequency distortion caused by flickering background radiation and the baseline wander effect in electrical circuits.

Conventional OFDM signals are complex-valued and bipolar in nature. Therefore, the standard RF OFDM technique has to be modified in order to become suitable for IM/DD systems. A straightforward way to obtain a real-valued OFDM signal is to impose a Hermitian symmetry constraint on the sub-carriers in the frequency domain as illustrated in Fig. 1. However, the resulting time-domain signal is still bipolar. One way for obtaining a unipolar signal is to introduce a positive direct current (DC) bias around which the amplitude of the OFDM signal can vary as shown in Fig. 2. The resulting unipolar modulation scheme is known as DC-biased optical OFDM (DCO-OFDM). The addition of the constant biasing level leads to a significant increase in electrical energy consumption. This can be easily visualized when Fig. 2(a) and Fig. 2(b) are juxtaposed. However, if the light sources are used for illumination at the same time, the light output as a result of the DC bias is not wasted as it is used to fulfil the illumination function. Only if illumination is not required, such as in the uplink of a Li-Fi system, the DC bias can significantly compromise energy efficiency. Therefore, researchers have devoted significant efforts to designing an OFDM-based modulation scheme which is purely unipolar. Some well-known solutions include: asymmetrically clipped optical OFDM (ACO-OFDM),[14] pulse-amplitude-modulated discrete multitone modulation (PAM-DMT),[15] unipolar OFDM (U-OFDM),[3] Flip-OFDM,[16] spectrally-factorized optical OFDM (SFO-OFDM),[17] etc.. The general disadvantage of all these techniques is a 50% loss in spectral efficiency, i.e., the data rates are halved. This limitation has recently been overcome by researchers at the University of Edinburgh and a patent application is pending.

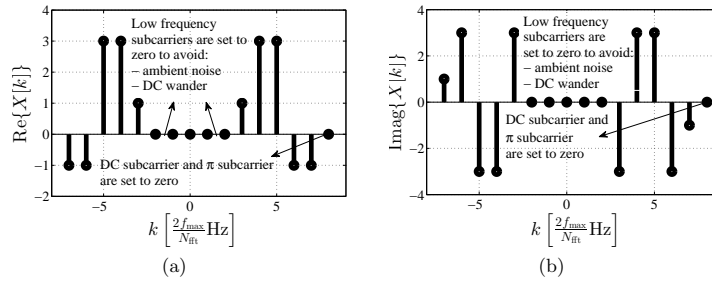(a)   (b)

Figure 1. Hermitian symmetry ensures a positive signal in the time domain: (a) real parts of the corresponding positive and negative frequency components are equal; (b) imaginary parts of the corresponding positive and negative frequency components are equal in absolute value, but have opposite signs.

From a networking perspective, OFDM offers a straightforward multiple access implementation as subcarriers can be allocated to different users resulting in orthogonal frequency division multiple access (OFDMA). The merits of OFDM have already been recognized, and OFDM is used in IEEE 802.11 Wi-Fi systems. The multiuser access version of OFDM, i.e., OFDMA, is used in the 4th generation (4G) Long Term Evolution (LTE) cellular standard. Therefore, the application of OFDM in optical mobile networks would allow the use of the already-established higher level communication protocols used in LTE and IEEE 802.11, which constitutes a major advantage.
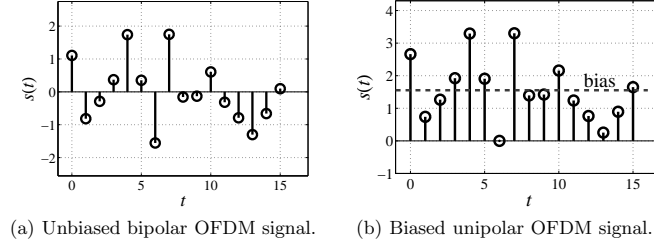
(a) Unbiased bipolar OFDM signal.   (b) Biased unipolar OFDM signal.

Figure 2. Real OFDM signal made bipolar through the addition of a DC bias – DCO-OFDM.

3. MULTIPLE ACCESS

A networking solution cannot be realized without a suitable multiple access scheme that allows multiple users to share the communication resources without any mutual cross-talk. Multiple access schemes used in RF communications can be adapted for OWC as long as the necessary modifications related to the IM/DD nature of the modulation signals are performed. OFDM comes with a natural extension for multiple access – OFDMA. Single-carrier modulation schemes such as M-PAM, OOK and PWM require an additional multiple access technique such as frequency division multiple access (FDMA), time division multiple access (TDMA) and/or code division multiple access (CDMA). The results of an investigation regarding the performance of OFDMA versus TDMA and CDMA are presented in Fig. 3.[18] FDMA has not been considered due to its close similarity
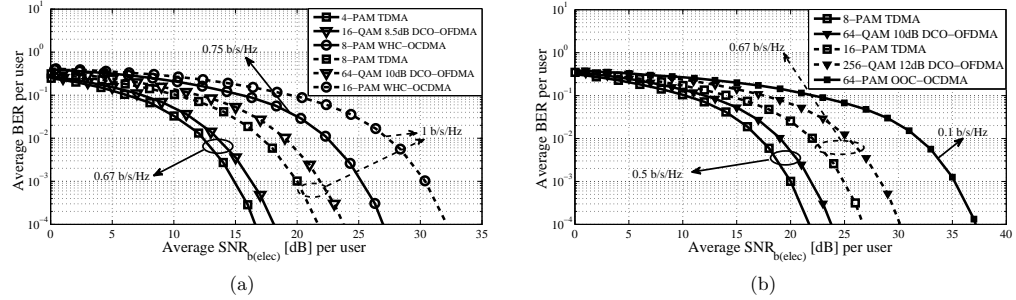

Figure 3. Comparison between different multiple access schemes:[18] (a) TDMA vs. OFDMA vs. CDMA (with Walsh-Hadamard code) in a three-user scenario; (b) TDMA vs. OFDMA vs. CDMA (with optical orthogonal code) in a six-user scenario.

to OFDMA, and the fact that OWC does not use superheterodyning. In addition, due to the limited modulation bandwidth of the front-end elements, this scheme would not present a very efficient use of the LED modulation bandwidth. As shown in Fig. 3, CDMA is very inefficient as the use of unipolar signals creates significant interchannel interference (ICI) and a substantial increase in the power requirements compared to its application in RF communications. At the same time, the performance of TDMA barely surpasses that of OFDMA for the different scenarios. The higher power requirement of OFDMA compared to TDMA is caused by its wider time-domain signal distribution. This leads to the need for higher DC biasing levels and as a consequence to a higher power consumption which is reflected in the shown signal-to-noise ratio (SNR). In a practical scenario where the functions of communication and illumination are combined, the difference in power consumption between the different schemes would diminish as the excess power due to the DC bias would be used for illumination purposes. It should be pointed out that this investigation has been performed for a flat linear additive white Gaussian noise (AWGN) channel where only clipping effects from below, applicable only to OFDMA, have been considered. This is due to the fact that nonlinear effects such as clipping from above as well as the

227

nonlinear relationship between the modulating current signal and the emitted optical signal are device-specific, while clipping from below is inherent to any IM/DD system. Furthermore, low-frequency distortion effects from the DC-wander in electrical components as well as from the flickering of background light sources are also not considered. In a practical scenario, these effects would not be an issue for OFDMA, but are expected to decrease the performance of TDMA and CDMA. Therefore, the design complexity of a TDMA or CDMA system increases as suitable techniques to deal with these problems need to be implemented. It is also worth noting that the non-flatness of the channel in a practical scenario would further degrade the performances of CDMA and TDMA compared to OFDMA.

In OWC there exists an additional alternative dimension for achieving multiple access. This is *color*, and the corresponding technique is wavelength division multiple access (WDMA). WDMA harnesses the different light wavelengths to facilitate multiple-user access. This scheme could reduce the complexity in terms of signal processing, however, it would lead to increased hardware complexity as well as to the need at each access point for multiple transmitter elements with narrow wavelength emission. This immediately puts strict requirements on the optical front-end elements, and compromises SNR and, hence, capacity. In addition, WDMA excludes the usage of a large variety of off-the-shelf LEDs as most of them are not optimized for WDMA. The typical emission profile of an off-the-shelf white LED is illustrated in Fig. 4(a). At the same time, light sources with different narrow wavelength emission spectra have different modulation frequency profiles as well as different optical efficiencies. When combined with the varying responsivity of photodetectors at different wavelengths, as shown in Fig. 4(b), these differences complicate immensely the fair distribution of communication resources between multiple users.
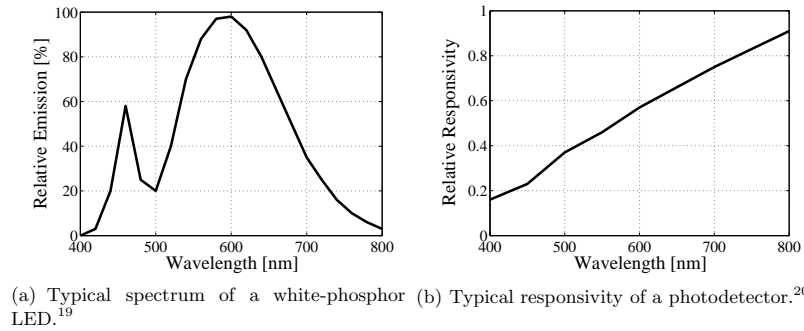

(a) Typical spectrum of a white-phosphor LED.[19] (b) Typical responsivity of a photodetector.[20]

Figure 4. Data provided by device data-sheets.

4. UPLINK

Up until now, research has primarily focused on maximizing the transmission speeds over a single unidirectional link.[4–6] However, for a complete Li-Fi communication system, full duplex communication is required, *i.e.*, an uplink connection from the mobile terminals to the optical AP has to be provided. Existing duplex techniques used in RF such time division duplexing (TDD) and frequency division duplexing (FDD) could be considered, where the downlink and the uplink are separated by different time slots, or different frequency bands respectively. However, FDD is more difficult to realize due to the limited bandwidth of the front-end devices, and because superheterodyning is not used in IM/DD systems. TDD provides a viable option, but imposes precise timing and synchronization constraints which is needed for data decoding, anyway. However, plain TDD assumes that both the uplink and the downlink transmissions are performed over the same physical wavelength. This could often be impractical as visible light emitted by the user terminal may not be desirable.[21] Therefore, the most suitable duplex technique in Li-Fi is wavelength division duplexing (WDD), where the two communication channels are established over different electromagnetic wavelengths. Using infrared (IR) transmission is one viable option for establishing an uplink communication channel.[21] A first commercially-available full duplex Li-Fi modem using

IR light for the uplink channel has recently been announced by pureLiFi.[22] There is also the option to use RF communication for the uplink.[21] In this configuration, Li-Fi may be used to do the "heavy lifting" and off-load data traffic from the RF network, and thereby providing significant RF spectrum relief. This is particularly relevant since there is a traffic imbalance in favor of the downlink in current wireless communication systems.

5. THE LI-FI ATTOCELL

In the past, wireless cellular communications has significantly benefited from reducing the inter-site distance of cellular base stations. By reducing the cell size, the network spectral efficiency has been increased by two orders of magnitude in the last 25 years. More recently, different cell layers composed of microcells, picocells and femto cells have been introduced. These networks are referred to as heterogeneous networks.[23, 24] Femtocells are short range, low transmission power, low cost, plug-and-play base stations (BSs) that are targeted at indoor deployment in order to enhance coverage. They use either cable Internet or broadband digital subscriber line (DSL) to backhaul to the core network of the operator. The deployment of femtocells increases the frequency reuse, and hence throughput per unit area within the system since they usually share the same bandwidth with the macrocellular network. However, the uncoordinated and random deployment of small cells also causes additional inter- and intra-cell interference which imposes a limit on how dense these small RF can be deployed before interference starts offsetting all frequency reuse gains.

The small cell concept, however, can easily be extended to VLC in order to overcome the high interference generated by the close reuse of radio frequency spectrum in heterogeneous networks. The optical AP is referred to as an attocell.[25] Since it operates in the visible light spectrum, the optical attocell does not interfere with the macrocellular network. The optical attocell not only improves indoor coverage, but since it does not generate any additional interference, it is able to enhance the capacity of the RF wireless networks. Li-Fi attocells allow
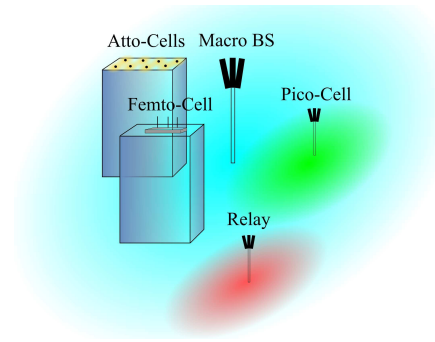

Figure 5. The attocell in the context of the heterogeneous network.

for extremely dense bandwidth reuse due to the inherent properties of light waves. The coverage of each single attocell is very limited, and walls prevent the system from suffering from co-channel interference between rooms. This precipitates in the need to deploy multiple access points to cover a given space. However, due to the requirement for illumination indoors, the infrastructure already exists, and this type of cell deployment results in the aforementioned very high, practically interference-free bandwidth reuse. A byproduct of this is also a reduction in bandwidth dilution over the area of each access point, which leads to an increase in the capacity available per user. The user data rate in attocell networks can be improved by up to three orders of magnitude.[26]

Moreover, Li-Fi attocells can be deployed as part of a heterogeneous VLC-RF network as illustrated in Fig. 5. They do not cause any additional interference to RF macro- and picocells, and can, hence, be deployed within RF macro-, pico- and even femtocell environments. This allows the system to vertically hand-off users between the RF and Li-Fi sub-networks, which enables both free user mobility and high data throughput. Such network structure is capable of providing truly ubiquitous wireless network access.

6. THE CELLULAR NETWORK

The deployment of multiple Li-Fi attocells provides ubiquitous data coverage in a room in addition to providing nearly uniform illuminance. This means that a room contains many attocells forming a very dense cellular attocell network. A network of such density, however, requires methods for intra-room interference mitigation while there is no inter-room interference if the rooms are separated by concrete walls. Interference mitigation techniques used in RF cellular networks such as the busy burst[27] technique, static resource partitioning,[28] or fractional frequency reuse[29] have been considered. The unique properties of optical radiation, however, offer specific opportunities for enhanced interference mitigation in optical attocell networks. Particularly important is the inability of light to penetrate solid objects, which allows interference to be managed in a more effective manner than in RF communication. According to,[26] for example, the VLC interference mitigation caused by solid objects in a typical indoor environment leads to a tremendous increase in area spectral efficiency (ASE) over an RF femtocell network deployment in same LTE indoor office environment. The presented results highlight that the improvement with respect to ASE can reach a factor of up to 1000 in certain scenarios.

Essential techniques for increasing wireless system capacity such as beamforming are relatively straightforward to use in VLC as the beamforming characteristic is an inherent, device specific property related to the field of view (FOV), and no computationally complex algorithms and multiple transmitting elements are required. A simple example is provided with the technique of joint transmission in indoor VLC downlink cellular networks proposed by Chen *et al.*[30] and illustrated in Fig. 6. The application of multiple simple narrow-emission-pattern transmitters at each attocellular AP results in significant co-channel interference reduction. The technique allows the cellular coverage area to be broken down further into areas of low interference and areas that are subject to higher interference – typically at the cell edges. The frequency allocation can then be performed in a more optimal way which allows the overall throughput distribution over the coverage area to increase significantly as indicated by the results in Fig. 7. A similar concept realized at the receiver side is illustrated in Fig. 8(a) where multiple receiver elements with a narrow FOV provide a means for enhanced interference mitigation capabilities. The narrow FOV causes each photodetector to scan only a fraction of the available space. The overall combination of all photodetectors provides a wide FOV. This discretization of the receiver eyesight allows interference to be avoided by careful recombination of the output signals from each receiver element. These are only some examples of the cellular network research that is being conducted in the field of OWC.

(a) Illustration of signal contributions to cell-center regions and to conflicting regions.

(b) Different frequency allocation schemes. Joint transmission 1 (JT1) allocates the same frequency to all conflicting regions. Joint transmission 2 (JT2) allocates non-overlapping frequency bands to neighboring conflicting regions.
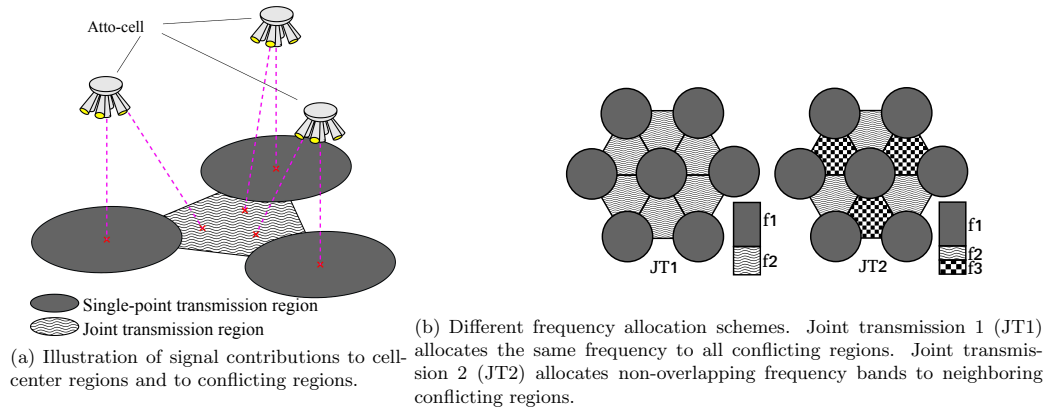
Figure 6. Resource allocation by using joint transmission. The adjacent APs transmit the same data at the cell-edge regions by coordinated transmissions. Note, in Li-Fi signals only add constructively which is a specific property that is exploited here. Frequency bands allocated to the high interference regions are different than frequency bands allocated to the cell-center regions.[30]

(a) CDF of the overall system throughput.[30]

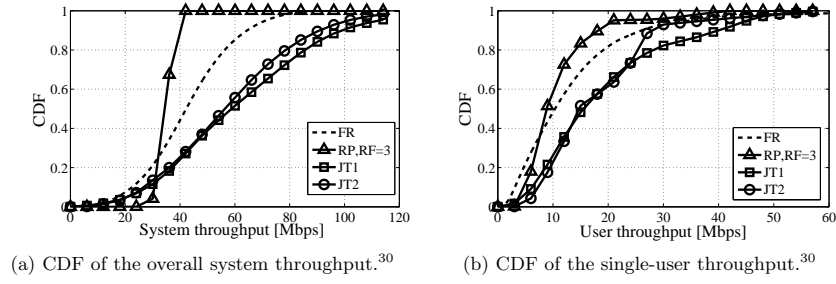(b) CDF of the single-user throughput.[30]

Figure 7. Performance comparison between four resource allocation schemes: full frequency reuse (FR), static resource partitioning (RP). joint transmission 1 (JT1), and joint transmission 2 (JT2).[30]

(a) Angle-diversity receiver and a conventional receiver.

(b) Performance conventional receiver (CR) vs angle-diversity receiver with three possible signal recombination techniques: equal-gain combining (EGC), select best (SB), and maximum-ratio combining (MRC).
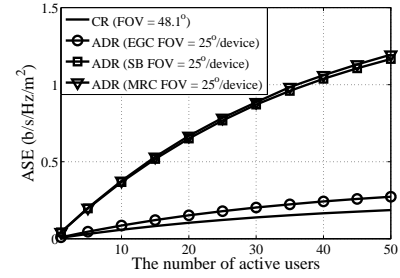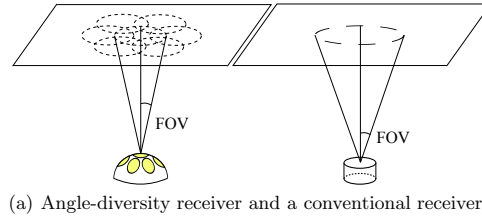
Figure 8. Performance of an angle-diversity receiver (ADR) vs. performance of a conventional receiver (CR). Parameters have been selected such that the effective area and the coverage of the two receivers are equivalent.

7. CONCLUSION

Research in VLC over the past ten years has primarily been focussed on finding an optimum modulation scheme for IM/DD assuming point-to-point VLC links by taking into account that VLC may serve two simultaneous functions: (a) illumination, and (b) gigabit wireless communication. The predominate sources for signal distortion are frequency dependent in such systems. This constitutes one key reason why there is now a general understanding that OFDM is the most suitable choice as a digital modulation scheme for Li-Fi, and there are good technical reasons to reconsider the IEEE 802.15.7 VLC standard. The straightforward multiple access technique that OFDMA provides at almost no additional complexity and its compatibility to state-of-the art wireless standards like LTE and IEEE 802.11 further favor the selection of this modulation/multiple access scheme.

The realization of a bidirectional connection also seems to have been addressed successfully to an extent that the first commercial bidirectional point-to-point Li-Fi systems are available. The most practical solutions to the uplink channel realization is to consider the IR or RF spectrum. The confidence brought by encouraging recent research results and by the successful VLC link-level demonstrations, has now shifted the focus towards an entire Li-Fi attocell networking solution. The unique physical properties of light promise to deliver very densely-packed high-speed network connections resulting in orders of magnitude improved user data rates. Based on these very promising results, it seems that Li-Fi is rapidly emerging as a powerful wireless networking solution to the looming RF spectrum crisis, and an enabling technology for the future Internet-of-Everything. Based on past experience that the number of wireless applications increases by the square of the number of available physical

connections, Li-Fi could be at the heart of an entire new industry for the next wave of wireless communications.

REFERENCES

[1] Ofcom, "Study on the future UK spectrum demand for terrestrial mobile broadband applications," report, realwireless (June 2013).

[2] Cisco Visual Networking Index, "Global Mobile Data Traffic Forecast Update, 2012-2017," White Paper, CISCO (Feb. 2013).

[3] Tsonev, D., Sinanović, S., and Haas, H., "Novel Unipolar Orthogonal Frequency Division Multiplexing (U-OFDM) for Optical Wireless," in [*Proc. of the Vehicular Technology Conference (VTC Spring)*], IEEE, IEEE, Yokohama, Japan (May 6–9 2012).

[4] Khalid, A. M., Cossu, G., Corsini, R., Choudhury, P., and Ciaramella, E., "1-Gb/s Transmission Over a Phosphorescent White LED by Using Rate-Adaptive Discrete Multitone Modulation," *IEEE Photonics Journal* **4**, 1465–1473 (Oct. 2012).

[5] Cossu, G., Khalid, A. M., Choudhury, P., Corsini, R., and Ciaramella, E., "3.4 Gbit/s Visible Optical Wireless Transmission Based on RGB LED," *Optics Express* **20**, B501–B506 (2012).

[6] Azhar, A., Tran, T., and O'Brien, D., "A Gigabit/s Indoor Wireless Transmission Using MIMO-OFDM Visible-Light Communications," *IEEE Photonics Technology Letters* **25**, 171–174 (Jan.15 2013).

[7] Tsonev, D., Chun, H., Rajbhandari, S., McKendry, J. J. D., Videv, S., Gu, E., Haji, M., Watson, S., Kelly, A., Faulkner, G., Dawson, M. D., Haas, H., and OBrien, D., "A 3-Gb/s Single-LED OFDM-based Wireless VLC Link Using a Gallium Nitride LED," *Photonics Technology Letter* **99**(99), to appear (2014).

[8] Dimitrov, S. and Haas, H., "Information rate of ofdm-based optical wireless communication systems with nonlinear distortion," *Journal of Lightwave Technology* **31**(6), 918–929 (2013).

[9] Tsonev, D., Sinanovic, S., and Haas, H., "Complete modeling of nonlinear distortion in ofdm-based optical wireless communication," *Journal of Lightwave Technology* **31**(18), 3064–3076 (2013).

[10] Elgala, H., Mesleh, R., and Haas, H., "Indoor Optical Wireless Communication: Potential and State-of-the-Art," *IEEE Commun. Mag.* **49**, 56–62 (Sept. 2011). ISSN: 0163-6804.

[11] Harald, B., Nikola, S., Dobroslav, T., Stefan, V., and Harald, H., "VLC: Beyond Point-to-Point Communication," *IEEE Communications Magazine* **pre-print available at: http://www.eng.ed.ac.uk/drupal/hxh/publications/** (2014).

[12] Vucic, J. and Langer, K.-D., "High-speed visible light communications: State-of-the-art," in [*Optical Fiber Communication Conference and Exposition (OFC/NFOEC), 2012 and the National Fiber Optic Engineers Conference*], 1–3 (2012).

[13] Afgani, M., Haas, H., Elgala, H., and Knipp, D., "Visible Light Communication Using OFDM," in [*Proc. of the 2nd International Conference on Testbeds and Research Infrastructures for the Development of Networks and Communities (TRIDENTCOM)*], 129–134 (Mar. 1–3 2006).

[14] Armstrong, J. and Lowery, A., "Power Efficient Optical OFDM," *Electronics Letters* **42**, 370–372 (Mar. 16, 2006).

[15] Lee, S. C. J., Randel, S., Breyer, F., and Koonen, A. M. J., "PAM-DMT for Intensity-Modulated and Direct-Detection Optical Communication Systems," *IEEE Photonics Technology Letters* **21**, 1749–1751 (Dec. 2009).

[16] Fernando, N., Hong, Y., and Viterbo, E., "Flip-OFDM for Optical Wireless Communications," in [*Information Theory Workshop (ITW)*], 5–9, IEEE, IEEE, Paraty, Brazil (Oct., 16–20 2011).

[17] Asadzadeh, K., Farid, A., and Hranilovic, S., "Spectrally Factorized Optical OFDM," in [*12th Canadian Workshop on Information Theory (CWIT 2011)*], 102–105, IEEE (May 17–20 2011).

[18] Fakidis, J., Tsonev, D., and Haas, H., "A Comparison Between DCO-OFDMA and Synchronous One-dimensional OCDMA for Optical Wireless Communications," in [*Proc. of the IEEE International Symposium on Personal, Indoor and Mobile Radio Communications (PIMRC 2013)*], IEEE, IEEE, London, UK (Sept. 8–11, 2013).

[19] OSRAM GmbH, "Datasheet: OS-PCN-2008-002-A OSTAR LED." Retrieved from http://www.osram.de (Feb. 2008).

[20] Vishay Semiconductors, "Datasheet: BPV10 Silicon PIN Photodiode, RoHS Compliant." Retrieved Aug 01, 2012 from www.vishay.com/docs/81502/bpv10.pdf (Aug. 2012).

[21] Rahaim, M. B., Vegni, A. M., and Little, T. D. C., "A hybrid radio frequency and broadcast visible light communication system," in [*IEEE Global Communications Conference (GLOBECOM 2011) Workshops*], 792–796 (5-9 Dec 2011).

[22] pureVLC, "pureVLC Li-1st." video. http://purevlc.co.uk/li-fire/purevlc-li-1st/.

[23] Ortiz, S., "The Wireless Industry Begins to Embrace Femtocells," *Computer* **41**, 14–17 (July 2008).

[24] Chandrasekhar, V., Andrews, J., and Gatherer, A., "Femtocell Networks: A Survey," *IEEE Communications Magazine* **46**(9), 59–67 (2008).

[25] Haas, H., "High-speed wireless networking using visible light." Retrieved from https://spie.org/x93593.xml (2013).

[26] Stefan, I., Burchardt, H., and Haas, H., "Area Spectral Efficiency Performance Comparison between VLC and RF Femtocell Networks," in [*Proc. of International Conference on Communications (ICC)*], 1–5 (June 2013).

[27] Ghimire, B. and Haas, H., "Self Organising Interference Coordination in Optical Wireless Networks," *EURASIP Journal on Wireless Communications and Networking* (2012).

[28] Marsh, G. W. and Kahn, J. M., "Channel Reuse Strategies for Indoor Infrared Wireless Communications," *IEEE Transactions on Communications* **45**, 1280–1290 (Oct. 1997).

[29] Chen, C., Serafimovski, N., and Haas, H., "Fractional Frequency Reuse in Optical Wireless Cellular Networks," in [*Proc. of the IEEE International Symposium on Personal, Indoor and Mobile Radio Communications (PIMRC 2013)*], IEEE (Sept. 8–11, 2013).

[30] Chen, C., Tsonev, D., and Haas, H., "Joint Transmission in Indoor Visible Light Communication Downlink Cellular Networks," in [*Proc. of the IEEE Workshop on Optical Wireless Communication (OWC 2013)*], IEEE (Dec. 9, 2013).

Avoiding Spectral Efficiency Loss in Unipolar OFDM for Optical Wireless Communication

Dobroslav Tsonev and Harald Haas

Institute for Digital Communications
Li-Fi R&D Centre
The University of Edinburgh
EH9 3JL, Edinburgh, UK
Email: {*d.tsonev, h.haas*} *@ed.ac.uk*

Abstract—**Unipolar orthogonal frequency division multiplexing (U-OFDM) has recently been introduced for intensity modulation and direct detection (IM/DD) systems. The scheme achieves higher power efficiency than the conventional direct-current-biased optical orthogonal frequency division multiplexing (DCO-OFDM) at the expense of half the spectral efficiency for the same M-ary quadrature amplitude modulation (M-QAM) order. This paper presents a modulation approach which doubles the spectral efficiency of U-OFDM and still allows it to achieve better performance in terms of both electrical power and optical power dissipation compared to DCO-OFDM. The simulation results and the theoretical analysis suggest that the performance improvement of the proposed scheme over DCO-OFDM increases with the modulation order. This trend is different from the inherently unipolar state-of-the-art techniques such as U-OFDM, asymmetrically clipped optical orthogonal frequency division multiplexing (ACO-OFDM) and pulse-amplitude-modulated discrete multitone modulation (PAM-DMT). It is typical for these schemes to exhibit a loss in the power efficiency as the spectral efficiency is increased. The novel approach is very promising for the achievement of high data rates in IM/DD systems. To the best of the authors' knowledge, this is the first design of a strictly unipolar orthogonal frequency division multiplexing (OFDM) scheme which requires no biasing and is able to demonstrate significant energy advantage over DCO-OFDM without sacrificing spectral efficiency.**

I. Introduction

Statistical data indicates that demand for wireless communication is growing exponentially. By 2017, data traffic of more than 11 Exabytes per month is expected in mobile networks [1]. Despite the significant technological advances in communication systems, forecasts indicate that meeting the future data rate demands will be challenging. The main reason for this stems from the fact that the radio frequency (RF) spectrum with favourable communication properties is almost completely depleted. A potential solution to the looming spectrum crisis lies in the expansion of wireless communication into new parts of the electromagnetic spectrum such as infrared and visible light wavelengths. Optical wireless communication (OWC) is a major candidate for providing a complementary alternative to RF communication. The optical spectrum features 100s of THz regulation-free bandwidth. Furthermore, optical radiation

does not interfere with the operation of sensitive electronic systems and the existing lighting infrastructure could be reused for backhauling. This would simplify the integration of OWC into future heterogeneous wireless networks. Moreover, OWC systems could potentially deliver significant energy savings when successfully combined with existing lighting fixtures.

The foremost candidates for low-cost front-end devices in OWC are commercially available light emitting diodes (LEDs) and photodiodes (PDs). Light emitted by off-the-shelf LEDs is incoherent and, therefore, information can be reliably encoded only in the signal intensity. Phase and amplitude of the light wave cannot be modulated or detected with LEDs and PDs. Hence, an OWC system can be realised only as an intensity modulation and direct detection (IM/DD) system. This limits the set of conventional modulation schemes that can directly be applied from the field of RF communication. Techniques like on-off keying (OOK), pulse-position modulation (PPM), and M-ary pulse-amplitude modulation (M-PAM) are relatively straightforward to implement. With the increase of transmission rates, however, the limited modulation bandwidth of the front-end devices and the limited bandwidth of the OWC channel lead to intersymbol interference (ISI).As a result, orthogonal frequency division multiplexing (OFDM) becomes a more appropriate choice. It enables cost-effective equalisation with single-tap equalisers in the frequency domain as well as adaptive data and energy loading in different frequency bands depending on the channel properties. This results in an optimal use of the communication resources. At medium access control (MAC) level, OFDM provides a straightforward multiple access scheme. It is less straightforward to achieve multiple access in OOK, PPM and M-PAM.

In practice, OFDM is realised by taking an inverse fast Fourier transform (IFFT) of a block of symbols from a conventional modulation scheme such as M-ary quadrature amplitude modulation (M-QAM). This effectively maps the M-QAM symbols to different subcarriers in the frequency domain of the resulting signal. The procedure, however, produces complex-valued time-domain samples, while intensity modulation requires real positive signals. Hence, modifications

3336

are required so that the OFDM signal becomes suitable for an IM/DD system. A real signal can be obtained by imposing a Hermitian symmetry in the information block which is passed through the IFFT. The resulting time-domain samples, however, are still bipolar. A number of approaches exist for obtaining a unipolar signal. A straightforward method is to simply add a bias value to all samples, which would make the resulting signal nonnegative. This scheme is called direct-current-biased optical orthogonal frequency division multiplexing (DCO-OFDM). The addition of the direct current (DC) bias increases the energy dissipation of the signal significantly. For example, 4-QAM DCO-OFDM requires a minimum bias which results in a power penalty of about 6 dB, compared to a bipolar OFDM signal. Hence, alternative methods for the generation of unipolar signals have been explored. This has lead to schemes such as asymmetrically clipped optical orthogonal frequency division multiplexing (ACO-OFDM) [2], pulse-amplitude-modulated discrete multitone modulation (PAM-DMT) [3], Unipolar orthogonal frequency division multiplexing (U-OFDM) [4], Flip-OFDM [5], *etc*. All these methods exploit the properties of the fast Fourier transform (FFT) and the properties of the OFDM frame structure in order to realise a unipolar signal without biasing. It is interesting to note that the underlying concepts presented for U-OFDM in [4] and for Flip-OFDM in [5] and [6] are the same. It is also interesting to note that all four approaches achieve the same performance in an additive white Gaussian noise (AWGN) channel [7]. For the same modulation order, the spectral efficiency of each of these four methods is halved when compared to DCO-OFDM. However, the power penalty when compared to a bipolar OFDM signal is only 3 dB for any M-QAM constellation size, which amounts to a significant energy advantage over DCO-OFDM. Improved decoders, which are equivalent in performance, have been developed for ACO-OFDM [8], U-OFDM [4] and Flip-OFDM [6]. Even though, to the best of the authors' knowledge, such an improved decoder is not presented in the literature for PAM-DMT, it would be straightforward to design. The improved decoders make the power efficiency of all four schemes almost equivalent to the case for a bipolar OFDM signal but can only work for a relatively flat communication channel. The real problem, however, stems from the decreased spectral efficiency, which requires M-QAM DCO-OFDM to be compared to M^2-QAM ACO-OFDM/U-OFDM/Flip-OFDM and to M-PAM PAM-DMT in order to keep the achievable data rate equivalent. This causes a substantial loss of energy efficiency compared to DCO-OFDM in all four schemes for a spectral efficiency above 1 bit/s/Hz [9]. Dissanayake *et. al.* have proposed a technique to simultaneously transmit ACO-OFDM and DCO-OFDM in an attempt to close the spectral efficiency gap [10]. However, this method still requires a DC-bias for the generation of DCO-OFDM. The current work proposes an algorithm to simultaneously transmit multiple unipolar data streams which

do not require any biasing. As a result, the spectral efficiency loss of U-OFDM is fully-compensated while a significant energy advantage over DCO-OFDM is retained.

The rest of this paper is organized as follows. Section II gives an overview of U-OFDM. Section III presents the modified modulation approach. Section IV makes a performance comparison between the proposed method and DCO-OFDM. Finally, Section V offers concluding remarks.

II. U-OFDM

In U-OFDM [4], after the IFFT operation from the OFDM modulation process, the time-domain signal is subjected to a simple transformation in order to make it unipolar with minimum or no biasing requirements. Each bipolar frame is split into two separate frames, transmitted one after the other. The first one holds the positive time-domain samples and zeros in the places of the negative ones. In the context of this work, this will be referred to as the *positive* frame. The second frame holds the absolute values of the negative samples and zeros in the places of the positive ones. This frame will be referred to as the *negative* frame. This transformation halves the achievable data rate and effectively halves the spectral efficiency which becomes:

$$\eta_{\text{U}} = \frac{\log_2(M)(N_{\text{FFT}} - 2)}{4(N_{\text{FFT}} + N_{\text{cp}})} \;\; \text{bits/s/Hz}, \quad (1)$$

as opposed to the spectral efficiency of DCO-OFDM:

$$\eta_{\text{DCO}} = \frac{\log_2(M)(N_{\text{FFT}} - 2)}{2(N_{\text{FFT}} + N_{\text{cp}})} \;\; \text{bits/s/Hz}. \quad (2)$$

The factor $\log_2(M)$ indicates the number of bits that are encoded in an M-QAM constellation; N_{FFT} is the FFT size; the factor $(N_{\text{FFT}} - 2)/2$ appears because the DC subcarrier and the π-shifted subcarrier are set to zero, and because only half of the subcarriers are modulated uniquely as part of the Hermitian symmetry requirement; N_{cp} is the length of the cyclic prefix.

At the U-OFDM receiver, each original bipolar frame is recovered by subtracting the samples in the *negative* frame from the samples in the *positive* frame. This combines the AWGN at both frames and leads to a signal-to-noise ratio (SNR) penalty of 3 dB when compared to a bipolar OFDM signal. The DC-bias in DCO-OFDM causes a substantial increase in the energy consumption. If the bias is defined as:

$$b_{\text{DC}} = k\sqrt{\text{E}\{s^2(t)\}} = k\sigma_{\text{s}}, \quad (3)$$

where $s(t)$ denotes the bipolar OFDM signal, and $\text{E}\{\cdot\}$ denotes statistical expectation, the energy dissipation of DCO-OFDM increases approximately by:

$$10\log_{10}\left(k^2 + 1\right) \text{dB} \quad (4)$$

when compared to bipolar OFDM [11]. The minimum biasing requirement of 4-QAM DCO-OFDM, for example, leads to a power penalty of about 6 dB. This penalty increases with the
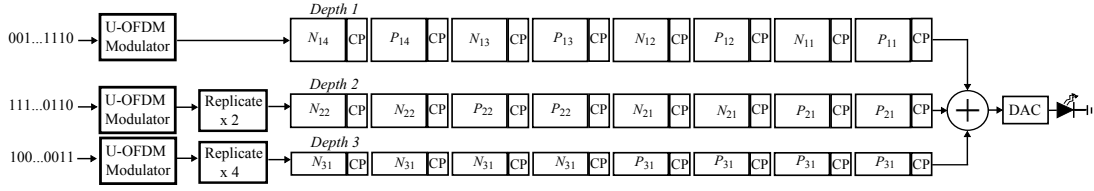
Fig. 1. Illustration of the enhanced U-OFDM concept up to *Depth 3*. CP is the cyclic prefix of each frame. P_{ml} signifies the unipolar frame which holds the positive samples of the *l*th original bipolar OFDM frame at *Depth m*. N_{ml} indicates the unipolar frame which holds the negative samples of the *l*th original bipolar OFDM frame at *Depth m*. The illustrated digital-to-analog converter (DAC) includes all necessary operations required for transition from a discrete-time-domain signal to a continuous analog signal. This block includes pulse-shaping and signal amplification. The resulting analog signal drives the LED transmitter.

modulation order. Hence, U-OFDM is more power efficient than DCO-OFDM for the same constellation size. However, as described in Section I, halving of the spectral efficiency means that M-QAM DCO-OFDM should be compared to M^2-QAM U-OFDM for the same spectral efficiency. As a result, U-OFDM very quickly loses its energy efficiency over DCO-OFDM as M increases.

An improved decoder for U-OFDM is presented in [4]. This decoder employs a recombination technique for the *positive* and *negative* frames, which at each position selects the sample with higher amplitude between the two frames. This ideally removes half of the AWGN. However, it is still insufficient to make up for the power penalty which results from the requirement for a higher constellation size compared to DCO-OFDM. Furthermore, this technique is only applicable in relatively flat communication channels where the ISI is negligible. If the ISI is considerable, then this demodulator requires equalisation to be performed in the time domain. In addition, since this method discards half of the U-OFDM samples, the channel attenuation at different frequency subcarriers is not consistent. This renders use of adaptive bit loading techniques difficult. Furthermore, frequency-dependent distortion effects caused by the DC-wandering in electrical circuits as well as by the flickering noise from ambient light sources could become unavoidable and could further aggravate the issues when using this demodulation algorithm.

III. ENHANCED U-OFDM

The current paper proposes a modification of U-OFDM which effectively doubles the spectral efficiency. The concept, as illustrated in Fig. 1, allows multiple U-OFDM information streams to be combined in a single time-domain signal used to modulate the LED. A single U-OFDM signal is represented by the information stream, labelled *Depth 1*. A frame labelled with P holds the positive samples of a bipolar OFDM frame and zeros in place of the negative ones. A frame labelled with N holds the absolute values of the negative samples of that same bipolar OFDM frame and zeros in place of the positive ones. The signal at *Depth 1* is generated exactly as described in Section II and in [4]. A second U-OFDM information stream,

indicated by *Depth 2*, is superimposed on the first one, and it does not affect the ability of the receiver to recover the transmitted bits as long as the additional stream follows a certain structure. In particular, at *Depth 2*, each U-OFDM frame is replicated and transmitted twice, where the second instance is an exact copy of the first one. Hence, in the figure, the second frame at *Depth 2* is an exact copy of the first one, the fourth frame is an exact copy of the third one, *etc..*, as indicated by their label. Since each frame is transmitted twice in the second stream, the power of each frame instance is scaled by $1/2$. A third stream can be added in the same way as the second one, and the structure requires the U-OFDM frames to be replicated four times now. The power of each frame instance is scaled by $1/4$ in this case. In a similar fashion, additional information streams could be added where each frame would be replicated into 2^{d-1} consecutive frames whose amplitude would be scaled by $1/\sqrt{2^{d-1}}$, where d indicates the depth of the stream.

At the receiver, the modulation stream at *Depth 1* can be demodulated using the standard techniques for U-OFDM. Each *negative* frame is subtracted from each *positive* frame, followed by conventional OFDM demodulation of the obtained bipolar frames. For example, at *Depth 1*, the first bipolar frame is obtained from the operation $P_{11} - N_{11}$, the second one is obtained from the operation $P_{12} - N_{12}$ and so on. The additional streams do not interfere with the successful demodulation because the interference that falls on P_{11} is equivalent to the interference that falls on N_{11} caused by $P_{21} + P_{31}$. Hence, the subtraction operation cancels out both interference terms. The same happens to the interference terms on all subsequent frames at *Depth 1*. Hence, the information at *Depth 1* can be successfully recovered with the conventional U-OFDM demodulator. Once the information bits are demodulated at *Depth 1*, they are remodulated again in order to recover the original U-OFDM signal at *Depth 1*. This signal is then subtracted from the overall received signal, and the result only contains the information streams from *Depth 2* and all subsequent levels. Every two equivalent frames at *Depth 2* are summed. For example, the first and the second

3338

frame at *Depth 2* are summed, the third and the fourth frames are summed, *etc.*. Then, the demodulation process continues with the conventional U-OFDM demodulator just like for the information at *Depth 1*. Again, subsequent streams do not interfere because the interference from the subsequent streams is structured in such a way that it is completely removed by the subtraction operation. After the bits are recovered, they are remodulated and the result is subtracted from the remaining received signal. This iterative demodulation procedure continues until the information at all depths is recovered.

The spectral efficiency of the new scheme is the sum of the spectral efficiencies of the information streams at all depths:

$$\eta_{\mathrm{eU}}(D) = \sum_{d=1}^{D} \frac{\eta_{\mathrm{U}}}{2^{d-1}} = \eta_{\mathrm{U}} \sum_{d=1}^{D} \frac{1}{2^{d-1}}, \tag{5}$$

where D is the maximum modulation depth of the scheme, which indicates the total number of streams that are superimposed in the modulation signal. As the maximum modulation depth increases, the spectral efficiency of this enhanced U-OFDM (eU-OFDM) converges to the spectral efficiency of DCO-OFDM:

$$\lim_{D \to \infty} \eta_{\mathrm{eU}}(D) = \eta_{\mathrm{U}} \lim_{D \to \infty} \sum_{d=1}^{D} \frac{1}{2^{d-1}} = 2\eta_{\mathrm{U}} = \eta_{\mathrm{DCO}}. \tag{6}$$

For a maximum modulation depth of $D=5$, η_{eU} is already 96.8% of η_{DCO}, which means the difference is negligible.

The average power of a U-OFDM signal is $\mathrm{E}\{\sigma_{\mathrm{s}}^2/2\}$, where σ_{s} is the standard deviation of the bipolar OFDM signal, introduced in (3). This result can be quickly deduced from the fact that half of the U-OFDM time-domain samples have the same absolute values as the bipolar OFDM samples and the other half of the U-OFDM samples are set to zero. The average electrical power of the eU-OFDM signal is higher due to the additional information streams. It can be calculated as:

$$\begin{aligned}
P_{\mathrm{elec,eU}}^{\mathrm{avg}} &= \mathrm{E}\{\mathrm{s}_{\mathrm{eU}}^2(t)\} = \mathrm{E}\left\{ \left(\sum_{d=1}^{D} \underline{\mathrm{s}}_d(t) \right)^2 \right\} \\
&= \sum_{d=1}^{D} \mathrm{E}\left\{\underline{\mathrm{s}}_d^2(t)\right\} + \sum_{d_1=1}^{D} \sum_{\substack{d_2=1 \\ d_1 \neq d_2}}^{D} \mathrm{E}\left\{\underline{\mathrm{s}}_{d_1}(t)\right\} \mathrm{E}\left\{\underline{\mathrm{s}}_{d_2}(t)\right\} \\
&= \frac{\sigma_{\mathrm{s}}^2}{2} \sum_{d=1}^{D} \frac{1}{2^{d-1}} + \sum_{d_1=1}^{D} \sum_{\substack{d_2=1 \\ d_1 \neq d_2}}^{D} \frac{\phi(0)\sigma_{\mathrm{s}}}{\sqrt{2^{d_1-1}}} \frac{\phi(0)\sigma_{\mathrm{s}}}{\sqrt{2^{d_2-1}}} \\
&= \frac{\sigma_{\mathrm{s}}^2}{2} \left(2 - \frac{1}{2^{D-1}} \right) + \frac{\sigma_{\mathrm{s}}^2}{2} 4\phi^2(0) \sum_{d_1=1}^{D} \sum_{\substack{d_2=1 \\ d_1 \neq d_2}}^{D} \frac{1}{\sqrt{2^{d_1+d_2}}}, \quad (7)
\end{aligned}$$

where $\mathrm{s}_{\mathrm{eU}}(t)$ is the time-domain eU-OFDM signal, $\underline{\mathrm{s}}_d(t)$ is the time-domain U-OFDM signal at depth d, and $\phi(0)$ is the probability density function (PDF) of the standard normal distribution. In (7), the time-domain expectation of the U-OFDM signal, $\mathrm{E}\{\underline{\mathrm{s}}_d(t)\} = \phi(0)\sigma_{\mathrm{s}}/\sqrt{2^{d-1}}$, can be quickly

derived from the fact that half of the U-OFDM samples follow a Gaussian distribution clipped at zero, and the other half of the samples are set to zero. The truncated Gaussian distribution and its statistical properties are described in more detail in [12]. The number of bits carried by eU-OFDM is $2 - 1/2^{D-1}$ times more compared to U-OFDM, and, as a consequence, the increase in the required SNR compared to U-OFDM for the same M-QAM constellation size becomes:

$$\alpha = 1 + \frac{4\phi^2(0)}{2 - 1/2^{D-1}} \sum_{d_1=1}^{D} \sum_{\substack{d_2=1 \\ d_1 \neq d_2}}^{D} \frac{1}{\sqrt{2^{d_1+d_2}}}. \tag{8}$$

The electrical SNR of the system is defined as:

$$\frac{E_{\mathrm{b,elec}}}{N_{\mathrm{o}}} = \frac{P_{\mathrm{elec,eU}}^{\mathrm{avg}}}{B\eta_{\mathrm{eU}} N_{\mathrm{o}}} = \frac{\mathrm{E}\{\mathrm{s}_{\mathrm{eU}}^2(t)\}}{B\eta_{\mathrm{eU}} N_{\mathrm{o}}}, \tag{9}$$

where B is the communication bandwidth of the system and N_{o} is the power spectral density (PSD) of the AWGN. Given that U-OFDM, decoded by subtraction of the negative frame, performs 3 dB worse than bipolar OFDM, a bound on the performance of eU-OFDM can be easily evaluated theoretically. This is achieved by applying a factor of 2 and a factor of α to the SNR in the formula for calculating the bit error rate (BER) of conventional real M-QAM OFDM. This bound is expected to coincide with the BER curve for the information stream at *Depth 1* of eU-OFDM where distortion is caused only by the AWGN as the inter-stream interference of any subsequent streams can be completely removed by the subtraction operation. The BER of the additional streams is expected to increase with the depth. This occurs because the performance of each stream is affected by the BER of the previous streams. Any errors in the demodulated bits at a given depth translate into imperfections in the iterative cancellation algorithm. This results in overall deterioration of the signal quality at all subsequent information streams. The performances of all streams are expected to converge to the performance of the one at *Depth 1* as the SNR increases. This expected trend is confirmed by the simulation results in Section IV.

In a similar fashion, the average optical power of the eU-OFDM signal can be calculated as:

$$P_{\mathrm{opt,eU}}^{\mathrm{avg}} = \mathrm{E}\{\mathrm{s}_{\mathrm{eU}}(t)\} = \mathrm{E}\left\{ \sum_{d=1}^{D} \underline{\mathrm{s}}_d(t) \right\} = \sum_{d=1}^{D} \mathrm{E}\{\underline{\mathrm{s}}_d(t)\} \tag{10}$$

$$= \phi(0)\sigma_{\mathrm{s}} \sum_{d=1}^{D} \frac{1}{\sqrt{2^{d-1}}}.$$

A closed-form bound can be calculated for the BER performance as a function of the optical SNR. The relationship between electrical SNR and optical SNR can be expressed as the ratio of (7) and (10). This means that for any optical SNR, the equivalent electrical SNR can be obtained, and for
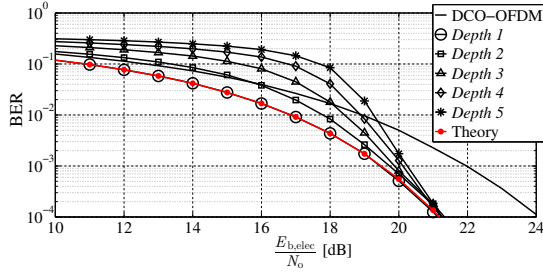
Fig. 2. 16-QAM eU-OFDM performance at different depths as a function of the electrical SNR. The optimum biasing level for 16-QAM DCO-OFDM is estimated at 7.5 dB, as described in (4).
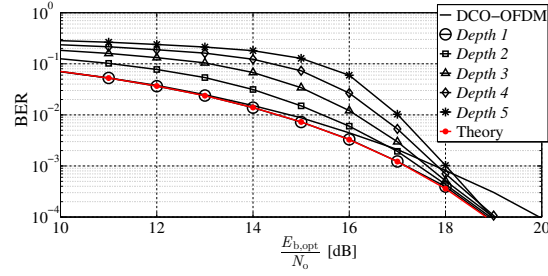

Fig. 3. 16-QAM eU-OFDM performance at different depths as a function of the optical SNR. The optimum biasing level for 16-QAM DCO-OFDM is estimated at 7.5 dB, as described in (4).

the electrical SNR a closed-form bound already exists. The optical SNR of the system is defined as:

$$\frac{E_{\mathrm{b,opt}}}{N_{\mathrm{o}}} = \frac{P_{\mathrm{opt,eU}}^{\mathrm{avg}}}{B\eta_{\mathrm{eU}}N_{\mathrm{o}}} = \frac{\mathrm{E}\left\{s_{\mathrm{eU}}(t)\right\}}{B\eta_{\mathrm{eU}}N_{\mathrm{o}}}. \qquad (11)$$

The calculations presented so far assume an eU-OFDM signal with zero bias. This occurs when at the lowest operational point the LED light intensity output is generally not visible. Then, a zero bias can be assumed for the estimation of the optical efficiency of the system. However, an LED normally requires a minimum bias current at which the device turns on. Therefore, for the calculation of the electrical efficiency, this bias needs to be taken into account. As long as it is small, relative to the span of the information signal, the bias will not introduce significant changes to the energy efficiency of the system. Therefore, in the current study, it is neglected.

IV. NUMERICAL RESULTS

This section compares the performance of DCO-OFDM and eU-OFDM in the context of a linear AWGN channel. The only nonlinear operation considered in this study is clipping of any negative values in the modulation signal. This occurs because an LED is active only for a positive signal. In practice, clipping of the signal from above is also present due to saturation of the optical output power and due to maximum current and optical radiation constraints. This effect is not considered in the current work as it is strongly dependent on the particular device which is used and also dependent on the signal level constraints. The clipping from below, however, is inherent and cannot be avoided in a scheme such as DCO-OFDM unless an impractically large signal bias is introduced. The peak-to-average power ratio (PAPR) of an OFDM signal is quite high and grows linearly with the number of active subcarriers in the frequency domain [13]. Hence, it is very inefficient to use a bias level which can make all possible negative values positive in DCO-OFDM. The novel modulation scheme, eU-OFDM, is strictly positive and so it requires no biasing. In the current study, the maximum modulation depth of eU-OFDM is set to $D=5$. The performance of the information streams at the

different depths is illustrated in Fig. 2. As expected, the stream at *Depth 1* performs best and its BER curve matches exactly the theoretical bound described in Section III. All subsequent streams converge to the performance of the first one as the SNR increases. The same behaviour is depicted in Fig. 3 where the performance of eU-OFDM is illustrated as a function of the optical SNR.

The average BER of the information at all depths is compared against the BER of DCO-OFDM for different M-QAM constellation sizes. Fig. 4 presents the results as a function of the electrical SNR. At BER=10^{-4}, the performance improvement of eU-OFDM over DCO-OFDM starts at 1 dB for $M=4$ and increases to about 5 dB for $M=256$. The bias levels for the different realisations of DCO-OFDM are optimised through Monte Carlo simulations, in agreement with previous works such as [12], [14]. This means that adding less bias would lead to more clipping and, hence, to higher BER values for a given SNR, while adding more bias would lead to higher SNR levels without actually reducing the BER. The bias level in each case is indicated as the estimated SNR increase in dB compared to the case for a bipolar OFDM signal as described in (4). It is interesting to note that, for a depth of $D=5$, the factor for the SNR increase of eU-OFDM, described in (8), is $\alpha=1.96$, which translates in an SNR penalty of less than 6 dB, compared to the real bipolar OFDM signal. This SNR penalty is constant for all values of the constellation size M. Therefore, it is easy to explain and quantify the increasing energy advantage of eU-OFDM over DCO-OFDM with the increase of the M-QAM modulation order. Fig. 5 illustrates the performance difference between eU-OFDM and DCO-OFDM for different modulation orders in terms of the BER as a function of the optical SNR. For $M=4$, the two schemes seem to perform equivalently at BER=10^{-4}. As the constellation size increases, the increasing biasing requirement of DCO-OFDM causes eU-OFDM to become more efficient. The savings in terms of optical power reach about 2 dB for 256-QAM.
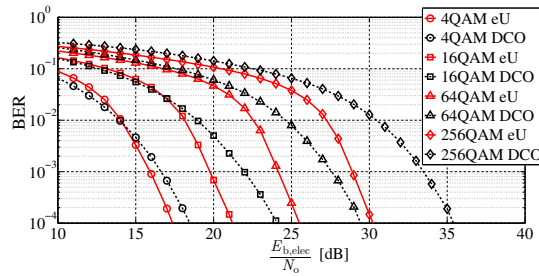
3340

238

IEEE ICC 2014 - Optical Networks and Systems

Fig. 4. eU-OFDM performance vs. DCO-OFDM performance for different M-QAM constellation size as a function of the electrical SNR. Optimum biasing levels for 4-QAM, 16-QAM, 64-QAM, and 256-QAM DCO-OFDM are estimated at respectively 6 dB, 7.5 dB, 9.5 dB, and 11 dB, as described in (4).
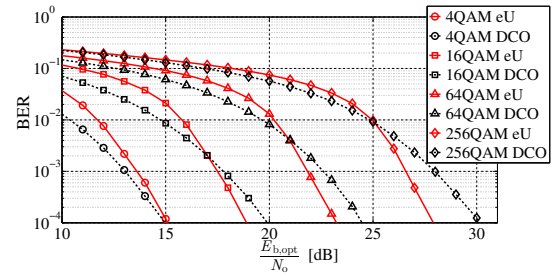
Fig. 5. eU-OFDM performance vs. DCO-OFDM performance for different M-QAM modulation order as a function of the optical SNR. According to (4), optimum biasing levels for 4-QAM, 16-QAM, 64-QAM, and 256-QAM DCO-OFDM are set at 6 dB, 7.5 dB, 9.5 dB, and 11 dB, respectively.

V. Conclusion

A novel approach for increasing the spectral efficiency of U-OFDM has been presented in this paper. It allows U-OFDM to approach the spectral efficiency of DCO-OFDM without the need to introduce any form of biasing, apart from the practical minimum around the turn-on voltage, and, as a consequence, the new scheme avoids energy efficiency losses due to LED biasing. The new method achieves significant improvements in terms of both electrical power dissipation and optical power dissipation. The better energy efficiency of the scheme comes at the cost of increased computational complexity in the modulation and demodulation procedures. At the same time, the design complexity of the analog circuitry is reduced, compared to DCO-OFDM, since the biasing level needs to be optimised only once for any signal strength and any constellation size.

The other two types of unipolar OFDM - ACO-OFDM and PAM-DMT - include a special structure within their time-domain frame which allows well-structured interference terms to be orthogonal to the useful information. As a consequence, the authors believe that the currently presented concept could be extended to those schemes as well. Further work on the subject may include a more detailed evaluation of ACO-OFDM and PAM-DMT. In addition, a performance analysis of eU-OFDM in the presence of nonlinear distortion, resulting from the electrical-to-optical characteristics of an LED, will also be conducted.

The other two types of unipolar OFDM - ACO-OFDM and PAM-DMT - include a special structure within their time-domain frame which allows well-structured interference terms to be orthogonal to the useful information. As a consequence, the authors believe that the currently .

Acknowledgement

References

[1] Cisco Visual Networking Index, "Global Mobile Data Traffic Forecast Update, 2012-2017," CISCO, White Paper, Feb. 2013. [Online]. Available: http://www.cisco.com/en/US/solutions/collateral/ns341/ns525/ns537/ns705/ns827/white_paper_c11-481360.pdf

[2] J. Armstrong and A. Lowery, "Power Efficient Optical OFDM," *Electronics Letters*, vol. 42, no. 6, pp. 370–372, Mar. 16, 2006.

[3] S. C. J. Lee, S. Randel, F. Breyer, and A. M. J. Koonen, "PAM-DMT for Intensity-Modulated and Direct-Detection Optical Communication Systems," *IEEE Photonics Technology Letters*, vol. 21, no. 23, pp. 1749–1751, Dec. 2009.

[4] D. Tsonev, S. Sinanović, and H. Haas, "Novel Unipolar Orthogonal Frequency Division Multiplexing (U-OFDM) for Optical Wireless," in *Proc. of the Vehicular Technology Conference (VTC Spring)*, IEEE. Yokohama, Japan: IEEE, May 6–9 2012.

[5] N. Fernando, Y. Hong, and E. Viterbo, "Flip-OFDM for Optical Wireless Communications," in *Information Theory Workshop (ITW)*, IEEE. Paraty, Brazil: IEEE, Oct., 16–20 2011, pp. 5–9.

[6] ——, "Flip-OFDM for Unipolar Communication Systems," *IEEE Transactions on Communications*, vol. 60, no. 12, pp. 3726–3733, Dec. 2012.

[7] D. Tsonev, S. Sinanovic, and H. Haas, "Complete Modeling of Nonlinear Distortion in OFDM-Based Optical Wireless Communication," *IEEE Journal of Lightwave Technology*, vol. 31, no. 18, pp. 3064–3076, Sep. 15 2013.

[8] K. Asadzadeh, A. Dabbo, and S. Hranilovic, "Receiver Design for Asymmetrically Clipped Optical OFDM," in *GLOBECOM Workshops (GC Wkshps)*. Houston, TX, USA: IEEE, Dec., 5–9 2011, pp. 777–781.

[9] S. Dimitrov, S. Sinanovic, and H. Haas, "A Comparison of OFDM-based Modulation Schemes for OWC with Clipping Distortion," in *GLOBECOM Workshops (GC Wkshps)*, Houston, Texas, USA, 5–9 Dec. 2011.

[10] S. Dissanayake, K. Panta, and J. Armstrong, "A Novel Technique to Simultaneously Transmit ACO-OFDM and DCO-OFDM in IM/DD Systems," in *IEEE GLOBECOM Workshops (GC Wkshps)*. Houston, TX, USA: IEEE, Dec. 5–9 2011, pp. 782–786.

[11] J. Armstrong and B. J. C. Schmidt, "Comparison of Asymmetrically Clipped Optical OFDM and DC-Biased Optical OFDM in AWGN," *IEEE Communications Letters*, vol. 12, no. 5, pp. 343–345, May 2008.

[12] S. Dimitrov, S. Sinanovic, and H. Haas, "Clipping Noise in OFDM-based Optical Wireless Communication Systems," *IEEE Transactions on Communications (IEEE TCOM)*, vol. 60, no. 4, pp. 1072–1081, Apr. 2012.

[13] D. Tsonev, S. Sinanović, and H. Haas, "Enhanced Subcarrier Index Modulation (SIM) OFDM," in *GLOBECOM Workshops (GC Wkshps)*, IEEE. Houston, Texas, USA: IEEE, Dec. 5–9, 2011.

[14] S. Dimitrov and H. Haas, "Information Rate of OFDM-Based Optical Wireless Communication Systems With Nonlinear Distortion," vol. 31, no. 6, pp. 918 – 929, Mar. 15 2013.

3341

Bibliography

[1] Cisco Visual Networking Index, "Global Mobile Data Traffic Forecast Update, 2012-2017," CISCO, White Paper, Feb. 2013. [Online]. Available: http://www.cisco.com/en/US/solutions/collateral/ns341/ns525/ns537/ns705/ns827/white_paper_c11-481360.pdf

[2] "Visible Light Communication (VLC) - A Potential Solution to the Global Wireless Spectrum Shortage," GBI Research, Tech. Rep., 2011. [Online]. Available: http://www.gbiresearch.com/

[3] L. Hanzo, H. Haas, S. Imre, D. O'Brien, M. Rupp, and L. Gyongyosi, "Wireless Myths, Realities and Futures: From 3G/4G to Optical and Quantum Wireless," *Proc. IEEE*, vol. 100, pp. 1853–1888, May 2012.

[4] J. M. Kahn and J. R. Barry, "Wireless Infrared Communications," *Proc. IEEE*, vol. 85, no. 2, pp. 265–298, Feb. 1997.

[5] H. Elgala, R. Mesleh, and H. Haas, "Indoor Optical Wireless Communication: Potential and State-of-the-Art," *IEEE Commun. Mag.*, vol. 49, no. 9, pp. 56–62, Sep. 2011, ISSN: 0163-6804.

[6] F. R. Gfeller and U. Bapst, "Wireless In-House Data Communication Via Diffuse Infrared Radiation," *Proc. IEEE*, vol. 67, no. 11, pp. 1474–1486, Nov. 1979.

[7] J. R. Barry, *Wireless Infrared Communications*. Springer, 1994, vol. 280.

[8] J. B. Carruthers and J. M. Kahn, "Modeling of Nondirected Wireless Infrared Channels," in *In the Proceeding of the IEEE Conference on Communications.: Converging Technologies for Tomorrow's Applications*, vol. 2, Dallas, TX, USA, Jun. 23–27, 1996, pp. 1227–1231.

[9] ——, "Modeling of Nondirected Wireless Infrared Channels," *IEEE Transactions on Communications*, vol. 45, no. 10, pp. 1260–1268, Oct. 1997.

[10] A. M. Khalid, G. Cossu, R. Corsini, P. Choudhury, and E. Ciaramella, "1-Gb/s transmission over a phosphorescent white LED by using rate-adaptive discrete multitone modulation," *IEEE Photon. J.*, vol. 4, no. 5, pp. 1465–1473, Oct. 2012.

[11] G. Cossu, A. M. Khalid, P. Choudhury, R. Corsini, and E. Ciaramella, "3.4 Gbit/s visible optical wireless transmission based on RGB LED," *Optics Express*, vol. 20, pp. B501–B506, 2012.

[12] A. Azhar, T. Tran, and D. O'Brien, "A Gigabit/s indoor wireless transmission using MIMO-OFDM visible-light communications," *IEEE Photon. Technol. Lett.*, vol. 25, no. 2, pp. 171–174, Jan.15 2013.

[13] Z. Ghassemlooy, W. Popoola, and S. Rajbhandari, *Optical Wireless Communications: System and Channel Modeling with MATLAB(R)*, 1st ed. CRC Press, 2012.

[14] S. Dimitrov, S. Sinanovic, and H. Haas, "Clipping Noise in OFDM-based Optical Wireless Communication Systems," *IEEE Transactions on Communications (IEEE TCOM)*, vol. 60, no. 4, pp. 1072–1081, Apr. 2012.

[15] ——, "Signal Shaping and Modulation for Optical Wireless Communication," *IEEE/OSA Journal on Lightwave Technology (IEEE/OSA JLT)*, vol. 30, no. 9, pp. 1319–1328, May 2012.

[16] D. Barros, S. Wilson, and J. Kahn, "Comparison of orthogonal frequency-division multiplexing and pulse-amplitude modulation in indoor optical wireless links," *IEEE Transactions on Communications*, vol. 60, no. 1, pp. 153–163, 2012.

[17] D. Tsonev, S. Sinanović, and H. Haas, "Enhanced Subcarrier Index Modulation (SIM) OFDM," in *GLOBECOM Workshops (GC Wkshps)*, IEEE. Houston, Texas, USA: IEEE, Dec. 5–9, 2011.

[18] ——, "Novel Unipolar Orthogonal Frequency Division Multiplexing (U-OFDM) for Optical Wireless," in *Proc. of the Vehicular Technology Conference (VTC Spring)*, IEEE. Yokohama, Japan: IEEE, May 6–9 2012.

[19] D. Tsonev and H. Haas, "Avoiding Spectral Efficiency Loss in Unipolar OFDM for Optical Wireless Communication," in *Proc. of the International Conference on Communications (ICC)*. Sydney, Australia: IEEE, Jun., 10–14 2014.

[20] D. Tsonev, S. Sinanović, and H. Haas, "Pulse Shaping in Unipolar OFDM-based Modulation Schemes," in *Proc. of the OWC'12 Workshop in conjuction with the Global Commu-*

nications Conference (GLOBECOM), IEEE. Anaheim, California, USA: IEEE, Dec. 3–7 2012, pp. 1208–1212.

[21] D. Tsonev, S. Sinanovic, and H. Haas, "Complete Modeling of Nonlinear Distortion in OFDM-based Optical Wireless Communication," *J. Lightw. Technol.*, vol. 31, no. 18, pp. 3064–3076, Sep. 15 2013.

[22] ——, "A Novel Analytical Framework for Modeling Nonlinear Distortions in OFDM-based Optical Wireless Communication," in *IEEE/CIC International Conference on Communications in China (ICCC 2013)*. Xi'an, China: IEEE, Aug., 12–14 2013, pp. 147–152.

[23] J. Campello, "Optimal Discrete Bit Loading for Multicarrier Modulation Systems," in *Proceedings of the IEEE International Symposium on Information Theory*, Cambridge, MA, USA, Aug. 16–21 1998, p. 193.

[24] D. Tsonev, H. Chun, S. Rajbhandari, J. J. D. McKendry, S. Videv, E. Gu, M. Haji, S. Watson, A. E. Kelly, G. Faulkner, M. D. Dawson, H. Haas and D. O'Brien, "A 3-Gb/s Single-LED OFDM-based Wireless VLC Link Using a Gallium Nitride μLED," *IEEE Photon. Technol. Lett.*, vol. 26, no. 7, pp. 637–640, Apr. 2014.

[25] A. G. Bell, "Selenium and the Photophone," *Nature*, vol. 22, no. 569, pp. 500–503, 1880.

[26] M. I. Nathan, W. P. Dumke, G. Burns, and F. H. Dill, "Stimulated Emission of Radiation from GaAs p-n Junctions," *Appl. Phys. Lett.*, vol. 1, no. 3, p. 62, 1962.

[27] R. N. Hall, G. E. Fenner, J. D. Kingsley, T. J. Soltys, and R. O. Carlson, "Coherent Light Emission from GaAs Junctions," *Phys. Rev. Lett.*, vol. 9, no. 9, pp. 366–369, Nov., 1 1962.

[28] P. Barker and A. C. Boucouvalas, "Performance modeling of the IrDA protocol for infrared wireless communications," vol. 36, no. 12, pp. 113–117, 1998.

[29] M. Afgani, S. Sinanović, K. Khashaba, and H. Haas, "Radio Frequency Signature Correlation Based Speed Estimation for Indoor Positioning," *Journal of Communications (Invited Paper)*, vol. 4, no. 2, pp. 96–107, Mar. 2009. [Online]. Available: http://www.academypublisher.com/jcm/vol04/no02/jcm0402096107.html

[30] D. O'Brien, G. Faulkner, H. Le-Minh, O. Bouchet, M. El Tabach, M. Wolf, J. Walewski, S. Randel, S. Nerreter, M. Franke, K.-D. Langer, J. Grubor, and T. Kamalakis, "Gigabit

Optical Wireless for a Home Access Network," in *IEEE Symposion on Personal, Indoor and Mobile Radio Communications (PIMRC 2009)*. Tokyo, Japan: IEEE, Sep. 13–16 2009, pp. 1–5.

[31] European Commission, "Technical briefing: Phasing out Incandescent Bulbs in the EU," Retrieved from http://ec.europa.eu, Sep. 2008.

[32] IEEE Std. 802.15.7-2011, *IEEE Standard for Local and Metropolitan Area Networks, Part 15.7: Short-Range Wireless Optical Communication Using Visible Light*, IEEE Std., 2011.

[33] J. Grubor, S. Randel, K. Langer, and J. Walewski, "Bandwidth Efficient Indoor Optical Wireless Communications with White Light Emitting Diodes," in *In the Proceeding of the 6th International Symposium on Communication Systems, Networks and Digital Signal Processing*, vol. 1, Graz, Austria, Jun. 23–25, 2008, pp. 165–169.

[34] J. J. D. McKendry, D. Massoubre, S. Zhang, B. R. Rae, R. P. Green, E. Gu, R. K. Henderson, A. E. Kelly and M. D. Dawson, "Visible-light communications using a CMOS-controlled micro-light-emitting-diode array," *J. Lightw. Technol.*, vol. 30, no. 1, pp. 61–67, 2012.

[35] J. J. D. McKendry, R. P. Green, A. E. Kelly, Z. Gong, B. Guilhabert, D. Massoubre, E. Gu and M. D. Dawson, "High-Speed Visible Light Communications Using Individual Pixels in a Micro Light-Emitting Diode Array," *IEEE Photon. Technol. Lett.*, vol. 22, no. 18, pp. 1346–1348, Sep. 2010.

[36] J. Wun, C. Lin, W. Chen, J. Sheu, C. Lin, Y. Li, J. Bowers, J. Shi, J. Vinogradov, R. Kruglov, and O. Ziemann, "GaN-Based Miniaturized Cyan Light-Emitting Diodes on a Patterned Sapphire Substrate With Improved Fiber Coupling for Very High-Speed Plastic Optical Fiber Communication," *IEEE Photon. J.*, vol. 4, no. 5, pp. 1520–1529, Oct. 2012.

[37] A. Neumann, J. Wierer, Jr., W. Davis, Y. Ohno, R. Brueck, and J. Tsao, "Four-color Laser White Illuminant Demonstrating High Color-rendering Quality," *OSA Optics Express*, vol. 19, no. S4, pp. A982–A990, Jul. 2011.

[38] C. Basu, M. Meinhardt-Wollweber, and B. Roth, "Lighting With Laser Diodes," *Advanced Optical Technology*, vol. 2, no. 4, pp. 313–321, 2013.

[39] R. Baets, D. Delbeke, R. Bockstaele, and P. Bienstman, "Resonant-cavity light-emitting diodes: a review," in *Proc. SPIE*, vol. 4996, Jul. 3 2003, pp. 42–49.

[40] L. Geng, J. Wei, R. Penty, I. White, and D. Cunningham, "3 Gbit/s LED-based step index plastic optical fiber link using multilevel pulse amplitude modulation," in *Proc. IEEE OFC/NFOEC*, Anaheim, CA, USA, Mar. 17–21 2013, pp. 1–3.

[41] I. Stefan, H. Burchardt, and H. Haas, "Area Spectral Efficiency Performance Comparison between VLC and RF Femtocell Networks," in *Proc. IEEE Int. Conf. Commun. (ICC)*, Budapest, Hungary, Jun. 9–13 2013, pp. 1–5.

[42] C. Chen, N. Serafimovski, and H. Haas, "Fractional Frequency Reuse in Optical Wireless Cellular Networks," in *Proc. IEEE 24th Int. Symp. Pers. Indoor and Mobile Radio Commun. (PIMRC)*, IEEE. London, UK: IEEE, Sep. 8–11, 2013, pp. 3594–3598.

[43] C. Chen, D. Tsonev, and H. Haas, "Joint Transmission in Indoor Visible Light Communication Downlink Cellular Networks," in *Proc. of the IEEE Workshop on Optical Wireless Communication (OWC 2013)*, IEEE. Atlanta, GA, USA: IEEE, Dec. 9, 2013.

[44] J. Liu, W. Noonpakdee, H. Takano, and S. Shimamoto, "Foundational Analysis of Spatial Optical Wireless Communication Utilizing Image Sensor," in *IEEE International Conference on Imaging Systems and Techniques (IST)*, Penang, Malaysia, May 17–18 2011, pp. 205–209.

[45] I. Takai, S. Ito, K. Yasutomi, K. Kagawa, M. Andoh, and S. Kawahito, "LED and CMOS Image Sensor Based Optical Wireless Communication System for Automotive Applications," *IEEE Photon. J.*, vol. 5, no. 5, pp. 6 801 418–6 801 418, Oct. 2013.

[46] Z. Wang, D. Tsonev, S. Videv, and H. Haas, "Towards self-powered solar panel receiver for optical wireless communication," in *Communications (ICC), 2014 IEEE International Conference on*, June 2014, pp. 3348–3353.

[47] S. Schmid, G. Corbellini, S. Mangold, and T. Gross, "An LED-to-LED Visible Light Communication System with Software-based Synchronization," in *IEEE Globecom Workshops (GC Wkshps)*, Anaheim, CA, USA, Dec. 3–7 2012, pp. 1264–1268.

[48] D. Giustiniano, N. Tippenhauer, and S. Mangold, "Low-complexity Visible Light Networking with LED-to-LED communication," in *IFIP Wireless Days (WD)*, Dublin, Ireland, Nov. 21–23 2012, pp. 1–8.

[49] R. Mesleh, R. Mehmood, H. Elgala, and H. Haas, "An Overview of Indoor OFDM/DMT Optical Wireless Communication Systems," in *IEEE International Symposium on Communication Systems, Networks and Digital Signal Processing (CSNDSP)*, Newcastle, U.K., 21–23 Jul. 2010, pp. 1–5, to appear.

[50] H. Elgala, R. Mesleh, and H. Haas, "Indoor Broadcasting via White LEDs and OFDM," *IEEE Transactions on Consumer Electronics*, vol. 55, no. 3, pp. 1127–1134, Aug. 2009.

[51] S. Cova, M. Ghioni, A. Lacaita, C. Samori, and F. Zappa, "Avalanche PPhotodiode and Quenching Circuits for Single-photon Detection," *OSA Applied Optics*, vol. 35, no. 12, pp. 1956–1976, Apr. 20 1996.

[52] D. C. O'Brien, Q. Shabnam, Z. Sasha, and G. E. Faulkner, "Multiple Input Multiple Output Systems for Optical Wireless; Challenges and Possibilities," in *Proceedings of SPIE*, San Diego, California, USA, Aug. 15–17 2006.

[53] L. Zeng, D. O'Brien, H. Minh, G. Faulkner, K. Lee, D. Jung, Y. Oh, and E. T. Won, "High Data Rate Multiple Input Multiple Output (MIMO) Optical Wireless Communications Using White LED Lighting," *IEEE J. Sel. Areas Commun.*, vol. 27, no. 9, pp. 1654–1662, Dec. 2009.

[54] D. Tsonev, S. Sinanović, and H. Haas, "Practical MIMO Capacity for Indoor Optical Wireless Communication with White LEDs," in *Proc. of the Vehicular Technology Conference (VTC Spring)*, IEEE.   Dresden, Germany: IEEE, Jun. 2–5 2013, pp. 1–5.

[55] J. Barry, J. Kahn, W. Krause, E. Lee, and D. Messerschmitt, "Simulation of multipath impulse response for indoor wireless optical channels," *IEEE J. Select. Areas Commun.*, vol. 11, no. 3, pp. 367–379, Apr. 1993.

[56] C. R. Lomba, R. T. Valadas, and A. M. De Oliveira Duarte, "Experimental Characterisation and Modelling of the Reflection of Infrared Signals on Indoor Surfaces," *IEE Proc. Optoelectronics*, vol. 145, no. 3, pp. 191–197, Jun. 1998.

[57] F. Tavernier and M. Steyaert, *High-Speed Optical Receivers with Integrated Photodiode in Nanoscale CMOS*. Springer, 2011.

[58] K. Schneider and H. Zimmermann, *Highly Sensitive Optical Receivers*. Springer, 2006.

[59] J. B. Carruthers and J. M. Kahn, "Multiple-subcarrier Modulation for Nondirected Wireless Infrared Communication," *IEEE Journal on Selected Areas in Communications*, vol. 14, no. 3, pp. 538–546, Apr. 1996.

[60] J. Armstrong and B. J. C. Schmidt, "Comparison of Asymmetrically Clipped Optical OFDM and DC-Biased Optical OFDM in AWGN," *IEEE Commun. Lett.*, vol. 12, no. 5, pp. 343–345, May 2008.

[61] J. Armstrong and A. Lowery, "Power Efficient Optical OFDM," *Electronics Letters*, vol. 42, no. 6, pp. 370–372, Mar. 16, 2006.

[62] S. C. J. Lee, S. Randel, F. Breyer, and A. M. J. Koonen, "PAM-DMT for Intensity-Modulated and Direct-Detection Optical Communication Systems," *IEEE Photonics Technology Letters*, vol. 21, no. 23, pp. 1749–1751, Dec. 2009.

[63] I. Neokosmidis, T. Kamalakis, J. W. Walewski, B. Inan, and T. Sphicopoulos, "Impact of Nonlinear LED Transfer Function on Discrete Multitone Modulation: Analytical Approach," *Lightwave Technology*, vol. 27, no. 22, pp. 4970–4978, 2009.

[64] H. Elgala, R. Mesleh, and H. Haas, "A Study of LED Nonlinearity Effects on Optical Wireless Transmission using OFDM," in *Proceedings of the 6th IEEE International Conference on wireless and Optical communications Networks (WOCN)*, Cairo, Egypt, Apr. 28–30, 2009.

[65] ——, "Impact of LED nonlinearities on optical wireless OFDM systems," in *2010 IEEE 21st International Symposium on Personal Indoor and Mobile Radio Communications (PIMRC)*, sept 2010, pp. 634 – 638.

[66] D. Dardari, V. Tralli, and A. Vaccari, "A Theoretical Characterization of Nonlinear Distortion Effects in OFDM Systems," *IEEE Transactions on Communications*, vol. 48, no. 10, pp. 1755–1764, Oct. 2000.

[67] J. Bussgang, "Cross Correlation Function of Amplitude-Distorted Gaussian Signals," Research Laboratory for Electronics, Massachusetts Institute of Technology, Cambridge, MA, Technical Report 216, Mar. 1952.

[68] H. E. Rowe, "Memoryless Nonlinearities With Gaussian Inputs: Elementary Results," *The Bell System Technical Journal*, vol. 61, no. 7, pp. 1519 – 1525, Sep. 1982.

[69] V. Kühn, *Wireless Communications over MIMO Channels*.   John Wiley & Sons Ltd., 2006.

[70] L. Hanzo, O. Alamri, M. El-Hajjar, and N. Wu, *Near-Capacity Multi-Functional MIMO Systems: Sphere-Packing, Iterative Detection and Cooperation*, ser. Wiley - IEEE.   Wiley, 2009.

[71] T. M. Duman and A. Ghrayeb, *Coding for MIMO Communication Systems*.   John Wiley and Sons, 2007.

[72] A. Burg, M. Borgmann, M. Wenk, M. Zellweger, W. Fichtner, and H. Bolcskei, "VLSI Implementation of MIMO Detection Using the Sphere Decoding Algorithm," *IEEE Journal of Solid-State Circuits*, vol. 40, no. 7, pp. 1566–1577, Jul. 2005.

[73] R. Blum, "MIMO Capacity with Interference," *IEEE Journal on Selected Areas in Communications*, vol. 21, no. 5, pp. 793–801, Jun. 2003.

[74] J. G. Andrews, W. Choi, and R. W. Heath Jr., "Overcoming Interference in Spatial Multiplexing MIMO Cellular Networks," *IEEE Wireless Communications Magazine*, vol. 14, no. 6, pp. 95–104, Dec. 2007.

[75] A. Alshamali and B. Quza, "Spatial modulation: Performance Evaluation in Nakagami Fading Channels," in *5th IEEE GCC Conf. Exhibition*, Mar. 2009, pp. 1 – 4.

[76] R. Mesleh, H. Haas, C. W. Ahn, and S. Yun, "Spatial Modulation – A New Low Complexity Spectral Efficiency Enhancing Technique," in *IEEE International Conference on Communication and Networking in China (CHINACOM)*, Beijing, China, Oct. 25–27, 2006, pp. 1–5.

[77] ——, "Spatial Modulation – OFDM," in *Proc. of the International OFDM Workshop*, Hamburg, Germany, Aug. 30–31, 2006.

[78] T. Fath, H. Haas, Marco Di Renzo, and R. Mesleh, "Spatial Modulation Applied to Optical Wireless Communications in Indoor LOS Environments," in *IEEE Proc. of the Global Commun. Conf. (GLOBECOM)*, Houston, Texas, USA, 5–9 Dec. 2011, pp. 1–5, 5 pages.

[79] T. Fath and H. Haas, "Performance Comparison of MIMO Techniques for Optical Wireless Communications in Indoor Environments," vol. PP, no. 99, 2012.

[80] R. Mesleh, H. Haas, Y. Lee, and S. Yun, "Interchannel Interference Avoidance in MIMO Transmission by Exploiting Spatial Information," in *Proc. of the 16th IEEE Int. Symp. on Personal, Indoor and Mobile Radio Commun. (PIMRC)*, vol. 1, Berlin, Germany, 11-14 Sep. 2005, pp. 141–145.

[81] R. Mesleh, H. Elgala, and H. Haas, "Optical Spatial Modulation," *IEEE/OSA J. Opt. Commun. Netw.*, vol. 3, no. 3, pp. 234–244, Mar. 2011, ISSN: 1943-0620.

[82] R. Abualhiga and H. Haas, "Subcarrier-Index Modulation OFDM," in *Proc. of the International Symposium on Personal, Indoor and Mobile Radio Communications (PIMRC)*, Tokyo, Japan, Sep. 13–16, 2009.

[83] T. Jiang and Y. Wu, "An Overview: Peak-to-Average Power Ratio Reduction Techniques for OFDM Signals," *IEEE Transactions on Broadcasting*, vol. 54, no. 2, pp. 257–268, Jun. 2008.

[84] F. Xiong, *Digital Modulation Techniques*, 2nd ed.   Artech House Publishers, 2006.

[85] M.-S. Alouini and A. Goldsmith, "A Unified Approach for Calculating Error Rates Of Linearly Modulated Signals over Generalized Fading Channels," *IEEE Trans. on Commun.*, vol. 47, no. 9, pp. 1324–1334, 1999.

[86] R. J. Green, H. Joshi, M. D. Higgins, and M. S. Leeson, "Recent Developments in Indoor Optical Wireless," *IET Communications*, vol. 2, no. 1, pp. 3–10, Jan. 2008.

[87] N. Fernando, Y. Hong, and E. Viterbo, "Flip-OFDM for Optical Wireless Communications," in *Information Theory Workshop (ITW)*, IEEE.   Paraty, Brazil: IEEE, Oct., 16–20 2011, pp. 5–9.

[88] ——, "Flip-OFDM for Unipolar Communication Systems," *IEEE Transactions on Communications*, vol. 60, no. 12, pp. 3726–3733, Dec. 2012.

249

[89] K. Asadzadeh, A. Dabbo, and S. Hranilovic, "Receiver Design for Asymmetrically Clipped Optical OFDM," in *GLOBECOM Workshops (GC Wkshps)*.   Houston, TX, USA: IEEE, Dec., 5–9 2011, pp. 777–781.

[90] S. Dimitrov, S. Sinanovic, and H. Haas, "A Comparison of OFDM-based Modulation Schemes for OWC with Clipping Distortion," in *GLOBECOM Workshops (GC Wkshps)*, Houston, Texas, USA, 5–9 Dec. 2011.

[91] S. Dissanayake, K. Panta, and J. Armstrong, "A Novel Technique to Simultaneously Transmit ACO-OFDM and DCO-OFDM in IM/DD Systems," in *IEEE GLOBECOM Workshops (GC Wkshps)*.   Houston, TX, USA: IEEE, Dec. 5–9 2011, pp. 782–786.

[92] S. Dimitrov and H. Haas, "On the Capacity of OFDM-based Optical Wireless Communication Systems with Non-linear Distortion," *J. Lightw. Technol.*, 2012, submitted.

[93] J. G. Proakis, *Digital Communications*, 4th ed.   New York, NY, USA: McGraw–Hill, 2000.

[94] ITU-T, "Forward Error Correction for High Bit-rate DWDM Submarine Systems," ITU, Tech. Rep. ITU-T G.975.1, Retrieved Nov. 19, 2013 from http://www.itu.int/rec/T-REC-G.975.1-200402-I/en, 2004.

[95] S. Dimitrov and H. Haas, "Information rate of OFDM-based optical wireless communication systems with nonlinear distortion," *J. Lightw. Technol.*, vol. 31, no. 6, pp. 918–929, Mar. 15 2013.

[96] A. Bahai, M. Singh, A. Goldsmith, and B. Saltzberg, "A New Approach for Evaluating Clipping Distortion in Multicarrier Systems," *IEEE Journal on Selected Areas in Communications*, vol. 20, no. 5, pp. 1037–1046, Jun. 2002.

[97] X. Li and J. Cimini, L.J., "Effects of Clipping and Filtering on the Performance of OFDM," *IEEE Communications Letters*, vol. 2, no. 5, pp. 131–133, May 1998.

[98] D. J. G. Mestdagh, P. Spruyt, and B. Biran, "Analysis of Clipping Effect in DMT-based ADSL Systems," in *Proc. IEEE International Conference on Communications ICC 1994*, vol. 1, New Orleans, LA, USA, 1–5 May 1994, pp. 293–300.

[99] B. Inan, S.C.J. Lee, S. Randel, I. Neokosmidis, A.M.J. Koonen and J.W. Walewski, "Impact of LED Nonlinearity on Discrete Multitone Modulation," *IEEE/OSA Journal of Optical Communications and Networking*, vol. 1, no. 5, pp. 439 –451, oct 2009.

[100] J. G. Proakis and D. K. Manolakis, *Digital Signal Processing: Principles, Algorithms and Application*, 4th ed., T. Robbins, Ed.   Prentice Hall, Apr. 2006.

[101] OSRAM GmbH, "Datasheet: OS-PCN-2008-002-A OSTAR LED," Retrieved from http://www.osram.de, Feb. 2008.

[102] Vishay Semiconductors, "Datasheet: BPV10 Silicon PIN Photodiode, RoHS Compliant," Retrieved Aug 01, 2012 from www.vishay.com/docs/81502/bpv10.pdf, Aug. 2012.

[103] F. Wu, C. Lin, C. Wei, C. Chen, Z. Chen, H. Huang, and S. Chi, "Performance comparison of OFDM signal and CAP signal over high capacity RGB-LED-based WDM visible light communication," *IEEE Photon. J.*, vol. 5, no. 4, p. 7901507, Aug. 2013.

[104] H. Chun, P. Manousiadis, S. Rajbhandari, D. Vithanage, G. Faulkner, D. Tsonev, J. McKendry, S. Videv, E. Xie, E. Gu, M. Dawson, H. Haas, G. Turnbull, I. Samuel, and D. O'Brien, "Visible Light Communication Using a Blue GaN LED and Fluorescent Polymer Color Converter," *IEEE Photon. Technol. Lett.*, vol. 26, no. 20, pp. 2035–2038, Oct. 15, 2014.

[105] A. Fasano, G. Di Blasio, E. Baccarelli, and M. Biagi, "Optimal Discrete Bit Loading For DMT Based Constrained Multicarrier Systems," in *Proceedings of the IEEE International Symposium on Information Theory*, 2002, p. 243.

[106] R. Sonalkar and R. Shively, "An Efficient Bit-loading Algorithm for DMT Applications," *IEEE Communications Letters*, vol. 4, no. 3, pp. 80–82, Mar. 2000.

[107] H. E. Levin, "A complete and optimal data allocation method for practical discrete multitone systems," in *Proc. IEEE Global Telecommun. Conf.*, vol. 1, San Antonio, TX , USA, 25–29 Nov. 2001, pp. 369–374.

[108] A. Fasano and G. Di Blasio, "Optimal Discrete Dynamic Loading Algorithms for Multicarrier Systems," in *Proceedings of the IEEE Workshop on Signal Processing Advances in Wireless Communications (SPAWC)*, Jun. 15–18 2003, pp. 373–377.

[109] J. Lee, R. Sonalkar, and J. Cioffi, "Multiuser Bit Loading for Multicarrier Systems," *IEEE Transactions on Communications*, vol. 54, no. 7, pp. 1170–1174, Jul. 17 2006.

[110] ITU-T, "Forward error correction for high bit-rate DWDM submarine systems," ITU, Tech. Rep. ITU-T G.975.1, Retrieved Nov. 19, 2013 from http://www.itu.int/rec/T-REC-G.975.1-200402-I/en, 2004.

[111] D. O'Brien, R. Turnbull, H. Le-Minh, G. Faulkner, O. Bouchet, P. Porcon, M. El Tabach, E. Gueutier, M. Wolf, L. Grobe, and J. Li, "High-speedpeed optical wireless demonstrators: conclusions and future directions," *J. Lightw. Technol.*, vol. 30, no. 13, pp. 2181–2187, Jul. 2012.

[112] H. Elgala, R. Mesleh, and H. Haas, "Non-linearity Effects and Predistortion in Optical OFDM Wireless Transmission Using LEDs," *Inderscience International Journal of Ultra Wideband Communications and Systems (IJUWBCS)*, vol. 1, no. 2, pp. 143–150, 2009.

[113] T. Kamalakis, J. Walewski, G. Ntogari, and G. Mileounis, "Empirical Volterra-Series Modeling of Commercial Light-Emitting Diodes," *J. Lightw. Technol.*, vol. 29, no. 14, pp. 2146–2155, Jul. 2011.

[114] K. Lee, H. Park, and J. Barry, "Indoor channel characteristics for visible light communications," *IEEE Communications Letters*, vol. 15, no. 2, pp. 217 – 219, Feb. 2011.